



**Study of the longitudinal and transverse cosmic ray
shower profiles at the Pierre Auger Observatory**

João Pedro Canhoto Espadanal

Supervisor: Doctor Mário João Martins Pimenta

**Thesis approved in public session to obtain the PhD Degree in
Physics**

Jury final classification: Pass with Distinction

Jury

Chairperson: Chairman of the IST Scientific Board

Members of the Committee:

Doctor Glennys Reynolds Farrar

Doctor Jorge Manuel Rodrigues Crispim Romão

Doctor Mário João Martins Pimenta

Doctor Jan Řídký

Doctor Sofia Andringa Dias

Doctor Patrícia Carla Serrano Gonçalves

2015

UNIVERSIDADE DE LISBOA
INSTITUTO SUPERIOR TÉCNICO

**Study of the longitudinal and transverse cosmic ray
shower profiles at the Pierre Auger Observatory**

João Pedro Canhoto Espadanal

Supervisor: Doctor Mário João Martins Pimenta

**Thesis approved in public session to obtain the PhD Degree in
Physics**

Jury final classification: Pass with Distinction

Jury

Chairperson: Chairman of the IST Scientific Board

Members of the Committee:

Doctor Glennys Reynolds Farrar, Professor, College of Arts and Science, New York University, United States of America.

Doctor Jorge Manuel Rodrigues Crispim Romão, Professor Catedrático do Instituto Superior Técnico, da Universidade de Lisboa.

Doctor Mário João Martins Pimenta, Professor Catedrático do Instituto Superior Técnico, da Universidade de Lisboa

Doctor Jan Řídký, Senior Researcher, Director of Institute of Physics, Academy of Sciences of the Czech Republic, Prague

Doctor Sofia Andringa Dias, Investigadora Principal do Laboratório de instrumentação e Física Experimental de Partículas, Lisboa

Doctor Patrícia Carla Serrano Gonçalves, Professora Auxiliar Convidada do Instituto Superior Técnico, da Universidade de Lisboa

Funding Institution:

Grant SFRH/BD/73202/2010
from FCT - Fundação para a Ciência e Tecnologia

To my Mother

Resumo

O Observatório Pierre Auger foi concebido para estudar os raios cósmicos acima de $10^{17.5}$ eV, através da análise de cascatas de partículas iniciadas quando o raio cósmico interage com a atmosfera. Auger é um detector híbrido que combina as duas técnicas de detecção de maior sucesso: detectores de superfície, que, usando tanques de Cherenkov; e detectores de fluorescência (FD), que colecta a luz de fluorescência emitida pelo azoto atmosférico, quando excitado pelas partículas secundárias do chuva. A construção do Observatório tem como aspiração, responder a várias incógnitas, como a origem, mecanismos de aceleração e propagação de raios cósmicos ao longo do universo, bem como a sua composição química e proporcionar uma janela única para o estudo das interações hadrónicas a altas energias (acima das obtidas nos aceleradores).

O objectivo desta tese foi construir ferramentas que permitam compreender melhor os dados e aumentar a sensibilidade tanto para a composição das partículas primária como para os modelos hadrónicos a alta energia usando o detector actual e o novo projeto MARTA, proposto para o Observatório Pierre Auger.

A simulação e reconstrução dos detectores de fluorescência em Auger, baseia-se numa análise unidimensional, usando parametrizações médias para recuperar a informação espacial. A primeira parte desta tese é desenvolver uma estrutura dedicada, que guarde a informação espacial das cascatas, ao nível do gerador e seja utilizada dentro da infraestrutura do Offline de Auger para simular os chuveiros. A fluorescência e o Cherenkov directo foram implementados e comparados com a simulação padrão. Esta estrutura de simulação pode ser aplicada em outros casos, como, obter o perfil de Cherenkov no solo.

Na superfície, os detectores medem as partículas electromagnéticas e muónicas simultaneamente. Actualmente, nos modelos, os muões não podem ser detectados directamente e os respectivos resultados não são consistentes com o sector electromagnético. Neste contexto, um novo detector dedicado a muões, como do projecto MARTA, é essencial para compreender as inconsistências.

MARTA permitiria recuperar o sinal electromagnético e muónico separadamente. Na tese, a energia do detector de superfície foi calibrada com a componente electromagnética, mostrando que para ângulos zenitais abaixo de $\sim 40^\circ$ a resolução conseguida é melhor ou da mesma ordem que a calibração actual com o sinal total. Assim, os muões podem ser medidos de forma quase independente da calibração de energia. Seguindo este raciocínio, um conjunto de detectores de muões abre várias possibilidades. A distribuição lateral média de muões pode ser construída e verificou-se, que os seus parâmetros de forma podem ser usados como estimador da composição e para restringir modelos hadrónicos. Além disso, a razão entre o parâmetro de tamanho do chuva, S_{1000} , no tanque, entre o sinal electromagnético e o sinal muónico pode ser utilizado para estimar o máximo do desenvolvimento electromagnético, acessível apenas no detector de fluorescência (em torno de 15% de todos os eventos).

Palavras-chave: Raios Cósmicos de altas energias; Observatório Pierre Auger; Simulação 3D da cascata de partículas; Emissões de luz de Fluorescência e Cherenkov directo; Calibração da energia nos detectores de superfície; Projecto MARTA; Distribuição Lateral Média nos detectores de superfície; Perfil Lateral Médio.

Abstract

The Pierre Auger Observatory has been conceived to study the cosmic rays above $10^{17.5}$ eV, through the analysis of the extensive air shower initiated by their interaction with the Earth's atmosphere. Auger is an hybrid detector that combines the two most successful detection techniques: a Surface Detectors, that sample the densities of particles at ground, using an array of Water-Cherenkov tanks (WCT); and a Fluorescence Detectors (FD), which collects fluorescence light emitted by atmospheric nitrogen, excited by the secondary charged particles in the shower. The Observatory construction has the aspiration to answer several unknowns, such as the origin, acceleration mechanisms and propagation of CRs throughout the universe, and their chemical composition. It also provides an unique window for the study of hadronic interactions at ultra high energies (above those achieved at man-made accelerators).

The objective of this thesis was to build tools that would allow to better understand the data and to increase the sensitivity both to the primary mass composition and to the high energy hadronic models using the current detector and the new MARTA project proposed for the Pierre Auger Observatory.

The Auger simulation and reconstruction of the Fluorescence Detectors is based on a one dimensional analysis, using average parametrizations to recover the spatial information. The first part of this thesis is to develop a framework that saves the spacial information at generator level and simulates it inside the Auger Offline framework. The fluorescence and direct Cherenkov light emissions were implemented and compared to the standard simulation. The framework could be applied to other purposes, such as to get the ground profile of Cherenkov light. On the surface, the detectors observe both electromagnetic and muonic particles. Currently, the muon content on the data is not directly accessible and the results are not consistent within the models, with the electromagnetic sector. In this context, a new dedicated muon detector is essential to disentangle the deviations, such as the one in the proposed MARTA project. MARTA would allow to recover the muonic and electromagnetic signal separately. In the thesis, the surface energy calibration were also performed with the electromagnetic component, showing that below $\sim 40^\circ$ the resolution achieved is better or at the same order as the current calibration with the total signal. So, the muon content can be measured almost independently from the energy calibration. Following this reasoning, a muon array opens several new possibilities. The average lateral distribution for muons could be built and it was shown that the shape parameters can be used as composition estimator and to constrain hadronic models. Moreover, the ratio between the tank electromagnetic and muonic signal, from the size parameter S_{1000} can be used to estimate the electromagnetic maximum, only accessible in the fluorescence detector (on around 15% of the events).

Keywords: Ultra High Energy Cosmic Rays; Pierre Auger Observatory; 3D Simulation of Extensive Air Showers; Fluorescence and Cherenkov light emissions; Surface Detectors Energy Calibration; MARTA project; average Lateral Distribution Function.

Acknowledgements

I would like to start by thanking to all people, who directly or indirectly, contributed for the elaboration of the work in my thesis and without whom it would have never been possible.

Obviously, I'm very grateful to my mother, who has always been there for me, no matter what. You have always help and support me, in all difficult and joyful situations. Thank you for being my mother.

To my grandmother, who passed away one and half years ago (I know she would like to be here for my thesis). I have to thank to João Franco, Lourdes and Ana Maria for all the help given to me and my mother, in the last 5 years, in so many occasions. Now, even more, for all the recent help to my mother and grandmother. I will be eternally in debt to you.

To Mario Pimenta, my supervisor, for all valuable help, all the support and beyond! I'm greatly indebted to Sofia Andriga, for helping me during this four years and for the advice and patience reviewing parts of the thesis. I would also thanks to Patrícia Gonçalves, specially on the 3D simulation work, to whom it would not been possible (particularly on CORSIKA). I would like to especially acknowledge Pedro Assis (with his fashionable haircut) and Ruben Conceição (with the English red face), for all the help and support writing scripts, Offline related problems and discussion about many problems. And also, for the extra time disposed for a coffee-break. To all my work colleagues, in particular Micael Oliveira, Lorenzo Cazon (sorry about the font size) and Fernando Barão for all discussions and coffee-breaks. Moreover, thanks to Bernardo Tomé, Catarina Espirito-Santo, Eva Santos, Francisco Diogo, Luís Mendes, Pedro Abreu, Raul Sarmiento and Rute Pedro (office partner and prima do Batalha!?). Thank you for your help solving daily problems, for your availability and for all coffee-breaks.

My deepest gratitude to my crazy family (especialy to Canhotos). A lot has happen during these last years. To Paula Canhoto and her young son António, whom I love, I hope you get better soon, so after my thesis defence and we could have more, special and funny, family moments. Like driving, out of Lisbon, without knowing the way, get lost at 1am around a police station and always return to the same position. To Zé, Patricia, Vanessa and especially to Tita Canhoto for always being there for us.

I'm owing a debt of gratitude to all my friends, which never have made me feel alone. To David Soares, Israel Gonçalves, Maria Fialho, Marcia Quaresma, Lenise Parreira, Ana Viegas e Pedro Caetano. Thank you for the support, endorsement, dinners and leisure nights to forget our problems. To my friends from Alentejo Ligia Silva, Rita Barradas and Nádia Cavaco. To David Soares, special thank you for being with me and support me for the last seven years.

I acknowledge the financial support given by the Portuguese Fundação para a Ciência e Tecnologia (FCT) under grant SFRH/BD/73202/2010. To LIP I wish to thank for providing the necessary conditions to develop the work presented in this thesis.

Contents

Resumo	vii
Abstract	ix
Acknowledgements	xi
Contents	xiii
List of Tables	xvii
List of Figures	xix
List of Abbreviations	xxv
1 Introduction	1
2 Ultra-High Energy Cosmic Ray physics	5
2.1 A short view through Cosmic Ray history	5
2.2 Cosmic Ray Radiation	13
2.2.1 Energy Spectrum	13
2.2.2 UHECR origin and acceleration	16
2.2.3 Cosmic Ray Propagation	20
2.3 Extensive Air Shower (EAS)	25
2.3.1 Electromagnetic Component	27
2.3.2 Hadronic Component	30
2.3.3 Muonic Component	38
2.3.4 Extensive Air Shower Simulations	39
2.4 Detection Techniques	40
2.4.1 Ground detection	41
2.4.2 EAS Light detection	43
3 The Pierre Auger Observatory	53
3.1 The surface array (SD)	54
3.1.1 Data acquisition and SD Calibration	55
3.1.2 SD Triggers	56
3.1.3 SD Reconstruction	59
3.2 The Fluorescence Detector (FD)	63
3.2.1 FD Calibration	65
3.2.2 Data acquisition and FD Trigger	67
3.2.3 FD Geometry Reconstruction	68
3.2.4 FD Energy Reconstruction	69
3.3 Hybrid Technique	74

3.3.1	HB Geometry Reconstruction	74
3.3.2	SD-FD Calibration	75
3.4	Atmospheric monitoring	76
3.5	Pierre Auger Enhancements	79
3.5.1	HEAT	79
3.5.2	AMIGA	80
3.5.3	R&D	80
3.6	<u>Offline</u> software framework	83
3.7	Latest results from the Pierre Auger Observatory	84
3.7.1	Energy Spectrum	84
3.7.2	Anisotropies and correlations	85
3.7.3	Mass composition	86
3.7.4	Multi-messenger information: photons and neutrinos	93
4	3D simulation of EAS for the FD	95
4.1	Framework and Method	96
4.1.1	CORSIKA Intervention	96
4.1.2	<u>Offline</u> Intervention	97
4.1.3	Validation strategy	102
4.2	Fluorescence Emission	104
4.2.1	CORSIKA and <u>Offline</u> Intervention	104
4.2.2	Validation	105
4.3	Cherenkov Emission	115
4.3.1	CORSIKA and <u>Offline</u> Intervention	115
4.3.2	Validation	118
4.3.3	Cherenkov Pool	127
4.4	Summary and prospects	133
5	Energy Calibration using WCT signals	137
5.1	Shower Size Determination	138
5.1.1	Fitting approach	138
5.1.2	LDF Parameterization	144
5.2	Energy Calibration	158
5.2.1	Intensities	158
5.2.2	Constant Intensity Cut (CIC)	160
5.2.3	Energy Estimator	167
5.3	Mixture Composition	178
5.4	Summary and prospects	183
6	Comparison between data and QGSJETII-04	185
6.1	Beta Parameter	185
6.2	CIC Function	188
6.3	Calibration Function	189
6.4	Summary and prospects	192
7	Studies with MARTA (Muon Auger RPC for the Tank Array)	197
7.1	MARTA project	198
7.1.1	MARTA design	198
7.1.2	MARTA studies	200
7.2	LDF's on MARTA	202

7.2.1	Fixed energy bin	205
7.2.2	Continuous energy bin	210
7.2.3	Applying the tank trigger	215
7.3	Perspective studies	219
7.3.1	Xmax reconstruction from signal fractions	219
7.3.2	MPD and L width	223
7.4	Summary and prospects	225
8	Summary and Conclusions	227
	Bibliography	231

List of Tables

3.1	Summary of the experimental parameters describing data SD energy calibration. . .	77
3.2	Parameters of the power law fit to the combined Auger spectrum	85
4.2	Reconstructed parameters of the fluorescence sample	112
4.3	Reconstructed parameters of the Cherenkov sample	123
5.1	LDF fit results from figure 5.1	139
5.2	Event cut efficiencies to fit the slope β	145
5.3	Parameters of the β parametrization with eq. 5.23	149
5.4	Fit parameters of eq. 5.33 to CIC with 170 intensity events	164
5.5	Fit parameters of eq. 5.33 for the average CIC	166
5.6	Parameters from the energy Calibration of the S_{38} to eq. 5.35	169
5.7	RMS of $(E_{SD} - E_{MC})/E_{MC}$ in four bins of zenith angle, for the three signal components and both samples	178
5.8	Fit parameters of eq. 5.33 for the average CIC of the 50% proton 50% iron composition	179
5.9	Parameters from the energy Calibration of the S_{38} to eq. 5.35	180
6.1	Parameters from the β dependence with eq. 6.1 in the simulations and data	187
6.2	Parameters from the CIC in eq. 6.2 to the simulation samples and data	189
6.3	Parameters from the total signal energy calibration, on the simulations and data . .	190
6.4	Parameters from the muonic signal energy calibration, on the simulations and data .	192
7.1	Parameters separation (according to eq. 7.2) from proton and iron, for the samples with energy and zenith (θ) fixed	207
7.2	Parameters separation (according to eq. 7.2) between EPOS-LHC and QGSJET-II.04 .	210
7.3	Parameters separation (according to eq. 7.2) between proton and iron, for the samples with the continue energy and zenith (θ)	211
7.4	X_{max} reconstruction parameters from eq. 7.3	221

List of Figures

2.1	A. Bennet and T. Wulf electroscopes	7
2.2	Photograph of Hess balloon flight and Kolhörster balloon flight	8
2.3	Air ionization with altitude from Hess and Kolhörste measurements	9
2.4	Cosmic ray coincidence rate from Kolhörster and Auger and Bothe and Kolhörster coincidence experiment	10
2.5	Positron in the cloud chamber photograph by C. D. Anderson; and pion and kaon decays from Powell	11
2.6	Cosmic ray spectrum, from solar cosmic rays up to the GZK cut-off	14
2.7	KASCADE-Grande spectrum and mean logarithmic mass for several experiments . .	15
2.8	Fermi’s acceleration mechanism	19
2.9	Hillas diagram	20
2.10	Cosmic rays propagation in the extraterrestrial magnetic fields	21
2.11	Energy loss length for protons and other nuclei	24
2.12	Proton propagation above the GZK cut-off and attenuation length for high energy photons	25
2.13	Schematic view of an Extensive Air Shower (Extensive Air Shower (EAS)).	26
2.14	Energy flow in an EAS development	27
2.15	Heitler model	28
2.16	Elongation rate curves for several models and compositions	29
2.17	Modified Heitler model for proton showers	31
2.18	Normal longitudinal profile and USP	33
2.19	L and R parameters in the USP	34
2.20	Particle density at the ground for low energy models	36
2.21	Predictions from the high energy hadronic models	38
2.22	Impact of hadronic interaction features on the shower maximum, X_{max}	39
2.23	Draft of the detection techniques.	41
2.24	Ground array scheme with a detected event; and scheme of several showers fronts. .	42
2.25	Fluorescence spectrum of the atmospheric nitrogen; and fraction of the missing energy (in %) in a EAS.	44
2.26	Fluorescence yield	45
2.27	Cherenkov emission scheme	46
2.28	Schematic representation of the image of a detection of a shower in a FD telescope. .	49
3.1	Layout of the Pierre Auger Observatory	54
3.2	Photograph and layout of a SD stations	55
3.3	VEM charge and current; VEM and muon tracklength	56
3.4	Schematics trigger system of the Auger surface detector	57
3.5	The T3 triggers modes	58
3.6	Minimal SD T4 configurations	59

3.7	SD Trigger Efficiency	60
3.8	Plane and spherical shower front and variables definition	61
3.9	Optimum distance for the SD energy estimator	62
3.10	Example on a SD event	62
3.11	FD building layout	63
3.12	Picture and layout of the telescopes	64
3.13	Camera and pixels photograph and layout	65
3.14	Drum and telescope calibrations scheme	66
3.15	Drum FD response	66
3.16	FD site scheme readout and the SLT trigger layout	68
3.17	shower geometry scheme and geometric time fit	69
3.18	Direct and scattered, fluorescence and Cherenkov light geometry	71
3.19	Real event seen by FD detectors	73
3.20	Missing energy correction for the FD	74
3.21	Angular and R_p resolutions for Hybrid and monocular reconstruction	75
3.22	Uptime fraction with the FD	76
3.23	Calibration for the different SD energy estimators	77
3.24	HEAT schematic view and event from HEAT and Coihueco together	80
3.25	HEAT and AMIGA map, AERA antenna and AERA event	81
3.26	EASIER, AMBER and MIDAS photograph; and EASIER event	82
3.27	General structure of the <u>Offline</u> framework and hierarchy registry of managers	83
3.28	Recent Cosmic Ray spectrum	84
3.29	Equatorial dipole amplitude and First harmonic phase	85
3.30	Average $\langle X_{max} \rangle$	87
3.31	X_{max} fluctuations	88
3.32	Average of the logarithmic mass, $\langle \ln A \rangle$, and $V(\ln A)$ from X_{max}	89
3.33	Proton-air and p-p cross-section	90
3.34	MPD geometry and average $\langle X_{max}^\mu \rangle$	90
3.35	Muon content of Auger data	91
3.36	The logarithmic mass $\langle \ln A \rangle$ from $\langle X_{max}^\mu \rangle$ and $\langle X_{max} \rangle$	92
3.37	Upper limits on the photon and neutrino fluxes	94
4.1	The BinTheSky framework data flow and representation	96
4.2	Depth variation per height bin of 100 m	97
4.3	Standard and 3D simulations light emission	99
4.4	Standard and 3D simulations photon times	100
4.5	Analysis procedure scheme and light components by geometry scheme	103
4.6	Fluorescence simulation sample: Cherenkov fraction; distance core-eye; $X_{max}^{data} - X_{max}^{Gen}$	106
4.7	Azimuthal and zenith reconstruction for fluorescence emission	107
4.8	Photons at the diaphragm	108
4.9	Photons at the diaphragm (including scattered Cherenkov)	108
4.10	Reconstructed energy of the fluorescence sample	109
4.11	dE/dX_{max} distribution for the fluorescence sample	109
4.12	Reconstructed X_{max} of the fluorescence sample	110
4.13	USP of the fluorescence sample	111
4.14	Energy vs X_{max} and L distribution	111
4.15	ζ and ξ definitions	112
4.16	Light profile as function of ζ	113
4.17	Light profile as function of ξ	114
4.18	Zeta Optimum from the reconstruction, for the fluorescence sample	114

4.19	Cherenkov angular α and ϕ' definitions	115
4.20	Cherenkov information saved in the SkyBins	116
4.21	Cherenkov simulation sample: Cherenkov fraction; distance core-eye; $X_{max}^{data} - X_{max}^{Gen}$	118
4.22	Geometry reconstruction for events with Cherenkov emission	119
4.23	Photons at the diaphragm for the Cherenkov sample	120
4.24	Photons at the diaphragm, in α_{sh} , for the Cherenkov sample and $\langle \alpha_{sh} \rangle$	121
4.25	Reconstructed energy of the Cherenkov sample	122
4.26	dE/dX_{max} distribution for the Cherenkov sample	122
4.27	X_{max} distributions for the Cherenkov sample	123
4.28	USP of the Cherenkov sample	124
4.29	Energy vs X_{max} and reconstructed energy vs true energy, for the Cherenkov sample	124
4.30	L distributions for the Cherenkov sample	125
4.31	Light profile as function of ζ , for the Cherenkov sample	125
4.32	Light profile as function of ξ , for the Cherenkov sample	126
4.33	Zeta Optimum from the reconstruction, for the Cherenkov sample	126
4.34	Cherenkov photon density arriving on the ground	127
4.35	Cherenkov photon density arriving on the ground for HEAT and normal telescopes Field Of View (FOV)	128
4.36	Cherenkov photons density for an event with 10^{18} eV	129
4.37	Cherenkov photons densities for several energies	130
4.38	Cherenkov lateral profile for the 3D and KG simulations	131
4.39	Cherenkov lateral profile for Tunka and respective 3D and KG simulations	132
4.40	Cherenkov lateral profile at Chacaltaya and respective 3D and KG simulations	132
5.1	Example of two LDF events with fits to Total, EM and MU signals	139
5.2	Tank signal uncertainty, $\sigma/Signal = f_S(\theta)$	140
5.3	The $p_S(\theta)$ function	142
5.4	LDF β evolution with $\log_{10}(S_{1000})$ and $\sec \theta$, for the total, electromagnetic and muonic signals	147
5.5	LDF β evolution with $\log_{10}(S_{1000})$ and $\sec \theta$, for the total, electromagnetic and muonic signals, for the iron sample	148
5.6	$\beta_i - \beta_{model}/\beta_i$ distribution for proton and iron	149
5.7	β dependence as function of $\log_{10}(S_{1000})$, for 1st and 2nd $\sec \theta$ bin	150
5.8	$\sigma_{S_{1000}}/S_{1000}$ as function of $\log_{10}(S_{1000})$ for the total component	151
5.9	$RMS(S_{1000}/Energy)/\langle S_{1000}/Energy \rangle$ for the total, electromagnetic and muonic signals, for the proton and iron samples	152
5.10	LDF β for the total signal, for proton and iron samples	153
5.11	LDF β for the electromagnetic signal, for proton and iron samples	154
5.12	LDF β for the muonic signal, for proton and iron samples	155
5.13	LDF β for the total, electromagnetic and muonic signals, in the proton sample	156
5.14	LDF β for the total, electromagnetic and muonic signals, in the iron sample	157
5.15	Cosmic rays frequency with zenithal angle	159
5.16	Event frequency on samples, in azimuthal and zenith angle	159
5.17	Intensity I plots, for all signals, in the proton and iron samples	161
5.18	Attenuation curves CIC for the total, electromagnetic and muonic signals, in the proton and iron samples	163
5.19	Normalized intensity CIC curves for the three signals components	165
5.20	$\sigma_{syst, S_{38}}/S_{38}$ as function of $\cos^2(\theta)$ on the total signal	166
5.21	EM and MU signal ratios at 1000 m	167
5.22	Energy calibration of the S_{38} estimator	168

5.23	Energy resolution with the distribution of $(E_{MC} - E_{SD})/E_{MC}$	170
5.24	Distribution of $P = \frac{E_{MC} - E_{SD}}{\sqrt{\sigma_{E_{SD}}^2 + \sigma_{E_{FD}}^2}}$	171
5.25	Error components on the reconstructed energy E_{SD} evolution with energy	172
5.26	Error components on the reconstructed energy E_{SD} evolution with zenith angle	173
5.27	$(E_{MC} - E_{SD})/E_{MC}$ evolution with energy	174
5.28	$(E_{MC} - E_{SD})/E_{MC}$ evolution with $\cos^2(\theta)$	175
5.29	Distribution of $(E_{MC} - E_{SD})/E_{MC}$ for the proton and iron samples with $\theta = 0^\circ - 29.9^\circ$	176
5.30	Distribution of $(E_{MC} - E_{SD})/E_{MC}$ for the proton and iron samples with $\theta = 48^\circ - 60^\circ$	177
5.31	RMS of $(E_{SD} - E_{MC})/E_{MC}$ in four bins of zenith angle	177
5.32	Attenuation curves CIC for the total, electromagnetic and muonic signals, in the 50% proton/iron samples	179
5.33	Energy calibration of the S_{38} estimator for the 50% proton/iron sample	180
5.34	Distribution of $(E_{MC} - E_{SD})/E_{MC}$ and $P = \frac{E_{MC} - E_{SD}}{\sqrt{\sigma_{E_{SD}}^2 + \sigma_{E_{FD}}^2}}$ for the mixture composition sample	181
5.35	Distribution of $(E_{MC} - E_{SD})/E_{MC}$ the 50% proton/iron sample, discriminating the proton and iron events	182
6.1	LDF β dependence with $\log_{10}(S_{1000})$ and $\sec\theta$ for the proton and iron samples	186
6.2	LDF β dependence with $\log_{10}(S_{1000})$ and $\sec\theta$ in the data	186
6.3	LDF β for proton and iron with $\sec\theta \in 1-1.1$ and $\sec\theta \in 1.9-2.0$	188
6.4	CIC curves for proton and iron samples and data	189
6.5	S_{38} energy calibration for the total signal on the simulations and data	190
6.6	S_{38} energy calibration for the muonic signal compared to the measured muons	191
6.7	LDF β evolution with $\log_{10}(S_{1000})$ and $\sec\theta$, for the total signal in the simulations and data	194
6.8	LDF β evolution with $\log_{10}(S_{1000})$ and $\sec\theta$, for the three signals in the proton simulations and data	195
6.9	LDF β evolution with $\log_{10}(S_{1000})$ and $\sec\theta$, for the three signals in the iron simulations and data	196
7.1	MARTA baseline configuration and RPC scheme	199
7.2	Slant mass over RPC and Electromagnetic over muonic ratio on the RPCs	200
7.3	Tank signal for atmospheric muons, with different cuts and Tyvek reflectivities	201
7.4	Combined fit for the tank and MARTA	201
7.5	Average lateral profile on MARTA	203
7.6	Toy model: LDF and residuals	203
7.7	Toy model for fitting the β and ρ_{1000} parameters	204
7.8	Average lateral profile on MARTA and fit to the average proton profile with 38° and 10^{19} eV	205
7.9	β parameter for fixed energy and angle	206
7.10	ρ_{1000} and β parameters for several primaries	206
7.11	$\langle N_\mu \rangle$ and $\langle X_{max} \rangle$ vs β parameter for fixed energy and angle	208
7.12	ρ_{1000} and β parameter for several primaries, for QGSJET-II.04 and EPOS-LHC models	209
7.13	β parameter for continuous energy and angle intervals	211
7.14	ρ_{1000} and β parameters for several primaries, for continuous energy and angle intervals	212
7.15	$\langle X_{max} \rangle$ vs β parameter for several primaries, for continuous energy and angle intervals	213
7.16	$\langle N_\mu \rangle$ and β parameter for several primaries, for continuous energy and angle intervals	214

7.17	Average $\langle LDF \rangle$ of the RPC densities hits on the MARTA stations	216
7.18	β evolution with energy and zenith angle, with and without silent stations	217
7.19	β with and without silent stations as function of the β including all stations	217
7.20	Average $\langle LDF \rangle$ of the Surface Detectors (SD) tank signals	218
7.21	β evolution with energy and zenith angle, with and without silent stations on tanks	219
7.22	β with and without silent stations as function of the β including all stations, on the tanks	219
7.23	X_{max} as function of $S_{1000,em}/S_{1000,\mu}$	220
7.24	Parameters b and m to the X_{max} reconstruction	221
7.25	$X_{max}^{MC} - X_{max}^{rec}$ resolution, for the iron and proton sample	222
7.26	X_{max} as function of $S_{1000,em}/S_{1000,\mu}$, for the mixture sample with 50% proton, 50% iron	222
7.27	X_{max} and X_{max}^{μ} results	223
7.28	$\langle X_{max} \rangle - \langle X_{max}^{\mu} \rangle$ and L parameter	224
7.29	$\langle X_{max}^{\mu,app} \rangle$ and $\langle X_{max} \rangle - \langle X_{max}^{\mu,app} \rangle$	225

List of Abbreviations

- ACR** Anomalous cosmic rays. 13
- ADC** Analog Digital Converter. 55
- AERA** Auger Engineering Radio Array. 51, 80
- AGASA** Akeno Giant Air Shower Array. 12, 43, 84, 93
- AGN** Active Galactic Nuclei. 17, 19, 85
- AIRES** AIRshower Extended Simulations. 39, 83, 95
- AIRFLY** AIR FLuorescence Yield. 45, 104
- AMBER** Air-shower Microwave Bremsstrahlung Experimental Radiometer. 51, 81
- AMIGA** Auger Muons and Infill for the Ground Array. 43, 80
- APF** Aerosol Phase Function. 78
- CDAS** Central Data Acquisition System. 54, 55
- CERN** European Organization for Nuclear Research (a particle physics laboratory in Geneva, Switzerland). 1
- CIC** Constant Intensity Cut. 76, 138, 150, 158, 160, 164, 178, 183, 185, 188, 228
- CLF** Central Laser Facility. 53, 77
- CMB** Cosmic Microwave Background Radiation. 21–24
- CODALEMA** COsmic ray Detection Array with Logarithmic ElectroMagnetic Antennas. 51
- CORSIKA** COsmic Ray SIMulations for KAscade. 39, 83, 95, 96, 99, 102, 104, 106, 115, 118, 129, 133, 207
- CR** Cosmic Ray. 1, 2, 13, 15, 17, 22, 40, 41, 60, 69, 89, 159, 160
- CROME** Cosmic Ray Observation via Microwave Emission. 51
- CTA** Cherenkov Telescope Array. 50
- DAQ** Data Acquisition. 67
- DPM** Dual Parton Model. 37

EAS Extensive Air Shower. xix, 1, 3, 25, 26, 41, 95, 96, 131

EASIER Extensive Air Shower Identification using Electron Radiometers. 51, 82

EM Electromagnetic signal component. 137, 228

Epos Energy conserving quantum mechanical multiple scattering approach, based on Partons, Off-shell remnants and Splitting of partons ladders. 37, 88, 90, 209, 225, 229

FADC Flash Analog to Digital Converter. 55

FD Fluorescence Detectors. 2, 3, 49, 53, 63, 95, 228

FLUKA FLUktuierende KAskade (German for fluctuating cascade). 35

FLY Fluorescence Light Yield. 44

FOV Field Of View. xxi, 63, 108, 127–129, 131, 135

FPGA Field-Programmable Gate Array. 67

FRAM The Photometric Robotic Atmospheric Monitor. 79

GCR Galactic Cosmic Rays. 13

GHEISHA Gamma-Hadron-Electron-Interaction SH(A)ower code. 35

GPS Global Positioning System. 54, 67

GZK Greisen-Zatsepin-Kuzmin. 2, 16, 22–24, 84, 94

HAM Horizontal Attenuation Monitors. 78

HAWC the High-Altitude Water Cherenkov Observatory. 43

HEAT High Elevation Auger Telescope. 79, 127

HESS High Energy Stereoscopic System. 50

HiRes High Resolution Fly’s Eye detector. 12, 15, 50, 84, 86, 88

ICS Inverse Compton Scattering. 24

IR Infra-Red radiation. 22

KASCADE KARlsruhe Shower Core and Array DETector. 14, 15, 43, 51, 84

LDF Lateral Distribution Function. 2, 61, 75, 101, 138, 145, 158, 164, 183, 185, 198, 202, 205, 210, 215, 225

LHC Large Hadron Collider. 1, 12, 53

LIDAR Light Detection And Ranging. 78

LOFAR Low Frequency ARray. 51

LOPES LOFAR Prototype Station. 51

LPM Landau-Pomeranchuk-Migdal effect. 29

MACFLY Measurement of Air Cherenkov and Fluorescence Light Yield. 45

MAGIC Major Atmospheric Gamma-ray Imaging Cherenkov. 50

MARTA Muon Auger RPC for the Tank Array. 2, 3, 79, 80, 197, 198, 202, 225

MC Monte Carlo. 39

MIDAS MICrowave Detection of Air Showers. 51, 81

MPD Muon Production Depth. 89, 197, 223

MU Muonic signal component. 137, 228

NKG Nishimura, Kamata and Greisen equation. 30, 35, 138, 202, 207

Opt Optical radiation. 22

PMT Photomultiplier Tube. 54, 55

QCD Quantum Chromodynamics. 36

QGSJet Quark Gluon String Model with mini-Jet. 36, 37, 77, 88, 91, 138, 185, 205, 209, 225, 229

RFT Gribov's Reggeon Field Theory. 36

RHIC Relativistic Heavy Ion Collider (at BNL). 37

RPC Resistive Plate Chambers. 79, 198, 199

SD Surface Detectors. xxiii, 1–3, 41, 53–55, 61, 137, 145, 183, 198, 200, 202, 204, 215, 217–220, 225, 228

SDP Shower Detector Plane. 68

SEP solar energetic particles. 13

SNRs Supernova Remnants. 13

SOPHIA Simulations Of Photo Hadronic Interactions in Astrophysics. 25

SUGAR The Sydney University array. 43

TA Telescope Array. 12, 43, 50, 84, 86, 88, 89, 93

TOT Total signal component. 137

TOTEM TOTAl Elastic and diffractive cross section Measurement. 37

UHE Ultra High Energy. 1, 131, 197, 221

UHECR Ultra High Energy Cosmic Rays. 1, 12, 13, 16, 36, 41, 53

URB Cosmic Universal Radio Radiation. 23

UrQMD Ultra-relativistic Quantum Molecular Dynamics model. 35

USP Universal Shower Profile. 34

UV Ultra-Violet radiation. 22

VCV Véron-Cetty and Véron catalogue. 85

VEM Vertical Equivalent Muon. 55

VERITAS Very Energetic Radiation Imaging Telescope Array System. 50

WCD Water Cherenkov detector. 42, 54, 55

WCT Water-Cherenkov tanks. 2, 137, 139, 140

XLF Extreme Laser Facility. 53, 77

XML eXtensible Markup Language. 83

Introduction

Our planet is constantly hit by extraterrestrial particles called Cosmic Rays (CRs). They consist in charged particles, such as ionized nuclei, protons and electrons and other particles like gammas and neutrinos. Their secondary particles arrive on the Earth surface, as a natural radiation which is on average about 0.4 mSv (average annual effective dose) of the total 2.4 mSv , environment radiation.

One century ago, at the turn of the 20th century, following a series of technological developments, the cosmic rays were discovered. In this new field, several elementary particles were discovered, such as positrons (e^+), muons (μ^-) and pions (π), which became known as the birth of elementary particle physics. After almost 100 years of studies, the cosmic ray spectrum spans over 11 orders of magnitude, from the GeV solar cosmic rays up to the Ultra High Energy Cosmic Rays (UHECR) with energies above 10^{20} eV .

The flux of CR decreases rapidly with increasing energy (by a power law). At lowest energies, cosmic rays can be detected directly in satellites, however at Ultra High Energy (UHE), they are expected with a rate of about 1 particle per century and square kilometer. With such small fluxes, huge detection areas are needed, so the atmosphere is used as the detector. Cosmic rays collide with atmospheric nuclei, producing new particles, these secondaries undergo the same process, eventually producing millions of particles that propagate through the atmosphere and reach the Earth surface, in the process known as Extensive Air Shower (EAS). These extremely rare events are only detectable indirectly through EAS. Studies try to extract information of the primaries from the analysis of the showers properties, which may vary depending on the nature and the energy of the primary particle inducing it. The Pierre Auger Observatory[1] is an experiment dedicated to the cosmic ray studies.

The technical challenge inherent to their detection makes the origin, acceleration mechanisms and propagation of CRs throughout the universe, chemical composition of UHECR, and of course, the study of hadronic interactions at ultra high energies, relatively unknown. At present, the man-made accelerators, namely the Large Hadron Collider (LHC) at CERN, allow to test the Standard Model (SM) at energies around 14 TeV. If one wants to explore the physics above those achieved at accelerators, only CRs are available and any increase in the knowledge of UHECR, directly influences particle physics. A curious fact, is that around 0.12 Higgs bosons per second are produced in the entire atmosphere[2], still ahead of the 2012 LHC running. However, their detection are not currently achievable on EAS experiments.

The Pierre Auger Observatory[1], covering more than 3000 km^2 , has been conceived to study the properties of cosmic rays in the end of the spectrum (with energies above $10^{17.5} \text{ eV}$). It uses a two of the most successful detection techniques (in an hybrid mode): a Surface Detectors

(SD), that samples the densities of particles on ground, using an array of Water-Cherenkov tanks (WCT); and a Fluorescence Detectors (FD), which collects the fluorescence light emitted by atmospheric nitrogen, excited by the secondary charged particles in the shower. The Pierre Auger Observatory collaboration performs many different physics analyses with the gathered data, with puzzling results. There are no clear evidence of anisotropies in the arrival direction in the sky, but there are indications of a dipole on the sky directions. The measurements of the upper-end of the energy spectrum could come from the Greisen-Zatsepin-Kuzmin (GZK) effect or source exhaustion. The cosmic rays mass composition seems to become heavier, however the electromagnetic and muonic components are not consistent, considering the existing models. Moreover, upper limits on the cosmic-ray photon and neutrino fluxes were derived and the proton-air cross-section was estimated at 57 TeV.

The Auger FD simulation and reconstruction, is currently based in one dimensional analysis along the longitudinal profiles. Nonetheless, the lateral width and the length from the time structure of the showers are lost in the analysis. A three dimensional reconstruction could be important to analyse the real 3D fluctuations in a shower. To perform a 3D reconstruction, it is necessary to simulate the shower anatomy on the atmosphere and not use average parametrization of the lateral profiles on the telescopes. To this aim a 3D simulation should be built to calculate the fluorescence and Cherenkov emission accordingly to the spacial information on the generator programs.

Moreover, the events rich in Cherenkov are very problematic, since the geometric reconstruction is worst (they have a high intensity light profile within a smaller detection time) and also, the fluorescence is much smaller than the Cherenkov. Both factors together make the energy reconstruction more difficult and less reliable, not being used in standard analysis. But, with the new telescope extension, HEAT (with a field of view more vertical), more Cherenkov rich events are measured. In this quadrature, a 3D simulation/reconstruction is expected to improve the analysis of these events and provides a possibility to increase the used statistics.

The FD can detect the electromagnetic lateral profile, which eventually can arrive on the ground. There, at the surface, the SD samples the Lateral Distribution Function (LDF), including the muonic component. The SD lateral signal includes both components together, but indirect techniques allow to obtain the muon content (with much less statistics than the standard SD). Those measurements seem quite enigmatic. The muon number is much higher than expected by the models and the interpretation of the maximum of the longitudinal muonic profile (X_{max}^μ) is not in agreement with the electromagnetic maximum (X_{max}) within each hadronic model. With this scenario it seems important to have a new muon purpose detector array, such as the Muon Auger RPC for the Tank Array (MARTA). This project would allow to detect the muons directly and the muonic/electromagnetic signal on the standard tank could be disentangled. Notice that, the SD energy calibration uses the total signal, and that signal is also used to obtain the muon content. Then they are correlated, but the muon content is much higher than expected by the models and the muonic sector interpretation is more difficult. An array similar to MARTA would allow to calibrate the SD energy using only the electromagnetic component, while measuring the muon content, with better systematic control than the current array. Such upgrades would also allow to perform other new analyses. The average lateral muonic profile could be built, and the shape parameter used to constrain the CR composition and eventually constrain the models. By having determined the muonic and electromagnetic fraction, it would be possible to determine the electromagnetic X_{max} together with the FD. This method would allow to dramatically increase the statistics and reach higher energies. It would give a resolution of at least $\sim 45 \text{ g/cm}^2$, comparable to the resolution in the muon sector.

This thesis is organized as follows:

Chapter 2 gives an overview of cosmic rays physics (section 2.2), the Extensive Air Showers (EAS) are defined and the detection techniques described (in section 2.3 and 2.4).

In chapter 3, the Observatory instruments, techniques and reconstructions of the showers are described. The Surface Detectors and Fluorescence Detectors are specified in sections 3.1 and 3.2 respectively. The Observatory enhancements are shown on section 3.5. Finally, the most recent results on cosmic rays are enumerated and described in section 3.7.

The 3D simulation framework is reported and discussed in chapter 4. The CORSIKA and Offline interventions are carefully described and the validation strategy shown in the section 4.1. The Fluorescence emissions and direct Cherenkov emissions implementation in Offline are shown with the validation in sections 4.2 and 4.3 respectively. The direct Cherenkov pool on the ground is also determined in section 4.3.3.

The SD energy calibration using the total, the electromagnetic and the muonic signals of SD separately, are performed in chapter 5. The calibration is done using the constant intensity cut (CIC) method. The LDF is fitted with a likelihood in which the parameter β can be parametrized to minimize the fluctuations in the size parameter S_{1000} (section 5.1). The $S_{1000}(\theta)$ attenuation curves are obtained using the CIC method and the S_{38} calculated. Then, this electromagnetic S_{38} is used as the energy estimator and calibrated with the MC energy (section 5.2). The same procedure is repeated for the total and for the muonic signal. The method is also applied to a sample with 50% proton/ 50% iron (section 5.3).

In chapter 6, the β parametrization, CIC and S_{38} energy calibration, for the total signal are compared to the simulations. The muonic S_{38} energy calibration is also compared with data.

In the chapter 7, the project MARTA is briefly described together with some prominent analysis. The slope parameter β and size parameter ρ_{1000} of the average LDF's are studied as a possible composition estimator (section 7.2). It is shown that the electromagnetic X_{max} can be obtained from a combination between the muonic and electromagnetic signals (section 7.3.1). And, a potential analysis for studying the hadronic models consistency between muonic and electromagnetic sector using MARTA array (section 7.3.2) is explained.

Finally, some conclusions are drawn in chapter 8.

Ultra-High Energy Cosmic Ray physics

The Ultra-High Energy Cosmic Rays are the most energetic particles known up to now. This chapter is a small review about the physics of these cosmic rays. The physics of these particles will be reviewed, such as their origin, acceleration and propagation in the universe (section 2.2) and their interaction in the atmosphere (section 2.3), as well as, a description on the detection techniques (section 2.4). The most recent results will be presented in the next chapter, together with the description of the Pierre Auger Observatory[1] (Chapter 3).

The "Cosmic Ray" terminology is somewhat misleading, since it is a radiation that consists mainly of ionized atomic nuclei. The term was assigned at the time of Victor Hess discovery that cosmic rays come from space. At that time, they were known by many names like "Höhenstrahlung" (high-altitude radiation), "Hesssche Strahlung" (Hess rays), and "Ultrastrahlung" (ultra rays). However, the name that remained was cosmic rays since Robert Millikan and other physicist thought they were high energetic X-Rays or gamma rays.

Nowadays, there are still many unknowns to answer in the current experiments such as:

- What are the causes for the different features of the spectrum?
- Is there an end to the cosmic rays spectrum? If so, is it caused by the sources or by the propagation?
- What are the sources of such energetic particles? and/or mechanisms to accelerate those particles?
- What is the composition of cosmic rays as a function of energy?
- The interactions are the same at those extreme energies?

2.1 A short view through Cosmic Ray history

A simple instrument, called electroscope, was the responsible for the discovery and further interest of the cosmic rays. Since the XVIII century and up to the beginning of the XX century, the electroscope become a standard instrument to study electric charges, radioactivity and the relative conductivity of the air. The first scientific electroscopes were the pith-ball electroscope and the gold-leaf electroscope, developed by John Canton (1754) and Abraham Bennet (in 1787) respectively.

The gold-leaf electroscope (figure 2.1) consists in a metal rod (at the time mainly brass), from the end of which hang two thin flexible gold leaves. In the other rod extremity, there is a disk or a ball where the tested charge is applied. After some applied charge, the gold leaves spread

apart in a "V" due to the Coulomb force. To avoid air drafts or other perturbation on the leaf, they are enclosed in a glass bottle, mounted over a conducting plate to absorb some leaking charge in the air (that could accumulate on the glass).

If the electroscope was perfectly isolated, then the charge contained in the gold would not change and they would stay in the same position. Nevertheless, around 1785, Charles-Augustin de Coulomb discovered that electroscopes can spontaneously discharge by the action of the air and not by defective insulation. Michael Faraday, around 1835, also verified the same result with greater precision. On that century, many developments on the initial designs were performed (by Thompson and Kelvin for example) and allowed W. Crookes to verify (in 1879) that the discharge speed of an electroscope decreases with air pressure increase. The cause of this ionization was unknown for several years, but fortunately it aroused much interest due to weather issues, such as atmospheric electricity.

In 1896 Henri Becquerel discovered the radioactivity. A few years later Marie and Pierre Curie discovered that the elements Polonium and Radium suffered transmutations generating radioactivity (radioactive decays). Close to these substances, the electroscopes discharge quicker, which means that some elements were able to emit charged particles. The electroscope was then used to estimate the level of radioactivity and these kind of studies became very popular in meteorology and research related to natural radioactivity. There were many studies about natural radioactivity and air ionization after their discoveries. For example, around 1900, Julius Elster and Hans Geitel isolated the electroscope by putting it in a thick metal box. They verified that the natural radioactivity decreased, but there were still discharge in the electroscope, meaning that the discharge was largely due to ionizing agents from outside the container and that such ionizing agents were highly penetrating. The question was if these ionization particles came from terrestrial, atmospheric or extra-terrestrial sources. Several other experiments were performed, like measuring the discharge in mines (by Charles Wilson, inventor of the cloud chamber). However, due to experimental uncertainties, a reduction of radioactivity with respect to the open air was not seen, as he expected to find if the extraterrestrial hypothesis had been true. An interesting note is that Nikola Tesla patented in 1901 in the US a power generator based on the fact that

"the Sun, as well as other sources of radiant energy, throws off minute particles of matter [which] communicate an electrical charge".

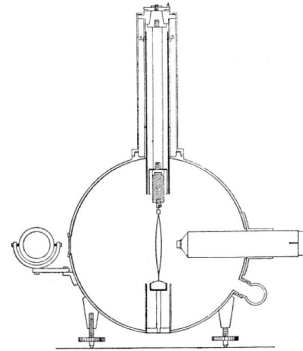
Since the electroscope was a very sensitive instrument, more reliable measurements were difficult. So, in 1909, a Jesuit monk in Vienna called Theodor Wulf, designed and built a more precise and transportable electroscope (figure 2.1b). The basic operation of this apparatus is a pair of quartz fibers at the center of the device. The pair is attached in the bottom to a bended quartz fiber which acts as a spring to adjust the tension on the pair and change the sensitivity of the device. To measure the distance between the fibers, a microscope is added inside the protective encapsulation. This device was mass produced and used across many countries. T. Wulf used it to determine small capacities and to study the radioactivity in the air. Again he found an anti-correlation between the radiation intensity and the ambient air pressure and also concluded that:

"We report on experiments, which prove that the penetrating radiation is caused by radioactive substances, which are located in the upper layers of soil up to a depth of about 1 m. If a fraction of the radiation originates in the atmosphere, it has to be so small, that it can not be detected with the present apparatus." [3]

To prove this hypothesis, Wulf measured the air radioactivity at the top of the Eiffel Tower, at about 300 m above the ground. He concluded that:



(a) A. Bennet electroscopes



(b) T. Wulf electroscopes

Figure 2.1: a) The gold-leaf electroscopes developed by Abraham Bennet in 1787. b) The electroscopes developed by T. Wulf consists in a 17 cm diameter cylinder with 13 cm depth made of Zinc. In the center there is a pair of quartz fiber which acts as the gold-leaf and the tension can be adjusted to change the sensitivity. In the right is the microscope to measure the distance between the two silicon glass wires, illuminated using the mirror on the left. The air was kept dry using Sodium in the small container below the microscope.

”[radiation] decreases at nearly 300 m [altitude] not even to half of its ground value”.

This decrease in radiation was too small compared with the expectations of ”just a few percent of the ground radiation” [4], if the radiation source was the ground. Despite not having discovered the radiation origin, he made measurements at different times of the year and different hours of the day, being considered as one of the most reliable measurements made at the time.

Around 1910, an Italian physicist, Domenico Pacini, carried out an experimental program of systematically measuring the air ionization. He measured the air ionization in several locations with different altitudes (to study local effects) and, more importantly, at the sea. One of his important measures was first to place the electroscopes on the ground, and after above the sea, a few kilometres off the coast (in the Gulf of Genova). He found that the radiation on the ground and above the sea were comparable, which meant that an important contribution of radiation could not come from the Earth crust. In 1910 and 1911, he developed a new experimental technique for radioactivity measurements a few meters underwater. In his papers [5, 6] (translated here [7]), he found a significant decrease, by 20% in the discharge rate, when the electroscopes was placed three meters underwater in the sea, consistent with absorption by water of a radiation coming from outside. Nevertheless, it was impossible to say if the radiation was extraterrestrial or atmospheric. He concluded:

”[it] appears from the results of the work described in this Note that a sizeable cause of ionisation exists in the atmosphere, originating from penetrating radiation, independent of the direct action of radioactive substances in the soil.”

Before Victor Hess had discovered the cosmic rays, several measurements were performed on balloons. For example, between 1902-1903 Franz Linke studied the air ionization at several altitudes. He found that, it was about the same between altitudes of 1000 m to 3000 m, and larger by a factor of four at 5500 m. However, the measurements accuracies were not very good

and the result was not considered reliable. Around 1909, Karl Bergwitz and Albert Gockel had also tried to do air ionization measurements with balloons. They didn't observe a decrease in the radiation, however, again problems with the detectors made difficult to draw definitive conclusions. Until 1909, the general consensus was that ionisation was caused by the natural radioactivity of the Earth.



(a) V. Hess



(b) W. Kolhörster

Figure 2.2: a) Historical photograph of Hess preparing for a balloon flight in 1912 (American Physical Society). b) Photograph of W. Kolhörster preparing for a balloon flight in 1913.

Only Victor Hess, figure 2.2b, would be able to claim the discovery that indeed this radiation was coming from extra terrestrial sources. But before, around 1910, Hess improved the electrometer by developing a calibration method using radium sources of different strengths. He used mass production spectrometers that, with his calibration, had an accuracy measuring the strength of unknown sources of about 5 per mil. While uncalibrated, the instrument achieved 3% accuracy. Furthermore, Hess also sealed the electrometer and maintained the air pressure inside constant. The particle number density inside the apparatus was kept constant, despite of the varying ambient temperature and air pressure during a balloon ascent.

From April 1912 to August 1912, Hess launched seven balloon flights with three instruments, one of them had a thin wall to estimate the effect of beta radiation from heavy particles (a photo of one of the launches is displayed in figure 2.2b). On August 7, 1912, the final flight reached 5200 m. The radiation recorded by Hess, showed a decrease until 1400 m consistent with previous measurements. After 1400 m the radiation showed a strong increase (see [8]). The results of the last flight are plotted in the figure 2.3a. Hess wrote:

”The results of the present observations can be most likely explained through a radiation of very high penetrating power, impinging onto the atmosphere from above, and being capable to cause the observed ionization in closed vessels even in the lowest layers of the atmosphere. The intensity of the radiation exhibits timely variations on hourly time-scales. Since I did not find a reduction of the radiation intensity during night or during a solar eclipse, the Sun can be excluded as the origin of this hypothetical radiation.” [8]

Hess won the Nobel Prize in 1936 for his discovery with Carl Anderson.

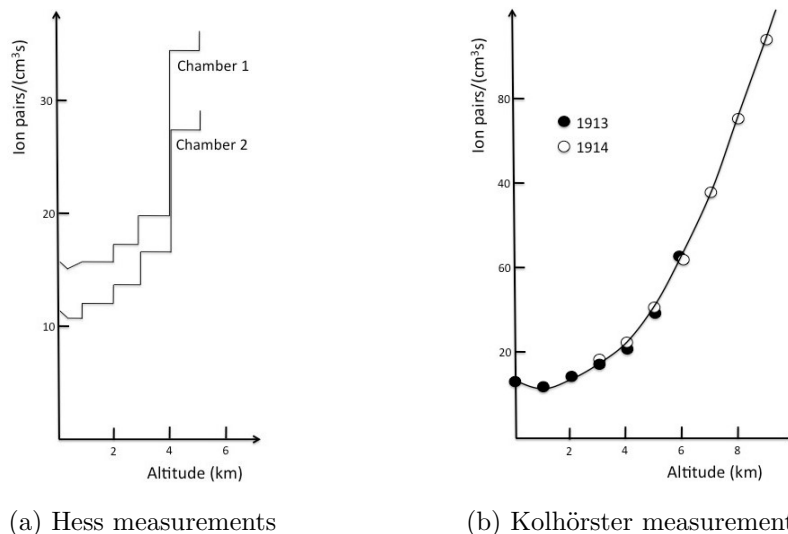


Figure 2.3: Variation of air ionization with altitude. a) Results of two electroscopes of the final Hess flight [8], b) the result of the two years sets of Kolhörster [9] .

After Hess, Werner Kolhörster performed balloon flights in 1913 and 1914, reaching heights around 6000 m and 9300 m respectively. The ionizations reached values above $80.4 \text{ ions cm}^{-3} \text{ s}^{-1}$, while on the ground were about $13 \text{ ions cm}^{-3} \text{ s}^{-1}$ (see figure 2.3b). It was a perfect confirmation that the high-energy radiation has an extraterrestrial origin.

In the 20's, many studies about the Latitude effect and barometric effect on the cosmic radiation were performed, throughout a worldwide measurement campaign. Meanwhile, new kinds of detectors were built. In 1911, C. T. R. Wilson developed of the cloud chamber, which allowed the first pictures of cosmic rays in this decade.

The big advance came with the new detector design by H. Geiger and W. Müller, the Geiger-Müller counter, in 1928. So, on the same year, W. Bothe, W. Kolhörster placed two Geiger-Müller counters, next to each other vertically (figure 2.4b), and operated them in coincidence to measure the absorption. The absorption measurements were taken with and without a gold block between the counters. They proved that the coincidences could only be caused by charged particles, and not by γ -rays as previously hypothesized. A γ -ray travelling through matter would be accompanied by secondary electrons resulting from the Compton effect. In coincidence, if the top signal was a γ -ray, then the second Geiger-Müller would detect the secondary electron. Nevertheless, they measure this electron (β ray) penetration power and found that the electron would not be able to cross the gold thickness. So, it must be a corpuscular particle with high penetrating power. Both won the Nobel Prize by the invention of the coincidence circuit. B. Rossi also improved the electronic coincidence circuit and performed measurements with three Geiger-Müller counters in coincidence with and without lead shielding on top. The coincidence rate increased with the shielding, even though the opposite had been expected.

In 1938, Kolhörster placed two Geiger-Müller counters at some distance of each other and operated them in coincidence. The number of coincidences measured exceeded the one expected for random coincidences (fig. 2.4a), which led to the discovery of extensive air showers. In [10] ("Coupled high-altitude rays"), he explains that the observed particle coincidences are secondary particles (a shower) from cosmic rays. Following these studies, Pierre Auger in 1938 also used two Geiger-Müller counters in coincidence, and his colleagues, Maze and Robley, detected extensive air showers (fig. 2.4a)[11]. They measured the rate at up to 300 m of counter distance

and estimated the energy of the primary cosmic particles to be about $10^{15}eV$ [12].

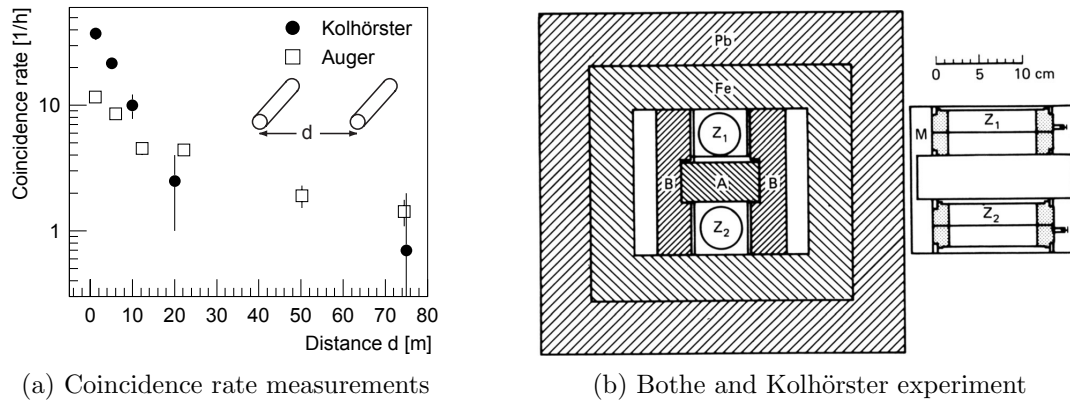


Figure 2.4: a) Coincidence rate as a function of the distance between two Geiger-Müller counters obtained by Kolhörster [10] in full dots and by Auger [11] in open squares. b) The experiment of Bothe and Kolhörster, Z_1 and Z_2 were two Geiger-Müller in coincidence, B were lead plates also. The observations were made with and without the 4.1 cm thick gold absorber (A).[13]

Apart from only studding new particles, their global properties were also studied. Rossi also observed showers of particles produced under lead plates, which were associated with the a maximum intensity of radiation found in the atmosphere. In 1937, Bhabha and Heitler[14], and at the same time Carlson and Oppenheimer[15] developed the theory of electromagnetic cascades. This was subsequently developed by Landau and Rumer and by Tamm and Belen'kii, who successfully used them to describe the extensive air showers.

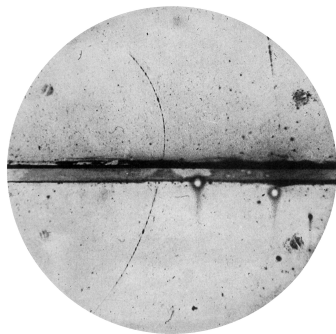
Meanwhile, the cosmic ray particles were being studied through cloud chambers with and without magnetic fields. Photographs like the one in the figure 2.5a, with the track particles in a strong magnetic field were studied to identify new particles. In this way, in 1932, Carl David Anderson discovered the positron[16] while studying cosmic ray tracks with negative and positive charges, which were interpreted as electrons and protons. However anomalous behaviour had already been evidenced in other papers and works. Since many positive track had similar trajectories as electrons, Anderson placed a 6 mm-thick lead plate into the chamber. With this procedure, he found tracks with a curvature matching the mass-to-charge ratio of an electron, with a positive charge. The particle was the positron predicted by Paul Dirac two years earlier and was the first evidence of anti-matter.

From the 1930's to the 1950's, many new particles were discovered within the cosmic rays, in what many call the beginning of Particle Physics. Just a quick review:

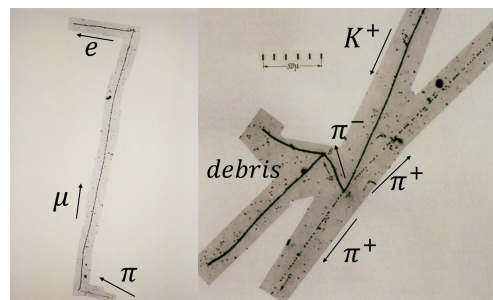
- 1936 Anderson and Neddermeyer discover the muon. They found about 25 events where the energy loss in the platinum absorber was much smaller than measured for electrons or positrons. They first call it mesotron and thought it was the pion as predicted by Yukawa in 1935.
- 1937 The photo-emulsion technique was developed by M. Blau.
- 1937 First cosmic ray nuclear interaction in a photo emulsion was seen in Hess's Hafelekar cosmic ray station at an altitude of 2300 m. This was a breakthrough, a cosmic ray interacted with an atom of the emulsion, producing eight tracks. From now on, many different nuclear interactions could be seen.

- 1947 discovery of the pion in photographic emulsions by D. H. Perkins, G. P. S. Occhialini and C. F. Powell (figure 2.5b). The predicted Yukawa particle had a lifetime of about 10^{-8} seconds, which was 100 times shorter than the measured lifetime of the muon. The problem was solved by them.
- 1947 George Rochester discovered the kaon (K-meson, figure 2.5b from Powell) one of the first sub-nuclear particles to be detected besides the neutron and the proton. The kaon had unusual properties that physicists at the time dubbed 'strange'. When quarks were discovered in the 1960s, it was clear that these characteristics came from a new quark within the kaon, and this became known as the 'strange' quark. Hyperons were also discovered by them but convincing proof of their existence was obtained only in 1950's.
- 1950 discovery of the neutral pion (π^0) at the Berkeley synchrocyclotron by Bjorklund.
- 1950 V. D. Hopper and S. Biswas discover the Lambda baryon (Λ^0), in photographic emulsions flown in a balloon at 21 km.
- 1952 The first discovery of a charged Xi baryon by Armenteros group and Tomasini group.
- 1955 Gell-Mann and Nishijima postulate the existence of a new quantum number, the strangeness (S), which is conserved in the processes of strong and electromagnetic interaction and could explain the peculiarities of the behaviour of hyperons and K-mesons. If the Kaons and Hyperons decays were caused by strong interaction, their lifetime should be on the order of 10^{-23} seconds, which is 13 orders smaller than that established experimentally. This made the necessity of a new quantum number. Now their lifetime can be explained through weak interaction decays.

The cosmic rays were essential in the beginning of the particle physics. Through CRs, new unpredictable particles were discovered like the muon and the strange particles like kaons and hyperons. They also allowed the discovery of hypothesized particles by the theory, like the positron and the pion.



(a) Cloud chamber photograph by C. D. Anderson



(b) A Pion and a Kaon decay

Figure 2.5: a) Cloud chamber photograph by C. D. Anderson from 1932, the track is a positron with an energy of 63 MeV entering the lead plate from below and leaving the plate with an energy of 23 MeV. If it was a proton, the track would be around 10 times shorter.[16] b) on the left, a pion decays into a muon (plus neutrino) and subsequently the muon decays into electron. On the right, a Kaon, K^+ , decays to 3 pions ($\pi^+ + \pi^+ + \pi^-$), the π^- subsequently causes a nuclear desintegration. From Powell and Perkins.

After the 1950's, with the design of particle accelerators, it was possible to produce particles with higher luminosities and better controlled environments. So the new discoveries would be made in accelerator and particle physics would separate from the cosmic rays field. In 1949, it was already possible to produce pions in the accelerators.

From then on, the cosmic rays field focused more in astronomy and astrophysical studies. Several new techniques were developed and starting in the mid 1950's, large detector arrays were built to measure EAS (with increasingly bigger areas of detection to detect the increasingly smaller fluxes). The pioneer experiment of ground arrays, consisting in an sparse arrays with particle detectors to increase the area of exposure was the Volcano Ranch experiment[17] (1959-1978) built by J. Linsley, in Volcano Ranch, New Mexico. Around 1962, they claim to had measured an air shower with energy greater than 10^{20} eV. This experiment was followed by many others using the same idea, such as: SUGAR-Sydney University Giant Air-shower Recorder[18](1968-1979) close to the town of Narrabri in northern New South Wales; Haverah Park [19] (1967-1987) with water Cherenkov detectors in an area of 12 km^2 on Haverah Park on the Pennine moorland near Harrogate, North Yorkshire; Yakutsk array [20](\approx 1970 until now) in the Soviet Union at longitude $129^\circ E$ and latitude $62^\circ N$, begun with 13 scintillation counters and also with air Cherenkov, muon detectors were later added. At the time, was the largest and most complex array; Akeno Experiment[21](1975-2004) near the town of Akeno, Japan, it was then expanded and upgraded into Akeno Giant Air Shower Array (AGASA) 1990.

These experiment made important contributions to understand the cosmic rays above 10^{17} eV. Haverah Park with AGASA found the "ankle" of the cosmic ray spectrum. The event with the highest energy was measured at 8.28×10^{19} eV.

In mid 1960's, a group under K. Greisen did a pioneer work trying to detect the fluorescence light produced when cosmic particle showers excite air molecules. The first prototype was built and tested by the University of Utah together in Haverah Park. In 1970's, the Fly's Eye detector array was built in the desert of Utah, with 67 detector units, each consisting of a container with a 1.5 m mirror and a light collection system. The array was able to register, on moonless nights, fluorescence light over an area of about 1000 km^2 [22]. It allowed to detect one ultra-high energy cosmic rays with energy $> 5 \times 10^{19}$ eV (confirming the existence of UHECR), which was called "Oh-My-God" particle. It was later upgraded into the High Resolution Fly's Eye or HiRes detector from May 1997 until April 2006. Together with Fly's Eye, the CASA-MIA array was built around 1992, the Chicago Air Shower Array (CASA) comprising an array of scintillation counters and the Michigan Anti Array (MIA) with buried muon detectors. In this way, in a prototype phase, the EAS could be detected in air and on the ground at the same time, in an hybrid detector.

Nowadays, hybrid detectors, with both techniques together, are built. For example, a follow-on experiment to the HiRes and AGASA is the Telescope Array (TA) Project in central Utah (collecting data since 2007)[23]. Similar, but with a ground array covered with water Cherenkov detectors (like Haverah Park), is the Pierre Auger Observatory, (collecting data since 2004)[1]. The Pierre Auger Observatory and new analysis methods for cosmic rays allow us currently to study the universe not only from an astrophysical point of view, but rather to understand the physics interactions at those energies. With Auger, it is possible to study cosmic rays until 10^{20} eV (around 150 TeV in mass center) one order magnitude higher than the current energies at the LHC, which is currently at our technological/financial limit. The Ultra High Energy Cosmic Rays are the most energetic particles observed in nature, with energies about 10^{20} eV. Nevertheless, there are many unknowns yet to be solved in the field.

2.2 Cosmic Ray Radiation

The Earth is continually exposed to a flux of cosmic rays with energies ranging from a few MeV to 100 EeV¹. The figure 2.6b, shows a general picture of the spectrum from the lowest to the highest Cosmic Rays (CRs) energies. The spectrum, flux as a function of the energy, follows a power law with almost no features and it has a dramatic decrease in flux. At energies around a few GeV, the flux is approximately 1000 particles per second and m², while at 100 EeV it is less than one particle per century and km².

The high CRs fluxes at low energies allows to detect them directly with balloons or satellites. Nonetheless, at higher energies the CRs flux is too small and huge detection areas would be needed to catch them. This is impossible in balloons or satellites so many experiments use the atmosphere as the detector (section 2.3), which means these particles interact in the atmosphere and it is possible to detect the shower development in the atmosphere instead of the CR directly. At lower energies it is possible to determine the CR composition, but at high energies, with increasing low flux and detecting the CR indirectly, our knowledge about the origins and compositions becomes increasingly limited. For the highest CR energies, called Ultra High Energy Cosmic Rays (UHECR), the composition is basically unknown and their origins and sources even more unknown.

2.2.1 Energy Spectrum

The detected cosmic rays spectrum extends over several orders of magnitude both in energy and in flux on Earth. The spectrum follows a simple power law $J(E) = \frac{dN}{dE} \propto E^{-\gamma}$, with the spectral index γ almost constant, being $\gamma \sim 2.7$ above the GeV. According to the few spectrum features, the cosmic rays are usually qualified as: solar cosmic rays, galactic cosmic rays and extreme energy cosmic rays (UHECR), see figure 2.6.

The lowest energy CR are produced in the Sun, being the solar cosmic rays (or solar energetic particles (SEP)). They are originated in violent events, like solar flares and coronal mass ejections, stirred up by the Sun. The energy is usually up to order of 100 MeV and may reach 10 GeV [24]. Between 1973 to 1988, the energy spectrum around 10-100 MeV showed relative abundances of some CRs compositions higher than expected, not compatible with solar and Galactic Cosmic Rays (GCR) abundances. This excess was found in nuclei like He, N, O, Ne, Ar and Mg, Si, and S[25]. The particles in this energy range were called Anomalous cosmic rays (ACR), they are originated from particles from the interstellar neutral gas that flows into the heliosphere. They become ionized by solar UV radiation and eventually accelerated by the solar wind termination shock (a mechanism called diffusive shock acceleration). The ions repeatedly collide with the termination shock wave in the solar wind, gaining energy in the process. As a result, the ACRs are predominantly singly ionized, these ions would be much less modulated than the fully ionized galactic cosmic rays or highly charged solar cosmic rays of the same velocity and thus could be observed in the inner heliosphere. The study of solar CR is also crucial for the future manned missions to the Moon and Mars, because they can constitute an important hazard for humans in space.

Cosmic Rays with energies higher than ~ 1 GeV don't come from the solar system, but from the galaxy, being called galactic cosmic rays. The GCR are believed to be accelerated at Supernova Remnants (SNRs) (it will be explained in section 2.2.2.1.1). With a rate of about three supernovae per century in a typical galaxy, they would account for the energy of galactic

¹1 EeV = 10¹⁸ eV

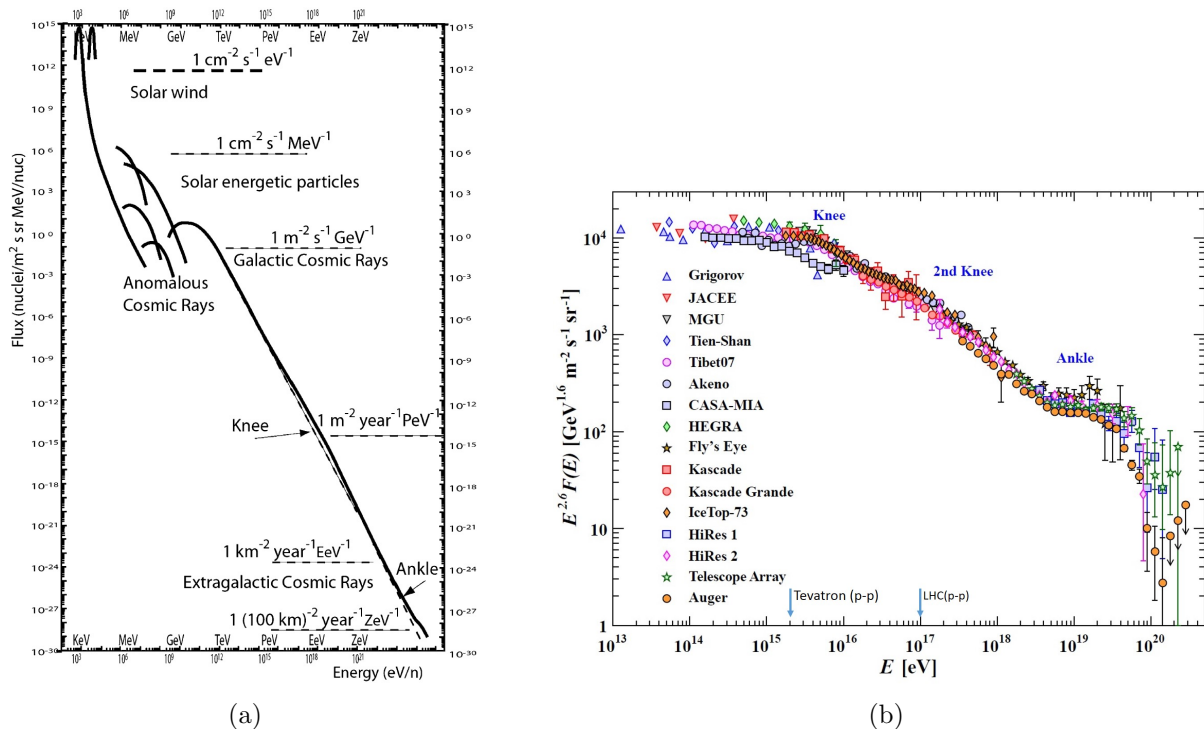
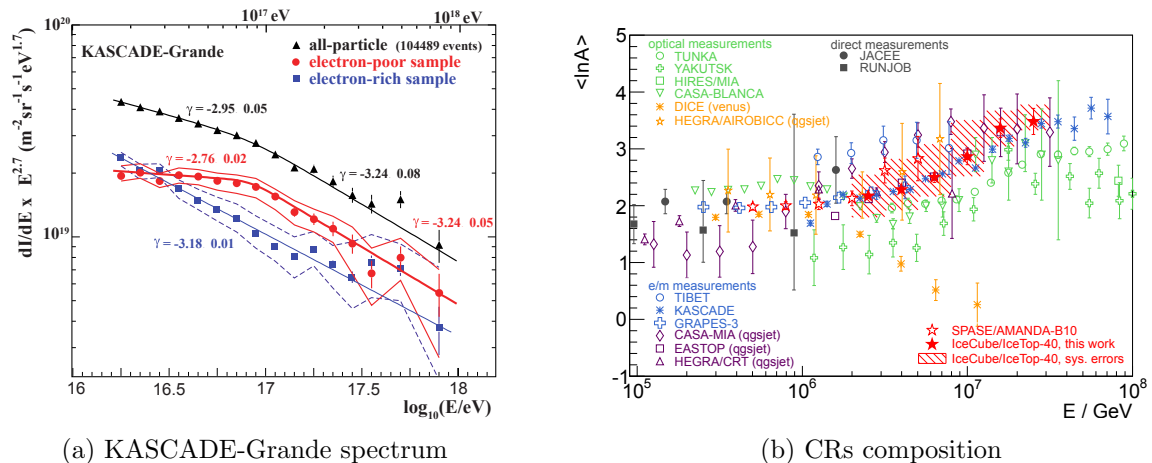


Figure 2.6: Left, cosmic ray spectrum, from solar cosmic rays up to the GZK cut-off, the dashed line corresponds to a power law with spectral index $\gamma = 3$ [24]. Right, spectrum as a function of energy, multiplied by $E^{2.6}$ for observation purposes, from several from air shower experiments [26].

cosmic rays if only a 5 – 10% of the kinetic energy released were transferred to accelerate particles. The composition of GCR is mainly protons (85%), nuclei (15%), electrons, positrons and antiprotons.

The spectral index in this region (from some GeV to 1PeV) is $\gamma = 2.70 \pm 0.01$, but at the energy $(4.0 \pm 0.8)10^{14}$ eV the slopes changes into $\gamma = 3.10 \pm 0.07$, as reported by Karlsruhe Shower Core and Array DEtector (KASCADE)[27]. This transition point was called knee. There are several hypothesis for the origin of the behaviour that can be group in four classes: from astrophysical scenarios, (i) the change of acceleration mechanisms at the sources of cosmic rays (supernova remnants, pulsars, etc.), or the finite limit of energy reached during the acceleration process; (ii) effects due to the propagation inside the Galaxy (diffusion, drift, leakage from the Galaxy during the diffusive propagation); to more exotic hypothesis like (iii) particle physics models with interaction of CRs with background particles during the propagation process (like relic neutrinos and background photons); and (iv) new hadronic interactions within the atmosphere, which transport a fraction of the energy into unobserved channels (see [28] for several others models description).

The acceleration mechanism at SNRs has an energy upper limit proportional to the nuclear charge number of the respective atomic nuclei Z and the strength of the magnetic field B in the acceleration region $E_{max} \propto Z \cdot B$ ($E_{max} \sim Z \cdot 10^{14}$ eV). This way, at knee energies, the cosmic ray sources can not accelerate protons to higher energy. Then the next nucleus, He, takes over and the process continues in order of charge until at some higher energy galactic cosmic rays contain only iron nuclei. This would explain the knee feature as being a successive limits in



(a) KASCADE-Grande spectrum (b) CRs composition

Figure 2.7: Left, KASCADE-Grande reconstructed energy spectrum of the electron-poor (heavier CRs) and electron-rich (light CRs) components together with the all-particle spectrum for the angular range $0^\circ - 40^\circ$. The error bars and the bands assign the statistical and systematic uncertainties respectively.[29] Right, the mean logarithmic mass vs primary energy, for several experiments in the region of the galactic cosmic rays. The result indicates a strong increase in mass through the knee. [30]

the accelerations for the increasingly heavier nuclei. But besides the acceleration mechanism, it should be added that the nuclei above some rigidity E/Z (since the Larmor Radius is proportional to E/Z) can escape the galaxy, because the galactic magnetic field are no longer able to confine the nuclei. This way, the spectrum has a diffusion cut-off that also depends on Z .

There is also some evidence of a second knee (see figure 2.6b) around $10^{17.6}$ eV. The slope before the second knee would be around $\gamma = 3.02 \pm 0.03$ and after $\gamma = 3.29 \pm 0.02$, reported in [31], using data from High Resolution Fly's Eye detector (HiRes), Akeno and Fly's Eye. KASCADE-Grande in [29] reported that the spectral slope γ for heavy primary cosmic rays, shows a kneelike structure around $\log_{10}(E/eV) = 16.92 \pm 0.04$ (8.10^{16} eV), where the $\gamma = 2.76 \pm 0.02$ changes to $\gamma = 3.24 \pm 0.05$ (see figure 2.7a).

The second knee is similar to the first one but for heavier particles. The figure 2.7 on the right, shows that the average composition of the CRs is getting heavier from 10^{14} eV to 10^{17} eV. The new results seems to exclude the (iii) and (iv) kinds of hypothesis. The third class can be excluded because interactions with background particles would result in a break-up of heavy nuclei, into lighter nuclei. The current result around 10^{16} to 10^{17} eV shows heavier composition. The fourth class is also disregarded due to the last measurement in KASCADE-Grande that shows that the predictions of the hadronic models in EAS, agree with measured observables on the 10% level, at these energies [32].

The acceleration mechanism could explain the slope between the knees, as being several energy limits on the acceleration mechanisms proportional to Z (the composition begin to get heavier). After the second knee, all nuclei begin to escape the galactic confinement, the heavier nuclei are the last ones to escape and composition also get heavier. The knees in the energy spectrum are probably a combination of a maximum energy in the sources and the leakage from the galaxy due to the propagation process.

At energies around 10^{18} eV a new change in the spectral index can be seen, the slopes turns again flatter and this feature in the spectrum is called ankle (latest Auger results on the spectral indexes are written on section 3.7.1). The reason for this change in the slope, is

probably due to the leakage of the heavier galactic nuclei and the beginning of an extragalactic cosmic ray component. These extremely energetic CRs are called Ultra High Energy Cosmic Rays (UHECR). The CR flux at those energies is extremely small, being necessary huge areas of detections for a few number of events. It means that the understanding of the particles composition is very reduced. Above that, since the extragalactic component becomes dominant after the ankle, an additional acceleration mechanism must be introduced to account for the energies above that limit. It is very difficult to explain how to transfer efficiently a macroscopic amount of energy, of the order of 20 Joules, to a microscopic particle.

In the end of the spectrum, a suppression in the flux appears around 10^{20} eV. Still, it is not clear if this suppression comes from a limit in the CR production or from the Greisen-Zatsepin-Kuzmin (GZK) cut-off (see section 2.2.3.1).

2.2.2 UHECR origin and acceleration

The most energetic cosmic rays are called Ultra High Energy Cosmic Rays (UHECR). There are two classes of model to describe how those particles get that extreme energies. The Bottom-Up theories, with CRs being accelerated in some mechanism and the Top-Downs theories with CRs being sub products of even more energetic particles.

The regular shape of the spectrum over its wide energy range may suggest a common acceleration mechanism, which could take place in different astrophysical sources. The productions or accelerations mechanism together with the energy process losses that could occur on those mechanisms, should match the observed spectral index. It is very difficult to know the composition of the most energetic particles, which makes room for several different origin models. Searches for significant anisotropies in arrival directions of UHE cosmic rays have been made in many experiments and it was found to be rather isotropic over a broad energy range. Only at the highest energies, a small anisotropy can be seen, but a conclusion on its origin is not clear yet.

2.2.2.1 Bottom-Up models

The Bottom-Up models assume that the CRs (charged particles) are accelerated by some mechanism. The conventional acceleration mechanisms are the direct acceleration of charged particles by electromotive force (emf) or very intense electric field and the stochastic acceleration in a magnetized plasma (Fermi acceleration).

The first kind of models, with CRs being accelerated by an electromotive force, is an idea from Swann[33], are inspired in the increased magnetic field of a sunspot (these were also called "one-shot" mechanisms). The particles are accelerated directly by a very intense electric field. This electric field may arise in rapidly rotating magnetized conductors, such as neutron stars or supermassive objects. This mechanism has the advantage of being fast, however the acceleration occurs in an environment of very high energy density, which means high energy losses exist. It is difficult and not obvious how to get a power-law spectrum to emerge from it, so this kind of mechanism is not widely favoured these days [34].

The second kind of models are based on statistical accelerations. The particles gain energy gradually by numerous encounters with regions of changing (moving) magnetic field (these processes are variants of Fermi's mechanism, see section 2.2.2.1.1). These models have the advantage that the energy is spread over many energy decades and a shock-wave region can give a spectrum with $\sim E^{-2}$. However, these are slow processes and it is hard to keep up with energy losses at the highest energies.

2.2.2.1.1 Fermi acceleration mechanism

In 1949, Fermi considered the hypothesis of CRs acceleration through their scattering on moving magnetized clouds [35]. The original model can be adapted to the case of shock accelerations in astrophysical objects, where the required extremely high energies could be possibly reached.

The scattering process is represented in figure 2.8a. A cosmic ray, with energy E_i and momentum p_i , entering a massive moving gas cloud of velocity V , with an angle of θ_i between the cloud velocity V and the CR direction. In the cloud, the CR undergoes diffuse scattering on the irregularities in the magnetic field. The CR initial energy in the cloud reference frame (E'_i) is given by:

$$E'_i = \gamma_{cloud} E_i (1 - \beta_{cloud} \cos \theta_i), \quad (2.1)$$

where γ_{cloud} and $\beta_{cloud} = V_{cloud}/c$ are the Lorentz factor and velocity of the cloud in units of the speed of light, respectively. In the rest frame of the cloud there's no change in energy, as the particle scatters collision-less on the magnetic field moving with the cloud. So $E'_f = E'_i$, there is elastic scattering between the CR and the cloud as a whole, which is much more massive than the CR. The CR leave the cloud with energy E_f , in the laboratory frame, given by:

$$E_f = \gamma_{cloud} E'_f (1 + \beta_{cloud} \cos \theta'_i). \quad (2.2)$$

Putting both together, the fractional energy change in the laboratory frame is then:

$$\frac{\Delta E}{E} = \frac{E_f - E_i}{E_i} = \frac{1 - \beta_{cloud} \cos \theta_i + \beta_{cloud} \cos \theta'_f - \beta_{cloud}^2 \cos \theta_i \cos \theta'_f}{1 - \beta_{cloud}^2} - 1. \quad (2.3)$$

Inside the cloud, the CR direction becomes randomized and so $\langle \cos \theta'_f \rangle = 0$. The average value of the $\cos \theta_i$ depends on the relation between the cloud and CR velocities. The probability per solid angle of having a scattering between the CR and the cloud is proportional to $v - V_{cloud} \cos \theta_i$ (and v is the CR velocity). Since at these energies the cosmic rays have an extreme energy, in the ultra-relativistic limit, so $v \approx c$, then:

$$\frac{dP}{d\Omega_i} \propto (1 - \beta_{cloud} \cos \theta_i), \quad (2.4)$$

so the average value is

$$\langle \cos \theta_i \rangle = \frac{\int \cos \theta_i \frac{dP}{d\Omega_i} d\Omega_i}{\int \frac{dP}{d\Omega_i} d\Omega_i} = -\frac{\beta_{cloud}}{3}, \quad (2.5)$$

putting in equation 2.3 and using $\beta \ll 1$ (clouds are not relativistic),

$$\frac{\langle \Delta E \rangle}{E} = \frac{1 - \beta_{cloud}^2/3}{1 - \beta_{cloud}^2} - 1 \approx \frac{4}{3} \beta_{cloud}^2. \quad (2.6)$$

The average magnetic field may vanish, however, there can still be a net transfer of the macroscopic kinetic energy from the moving cloud to the particle with $\frac{\langle \Delta E \rangle}{E} = \frac{4}{3} \beta_{cloud}^2$. The gain is small since it is on the second order and $\beta_{cloud} \ll 1$.

There is also a more efficient acceleration, of the first order in β_{cloud} [36], thought to take place in regions of strong shocks, as for example in supernovae and Active Galactic Nuclei (AGN) jets. In this case, with a large shock wave propagating with velocity V_S , as depicted in figure 2.8b. Relative to the shock front, the downstream shocked gas is receding with velocity V_P , where $|V_P| < |V_S|$. The CR scatters inside the magnetic irregularities on either side of the shock, as on the clouds of magnetized plasma in the 2nd order Fermi mechanism discussed previously, and can cross the shock front several times. Considering the rate at which cosmic rays cross the

shock from downstream to upstream, and upstream to downstream, one finds $\langle \cos \theta_i \rangle = -2/3$ and $\langle \cos \theta_f \rangle = 2/3$. Re-writting equation 2.3, it gives:

$$\frac{\langle \Delta E \rangle}{E} = \frac{1 + 4/3\beta + 4/9\beta^2}{1 - \beta^2} - 1 \approx \frac{4}{3}\beta, \quad (2.7)$$

which is on the first order in β and $\beta = \frac{V_p}{c}$ and therefore more efficient than Fermi's original mechanism.

The rate at which CRs cross from upstream to downstream is given by the projection of the isotropic CR flux, n_{CR} onto the shock front plane. Cosmic rays travelling at speed v at angle θ to the shock normal (as seen in the laboratory frame) approach the shock with speed $(V_S + v \cos \theta)$. So, to cross the shock, $\cos \theta > -V_S/v \sim 0$. Then, the rate is given by:

$$\tau_{cross} = \frac{n_{CR}}{4\pi} \int_{-V_S/v \sim 0}^1 \left[\int_0^{2\pi} (V_S + v \cos \theta) d\phi \right] d(\cos \theta) \approx \frac{n_{CR}v}{4}. \quad (2.8)$$

The rate of downstream CRs (see figure 2.8) away from the shock front is

$$\tau_{loss} = n_{CR}(V_S - V_p), \quad (2.9)$$

the probability of crossing the shock once and then escaping from the shock is

$$Prob.(escape) = P_{esc} = \frac{\tau_{loss}}{\tau_{cross}}. \quad (2.10)$$

The probability of crossing the shock front again after crossing from upstream to downstream is

$$Prob.(return) = 1 - Prob_{esc}, \quad (2.11)$$

and the probability of returning to the shock n times is

$$Prob.(cross n times) = [1 - Prob_{esc}]^n. \quad (2.12)$$

Considering that after n shock crossings, the energy is given by

$$E = E_0 \left(1 + \frac{\langle \Delta E \rangle}{E} \right)^n, \quad (2.13)$$

with $\langle \Delta E \rangle$ the average energy gain per shock crossing and E_0 the initial energy. So, the number of n shock crossings, until the CR reach a particular energy E is

$$n = \frac{\ln(E/E_0)}{\ln(1 + \langle \Delta E \rangle/E)}. \quad (2.14)$$

The cosmic ray flux above some energy should be proportional to the probability of returning to the shock n times, $N(\geq E) \propto [1 - Prob_{esc}]^n$. So, substituting equation 2.14 and rearranging, the flux becomes

$$\ln N(\geq E) \propto \frac{\ln(E/E_0)}{\ln(1 + \langle \Delta E \rangle/E)} \ln(1 - P_{esc}) \propto -\gamma \ln E, \quad (2.15)$$

where

$$\gamma = -\frac{\ln(1 - P_{esc})}{\ln(1 + \langle \Delta E \rangle/E)}. \quad (2.16)$$

In this way Fermi's mechanism yields a Cosmic Rays spectrum with a power law with spectral index γ . In the first order mechanism, the index γ doesn't depend on the plasma velocities but depends only on the ratio of the upstream and downstream velocities.

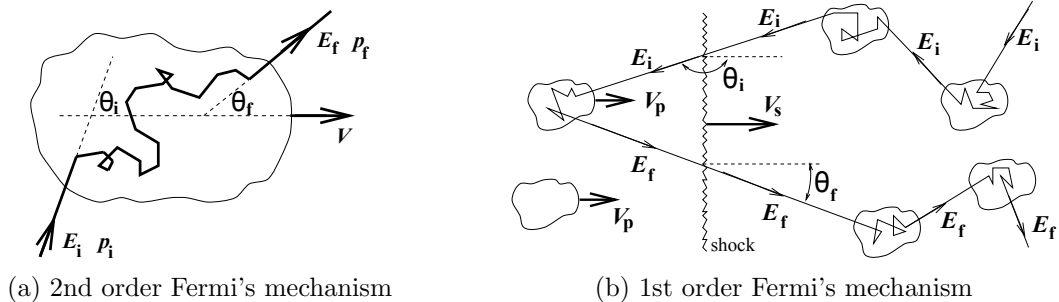


Figure 2.8: Left, scheme of the second order Fermi acceleration mechanism in a moving magnetized cloud. Right first order Fermi acceleration mechanism in strong plane shocks. [36]

2.2.2.2 Sources and Hillas Diagram

In accelerations of the type bottom-up, like Fermi mechanism, the CRs must be constrained within the acceleration region. If the magnetic field is not enough to constrain the CR, then it will escape that region and it won't be further accelerated. Also, the CR interaction with the plasma (like Fermi's) may be finite in time, as supernovae shock waves dissipate after about 10^4 yr. This must be also accounted for, in order to obtain the final spectrum and the maximum possible energy achieved.

The UHECR can have energies that the magnetic field can not constrain in the acceleration region. The Larmor radius (r_L), of a cosmic ray with charge Ze , at a given region, in parsec (pc), is given by:

$$r_L \simeq 110 \frac{E/10^{19} \text{ eV}}{Z B_{\mu G}} \text{ kpc}, \quad (2.17)$$

$B_{\mu G}$ is the magnetic field in units of μG . Including the effect of the characteristic velocity βc of the magnetic scattering centers, the maximum energy reached in a particular region is:

$$E_{max} \approx 2\beta c Z e B r_L = \beta c Z e B L, \quad (2.18)$$

L is the acceleration region size, this holds for strong shocks and very inclined B with respect to the shock normal, and for relativistic particles. For small magnetic field, huge areas are needed to accelerate to high energies while in strong magnetic field the region can be small. This is many times called "Hillas criterion".

There are many structures in the universe candidates to sources of CRs like Supernovae explosions, Large scale Galactic wind termination shocks, Pulsars, AGN and so on (see [37] for more information). These objects are usually summarized in the Hillas diagram on figure 2.9. On the diagram, the objects are distributed according to their size and corresponding maximum CR energy achieved inside. Only a few astrophysical sources seem to satisfy the conditions necessary for acceleration of protons up to 10^{20} eV (red dashed line).

2.2.2.3 Top-Down models

An alternative type of models are called the Top-Downs models. These mechanisms have the advantage that they avoid the need of an accelerator and are based on the decay or annihilation of exotic particles (X-particles) into the Ultra High Energy Cosmic Rays. These X-particles decay in quarks and leptons. The quarks produce jets of hadron, mainly pions (that decay to photons, muons, neutrinos and electrons), and a few percent of nucleons. This would cause a

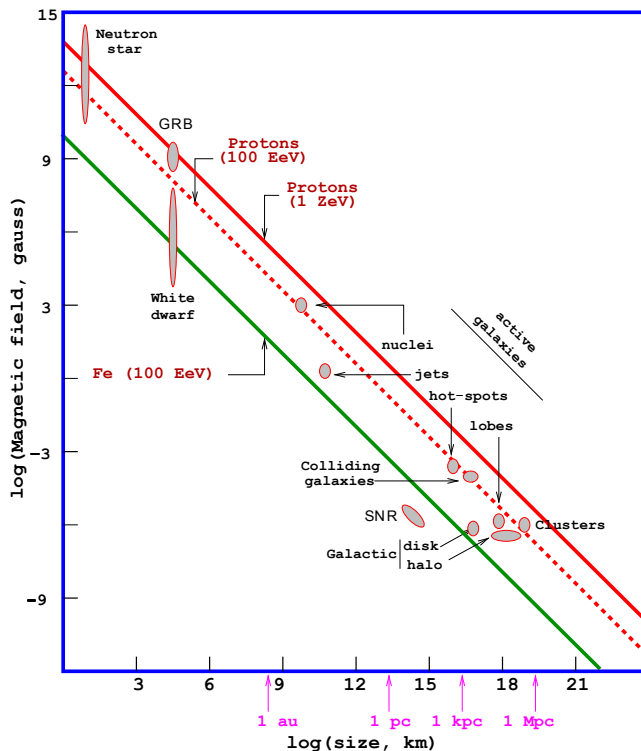


Figure 2.9: Hillas diagram [34] from [37], magnetic and size characteristics of several astronomical objects. Below the diagonal lines, particles couldn't be explained by models processes, at that energy, with the astrophysical objects.

spectrum dominated by photons at high energies. The initial particles would be super-massive with energies far above 10^{20} eV and have a sufficient density to maintain the CR flux. Also, to avoid energy losses, they must decay within a distance around ≈ 100 Mpc. A more detailed description can be seen in [38].

These particles could be Topological Defect model (TD). The Grand Unification Theory predicts the formation of topological defects in early universe like magnetic monopoles, strings and others. These models easily produce particles with masses around $10^{22} - 10^{25}$ eV, since the symmetry breaking scales are typically 10^{21} eV.

Other hypothesis could be the super-heavy dark matter model (SHDM). These super heavy metastable relic particles or wimpzillas, produced in the early stages of the Universe would be part of the cold dark matter and would decay or annihilate producing the CRs.

Another model is the Z-burst, where UHE neutrinos interact with cosmic neutrinos background at the Z-resonance. The Z would then decay into protons, neutrinos and photons. These neutrinos would come from even more energetic particles, which is difficult to explain.

This kind of models often predicts a huge fraction of photons and neutrinos at high energies which was not seen in the Pierre Auger Observatory [39, 40] (see section 3.7.4).

2.2.3 Cosmic Ray Propagation

The Cosmic Rays propagate throughout the universe, from their sources until they reach us. Since they are charged particles, they may be deflected by magnetic fields.

Our galaxy has magnetic fields with typical intensities of some μG . Those fields extend uniformly over scales of the order of a few kpc and the field lines follow the spiral lines. In figure 2.10a, cosmic rays with rigidity $E/Z = 1$ and 10 EeV (dashed lines) are drawn (with solid and dotted

lines respectively), within the BSS-S galactic magnetic field model [41]. The galaxy spirals are in dashed lines. The particles with rigidities of $E/Z = 1$ are trapped in the magnetic field lines with helicoidal trajectories. Thus, they arrive at Earth with almost random trajectories, losing the direction to their source. The gyroradius of a 1 EeV proton in a $3 \mu\text{G}$ is around 300 pc, which is the thickness of the Galactic disc.

A CR nucleus with $E/Z = 10$ EeV in a uniform magnetic field should be in general not very different from a quasi-rectilinear trajectory. And, they should point their source directions.

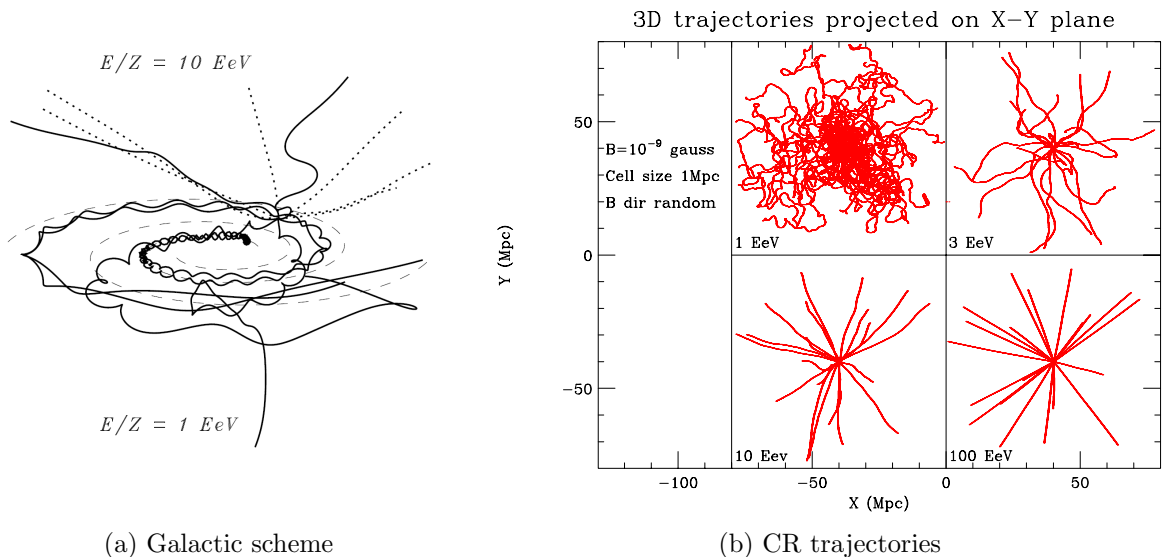


Figure 2.10: Left: Cosmic rays with rigidity $E/Z = 1$ and 10 EeV are drawn (with solid and dotted lines respectively), within the BSS-S galactic magnetic field model [41]. Right: Trajectories of 20 protons emanating from a point for several energies. The trajectories are followed until 40 Mpc, with $B = 1 \mu\text{G}$ in cells of 1 Mpc[42].

Out of the galaxy, a regular intergalactic field is strongly constrained in area and with $B < 10^{-9}\text{G}$, but galaxy clusters may have stronger magnetic fields, coherent over Mpc scales, with $\sim \mu\text{G}$ [43]. In figure 2.10b, several trajectories are plotted for a CR with $E/Z=1, 5, 10$ and 100 EeV, until 40 Mpc. The magnetic field is considered to be $1 \mu\text{G}$ in cell of 1 Mpc. For protons with 1 EeV, the trajectories are basically random. At 10 EeV the trajectories are almost rectilinear and if a proton were produced inside our galaxy with $B \sim 3 \mu\text{G}$ it would have a Larmor radius of 3 kpc (much larger than the galaxy width and the proton would escape from the galaxy). At 100 EeV a proton have basically rectilinear trajectories and the directions on Earth would point to their sources.

2.2.3.1 Energy losses and GZK effect

Cosmic rays with energies of 100 EeV are expected to have rectilinear trajectories across the galaxy. Nevertheless, at those energies, they will interact and lose much of their original energy, so the spectrum has a strong suppression in its flux at these energies (see section 2.2.1). This means that the large scale universe is no longer transparent, becoming opaque to these energies. In 1965, Penzias and Wilson discovered the Cosmic Microwave Background Radiation (CMB)[44], a constant radiation in every direction of the universe which are remnant photons of the Big Bang, whose temperature is currently around 2.7 K. Shortly after, Greisen [45] and Zatsepin and

Kuz'min [46], predicted that, the CRs interacts with the CMB due to photopion production, inducing a cut-off the spectrum of cosmic rays around 5×10^{19} eV, if CRs were protons. This cut-off become known as GZK cut-off. A few months later Hillas, [47] proposed another possible effect of pair production on extragalactic protons above 10^{18} eV.

The most important processes of energy losses are:

- photoproduction of hadrons (eq. 2.19 and 2.20), and
- Bethe-Heitler (BH) production of e^+e^- pairs (eq. 2.21).

Which are given by:

$$p + \gamma_{CMB} \rightarrow p + \pi^0 \quad (2.19)$$

$$\rightarrow n + \pi^+ \quad (2.20)$$

$$\rightarrow p + e^+ + e^- \quad (2.21)$$

There is also adiabatic loss due to the cosmological expansion of the Universe. And, besides CMB, the cosmic rays can interact with infra-red, optical and ultra-violet photons (IR/Opt/UV photons). The difference between IR/Opt/UV photons and CMB is the energy threshold, which is lower for IR/Opt/UV photons. Also, the attenuation length for CMB is much lower, since CMB represents the densest photon background.

Considering cosmic ray protons, for the photoproduction or photopion production, in the laboratory frame, the center of mass energy squared is:

$$s = m_p^2 + 2E_p\epsilon(1 + \beta \cos\theta) , \quad (2.22)$$

where ϵ is the energy of the photon m_p , E_p and β ($\beta^2 = 1 - \frac{m_p^2 c^4}{E_p^2} \simeq 1$) are the mass, energy and speed of the proton. In a head-on collision, the energy threshold to produce a pion is given by:

$$E_{th} = \frac{m_\pi}{4\epsilon} (2m_p + m_\pi) \simeq 6.8 \cdot 10^{16} \left(\frac{\epsilon}{\text{eV}} \right)^{-1} \text{ eV} . \quad (2.23)$$

For CMB photons as a black body with temperature $T \approx 2.725$ K, $\langle \epsilon \rangle \approx 6.34 \cdot 10^{-4}$ eV, the proton cosmic ray energy threshold is about $E_{p/\pi,th} \approx 1 \cdot 10^{20}$ eV. This value can be smaller since the microwave spectrum extends to higher energies (10^{-3} eV), but its density decreases. The mean free path of a nucleon is given by [48, 49, 50]

$$\frac{1}{\lambda_{N\gamma}} = \frac{1}{8\beta E_N^2} \int_{\epsilon_{th}}^{\text{inf}} \frac{n(\epsilon)}{\epsilon^2} d\epsilon \int_{s_{min}}^{s_{max}} (s - m_N^2) \sigma_{N\gamma}(s) ds , \quad (2.24)$$

where $n(\epsilon)$ is the photon density per energy, the energy threshold for the considered nucleon, ϵ_{th} , s_{min} and s_{max} are the squares of minimum and maximum energies in the center of mass system. For the proton-photon, The threshold ϵ_{th} is given by eq. 2.23. The cross-section is $\sigma_{p\gamma}(s)$ and can be considered to be about $\sigma_{N\gamma}(s) = \sigma_{p\gamma}(s) \approx 10^{-28}$ cm² (at the threshold energy). Note that the most important process to the total cross-section is the production of the $\Delta^+(1232)$ resonance, exceeding 0.5 mb [49].

According to [51], the average CMB photons density $\langle n_{CMB} \rangle \simeq 411$ cm⁻³, so approximately, the mean free path $\lambda_{p\gamma} = 1/(\sigma_{p\gamma} \cdot \langle n_{CMB} \rangle) \approx 2.4 \cdot 10^{24}$ cm = 8 Mpc. These values are estimations, for more precise description on the cross-sections and processes see [49, 52, 50].

It usual to define the mean energy loss distance (χ_{loss}) or attenuation length, as the mean free path over the energy loss per interaction, defined as:

$$\chi_{loss} = \frac{E}{dE/dx} = \frac{\lambda(E)}{k(E)}, \quad (2.25)$$

with the mean free path $\lambda(E)$ and the inelasticity k given by:

$$k(E) = \frac{\langle \Delta E \rangle}{E}. \quad (2.26)$$

In pion-photo production, the inelasticity can be considered as $k \approx 0.2$ ($k \approx 0.2 - 0.5$ [50]). Thus, the attenuation length is of the order of some tenths of Mpc, beyond which the proton energy falls below the GZK threshold. This means that the source of the proton cosmic ray should lie within a sphere of that size.

The Bethe-Heitler (BH) production of e^+e^- pairs (eq. 2.21) occurs at a lower energy threshold (due to lower e^+/e^- mass), give by:

$$E_{th} = \frac{m_e(m_p + m_e)}{\epsilon} \simeq 4.8 \cdot 10^{14} \left(\frac{\epsilon}{\text{eV}} \right)^{-1} \text{eV}. \quad (2.27)$$

Considering the CMB, the proton energy threshold is about $E_{p/e^+e^-,th} \approx 4.8 \cdot 10^{17}$ eV. In this process, the inelasticity is much lower, being around $k \approx 10^{-3}$, giving attenuation lengths of around 1 Gpc[50].

The mean energy loss distance, in pion production, is drawn in the figure 2.11a with a red line. For energies above 10^{20} eV, the attenuation length is lower than 100 Mpc decreasing to 15 Mpc with energy, due to pion production. This produce a huge cut-off in the spectrum and means that particles with those energies should lie within tenths of Mpc. The turning point from pion production loss dominance to pair production loss dominance is around $E \approx 6 \cdot 10^{19}$ eV, with a mean energy loss distance of ≈ 1 Gpc. The minimum of the pair production loss length is reached at $E \approx (2 - 4) \cdot 10^{19}$ eV. For $E \leq (2 - 3) \cdot 10^{18}$ eV continuous losses due to the expansion of the universe dominate[52]. The pair production is weaker than the pion production, however it might be important to explain some spectrum features in the region where it is dominant [53]. There is also interaction between cosmic rays and IR (infra-red), optical and UV photons (IR/Opt/UV) and Cosmic Universal Radio Radiation (URB) photons. It is much smaller than the other contributions (see green lines in the figure 2.11a).

In figure 2.11b, the attenuation length is drawn for several different nuclei. The different channels can highly vary from one nucleus to another, some nuclei, for instance, being more likely to emit a proton or sometimes an α particle depending on the details of its nuclear structure [52]. A nuclei of mass A undergoes photo-disintegration and pair production, with CMB and IR/Opt/UV photons, according to:



The threshold energy for the processes increase, since energy is shared between the nucleons. The inelasticity goes with $\sim 1/A$ and the cross section increases with Z^2 . So the loss length would be smaller than in the proton case. If neutrons appear, they interact similarly as the proton, but if the energy is less than around $\sim 8 \cdot 10^{20}$, they will decay ($n \rightarrow pe^- \bar{\nu}_e$). The line

corresponding to the neutron decay is in grey, in figure 2.11b. The neutron range of propagation is $R_n = \tau_n \frac{E}{m_n} \simeq 0.9 (E/10^{20} \text{eV}) \text{ Mpc}$, with the laboratory lifetime $\tau_n \simeq 888.6 \pm 3.5 \text{ sec}$. The neutron decays are important for the production of PeV neutrinos.

The actual value of χ_{loss} depends on the energy and density of the photon background which evolves with redshift, that's why the lines are drawn for redshift $z = 0$, excluding this effect.

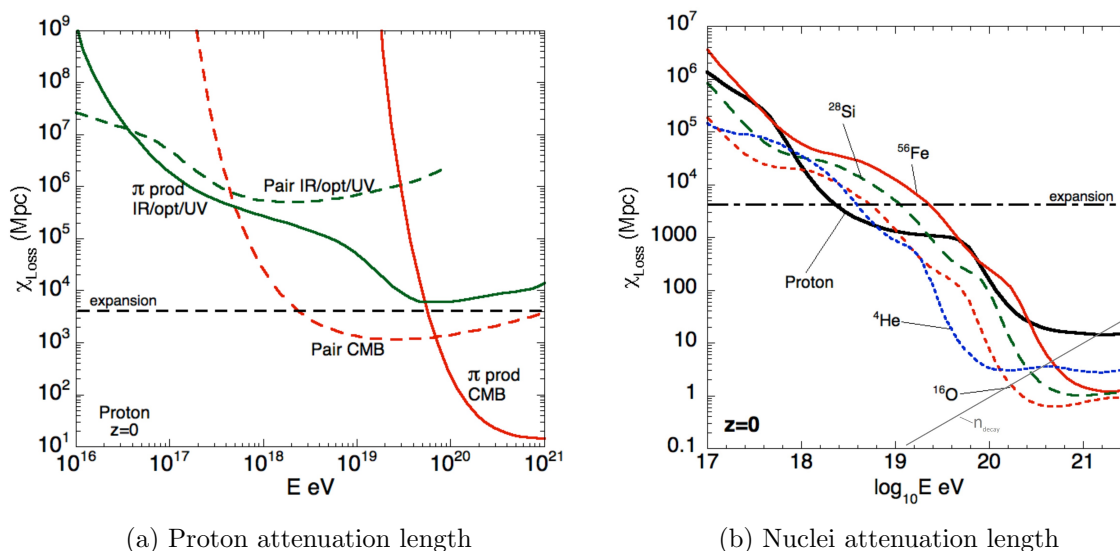


Figure 2.11: left: energy loss length χ_{loss} evolution for proton cosmic ray at $z=0$. Different energy loss processes are displayed, pair production and pion production in full and dashed lines. In green and red are the interaction with IR/Opt/UV photons and CMB photons. Losses due to adiabatic expansion in black dotted line [52]. Right: Comparison of the attenuation length of different nuclei at $z=0$ [52].

In figure 2.12a, the energy loss of several protons above the GZK limit, along their trajectories is plotted. From there, if a proton is detected with energy above the GZK cutoff, its source must lie within less than 100 Mpc, or its energy would fall below the cut-off.

The photons also have a cutoff through the interaction with CMB. The dominant process is pair production:

$$\gamma + \gamma_{CMB} \rightarrow e^+ + e^-, \quad (2.29)$$

and the energy threshold is given by:

$$E_{\gamma\gamma_{CMB,th}} = \frac{m_e^2}{\epsilon} \simeq 2.6 \cdot 10^{11} \left(\frac{\epsilon}{\text{eV}} \right)^{-1} \approx 2.6 \cdot 10^{14} \text{ eV}. \quad (2.30)$$

In figure 2.12 right, the attenuation length for high energy photons with IR (infra-red), CMB (cosmic microwave) and URB (universal radio) backgrounds is plotted. The photo fluxes are extremely suppressed around $\sim 10^{15} \text{ eV}$. The high energy photons produces pairs that by their turn undergo Inverse Compton Scattering (ICS) producing a photon which carries most of the initial energy and can produce a secondary electron-positron pair. This develops an electromagnetic cascade that produces photons with energies below the threshold. At that point losses from IR dominates until ending up with photons around $\sim 100 \text{ GeV}$. See photon fluxes in section

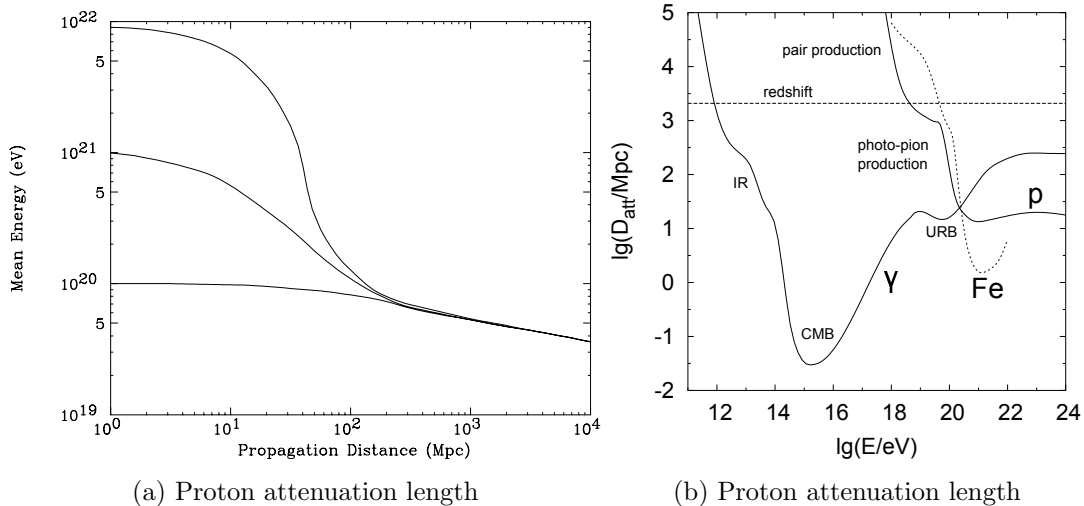


Figure 2.12: Left: The mean energy of a proton moving through the universe with CMB, with 3 initial energies[54]. Right: attenuation length for high energy photons with IR (infra-red), CMB (cosmic microwave) and URB (universal radio) backgrounds[55].

3.7.4.

There are several simulation codes for Ultra High Energy Cosmic Ray propagation that use all these interactions, several composition scenarios and sources to try to obtain the measured spectrum and other CRs results. For further information see for instance the simulation codes SimProp [56], CRPropa 2.0 [57] and SOPHIA [49].

2.3 Extensive Air Shower (EAS)

In 1938, Pierre Auger and Roland Maze showed that cosmic rays (CRs) separated by more than 20 m were simultaneously detected in coincidence, proving that they are originated from a single high energy cosmic ray. A year after, they already had proven the existence of particles up to 10^{15} eV [12] as shown in the beginning of the chapter. At these energies, the CR flux is very small and direct detection is not possible. Huge areas of detection would be needed to have some events. In this way, the atmosphere is used as the detector. It acts as a calorimeter² where the CR disintegrates forming a cascade of particles.

A Cosmic Ray enters the atmosphere and interacts with air nuclei, typically with nitrogen or oxygen. In this hadronic interaction several particles are produced, since they still are highly energetic, they will interact again (or decay) producing more particles and so on, in a cascade of particles called Extensive Air Shower (EAS). A schematic representation of the EAS development is drawn on the figure 2.13.

The cascade develops through different interaction processes (see fig. 2.13) within three main components:

²The atmosphere provides approximately a vertical thickness of 26 radiation length for electron and 15 interaction length for a proton, very similar to the values for the CMS at LHC. The CMS electromagnetic and hadron calorimeter have about 25 radiation lengths and 11 interaction lengths respectively.

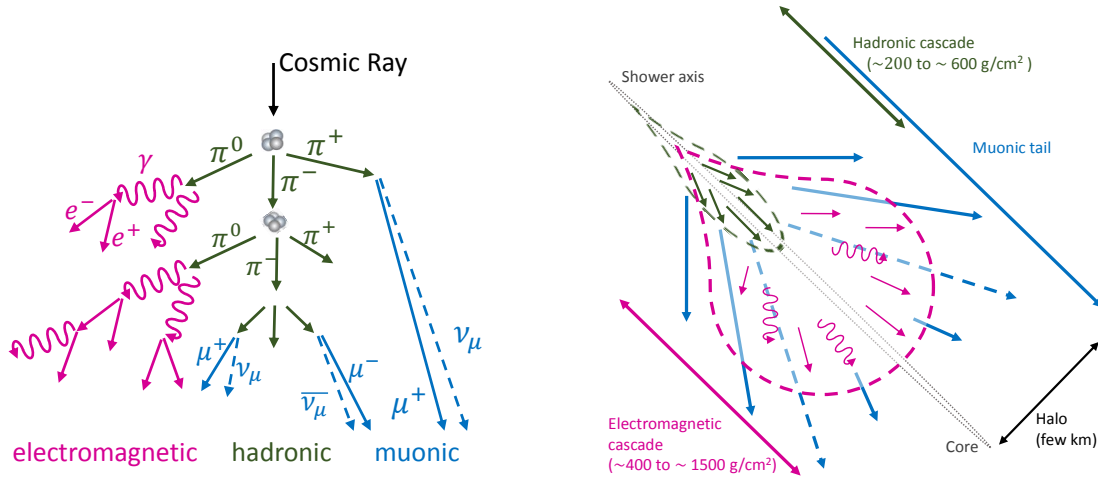


Figure 2.13: Schematic view of an Extensive Air Shower (EAS).

- **Hadronic component:** the primary particle interacts with atmospheric nuclei producing high energy hadrons that interact again or decay giving a new generation of particles. It is close to the shower axis (direction) and the majority of produced hadrons are mesons, mainly pions and a few Kaons.
- **Electromagnetic component:** in each hadronic interaction 1/3 of the parent particle energy goes into π^0 , that decay into photons originating a electromagnetic cascade.
- **muonic component:** approximately 2/3 of the energy goes to charged pions. When they have lower energy, they will decay (also the K) into muons and neutrinos. Most of the muons arrive at the ground. Since both muons and neutrinos are unlikely to interact with the atmosphere, it means that the energy carried by these particles is undetectable (on the atmosphere).

Usually the muonic and neutrinos part of the cascade is called "hard" component, while the electromagnetic and hadronic part are called "soft" component. The cascade develops with these components and the particle production growth continue, until the average energy lost by ionization by secondary particles, becomes of the same order of the average energy needed to produce a new particle generation. After that, the particles produced in each generation decreases down to zero and the remaining particles are absorbed in atmosphere. The evolution of the electromagnetic particle number in the cascade can be seen on the figure 2.14 in red.

A 10^{11} GeV proton shower reaches the ground with around $\sim 10^{11}$ secondaries with energy above 90 keV in the region extending from 8 m to 8 km from the shower core. In these particles, 99% are photons, electron and positrons, with a typical ratio of γ to e^+e^- of 9 to 1 and with a mean energy of 10 MeV [58]. The remaining are hadrons, muons and neutrinos. At this development stage, around 90% of the CR energy has been dissipated through the electromagnetic component (see figure 2.14, the Earth ground corresponds roughly to 1000 g/cm^2).

The shower propagates around the shower axis (direction of the primary particle). The point it hits the ground is called shower core. At this point, some definitions should be introduced. The number of interactions that had occurred in the shower depends on the matter traversed and not the altitude (since the atmospheric density changes with altitude). So, the good variable

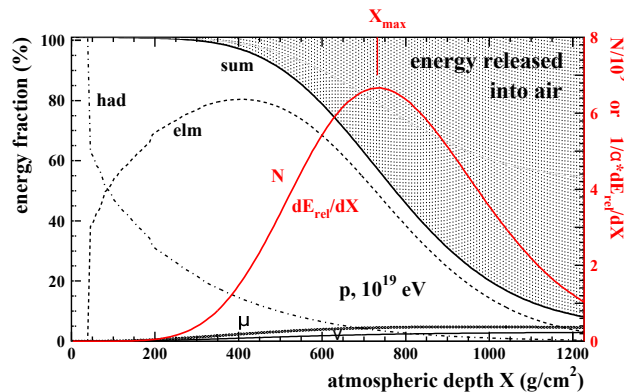


Figure 2.14: Energy flow in EAS for each component, in the left scale, the gray region corresponds to the energy released into the air. In red (and red right scale) is the number of particles $N(X)$ in the cascade with the X_{max} indicated. Taken from [59].

is the slant depth X measured in gcm^{-2} :

$$X_v = \int_h^\infty \rho_{atm}(z) dz, \quad (2.31)$$

ρ_{atm} is the atmospheric density, which is a function of the altitude h and the integration is done from the point to the top of the atmosphere (here with infinity). X_v denotes the vertical depth, if the shower is inclined, the depth can be considered to be $X \sim X_v / \cos \theta$. For very inclined showers, this is not valid and the Earth curvature should be taken into account. The ground depth may vary from around 1000 g/cm^2 (vertical) to 36000 g/cm^2 (horizontal).

The shower particle number (shower size) as a function of the traversed atmospheric depth X , the longitudinal profile, is denoted by $N(X)$. The point where it reaches the maximum number of particles is the X_{max} (in g/cm^2). Finally, the particle density at distance r from shower axis, in the plane perpendicular to the axis, the lateral distribution, is usually expressed with $\rho(r)$.

2.3.1 Electromagnetic Component

The electromagnetic component of any EAS has essentially the same behaviour as an EAS induced by a photon cosmic ray. This component begins fundamentally in the π^0 produced in the hadronic interaction (in the case of nuclei cosmic rays) and by the interaction of γ particles (from those interactions or as a primary cosmic ray). It is composed by e^- , e^+ and γ that feed each other.

The π^0 meson has a very short lifetime and decay into $\pi^0 \rightarrow \gamma + \gamma$ (with 98.798% branching ration) or into $\pi^0 \rightarrow e^+ + e^- + \gamma$ (with 1.198% branching ration).

The two dominant processes that contribute to the development of an electromagnetic shower are e^+e^- pair creation and bremsstrahlung radiation (see the scheme on figure 2.15). Photons will convert into e^+e^- pairs, these by their turn will radiate photons by bremsstrahlung feeding the cycle in a chain reaction, while there is enough energy. These two processes have similar radiation length (λ) with $\lambda|_{brem} \approx \lambda|_{pair}$, with $\lambda|_{pair}$ around 37 g/cm^2 [51].

In each cycle the particle number increases and the energy of each one decreases, until the energy is low enough and the main mechanism of energy loss is through ionization and collisions, rather than by Bremsstrahlung or pair production. The atmosphere will absorb the particles and the cascade begins to decrease. The critical energy ξ_c for the absorption of particles is roughly defined as the energy at which the ionization loss is equal to the bremsstrahlung loss, from [60]

$$\xi_c = \frac{710\text{MeV}}{Z_{eff} + 0.92} \approx 86\text{MeV}. \quad (2.32)$$

Where is the $Z_{eff} = 7.3$ is the effective atomic charge [61]³. A similar definition is given by Berger and Seltzer [62].

The electromagnetic component descends mainly from the π^0 . For a photon primary particle, the shower would correspond fundamentally to this component. The Bethe-Heitler[63] cross section for pair production, for UHE 10 EeV is about 500 mb [64]. Moreover, the photonuclear cross section for these energies is about 1 mb[26, 64], and extrapolations to other more exotic scenarios gives ~ 10 mb[64, 65], so the ratio of the photohadronic cross-section to the pair production cross-section will be,

$$Q = \frac{\sigma_{\gamma \rightarrow \text{hadrons}}}{\sigma_{\gamma \rightarrow e^+e^-}} \simeq \frac{1(10)}{500} \simeq 0.2\%(2\%), \quad (2.33)$$

where it can be seen, that the hadronic interactions in γ showers are unlikely and photons produce mainly electromagnetic cascades. Anyhow, if the first photon interaction is hadronic, the shower development will be more similar to the proton shower [64].

2.3.1.1 Heitler model

The first models for the EAS were proposed by Rossi and Greissen around 1941. But most of the main features of EAS may be deduced by the Heitler toy model [63](see also [66]).

In Heitler model (figure 2.15), at each step, electrons and positrons radiate a photon via bremsstrahlung, and photons split into a e^+e^- pair. The steps happens after travelling an interaction or splitting length, $d = 2 \ln \lambda_r$, with the radiation length $\lambda_r = 37 \text{ g/cm}^2$ in air. In each splitting, a particle split into two new particles, so the particle number increase by a factor of 2 and the energy is equally divided by the new particles. The number of particle at step n is $N = 2^n$ and the energy is $E_n = E_0/2^n$. The process of particle multiplication continues until the energy of the particles falls below a critical energy, ξ_c^e . It is supposed that in the process of bremsstrahlung, the photon and $e^-(e^+)$ share the initial energy of the $e^-(e^+)$. The cascade is one-dimensional and all splitting occur after the same distance d. This picture does not capture all the details of EM showers, but is able to account for three important features.

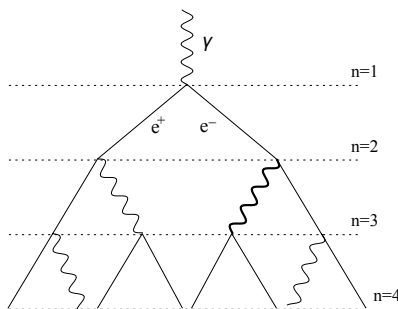


Figure 2.15: Schematic representation of the Heitler model, for an electromagnetic shower, initiated by a photon. At each level n the number of particles duplicates by bramstrahlung or pair production.

³At high altitude the atmosphere consists of 78.09% N_2 , 20.95% O_2 and 0.96% other gases. It can be considered as an homogeneous gas with $Z_{eff} = 7.3$ and $A_{eff} = 14.6$.

The number of particles at the shower maximum is proportional to the energy of the primary particle.

$$\begin{aligned} E_0 &= \xi_c^e \cdot N_{max} \\ N_{max} &= E_0 / \xi_c^e. \end{aligned} \quad (2.34)$$

The depth of maximum shower development (X_{max}) is logarithmically proportional to E_0 . The maximum depends on the maximum number of interaction n_{max} to reduce the energy per particle into ξ_c^e .

$$\begin{aligned} N_{max} &= 2^{n_{max}} \\ n_{max} &= \ln(E_0 / \xi_c^e) / \ln 2 \\ X_{max} &= \lambda_r \ln 2 \cdot n_{max} = \lambda_r \cdot \ln(E_0 / \xi_c^e). \end{aligned} \quad (2.35)$$

The elongation rate is the evolution of X_{max} with energy given by:

$$\Lambda_{10} \equiv \frac{dX_{max}}{d \log_{10} E_0} = 2.3 \lambda_r \simeq 85 \text{g/cm}^2. \quad (2.36)$$

The predicted number of particles at the shower maximum is overestimated by a factor 2-3 and the ratio of electrons to photons is overestimated by a factor 10-12. These discrepancies appear because the absorption of particles above the critical energy is not accounted for, multiple photons are often radiated during bremsstrahlung, and electrons lose energy much faster than photons do.

Nevertheless, the photon elongation rate curve estimated is quite similar to the photon curve until $E_0 \sim 10^{17}$ eV (see figure 2.16). At higher energies the photon showers start to get more deeply penetrating due to the appearance of small hadronic showers. At energies around $E_0 \sim 10^{19}$ eV the X_{max} (and λ_r) increases dramatically due to the Landau-Pomeranchuk-Migdal effect (LPM)[67, 68]. The effect suppresses the cross sections for pair production and bremsstrahlung at high energies (above roughly 10 EeV) or high matter densities due to the interference from successive scattering centres. At the highest energies, the photons can interact with Earth's magnetic field with pair production, which make the photon produce the cascade before reaching the atmosphere, reducing the average photon showers X_{max} . This is commonly known as pre-shower effect.

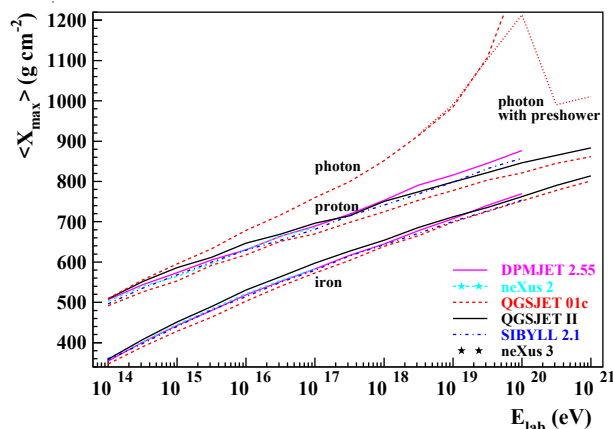


Figure 2.16: Elongation rate curves for shower induced by different primary composition and different hadronic models using MC simulations (from [64]).

2.3.1.2 Electromagnetic Longitudinal Parametrization

The Heitler model is rather simplistic and is not enough to completely describe the longitudinal profile of a shower development. It is not easy to obtain an analytical solution of the cascade due to the statistical fluctuations. Around 1952, Greisen proposed an analytical solution of the longitudinal profile for the number of electrons, a function of depth X , given by [69]:

$$N_e = \frac{0.31}{\sqrt{\beta_0}} e^{X(1-3/2 \ln s)}, \quad (2.37)$$

where $\beta_0 = E_0/\xi_c^e$ and s is the shower age given by:

$$s = \frac{3X}{X + 2X_{max}}. \quad (2.38)$$

The shower age is 1 at the X_{max} depth and is 0 when the shower development begins.

2.3.1.3 Electromagnetic Lateral Parametrization

The shower development also gives rise to a transverse or lateral distribution of particles. The electromagnetic particles have multiple Coulomb Scattering in the nuclei of the atmosphere, this causes them to gain transverse momentum. The lateral development of the cascades was parametrized by Nishimura, Kamata and Greisen equation (NKG) [70, 69] and takes the form for pure electromagnetic showers:

$$\rho(r) = c(s) \frac{N_e}{r_0^2} \left(\frac{r}{r_0} \right)^{s-2} \left(1 + \frac{r}{r_0} \right)^{s-4.5}, \quad (2.39)$$

where $c(s) = 0.366.s^2 (2.07 - s^{1.25})$, $\rho(r)$ is the density of particles with respect to the distance r of the axis shower. N_e is the total number of electrons, s is the age parameter and r_0 is the Molière radius⁴. In such showers, only about 10% of the energy is contained in particles outside the cylinder with radius r_0 .

2.3.2 Hadronic Component

The hadronic component originates from the interaction of primary nuclei (such as protons and iron and very rarely of photons) with atmospheric nuclei. These interactions are the major source of uncertainty in the analysis of EAS, since the energies of the CR are several orders of magnitude above the accelerators data. The interaction of a proton with the atmosphere can be seen as $p + p \rightarrow p + p + N(\pi^0 + \pi^+ + \pi^-)$ and the production of K , Λ , η , Ω , Σ ... can be neglected, because their quantity is small compared to pions. In each generation, on average, the neutral pions carry one third of energy and charged pions about 2/3.

2.3.2.1 Modified Heitler model

In a similar approach to the Heitler model for photon showers, the model can be modified for nuclei induced showers with hadronic component (see [66]). A scheme of this version can be seen on the figure 2.17. An hadronic particle interacts with the atmosphere producing N_{mult}

⁴The Molière radius, r_0 or $r_{Moliere}$ is a characteristic constant of a material giving the natural transverse scale set by multiple scattering. Inside this radius should be on average 90% of the shower's energy deposition. It can be approximated by $r_0 = 0.0265\lambda_r(Z + 1.2)$ (see the review [71]). It depends on the material density (which means that depends on the atmospheric altitude), at sea level is around 78 m.

new particles. For simplicity, only pions shall be considered and so, 2/3 would be charged pions and 1/3 would be neutral pions.

The neutral pions quickly decay in $\pi^0 \rightarrow \gamma\gamma$, feeding the electromagnetic sub-showers (equals to the showers described before).

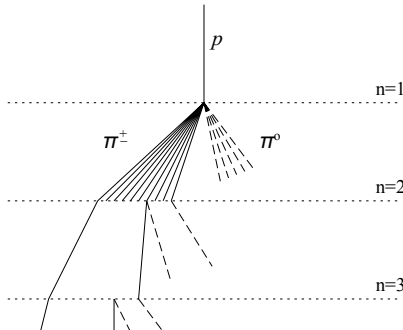


Figure 2.17: Schematic view of a hadronic shower with the modified Heitler model. The dashed lines represent π^0 , while the full lines indicate charged pions. At each step n , the particle number increases by the factor N_{mult} (multiplicity).

The 2/3 charged pions interacts again with air molecules in a similar way producing again new particles, 1/3 neutral pions and 2/3 charged pions that feed the cycle until their energy falls below the critical energy. The critical energy is the energy at which the pion decay probability overcomes the interaction probability. Below that energy, the charged pions should decay into muons. Each new interaction happens at step with distance $d = \lambda_I \ln 2$. The interaction length (λ_I) is assumed to be constant, with $\lambda_I \approx 120\text{g/cm}^2$. This is a fairly good approximation for interactions in the range 10-1000 GeV[66].

The critical energy for the pions ξ_c^π can be approximated to be 20 GeV. Note that this cut depends on the energy of the primary, since the pions decay length in depth depends on the atmospheric density. So for a primary with $E_0 = 10^{14}$ eV the $\xi_c^\pi \sim 30$ GeV (higher in altitude) while for $E_0 = 10^{17}$ eV, $\xi_c^\pi \sim 10$ GeV (see also section 2.3.3).

In each step, N_{mult,π^\pm} charge pions are produced. After n interactions, or atmospheric layers, there are $N_{\pi^\pm} = (N_{mult,\pi^\pm})^n$ total charged pions. N_{mult,π^\pm} is the multiplicity of charge pions. These pions carry a total energy of $(2/3)^n E_0$. Then, the energy per pion is $E_\pi = (2/3)^n E_0 / (N_{mult,\pi^\pm})^n = E_0 / (3/2 N_{mult,\pi^\pm})^n$. The critical energy is reached at the step $n_c = \frac{\ln(E_0/\xi_c^\pi)}{\ln(3/2 N_{mult,\pi^\pm})}$. In this way, some predictions can be made.

The muon number at the shower maximum is given by:

$$N_\mu = N_{\pi^\pm} = \left(\frac{3}{2} N_{mult,\pi^\pm}\right)^{n_c} = \left(\frac{E_0}{\xi_c^\pi}\right)^\beta. \quad (2.40)$$

The β parameter of the model can be given by:

$$\beta = \frac{\ln(N_{mult,\pi^\pm})}{\ln\left(\frac{3}{2} N_{mult,\pi^\pm}\right)}. \quad (2.41)$$

Assuming an hadronic interactions multiplicity between $N_{mult} = 10 - 100$, the β parameter would range between $\beta = 0.84$ and 0.92 [72]. The X_{max} can also be derived, in a similar way as for electromagnetic Heitler model. The X_{max} continues to be in the electromagnetic component, but this time it is related with the pion interactions, however the radiation length of the electromagnetic shower will be considered for the respective component.

The depth of maximum shower development can be written as, an EM shower, initiated only in the first generation, with energy $\frac{1}{2}E_0/(\frac{3}{2}N_{mult,\pi^\pm})$ starting at depth X_0^p :

$$X_{max}^p = X_0^p + \lambda_r \ln \left(\frac{E_0/\xi_0^e}{3N_{mult,\pi^\pm}} \right) = X_{max}^\gamma + X_0^p - \lambda_r \ln(3N_{mult,\pi^\pm}), \quad (2.42)$$

X_0^p is the first interaction depth for proton primary in the atmosphere, it can be approximately by $X_0^p = \lambda_I \ln 2 = (61 \text{ gcm}^{-2}) (1.0 - 0.1 \ln[E_0/\text{PeV}]) \ln 2$ [66]. The main difference to the equation 2.35 is the multiplicity and the first interaction length, making the X_{max} for photons more penetrating (see figure 2.16). Using only the first interaction will certainly underestimate X_{max} , since it neglects the following sub showers, but it will capture well the elongation rate Λ^p (the rate of increase of X_{max} with E_0).

The superposition model considers that an iron shower is equal to 56 proton showers with energy $E_0/56$. Thus, equation 2.42, can be modified to compare protons and iron showers.

$$X_{max}^I = X_0^I + \lambda_r \ln \left(\frac{E_0/\xi_0^e A}{3N_{mult,\pi^\pm}} \right) \propto \ln \left(\frac{E_0}{A} \right) \sim X_{max}^p - \lambda_r \ln A. \quad (2.43)$$

Proton showers are more penetrating than iron, because X_0^p is higher than X_0^I and also because the logarithm $\frac{E_0}{A}$ for iron is smaller. the iron X_{max} is higher than for proton showers by $\lambda_r \ln 56 = 150 \text{ gcm}^{-2}$ at all energies, similar to the simulations.

The muon number in a shower from a nuclei A is $N_\mu = N_\mu^p \cdot A^{0.15}$. This means that an iron shower will have $(56)^{0.15} = 1.8$ times more muons than protons.

This very simple model don't consider the inelasticity effect on the interactions. In each hadronic interaction a significant fraction of the energy is carried by a leading particle. This leading can carry energy further deep, with the respective sub shower developing later. In this way, it can lead to a significant increase in the X_{max} and a decrease in the muon number. Nonetheless, it can gives us a remarkably good view of the shower parameters.

The elongation rate for a proton initiated shower is

$$\Lambda^p = \Lambda^\gamma + \frac{d}{d \log_{10} E_0} [X_0^p - \lambda_r (3N_{mult,\pi^\pm})] \simeq 58 \text{ g/cm}^2 \text{ per decade}. \quad (2.44)$$

This value is lower than for photons due to increasing multiplicity N_{ch} and increasing cross-section (decreasing X_0). The result agrees with the Linsley's elongation rate theorem, which pointed out that Λ^γ for electromagnetic showers represents an upper limit to the elongation rate for hadron showers. The elongation rate is lower for hadronic shower than for photon shower. In figure 2.16, the X_{max} is plotted for photons, protons and irons, for several energies, where the previous behaviours can be seen.

2.3.2.2 Longitudinal Parametrization

As said before, the Heitler model is rather simplistic. The model does not treat the loss of particles as they range out, or even the particle absorption before X_{max} . A better parametrization was needed, and despite the longitudinal profile can not be achieved analytically, Gaisser and Hillas proposed a parametrization for the average number of particles, N , for an hadronic shower with a primary energy E_0 given by [73]

$$N = S_0 \frac{E_0}{\epsilon} e^{t_m} \left(\frac{t}{t_m} \right)^{t_m} e^{-t}, \quad (2.45)$$

with $S_0 = 0.045$, $\epsilon = 0.074$ GeV and $t = X/\lambda$ is the average number of interaction at the point X considering a characteristic length parameter λ . The shower maximum depth in units of radiation length is $t_m = \frac{X_{max}}{\lambda}$.

This parametrization was very successful describing the longitudinal shower profiles. Nevertheless, currently, a more useful parametrization derived from the previous is consider, since it doesn't rely on so many parameters. It is:

$$N(X) = N_{max} \left(\frac{X - X_0}{X_{max} - X_0} \right)^{\frac{X_{max} - X_0}{\lambda_{GH}}} e^{-\frac{X_{max} - X}{\lambda_{GH}}}, \quad (2.46)$$

where N_{max} is the maximum number of particles in the shower maximum at $X = X_{max}$ in depth. X_0 is an effective first interaction point, since it can be negative. The Parameter λ gives an indication about the interaction length. This function is known as *Gaisser-Hillas function* with 4 free parameters. In figure 2.18 left, some longitudinal profiles are drawn. It can be seen that they look quite different (even within the same energy and composition, due to natural fluctuations). This profile is normally applied to the electromagnetic particle number, $N(X)$, however, instead of using the $N(X)$, it could be applied to the $dE/dX(X)$, since they are proportional.

2.3.2.2.1 Universal Shower Profile

Figure 2.18 left, shows some shower profiles with the same energy. They look very different from each other, some of them developed more or less quickly and have a bigger or smaller X_{max} . They also have different N_{max} , since only the integral $\int dE/dX_{max} dX$ should be equal (for the same energy).

The longitudinal profiles are very similar however, if the shower is normalized to N_{max} and translated with X_{max} (see figure 2.18 right). The Gaisser-Hillas function can be rewritten as a function of $N' = N/N_{max}$ and $X' = X - X_{max}$ ($X'_0 = X_0 - X_{max}$) with the form:

$$N' = \left(\frac{X'}{X'_0} - 1 \right)^{\frac{X'_0}{\lambda}} \exp\left(-\frac{X'}{\lambda}\right). \quad (2.47)$$

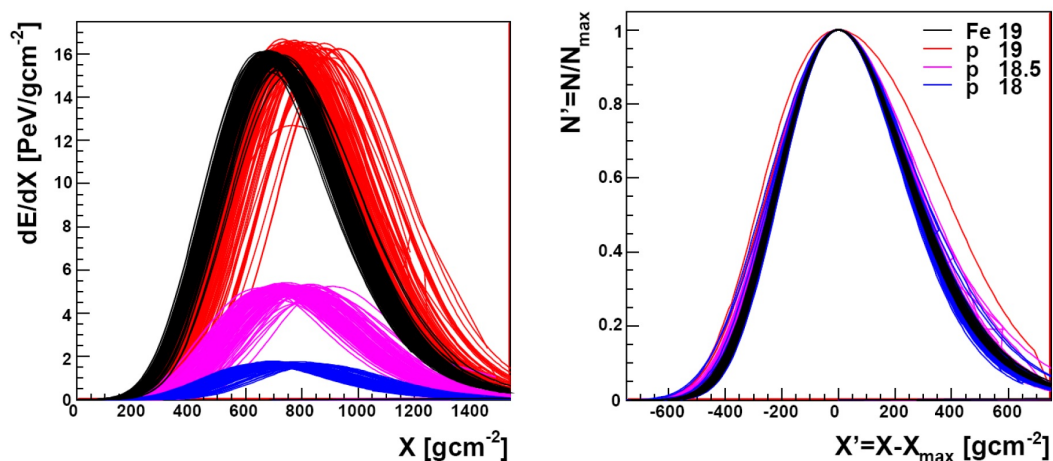


Figure 2.18: Left: Normal longitudinal profile as function of $X[\text{g/cm}^2]$. Right: longitudinal profile normalized to N_{max} and translated with X_{max} (Universal Shower Profile) as function of $X' = X - X_{max}$.

In this mode, the profile is known by Universal Shower Profile (USP) (see [74, 75, 76]). In figure 2.18, the same events are drawn in USP profiles and normal profiles mode. In the USP, most of the showers present the same characteristics and a few have different shapes (wider or thinner) and even less have a very different behaviour.

The USP equation can be expanded around $X' \sim 0$ (around the X_{max}) giving [75]:

$$\begin{aligned}
 N' &\sim \exp\left(-\frac{X'^2}{2|X'_0\lambda|}\right) \prod_{n=3}^{\infty} \exp\left(\frac{1}{n} \frac{X'_0}{\lambda} \left(\frac{X'}{X'_0}\right)^n\right) \\
 &= \exp\left(-\frac{1}{2}\left(\frac{X'}{L}\right)^2\right) \prod_{n=3}^{\infty} \exp\left(\frac{R^{n-2}}{n} \left(-\frac{X'}{L}\right)^n\right) \\
 N' &= \left(1 + \frac{RX'}{L}\right)^{R-2} \exp\left(-\frac{X'}{LR}\right).
 \end{aligned} \tag{2.48}$$

With the Taylor expansion, it seems like a Gaussian with width $L = \sqrt{|X'_0\lambda|}$ and distorted by $R = \sqrt{\lambda/|X'_0|}$ (see figure 2.19) with the effect of different R and L in the profiles). These parameters are less correlated than the previous X_0 and λ (see ref. [75]) and L will be something like the width and R will be a rotation of the shower (see fig. 2.19).

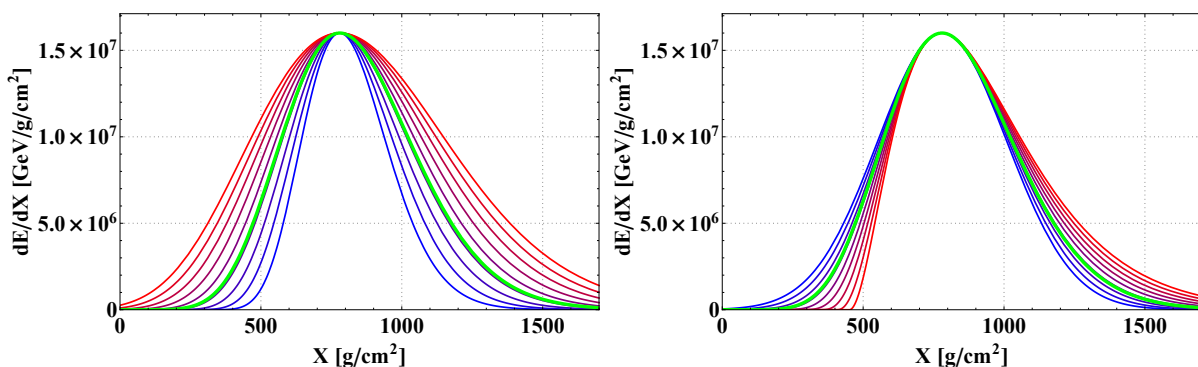


Figure 2.19: In green is the GH equation with the parameters $L = 250 \text{ g/cm}^2$ and $R = 0.25$ in dashed green. In right, the evolution of the profile from $L = 150 \text{ g/cm}^2$ (blue) to $L = 350 \text{ g/cm}^2$ (red) with constant $R = 0.25$. In left, evolution from $R = 0.01$ (blue) to $R = 0.70$ (red) with constant $L = 230 \text{ g/cm}^2$.

The L parameter will be related with the electromagnetic interactions and it should not vary much either with primary particle type or its energy. The energy deposited (dE/dX) along the shower is proportional to the number of particles N , so the integral of the distribution is used to compute the electromagnetic shower energy. The integral of an USP is:

$$\begin{aligned}
 E/\frac{dE}{dX}_{max} &= \lambda A^A \exp(A) \Gamma(A+1) \\
 E/\frac{dE}{dX}_{max} &\sim \lambda \sqrt{2\pi A} = \sqrt{2\pi} L,
 \end{aligned} \tag{2.49}$$

where $A = R^{-2}$ and the approximation results in a small underestimation of the integral ($< 1\%$ for $R < 0.35$ and $\sim 9\%$ for $R = 1$ [75]). The variable R , for the rotation of the shape is related with the rate at which the energy is transferred from hadronic to the electromagnetic component. At the same energy, a heavier nucleus will interact sooner and more efficiently than a proton, so R will be bigger for iron, which means that the hadronic component transforms more

quickly into electromagnetic component. An interesting feature is that the R can be related with $\Delta_0 = X_{max} - X_0$, where X_0 is the the depth of the first interaction. So Δ_0 decreases linearly as R increases (see [74]). R can be used in a event-by-event basis to study the showers and the first interactions.

2.3.2.3 Lateral Parametrization

The transverse shower profile of a shower induced by a hadron is parametrize using a modified NKG equation (from equation 2.39). It is needed to account for the transverse momentum gained in the hadronic interaction and to account for the presence of an hadronic component which feeds the electromagnetic bulk shower. Greisen[69] suggest the modified NKG given by:

$$\rho(r) = \frac{C_1(s)N_e}{2\pi r_0^2} \left(\frac{r}{r_0}\right)^{s-2} \left(1 + \frac{r}{r_0}\right)^{s-45} \left[1 + C_2 \left(\frac{r}{r_0}\right)^\delta\right], \quad (2.50)$$

where δ is a free parameter, r_0 is the Molière radius and the other constants corresponds to same as in equation 2.39.

There are some differences in the lateral shape for different primaries, but at energies around 10^{19} eV the lateral profile gets almost universal. From a Monte Carlo Simulation [77], a cumulative function of the lateral distribution was obtained, being given by⁵

$$F\left(\frac{r}{r_0}\right) = 1 - \left[1 + a(s)\frac{r}{r_0}\right]^{-b(s)}, \quad (2.51)$$

where the parameters $a(s)$ and $b(s)$ depends only on the shower age and were fitted to the simulation results with a polynomial expressions given by:

$$\begin{aligned} a(s) &= 5.515s^4 - 28.925s^3 + 60.056s^2 - 56.718s + 22.331 \\ b(s) &= -1.039s^2 + 2.251s + 0.676 . \end{aligned} \quad (2.52)$$

2.3.2.4 Low energy hadronic models

In the air shower simulation programs, below an energy threshold in the range from 80 GeV to 500 GeV, the interactions are simulated by low energy interaction models, like FLUKA[78], GHEISHA[79] or UrQMD[80], and above that energy by high energy interaction models described in section 2.3.2.5.

The longitudinal shower observables like X_{max} and $RMS(X_{max})$ do not change too much with the low energy hadronic models, since they depend mainly on the proprieties of the first interactions. At low energies, the particle statistics is to high to change considerably the X_{max} behaviour, while the first interaction at high energies define the X_{max} nature.

Nonetheless, the low energies models are more important to predict the total number of secondary particles at latter stages of the shower development. The models can have a big impact on the number of particles measured at the ground.

In figures 2.20a and 2.20b, the lateral density of μ^\pm and e^\pm respectively, are compared between GEISHA and FLUKA models. The large dependence on the distance to the shower axis is mainly due to different transverse momentum distributions predicted by the models. At radius larger than 1000 m, GEISHA predicts 5-20% more muons than FLUKA (which correspond to the region relevant to Auger). The number of e^\pm is not so problematic, but differences can arrive to 10%.

⁵this parametrization is known in The Pierre Auger Observatory as Gora parametrization.

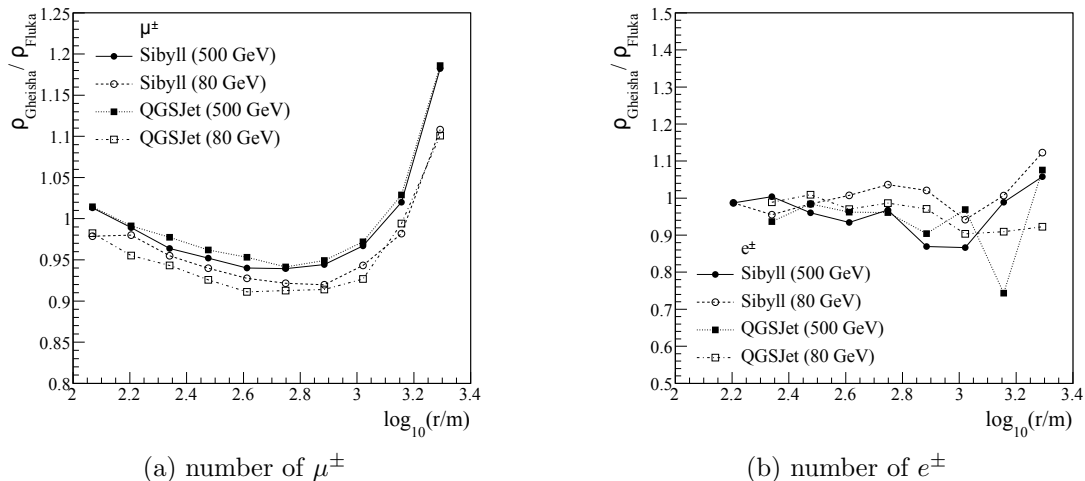


Figure 2.20: The lateral particle density at the ground, predicted by GEISHA divided by the one predicted by FLUKA, for the high energy models SIBYLL and QGSJET, for the μ^\pm component (a) and e^\pm component (b). In brackets is the energy transition between the low and high energy models. From [81]

2.3.2.5 High energy hadronic models

At high energies, the hadronic interactions are described by the Quantum Chromodynamics (QCD) theory. The strong force is carried by the gluon boson which can couple to itself emerging two special properties: the asymptotic freedom and confinement.

At high energies, or equivalently, at short distances, the partons (quarks and gluons) can be considered as almost free particles where perturbative treatment can be used to describe experimental data from high energy hadronic interactions with extreme accuracy. This characteristic is known as asymptotic freedom. On the opposite side, as quarks and gluons are separated, the coupling constant starts to increase very quickly and the perturbative methods can no longer be applied (confinement). The scale Λ_{QCD} separates the long distance regime (soft processes) from the short one (hard processes). It is generally accepted to be on the order of a few hundred MeV. The hadronic models built to describe the hadronic interactions, must handle hard and soft physics, and extrapolate the physical parameters, tuned at man-made accelerator energies, many orders of magnitude up to the UHECRs energies. Moreover, the accelerators data lies in the transverse plane of the collision, described by perturbative QCD, while at cosmic rays, the forward region, where soft processes dominates, is extremely important.

The models employ algorithms to treat both soft and hard interactions. They use perturbative QCD using parton-parton scattering calculations to predict the cross-section of minijet production. At energies/distances where perturbative theory can not be used, they apply Gribov's Reggeon Field Theory (RFT)[82]. In this theory, the interactions are described by the exchange of quasi-particles called Reggeons and Pomerons. The pomerons amplitudes are not calculated from first principles, but extrapolated from parametrizations of the data (at lower energy than cosmic rays). The extrapolations and parametrizations differs between each model, creating a significant uncertainty in the result at the energies of the UHECR.

The hadronic interactions can be calculated using these theories for proton-proton collisions, however they need to be extrapolated to nucleus-nucleus collisions (since in the atmosphere the collision would be proton-nitrogen or proton-oxygen). This extrapolation is performed applying Glauber Theory.

There are three principal high energy hadronic models described in the following:

QGSJET

The QGSJET [83] is based on the Quark-Gluon-String (QGS) model. The older version, the QGSJET01 model, included a minijet component and used parton densities from pre-HERA data. It was updated to the QGSJET-II, which includes non-linear effects coming from pomeron-pomeron interactions and HERA data. Currently, it was tuned to the new LHC data with the release version QGSJET-II.04 [83]. The model uses non-perturbative framework from the Regge theory and hadrons parton structure. The interactions take into account the interaction between valence quarks, diquarks and sea quarks (antiquarks). In each interaction a string between partons is formed, these strings diverge and their color charge increases, breaking up at some point with the formation of baryons, mesons and charmed particles. Multiple scattering is considered as a superposition of coloured strings of parton collisions.

EPOS

The EPOS model[84], the successor of neXus, is based in a Gribov's RFT, applied to individual partons instead of hadrons (pomerons are exchanged between partons and not hadrons). It predict a very hard pion spectrum in proton-induced interactions (characteristic for this model). The model parameters were tuned to RHIC measurements, in version EPOS1.99 and recently tuned to LHC data in the latest version EPOS-LHC . It is very successful describing accelerator data, for proton-proton and Au-Au collisions.

SIBYLL

The SIBYLL2.1 model[85] is a minijet production model (multiple hard processes), superimposed with a Dual Parton Model (DPM), in which only up to one soft interaction is generated per hadron-hadron collision. An energy-dependent transverse momentum cut-off is applied for the minijet cross section calculation to avoid high-density regions, but an additional degree of freedom is added to the high energy extrapolation. SIBYLL2.1 is the model which predicts the highest proton-proton and proton-air cross section at high energy. It is not yet tuned to the LHC data, so many times is not considered in the most recent analysis.

There are many important model parameters in order to describe the accelerators and cosmic rays data. The cross section is very important for the development of air showers and in particular for the depth of shower maximum. The TOTEM experiment at 7 TeV reduced the difference between the models by a factor of 5 (50 to 10 mb)[86]. In figure 2.21a, the recent results and model prediction for the p-p cross section are shown.

The multiplicity is also very important, since it plays a similar role as the cross section, but with a weaker dependence. In figure 2.21b, the average multiplicity for p-p interactions at 7 TeV is plotted. After the re-tuning, the multiplicity (and the fluctuations) in the number of produced particles are now more similar for the models, which is important for the X_{max} fluctuations.

The number of muons in EAS depends on the baryon production, or better on the ratio R between all particle types except π^0 and the total number of particles. Since the π^0 carry energy into the electromagnetic cascade, removing energy from the muon production. The ration is sensitive to the number of (anti)baryons produced in the hadronic interactions. So it is important to check the production of such particles in LHC data. In figure 2.21c is the ratio between anti proton and π^- , it can be seen that the models predict different results, being the EPOS-LHC the one compatible with data. When the data is extrapolated for the cosmic rays, the extrapolations are done for higher energies and between the p-p results to p-air and π -air calculations. At the highest energies in π -air the multiplicities predicted by the models have a difference that can be as high as a factor of 10 (see figure 2.21d, since no direct data is available).

Adjusting the models to the cosmic ray data is not an easy task. Many model parameters produce the same behaviour in the final result on the CR measurements. In figure 2.22, cross

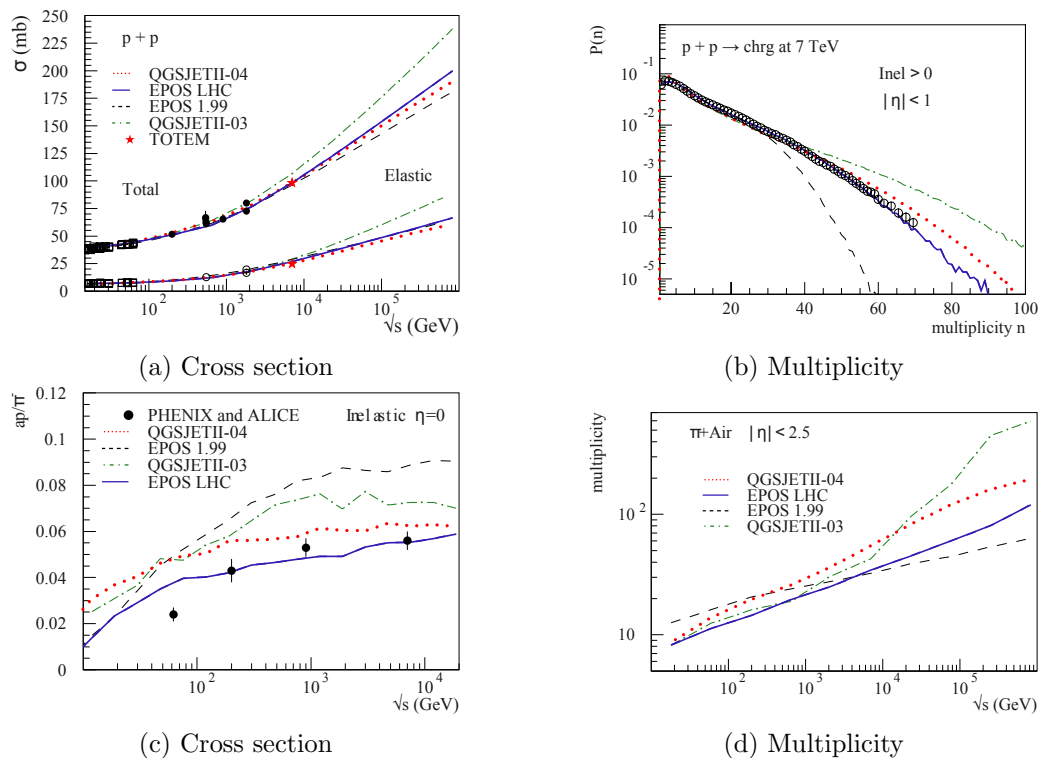


Figure 2.21: a) Total and elastic p-p cross sections, b) multiplicity distribution for events with at least one charged particle with $|\eta| < 1$ for p-p interactions at 7 TeV. c) anti-proton over pion ratio at $y = 0$ for p-p collisions and d) multiplicity for $|\eta| < 2.5$ of π -air collisions as a function of center of mass energy. Taken from [86].

section, multiplicity, elasticity and charge ratio are change by a factor defined on the x axis and the change in X_{max} and $X_{max} RMS$ is plotted on the y axis. The macroscopic parameters are, in fact, interconnected, however, these changes can lead to unexpected changes on the number of muons and X_{max}^μ for example. The elasticity is defined as the energy of the more energetic particle over the collision total energy, $k_{elas} = E_{max}/E_0$.

Since the hadronic models described here are not consistent themselves with different measurement, it opens the possibility for an unforeseen change in the nature of particle interactions at ultra-high energy. For example, a model where chiral symmetry is restored at the extreme energy densities produced in UHE collisions [88], which allows to describe the apparent trend to heavier composition with proton primaries. Other model comes from percolation theory[89], arguing that the proton approaches a black body, close to the Froissart bound, increasing the cross section drastically.

2.3.3 Muonic Component

The muonic component, comes from the decay of charged pions and kaons from hadronic interactions. The muons have a considerable large lifetime (considering their large boost in the EAS) and low cross-section, which means the majority of the produced muons reach the Earth surface and even penetrate the ground. The muon content of a shower depends heavily on hadronic models and the composition of the primary particle and can be used to constrain models and composition.

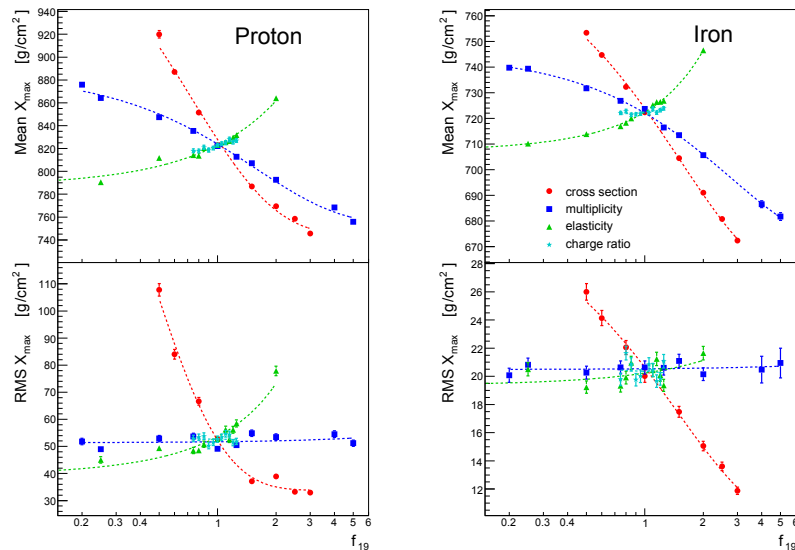


Figure 2.22: Impact of hadronic interaction features on the shower maximum, X_{max} and $X_{max} RMS$, changing some parameters individually by a factor on the x axis (from [87]).

The lifetime of the neutral pions is $\tau_{\pi^0} = 8.4 \cdot 10^{-17}$ s, so at about ~ 13 km altitude it would require at least an energy of $E \sim 2.5 \cdot 10^{19}$ eV for the neutral pion to interact. This energy is too extreme and the neutral pion will not interact, but decay into two photons (as seen before). Even at 1 km, the π^0 would require an energy $\sim 5.4 \cdot 10^{18}$ eV, in order to cross ~ 1000 m. In conclusion, the π^0 always decays.

For charged pions the case is different, since the average lifetime is $\tau_{\pi^{+/-}} = 2.6 \cdot 10^{-8}$ s, so at ~ 13 km, with approximately $E \sim 8.4 \cdot 10^{10}$ eV, these pions can cross 4700 m. At ~ 1 km, the charged pions could cross 1000 m, with an energy of about $\sim 1.8 \cdot 10^{10}$ eV. If the pions have energy above a threshold that will be around $\sim 10^{10}$ eV, then they can interact, producing again one third of π^0 and two thirds of $\pi^{+/-}$. If their energy is below this limit, the charged pions will decay to produce muons in the reaction,

$$\pi^+(\pi^-) \longrightarrow \mu^+(\mu^-) + \nu(\bar{\nu}). \quad (2.53)$$

Due to the bust of hadron particle, the hadronic component remains very close to the axis of the cascade in relation to e^- , e^+ , photons and muons. Note, however, that at large distances from the core, the atmospheric depth crossed by the particles is much higher and probably only muons can survive (see chapter 5 for a better close up).

2.3.4 Extensive Air Shower Simulations

To study coherently the extensive air showers, it is not useful to only use parametrization and functions that describe the average behaviour of the shower like equations 2.46, 2.50 or 2.51. The shower development has a statistical behaviour with many fluctuations with physics implications that became difficult to understand in data without a Monte Carlo (MC) simulation of the particles.

The MC simulations most widely used in the cosmic rays community are the programs AIR-shower Extended Simulations (AIRES) [90] and COsmic Ray SIMulations for KAScade (CORSIKA) [91]. The particle number grow with energy (as seen previously), so at ultra high energies, the particle number is so big that treat and track each individual particle make these programs

very time consuming. A complete simulation of a 100 EeV shower can easily consume one month and occupy 1 Terabyte of information.

This kind of time and space consumption lead to the development of thinning methods. The sub-adjacent idea is that, in the showers with those extremely high particle number is redundant to follow every particle. In this way, only some particles need to be followed, with the weight that represents a bunch of particles, or in other words, some particles are killed and the surviving particle carries a weight symbolizing the number of particles killed (that this single particles represents). The thinning is not applied to the highest energetic particles, since they are the most relevant for the shower fluctuations. Essentially, it is only applied when particles reach a lower energy threshold (user defined) or when the density of particles is extremely high, creating redundancy.

Other way to reduce the computation time of the Monte Carlo simulations is to follow some particles and combine cascade equation to represent the development of other particles. Examples of this hybrid EAS simulations are CONEX [92] and SENECA [93] simulation programs.

In this approach, the particles that carry a large fraction of the primary energy are tracked using the conventional Monte Carlo methods (for the shower fluctuations). For the particles that reach an energy bellow some threshold (also user defined), the particles are not followed, but the subsequent sub-shower development is described by cascade equations. The cascade equations are parametrizations that represent the average values of the showers development without any natural fluctuations. Nevertheless, since they are used in particles with less energy (where already exist a high multiplicity in the development), it is considered that those particles would not contribute significantly to the total fluctuations.

The CONEX program, for instance, uses cascade equations that don't have time and geometric information, leading to a final shower development in one dimension. The SENECA program solved this problem using parametrizations of the lateral profiles.

The huge particle number reduction in both methods, allows us to simulate showers in a practical time scale. It should be noticed that the threshold used in both hybrid and thinning programs specifies the speed/quality of the shower development.

2.4 Detection Techniques

The study of Cosmic Rays with energies up to 10^{14} eV can be done directly, detecting the primary particles using balloons and satellite experiments (as seen in the beginning of the chapter). At higher energies, the CR flux becomes too low to detect such particles directly (it would be impossible to have huge areas of detection in balloons, or in space). The alternative is to use the atmosphere as the detector and detect indirectly the cosmic ray through their development in the atmosphere. Once the primary particle collide with atmospheric nuclei and initiate an EAS, the particle properties such as energy, mass and arrival direction cannot be measured directly. Rather, they have to be inferred by the properties of the shower development. There are various complications in the indirect measurements, when the atmosphere became part of the detection system, acting as a calorimeter, it needs to be carefully monitored. Moreover, it is not possible to detect all shower development, but rather some sampling imposed by the detector discreteness. This increases fluctuations measured in the showers development, which is a stochastic process. And also, some cascade proprieties must be inferred using extrapolation of models at lower energies.

The study of the EAS can be done through two types of detection techniques. On the one hand, the secondary particles can be sampled at ground level with arrays on the ground (SD). On other hand, the emitted radiation from the shower front, as it traverses the atmosphere, can be detected (atmospheric radiation detectors). The surface arrays are detectors on the surface, detecting all particles arriving to the ground (blue cylinder in the figure 2.23). They can be scintillator arrays and Water-Cherenkov tank arrays. The atmospheric detectors record the radiation emitted by the secondary particles through the shower development in different frequencies. As example, the fluorescence detectors, the air Cherenkov detectors, and radio and microwave antenna arrays. In figure 2.23, the fluorescence detectors are represented by the right telescope, the radio and microwave detection are represented in the antennas (in the middle).

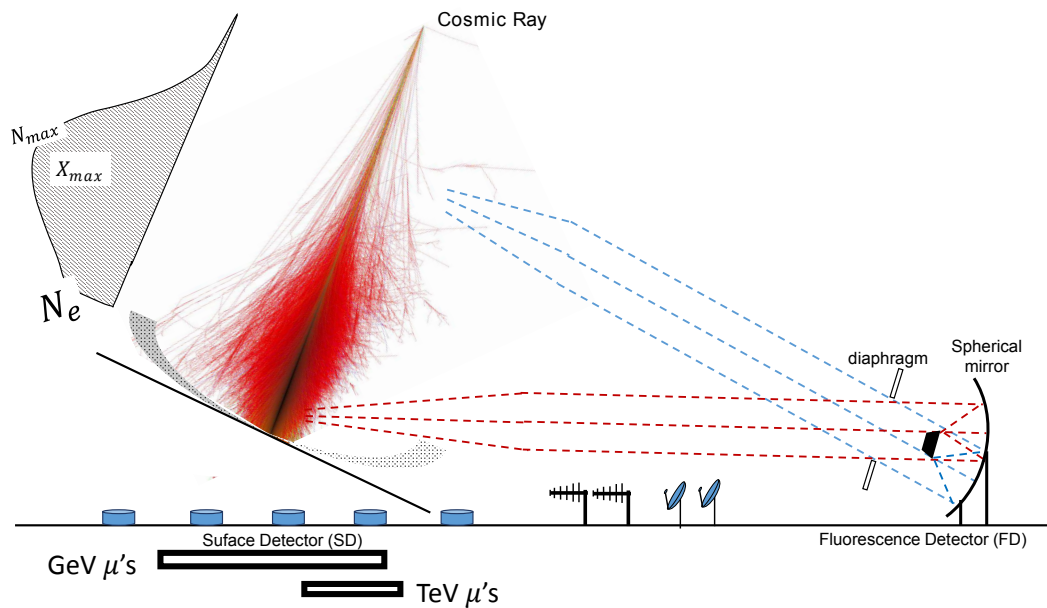


Figure 2.23: Draft of a shower development and it's detection with several types of detection techniques.

2.4.1 Ground detection

The ground arrays, measures the secondary particles of an EAS at a determined observation level corresponding to a particular point of the longitudinal EAS development. The altitude where these detectors are installed, depends on CR energy. If the energies to measure are of the order of $10^{15} eV$, the detectors should not be placed at sea level, since they would detect very few particles. On the other hand, if the altitude is too high, the detectors could be above the X_{max} development of the EAS of UHECR and therefore it would not be sensitive to these showers.

The CR flux reduces very quickly with energy, so the areas needed for detection depends much on the interest energies. At $10^{19} eV$ the CR flux is lower than 1 particle per km^2 per century, which means several thousands of km^2 are needed to have a significant amount of data. At these energies, the lateral development spans several thousand meters, so individual detectors sample the lateral profile instead of a continuous detector (which would be impossible). The space between each detector is optimized to sample the shower in some energy range at a given altitude. For example, in a triangular grid, the detector spacing of 666 m, 1332 m and 1880 m becomes fully efficient at 0.5, 4.5 and 20 EeV respectively [94]. The total number of individual

detector is a compromise between the total detection area and the grid spacing for a given interest energy range.

In figure 2.24, a possible event is represented, where each number expresses the density of particles detected by each ground detector. The circles join detectors with the same density and x represents the core of the shower. If the event is vertical, the lateral profile can be fitted with the equation 2.50, however, for inclined events, the event geometry is needed, because the lateral profiles are perpendicular to the propagation.

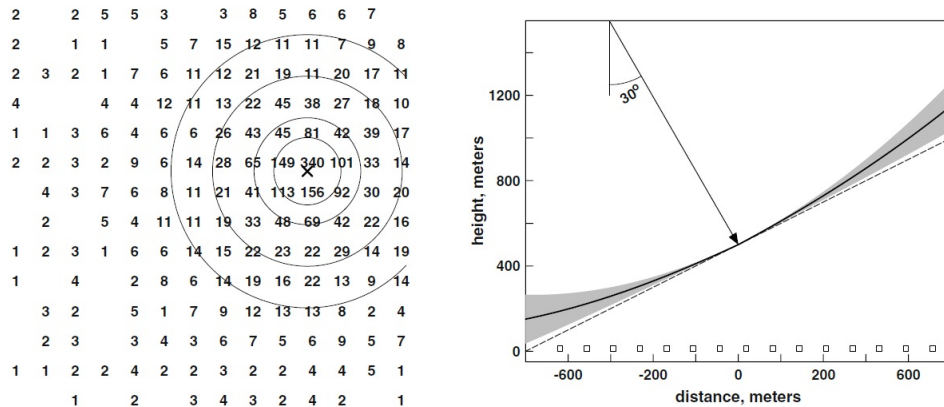


Figure 2.24: In left, a ground array scheme with an hypothetical detected event. The numbers are the intensity signal in each detector, the circles represents equal particle densities and since the signal fluctuate with Poissonian distribution, some detectors are not triggered. In right, is a scheme of a plane front in dashed line, in the grey shadow a realistic front and in the black line a curved front.[51]

The shower axis (and direction) of the primary particle is obtained from the relative signals arrival times, at a minimum of three non-collinear detectors (if it is considered that the shower front have the shape of a flat disc). As shown in figure 2.24, the front of the EAS is curved instead of flat and its thickness increases with distance from the event axis. Fluctuations in the detectors further away from the core will increase and there is still the background from particle simultaneously detected with the EAS. Each experiment uses different parametrizations for these effects in reconstruction, for which they depend on the installed systems. With the given geometry and lateral profile, the energy of primary particle can be estimated accordingly to the total signal at some point. This method is also dependent on hadronic models in Monte Carlo, as in the case of fluorescence methods, for the lateral parametrizations and comparison to different compositions. The advantage of this method compared to light emission is that, it does not depend on the background light, having a duty cycle of 100%. And, it may be sensitive to the muon and hadronic components. There are several types of surface detectors briefly described below.

Water Cherenkov Detectors

The Water Cherenkov detector (WCD) with the scintillators are the mostly used. They are tanks filled with purified water to measure the Cherenkov light produced by the charged particles crossing the tanks (essentially electrons, positrons, muons and converted photons). Muons leave a signal proportional to the track length, while the others develop an electromagnetic cascade inside the tank emitting light according to their energy. Since they can have an water height on the other of 1-5 m, they are suitable to detect very inclined events. Example of this

kind of detectors are Haverah Park [19], the Pierre Auger Observatory[1] and HAWC (the High-Altitude Water Cherenkov Observatory)[95].

Scintillators

Scintillators are commonly made of plastic and sensitive to all charged particles and converted photons. They can cover areas of some m^2 , but only a few centimetres height, which means their use is usually restricted to angles below 45° . Scintillators experiment examples are The Volcano Ranch array [17], Yakutsk [20], Akeno [96] and AGASA[97], KASCADE (KARlsruhe Shower Core and Array DETector)[98], KASCADE-Grande[99] and Telescope Array [23].

Muonic and hadronic detectors

The detectors (usually scintillators) can be placed under a shielding or buried on the ground to absorb the electromagnetic component. Since the muons can penetrate from a few meters to several hundred meters underground, the detectors are used as muon detectors. According to the ground depth, they can detect muons with different energy thresholds (see figure 2.23). Several examples of experimental muon detector are Yakutsk [20], AGASA muon detectors [97], SUGAR (The Sydney University array) [18] and AMIGA (Auger Muons and Infill for the Ground Array) [100].

Close to the shower core, some part of the hadronic component can be detected. The hadronic component is measured with hadronic calorimeters on experiments like EAS-TOP[101], or KASCADE[98, 99].

2.4.2 EAS Light detection

During the EAS development through the atmosphere, it is not possible to detect the secondary particles directly. However, these secondary particles dissipate most of their energy by ionization and it is possible to record the fluorescence emission of an EAS. The fluorescence emission is the most widely used technique, but it is also possible to detect Cherenkov and radio radiation, or maybe even coherent synchrotron radiation emitted by charged particles in the Earth magnetic field (microwave radiation)[102]. Radiation emissions can vary from the low frequency radio emission to UV fluorescence emission.

The light emissions are very dependent on the atmospheric properties. The emissions are also attenuated in air (with Rayleigh and Mie scattering), which depends heavily on the composition and characteristics of the atmosphere. So it is strictly necessary to manage, day to day, the atmospheric parameters. Even using an annual model of the atmosphere is not enough, since variations in clouds, dust and pollutants may vary very quickly and need to be measured.

2.4.2.1 Fluorescence light

The cosmic rays induces a cascade of secondary particles and the electromagnetic component dissipates its energy into the atmosphere. The shower particles, mostly electrons and positrons, deposit energy in the atmosphere by ionization or excitation of air molecules. The excited nitrogen molecules, subsequently return to their ground state partially by the emission of photons near UV region, isotropically, with wavelengths between about 300 and 400 nm. This is called fluorescence light instead of scintillation light, considering the atmosphere as a scintillation calorimeter. In this way, the energy deposited measurements in the atmosphere are proportional to the primary energy, like a calorimetric energy measurement. The amount of fluorescence light emitted along the shower path is a part of the energy loss rate by means of collisional processes

(other part can go into internal quenching⁶). The energy losses due to collisional processes affects those with lower ionization power, like electrons or positrons. Simulation studies show that most of the energy deposited into the atmosphere comes mainly from electrons (and positrons) with energies below 1 GeV with a maximum at about 30 MeV[103].

It is considered that the number of fluorescence photons is proportional to the deposited energy in air. The conversion factor between the deposited energy and the number of emitted fluorescence photons is the Fluorescence Light Yield (FLY), $FLY(\lambda, T, P)$ ⁷ which depends on the air pressure P , temperature T as well as on the wavelength.

The fluorescence light is produced by electronic transitions in the nitrogen, N_2 and N_2^+ . Each electronic state is split into vibrational levels, and in addition, each vibrational level is split in rotational sub-levels following a complicated structure (in a band system per electronic state). The two most important transitions come from the N_2 second positive system (2P) and the N_2^+ first negative system (1N), see the spectrum in the figure 2.25. The 1N fluorescence system can be excited directly, as a consequence of the molecular ionization, from high energy particles in $N_2 + 2 \rightarrow N_2^{+*} + e + e$. The 2P systems, the upper levels cannot be excited directly by high energy interactions because the final electronic spin of the molecule is forbidden. They can however occur with excitation, with low energy electron involving spin change, or by decay from higher levels, in the processes $N_2 + e(\uparrow) \rightarrow N_2^+e(\downarrow)$ and $N_2^+ + e \rightarrow N_2^*$.

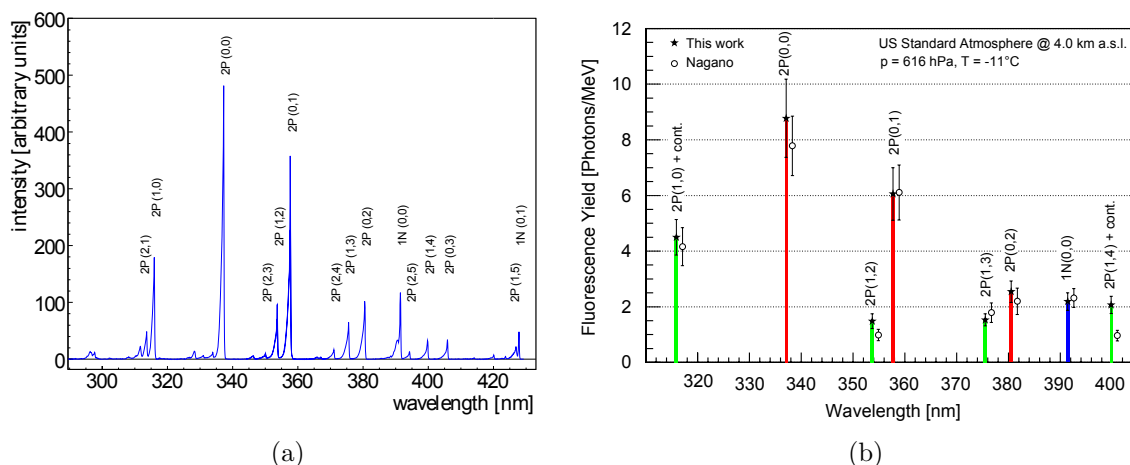


Figure 2.25: a) Air fluorescence spectrum excited by a current of $\sim 10 \mu\text{A}$ with 3 MeV electrons at 800 hPa [104]. b) fluorescence spectrum measured by by AirLight in black stars[105] for nitrogen transitions in dry air at 4 km height considering the US standard Atmosphere and results from Nagano et. al. in open circles [106].

The number of emitted photons can be given by:

$$n[\text{photons}] = \frac{\epsilon_\lambda(P, T, \lambda) \cdot E_{dep}}{E_\lambda} = \epsilon_\lambda(P, T, \lambda) \frac{\lambda}{hc} E_{dep}, \quad (2.54)$$

where ϵ_λ is known as fluorescence efficiency, it denotes the fraction of energy emitted as fluorescence light over the total energy loss into the atmosphere. This value depends on the pressure,

⁶The internal quenching is the process where molecules have a de-excitation or downward electronic transition without radiation, electronic excitation energy can be transferred to high vibrational levels of a lower electronic state with a consequent emission of infra-red radiation.

⁷Usually, the fluorescence light yield is rather defined as photons per meter $FLY/l(\lambda, T, P)$ or photons per energy deposited in the atmosphere $FLY/E_{dep}(\lambda, T, P)$.

temperature and wavelength of the emitted photon. It is related with the lifetime of a specific excited state and the energy losses by internal quenching (not going into fluorescence), which depends mainly on temperature and pressure. The fluorescence light yield can be given in two ways, in photons per meter or photons per deposited energy.

$$FLY/E_{dep}(\lambda, T, p) = \epsilon(p, T, \lambda) \cdot \frac{\lambda}{hc} \left[\frac{\text{photons}}{\text{MeV}} \right],$$

$$FLY/l(\lambda, T, p) = \epsilon(p, T, \lambda) \cdot \frac{\lambda}{hc} \cdot \frac{dE}{dX} \cdot \rho_{air} \left[\frac{\text{photons}}{m} \right],$$
(2.55)

where ρ_{air} is the atmospheric density and dE/dX is the energy loss rate into the atmosphere.

Energy, pressure and temperature dependences of FLY have been measured between 300 and 400 nm in dry air using electron beams of several energies. The FLY/l (left axis of figure 2.26a) is drawn as function of the electron energy, the full line corresponds to the dE/dX of the electrons obtained in [107](right scale). The dotted line is the total energy loss of the electron using Berger-Seltzer formula, used by GEANT4[108] simulation toolkit. The difference between the two curves reflects the energy carried away by the high energy δ -rays and γ -rays beyond the used chamber.

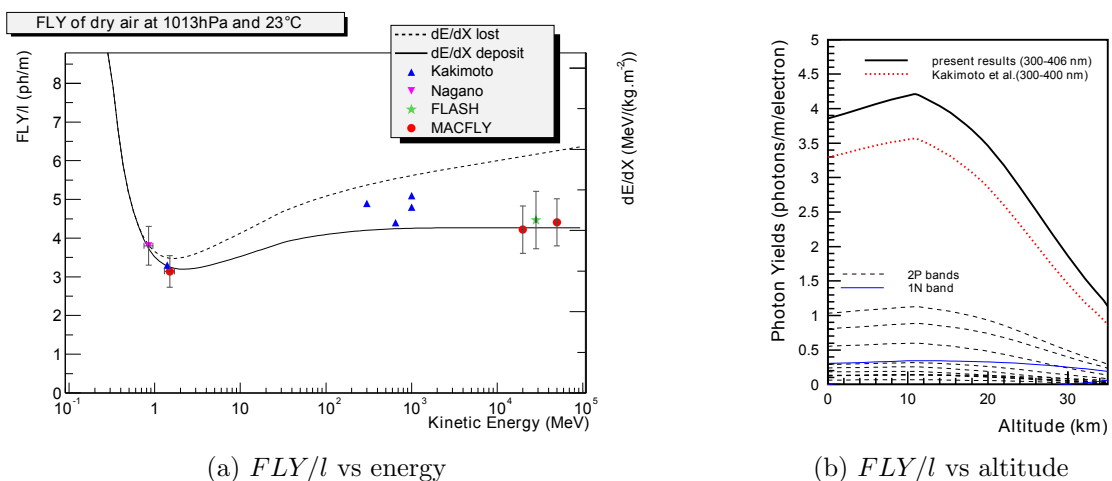


Figure 2.26: Left, FLY per electron track length FLY/l (in photon/meter) as a function of electron energy measured by several experiments (Kakimoto[109], Nagano [106], FLASH[110] and MACFLY [107]). Right, is the FLY/l as function of atmospheric altitude (from [106]). .

In an atmospheric dry air at 1013 hPa and 23°C, for the fluorescence wide spectrum, it gets $FLY/E_{dep} = 17.6$ photon/MeV, with a systematic error of 13.2%[107]. Currently the values of the fluorescence yield at 337 nm were updated with the value of $FLY/E_{dep337nm} = 5.61 \pm 0.06_{stat} \pm 0.21_{syst}$ (around 4% systematic error), from AIRFLY Collaboration [111]. In figure 2.26 right, the FLY/l per electron is drawn as function of atmospheric altitude. The value is around $FLY/l \sim 4$ photons/m/electron.

2.4.2.2 Cherenkov radiation

In the EAS, the relativistic particles also generate a large amount of Cherenkov light. The amount of Cherenkov light at any point of the shower depends on the previous history of the

shower, so it is not proportional to the local shower size, as in the case of fluorescence light. Moreover, Cherenkov is also primarily beamed in the forward direction of the parent particles (against the isotropically radiated fluorescence). The Cherenkov emission is very intense, at observation points with angles smaller than $\sim 25^\circ$ with respect to the shower axis and dominates the fluorescence light. Even if the direct beam is not pointing towards the observation point, additional scattered Cherenkov light also contributes to the shower image.

The Cherenkov radiation was first observed by Pavel Cherenkov in 1934, as a blue glow in a liquid due to radioactivity effects. After, a theory to describe the radiation was purposed by Igor Tamm and Ilya Frank.

A charge particle crossing a dielectric medium, turns the medium polarized. Its electrons will assume a given configuration in the presence of a charge and then return to its initial positions, emitting electromagnetic waves. The waves interfere destructively if the velocity of the charge particle, v , is less than the velocity of the light in that medium c/n (figure 2.27). However, if the particle velocity is higher than the light in the medium (figure 2.27 right) the waves may interfere in a constructive way giving origin to the so-called Cherenkov radiation.

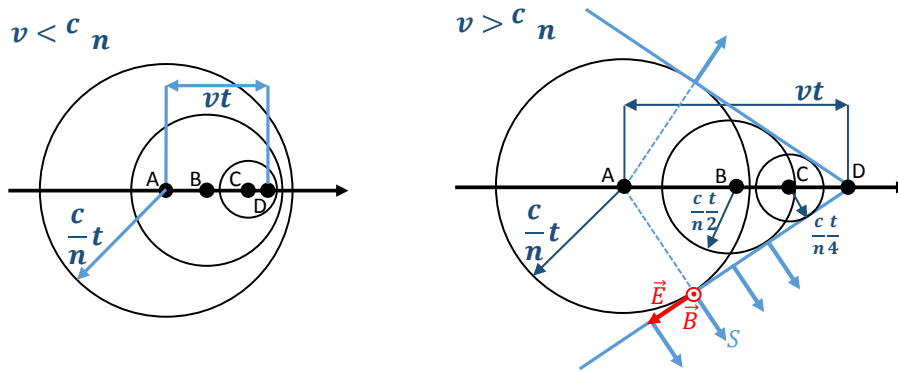


Figure 2.27: In the left a charge particle crossing a medium with $v < c/n$ with no constructive interference. In the right, a charge particle with $v > c/n$ occurring constructive interference in the blue line.

According to the picture, the condition for constructive interference is the triangle formed with the distance that the particle moved vt from a particular point and the distance travelled by the photons from that point, ct/n . This triangle happens in all particular points (changing only the time t) and the waves interfere constructively. It is summarized by:

$$\cos \theta = \frac{ct/n}{vt} = \frac{1}{\beta n}, \quad (2.56)$$

with $\beta = v/c$ and θ the emission angle of the radiation with relation to the particle direction. For ultra-relativistic particles, $\beta \approx 1$ the maximum angle radiation is $\cos \theta_{max} = 1/n$. At sea level the refractive index of air is $n = 1.00029$ [112] and $\cos \theta_{max} = 1.3^\circ$. Thus, the radiated light is closely directionally related to the radiating parent particle path. The radiation is only possible if $v > c/n$ as said before and a energy threshold can be calculated for different shower particles. For electrons the energy is $E_{e,thr} = 21$ MeV, for π mesons $E_{\pi,thr} = 4.4 \cdot 10^3$ MeV and for protons $E_{p,thr} = 39 \cdot 10^3$ MeV. The energy threshold for electrons is lower and since the number of electrons can be around 95% of the total particles number, this means that the Cherenkov radiation will be mainly produced by electron.

The number of emitted photons per unit length, for some region $[\lambda_1, \lambda_2]$ is given by the following equation:

$$\frac{dN_\gamma}{dl} = 2\pi\alpha \int_{\lambda_1}^{\lambda_2} \left(1 - \frac{1}{\beta^2 n^2(\lambda)}\right) \frac{1}{\lambda^2} d\lambda, \quad (2.57)$$

where α is the fine structure constant and n the refraction index (see [113, 114]). The number of Cherenkov photon produced during an EAS development can be approximated by:

$$\frac{dN_\gamma}{dX} = N(X) \int_{E_{thr}}^{\infty} f_e(X, E) y_\gamma^e(h, E) d \ln E, \quad (2.58)$$

with $N(X)$, the charged particle number as function of depth X , E_{thr} is the electron energy threshold for Cherenkov. $f_e(X, E) = \frac{1}{N_e(X)} \frac{dN_e}{d \ln E}(X, E)$ is the normalised differential electron energy spectrum at depth X and $y_\gamma^e(h, E) = \frac{dN_\gamma}{dE} \frac{1}{\rho(h)}$, with $\rho(h)$ the atmospheric density. An exact calculation of the Cherenkov light signal (both direct as well as scattered) is quite complicated and must be carried out numerically.

2.4.2.3 Scattering of the light in the atmosphere

The EAS light emission has to cross some atmosphere before being detected. So, despite the photon production mechanisms, it is also necessary to understand the scattering of that light across the air. Within the wavelength of interest (roughly 300-400 nm), attenuation is essentially caused by air molecules, the Rayleigh Scattering, as well as the aerosol particles, Mie scattering. The fluorescence light emitted isotropically in the shower development is attenuated in its path through the atmosphere. The Cherenkov radiation, with directions close to shower axis, is also scattered across the air. This means that even if the observation point is in an angle bigger than $\sim 25^\circ$ (where almost no direct Cherenkov can arrive) the diffusive Cherenkov light can be detected with an intensity that may compete with fluorescence. In the next section, the light scattering will be addressed.

2.4.2.3.1 Rayleigh scattering

The Rayleigh scattering is the elastic scattering of light with particles much smaller than the light wavelength. The cross-section depends strongly on the wavelength ($1/\lambda^4$) as pointed by Lord Rayleigh in the 19th century. The total cross-section per molecule of air can be given by[115]:

$$\sigma(\lambda) = \frac{24\pi^3 (n_s^2 - 1)^2}{\lambda^4 N_s^2 (n_s^2 + 2)^2} \left(\frac{6 + 3\rho_n}{6 - 7\rho_n} \right), \quad (2.59)$$

where n_s is the air refractive index at a given wavelength, N_s the molecular number density, and ρ_n is the depolarization factor⁸, that accounts for the anisotropy of the air molecule and varies with wavelength. The depolarization factor is difficult to parametrize with wavelength, with a variance around 60% from the near IR to the UV spectral region.

The differential cross-section, or phase function, is given as (in [115])

$$\frac{1}{\sigma} \frac{d\sigma}{d\omega} = \frac{3}{16\pi (1 + 2\gamma)} \left[(1 + 3\gamma) + (1 - \gamma) \cos^2 \theta \right], \quad (2.60)$$

where the γ parameter comes from the depolarization factor and is given by $\gamma = \frac{\rho_n}{2 - \rho_n}$. If $\rho_n = 0$, the differential cross-section becomes proportional to $1 - \cos^2 \theta$, recovering the classical

⁸ ρ_n account of the anisotropy of the air molecules, point-like scatters should have $\rho_n = 0$ and in air is expected to be around 0.03 .

Rayleigh formula. In this way, the scattering emission has a maximum intensity in the forward and backward directions.

In the range of interest is preferable to have a description of the scattering in some amount of atmosphere instead of individual scattering centers. So, the number of photons undergoing an atmospheric thickness dl is approximately (see [113]):

$$\frac{dN_\gamma}{dl} = -\frac{\rho N_\gamma}{X_R} \left(\frac{400\text{nm}}{\lambda} \right)^4, \quad (2.61)$$

where $X_R = 2974 \text{ gcm}^{-2}$ is the characteristic Rayleigh path length [113]. The differential emission would be given by,

$$\frac{d^2 N_\gamma}{dl d\Omega} = \frac{3}{16\pi} (1 - \cos^2 \theta) \frac{dN_\gamma}{dl}. \quad (2.62)$$

The transmission coefficient between a depth X_1 and X_2 is,

$$T_R = e^{-\frac{|X_1 - X_2|}{X_R} \left(\frac{400\text{nm}}{\lambda} \right)^4}. \quad (2.63)$$

2.4.2.3.2 Mie scattering

Mie scattering is the light scattering with particle in the atmosphere, whose size is comparable to the wavelength of the light itself. These particles are called aerosols, have typical radius around 0.1 to 10 μm like dust, pollutants, liquid droplets, etc. Instead of Rayleigh scattering, it is described by Mie Theory and it has to deal with the aerosols dimension, chemical composition and even their shape.

The aerosol density can be considered as falling exponentially with altitude, so the amount of Mie scattered light is approximately [113],

$$\frac{dN_\gamma}{dl} = -\frac{N_\gamma}{l_M} e^{-h/h_M}, \quad (2.64)$$

where h is the height, h_M is the scale height factor and l_M is the Mie scattering mean free path, they depend on the atmospheric properties. Its angular distribution can be approximately given by,

$$\frac{d^2 N_\gamma}{dl d\Omega} = a_M \cdot e^{-\theta/\theta_M} \frac{dN_\gamma}{dl} \approx \frac{dN_\gamma}{dl} 0.80 e^{-\theta/\theta_M}, \quad (2.65)$$

for angle between 5° and 60° , where $\theta_M = 26.7^\circ$, a_M, θ_M, h_M and l_M , are parameters, and they correspond to mean values for aerosol conditions. The angular distribution depends also on the aerosol properties and is strongly peaked in the forward direction. The diffusion is mainly driven forward. The coefficient of transmission between position 1 and 2 [116] is,

$$T_M = e^{\frac{1}{l_M(\lambda)} \int_1^2 e^{-h/h_M} dl}. \quad (2.66)$$

Using the approach $dl = dh/\cos \theta'$ (θ' being the angle between the vertical and the photon path), it will be,

$$T_M = e^{\frac{h_M}{l_M(\lambda) \cos \theta'} |e^{-h_1/h_M} - e^{-h_2/h_M}|}. \quad (2.67)$$

It should be noted that a_M, θ_M, h_M and L_M strongly depend on the composition of the atmosphere and therefore a good control of the atmosphere is needed. From [116], $h_M \simeq 1.2 \text{ km}$ and $l_M \simeq 14 \text{ km}$ at $\lambda = 360 \text{ nm}$.

2.4.2.3.3 Attenuation

The fluorescent light that reaches the detector must be corrected by the geometry and the attenuation of the Mie and Rayleigh diffusion. Thus, being I_0 the intensity of photon emission, at the detector the photon intensity will be,

$$I = I_0 \cdot T_R \cdot T_M \cdot (1 + \varepsilon) \frac{\Delta\Omega}{4\pi}, \quad (2.68)$$

where $\Delta\Omega$ is the angular interval and ε corresponds to higher order correction due to multiple scatterings.

2.4.2.4 Fluorescence technique

It is possible to detect the fluorescence light using FD and reconstruct the shower development. Nevertheless, the fluorescence intensity is lower than the Cherenkov radiation, so the detectors should not be placed in the direction of showers (or fluorescence will be small compared with Cherenkov). It is only possible to detect very high energy EAS, usually for energies above $10^{17}eV$, since the fluorescence is isotropic and the fluorescence yield, with the attenuation, is very low. The shower may develop far away from the detector, if the photon intensity is enough, increasing the exposure of the detectors.

If 10^6 electrons pass by 700 m of atmosphere, at about 20 km from the detector, it will produce $2.8 \cdot 10^{12}$ photons [51], but since the area of the ~ 20 km distance sphere is $\sim 5 \cdot 10^{13}cm^2$, then the density of photons in the detector will be $\sim 0.056 \gamma/cm^2$. In this way, mirrors are used to concentrate the photons to an acceptable level. The concentrated light is collected by a PMT camera that divides the image into pixels (fig 2.28), recording the density of photons. So, it is possible to obtain the longitudinal profile of the showers.

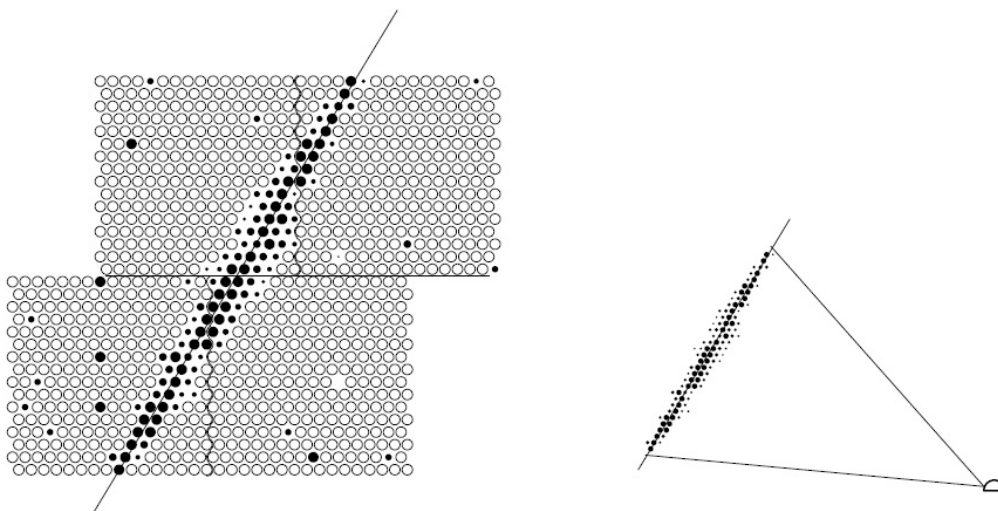


Figure 2.28: Schematic representation of the image of a detection of a shower in a FD telescope. [51]

The detector sees the shower as a point moving at the speed of light in the atmosphere. From the pixels time and direction it is possible to reconstruct the geometry of the event. After knowing the geometry, the amount of photons that passes through the atmosphere towards the detector can be known. In addition, it is necessary to take into account the Rayleigh and Mie

attenuation of these photons accordingly with the geometry. It is also needed to calculate the direct Cherenkov and indirect Cherenkov (Cherenkov diffused by Rayleigh and Mie), which is highly dependent on the geometry and detectors position. All these components must be considered to recover the fluorescence profile and the longitudinal profile in dE/dX and number of charge particles. Consequently the N_{max} and X_{max} are also known.

The energy of primary particle is known integrating the particle number, for instance, $E_p = \alpha \int_0^\infty N_e(X) dX$, where the constant is $\alpha \sim 2.2 MeV/g/cm^2$ [51] and expresses the average ionization energy loss rate for the shower. The value of the constant is the energy losses of the shower particles in atmosphere but it comes mainly from electrons, positrons and gammas while hadrons, muons, neutrinos hardly excite the air producing fluorescence radiation. This means that some part of the primary energy will not excite the air and it continues in the hadronic and muonic component until the ground. So the total energy integrated will be approximately $\sim 90\%$ of the primaries energy, the remaining energy is called the missing energy. The missing energy is calculated by Monte Carlo simulation and is therefore dependent on the model. Moreover, it still depends on the composition of the primary particle.

The biggest problem with this method is that it only runs on moonless nights and good weather, which leads to a duty cycle of $\sim 10 - 15\%$. An experience of this type is the Fly's Eye[22], it is located on hilltops above the desert in Utah, USA and operated from 1981 to 1993. In the initial phase, the detector, consisted of 67 spherical mirrors with ~ 1.6 m in diameter and between 12 to 14 PMTs each, with a total of 880 PMTs. The PMTs had a time resolution of 25 ns. With this system the detector covered the entire sky (each PMT was $5^\circ \times 5^\circ$ of the sky). Later in 1986, has installed a second detector with 36 mirrors at 3.4 km away from the original to make stereoscopic reconstructions. Other examples are HiRes[117], the Pierre Auger Observatory [1] and the Telescope Array (TA) [23].

2.4.2.5 Cherenkov detectors

The Cherenkov radiation is emitted into the air in a cone with a very small angle of aperture and it is delivered very close to the shower axis. Therefore, the optical detectors must be aligned with the showers axis in order to detect direct Cherenkov. If the observation point is not in the front of the shower axis, it will only detect fluorescence light and Mie and Rayleigh scattering light.

The big advantage comes from the high density of emitted photons, but is difficult to reconstruct the features of EAS and Monte Carlo simulations are necessary to estimate the X_{max} or primary energy.

Currently, this type of detectors (system of Imaging Atmospheric Cherenkov Telescopes) are used primarily to detect gamma-rays, at lower energies. Some examples are the Very Energetic Radiation Imaging Telescope Array System (VERITAS) and the Major Atmospheric Gamma-ray Imaging Cherenkov (MAGIC)[118], in the island of La Palma, Canary Islands, Spain. The High Energy Stereoscopic System (HESS)[119], Cherenkov Telescope Array (CTA)[120] and Tunka experiment [121] are other examples.

2.4.2.6 EAS detection in other frequencies

The EAS development can also be studied at other frequencies, like radio and microwave radiation. The idea of radio detection from EAS was proposed for the first time by Askar'yan in 1962. He concluded that in an electron-photon shower there is an excess of negative charge (excess of electrons) due to electrons knocked out from atoms either by photoelectric effect or ionization and annihilation of positrons in flight. Thus, there is an electric current created by the electrons

excess associated with shower, being a source of electromagnetic radiation. In 1965, the first evidences of radio emission were seen[122].

Radio

In the radio band, there is a Very Low Frequency (VLF) radiation (generally around 0.1-1 MHz) from a mechanism called Transition Radiation [123] (see [124] for a review). Transition radiation is emitted when a uniformly moving charged particle traverses the boundary separating two media having different dielectric properties. Currently, no detector is working on this frequency range, however LOFAR (Low Frequency ARray) conceived for purely astronomical purposes, can offer the possibility for EAS studies.

The Very High Frequency (VHF) radiation (around 10-200 MHz) is caused mainly by Cherenkov radiation from a charge excess moving with a velocity higher than the speed of light in the traversed medium and by geosynchrotron emission. The geomagnetic emission mechanism, a coherent synchrotron emission from electron-positron pairs deflected in the earth's magnetic field, is dominant for radio emission from EAS in air and has a firm theoretical background. Some examples of radio experiments are LOPES (LOFAR Prototype Station) experiment [125] in the range 40-80 MHz and CODALEMA (COsmic ray Detection Array with Logarithmic ElectroMagnetic Antennas) [126] in the range 1-200 MHz. The AERA (Auger Engineering Radio Array)[127] and EASIER (Extensive Air Shower Identification with Electron Radiometer)[128] are the radio extensions of the Pierre Auger Observatory.

Radio detection of showers presents two principal advantages. The detectors are cheap and easy to deploy (built only with wire antennas). The absorption at radio frequencies in the atmosphere is negligible and the signal remains unaltered. However is not easy to trigger independently and reconstruct the shower.

Microwave

Microwave emissions with frequencies $\gtrsim 1$ GHz have been proposed in [129]. This radiation has been attributed to molecular bremsstrahlung radiation (MBR) from the interaction of electrons with neutral air molecules. Low-energy electrons in extensive air showers (EAS) might produce an unpolarized and isotropic microwave radiation (see also [130]). The Giga Hertz range has the advantages of a very low natural background radiation, very little human-made radio frequency interference and negligible absorption in the atmosphere.

Some experiments are the AMBER (Air shower Microwave Bremsstrahlung Experimental Radiometer) and EASIER [128, 131] prototypes, installed at the Pierre Auger Observatory. MIDAS (Microwave Detector of Air Showers)[132], a self-triggering system foreseen to be installed at the Pierre Auger Observatory and the CROME (Cosmic Ray Observation via Microwave Emission)[130] experiment installed within the KASCADE-Grande array.

The first experimental characterization of microwave emission from cosmic ray air showers was performed by CROME [133]. The microwave signals have been detected for more than 30 showers with energies above $3 \cdot 10^{16}$ eV, consistent with a mainly forward-directed and polarised emission process in the GHz frequency range.

The Pierre Auger Observatory

The Pierre Auger Observatory [1] project is currently the biggest cosmic rays experiment, designed to measure the properties of the UHECRs (energies above 10^{18} eV). In 1992, two physicists, Jim Cronin and Alan Watson, created the project, whose name comes from the french physicist that discovered the extended air shower existence. The experiment involves several universities and research institutes from 15 countries, with more than 500 physicists.

The Observatory was designed and purposed to study open questions such as: the spectrum in the GZK-region; observation of point-like sources of cosmic rays (anisotropy on small scale); estimation of intergalactic magnetic field; observation of large scale anisotropy; mass composition in the GZK-region; and studies of the hadronic interaction at energies above LHC.

The Observatory is gathering data since 2004 and it became fully operational in 2008. It is located near Malargüe in the province of Mendoza, Argentina (69°W , 35°S). The site is relatively flat, near the base of the Andes mountains at an altitude around 1400 m, corresponding to a vertical atmospheric depth of $\sim 880 \text{ g}\cdot\text{cm}^{-2}$. Auger is an hybrid air shower experiment that uses two independent, well-established techniques to detect UHECR, an array of Surface Water-Cherenkov Detectors (SD) combined with air Fluorescence Detectors (FD).

The Pierre Auger Observatory has over 1600 surface detectors arranged as an array on a triangular grid with 1500 m spacing. This 3000 km^2 array is overlooked by 24 fluorescence telescopes grouped in units of 6 at four locations on its periphery. The configuration of the Observatory appears in the figure 3.1.

In addition to the SD (section 3.1) and the FD (section 3.2), other instruments are installed or foreseen to be. There are some enhancements (section 3.5) of the observatory lower energies, AMIGA and HEAT. The AMIGA project is an infill of 61 water Cherenkov tanks separated 750 m with muon counters buried alongside [100], fully efficient at 10^{17} eV. And HEAT is a set of three high elevation telescopes located close to one of the FD stations. There are also projects to study the radio and microwave emissions like AERA to study radio in a frequency range from 30 to 80 MHz. AMBER, EASIER and MIDAS prototypes, were developed to measure the microwave emission between 3 and 15 GHz. Since the atmospheric characteristics are very important for the FD, there are several monitoring systems (section 3.4). The Central Laser Facility (CLF) and the Extreme Laser Facility (XLF) that produce UV laser tracks to estimate the aerosol distribution in the atmosphere at different heights. Four LIDAR stations to detect clouds and aerosols, and infra-red cameras are installed on the top of each FD building.

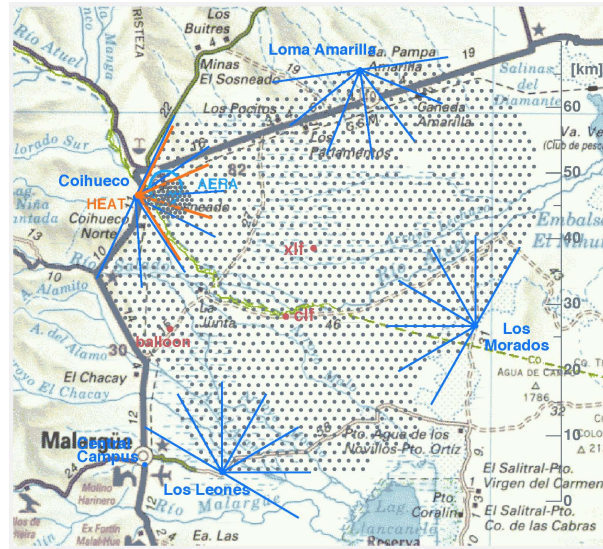


Figure 3.1: Layout of the Pierre Auger Observatory at Malargüe. The dots represent the Surface detector stations, the fluorescence detector stations are in blue on the boundaries of the array (HEAT in orange).

3.1 The surface array (SD)

The secondary particles in a cosmic ray shower arriving the ground can be detected using Surface Detector (SD). The SD of the Pierre Auger Observatory [1, 134, 135] is an array of approximately 1600 WCD, or water Cherenkov tanks, covering $\sim 3000 \text{ km}^2$, in a triangular grid, spaced by a distance of 1.5 km from each other. The final array configuration is slightly different from the initially proposed, since there are small regions in which the deployment was not possible. Water Cherenkov tanks were chosen for their robustness, low cost, good sensitivity in detecting particles at high zenith angles and because they were successfully used in other experiments.

Each unit is a complete autonomous station (see picture and layout on the figure 3.2), equipped with solar panels providing an average of 10 W and two 12 V batteries power the Photomultiplier Tube (PMT)s and the electronics. A commercial Motorola GPS board at the station give the tank trigger time and location with a time precision of $\sim 8 \text{ ns}$. Communication antenna sends the data by WLAN to the Central Data Acquisition System (CDAS) at Malargüe. The ground detector unit is a cylinder tank, produced with rotationally moulded polyethylene, with 3.6 m diameter and 1.55 m high, enclosing a liner filled with 12 m^3 of high purity water, the tank structure is shown in figure 3.2b. The liner is an olefin polymer bag (or Tyvek®) which seal the water inside, protecting it from contamination and is an efficient reflector of Cherenkov light. The top of the tank houses three photomultiplier tubes ($9''^1$ Photonis XP1805), symmetrically distributed at 1.2 m from the center of the tank. The PMTs see the water in the tanks through three clear polyethylene windows set into the top surface of the liner. Each PMT records two signals, an amplified ($\times 32$) signal from the last dynode, and a signal from the anode. The signals are digitalized and various trigger levels are applied, then they are sent to the CDAS. For further information about the water quality and production, PMT enclosure and assembly, liners, power cabling, solar panels and battery box system see reference [134].

¹22.86 cm

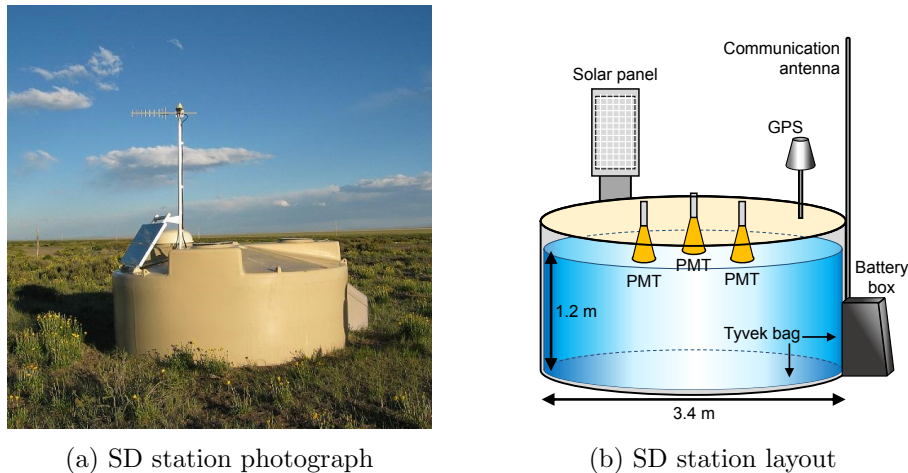


Figure 3.2: A SD station photograph in the left. In the right is the layout of the SD tank.

3.1.1 Data acquisition and SD Calibration

The PMTs detect the Cherenkov light emitted by the particles crossing the tank. The six signals in each tank (amplified dynode and anode signals for 3 PMTs) are read using front-end electronics having 40 MHz Flash Analog to Digital Converters (FADCs). Each FADC bin corresponds to 25 ns. Digitized signals are sent to a PLD (programmable logic device) board, which implements various trigger levels, and then sent to the Central Data Acquisition System.

The WCD signal recorded by the FADC is referred to in units of ADC counts, it measures the current from the PMT or PMT photocurrent (I). It is also possible to obtain an integrated charge (Q). These counts need to be calibrated in each tank to some reference. The calibration unit adopted is the Vertical Equivalent Muon (VEM), defined as the average charge collected in a tank that is fully traversed by a single high-energy muon impinging vertically at the center. In the observatory, it is not possible to choose vertical muons so the best way to calibrate the signal is using the known background muon signal. The atmospheric muons provide the baseline, a peak in the charge histogram ($Q_{\text{VEM}}^{\text{peak}}$) and a peak in a pulse height histogram ($I_{\text{VEM}}^{\text{peak}}$), see figure 3.3.

The PMT calibration is performed in three steps (see references [1, 136, 137]). First, the three PM tubes are matched in gain by adjusting their voltages to have the same rates above a common threshold; the evolution of the gains is monitored and included in the data flow; and finally the absolute calibration is determined from a sequence of measurements made on an identical test tank.

The ADC counts have been chosen to be around 50 channels for $1 I_{\text{VEM}}^{\text{peak}}$. From several test studies, the signal rate above approximately $3 I_{\text{VEM}}^{\text{peak}}$ is 100 Hz. In this way, the voltage in the three PMTs is adjusted until the rate above 150 channels is 100 Hz. Once tanks are calibrated using this method the muon peak is expected with a value around 50. The dispersion at this level is $\sim 8\%$, sufficiently small to allow the next calibration step. The next step is an on-line refinement. For this step, in the data acquisition mode, a first level trigger is applied, which consists of a 3-fold coincidence above a specific threshold ($1.75 I_{\text{VEM}}^{\text{peak}}$). After this trigger, each individual PMT is expected to have a 70 Hz rate above $2.5 I_{\text{VEM}}^{\text{peak}}$. If the single rate is greater than $70 + \sigma$ Hz, the $I_{\text{VEM}}^{\text{peak}}$ is incremented by δ . If it is below $70 - \sigma$ Hz, the $I_{\text{VEM}}^{\text{peak}}$ is decreased by δ . With $\sigma = 2$ Hz and $\delta = 1$ channel, until it converges. The local stations also compute charge associated with the PMT signals by integrating the signal over 625 ns and obtain the

$Q_{\text{VEM}}^{\text{peak}}$. The VEM values associated with the peak and charge for each PMT are sent to CDAS along with the data of those events that are forwarded for reconstruction.

In the final step, in every 4 hours, histograms are compiled, taking data at low threshold (0.15 VEM threefold) to compute the position of the muon peaks. Then this peak is related with reference physical value, namely the signal associated with 1 VEM. This value has been measured using a muon telescope, with two scintillators, placed above and below a test tank. In figure 3.3 b, the 3-fold trigger peak is shown in heavy line and the real VEM peak, from the telescopes in light trace. The peaks are displaced $Q_{\text{VEM}}^{\text{peak}} = 1.09Q_{\text{VEM}}$ [136], since the peak from the telescope comes from vertical muons traversing essentially 1.2 m of water and the other have a continuous distribution of track lengths. The first peak appearing at low charge values is due to charge deposited by short-tracked muons and other particles (gammas after conversion, electrons, slow muon decays, and electronic noise). Using this telescope was also possible to see the correlation between the muon signal and track length in the tank (see figure 3.3 c). Stations are calibrated with respect to this absolute value of the VEM with an overall precision of 5%.

Additional monitoring data is also sent to CDAS like temperature, current and voltage measurements and added to the already defined calibration constants. The ratio between the total charge (Q^{peak}) and the maximum amplitude value (I^{peak}) of the muon signals is directly proportional to the signal decay time and is therefore a useful parameter for the detector quality monitoring.

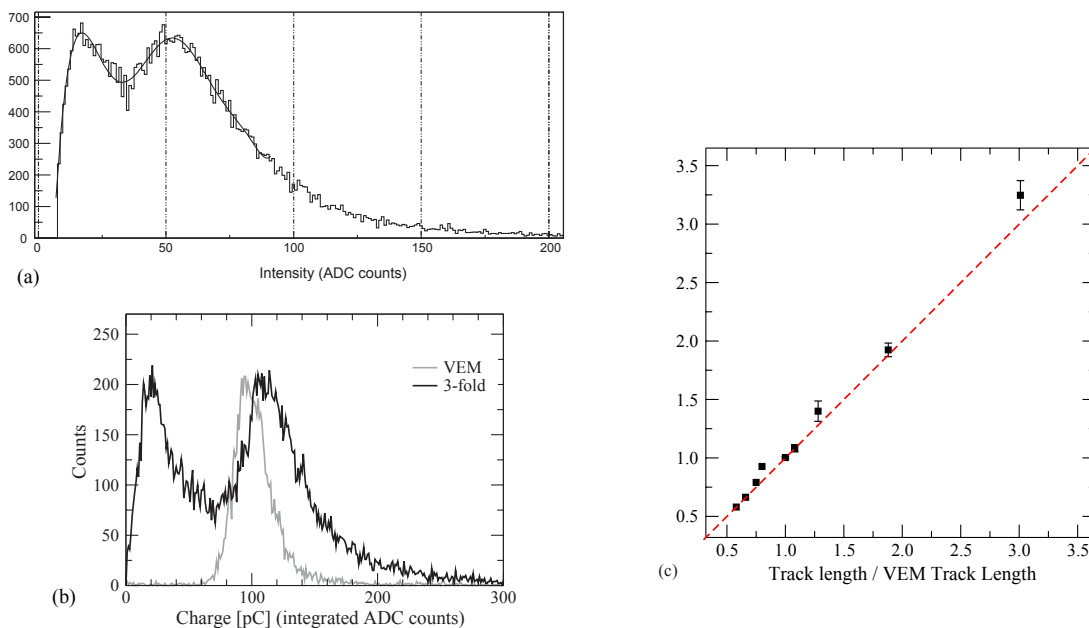


Figure 3.3: a) current intensity in ADC counts ($I_{\text{VEM}}^{\text{peak}}$ should be around 50 channel, from [1]. b) integrated current or charge histograms for the 3-fold trigger darker line and for vertical muons selected with scintillator telescopes in light lines, from [138]. c) VEM signal as function of the muon track length in the WCD, from [138].

3.1.2 SD Triggers

The tanks are being continually hit by particles and most of those are not coming from high-energy EAS (that interest us). The trigger is important to distinguish between the physical events from the background particles. The total gathered data is mainly imposed by the limita-

tions on the wireless communication system. The total bandwidth available for data transmission from the detectors to the CDAS is 1200 bits.s^{-1} . The maximum sustainable rate of events per detector is less than 1 per hour, while each station has a counting rate of around 3 kHz. In this way, to not use the essential bandwidth, the first and second level triggers are performed at the station level (a review of the triggers can be seen in ref. [139]). The triggers sequential order can be seen in the figure 3.4.

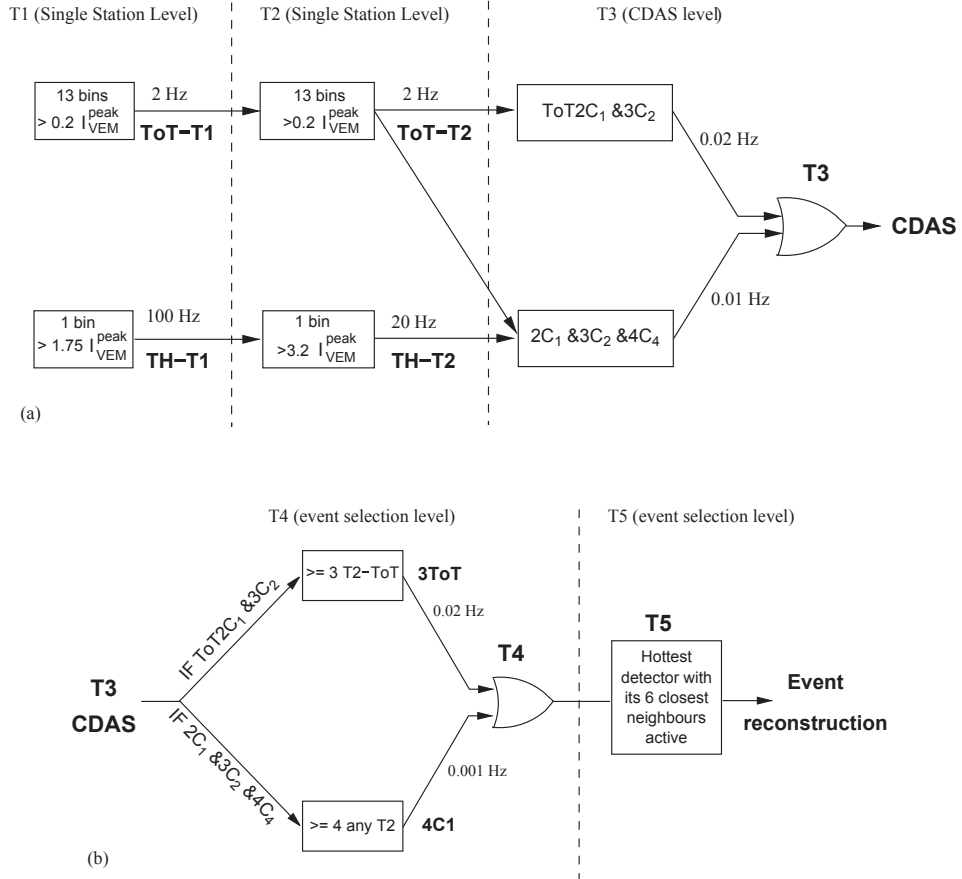


Figure 3.4: Schematics of the hierarchy of the trigger system of the Auger surface detector, from the T1 to the T5, taken from [139].

Local single detector triggers

The first and second level triggers, **T1** and **T2**, are applied locally on the stations. At the level of the T1, there are two independent triggers, the T1 Simple Threshold trigger (**TH**) and the Time-over-Threshold (**ToT**) conceived to detect the muonic and electromagnetic components respectively.

The TH trigger requires a three-fold coincidence of the PMTs in a single time bin, each above $1.75 I_{\text{VEM}}^{\text{peak}}$ and it is efficient selecting large and narrow signals, like the muons, reducing the rate of atmospheric muons from $\sim 3 \text{ kHz}$ to $\sim 100 \text{ Hz}$. The ToT requires a two fold (in three PMTs) coincidence of 13 bins (325 ns) in 120 FADC bins (sliding window of $3 \mu\text{s}$), with signals above $0.2 I_{\text{VEM}}^{\text{peak}}$. The ToT rate at each detector is $< 2 \text{ Hz}$ and is mainly due to the occurrence of two muons arriving within $3 \mu\text{s}$ (since the average signal duration of a single muon is about 150 ns). The second level trigger (T2) is applied to reduce the event rate from 100 Hz to around 20 Hz.

The TH-T1 triggers need to pass a further higher threshold of $3.2 I_{\text{VEM}}^{\text{peak}}$ in coincidence among the three PMTs². The ToT-T1 are automatically promoted to the T2 level.

Array triggers

Once the T2 triggers occur, the stations begins to communicate with the CDAS. The third level trigger (**T3**) is based on the spatial and temporal combination of second level triggers and have two modes. One mode requires a spacial configuration called ToT2C₁&3C₂³. This trigger requires that one of the triggered detectors must have one of its closest neighbours and also one of its second closest triggered, see figure 3.5 left. It gives around 1600 events per day (each detector participates in an event around 3 times per day), where about 90% are real showers. The other T3 selection is 2C₁&3C₂&4C₄ (see footnote 3 and figure 3.5 right). This trigger selects about 1200 events per day where 10% are real showers. The timing criteria for each mode is that each T2 must be within $(6 + 5C_n)$ μs of the reference one.

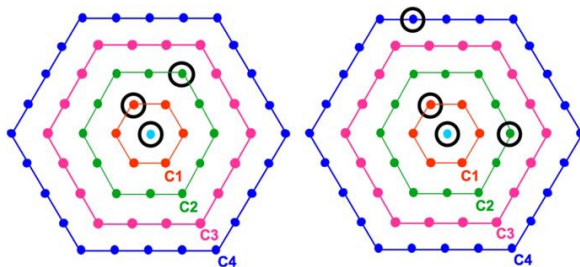


Figure 3.5: The T3 triggers modes. In the left, the the 3-fold T3 mode ToT2C₁&3C₂ and the 4-fold mode 2C₁&3C₂&4C₄ in the right.

The next trigger level is the physics trigger **T4**, to select real shower from the set stored as T3, with two criteria defined with different aims. The first one corresponds to a ToT-3C₁ configuration (denoted by **3ToT**), which means it requires three nearby stations, passing the T2-ToT, in a triangular pattern (drawn in the figure 3.6). Real physics events up to 60° are selected with high efficiency (above 98%). The second criterion T2-4C₁ (denoted by **4C1**) needs four nearby stations with any T2 trigger, the figure 3.6 shows the three minimal configurations. The stations should be compatible in time, so there are also time criterions to fulfil. The stations time must fit a plane shower front moving at the speed of light. To this aim, a "seed" made by the highest signal, three neighbouring detectors in a non-aligned configuration, are chosen in the event. This seed has three stations (that maximize the sum of the signals on the seed configuration) and must be compatible with a planar shower front propagating with speed of light, then:⁴

$$c(t_i - t_1) = -\hat{a}(\check{x}_i - \check{x}_1) \quad \text{for } i \in \{1, 2, 3\}, \quad (3.1)$$

for $i = 1$ is trivial, a provisional axis \hat{a} is obtained and signal time of one of the seed stations, t_1 , considered. At this point, all stations start times are checked for compatibility with a planar front around that seed. Accordingly, the predicted times t_{sh} for the station \check{x} is given by:

$$t_{sh}(\check{x}) = t_1 - \check{a}(\check{x} - \check{x}_1)/c. \quad (3.2)$$

²For detectors with only two(one) operating PMTs the threshold is set to 3.8 (4.5) $I_{\text{VEM}}^{\text{peak}}$.

³ mC_n means m triggered stations inside the n th ring

⁴**Notations:** \vec{a} represents a vector and \check{x} stands for a position point with absolute value of coordinates. In this way, a vector can be defined as $\vec{a} = \check{x}_2 - \check{x}_1$.

The difference between the predicted times and the station real time is $\Delta t_i = t_i - t_{sh}(\check{x}_i)$. The event must satisfy:

$$-1000 \text{ ns} < \Delta t_i < 2000 \text{ ns} . \quad (3.3)$$

If the station delay lies outside this interval, then it is flagged as *accidental* station.

The detectors with no triggered neighbours within 3 km are flagged as *lonely*. Also lightning-originated signals are classified as *lightning*. If the signal does not exceed 1000 FADC counts and makes more than three baseline crossings, it is considered to be generated from a lightning. Both are removed from the reconstruction.

The joint detection efficiency of the two criterion are about 99.9%.

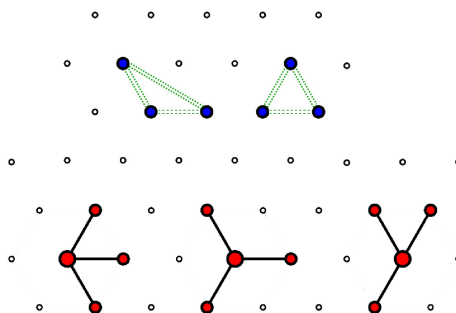


Figure 3.6: Minimal T4 configurations: 3ToT (on top) and $4C_1$ (bottom).

After this trigger levels, there are some events that may lie in the borders of the array. Missing information on these events may lead to incorrect core reconstructions and wrong energy estimations. The trigger **T5** (or fiducial trigger) selects events well contained within the array. It requires that the station with the largest signal must have at least 5 working stations (not necessarily triggered) in its closest neighbours (also denoted by **5T5**). The event can also be classified as **6T5** requiring 6 working stations.

The complete trigger sequence can be seen on the previous figure 3.4. The final triggers efficiency computed for different primary types as a function of the energy with Monte Carlo simulation is plotted in the figure 3.7. The Auger SD array is full efficient above 3 EeV for both proton and iron primaries.

3.1.3 SD Reconstruction

The event can be reconstructed using only the SD information such as the coordinates of the triggered stations (given by the GPS) and the timing of the triggered station (arrival time of shower front t_i , given by the PMTs ADC). With this, the shower direction and front curvature can be extracted and the energy can be estimated using the lateral distribution of the signals. In the reconstruction process, only stations classified as *candidates* are used. The stations considered as *accidental*, *lonely* or *lightning* are excluded. The shower core position is calculated by weighting the average triggered stations coordinates, x_i, y_i , with the weight $W_i = \sqrt{S_i}$, where

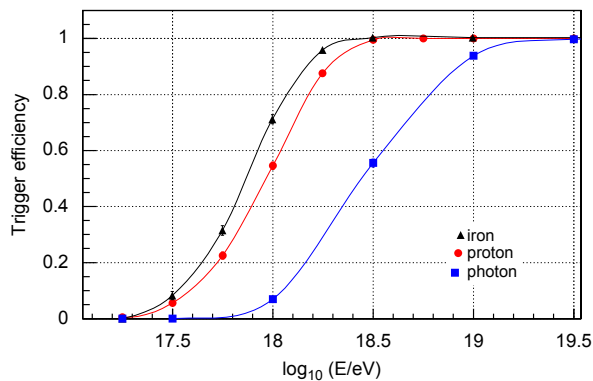


Figure 3.7: SD trigger efficiency as a function of Monte Carlo energy for proton, iron and photon primaries in circles, triangles and squares respectively (for zenith angles up to 60°), from [139].

S_i is the station signal,

$$\begin{aligned} x_c &= \frac{\sum W_i x_i}{\sum W_i}, \\ y_c &= \frac{\sum W_i y_i}{\sum W_i}. \end{aligned} \quad (3.4)$$

The signal weighted barycenter $\check{b} = (x_c, y_c)$ and barytime t_0 are set as the origin at which the distances and times are measured. The shower plane is the first approximation to the shower front. A shower track \check{x} moving at the speed of light along the axis defined by \check{a} (normalized) and passing the origin at time t_0 obey the relation:

$$\check{x}(t) - \check{b} = -c(t - t_0)\hat{a}, \quad (3.5)$$

see the geometry displayed in figure 3.8. The vector \hat{a} is pointing towards the CR source. The shower plane is a plane perpendicular to the shower axis moving along with the same speed and containing the shower forehead. So, the time $t(\check{x})$ at which the shower crosses the ground in the position \check{x} is given by the point projection in the axis:

$$ct(\check{x}) = ct_0 - (\check{x} - \check{b})\hat{a}. \quad (3.6)$$

Considering only the time uncertainty σ_t of the signal start, the shower plane is then obtained minimizing the sum of the squared time differences between the measured signal start times and the predicted times. It takes the form:

$$\chi^2 = \frac{1}{\sigma_t^2} \sum_i [t_i - t(\vec{x}_i)]^2 = \frac{1}{c^2 \sigma_t^2} \sum_i [ct_i - ct_0 + \vec{x}_i \cdot \hat{a}]^2, \quad (3.7)$$

where $\vec{x}_i = \check{x}_i - \check{b}$ and t_i are the position and time of the i^{th} station. Considering the components of $\check{a} = (u, v, w)$ and $\vec{x}_i = (x_i, y_i, z_i)$, it gets:

$$\chi^2 = \frac{1}{c^2 \sigma_t^2} \sum_i [ct_i - ct_0 + x_i u + y_i v + z_i w]^2. \quad (3.8)$$

The vector \hat{a} must be unitary by construction. This may be simplified, assuming that all station are close to some plane and $z_i \ll x_i, y_i$, the z component is neglected and a linear approximation

to equation 3.8 can be used (see ref [140]).

The plane shower front is an approximation that can be refined assuming a curved front, such as shown in figure 3.8 (right). The angular resolution of the axis is determined from simulations and depends on the number of tanks used in the reconstruction. It is around 2.2° for events with energy $E \geq 4$ EeV, which on average only have 3 candidate tanks, and is better than 1° above $E \geq 10$ EeV, where events show a large multiplicity.

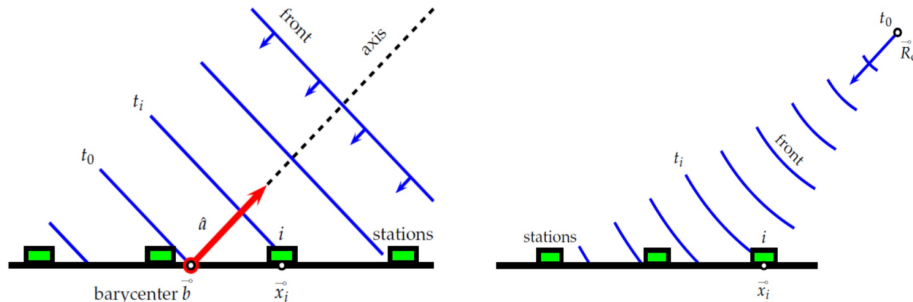


Figure 3.8: Scheme of the plane (left) and spherical (right) shower front arriving the SD tanks.

3.1.3.1 Energy Reconstruction

The energy estimation, in the SD, with the stations signal, using the (LDF). The energy estimator in the SD is the expected signal at a chosen distance from the core. In Auger, the expected signal $S_i(r)$ (in VEM) on the ground at a perpendicular distance r to the shower axis, is described by:

$$S(r) = k \cdot f_{LDF}(r, \theta, E), \quad (3.9)$$

the $f_{LDF}(r, \theta, E)$ is the lateral shape, that depends on the zenith angle of the shower axis (θ) and the primary energy (as seen in the equation 3.10). Usually, $f_{LDF}(r, \theta) = 1$. The parameter k is the size parameter used for the energy estimator. The SD signal at a particular distance chosen as the energy estimator must be sufficiently insensitive to shower fluctuations (due to statistics). Moreover, the exact functional of the LDF is not known, so the optimum point for the estimator should also be in the region where it is less dependent on the functional form. This region is completely dependent on the geometry of the sparse array.

A way to find the optimum distance, r_{opt} , is to fit an event several times with different LDF shapes. In figure 3.9 left, the same event was fitted 50 times with different slopes and the optimum distance was found to be around $r_{opt} = 970$ m. In the right of the same figure, the optimum distance as function of the array spacing can be seen.

So, given the Auger surface array configuration, the optimum point, where the impact of the fluctuation is minimal, is the region around 1 km away from the shower core (see [141]).

Also, as saw in the previous chapter, the LDF can be described as a NKG function, the $f_{LDF}(r, \theta, E)$ chosen in Auger is:

$$S(r) = S(1000) \left(\frac{r}{1000} \right)^\beta \left(\frac{r_s + r}{r_s + 1000} \right)^{\beta + \gamma}, \quad (3.10)$$

where β is the LDF slope, which depends on the zenith angle (see section 5.1.2) and γ is small, but it could be left free, if the event have a high station multiplicity. The parameter $r_s = 700$ m is fixed. The $S(1000)$ is the signal at $r = 1000$ m, it is later used as the energy estimator

and calibrated with the FD energy using the CIC method (see chapter 5) for the procedure description). One SD event can be see in figure 3.10.

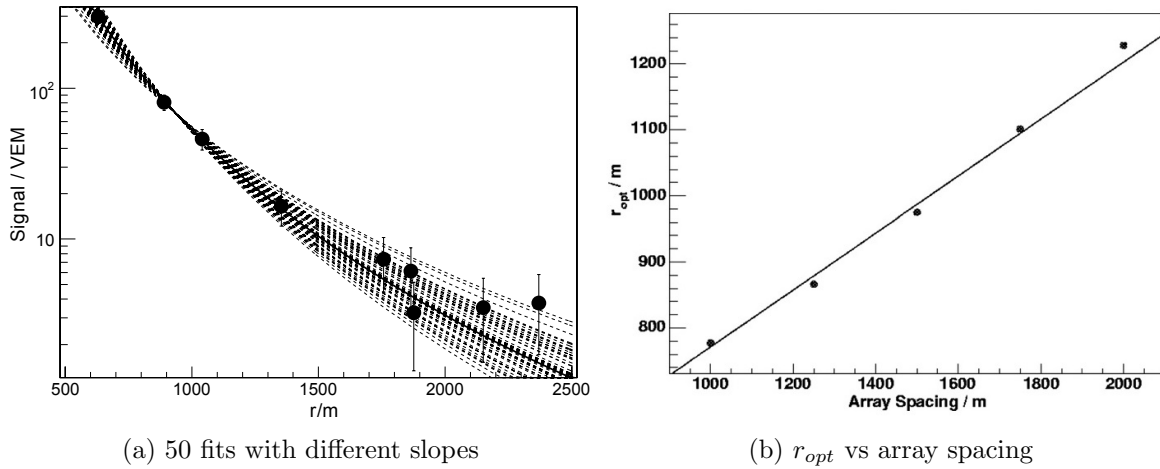


Figure 3.9: Left: Reconstructing the same event 50 times with different slopes allowing the optimum ground parameter, r_{opt} to be found. Right: r_{opt} as a function of the surface array spacing, from [141].

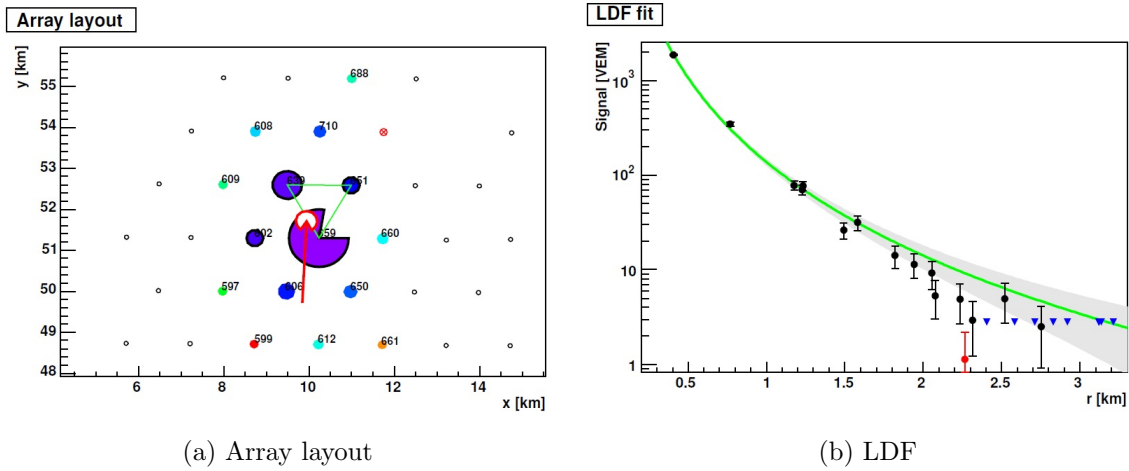


Figure 3.10: Array layout a), and LDF fit result b), for the event ID 1153192, from [140].

3.2 The Fluorescence Detector (FD)

The Fluorescence Detector (FD)[142, 135] was built to measure the fluorescence light (section 2.4.2) emitted by the atmospheric nitrogen and follows the development of the shower through the atmosphere. It was projected to have a resolution of $\sim 20 \text{ g.cm}^{-2}$, since the difference between X_{max} in iron and protons in the models is about $\sim 100 \text{ g.cm}^{-2}$ (and thus would be possible to distinguish between the two). It consists in four Fluorescence Detector sites⁵ (figure 3.11a); Los Leones, Los Morados, Loma Amarilla and Coihueco. The layout of the site is draw in the figure 3.11b. Each one has six independent telescopes with a FOV of 30° in azimuth angle and 28.6° in vertical angle and an inclination of 16 degrees to the horizontal. Consequently, each site has a total FOV of $28.6^\circ \times 180^\circ$ (see figure 3.11).

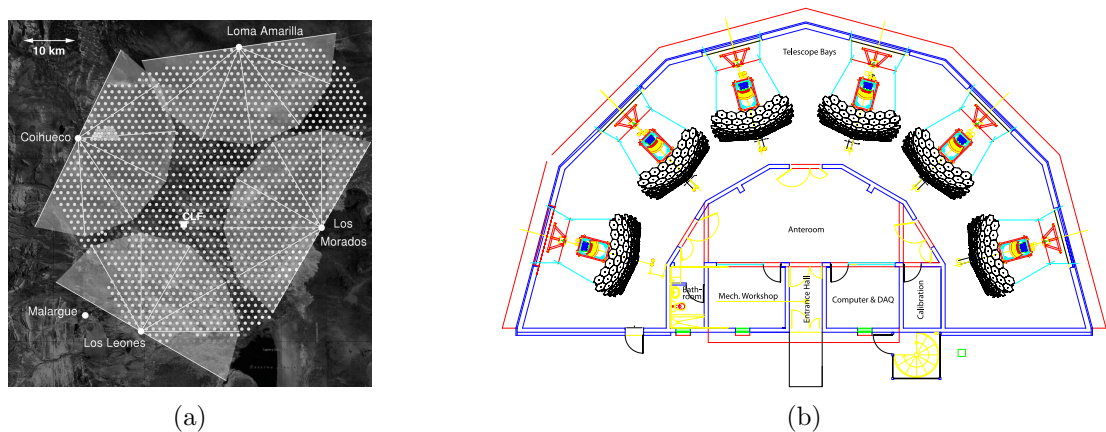


Figure 3.11: Left: the four FD sites with the respective telescopes field of view in gray area, gray dots show the positions of surface detector stations. Right: layout of the FD building with six fluorescence telescopes. From [142].

A photograph and the layout of the telescopes can be seen on the figure 3.12. They are housed in a clean, climate-controlled house, consisting in a shutter, a filter at the entrance window, a circular aperture, a corrector ring, a mirror and a camera with photomultipliers. Due to the large FOV needed, the telescopes are modified Schmidt cameras (except for the shutter and filters) design, that partially corrects spherical aberration and eliminates coma aberration[142].

The entrance window of the aperture system is a optical filter made of Schott MUG-6 glass⁶ with 3.25 mm thick and $80 \text{ cm} \times 40 \text{ cm}$, having a transmission of 85% for wavelength of 350 nm and decreases to 20% at 300 nm and 400 nm. This is important to reduce the amount of background light especially in other frequencies. The filter seals the FD light entrance and is reinforced mechanically by a metallic grid (the shutter) to protect the telescope from wind, dust, rain and light. In the aperture box, the diameter of the diaphragm was set at 1.7 m, which ensures a nearly uniform spot of about 0.5° with this optics, and giving an effective area for light collection of 1.5 m^2 (after taking account of the shadow of the camera). After the diaphragm, the corrector ring is placed (with radius between 0.85 m and 1.10 m) in order to double the aperture[143], while maintaining the quality of the spot⁷.

⁵Each site is known as *Eye*

⁶from Schott Glaswerke, Mainz, Germany <http://www.schott.com>

⁷or "point spread function", is the photons spread of a point-like source, at the focal plane, due to aberrations. This spread increases with the distance to the geometry center and the size of the spot characterizes the quality

The light that passes the aperture box is focus into the camera with mirrors of 3.6×3.6 m and 3.4 m radius. Due to the large area of the primary mirror, it was segmented. The segments are fixed to a strong and precise supporting structure through an adjustable set, so that a good overall alignment is achieved. There were two segmentation configurations⁸. At the Los Leones and Los Morados, a tessellation of 36 rectangular anodized aluminium mirrors of three different sizes was used. It consists in two layers, glued to the aluminium surface, a sheet of $AlMgSiO_5$ to achieve reflectivity, and an aluminium-oxide layer to provide additional protection. At Loma Amarilla and Coihueco was used a structure of 60 hexagonal glass mirrors (of four shapes and sizes) with reflective coatings. The glass segments were coated under high vacuum with a layer of 200 nm of aluminium and anodised for protection. In both types of mirrors, the average reflectivity at $\lambda = 370$ nm exceeds 90%.

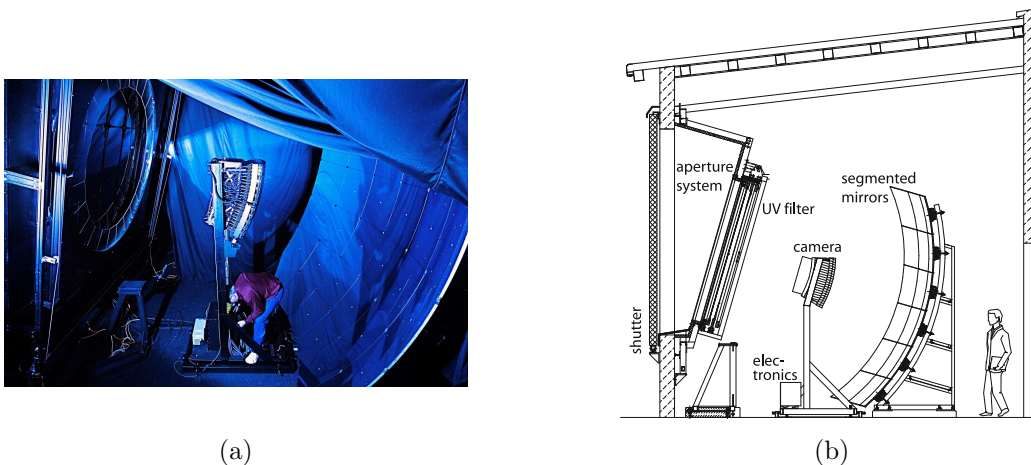


Figure 3.12: Left: picture of a telescope bay, by L. Wiencke at National Accelerator Laboratory, in Menlo Park (USA), 2009. Right: layout of the telescopes from [142]

The camera has 440 hexagonal pixels (in a matrix of 22 rows by 20 columns, with $6 \text{ cm} \times 94 \text{ cm}(w) \times 86 \text{ cm}(h)$) located on the focal surface of the telescope mirror, which is a sphere of 1.743 m radius. It is fixed to a massive steel support to guarantee mechanical stability. Each pixel is a hexagonal PMTs Photonis XP3062⁹, inside a hexagonal window with 40 mm from side to side. They have a field of view of 1.5° . Some space between the PMT is needed for a safe mechanical packing. In this way, for a better light collection efficiency and to have a smooth efficient transition between the pixels, each PMT is surrounded by a simplified version of the classical "Winston cones", which are called the *Mercedes stars* (see figure 3.13). These reflective surfaces are inclined, to reflect about 90% of the light into the PMT.

The spot⁷ indicated in figure 3.13 is the circle of least confusion, ie, due to aberrations, photons entering the telescope can be seen in the camera with a displacement from the original position and so the spot is the area where those photons can be detected. The Schmidt optics was chosen in order to maintain this constant distance. The spot has an angular size of 0.5° (0.25° radius) which corresponds to about one third of the pixels with 1.5° opening angle. This means that the aberrations effects are not very significant, taking into account the pixels size. Several spots shapes, accordingly with the photon angular direction can be seen in [142].

The FD only operates in nights with moon fraction below 60% and without poor or dangerous weather conditions for operation (rain, snow, high wind speed). Each telescope only work if the

of the optical system.

⁸The two different configurations were used due to production reasons, to be divided in to two laboratories.

⁹by PHOTONIS <http://www.photonis.com>

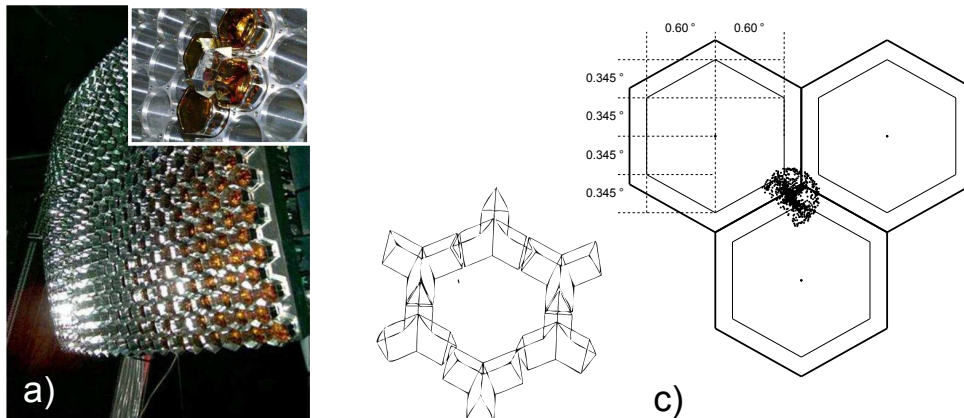


Figure 3.13: a) camera photograph with zoom of a few pixels, from [142]. b) six Mercedes star (Winston cones) around the space of one pixel, to reflect the light into the PMT, that would be lost in the PMTs interstices. c) pixels angular dimensions and an example of a spot light, from [144].

moon in any phase is 5° away from the telescope field of view. The average observation period lasts 16 days per month, with an average observation time of about 10 h (a maximum of 14 h in June and a minimum of 5 h in December). The fraction of the total time during which the FD is acquiring data, uptime, is on average $\sim 15\%$.

3.2.1 FD Calibration

The FD detector follows the longitudinal development of the shower, being the basis for the energy measurement of the primary particle. Along these lines, the ability to convert pixel ADC counts into a light flux, through the calibration, is very important. It is calibrated in two processes: an absolute calibration (made from time-to-time and serving as a reference for the relative calibration); and a relative calibration (that is made regularly).

A calibration step-by-step would be extremely difficult. It would need to include diaphragm area projection, optical filter transmittance, mirror reflectivity, pixel light collection efficiency and area, cathode quantum efficiency, PMT gain, pre-amp and amplifier gains, and digital conversion. So, a single end-to-end calibration is performed [142, 145, 135], taking into account all the effects (this is the absolute calibration). For this purpose, a calibrated 2.5 m diameter light source, called the "drum", is installed at the telescope aperture. The drum is a cylinder with 2.5 m diameter and 1.4 m depth (figure 3.14) illuminated by a pulsed UV LED (375 ± 12 nm), mounted against the face of a 2.5 cm diameter \times 2.5 cm long TeflonTM (good light diffuser) cylinder cup. This cup illuminates the interior of the drum, which is made in Tyvek on the side with a front sheet of 0.38 mm thick Teflon, which transmits light diffusively. This produces a uniform light within 2%. The drum is calibrated measuring the absolute light flux using a NIST-calibrated photodiode leading to a precision of about 7%. The FD camera PMTs can be calibrated with a uncertainty of 9%, performed once per year. The average response of the FD is 5 photons/ADC bin. In figure 3.15, is the FD response relative to 380 nm using the drum.

A remote vertical laser shots of known intensity and wavelength are used as a cross-check of the drum calibration. The called Roving Laser, is a portable nitrogen laser, with 337 nm, with about $100 \mu\text{J}$ per pulse fired in each telescope field of view. The light collected by the telescope depends on the Rayleigh scattering and the aerosol attenuation. The second can be neglected,

if the laser is close to the telescopes, so the number of photons detected by the telescope can be predicted within an uncertainty of 12% allowing to check the previous telescope absolute calibration.

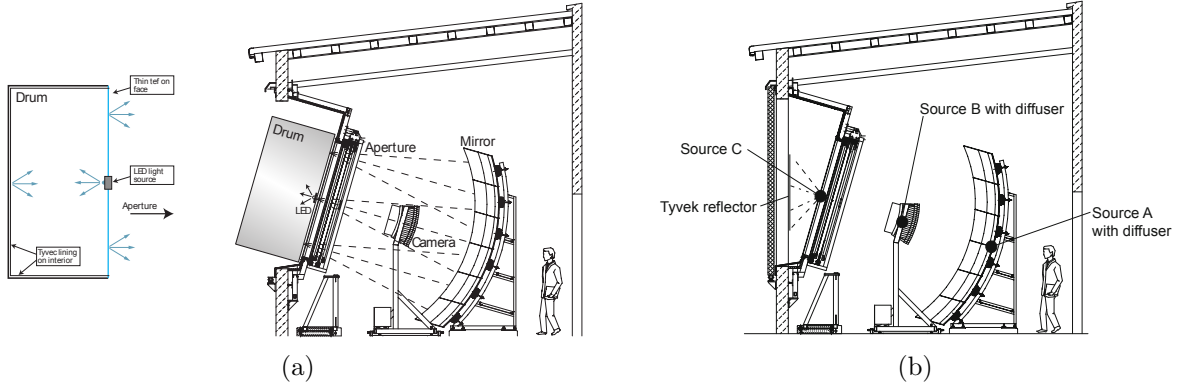


Figure 3.14: Left: Scheme of the drum placed on the telescope. Right: Telescope picture with the A, B and C calibrations positions.

The relative calibration is done every night, before and after data collection, to detect possible time modifications that the calibration might suffer. It is done with three light sources coupled to optical fibres, which distributes the light into three destinations on each telescope (see figure 3.14 right). The A light source is a 470 nm LED and each of the B and C light sources are xenon flash lamps.

In the **Calibration A**, the source is brought to the centre of the mirror, by optical fibres, with the light directed to the camera. This allows to monitor the stability and linearity of the PMTs. In the **Calibration B**, a light source is placed at the centre of the two sides of the camera with the light directed at the mirror (through a Teflon diffuser in the end). It includes a Johnson-U filter, approximating the full wavelength acceptance of the fluorescence telescopes. It allows to monitor the mirror reflectivity.

In the **Calibration C**, the third source is sent to ports on the sides of the entrance aperture, where the light was directed at reflective Tyvek targets mounted on the telescope doors, and from which the light is reflected back into the telescopes. It contains interference filters centred at wavelengths of 330, 350, 370, 390 and 410 nm, for monitoring detector stability at wavelengths spanning the spectral acceptance.

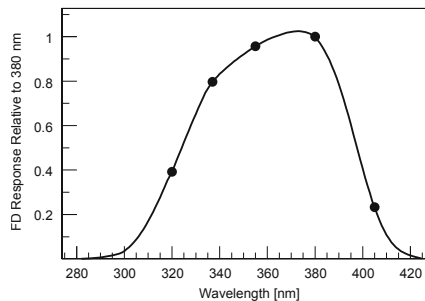


Figure 3.15: Results of the multi-wavelength measurements for the FD response relative to 380 nm using the drum (from [142]).

3.2.2 Data acquisition and FD Trigger

All Telescopes operate independently and have to detect a widely varying intensity, over a background of intense and changing light.

The PMTs high voltage is provided by a CAEN SY527 system, in groups of 44 PMTs with similar gains (10 groups per camera) and a commercial power supply provides the low voltage. The high and low voltage are distributed by 10 power control boards at the back of the camera. The PMT signals are received by a set of 20 front-end boards, for groups of 22 pixels from camera columns. The signals are continuously digitized by 10 MHz 12 bit FADCs. The electronics and DAQ are hierarchical according with the physical layout of the FD buildings, divided into four logical units (see figure 3.16): head electronics for 440 PMTs in each 6 telescopes, which provide low and high voltage; front-end (FE) sub-racks, where the signals are shaped and digitized, and where threshold and geometry triggers are generated; the DAQ subnet, in which six telescope PCs (Mirror PCs) readout the stored data and perform additional software-based background rejection; and one FD site network, in which a single computer (named EyePC) merges triggers from the six telescopes and transfers them to the CDAS in Malargüe. The FD site network also contains a Slow Control PC for remote operation of the building. The camera electronics and PCs are synchronized by a clock module based on the Motorola On core UT+GPS receiver, the same receiver used in the SD array.

The electronics and data acquisition system need to have large dynamic range and provide a strong background rejection while accepting any physically plausible air shower (using three trigger levels).

The first level trigger (**FLT**), or pixel trigger is done by the Field-Programmable Gate Arrays (FPGAs) in the front-end. While the ADC values are continuously written to memory, the running sum of the last n ADC bins ($5 < n < 16$) is compared to an adjustable threshold. The pixels trigger, whenever the running sum exceeds an adjustable threshold. The threshold value is dynamically adjusted to keep the trigger rate as close as possible to 100 MHz. When the signal drops below the threshold, the pixel trigger is extended for an adjustable period of 5-30 μ s, increasing the chance of coincidence with other triggered pixels.

The second level trigger (**SLT**), also made by the FPGAs, is designed to detect straight-track patterns in the FLT triggered pixels. It requires that, in a time window between 1 and 32 μ s, there are at least five adjacent triggered pixels in any of the patterns depicted in figure 3.16 or those generated by their rotations. If some PMT is not collecting enough data or having problems, the trigger can require that only four out of five pixels triggers, giving rise to 108 different combinations of four-fold patterns from the previous five-pixel track segments.

Once the data is considered as SLT, it is analysed in the MirrorPCs, with a software algorithm intended to remove noise events that survive the first and second level triggers. This is the Third Level Trigger (**TLT**) or hybrid trigger, designed to check the time structure of the event and neglect sequences generated by pixels not correlated in time. In normal conditions, the SLT detect one or two events per minute per telescope, but a lightning can trigger hundreds of pixels at the same time and several tens of events per second, increasing the dead-time considerably. The TLT filters lightning events, reading the FLT multiplicities. The rejections made, based on the time development, multiplicity and its integral over the whole event, are able to cut approximately 99% of all lightning events in a 50 μ s decision window. The TLT is also optimized for rejection of triggers caused by muon impacts on the camera and randomly triggered pixels.

The events that surviving the TLT are collected by the EyePC, performing a final level trigger **T3**. The software system merges coincident events from adjacent telescopes, perform a preliminary event reconstruction of the direction, time and impact on the ground, and sends the event to the CDAS. The T3 also acts as an external trigger for the SD, allowing to record events below

$3 \cdot 10^{18}$ eV, where the array is not fully efficient and would not often generate an independent trigger. This is important since even limited SD data (one or two SD stations) are sufficient for high-quality hybrid reconstruction.

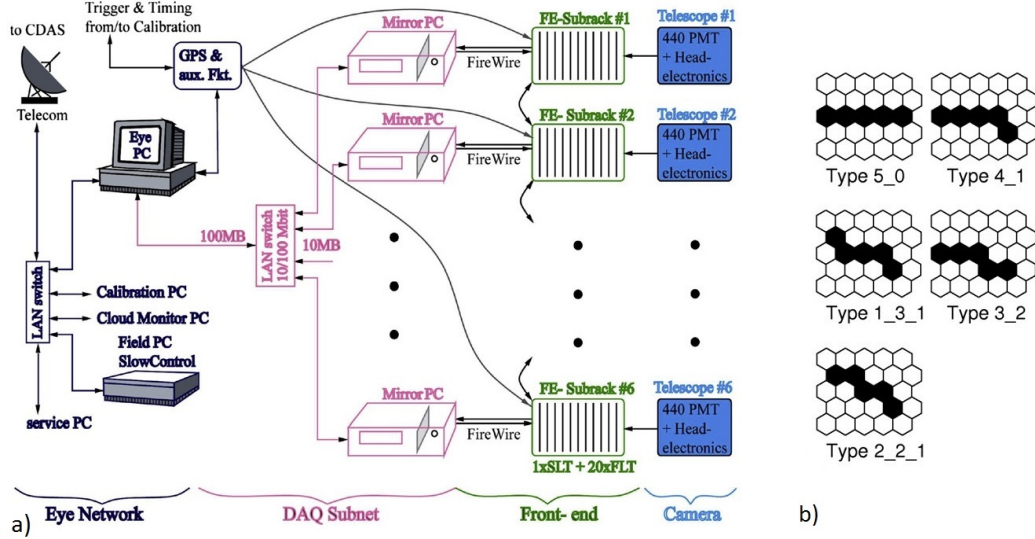


Figure 3.16: a) Readout scheme of an FD site, into four logical units, where the data flow is right to left. b) Types of pattern regarded as straight track segments for the SLT trigger.

3.2.3 FD Geometry Reconstruction

The FD geometrical reconstruction is done in two steps, first the plane containing the shower axis and the observation point, called the Shower Detector Plane (SDP) must be determined and then the arrival time of the photons to the detector is used to determine shower direction within the SDP (see figure 3.17).

Each camera pixel sees in a direction r_i , so the shower plane will intersect the FD on the corresponding pixels that have been triggered. These candidate pixels, to the SDP reconstruction, should lay less than 4 columns or rows away from any other. The SDP normal vector n_{SDP} can be found by minimizing the amount:

$$\chi^2 = \sum_i (\vec{r}_i \cdot \vec{n})^2 \cdot w_i, \quad (3.11)$$

where w_i is a weight proportional to the i^{th} pixel signal. After the SDP is known, in the next step, the geometrical reconstruction of the shower is reduced to a 2-dimensional problem. If the event is only seen by one FDeye is called FD-Mono reconstruction. This step is accomplished using the trigger times of the pixels. In this way is necessary to estimate the nearest distance of the shower to the observation point (FD), the R_p , the time t_0 at which the shower front passes by the closest point to the telescope and the angle χ_0 between the shower axis, in the SDP plane, and the detector plane (see figure 3.17). These parameters can be obtained minimizing the χ^2 of the times:

$$\chi^2 = \sum_i \frac{(t_i - t_i^{exp})^2}{(t_i^{err})^2}, \quad (3.12)$$

where t_i is the time of the i^{th} pixel¹⁰, t_i^{exp} the expected arrival time to the same position and t_i^{err} is the centroid error for that pixel.

According with the figure 3.17, the time expected t_i^{exp} is the time t_0 less the time of the shower propagation (τ_i^{sh}) between the i^{th} position and the t_0 position plus the propagation time from the i^{th} position to the detector (τ_i^{prop}). The expected arrival time can be written in terms of R_p , t_0 and χ_0 as,

$$\begin{aligned} t_i^{\text{exp}} &= t_0 - \tau_i^{\text{sh}} + \tau_i^{\text{prop}} \\ &= t_0 - \frac{R_p}{c} \left[\frac{1}{\sin(\chi_0 - \chi_i)} - \frac{1}{\tan(\chi_0 - \chi_i)} \right] \\ &= t_0 + \frac{R_p}{c} \tan\left(\frac{\chi_0 - \chi_i}{2}\right). \end{aligned} \quad (3.13)$$

An example of this fit is in the figure 3.17 right, in red. The equation 3.13 only uses simple geometry, which can be further improved taking into account phenomena like larger fluorescence de-excitation times, a reduced speed of light and the bending of the fluorescence photons due to a refractive index, $n_i > 1$. This would give rise to geometry corrections up to 0.2° and a few percent in the primary reconstructed energy. The shower can be seen by more than one FD, in these called stereo events, the shower axis can be defined by the intersection of the several SDP planes improving the determination of the geometry parameters.

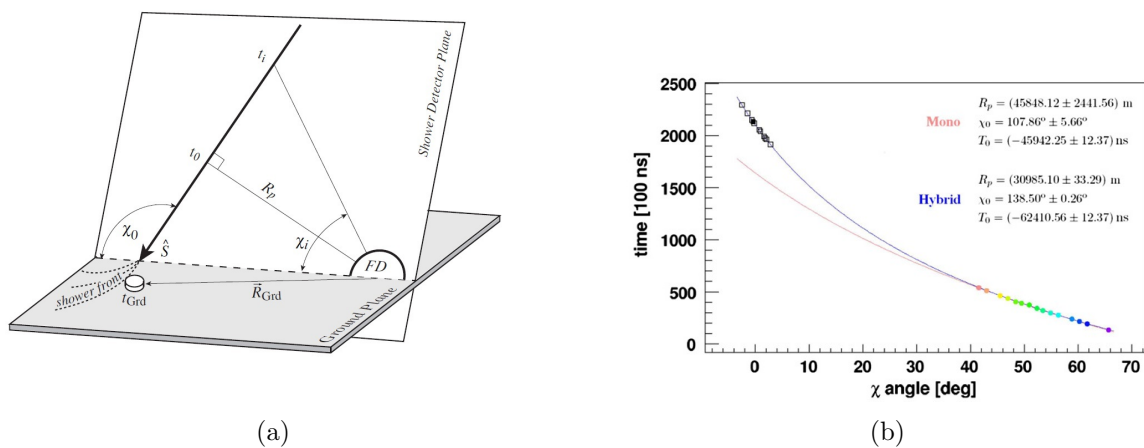


Figure 3.17: left: Scheme of the shower geometry with the important parameters. Right: the light arrival time at each pixel in relation to the angle between the pointing direction of that pixel and the horizontal line. The color points came from FD data and the black squares from SD, the monocular (red line) and hybrid (blue line) are reconstruction fits to equations 3.13 and 3.30.

3.2.4 FD Energy Reconstruction

The energy of the primary CR can be obtained integrating the longitudinal profile, in dE/dX from the FD and applying a small correction due to the invisible energy. As said before, the atmosphere works like a calorimetry, where the shower deposits its energy. To obtain this longitudinal profile, first, it is necessary to determine the light profile as a function of FADC

¹⁰normally is the the weighted time of the centre of the PMT signal.

time bins. Then the time is converted in atmospheric depth $X[\text{g}/\text{cm}^2]$ using the geometry information. And finally, the different light contributions are estimated in order to obtain the fluorescence light profile, which is the one proportional to the primary energy.

After the ADCs signal are converted into photons, they must be summed in a specific distance around the shower plane. Since the shower image has some width (due to shower, atmosphere and telescopes characteristics), it will deposit photons in several pixels. Let ζ be the angular distance between the pixel alignment direction \vec{R}_{pix} and the direction of the shower at a specific time, \vec{R}_t , so that

$$\zeta = \arccos \left(\vec{R}_{pix} \cdot \vec{R}_t \right). \quad (3.14)$$

The pixel with $\zeta < \zeta_{opt}$ are selected. The optimal, ζ_{opt} is chosen as the ζ that maximizes the signal (S) to noise (N) ratio, plus 0.2° , with

$$\frac{S}{N} = \frac{\sum_t \sum_{\zeta < \zeta_{opt}} [n_{adc}(t_i) - n_{ped}]}{\sum_t \sum_{\zeta < \zeta_{opt}} \sigma_{ped}^2}, \quad (3.15)$$

where $n_{adc}(t_i)$ is the FADC trace value at time t_i , the parameter n_{ped} and σ_{ped} is the mean and the variance of the baseline, respectively. $n_{ped} \sim 100$ ADC is considered the baseline for the background.

With the ζ_{opt} the light flux in each time bin (of 100 ns) can be obtain as

$$n_\gamma^{370\text{nm}} = \sum_{PMT} C_{PMT}^{370} [n_{adc}(t_i) - n_{ped}]. \quad (3.16)$$

The C_{PMT}^{370} is the absolute calibration, given in 370 nm photons at the diaphragm over FADC count units (seen in section 3.2.1).

The next step is to obtain the longitudinal profile in atmospheric depth. Since the geometry is already known, is easy to get the slant depth at position i , $X_i = \int_{z_i}^{\infty} \rho(z) \frac{dz}{\cos \theta}$, where θ is the shower zenith angle and $\rho(z)$ is the atmospheric density. The equation is valid if $\theta < 60^\circ$, above that the calculations must consider the Earth curvature.

In the last step, the fluorescence light is determined considering the specific geometry of the shower. In this way, all contributing light sources need to be disentangled[146]: fluorescence light [77, 105, 106], direct and scattered Cherenkov light [114, 147] as well as multiple-scattered light [148, 149].

The fluorescence light is emitted isotropically and depends on the deposited energy along the atmosphere. The Cherenkov light comes mainly from electrons/positrons and have directions very close to the shower axis. So, an observation point close to the shower axis will be dominated by Cherenkov light, while if it is on a side position, the light would be dominated by fluorescence light.

Moreover, both light components are scattered across the air and it need to be accounted for. This means that even an observation point far away from the shower axis can have a considerable Cherenkov scattered light, this effect is higher in late stages of the shower development due to the presence of aerosols in the atmosphere near the Earth surface(see figure 3.18).

The fluorescence light flux y_i^f , measured at the FD pixel i can be given by:

$$y_i^f = \frac{A\epsilon T_i}{4\pi r_i^2} N_\gamma^f(X_i) = \frac{A\epsilon T_i}{4\pi r_i^2} Y_i^f \frac{dE}{dX_i}, \quad (3.17)$$

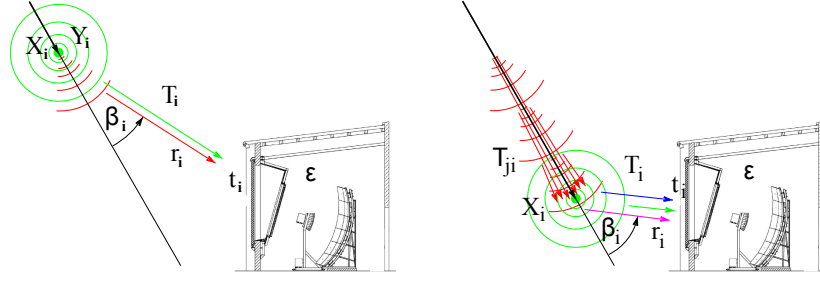


Figure 3.18: Direct fluorescence and Cherenkov light (a) and scattered Cherenkov light (b) received at diaphragm. Isotropic fluorescence light in green, direct Cherenkov light in red, Rayleigh-scattered Cherenkov light in blue and Mie-scattered Cherenkov light in magenta. From [150].

for fluorescence photons. It depends on the detection efficiency ϵ , on the aperture A and on the fraction T_i due to Rayleigh and Mie attenuation, for the geometrical path corresponding to the pixel i . The fluorescence yield is denoted by Y_i^f .

The direct Cherenkov, at the FD aperture emitted at an angle β_i with respect to the shower axis is given by:

$$y_i^{Cd} = \frac{A\epsilon T_i}{4\pi r_i^2} f_C(\beta_i) N_\gamma^C(X_i) = \frac{A\epsilon T_i}{4\pi r_i^2} f_C(\beta_i) Y_i^C \Delta X_i N_e(X_i), \quad (3.18)$$

where $f_C(\beta_i)$ is the fraction of Cherenkov photons emitted at an angle β_i with respect to the shower axis, since Cherenkov is emitted mostly in a narrow cone along the particle direction. The number of electrons and positrons above a certain energy cutoff is given by $N_e(X_i)$. The details of Cherenkov light production, like particle energy threshold for Cherenkov emission are included in the Cherenkov yield factor Y_i^C (ref. [114, 147]). The term ΔX_i is the variation depth in the i th pixel with corresponding time bin, since the Cherenkov depends on the length travelled by the particles.

The Cherenkov light scattered across the atmosphere must also be accounted for. The amount of Cherenkov light on a point X_i depends on the previous history of the shower, so in a one dimensional model, the number of photons present in the beam at a given X_i is just the sum of the photons produced in all previously depths X_j , attenuated from the initial depth by T_{ji} . It gives

$$N_\gamma^{beam}(X_i) = \sum_{j=0}^i T_{ji} Y_j^C N_e(X_j). \quad (3.19)$$

Details on the T_{ji} can be seen in ref. [114]. The scattered Cherenkov light received at the detector is then

$$y_i^{Cs} = \frac{A\epsilon T_i}{4\pi r_i^2} f_s(\beta_i) \sum_{j=0}^i T_{ji} Y_j^C \Delta X_j N_e(X_i). \quad (3.20)$$

The total light received at the detector at the time t_i is the sum of the three contributions:

$$y_i = y_i^{Cs} + y_i^{Cd} + y_i^f. \quad (3.21)$$

In the y_i value, the individual light contributions are experimentally indistinguishable, and it seems difficult to separate them. Even worst, y_i depends on dE/dX and N_e at the same time. Nevertheless, using the universality of the energy spectra of the secondary electrons and positrons in EAS, some parametrizations can be used and the total energy deposit of the air shower can be given by the sum of the energy loss of individual electrons, such that,

$$\frac{dE}{dX_i} = N_e(X_i) \int_0^\infty f_e(E, X_i) \frac{dE}{dX_e(E, X_i)} dE = N_e(X_i) \alpha_i, \quad (3.22)$$

where $f_e(E, X_i)$ is the normalized electron energy distribution and $dE/dX_e(E, X_i)$ is the energy loss of a single electron with energy E . the parameter α_i is the average energy deposit per unit depth per electron at shower age s_i , which can be parametrized in simulations. Using equation 3.22, N_e can be related to dE/dX . Then, equation 3.20 can be rewritten and together with equations 3.17 and 3.18:

$$\begin{aligned} y_i^f &= c_i^f \frac{dE}{dX_i} = \frac{A\epsilon T_i Y_i^f}{4\pi r_i^2} \frac{dE}{dX_i} \\ y_i^{Cd} &= c_i^{Cd} \frac{dE}{dX_i} = \frac{A\epsilon T_i}{4\pi r_i^2} f_C(\beta_i) \frac{Y_i^C}{\alpha_i} \Delta X_i \frac{dE}{dX_i} \\ y_{ij}^{Cs} &= c_{ij}^{Cs} \frac{dE}{dX_i} = \frac{A\epsilon T_i}{4\pi r_i^2} f_s(\beta_i) \sum_{j=0}^i T_{ji} \frac{Y_j^C}{\alpha_j} \Delta X_j \frac{dE}{dX_j}. \end{aligned} \quad (3.23)$$

Rewriting the system above in matrix notation,

$$\mathbf{Y} = \mathbf{C}\mathbf{w}, \quad (3.24)$$

with $\mathbf{y} = (y_1, y_2, \dots, y_n)^T$ is the vector, time ordered, that contains the measured photon flux at the aperture and $\mathbf{w} = \left(\frac{dE}{dX_1}, \frac{dE}{dX_2}, \dots, \frac{dE}{dX_n}\right)^T$ is the energy deposit at the shower track. To summarize, the matrix \mathbf{C} will be:

$$C_{ij} = \begin{cases} 0 & i < j \\ c_i^f + c_i^{Cd} + c_{ii}^{Cs} & i = j \\ c_{ij}^{Cs} & i > j \end{cases} \quad (3.25)$$

Inverting equation 3.24, the dE/dX profile is obtained, $\mathbf{w} = \mathbf{C}^{-1}\mathbf{y}$. Given a statistical uncertainty on the light detection \mathbf{V}_y , the error on the profile can be calculated as $\mathbf{V}_w = \mathbf{C}^{-1}\mathbf{V}_y(\mathbf{C}^T)^{-1}$. With the shower energy deposit profile, a Gaisser-Hillas function can be fitted and the integral of this energy should be proportional to the primary energy:

$$E_{cal} = \int_0^\infty f_{GH}(X) dX, \quad (3.26)$$

despite an invisible missing energy (described afterwards).

In figure 3.19, a real event is plotted where two FD eyes see the same event. One of the eyes is close to the shower axis, being dominated by the Cherenkov light (plot c), the other eye is dominated by the fluorescence (b). After the previous corrections, the different light contributions are calculated. Then, considering only the reconstructed fluorescence photons, the deposit energy profile is obtained. Since the event is the same, both dE/dX profiles must be similar within the error bars, as can be seen in plot d) and f).

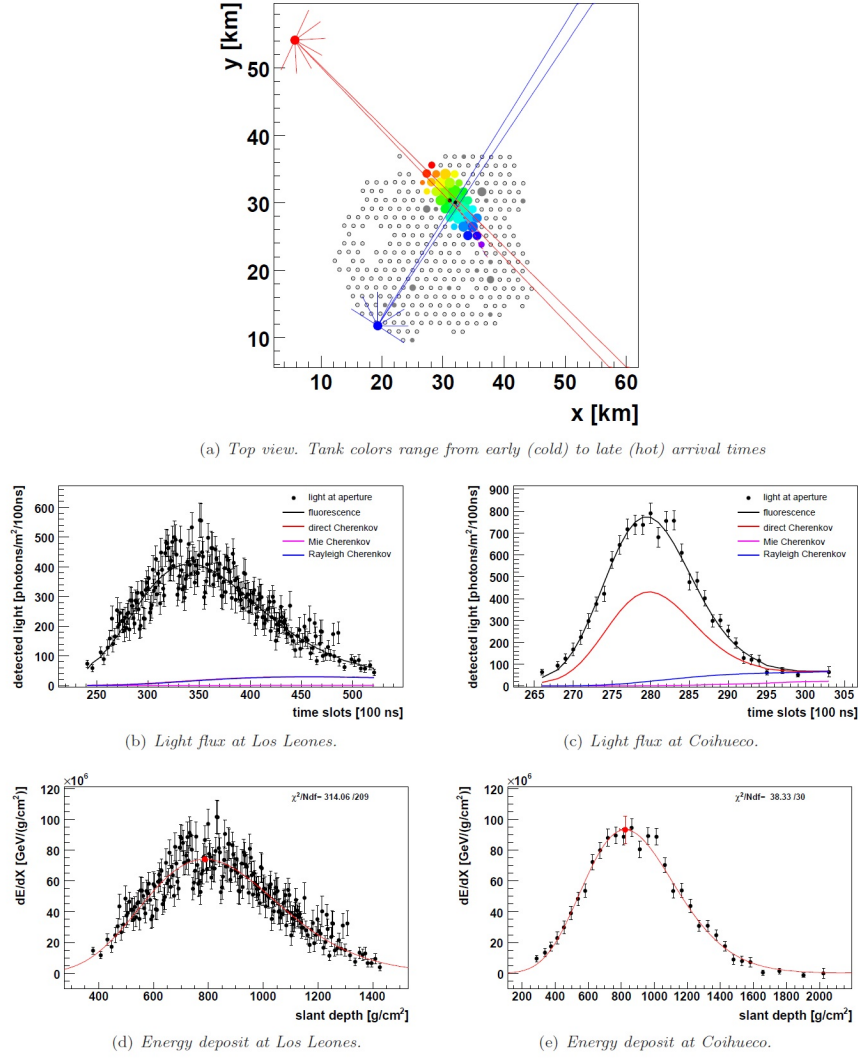


Figure 3.19: Reconstruction of a real event (at 772256331 GPS-seconds) seen by two FD eyes where one of the telescope is relatively close to the shower axis, being dominated by Cherenkov, and the other is dominated by fluorescence light. Both reconstructions are similar in the dE/dX .

Additionally, there are fluorescence and Cherenkov multiple scattering light that can be estimated. The previous Cherenkov scattered light is considered as singly scattered Cherenkov photons, while fluorescence scattered photons were not considered. The signal from multiply scattered light is larger at later stages of shower development, and may finally reach a few percent of the total signal from the shower (see [148, 149]).

According to ref. [149], multiple scatter light can be parametrized as a function of ζ angle¹¹ (in eq. 3.14), the shower-detector distance d and an exponential function of altitude above ground h :

$$M = \frac{y^f_s + y^{f_{ms}} + y^{C_{ms}}}{y^f + y^{C_d} + y^{C_s}} = A\zeta d \exp\left(-\frac{h}{B}\right) [\%], \quad (3.27)$$

where the parameters A and B are $A = 0.5830 \pm 0.0011\%/deg$ and $B = 2.4986 \pm 0.0062$ km.

¹¹ ζ is the angle distance between a pixel camera and the shower axis position at a specific time.

The electromagnetic component of an EAS does not account for the whole energy of the shower. Some particles, like neutrinos escape undetected, other like muons need long path lengths to release their energy, arriving on the ground without being absorbed in the atmosphere. This *missing energy* needs to be accounted in the final. So the FD energy will be:

$$E_{FD} = E_{miss} + E_{cal} = f_{inv} \cdot E_{cal} . \quad (3.28)$$

This correction is shown in the figure 3.20 from Monte-Carlo simulations, for different primaries and models as function of the primary energy. The invisible energy give an uncertainty around 4.4% for the FD energy and 1.5% for the SD energy. A parametrization of the missing energy can be seen in the Ref. [151].

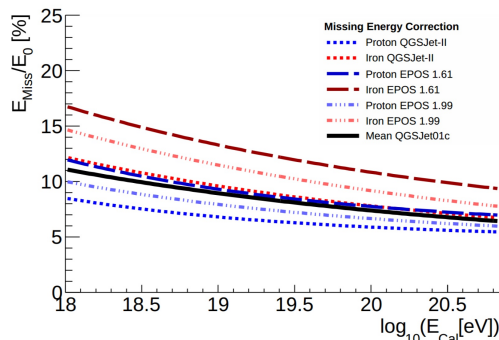


Figure 3.20: Missing energy correction as a function of the calorimetric energy for different hadronic models and primary masses.

3.3 Hybrid Technique

The Fluorescence Detector and Surface Detector, described before, are completely independent. Nonetheless, useful constrains on the geometry and energy reconstruction can be obtained using both detectors information. Also, the FD energy reconstruction is much more model independent than SD. So, the SD energy estimators are calibrated using the FD energy. The combined data of each detector is in this way very profitable.

3.3.1 HB Geometry Reconstruction

In the section 3.2.3 the FD geometry reconstruction was described. Despite being possible to recover the shower geometry using only FD, if SD timing information is added (even one or two SD stations in the T3 trigger), the resolution of the core position and the shower direction can be significantly improved.

The expected extra SD time t_{SD}^{exp} can be related with the FD reference time t_0 by:

$$t_{SD}^{exp} = t_0 - \frac{\vec{R}_{SD} \cdot \hat{S}}{c} , \quad (3.29)$$

where \vec{R}_{SD} is the vector pointing from the telescope to the SD tank and \hat{S} is the shower axis. Again, this result is assuming a planar front, travelling at the speed of light. With this

information, the geometry is determined minimizing:

$$\chi^2 = \sum_i \frac{(t_i - t_i^{exp})^2}{(t_i^{err})^2} + \sum_i \frac{(t_{SD,i} - t_{SD,i}^{exp})^2}{(t_{SD,i}^{err})^2}, \quad (3.30)$$

adapted from equation 3.12, where $t_{SD,i}$ and $t_{SD,i}^{err}$ are the SD tanks time and error in time, respectively. In the figure 3.17 left, this fit is plotted in black versus the one for mono FD reconstruction. In that picture, the FD stops seeing the shower before it reaches the ground. However, the inclusion of the tanks times on the ground, allows to put a strong constraint to the time geometry curve as it is considerably far from the FD (t, χ) pairs.

The best way to test the reconstruction is to use a laser with known position and direction such as the CLF. The CLF position is known with 5 m error in R_p and 0.01° in the angle. Also, the CLF is connected to a tank in order to give a time T_0 and simulate an hybrid reconstruction. In figure 3.21, the monocular and hybrid reconstruction of the CLF laser is plotted. The resolution in the R_p and χ is much better in the hybrid than in the monocular reconstruction. In this way, this reconstruction is very good, namely to carry out studies of anisotropies.

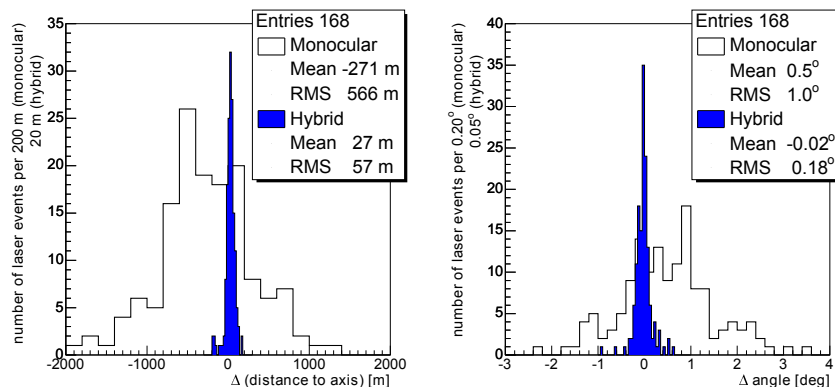


Figure 3.21: The difference in the reconstructed distance R_p (left) and the angular direction χ (right) with respect to the known position of the laser CLF. From [152]

3.3.2 SD-FD Calibration

The FD performs a quasi-calorimetric measurement of the shower energy, being less model dependent, while the energy estimator of the SD, $S(1000)$, is very dependent on the models, depending on the development of the shower and thus on the knowledge of the physical processes that rule the shower development. Nevertheless, it is possible to calibrate the SD energy estimator with the FD energy. Since the SD duty cycle is 100% and the FD is $\sim 15\%$ (see figure 3.22), with this cross calibration, it is possible to have an energy reconstruction around 100% of the events less dependent on the models.

In the normal spacing array (with 1500 m), the optimum distance, where the signal is less dependent on the LDF is $r = 1000$ m (seen in section 3.1.3.1), that way the S_{1000} is used as energy estimator. However, the SD signal S_{1000} is not yet the appropriate one to use in this cross calibration since this value change with angle for the same energy. The value of the signal at a fixed distance changes with zenith angle, due to the attenuation of the shower particles travelling larger distances from their production point to the detector. If the shower is vertical,

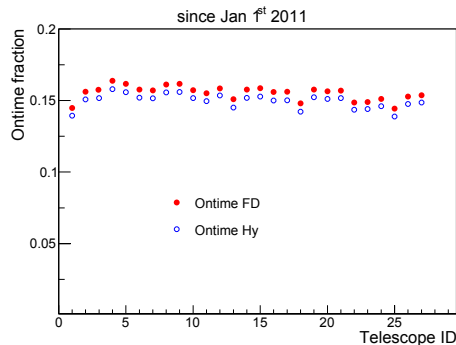


Figure 3.22: FD and hybrid on-time of individual telescopes since 1 Jan 2011. (1-6), (7-12), (13-18), (19-24), (25-27) for the sites of Los Leones, Los Morados, Loma Amarilla, Coihueco and HEAT, respectively [135].

the ground would correspond to a lower depth than in the inclined events, meaning that at higher zenith angle the shower would be in a later development stage, where more particles would be attenuated. The best way to handle this, is to convert the S_{1000} to the value it should have at 38° , S_{38} and use this as the reference value. This angle is considered since is the median angle, with higher statistics (at this geometry). The S_{38} is obtained for zenith angle $\theta < 60^\circ$ and given by:

$$S_{38} = S_{1000}CIC(\theta). \quad (3.31)$$

The $CIC(\theta)$ (Constant Intensity Cut)[153] is the attenuation function of the SD signal, which depends on the zenith angle θ . Further discussion can be seen in the chapter 5.

For a smaller spacing array of 750 m, like AMIGA, the optimum distance is not 1000 m, but rather $r_{opt} \approx 450$ m. So the estimator is $S(450m) = S_{450}$, which for the same reason, is converted into the reference value S_{35} , at 35° . Only events with zenith angle below 55° are accepted.

For very inclined events ($62^\circ < \theta < 80^\circ$), the electromagnetic component is mostly attenuated, so the signal is considered as muon signal. Here the energy estimator is the N_{19} , which is the muon content relative to simulated proton showers with energy 10^{19} eV, at $r = 1000$ m. See reference [154] for the reconstruction of inclined events.

The calibration is performed fitting the power law given by:

$$E_{SD} = aS_{38}^b, \quad (3.32)$$

or using S_{35} or N_{19} . The three calibration with respect to the FD energy are plotted on the figure 3.23 and written on table 3.1. In figure 3.23 right, the ratio between the calibrated SD energy (for 1500 m array) and the FD energy. The observed distributions are well reproduced by Monte-Carlo simulations.

3.4 Atmospheric monitoring

The EAS develops through the atmosphere until the ground. The FD detects the light emitted in the atmosphere and uses it as a calorimeter to measure the energy of the primary cosmic ray. The properties and local composition of the atmosphere are highly variable, varying with altitude and time and any shower measurement depends strongly on the integrated amount of matter in the atmosphere, as well as its density profile and composition. Moreover, atmosphere is not only responsible for producing light, but also the medium in which it is transmitted to

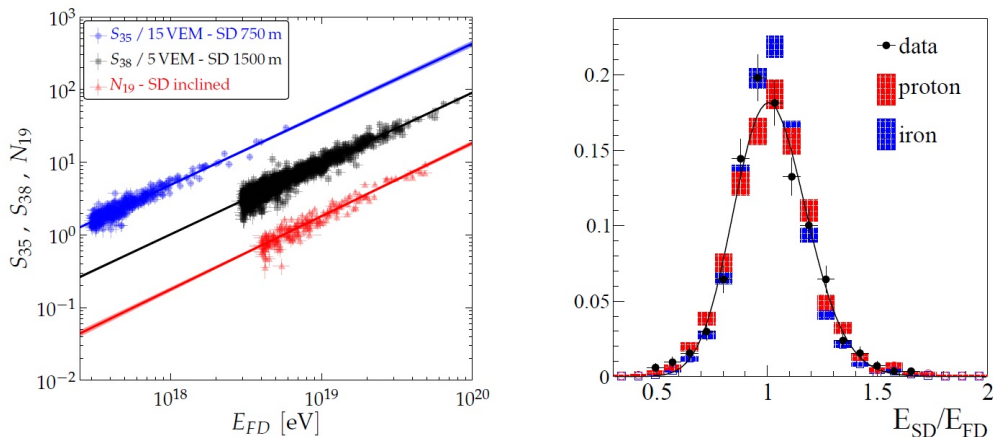


Figure 3.23: Left: Calibration for the different energy estimators S_{38} , S_{35} and N_{19} with the FD energy. Fits to equation 3.32 and parameters in table 3.1. Right: ratio of calibrated SD over FD energy for proton (blue) and iron (red) for QGSJET -II.03 simulations and for data (black dots with error bars). From [155]

Table 3.1: Summary of the experimental parameters describing data SD energy calibration. From [155]

	Auger SD		
	1500 m vertical	1500 m inclined	750 m vertical
Data taking period	01/2004 - 12/2012	01/2004-12/2012	08/2008-12/2012
Exposure[km ² sr yr]	31645±950	8027±240	79±4
Zenith angles[°]	0-60	62-80	0-55
Threshold energy E_{eff} [eV]	$3 \cdot 10^{18}$	$4 \cdot 10^{18}$	$3 \cdot 10^{17}$
No. of events ($E > E_{eff}$)	82318	11074	29585
No. of events (golden hybrids)	1475	175	414
Energy calibration (A)[EeV]	0.190 ± 0.005	5.61 ± 0.1	$(1.21 \pm 0.7) \cdot 10^{-2}$
Energy calibration (B)	1.025 ± 0.007	0.985 ± 0.02	1.03 ± 0.02

the detector. The attenuated light is detected and also the scattered light produce elsewhere in the shower, as seen in the previous section. The vertical density profile of aerosols (for Mie scattering), as well as their size, shape and composition, vary strongly with location and time, even on an hourly basis. If it is neglected or not measured properly, such dynamic and variable conditions can bias the shower reconstruction. The energy can be underestimated from 8% at the lowest energies up to 25% at the highest energies[156], and a shift in X_{max} between -1 g/cm^2 and 10 g/cm^2 . Therefore, several atmospheric monitoring systems exists in the Auger Observatory, such as LIDARs, cloud monitors, Horizontal Attenuation Length Monitor, phase function monitors, meteorological stations, and radiosondes, described in the following:

CLF and XLF

Close to the center of the array, there are two laser facilities; the Central Laser Facility (CLF) and the Extreme Laser Facility (XLF)[157, 158]. They are basically UV lasers (355 nm), with a steerable system, that directs the depolarized laser into well known sequences of shots into the sky (with an accuracy of 0.2°), with an energy of 7 mJ¹². CLF is connected by a optical fiber cable to the closest SD tank, Celeste, where a fraction of the laser light is injected in order to

¹²7 mJ is approximately equivalent to a 10^{20} eV induced shower.

allow hybrid reconstructions of the laser track. The laser produces beams, whose intensity and width depends on the atmosphere properties. It is used to monitor geometric alignment, FD timing, efficiency and reconstruction systematics from the FD, FD-SD timing and aerosol scattering in the atmosphere. Information about techniques for measuring the aerosol attenuation can be seen in ref. [158] and studies about the origin of atmospheric aerosols at Auger in ref. [159].

It is also possible to use a portable nitrogen laser (Roving Laser), a 337 nm laser, of known power, on a truck, which is able to fire the laser in each telescope field of view at different distances. In this way, atmospheric scattering effects and detectors effects can be disentangled.

LIDAR stations

There are four Light Detection And Ranging (LIDAR) stations [160, 157], each one located near one FD building. The LIDAR continuously operate in a steerable platform outside the FD field of view (FoV) with high energy UV laser, that emits pulses at a wavelength of 351 nm with a repetition rate of 333 Hz, and three parabolic glass mirrors that focus the backscattered light into PMTs. It can detect clouds and aerosols in any direction, up to 25 km of distance and 20 km of altitude.

It operates in two modes: a continuous scan of the sky outside the FD FoV; and the shoot-the-shower mode, in which the LIDAR scans the atmosphere crossed by a very high energy shower event, short after its detection.

A Raman LIDAR is also installed at the Los Leones FD site, with a laser of 10 mJ, which emits pulses of 355 nm into the atmosphere and collects the backscatter light. It detects the backscattered light by Raman scattering, 3 orders of magnitude smaller than Rayleigh, this allows a higher accuracy in measurements and identification of the constitution of the atmosphere, however, it requires very intense lasers that would affect the FD and it operates only before and after the FD normal data acquisition.

Horizontal Attenuation Monitors (HAM)

Complementary to the LIDARs, the Horizontal Attenuation Monitors (HAM) system is installed to measure the aerosol attenuation length in horizontal path between Coihueco (emitter) and Los Leones (receiver). The system has a DC light, with a 365 nm, 405 nm, 436 nm and 542 nm filters and a camera sensitive to UV. Measurements are made every hour during FD data acquisition.

Aerosol Phase Function Monitor (APF)

The Aerosol Phase Function (APF) monitor systems[161], one in Coihueco and another in Los Morados, measure the normalized aerosol differential scattering cross section as a function of the scattering angle from the initial light direction, which means the Mie scattering phase function, that depends on the characteristic of the aerosols. A Xenon flash tube source fires a set of five horizontal shots through the field of view of five telescopes with a repetition rate of 0.5 Hz, once every hour. The scattered light is observed by the FD, allowing the parameters of the Mie scattering phase function to be determined.

Cloud cameras and FRAM

Clouds can block the transmission of light from EAS to the detectors, or enhance the observed light flux due to multiple scattering of the intense Cherenkov in a cloud. Cloud cameras¹³[162] are installed on top of each FD building to monitor the cloud coverage, using digital cameras with infra-red spectrum between 7 and 14 μm , tanking a photograph every 5 minutes. It is

¹³infra-red Raytheon 2000B cameras.

suitable for distinguishing warm clouds from the cold clear sky. They do not give the clouds height, where measurement is possible only through the LIDARs. The determination of cloud composition is non-trivial and highly unreliable, so it is safer to remove cloudy periods from the data taking process. If the cloud fraction is larger than 25%, events are rejected as a whole and approximately 30% of the events are rejected due to cloudy conditions[163]. Currently, it is also possible to detect the clouds using infra-red satellite data [164].

A optical telescope, the The Photometric Robotic Atmospheric Monitor (FRAM) [165], equipped with CCD camera and a photometer that observe a set of selected bright ultraviolet stars and a calibrated terrestrial source. Comparing both, the dependence of the light attenuation in the atmosphere with the wavelength can be obtained.

Weather stations and balloon launches

Each FD site is equipped with weather station, which allows to record the temperature, pressure, relative humidity, and wind speed every 5 min, with an accuracy about $0.2 - 0.5^\circ\text{C}$ in temperature, $0.2 - 0.5$ hPa in pressure, and 2% in relative humidity.

Several balloon radiosonde campaigns were also performed[166]. The radiosonde record the temperature, pressure, relative humidity, and wind speed and direction, about every 20 m up to an average altitude of 25 km, covering completely the fiducial volume of the fluorescence detectors, with an approximately accuracy of 0.2°C for temperature, $0.5 - 1.0$ hPa for pressure, and 5% for relative humidity.

3.5 Pierre Auger Enhancements

The surface detector of the Pierre Auger Observatory reaches full shower detection efficiency at $10^{18.5}$ eV and the FD at 10^{18} eV. However, many unsolved questions arise from the data at those energies due to composition or hadronic models. A better discrimination between astrophysical models and afterwards, hadronic modes, requires the knowledge of the evolution of the cosmic ray composition since at least the knee. A way to better understand the data is to extend the energy detection efficiency to lower energies both in the SD and the FD, providing full detection efficiency starting at $E \approx 10^{17}$ eV. This allows to observe the composition evolution with energy and to analyse the hadronic models results where the accelerators data is available.

Activities of R&D have also been developed in order to access other possible variables and other frequencies of information about the showers. Studies on other frequencies of light emissions, such as radio and microwave, are been carried out. Also, new kinds of detectors that could open possibilities to measure the electromagnetic and muonic particles on the ground. The MARTA Project that uses Resistive Plate Chambers (RPCs) to detect the muons bellow the normal SD tank, can allow to separate the muonic and electromagnetic component. MARTA will be discussed on chapter 7.

3.5.1 HEAT

In extensions to lower energies, the longitudinal profiles develops faster and the maximum of the shower is displaced to higher altitudes in the atmosphere. So, the telescopes field of view must be placed with a higher elevation (for lower depth). The Telescopes enhancements was the High Elevation Auger Telescope (HEAT)[167] installed in 2009. It consist in three telescopes close do Coihueco site, with the same field of view as the regular telescopes, but with the possibility to be placed in two elevation positions (see figure 3.24 left and figure 3.25 a). One similar to Coihueco, with overlapping field of views and another with 30° elevation allowing to see the field of view above the normal telescope and overlook lower depths in the atmosphere.

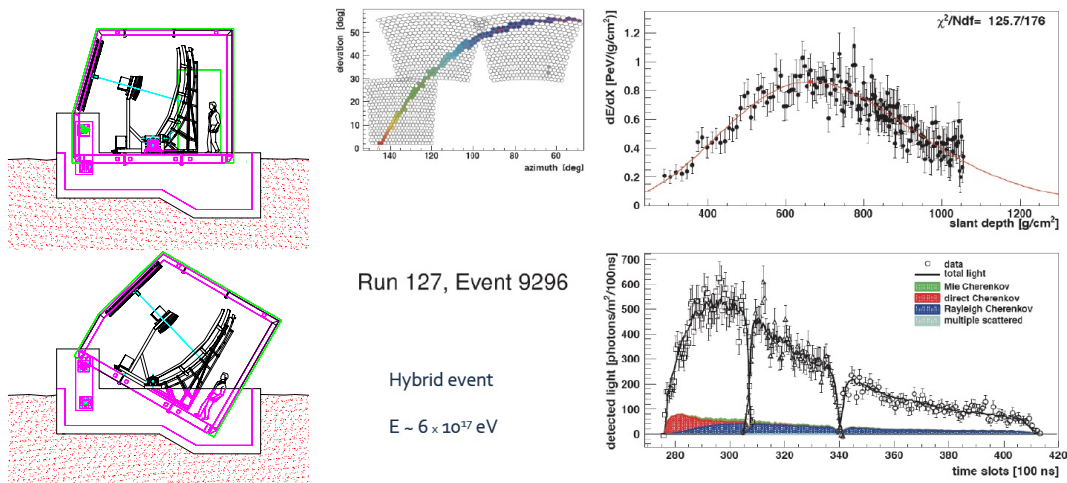


Figure 3.24: Left: Schematic view of the HEAT telescopes, in Horizontal mode (top) and data-taking mode in tilted orientation (bottom). Right: An event detected both by one Coihueco and two HEAT telescopes, with respective light detected at the diaphragm and longitudinal profile reconstructed.

The energy threshold is lowered down to around 10^{17} eV. Working together, Coihueco and HEAT allows to record the initial development of some showers that otherwise would be lost. One event detected both by HEAT and Coihueco is in the figure 3.24 right.

3.5.2 AMIGA

The SD lower energy extension is the Auger Muons and Infill for the Ground Array (AMIGA)[100, 168], which consists of an array of Water-Cherenkov tanks close to HEAT inside the regular 1.5 km grid, with accompanying scintillators buried alongside (see figure 3.25 a). It has 61 surface stations in a 750 m grid and 24 stations on a 433 m grid, to provide full efficiency detection of EAS down to $3 \cdot 10^{17}$ eV and 10^{17} eV, respectively.

The array of scintillators is being installed under the infill array (buried next to each of the stations), the first seven muon detectors are being deployed in an engineering array, consisting of 30 m² counters, to validate the detection technique and the detector design. The earth shielding on the scintillators strongly absorb the electromagnetic component, allowing to count muons above 1 GeV. Moreover, since it is close to HEAT, it is possible to have hybrid events at lower energies.

3.5.3 R&D

Others R&D projects have been developed with the purpose to detect the radio and microwave emission from the EAS development. There were several purpose detectors from low frequency range MHz to GHz. These enhancements can be seen distributed in Auger in the figure 3.25 b) and photographs can be seen in figure 3.25 and 3.26.

There are other projects, like MARTA described on chapter 7.

AERA: the Auger Engineering Radio Array (AERA)[127] operates in the frequency range from 30 to 80 MHz and is expected to record several thousands of cosmic rays showers in the range 10^{17} to 10^{19} eV. The first phase AERA24, deployed in April 2011, consisted of 24 stations

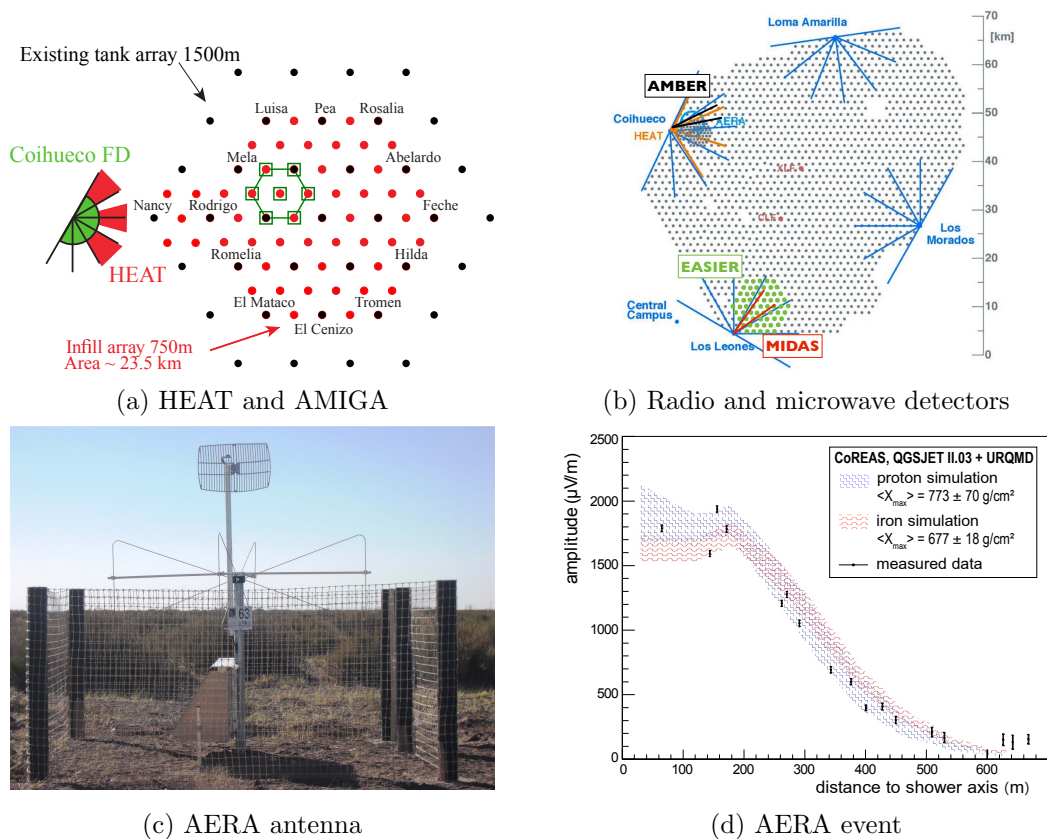


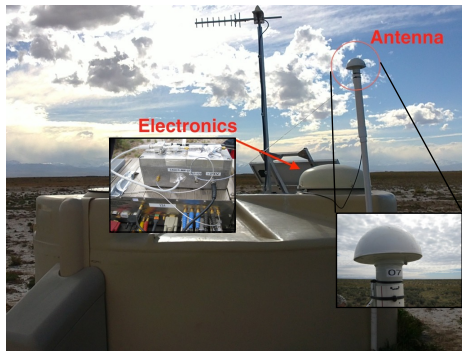
Figure 3.25: a) HEAT and AMIGA map[167]. The green hexagon is the unitary cell, where the squares represents the burred muon scintillators. b) Location of AERA (blue), EASIER (green), AMBER (black) and MIDAS (red). Photographs of AERA (c) with one AERA event (d) with an energy of 4.3 EeV, and a zenith angle of 58.4°. The band colors corresponds to simulation of the radio emission from protons and irons air-showers[127].

with logarithmic periodic dipole antennas (LPDAs) distributed over an area of 0.5 km² with a spacing of 144 m. Currently, there are 153 radio detection stations installed, spreading over an area of roughly 17 km² with different distances between each others. There are 29 with the 144 m spacing between each others, plus 55 station with a spacing of 250 m, 52 with 375 m spacing and 17 stations 750 m spacing. It is located over AMIGA to maximize the number of showers detected in coincidence with the other detectors. A photograph and one event from AERA can be seen in figures 3.25c and 3.25d. It has reported that the electric field detected cannot be described only with geomagnetic emission process and a radial dependence with respect to the shower axis is in agreement with predictions made by Askaryan using a charge-excess model[169, 170] (section 2.4.2.6). Some discrepancies between the modelled and measured polarization characteristics are not yet fully understood, underestimate of (systematic) errors in the data sets or the effect of strong electric fields in the atmosphere can be the cause.

MIDAS and AMBER: The MICrowave Detection of Air Showers (MIDAS) and Air-shower Microwave Bremsstrahlung Experimental Radiometer (AMBER) [128, 132] are prototypes of an imaging parabolic dish detector, intended to observe air showers at GHz frequencies (figures 3.26b and 3.26d). The major difference between both detectors is their trigger, MIDAS works with a self-triggering system, while AMBER uses a SD trigger. MIDAS is a radio telescope

instrumented with a 5 m^2 parabolic dish and a 53 pixels camera at its focal plane. Each pixel is a C-band LNBF covering approximately $1.3^\circ \times 1.3^\circ$ of the sky, for a total field of view of approximately $20^\circ \times 10^\circ$. MIDAS is now installed at the Pierre Auger Observatory, next to the FD building Los Leones. No clear event candidate was found, thus excluding a quadratic scaling with the air shower energy. AMBER is a 2.4 m off-axis parabolic dish imaging a section of $14^\circ \times 14^\circ$ of the sky at 30° elevation angle with 16 pixels, at the Coihueco FD site. It has acquired more than 18 months of data, and the data analysis is underway.

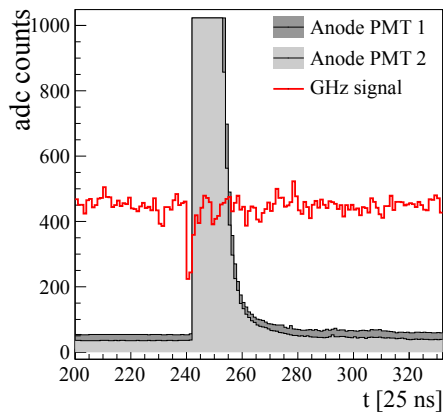
EASIER: The Extensive Air Shower Identification using Electron Radiometers (EASIER)[128, 131] is a radio detector array integrated with the Auger SD and triggered by the SD, to observe radio emission in both the GHz and MHz regime. Each detector is composed with a C-band horn antenna, 3 m above the ground, covering a large field of view, mounted on the tanks of the surface detector. EASIER is now an array of 61 detectors with 33 antennas oriented with a North-South polarization and the other 28 ones with East-West polarization. It has been taking data since 2011 and has recorded a total of three unambiguous radio signals in coincidence with an air shower detected by the SD array. A photograph and one EASIER event trigger by the SD can be seen in the figures 3.26a and 3.26c, respectively.



(a) EASIER antenna



(b) MIDAS antenna



(c) EASIER event



(d) AMBER antenna

Figure 3.26: Photographs of EASIER (a), AMBER (b) and MIDAS (d) antennas. c) one EASIER event trigger by the SD, in red the radio trace with the signal of two low gain PMT channels of the SD tank in gray. The PMT signals are saturated as expected for a shower with the core at 136 m of the detector.

3.6 Offline software framework

The Pierre Auger Collaboration developed a software framework, called Offline Software Framework [171, 172], to process data from air shower detectors, like event simulation and reconstruction. The software is implemented in C++ and consists in three principal parts (figure 3.27): a collection of processing modules which can be assembled and sequenced through instructions contained in an XML file or in a Python script; an event data structure through which modules deliver data to one another and accumulates all simulation and reconstruction information; and a detector and atmospheric description which constitutes the data environment conditions, allowing to test the configuration and performance of the observatory as a function of time.

The tasks and algorithms can be factorized into sequences of self-contained processing steps, so-called *modules*. The *modules* inherit a common interface, are computed in a sequential order instructions, through a run controller and allow an easy exchange and comparison of code fragments between users.

The data are stored in a hierarchy of XML files, accessible from the central configuration points modules and framework components and creates Xerces-based XML parsers to assist in reading information.

The Offline framework includes two parallel hierarchies for accessing data. The detector description provides a unified interface, including the detector geometry, calibration constants, and atmospheric conditions. Data requests are passed by this interface to a manager, capable of extracting a particular sort of information from a given data source. Usually, XML files contains the information about static detectors, while time-varying monitoring and calibration data, including the atmosphere monitoring, are stored in MySQL databases. The other hierarchy is the Event data model for reading and writing information that changes per event. It contains the raw, calibrated, reconstructed and Monte Carlo information. To write the event into a file, the data are transferred from the transient event through a file interface to the persistent event, which uses ROOT environment. The file interface mechanism, must handle several file formats including raw event and monitoring formats as well as the different formats employed by the AIRES, CORSIKA, CONEX and SENECA air shower simulation packages.

Moreover, there are collection of utilities, including an XML parser, an error logger, various mathematics and physics services like a geometry package, testing utilities and a set of foundation classes to represent objects such as signal traces, tabulated functions and particles.

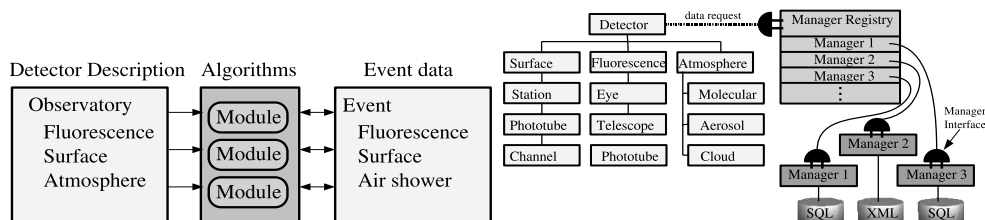


Figure 3.27: Left: General structure of the Offline framework. Simulation and reconstruction algorithms in modules, which are able to read information from the detector description and read/write information, to event. Right: detector description, a hierarchy of objects describing the various components of the observatory can be accessed through registry of managers.

3.7 Latest results from the Pierre Auger Observatory

In this section, the most recent result from Auger, that have not been addressed, will be described. Results such as the energy spectrum, elongation rate, composition, muon number, anisotropies and photon and neutrino fraction limit.

3.7.1 Energy Spectrum

The energy spectrum of cosmic rays obtained with the Auger data until 31 Dec 2012 is displayed on the figure 3.28 left. The energy spectra is obtained for the normal 1500 m arrays SD events, inclined events, hybrid and 750 m array events. The SD energies share the uncertainty of the FD energy scale of 14% and the measurements are affected by the energy calibrations uncertainties, in table 3.1.

The combined energy spectrum is shown in fig. 3.28, right together with the number of observed events within each bin. To match the energy spectra, the SD 750 m spectrum had to be scaled up by 2%, the inclined spectrum up by 5% and the hybrid down by 6%[155]. The data was described with a power law $J(E) \propto E^{-\gamma_1}$, below the ankle and a power law with smooth suppression above given by:

$$J(E; E > E_a) \propto E^{\gamma_2} \left[1 + \exp \left(\frac{\log_{10} E - \log_{10} E_{1/2}}{\log_{10} W_c} \right) \right]^{-1}, \quad (3.33)$$

γ_1 and γ_2 are the spectral indices below/above the ankle at E_a , $E_{1/2}$ is the energy at which the flux has dropped to half of its peak value before the suppression and W_c gives the steepness of the suppression.

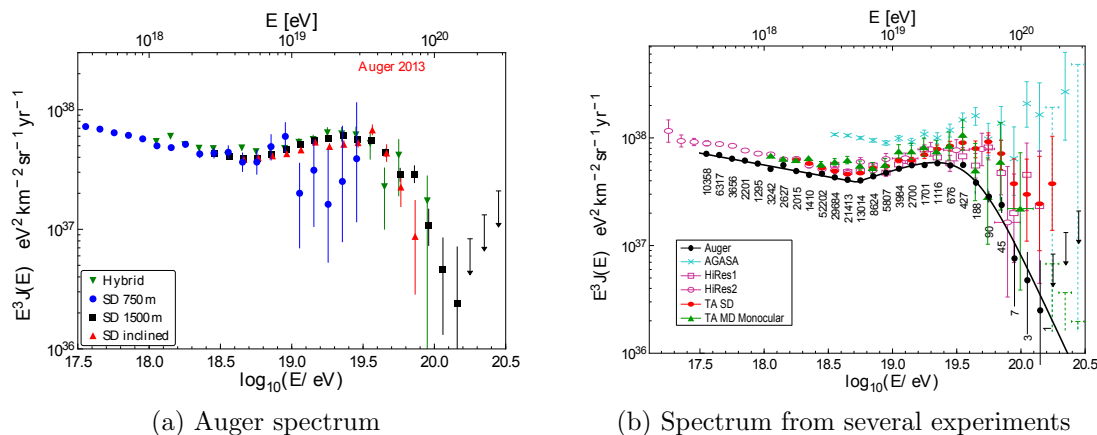


Figure 3.28: left: The Auger cosmic ray spectrum, derived from SD and from hybrid data until 31 Dec 2012 [155]. Right: Combined Auger spectrum, with fit to power law of eq. 3.33, compared with Telescope Array [173], HiRes-1/HiRes-2 [174] and AGASA [175].

The results for the power law fit are written on table 3.2. The overall spectrum is slightly shifted with respect to Telescope Array, HiRes and AGASA, but comparable within the 14% systematic uncertainty on energy scale. The 750 m array spectrum is compatible with the one obtained in KASCADE-Grande[155]. The combined energy spectrum is comparable to fluxes from several astrophysical scenarios and it is not clear if the suppression comes from the sources or from the GZK effect.

Table 3.2: Parameters of the power law fit (eq. 3.33), to the combined Auger spectrum[155].

Parameter	Results($\pm\sigma_{stat} \pm \sigma_{sys}$)
$\log_{10}(E_a/eV)$	$18.72 \pm 0.01 \pm 0.02$
γ_1	$3.3 \pm 0.01 \pm 0.07$
γ_2	$2.63 \pm 0.02 \pm 0.04$
$\log_{10}(E_{1/2}/eV)$	$19.63 \pm 0.01 \pm 0.010$
$\log_{10} W_c$	$0.15 \pm 0.01 \pm 0.02$

3.7.2 Anisotropies and correlations

The UHECRs distribution over the sky is crucial to understanding the nature of the particles. Combining the anisotropies measurements in the distribution of arrival directions with their chemical composition, they can provide valuable information on the nature of the sources and acceleration mechanisms. It has been seen in section 2.2.3 that a 10^{20} eV proton can travel large distances without suffering a big deflection on the galactic and extragalactic magnetic fields. So, these particles would have rectilinear trajectories from their sources, appearing on Earth with an anisotropic distribution in the sky. Moreover, their sources should be within a radius of about 100 Mpc, due to the GZK effect. For smaller energies or heavier compositions, the cosmic ray distribution in the sky would be more isotropic.

The Pierre Auger Observatory is able to reconstruct the direction of cosmic rays with an accuracy of $\sim 1^\circ$. Point-like sources searches show no significant evidences for anisotropy for the highest energies. The event fractions of cosmic rays above 53 EeV, correlating with the positions of nearby (within $\lesssim 75$ Mpc) AGNs in the VCV catalogue¹⁴, within an angular scale of $\sim 3^\circ$ is $28_{-3.6}^{+3.8}\%$, to be compared with the 21% expected to occur by chance if the flux were isotropic[177]. Other tests were performed with no significant excesses. The largest departures from isotropy were obtained around Swift-BAT[178] AGNs closer than 130 Mpc and around Centaurus A, with a 1.4% probability of arising by chance from an isotropic distribution.

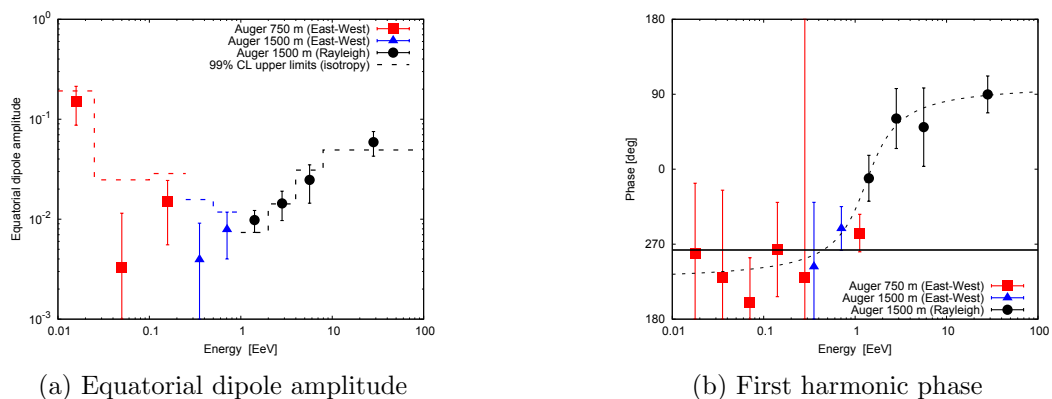


Figure 3.29: Left: Equatorial dipole amplitude as a function of energy, for three different methods, the 99% CL upper values of the amplitude coming from fluctuations of an isotropic distribution are in dashed lines. Right: first harmonic phase as a function of energy, the continuous line ($\phi = 263^\circ$) comes from a fit to the infill measured phase and the smooth fit to all data (dashed line). [179].

¹⁴Véron-Cetty and Véron catalogue[176]

Large scale anisotropies are also studied for lower energies ($0.1 < E < 20$ EeV), see references [179, 180, 181]. A recent study on the analysis of the first harmonic modulation in the right ascension distribution of events above 10^{18} eV has been done. In figure 3.29, the results of these analysis for the amplitude and phase of the dipole is displayed. The dashed line in the amplitude plot, are the 99% CL upper values for the amplitude which may arise from fluctuations of an isotropic distribution. No clear evidence for anisotropy has been found yet, however, in the range above 1 EeV, 3 points are above the 99% CL line. The probabilities for the dipole amplitudes that are measured to arise by chance from an isotropic flux are of about 0.03% in the energy range from 1-2 EeV, 0.9% for 2-4 EeV and 0.1% above 8 EeV. The phase evolution with energy has a smooth transition from the galactic center directions (270°) to 90° . In combined studies between Auger and Telescope Array, of anisotropy searches performed for energies above 10^{18} eV, no significant deviation from isotropy could be captured at any angular scale. Upper limits on the dipole and quadrupole amplitudes were given in [181]. The weakness of the anisotropy points to a scenario there could be some point-sources of UHE-CRs (maybe some of them would be AGNs), with a large isotropic background.

3.7.3 Mass composition

The cosmic rays are indirectly detected through their development into air showers, so the composition of the CRs is lost, but may be inferred using the EAS data. The main results used to infer composition are the elongation rate, average X_{max} , the variation of X_{max} ($RMS(X_{max})$), and the number of muons measured at the ground. However, the interpretation of these results is difficult and strongly rely on the hadronic models, with extrapolations of accelerator measurements, which mean different models would infer different compositions. The primary mass is extremely difficult to be measured on an event-by-event basis, but can be inferred statistically from the distribution of shower maxima for example, in an ensemble of air showers. In this section some of these parameters will be discussed.

3.7.3.1 X_{max} Results

Elongation Rate

The evolution of the average X_{max} , $\langle X_{max} \rangle$, is drawn in the figure 3.30a, using the Quality and fiducial selection cuts of reference [182]. For identical energies, the average shower maximum of proton-induced showers is around 100 g/cm^2 larger than that of showers generated by iron primaries. The results obtained by the Pierre Auger Collaboration seems to become heavier with energy, which are in contradiction with the Telescope Array and HiRes results on figure 3.30b. The TA and HiRes data favours a pure proton composition. There are several factors that could explain the differences. On one hand, different analysis to obtain the average X_{max} could bias the results. On other hand, the experiments are located in different places, Auger point toward the south hemisphere, while the others to the north, which mean the astrophysical composition could be different in the two directions. In the anisotropy analysis, the CRs energy is greater than 56 EeV, so composition is not reflected on those plots.

The evolution of $\langle X_{max} \rangle$, with the logarithm of energy is usually referred as the elongation rate, $D_{10} = \frac{d\langle X_{max} \rangle}{d \log_{10}(E/\text{eV})}$ discussed in the sections 2.3.1.1 and 2.3.2.1. According with the superposition model, a nucleus with mass A and energy E is a group of A nucleons with energy $E' = E/A$ and the elongation rate is expected to be the same for any type of primary. If some difference in D_{10} is observed, it is due to composition changing:

$$D_{10} = \hat{D}_{10} \left(1 - \frac{d\langle \ln A \rangle}{d \log_{10}(E/\text{eV})} \right), \quad (3.34)$$

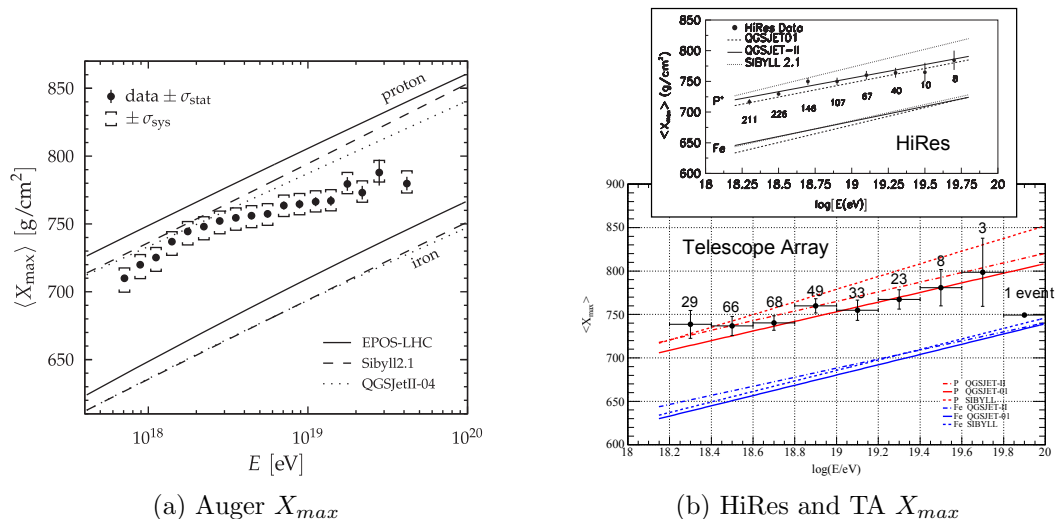


Figure 3.30: Average $\langle X_{max} \rangle$ as function of energy. Left: Auger results [182], right Telescope Array [183] and HiRes [184] results.

and \hat{D}_{10} is the expected elongation rate.

A single linear fit would not describe the Auger data, so the X_{max} evolution is divided in two regions, at the break point $\log_{10}(E_0/eV)$, it yields an elongation rate of:

$$\begin{aligned}
 D_{10} &= 86.4 \pm 5.0(stat) \begin{matrix} +3.8 \\ -3.2 \end{matrix} (sys) g/cm^2/decade & E < E_0 \\
 D_{10} &= 26.4 \pm 2.5(stat) \begin{matrix} +7.0 \\ -1.9 \end{matrix} (sys) g/cm^2/decade & E > E_0 ,
 \end{aligned}
 \tag{3.35}$$

with the break point at $\log_{10}(E_0/eV) = 18.27 \pm 0.04(stat) \begin{matrix} 0.06 \\ -0.07 \end{matrix} (sys)$. The elongation rates predicted by air-shower simulations for a constant composition range from 54 to 64 $g.cm^2/decade$. Therefore, equation 3.34 gives:

$$\begin{aligned}
 \frac{d\langle \ln A \rangle}{d \log_{10}(E/eV)} &= -1.07 \pm 0.20(stat) \begin{matrix} +0.15 \\ -0.13 \end{matrix} (sys) \begin{matrix} +0.26 \\ -0.31 \end{matrix} (model) & E < E_0 \\
 \frac{d\langle \ln A \rangle}{d \log_{10}(E/eV)} &= +1.23 \pm 0.10(stat) \begin{matrix} +0.07 \\ -0.27 \end{matrix} (sys) \begin{matrix} +0.09 \\ -0.10 \end{matrix} (model) & E > E_0 .
 \end{aligned}
 \tag{3.36}$$

This implies an evolution of the average composition of cosmic rays towards lighter nuclei up to energies of $10^{18.27}$ eV and a trend to heavier composition, above this energy.

X_{max} fluctuations

The second momentum of the X_{max} distribution, the RMS, also depends on the composition and/or hadronic model. The iron showers, equivalent to 56 protons, have high multiplicity, so fluctuates less than a proton shower at the same energy. The same happens between different hadronic model with different multiplicities, inelasticities and so on (see section 2.3.2.5). In figure 3.31, the $\sigma(X_{max})$ (or RMS) results for Auger and HiRes are drawn. A similar behaviour is found for the width of the X_{max} distribution. The Auger data gets narrower towards high energies, meaning again that the composition is getting heavier. In HiRes, the $\sigma(X_{max})$ is consistent again with pure proton composition.

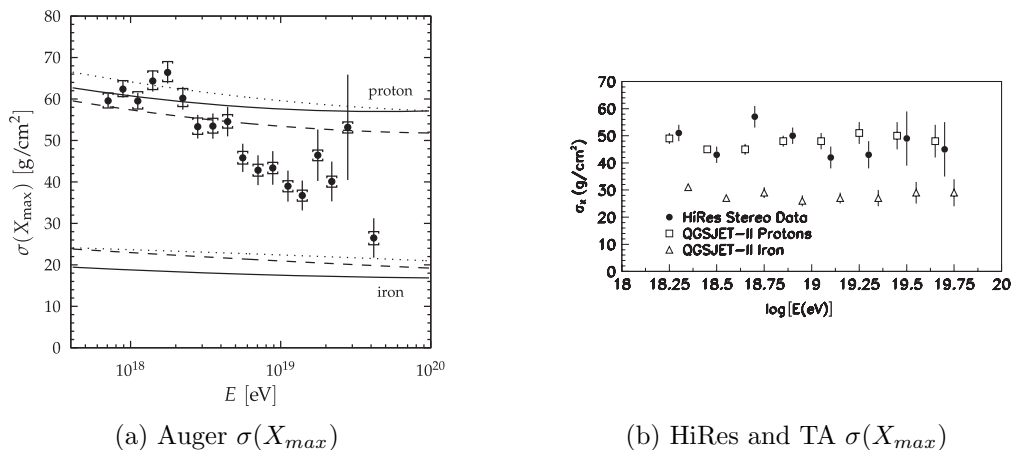


Figure 3.31: X_{max} fluctuations, $\sigma(X_{max})$, as function of energy for the Auger[182] (left) and HiRes[184] (right) results.

Both X_{max} in the Auger and HiRes are not directly comparable, because they use different definitions, but the final conclusions with respect to the hadronic models should be the same. In Auger, anti-bias selection cuts are applied (called fiducial cuts) to obtain a final X_{max} with no shifts due to the detector. Since this is slightly dependent on the models, the TA uses the measured X_{max} directly without anti-bias cuts. Currently, a composition matching the Auger results on FD, were simulated on the TA framework with respective quality selection cuts. According to [185], the X_{max} , from a selection with Auger composition and the TA detector reconstruction, is compatible with the TA measurements. This means that the difference on the measurements, probably comes from the analysis itself, however the composition on Auger is not completely known and it is not consistent with the muon sector (see section 3.7.3.2)

Composition in ln A

For a more quantitative study of the composition evolution, using the hadronic model predictions, the X_{max} and $\sigma(X_{max})$ can be converted into $\ln A$ distributions[186, 187]. The composition obtained from this method is drawn in the figure 3.32 for the models SIBYLL2.1, EPOS-LHC and QGSJET-II.04. In a pure iron sample, $\langle \ln A_{iron} \rangle \approx 4$ and for proton would be $\langle \ln A_{proton} \rangle \approx 1$. In respect to the variance of $\ln A$, a maximal mixing of 50% proton 50% iron would give $V(\ln A) \approx 4$ while a pure composition would give $V(\ln A) = 0$. The composition is lightest at around $10^{18.3}$ eV and the different features of hadronic interactions implemented in the three models give rise to differences in $\ln A$ of about 0.3. The EPOS-LHC model gives the heavier interpretation of the data and in both three models, the composition is getting heavier. The variance of $\ln A$ suggests the cosmic rays are composed of different nuclei at low energies and dominated by a single type of nucleus above $10^{18.7}$ eV, since the variance, $V(\ln A)$, is close to zero. The QGSJET-II.04 model leads to unphysical variances ($V(\ln A) < 0$) above $10^{18.4}$ eV and therefore this model is disfavoured by Auger data (but still within the systematics plus statistical uncertainty).

Further analysis on these results can be seen in [188], to interpret the fraction of elements in cosmic rays and how it evolves with energy. The Auger data are not well described by a mix of protons and iron nuclei over most of the energy range, independently of the considered model. A strong energy dependence in proton fractions is observed, and any of the models support a significant contribution from iron nuclei. Intermediate masses is favourable describing the data.

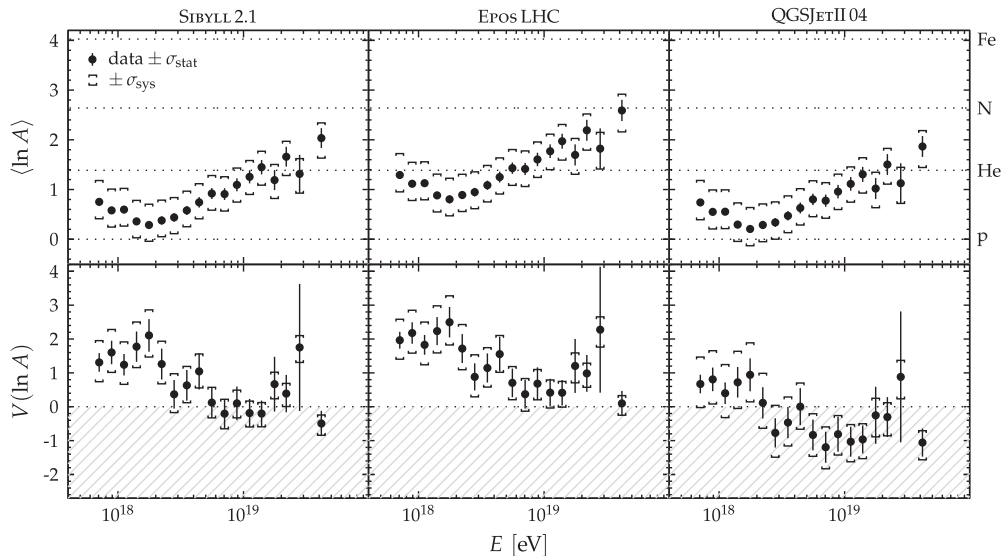


Figure 3.32: Average of the logarithmic mass, $\langle \ln A \rangle$, and its variance, $V(\ln A)$, estimated from data using different interaction models. The gray dashed region represents the non-physical negative variance region. From [182].

The azimuthal asymmetry of the rise-time of signals between detectors carries information about the longitudinal development of the showers as well[189].

Cross-section

The slope of the right tail in the X_{max} distribution, at a specific energy, is proportional to the first primary cosmic particle interaction length in the atmosphere. In this way, it is possible to recover the CR inelastic cross-section with air. Assuming a proton composition, the inelastic proton-air cross-section have been reported at 57 TeV and 95 TeV at Pierre Auger Observatory and TA respectively. The Glauber formalism allows to recover the proton-proton cross-section. The results of both experiments are compatible with the models as can be seen in the figure 3.33.

3.7.3.2 Muon Content

Despite the precision achieved by the fluorescence technique, it has a reduced duty cycle and is only sensitive to the electromagnetic component, so it is worth to analyse other SD observables that may be sensible to composition and hadronic models, like the muons. Since muons come from the decay of pions and kaons, the shape and absolute value of the muons distribution contains information about the evolution of the hadronic cascade.

Muon Production Depth (MPD)

It is possible to reconstruct the Muon Production Depth distribution (MPD)[192, 193, 194, 195] using the signals of the surface detectors far from the shower core. The electromagnetic signal on the SD is treated as a background, so the results are only applied for events with zenith angles in the interval $[55^\circ, 65^\circ]$. In inclined events, the electromagnetic signal are highly attenuated. Far from the core, the particle's arrival time is spread enough and with lower electromagnetic contamination, so using the timing information of the signals and the geometry, it is possible to reconstruct a muon production depth distribution (see figure 3.34). Despite the geometric

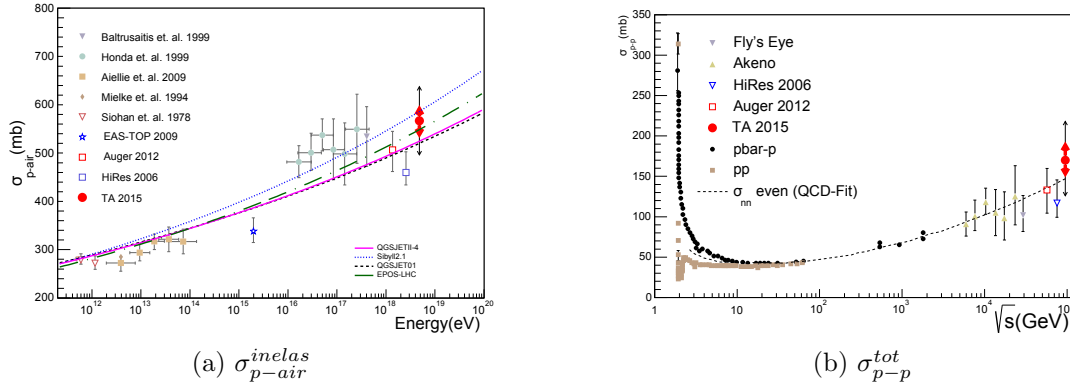


Figure 3.33: (a) Inelastic Proton-Air cross-section with the results [190, 191]

$$\sigma_{p-air}^{inelas} = [505 \pm 22(stat)_{-36}^{+28}(syst)] \text{ mb at 57 TeV in Auger}$$

$$\text{and } \sigma_{p-air}^{inelas} = [567 \pm 70.5(stat)_{-29}^{+25}(syst)] \text{ mb at 95 TeV in TA.}$$

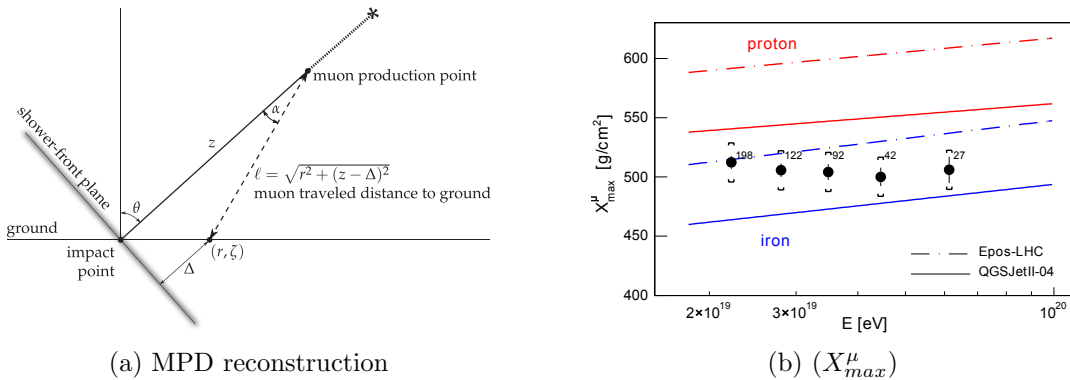
(b) total p-p cross-section with the results

$$\sigma_{p-p}^{tot} = [133 \pm 13(stat)_{-20}^{+17}(syst) \pm 16(Glauber)] \text{ mb at 57 TeV in Auger}$$

$$\text{and } \sigma_{p-p}^{tot} = [170_{-44}^{+48}(stat)_{-19}^{+17}(syst)] \text{ mb at 95 TeV in TA.}$$

delay expressed in the figure, other corrections must be accounted for, like the kinematic delay (muons travel below the light velocity); the deflection of muons due to their elastic scattering on nuclei and the geomagnetic field affects the trajectory of the muons, delaying their arrival times even more.

From MPD distributions, it is possible to obtain the X_{max}^{μ} , as the depth along the shower axis where the production of muons reaches the maximum. In figure 3.34 right, the average $\langle X_{max}^{\mu} \rangle$ is drawn. Accordingly with the two models presented, the composition seems to become heavier and for EPOS-LHC it becomes heavier than iron. The models predict $\frac{d\langle X_{max}^{\mu} \rangle}{d \log_{10} E / \text{eV}}$ for pure proton and pure iron to be about 35.9 ± 1.2 and $48.0 \pm 1.2 \text{ g/cm}^2/\text{decade}$, respectively¹⁵. The data is $-25 \pm 22(stat) \pm 21(syst) \text{ g/cm}^2/\text{decade}$ [194].


 Figure 3.34: Left: Geometry used to obtain the muon travelled distance and the geometric time delay for the MPD. Right: the average $\langle X_{max}^{\mu} \rangle$ obtained from the MPD, from [194].

Muon number

¹⁵Mean values between QGSJET-II.04 and EPOS-LHC predictions.

Extensive air showers with zenith angles above 62° are dominated by secondary energetic muons at the ground since the electromagnetic component has been largely absorbed in the large atmospheric depth crossed by the shower. The SD signals of those events provide a direct measurement of the muon number on the ground. The muon number in inclined air showers is measured using the relative scale factor N_{19} (section 3.3.2) which relates the observed muon densities at the ground to the average muon density profile of simulated proton-induced air showers of fixed energy 10^{19} eV, with QGSJET01. In the simulations, the N_{19} is bias with respect to the true number of muons, so it is corrected with that bias, and after that, is called R_μ . With this procedure, the systematic uncertainty of R_μ is about 11%.

The data set consists of hybrid events with zenith angles $62^\circ < \theta < 80^\circ$, energy above 4×10^{18} eV, passing quality cuts, between 1 January 2004 to 1 January 2013. In figure 3.35 left, the average number of produced muons, which is proportional to $\langle R_\mu \rangle$, is plotted as function of energy, together with its fit to equation $\langle R_\mu \rangle = a (E/10^{19} \text{ eV})^b$. The data gives the results[196]:

$$\begin{aligned} a &= \langle R_\mu \rangle (10^{19} \text{ eV}) = 1.841 \pm 0.029 \pm 0.324(\text{sys}) \\ b &= d\langle \ln R_\mu \rangle / d \ln E = 1.029 \pm 0.024 \pm 0.0308(\text{sys}) . \end{aligned} \quad (3.37)$$

The systematic uncertainty of the absolute scale of $\langle R_\mu \rangle (E/10^{19} \text{ eV})$ is about 18%, where 11% come from the intrinsic uncertainty of the R_μ measurement and 14% from the uncertainty of the Auger energy scale.

To compare the data with the models, the same plot is rescaled as $\langle R_\mu \rangle / (E/10^{19} \text{ eV})$, in figure 3.35 right. In this way, most of the energy scaling is cancelled and emphasizes the effect of the cosmic-ray mass A on the muon number. The high abundance of muons in the data reflects a discrepancy between the models and the data. The measured muon number is higher than in pure iron showers, suggesting contributions of even heavier elements. This interpretation is not in agreement with studies based on the depth of shower maximum (described after). A pure proton composition would be very disfavoured with these results, based on the hadronic models.

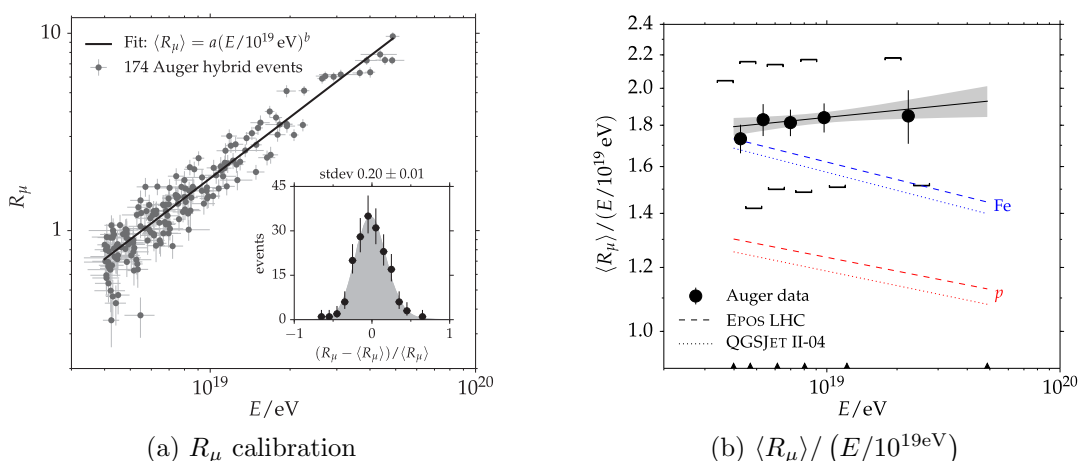


Figure 3.35: Left: R_μ values for the selected hybrid events above 4×10^{18} eV and a fit of the power law $\langle R_\mu \rangle = a (E/10^{19} \text{ eV})^b$. The inset shows the residuals around the fitted curve. Right. Average muon content $\langle R_\mu \rangle$ normalized by $E/10^{19}$ eV as a function of the shower energy E . The square brackets indicate the systematic uncertainty of the measurement. From [196].

The muon number in less inclined air showers has also been explored [197], using the different characteristics of the muonic and electromagnetic components in individual detectors. The muonic part is composed of peaks above a smooth background due to the lower energy deposition of the latter photons and electrons. Applying different filtering techniques to the temporal distribution of the signals, each component can be separated (see summary in [198]). Also, studies rescaling both the electromagnetic and muonic component were performed in reference [199] to describe the data and found that the ground signals of simulated events have a factor 1.3-1.6 deficit of hadronically-produced muons relative to observed showers, while the electromagnetic part simulated was similar to the data with negligible change.

3.7.3.3 Combined results

Combining observables from both electromagnetic and muonic components, the internal consistency of hadronic interaction models can be tested.

It is possible to obtain the $\langle \ln A \rangle$, using the $\langle X_{max}^\mu \rangle$ results in the same way as done previously

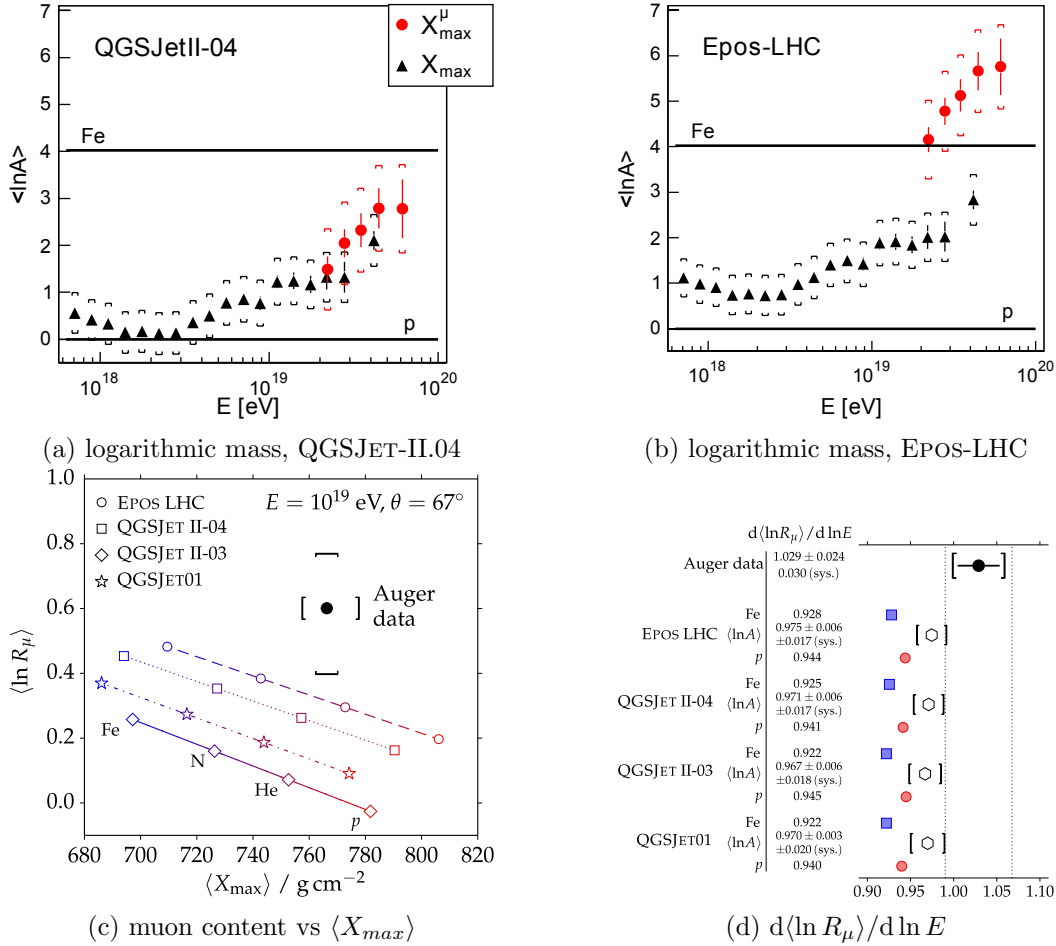


Figure 3.36: Top: the logarithmic mass $\langle \ln A \rangle$ obtained from $\langle X_{max}^\mu \rangle$ (red) and $\langle X_{max} \rangle$ (black) as a function of energy, for QGSJET-II.04 (a) and EPOS-LHC (b). [194] Bottom: c) Average logarithmic muon rescaling factor $\langle \ln R_\mu \rangle$ as a function of the $\langle X_{max} \rangle$ and d) the Auger logarithmic gain $d\langle \ln R_\mu \rangle / d \ln E$ between 4×10^{18} and 5×10^{19} eV with model predictions for proton, iron and mix composition obtained from the $\langle X_{max} \rangle$ within each model [196].

in figure 3.32. If the hadronic models are consistent in the electromagnetic and muonic component, then the average $\langle \ln A \rangle$, from $\langle X_{max} \rangle$ and $\langle X_{max}^\mu \rangle$ would overlap within the same model, despite different results between models. On the figure 3.36 a) and b), the combined results of $\langle \ln A \rangle$ are drawn for EPOS-LHC and QGSJET-II.04. In the case of EPOS-LHC, the mean $\ln A$ values extracted from the X_{max} and X_{max}^μ are incompatible at a level of at least 2.5σ . With QGSJET-II.04 the $\ln A$ values are compatible, however, it should be remembered that this model has problems to describe $\langle \ln A \rangle$ and $V(\ln A)$ in a consistent way. None of the interaction models recently tuned to LHC data provide a consistent description of the Auger data on EM and MPD profiles.

In figure 3.36 c), the average $\langle \ln R_\mu \rangle$ versus $\langle X_{max} \rangle$ for an energy 10^{19} eV is plotted. The Auger result falls completely out of the phase space allowed by the hadronic models. In plot d), the $d\langle \ln R_\mu \rangle / d \ln E$ values for the data and models are drawn. In blue squares and red circles are the respective values for iron and proton showers. The white hexagon is a $d\langle \ln R_\mu \rangle / d \ln E$ corresponds to the average $\langle \ln A \rangle$ obtained from the X_{max} within each model. None of the models is covered by the total uncertainty interval. The deviation between measurement and $\langle \ln A \rangle$ -based predictions is 1.3 to 1.4 σ . The large measured value of $d\langle \ln R_\mu \rangle / d \ln E$ disfavors a pure composition hypothesis.

The muonic and electromagnetic components don't seem to be described in a consistent way by the hadronic models. The Auger data favour heavier composition, this result is compatible with those found from independent studies for showers with $\theta < 60^\circ$. Nevertheless, Telescope Array points toward a pure proton composition [183]. The hadronic and muonic components of air showers are less well understood than the electromagnetic component, but all three are physically connected. Without a self-consistent description of air shower observables, the chemical evolution of cosmic rays is still an unsettled issue.

3.7.4 Multi-messenger information: photons and neutrinos

Neutrinos and photons are predicted essentially in all models of UHECR production. The interactions of cosmic rays within their sources and with background radiation during their propagation, produce charged and neutral pions which decay to neutrinos and photons, respectively. These UHE neutrinos and photons propagate along straight lines, not deflected by magnetic fields, and point to their production sites. Since they point toward their sources and are related with the cosmic ray production, they can give important limits on the astrophysical scenarios.

Photon fraction limit

A photon shower is considerably different from an hadronic one, the X_{max} is much deeper, due to the reduced number of secondary particles per interaction. The muon content is very small, photon hadron-production cross-sections are roughly 3 orders of magnitude smaller than pair production cross-sections. The properties of the shower front are different (larger curvature and width of the shower front). So it is possible to constrain the fraction of photons present in data. Current upper limits on the photon fraction, as a function of the primary energy, derived by the Pierre Auger Observatory, AGASA, Yakutsk and Telescope Array (TA) are plotted in the figure 3.37 left. The derived limits on the photon fraction, by the Pierre Auger Observatory, correspond to 0.4%, 0.5%, 1.0%, 2.6% and 8.9% for energies above 1, 2, 3, 5 and 10 EeV, respectively [39]. These fluxes already exclude many top-down scenarios.

A search for point sources of EeV photons, around the observable sky, had been carried out in [200]. No candidates have been found, on the pixelized sky, that stands out with statistical significance among the large number of trials pixels.

The studies of neutrons fluxes [201, 202] give no evidence for point sources of EeV neutrons. The absence of any detectable neutron flux might suggest that the sources are extragalactic,

or transient, or emitting in jets, or optically thin to escaping protons, or individually weak but densely distributed.

Neutrino fraction limit

The surface detector (SD) of the Pierre Auger Observatory can detect and identify UHE neutrinos (UHE ν s) in the 0.1 EeV range and above. Neutrinos of all flavours can interact in the atmosphere and induce inclined showers close to the ground (down-going). The probability of a neutrino to initiate an air shower at all is quite small ($\sim 10^{-5}$ at 1 EeV within a depth of 1000 g/cm²). But near-horizontal showers starting at very large depths could happen. The sensitivity of the Surface Detector to tau neutrinos is further enhanced through the "Earth-skimming" mechanism (up-going). In this case, the showers would be induced by the decay products of an emerging τ lepton, after the propagation and interaction of a ν_τ inside the Earth.

So far, no UHE neutrinos have been reported at Auger[40, 203], the current limit on the neutrino fluxes are plotted in the figure 3.37 right. The Auger results are competitive with other neutrino purpose experiments. The current Auger limit is below the Waxman-Bahcall bound on neutrino production in optically thin sources. It also constrains models of cosmogenic ν fluxes, assuming a pure primary proton and normalised to Fermi-LAT data. The two most energetic events in the PeV energy range were reported by the IceCube, if a power law of the flux is extended to higher energies, Auger would expect ~ 2.2 events in Auger while none is observed.

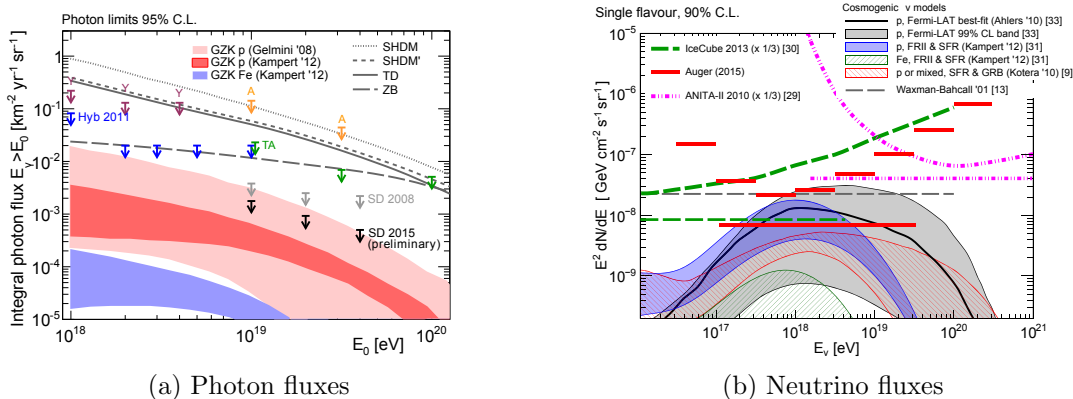


Figure 3.37: Left: Upper limits on the photon flux above 1, 2, 3, 5 and 10 EeV for Auger and Other limits from AGASA, Yakutsk and Telescope Array. the predictions for the GZK photon flux and for top-down models (TD, Z-Burst, SHDM and SHDM') also included[39]. Right: Differential and integrated upper limits, at 90% C.L., from the Pierre Auger Observatory for a diffuse flux of UHE neutrinos. The integrated limits from other experiments and expected fluxes for several cosmogenic neutrino models and astrophysical sources are also shown[203].

3D simulation of EAS for the FD

The standard Extensive Air Shower (EAS) simulation for the FD, in the Pierre Auger Offline framework[172], is based in a one dimensional, longitudinal analysis, taking the longitudinal shower information as input and not taking into account the 3D shower information. The Offline framework recovers the spacial structure later with average shower parametrizations. These average distributions do not account for shower to shower fluctuations which can be important in the interpretation of the Fluorescence Detector (FD) measurements, like double bangs for example.

The BinTheSky framework was developed with the purpose of keeping the spatial information related to the EAS development from the shower particle generator and using it directly in the production of fluorescence and Cherenkov light, without having to use a parametrization for the transverse distribution of the particles in the shower. In order to achieve this, the information required for computing the light (fluorescence and Cherenkov) produced by the charged particles in the shower, is saved in a structure whose building blocks are volumes in the sky: the SkyBins.

The development of the BinTheSky framework was also motivated because of its complementarity to the ongoing development of a "3D reconstruction method"[204]. The standard shower reconstruction neglects the time signal structure on the pixels and also projects the pixel information on the longitudinal line of the shower development (more precisely the SDP), losing information. This line propagation approach is good for distant showers, however in close-by events, it neglects the structure of the lateral shower profiles. Furthermore, in each time slot, the signals, for the profile reconstruction, are summed in nearby pixels. Although the same time bins on different pixels correspond to different emission times. The 3D simulation can use the relevant time bins in the pixels and considers that the shower propagates as a disk.

In this chapter, data events close to the telescopes with very small fraction of Cherenkov (fluorescence samples) and dominated by Cherenkov light (Cherenkov sample) were selected. Its characteristics were simulated with the standard and 3D simulations and after that, both simulations were reconstructed with the standard reconstructions. Finally, the fluorescence (section 4.2) and direct Cherenkov (section 4.3) emission simulations were compared with the data they represent with compatible results.

The standard longitudinal information can be produced by different codes for shower development, such as CORSIKA[91], AIRES [90], SENECA [93] or CONEX [92], as the input to the Pierre Auger Offline framework[172], where Cherenkov and fluorescence photons are produced from EAS calorimetric energy longitudinal profiles, propagated and attenuated to the telescope diaphragms. The surviving photons of fluorescence, direct Cherenkov and scattered light, are spread according to transversal parametrizations of the light profile available inside the Offline framework. The most commonly used for describing both Cherenkov and fluorescence light

components is the Gora function [77]. Currently, the 3D information is obtained at the generator level from the CORSIKA program only. It is inserted into Offline, in a dedicated *module*, without lateral parametrizations, to simulate the Auger detectors.

4.1 Framework and Method

The BinTheSky framework, developed here, has the objective of keeping the spatial information related to the EAS development produced by the shower particle generator, the CORSIKA program version 6.616. This is accomplished by writing a ROOT [205] structure, where the information can be retrieved and used to simulate the production of light in the atmosphere and the subsequent reconstruction of the simulated shower using the same principles and information as in the reconstruction of real data.

The distributions of the variables of charged particles (mainly electrons and positrons, and muons) relevant for light production, obtained with the shower generator, are saved as a function of their spatial location with respect to the shower axis, defined by the direction of the primary particle. The amount of light emitted, from fluorescence and Cherenkov processes, is then computed inside the Auger Offline framework, version 2.9.1-Valentine. It provides all the necessary information, such as the description of the atmosphere and physical description of the FD, including field of view, location, etc (figure 4.1a).

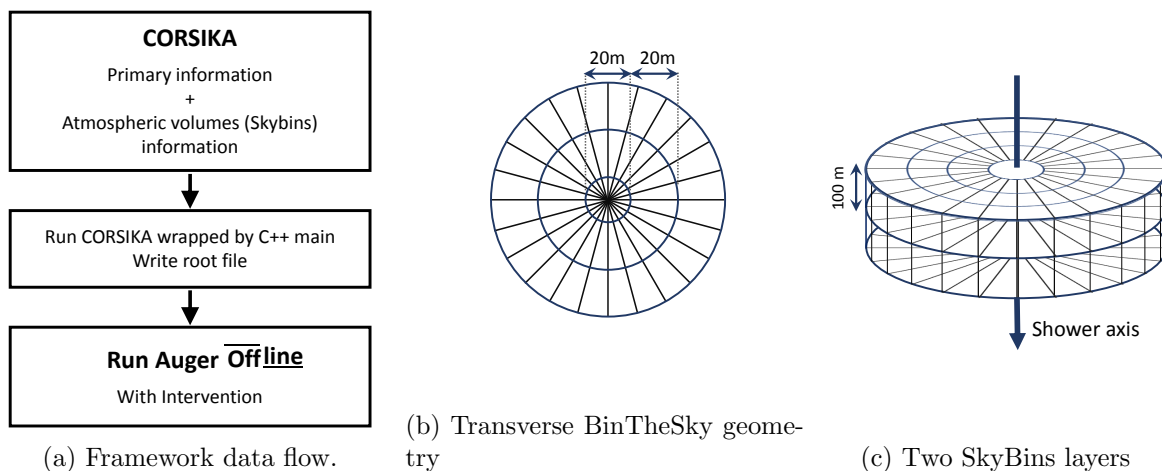


Figure 4.1: a) Representation of the data flow of the BinTheSky framework. Representation of the transverse structure of the BinTheSky geometry (b) and two SkyBins layers in the BinTheSky geometry (c), for a fixed z coordinate. The dark arrow represents the shower axis, i.e. the direction of the primary particle.

4.1.1 CORSIKA Intervention

In order to pass on the required information from CORSIKA to the Offline in the form of a ROOT structure, it was necessary to develop a C++ interface with CORSIKA, where the shower spatial structure is written to a ROOT tree object. The basic element in the data structure, where the required information is passed from CORSIKA, the SkyBin, corresponds to a volume in the sky, where the particles resulting from the development of the shower are located. The full set of SkyBin volumes forms a cylinder centred on the axis defined by the primary particle

direction (figure 4.1b and 4.1c). SkyBins are defined as $(\Delta r, \Delta \phi, \Delta z)$ intervals, and each SkyBin is identified by its geometric centre coordinates (r_c, ϕ_c, z_c) . In this definition, r is the radial distance from a given position in the sky to the axis defined by the direction of the primary, ϕ is the azimuthal angle corresponding to that position and z is its vertical coordinate with respect to the maximum shower height (height of the first interaction as defined in CORSIKA). In the center there are 24 SkyBins, with $\Delta \phi$ segmentations and radius $r = \Delta r/2$. The bins located near the shower axis have a smaller volume, appropriate for describing the denser shower region. Note that in the SkyBin definitions, $z_c = 0$ is the height of the first interaction, while in the Shower Axis coordinates frame of reference, $z_{sh} = 0$ corresponds to the altitude of the shower core.

The cylindrical geometry was chosen due to the shower azimuthal symmetry. The $(\Delta r, \Delta \phi, \Delta z)$ intervals can be chosen before compiling the CORSIKA with C++. In this chapter, the SkyBins intervals were chosen with a constant radius of $\Delta r = 20$ m, $\Delta \phi = 15^\circ$ in azimuthal angle and $\Delta z = 100$ m in height, for $r > 10$ m. For $r < 10$ m, the bin width in r is 10 m. As we can see in figure 4.2, using height bins of 100 m, close to the ground, we have approximately 12 g/cm² column depth variation per bin, which is acceptable. On other side, in the validation, nearby events with a distance between the shower and telescopes from 2 km to 7 km will be considered. For events with ~ 2 km, each pixel with 1.5° would correspond to 500 m of the shower, so we will have ~ 5 bins per pixel in this configuration.

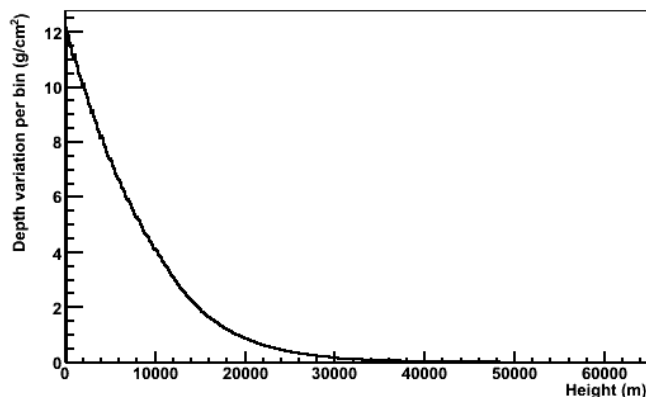


Figure 4.2: Depth variation per height bin of 100 m.

In CORSIKA, the electromagnetic particles and muons are followed and the necessary information to calculate the light emission is saved in distributions. The distributions and values saved will be discussed for each light component in sections 4.2 and 4.3, respectively.

4.1.2 Offline Intervention

In the current Offline framework, the detector simulation is embedded within it and the FD simulation can be separated in different *modules* steps. The standard `ModuleSequence` with all *modules* needed for a full simulation are listed here[206]:

```
<module> EventFileReaderOG      </module>
<module> EventGeneratorOG       </module>

<module> FdSimEventCheckerOG    </module>
```

```
<module> ShowerLightSimulatorKG      </module>
<module> LightAtDiaphragmSimulatorKG </module>
<module> ShowerPhotonGeneratorOG     </module>
<module> TelescopeSimulatorKG        </module>

<module> FdBackgroundSimulatorOG     </module>
<module> FdElectronicsSimulatorOG    </module>
<module> FdTriggerSimulatorOG       </module>

<module> EventBuilderOG              </module>
<module> EventFileExporterOG        </module>
```

Some *modules* are needed, but don't belong to the FD simulation, such as: the `EventFileReaderOG` that reads the profile and ground particle data from an EAS simulation program; the `EventGeneratorOG` generates an event time and core location; the `EventBuilderOG` combines all FD and SD data to build a valid `IoAuger` data object; and the `EventFileExporterOG` that writes the resulting event at the end of the *module* chain to the disk.

The module `FdSimEventCheckerOG` works as an event preparation, which sets the status of the components that are existing at the timestamp of the simulation to `eInDAQ`.

With the event already set, the light emissions, fluorescence and Cherenkov, are calculated in the module `ShowerLightSimulatorKG` and the propagation of those photons throughout the atmosphere until the telescopes diaphragm is done in the `LightAtDiaphragmSimulatorKG` module. Both modules works in one dimension using longitudinal profiles. At the telescopes, the lateral profile is recovered in the module `ShowerPhotonGeneratorOG` according to some parametrizations.

The photons on the diaphragm are traced in the telescopes to the PMTs in the `TelescopeSimulatorKG` module. It determines the reflection and refraction at the corrector lens, mirror, light collectors and PMT window. It uses measured telescope responses (relative to $\lambda_{norm} = 370$ nm), so the simulated events can be consistently reconstructed with the same settings as used for real data. Instead, it is possible to simulate the telescopes in a GEANT4-based simulation substituting this module by the `TelescopeSimulatorLX` module. It tracks the diaphragm photons through the GEANT4telescope simulation and outputs the total photon signal in each pixel and for each time bin.

The background light fluctuations, from bright stars, the milky way, the moon, the atmosphere and other sources are performed in the `FdBackgroundSimulatorOG`. The electronics and sampling effect are added through the `FdBackgroundSimulatorOG` module. The total photon flux at each PMT is converted into generated PEs (Photoelectrons) at the photocathode at time t_{ADC} given by:

$$n_{PE}^{PMT_i} = \text{Poisson} \left[\left(n_{ph,bg}^{PMT_i} + n_{ph,shower}^{PMT_i} \right) \cdot Q_{eff} \right], \quad (4.1)$$

with the PMTs quantum efficiency Q_{eff} , number of photon at the PMT, $n_{ph,bg}^{PMT_i}$ and $n_{ph,shower}^{PMT_i}$, from background and shower respectively. And the PEs are converted into ADC signals by:

$$s_{ADC}^{PMT_i}(T_{ADC}) = \left(n_{PE}^{PMT_i}(t_{ADC}) + \text{Gauss}[0, \sigma_{dynodes}] - \langle n_{ph,bg}^{PMT_i} \rangle \cdot Q_{eff} \right) \cdot g \\ + \text{Gauss}[0, \sigma_{noise}] \\ + \text{baseline}, \quad (4.2)$$

where g is the gain, the Poissonian fluctuations are combined with the Gaussian fluctuations and then reduced by the mean number of background light PEs, since the baseline is later added, but it is needed to produce the right fluctuations. The electronics fluctuations σ_{noise} and the baseline are also added. The generated ADC signal is in the end corrected for electronics filters and the total telescope response in each pixel. And finally, the trigger system described earlier in section 3.2.2 is simulated in the module `FdTriggerSimulatorOG`.

The `BinTheSky` root tree structure, containing the event properties needed inside the `SkyBins`, written by the `CORSIKA` wrapper are inserted in the `Offline` chain of modules, substituting some modules. Currently, the `ShowerLightSimulatorKG`, `LightAtDiphragmSimulatorKG` and `ShowerPhotonGeneratorOG` modules are substituted by the new `ShowerSimulatorLX`. Inside this module, light is emitted, but only for those `SkyBins` in the field of view of the relevant telescopes, and then propagated and attenuated until it reaches the telescopes.

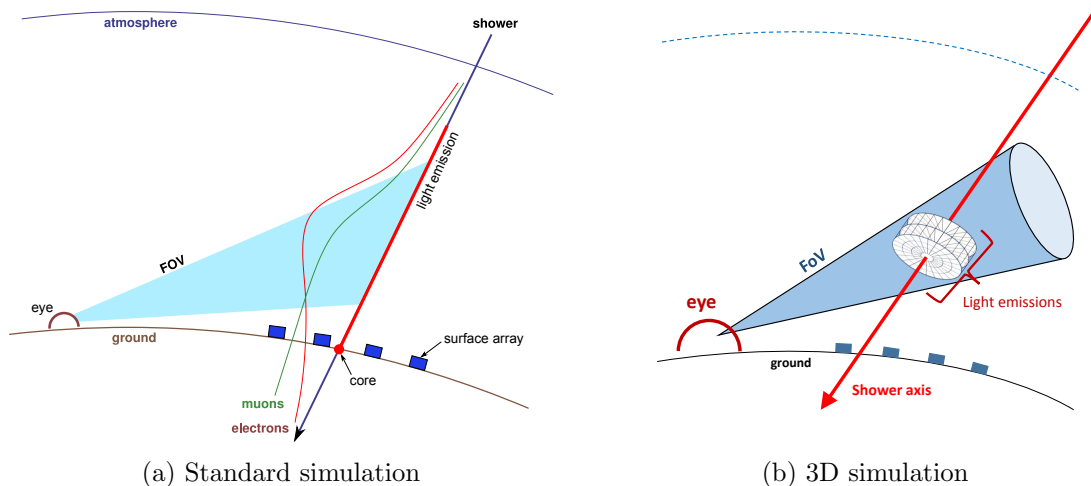


Figure 4.3: Light emissions in `Offline` inside a specific field of view. a) in the standard `Offline`, light is emitted along the shower axis (from [206]). b) in the 3D simulation, light is emitted in each `SkyBin`.

In the `ShowerLightSimulatorKG`, the light is calculated along the shower axis in steps of length dl that can be specified by the user (fig. 4.3a), using longitudinal profiles. Time simulation is fast, with the cost of not having the shower 3D information. In this new module, the light

is calculated in each Skybin, having the real 3D shower structure (fig. 4.3b). The precise description of each light emission is described afterwards.

In our framework, in fact, keeping the three Offline modules separately would be unnecessarily costly in terms of memory and time. Costly, since, for each longitudinal shower bin, the information input into the Offline is multiplied by the number of bins with information in the transverse profile. Consequently, there is a large increase in the amount of information that should be saved by ShowerLightSimulator module (where the light is produced) to be treated by LightAtDiaphragmSimulator module (which identifies which amount of light arrives at the telescope diaphragm).

In the standard Offline configuration, in the LightAtDiaphragmSimulator, the photons propagation times are calculated along the shower axis and from the shower axis to the telescope (figure 4.4a). In the ShowerSimulatorLX, after the calculations for the photon emissions, the photons arrival times are calculated in two parts, the emission time plus the propagation times ((figure 4.4b). The time calculations are based on the *time stamp* of the shower core, t_{core} . The shower *starting time*, t_0 , is obtained subtracting the propagation time from the core to the the maximum recorded height in the root structure. So $t_0 = t_{core} - (z_{core} - z_{max})/c$. The emission time is the time at which the photons are emitted, given by the propagation from the starting time to the position z_i along the shower axis, $t_e = (z_{max} - z_i)/c$. And the propagation times corresponds to the photons travel time from the emission point to the telescope, given by $t_{prop} = |\vec{p}_{e,i} - \vec{p}_{eye}|/c$, with the emission position, $\vec{p}_{e,i}$. The final photon times at the diaphragm are

$$t_{dia} = t_0 + t_e + t_{prop} . \quad (4.3)$$

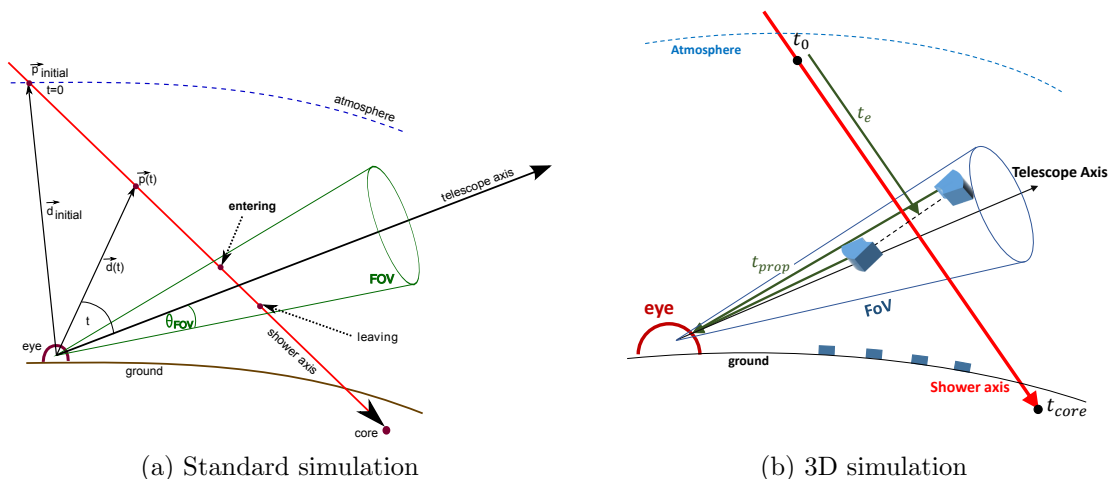


Figure 4.4: a) in the standard simulation, times are calculated along the shower axis (LightAtDiphragmSimulatorKG) plus an extra factor from LDF parameterizations (in ShowerPhotonGeneratorOG). b) in the 3D simulation, times are calculated for each SkyBin, considering a planar front wave.

To obtain the final continuous distributions, the photon emission position, $\vec{p}_{e,i}$, is randomly defined inside the corresponding SkyBin. The point is randomly distributed in $(\Delta z, \Delta r, \Delta \phi)$ and dividing uniformly the total number of photons computed for this SkyBin. An uniform distribution of emitters in $(\Delta z, \Delta r, \Delta \phi)$ is assumed (other functional forms could be used, but in this work parametrizations are being avoided). Currently, it is divided 10 times (but it is user defined). This means that the information of transverse distribution for light coming from the showers is contained in the SkyBin structure with a spatial (and temporal) resolution imposed by the SkyBin width only.

After the emission point inside the SkyBin is found, the photon's travelling distance to the detector, emission and propagation times are recomputed and the methods available in the Offline framework to compute photon attenuation from Rayleigh and Mie processes are applied to the photons pointing to the detector in each wavelength interval.

The third module, ShowerPhotonGenerator, where, for the longitudinal profile based shower simulation, the light is spread on the telescope diaphragm according to the chosen LDF, is unnecessary. Since in the present work, the transverse distribution of the shower energy deposited in the SkyBins is simply inherited from generator level and input into the Offline framework.

After calculate the photons until the diaphragm, they are traced in the telescope. Since there are many SkyBins and they are still divided, it would be very time consuming to trace all bunches of photons introduced in the telescopes. In this way, the photons are summed in 100 ns/*binning* (currently *binning* = 10 ns) and accordingly with their positions on the telescope:

$$n_{ph,xy}^{dia}(t_i) = \sum_{t_i-10ns < t < t_i+10ns} n_{ph,xy}^{dia}(t), \quad (4.4)$$

where $n_{ph,xy}^{dia}(t)$ are the number of photons at the diaphragm for fluorescence and Cherenkov (in equations 4.7 and 4.13) at the telescope position (x, y) .

Module configuration

The following options can be used in order to modify the behaviour of the module:

Name	Type	Default-value
InpuFileNames	ROOT filename	-
fluorDirect	boolean	true
cherDirect	boolean	true
binning	integer	10
Deltabinning	integer	10
FluorescenceLDF	off, S3D, NKG,Gora	S3D
DirectCherenkovLDF	off,S3D,NKG,Gora	S3D
ScatteredCherenkovLDF	-	off
MultipleScattering	-	-
MaxNRayTracePerBin	integer	75
MinNRayTracePerBin	integer	0.001

InpuFileNames The ROOT file name which contains the shower BinTheSky information.

fluorDirect To emit fluorescence photons at the shower axis.

cherDirect To emit Cherenkov photons at the shower axis.

binning Time binning of photon fluxes at the telescope aperture. The number gives the fraction with respect to the final ADC trace binning of the simulated telescope electronics. For standard Auger telescopes this is 100 ns but for HEAT it may get as small as 25 ns.

Deltabinning Number of random SkyBin divisions for an uniform distribution of emitters inside the bin.

FluorescenceLDF Choose how the fluorescence 3D structure of the air shower is taken into account. Options: without structure, using SkyBins spacial information; or it could allow NKG and Gora parametrizations.

DirectCherenkovLDF Choose how the direct Cherenkov 3D structure of the air shower is taken into account.

ScatteredCherenkovLDF Not yet implemented, to choose how to handle the Scattered Cherenkov light.

MultipleScattering To choose how to handle the Multiple Scattering light, not yet implemented neither here nor in standard Offline.

MaxNRayTracePerBin maximum photon bunch weight allowed to be traced in the telescope. If the value is higher than MaxNRayTracePerBin, the weight is equally divided until it is lower than the limit.

MinNRayTracePerBin minimum value of a photon bunch weight allowed to be traced on the telescope.

4.1.3 Validation strategy

The validation strategy for the BinTheSky framework based on data is described in the diagram presented in figure 4.5a. A data sample is selected according to specific criteria and then CORSIKA is used to generate events with the same characteristics of the data events. The characteristics of these events after data reconstruction (core coordinates, zenith angle, azimuthal angle, primary Energy and X_{max}^{dat}) were used to generate an equivalent sample with CORSIKA. Each generated shower was produced repeated times, with its geometry and energy until a CORSIKA shower with X_{max} within 50 g/cm² of the reconstructed X_{max}^{dat} from the corresponding data event was obtained. Both the standard CORSIKA output and the BinTheSky tree are saved for each event so that the standard shower simulation, based on the longitudinal profile of

the showers, and the 3D BinTheSky simulation can be compared with data, in an event by event basis, after being passed through the full Offline simulation and reconstruction framework. The standard reconstruction were applied to both 3D and standard simulations.

As for the SD signal, to reduce the computation time, the SdSimpleSimKG module was used to better constrain the reconstruction procedure, by fixing the shower arrival time at ground and forcing the trigger of the closest SD tank (allowing an hybrid event). Although, the BinTheSky framework was developed to enable a more realistic simulation of the transverse distribution of light produced by extensive air showers. The validation of the whole BinTheSky chain can, in first approximation, be performed by comparing the geometric and longitudinal reconstructed variables in the 3D simulated showers with those of reconstructed data and of the standard simulation (based on the longitudinal shower profiles). Therefore, for the present validation, the reconstruction of the shower profile can be performed by the module FdEnergyFinderKG.

From here on, the standard simulation based on the one dimensional longitudinal profiles will be denoted by KG simulation.

The aim of this analysis is validating the fluorescence and Cherenkov emissions with the BinTheSky framework. To this purpose, two data samples were chosen. Both samples were chosen with events close to the eye, because in this condition, the multiple scattering contribution in data is naturally kept low. Additionally, the 3D structure of the shower is more important. One of the data samples consists of events rich in fluorescence photons, with several event selection criteria in order to have a small contribution of Cherenkov light in the data sample. Note that, the Cherenkov is emitted close to the shower axis, so the presence of detected Cherenkov photons is favoured in events with geometric configurations where the shower direction points at the telescope, as illustrated in figure 4.5 b). By choosing events pointing away from the

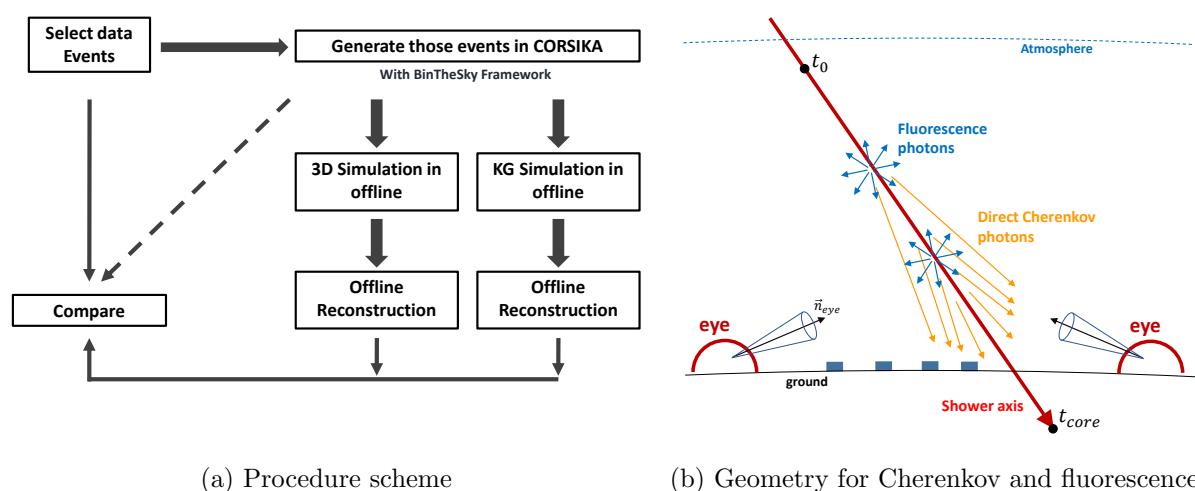


Figure 4.5: a) Scheme of the analysis procedure. b) Geometry of Cherenkov and fluorescence photon emission and propagation. The left eye is dominated by fluorescence photons while the right one is dominated by Cherenkov.

telescope, this type of contribution for the detected light can thus be reduced. The other sample is dominated by Cherenkov light. In this case, the shower should point toward the eye.

4.2 Fluorescence Emission

The emission and propagation of fluorescence photons through the atmosphere up to the detector, as well as their validation [207] will be described on this section.

4.2.1 CORSIKA and Offline Intervention

4.2.1.1 Fluorescence information

Fluorescence light is emitted when atmospheric molecules return to their fundamental states after being excited by the charged particles in the shower. Although all charged particles contribute to fluorescence light emission, electromagnetic particles are responsible for most fluorescence light. The fluorescence emission is isotropic and is proportional to the deposited energy in the atmosphere, so there aren't any reasons to save all particles information inside each SkyBin, but rather to save only the total deposited energy in it. In this way, in CORSIKA, all energy deposition inside a SkyBin was saved into the output ROOT file.

4.2.1.2 Photon emission and propagation

In any given shower, only the SkyBin in the field of view are considered. Using the deposited energy in each SkyBin, it's easy to compute the number of fluorescence photons per bin, as given by:

$$dn_{ph,fluo}^{SkyBin,i}(\lambda_{fluo}) = E_{dep,i} \cdot Y_{fluo}(T, \rho_i, \lambda_{fluo}) \cdot \left(\frac{dE}{dX_0} \cdot \rho_i \right)^{-1}, \quad (4.5)$$

where $E_{dep,i}$ is the deposited energy in the i SkyBin, $\frac{dE}{dX_0}$ is the energy deposit of electrons and ρ_i is the atmospheric density. The measured fluorescence yield is $Y_{fluo}(T, \rho_i, \lambda_{fluo})$, it includes temperature and density dependence, for the ultraviolet fluorescence emission bands λ_{fluo} of interest. The parametrization from AIRFLY (reference [111]) was used for both simulations.

The emitted photons in each SkyBin are propagated until the diaphragm. The timing is calculated through equation 4.3 and the geometrical spreading and attenuations until the detector are computed. Assuming the fluorescence light emission to be isotropic, a geometric factor for fluorescence light detection given by equation 4.6 is applied to the emitted fluorescence photons in each SkyBin,

$$f_{geo}(\vec{p}_i) = \frac{1}{4\pi d_i^2}, \quad (4.6)$$

where \vec{d}_i is the vector connecting the centre of the diaphragm to the random position, \vec{p}_i , inside the i th SkyBin, with module d_i . The number of fluorescence photons arriving at the diaphragm,

from a given SkyBin i can then be written as

$$\begin{aligned} dn_{ph,fluo}^{dia,i}(\lambda_{fluo}) &= f_{geo} A_{dia} \cdot \cos(\theta_{\vec{n}_{dia},\vec{p}_i}) dn_{ph,fluo}^{SkyBin,i}(\lambda_{fluo}) \cdot T_{Mie} \cdot T_{Rayleigh} \\ &= \frac{R_{dia} \cos(\theta_{\vec{n}_{dia},\vec{p}_i})}{4d_i^2} \cdot dn_{ph,fluo}^{SkyBin,i}(\lambda_{fluo}) \cdot T_{Mie}(\lambda_{fluo},\vec{p}_i) \cdot T_{Rayleigh}(\lambda_{fluo},\vec{p}_i), \end{aligned} \quad (4.7)$$

with the radius of the telescope diaphragm, R_{dia} , and the angle $\theta_{\vec{n}_{dia},\vec{p}_i}$, which is the angle between \vec{d}_i and the telescope axis (\vec{n}). The factors $T_{Mie}(\lambda_{fluo},\vec{p}_i)$ and $T_{Rayleigh}(\lambda_{fluo},\vec{p}_i)$ are the attenuations for Mie and Rayleigh scattering respectively. The attenuation factor depends on the photon wavelength and the position of the i th SkyBin with respect to the eye.

The de-excitation time of the fluorescence light was also taken into account. The de-excitation probability is an exponential with the form $P_{de-exc} \propto e^{t/\tau}$. It was considered an average value $\tau \sim 50$ ns[208]. In the code, the light was divided in steps of 25 ns according to $dn_k(t + k \cdot 25 \text{ ns}) = dn(t) \cdot P_{de-exc,k}$ and the extra time $k \cdot 25$ ns were added to the time calculations. The function used was $P_{de-exc,k} = 0.3934e^{(k \cdot 25)/\tau}$, obeying to $1 = \sum_{k=0}^{\infty} P_{de-exc,k}$, it was summed until $k = 7$, which includes the weight of the remaining terms.

4.2.2 Validation

A data sample composed of golden events with negligible amount of direct Cherenkov light, and with shower core near the telescopes was selected using a dedicated function of the CuscaLX module[209]. This fluorescence rich data sample had to fulfil the criteria:

1. θ shower $< 45^\circ$;
2. distance(Core-Telescope) < 7.5 km;
3. $\log_{10}(E_{Shower}) > 18$;
4. Cherenkov component $< 10\%$ of the total light
5. Showers moving away from the eye (see figure 3).

A sample with 66 events was selected from 2007 to 2010 Pierre Auger Observatory data. In figure 4.6, the Cherenkov fraction and shower-eye distance is plotted, as well as the difference in X_{max} between generated and data events.

This sample generated with CORSIKA was then simulated within the Offline framework using both the standard shower simulation for the FD and the developed simulation based on the BinTheSky framework. Since the selected sample is used to study the fluorescence emission, the contributions from direct Cherenkov light emission and from the multiple scattering of light in the atmosphere were turned off in the simulation and in the reconstruction. The events were simulated using the core coordinates and the TimeStamp of the corresponding events in the

data sample. In this section both the standard and KG simulations will be compared to the data they represent.

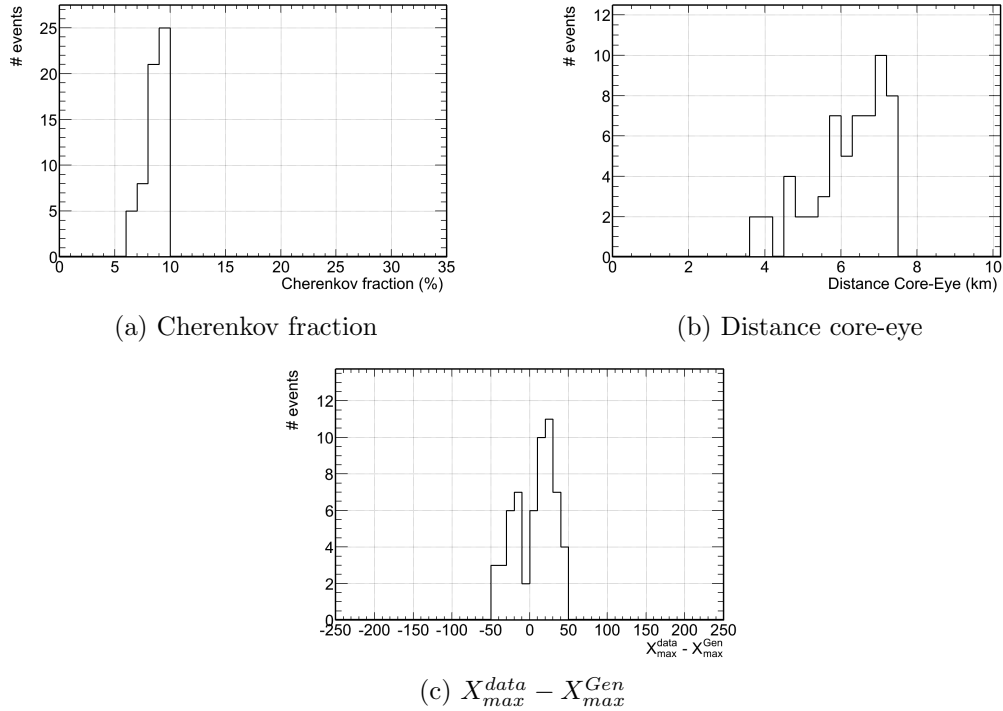


Figure 4.6: a) the event Cherenkov fraction. b) distance core-eye for the sample. c) difference between data and generated X_{max} .

4.2.2.1 Geometric reconstruction

The first step is to check the geometry reconstruction. The reconstructed zenith and azimuthal angles, for the shower axis, for the KG and the 3D simulated events were compared with the data events in the figure 4.7.

The geometry reconstruction of the 3D Simulation is in agreement with the data geometry that it should reproduce, and it is very similar to the KG simulation behaviour. For the azimuth, it gets a fraction $\langle \phi_{3D} - \phi_{data} \rangle = 0.08 \pm 0.83^\circ$, while in the KG simulation for this sample, it gets $\langle \phi_{KG} - \phi_{data} \rangle = 0.15 \pm 1.14^\circ$. There are basically no bias and the RMS is around 1° as expected from the Auger resolution. The zenith reconstruction is similar, the simulations give the values $\langle \theta_{3D} - \theta_{data} \rangle = -0.11 \pm 0.98^\circ$ and $\langle \theta_{KG} - \theta_{data} \rangle = -0.21 \pm 0.25^\circ$. These values are important to realize that the new module is getting the right geometry from the CORSIKA and correctly introduce it in the Offline.

From the analysis of table 4.2 and from figure 4.7 it can be stated that the geometric reconstruction of the shower axis for both simulations is in good agreement with the the geometric reconstruction of the data events.

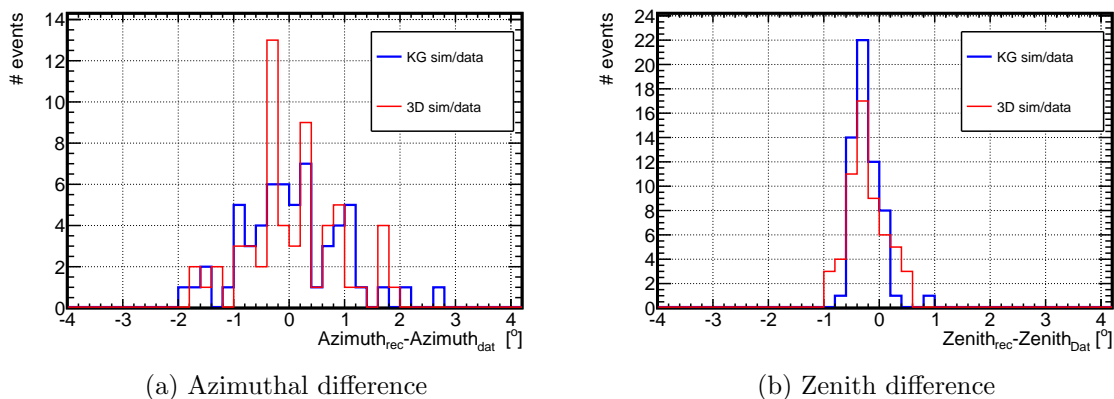


Figure 4.7: Relative differences between the simulation and data of the reconstructed azimuthal angle (left) and zenith angle (right), for the 3D and KG simulations. The KG is represented by the blue line whereas the red line corresponds to the 3D simulation.

4.2.2.2 Longitudinal shower parameters

The longitudinal profile and parameters such as the energy reconstruction, X_{max} can be compared in the next step.

The first thing to look for, is the light obtained at the diaphragm and sum it for all events, as function of the detection time slots. In figure 4.8, the light sum at the diaphragm is plotted for both simulations and data, left, and the same distribution is plotted normalized to the peak on the right. The time traces were added event-by-event, in each profile, placing the first signal time on the same position in time. The number of fluorescence photons (left) and shape (right) is very similar between the KG and 3D simulation however both of them are smaller than the photon distribution in the data. This happens because the scattered Cherenkov light was not simulated, but it is present in the data. The normalized profiles are in a good agreement with each other, but the data is narrower, since the scattered light is higher close to the shower maximum.

In figure 4.9 the KG simulation sample was simulated again considering the scattered light. In this way, it is much closer to the data and justify the previous argument. The small difference between the KG and data comes from the multiple scattering currently not simulated in the standard simulation.

To analyse the energy and X_{max} , the event needs to be fully reconstructed. The light needs to be converted into dE/dX and the time into depth, $X[\text{g}/\text{cm}^2]$. Both simulations were reconstructed with the standard reconstruction. Just a quick reminder, after the event is obtained in dE/dX , it is fitted to the Gaisser-Hillas function, $dE/dX = dE/dX_{max} \left(\frac{X-X_0}{X_{max}-X_0} \right)^{\frac{X_{max}-X_0}{\lambda_{GH}}} e^{-\frac{X_{max}-X}{\lambda_{GH}}}$ (eq. 2.46), where the X_{max} is obtained and the integral is proportional to the energy.

In figure 4.10a, the reconstructed shower energy is presented with the $\log_{10}(E/eV)$ distribution, where it is compared to the reconstructed energy of the events in the real data. On the right,

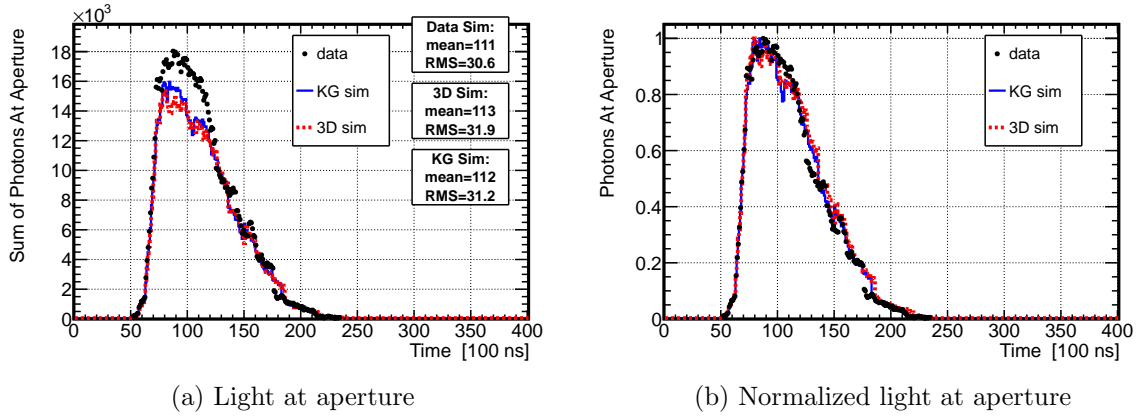


Figure 4.8: Sum of the photons at the diaphragm for all events as function of ADC time bins (left). The same normalized profiles on the right. In black dots, blue and red lines are the data, KG and 3D simulations respectively. Only fluorescence light was produced on the simulations.

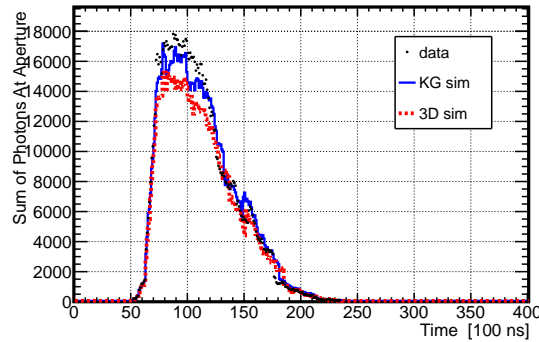


Figure 4.9: Sum of the photons at the diaphragm for all events as function of ADC time bins for data (black dots), KG (blue line) and 3D (red line) simulations. In the KG simulation the production of Cherenkov and scattered Cherenkov were turned on.

figure 4.10b, the distributions of the relative difference between the reconstructed energy in both simulations and that of the data sample is displayed.

The reconstructed energy distributions for both simulations are in fair agreement. However, both simulations display $\sim 3\%$ excess in the average value of the reconstructed energy with respect to the average value of the energy reconstructed for the data events, as presented in table 4.2.

The selected data sample is composed by events occurring close to the telescope. Therefore, only a fraction of the EAS is detected and the extrapolation of the dE/dX curve outside the telescope FOV yields a significant uncertainty (when compared to the reconstruction of distant showers). Since the shower energy is proportional to the integral of the dE/dX curve, this translates into a larger uncertainty in the reconstructed energy. Additionally, both simulations seem to be wider than the data (see figure 4.13 and 4.14), with a consequent larger value for the reconstructed energy.

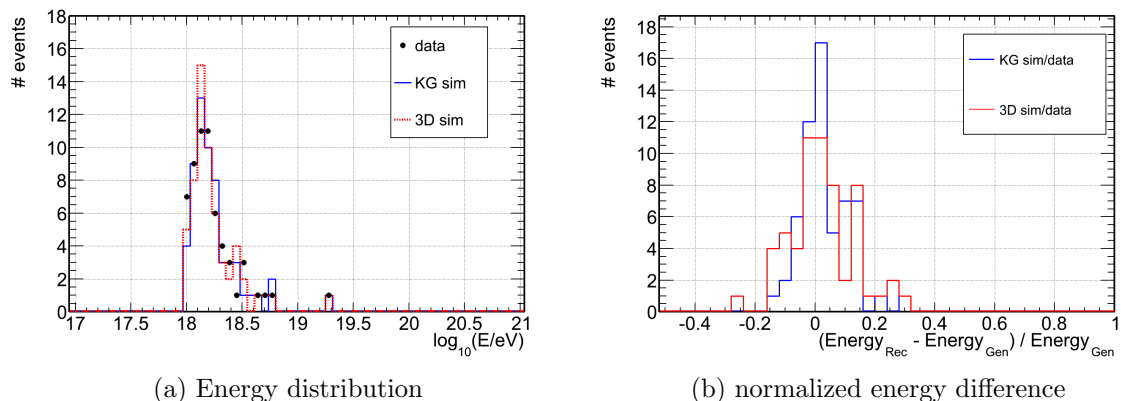


Figure 4.10: a) The plot shows the distribution of the reconstructed energy of the events in the data sample (black dots) compared to the simulated samples, KG (blue) and 3D (red) in the form of $\log_{10}(E/\text{eV})$ (left); on b) the relative difference between the simulated and real data reconstructed energy for both simulated samples, KG (in blue) and 3D (in red) is displayed. The generated energy matches the RE reconstructed energy on data.

To compare the longitudinal profile on data and simulation, it is possible to observe the reconstructed X_{max} and dE/dX_{max} of the energy deposition obtained from the fluorescence light alone. The dE/dX_{max} results are plotted on the figure 4.11, the generated, data and simulation values are consistent with each other showing a good behaviour of the simulation and reconstruction methods. The generated dE/dX_{max} should be the value obtained from the one dimensional longitudinal profile (in CORSIKA) without propagation, attenuations and 3D informations. These values are written on table 4.2. The maximum is around $\sim 4\%$ smaller in both simulations than the generated ones, but similar to the one obtained for the data.

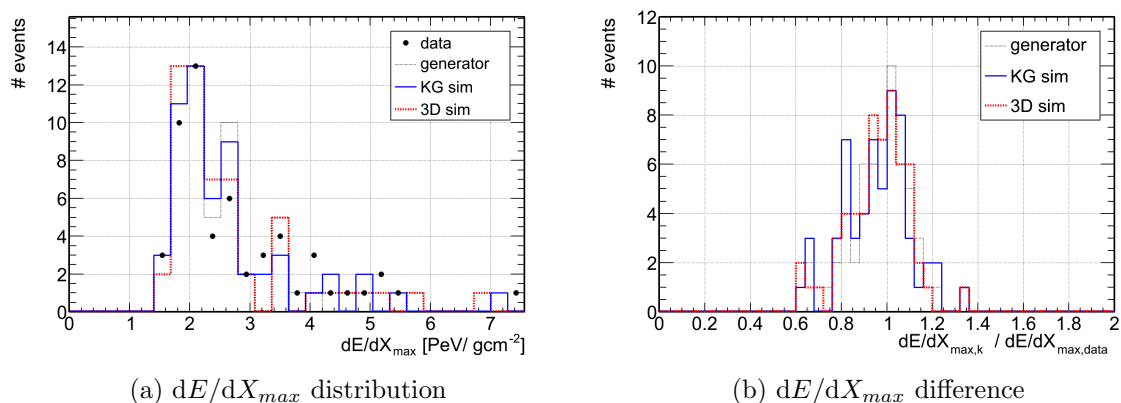


Figure 4.11: The reconstructed longitudinal maximum profile, dE/dX_{max} , the data sample (black dots), KG (blue) and 3D (red) simulations (left); and the $(dE/dX_{max,k} - dE/dX_{max,data})$ distribution (right).

To compare the shower maximum in both simulations, the value of X_{max} at generation level

should be considered instead of the value of X_{max} in data. In figure 4.12, the distributions of the X_{max} reconstructed for both simulations and the generated values are displayed on the left, whereas, on the right, the relative difference (in g/cm^2) between the reconstructed values of X_{max} for both simulations and the corresponding X_{max} values at generator level are compared. In average, the simulations give around $+3.9$ and $+1.1$ g/cm^2 (for 3D and KG respectively) with respect to the generated values. For both simulations, the difference between generated and reconstructed X_{max} values is below 1%. These values are negligible within the X_{max} resolutions.

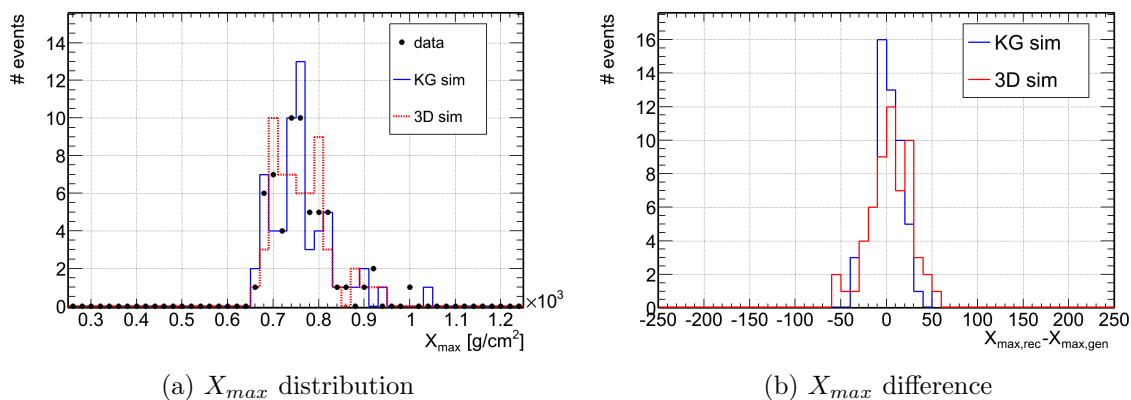


Figure 4.12: On the left, the X_{max} values are displayed for the generated events (black dots) and for the simulated sets. On the right the relative difference between the simulation reconstructed X_{max} values and the corresponding generated values for both simulated samples are compared. KG is represented in blue and 3D is shown in red.

In the figure 4.13, the dE/dX is summed for all events as function of $X' = X - X_{max}$, for the two simulated samples and for data. With the translation in X , all events should become similar and the fluctuations decrease (see section 2.3.2.2.1), so it's easy to see if there are some regions with more or less production of light. However it is very dependent on the X_{max} reconstruction. These distributions display a similar structure for both simulations and differ from the corresponding real data sample at $X' = 0$ g/cm^2 . This was expected because data contains the contribution from Cherenkov light (mostly scattered Cherenkov photons), which was not simulated for the present study. The average value of the Cherenkov contribution for the total detected light is of around 8% in the selected data sample. This value corresponds approximately to the difference between the area of the data dE/dX distribution and the total area of the dE/dX distributions for each of the simulated sets and it is compatible with the fact that the larger contribution from Cherenkov scattered light comes from the region of the shower around X_{max} , or later.

In figure 4.14 left, the relative difference between the simulation and data reconstructed shower energy is plotted against the relative difference between the simulated and data X_{max} values, for both simulated sets. It can be observed that there is no correlation between both

variables in KG and 3D simulations with similar dispersions.

In the right, the L parameter of equation 2.48, $L = \sqrt{|X'_0|\lambda}$, which is basically the longitudinal width of the shower is plotted. Both KG and 3D simulation seems to have similar width, but slightly higher than the one for data. There are some data events with much lower L parameter than the one in the simulations. Those events producing the lower average L on data and come probably from a worse longitudinal profile reconstruction not seen on the simulation. Note that the differences are compatible within the RMS.

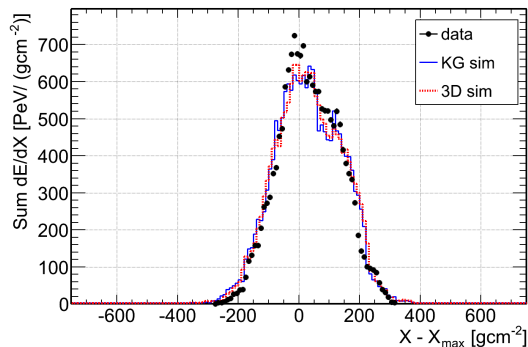


Figure 4.13: dE/dX sum of all events, as a function of $X' = X - X_{max}$ of each event, for the two simulated sets, 3D simulation (red) and KG Simulation (blue) and compared to the corresponding distribution on data (dots).

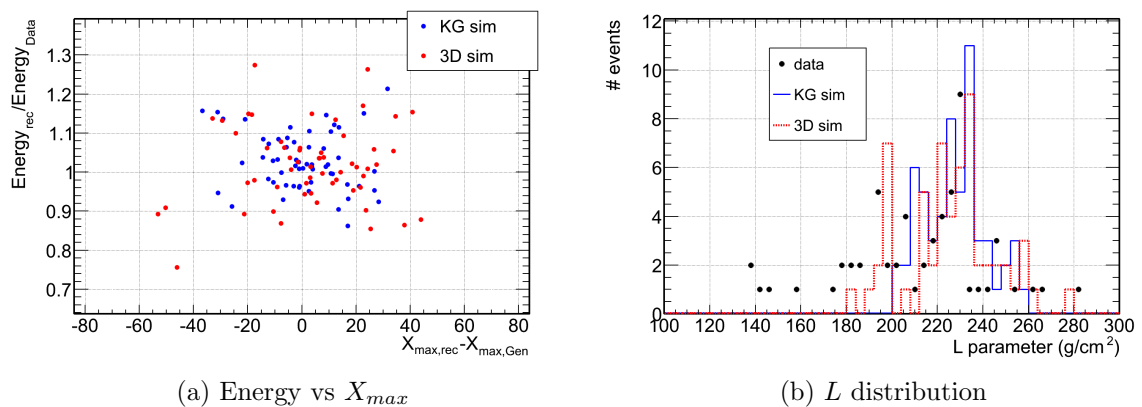


Figure 4.14: Relative difference between the reconstructed shower energy in the simulations and the reconstructed shower energy for data versus the difference between the reconstructed X_{max} value obtained for the simulations and at generation level. The KG simulation is represented by the blue dots and the 3D simulation by the red dots. b) width L distribution (data in black points).

4. 3D SIMULATION OF EAS FOR THE FD

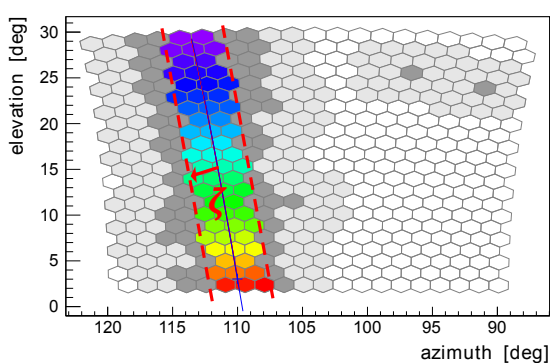
x	$\langle x_{gen} \rangle$	$\langle x_{KG} \rangle$	$\langle x_{3D} \rangle$	$\langle \frac{x_{KG} - x_{gen}}{x_{gen}} \rangle$	$\langle x_{KG} - x_{gen} \rangle$	$\langle \frac{x_{3D} - x_{gen}}{x_{gen}} \rangle$	$\langle x_{3D} - x_{gen} \rangle$
$\phi(^{\circ})$	-	-	-	-0.0001 ± 0.0096	0.08 ± 0.83	0.0010 ± 0.0194	0.15 ± 1.14
$\theta(^{\circ})$	-	-	-	-0.012 ± 0.015	-0.11 ± 0.98	-0.0009 ± 0.0459	-0.21 ± 0.25
$\log_{10}(E/eV)$	18.23 ± 0.22	18.24 ± 0.22	18.24 ± 0.22	0.033 ± 0.082	0.013 ± 0.034	0.027 ± 0.109	0.009 ± 0.046
$X_{max,gen} [g/cm^2]$	762.5 ± 64.6	763.6 ± 70.7	762.4 ± 61.5	0.001 ± 0.021	1.1 ± 16.6	0.010 ± 0.049	3.9 ± 22.8
$dE/dX_{max,data} [PeV]/g/cm^2]$	3.31 ± 3.70	3.29 ± 3.71	3.31 ± 3.70	-0.008 ± 0.038	-0.020 ± 0.084	-0.006 ± 0.035	-0.008 ± 0.116
$dE/dX_{max,gen} [PeV]/g/cm^2]$	3.45 ± 3.50	3.29 ± 3.71	3.31 ± 3.70	-0.040 ± 0.145	-0.157 ± 0.556	-0.040 ± 0.137	-0.145 ± 0.548
$L_{data} [g/cm^2]$	211.6 ± 30.3	227.8 ± 13.9	225.9 ± 20.1	0.102 ± 0.197	14.7 ± 32.3	0.093 ± 0.208	12.7 ± 35.43

Table 4.2: Average values of the reconstructed geometry, energy, dE/dX_{max} , X_{max} and L for the simulated samples with KG and 3D methods. The difference and relative difference between the reconstructed parameters of the simulations and the generated ones, along with the rms of the distributions. The value dE/dX_{max} of the data and generated is considered separately in the lines 5 and 6. The results are presented as *mean* \pm *RMS*.

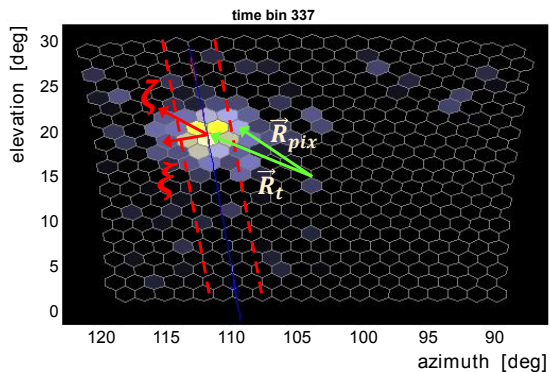
4.2.2.3 Lateral parameters

After validating the longitudinal light profiles, it is more important to see the behaviour of the lateral profile, comparing the 3D simulation to the KG simulations (or equivalent to the lateral parametrizations inside ShowerPhotonSimulatorKG) and with the data. The longitudinal structure of the shower is more easily reproduced, but the lateral profiles on the standard simulations are obtained from average parametrizations, and it should be checked if they are compatible. Moreover, in the future it will be important to study the fluctuations of the lateral profiles.

In each time slot, the shower is seen in the camera with an oval shape around the corresponding point in the shower axis, as the picture displayed in the figure 4.15b. After adding up all time slots, the traditional camera view appears, like in figure 4.15a. Considering the point, \vec{R}_t , on the shower axis, where the shower front is at time t , it is possible to see the light profile as function



(a) ζ on the camera



(b) ζ, ξ on the camera at time t

Figure 4.15: left, event on the camera, adding the light in all time slots, the color represents the time evolution. Right: light in the camera at a give time slot with the representation of the ζ and ξ .

of the angular distance (ζ) to that point, or as a function of the perpendicular distance (ξ) to that point, with respect to the shower axis on the camera.

Let ζ be the angular distance between the pixel alignment direction \vec{R}_{pix} and the direction of the shower at a specific time, \vec{R}_t , in the camera (α, β) coordinates, so that

$$\zeta = \left| \vec{R}_{pix} - \vec{R}_t \right|. \quad (4.8)$$

In the figure 4.16, the light is summed for all events and time slots, as function of the ζ angle. The light is considerably similar to the data and KG simulations.

The first two bins in ζ are smaller, due to the size of the pixels. Since the pixels have a size of about 1.5° from side to side, below 0.75° the probability of having an \vec{R}_{pix} decreases, decreasing the summed light.

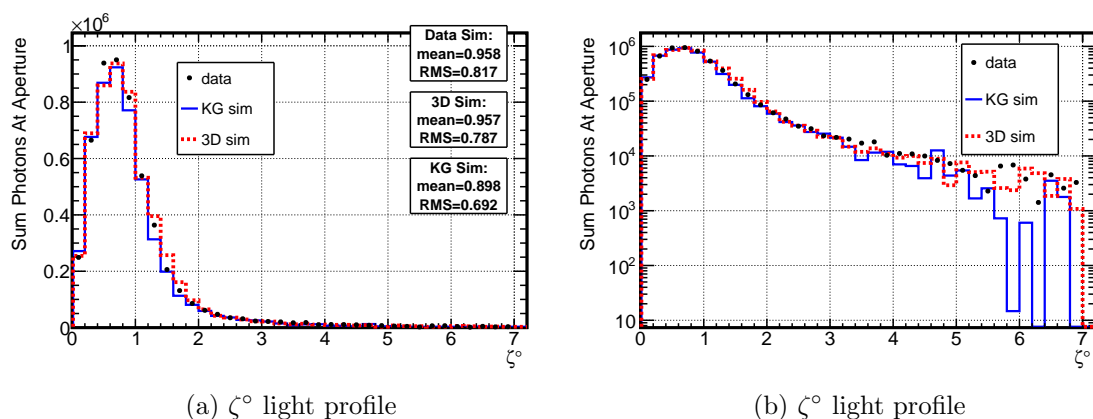


Figure 4.16: Light profile as function of ζ , in normal (left) and \log_{10} scale (right), for the 3D (red), KG (blue) simulations and data (black).

To see the light evolution with the perpendicular angular distance to the shower axis, we plot the angular distance ξ , given by:

$$\xi = \left| (\vec{R}_{pix} - \vec{R}_t) \cdot \vec{e}_{sh,\perp} \right|, \quad (4.9)$$

where $\vec{e}_{sh,\perp} = (\vec{e}_{sh,\alpha}, -\vec{e}_{sh,\beta})$ and \vec{e}_{sh} is the shower direction in the camera (α, β) coordinates. In figure 4.17, the light is displayed as function of ξ . Again, the 3D simulation light is consistent with the KG simulation and data.

Extra light photons on data, would be expected for higher angles than $\sim 3^\circ$ due to the multiple scattering, which is not implemented on the 3D or KG simulations. This contribution is not so important here as in the Cherenkov sample (figure 4.31) because the events are very close and with directions from the telescope into the Auger array.

As said before, to reconstruct the energy, for each time bin, only the light within the zeta optimum, $\zeta_{otpimum}$ is summed to obtain the profile. The $\zeta_{otpimum}$ is obtain in order to maximize the signal over background, but there are some light outside the $\zeta_{otpimum}$ that should be accounted based on models. A good way to compare nearby fluorescence events is to compare

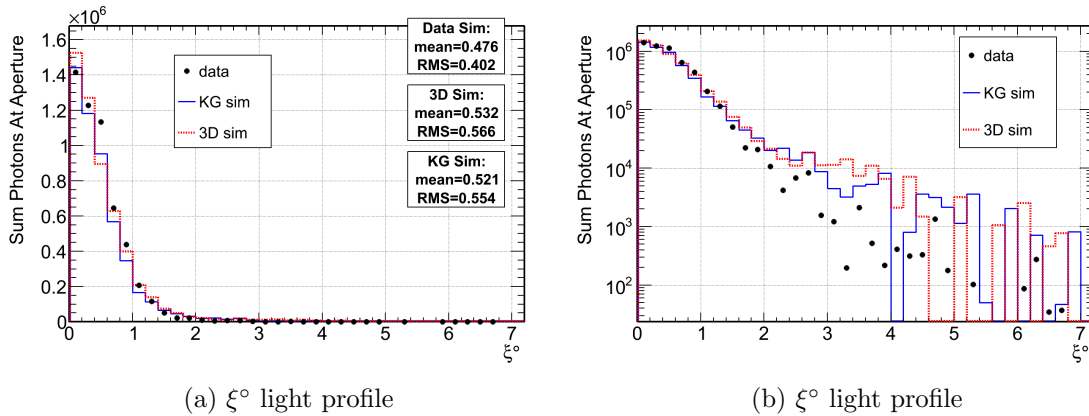


Figure 4.17: Light profile as function of ξ , in normal (left) and \log_{10} scale (right), for the 3D (red), KG (blue) simulations and data (black).

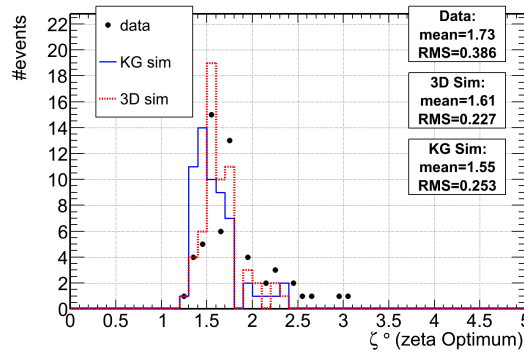


Figure 4.18: Zeta optimum, $\zeta_{optimum}$ considered in the reconstruction, for the 3D (red), KG (blue) simulations and data (black).

the $\zeta_{optimum}$ between the simulations and data. In figure 4.18, the zeta optimum is plotted and the simulations and data are slightly different but within the systematics. Nevertheless, the 3D simulation considers a large angle ζ , when summing the light, than the KG simulation. The data reproduce a even larger average angle ζ . This fact shows us that the real shower might be larger, transversely, than expected and the corrections for the light outside the $\zeta_{optimum}$ must be carefully considered.

4.2.2.4 Review

With the BinTheSky framework it was possible to simulate the air shower without using any lateral parametrizations. With the previous distributions, the fluorescence light is consistent with the data and parametrizations in the KG simulation. After the validation, it would be important to simulate a bigger sample and reconstruct it with the 3D reconstruction in order to see the fluctuation around the average lateral and longitudinal parametrizations.

On the next section, the Cherenkov emission will be treated. This is much harder than the fluorescence emission since it depends on the particle's direction on the sky rather than the energy deposited.

4.3 Cherenkov Emission

4.3.1 CORSIKA and Offline Intervention

4.3.1.1 Cherenkov information

The Cherenkov light is emitted from particles with velocity, $\beta = v/c$, higher than the speed of light on the atmosphere, in a light cone with $\cos \theta = \frac{1}{\beta n}$ around the particle direction, with the atmospheric refraction index n (section 2.4.2.2).

Since the Cherenkov emission depends on the particle's direction, it is more difficult to save the relevant information inside CORSIKA and simulate the shower. There are millions of particles in the shower development, so it is not possible to save the directions and energy of all particles that cross one SkyBin. The best way to handle this, is to save the distributions of the particle directions inside the SkyBin, instead of each particle direction.

The directions inside the SkyBin are defined as the angle α , from the shower axis direction to the charged particles directions (see figure 4.19). It is also defined, an angular direction ϕ' , which is the azimuthal direction of the charged particle with respect to the SkyBin azimuthal angle, ϕ (see figure 4.19a).

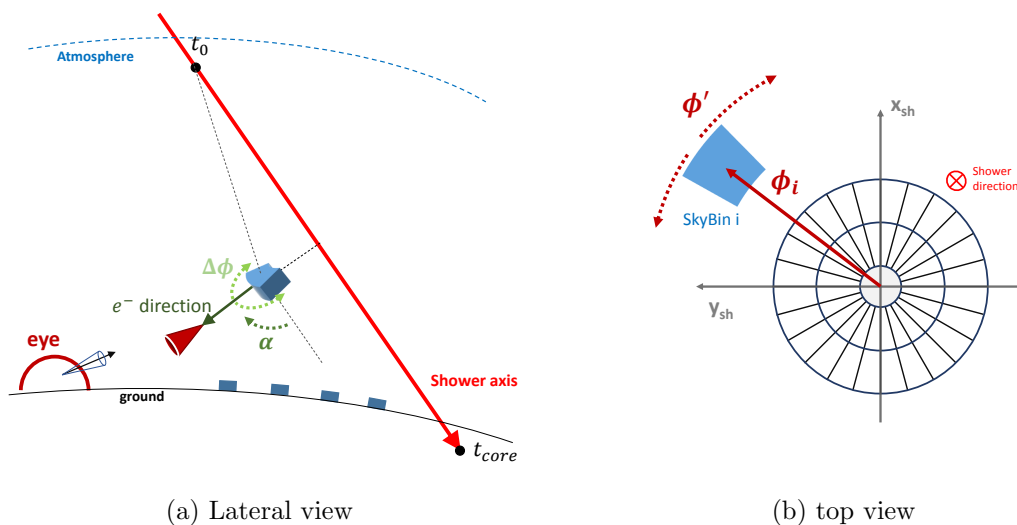


Figure 4.19: Angular definitions, α and ϕ' , inside the SkyBin, in a lateral view (left) and from a top view (right).

The information that needs to be saved are the distribution of charged particle number as function of the angular direction α and the length travelled by those particles as function of the α direction also. The distribution has an interval $\Delta\alpha = 1^\circ$ (see the distributions in the figure 4.20c and 4.20e).

For the ϕ' angular dependence, it is also necessary to save the length travelled by those particles as function of the ϕ' in a distribution with intervals $\Delta\phi' = 1^\circ$ (figure 4.20a).

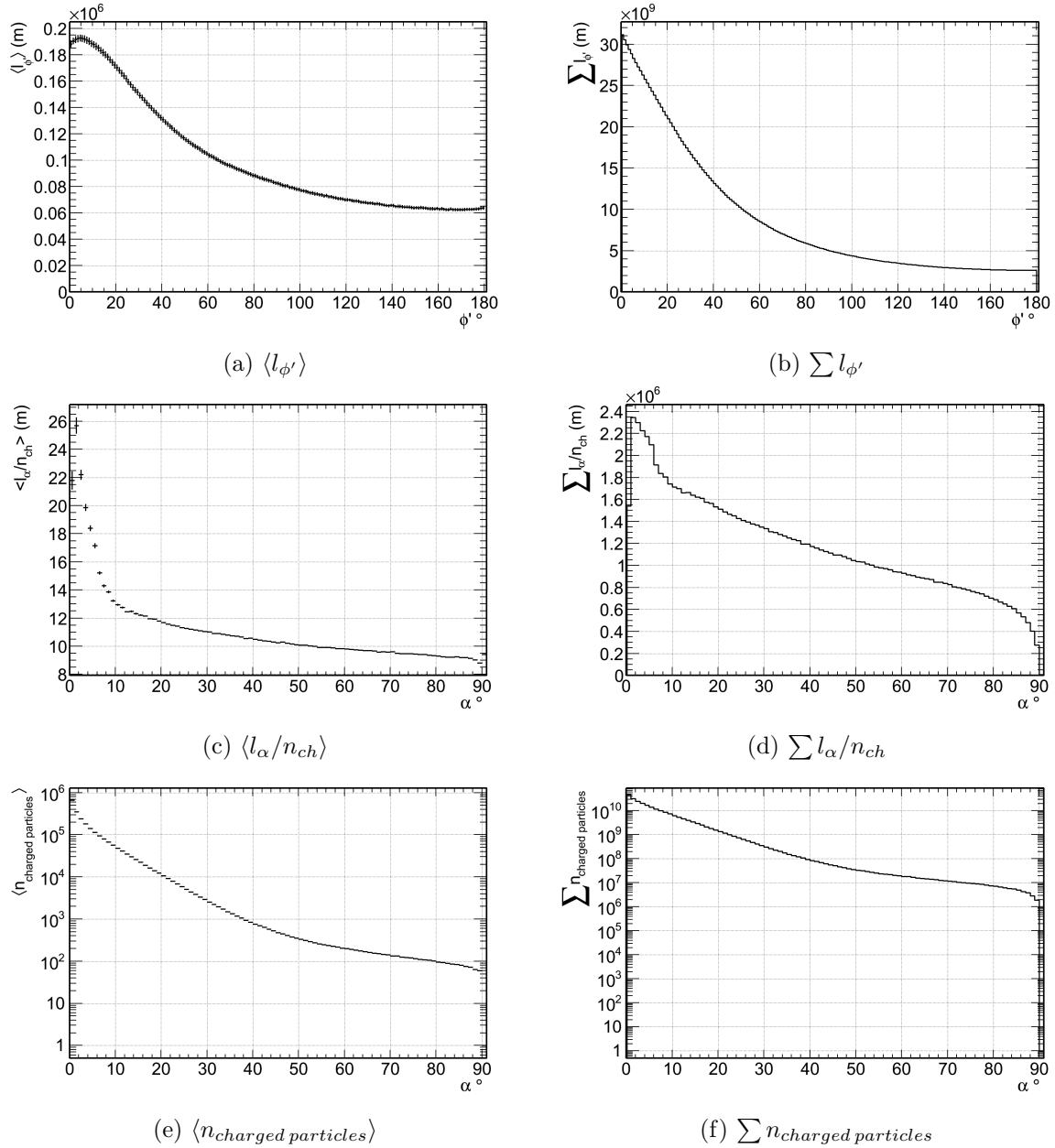


Figure 4.20: Average number of charged particles as function of α for all SkyBins, in (e), and the summed number for all boxes in (f). Average length travelled by those particles as function of α (c) and ϕ' (a), summed lengths for all boxes in (b) and (d), see definitions in the figure 4.19. These profiles were obtained from one event with 10^{19} eV.

4.3.1.2 Photon emission and propagation

With the information displayed in the figure 4.20 and described before, it is possible to calculate the Cherenkov emission. As previously, only the SkyBins inside the field of view are considered. The Cherenkov emission can be given by equation 2.57 described on the section 2.4.2.2.

The number of emitted photons depends on the number of charged particles above the velocity limit and the length travelled by those particles. The calculation for the emissions should begin by calculating the average length times the number of charged particles with direction to the eye. Basically, in the i th SkyBin, the eye direction is calculated in α and ϕ' coordinates. The charged particles times length in α direction is $N_{i,\alpha}^{ch} \cdot l_{i,\alpha}$. It is only missing the ϕ' distribution. Since it already contains the travelled length (in α), it is only necessary to correct this value to the fraction of total length in ϕ' direction, $l_{i,\phi'}$, to the total length travelled in the SkyBin, l_i . The charged particles times the travelled length in α and ϕ' direction is given by:

$$\left(l_i \cdot N_{Ckov,i}^{ch} \right)_{\alpha,\phi'} = N_{i,\alpha}^{ch} l_{i,\alpha} \cdot \frac{l_{i,\phi'}}{l_i}. \quad (4.10)$$

According with equation 2.57, the number of photons emitted from a SkyBin, i , to the eye direction, (α, ϕ') , between λ_1 and λ_2 is:

$$n_{ph,Ckov}^{SkyBin,i,\alpha,\phi'}(\lambda_1, \lambda_2) = \left(l_i N_{Ckov,i}^{ch} \right)_{\alpha,\phi'} \cdot k_{Ckov} \left(1 + \frac{1}{n^2} \right) \cdot \left(\frac{1}{\lambda_1} - \frac{1}{\lambda_2} \right), \quad (4.11)$$

with the Cherenkov constant $k_{Ckov} = 2\pi\alpha_e$, and the refractive index n .

Actually, the Cherenkov is emitted in a cone and not in the particles direction. Nevertheless, the maximum opening angle at sea level is around 1.3° , the bins have $(\Delta\alpha = 1^\circ, \Delta\phi' = 1^\circ)$ and there are millions of particles. In this way, the photons that would cross to another (α, ϕ') bin, would be compensated by the photons coming from the others bins around.

These photons then propagates until the telescopes, decreasing the density with the corresponding solid angle. The geometric factor is given by:

$$f_{geo,\alpha}(d_i) = \frac{1}{2 \sin(\alpha) \sin(\Delta\alpha/2) \Delta\phi \cdot d_i^2}. \quad (4.12)$$

The number of photons arriving at the diaphragm, given by eq. 4.13, is just the eq. 4.11 times the geometric factor, projected diaphragm area and corresponding attenuations by Mie and Rayleigh scattering.

$$\begin{aligned} dn_{ph,Ckov}^{dia,i}(\lambda_1, \lambda_2) &= f_{geo,\alpha} A_{dia} \cdot \cos(\theta_{\vec{n}_{dia}, \vec{p}_i}) dn_{ph,Ckov}^{SkyBin,i,\alpha,\phi'}(\lambda_1, \lambda_2) \cdot T_{Mie} \cdot T_{Rayleigh} \\ &= \frac{\pi R_{dia}^2 \cos(\theta)}{2 \sin(\alpha) \sin(\Delta\alpha/2) \Delta\phi \cdot d_i^2} \left(l_i N_{Ckov,i}^{ch} \right)_{\alpha,\phi'} \cdot k_{Ckov} \left(1 + \frac{1}{n^2} \right) \cdot \left(\frac{1}{\lambda_1} - \frac{1}{\lambda_2} \right) \\ &\quad \cdot T_{Mie} \cdot T_{Rayleigh}. \end{aligned} \quad (4.13)$$

In the end, the photons are added for the λ intervals and the attenuations are the average attenuations in the wave length interval.

4.3.2 Validation

A data sample composed of events with high amount of direct Cherenkov light, and with shower core near the telescopes was selected using a dedicated function of the CuscaLX module. This Cherenkov rich data sample had to fulfil the criteria:

1. θ shower $< 55^\circ$;
2. distance(Core-Telescope) < 7.5 km;
3. $\log_{10}(E_{Shower}) > 17$;
4. Cherenkov component $> 70\%$ of the total light
5. Showers moving to the eye (see figure 3).

A sample with 85 events was selected from 2007 to 2010 Pierre Auger Observatory data. In the figure 4.21, the Cherenkov fraction and distance shower-eye is plotted, as well as the difference X_{max} between generated and data events.

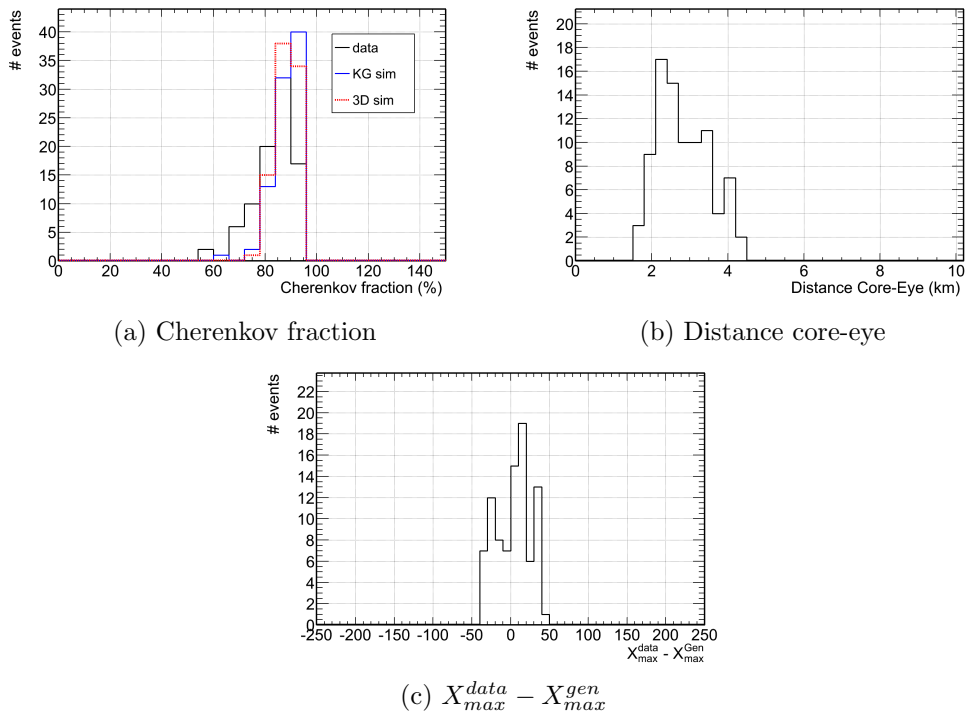


Figure 4.21: a) the event Cherenkov fraction. b) distance core-eye for the sample. c) difference between data and generated X_{max} .

This sample generated with CORSIKA was then simulated within the Offline framework using both the standard shower simulation for the FD, based on the longitudinal shower profile and the developed simulation based on the BinTheSky framework. Since the selected sample is

used to study the Cherenkov emission, only the contributions from direct Cherenkov light and fluorescence emission were considered. The multiple scattering of light in the atmosphere was turned off in the simulation and in the reconstruction. The events were simulated using the core coordinates and the TimeStamp of the corresponding events in the data sample.

4.3.2.1 Geometric reconstruction

The standard and KG simulations will be compared to the data they represent, the first step is to check the geometry reconstruction. The reconstructed zenith and azimuthal angles for the shower axis for the events in the KG and the 3D simulations divided by the corresponding data event values are compared in figure 4.22.

The geometry reconstruction of the 3D Simulation is in agreement with the data geometry and it is very similar to the KG Simulation behaviour. For the zenithal angle, the reconstruction gave the fraction $\langle \theta_{3D} - \theta_{data} \rangle = 0.16 \pm 0.54^\circ$, while in the KG simulation for this sample it was $\langle \theta_{KG} - \theta_{data} \rangle = 0.23 \pm 0.39^\circ$. The reconstructed azimuthal angle gave the values $\langle \phi_{3D} - \phi_{data} \rangle = -0.11 \pm 0.55^\circ$ and $\langle \phi_{KG} - \phi_{data} \rangle = 0.17 \pm 0.46^\circ$. Both mean values and RMS are within the normal Auger resolution. These values are important to realize that the new simulation are getting the right geometry in the CORSIKA, correctly introducing it in the Offline and that the new emissions approach don't destroy the times and geometry of the shower. From the analysis of table 4.3 and from figure 4.22 it can be stated that the geometric reconstruction of the shower axis for both simulations is in good agreement with the the geometric reconstruction of the data events.

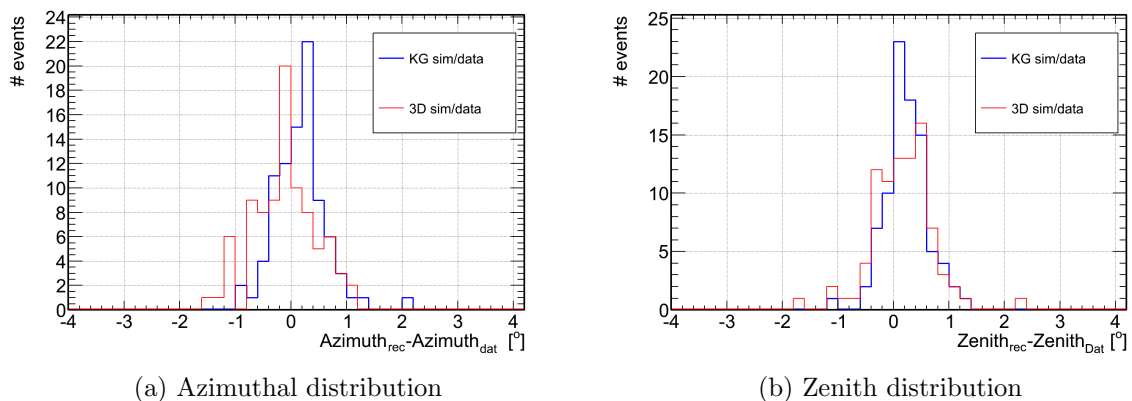


Figure 4.22: For the Cherenkov emission, the relative differences between the simulation and data reconstructed zenith angle (left) and azimuthal angle (right), for the 3D and KG simulations. The KG is represented by the blue line whereas the red line corresponds to the 3D simulation.

4.3.2.2 Longitudinal shower parameters

The longitudinal profile and parameters such as the energy reconstruction and X_{max} can be compared in the next step, for the Cherenkov sample.

The first thing to look for is the light obtained at the diaphragm and summed it for all events, as function of the time slots of detection. In the figure 4.23 the light sum at the diaphragm is plotted for both simulations and data, left, and the same distribution is plotted normalized on the right. The number of Cherenkov (plus some fluorescence) photons (left) and shape (right) is very similar between the data and simulations, which should be expected if the 3D simulations was corrected. The 3D simulation have a light profile much similar to the one found on data. The light in the data is slightly higher than on the simulations, but the normalization of the 3D simulation is closer than the KG one. The extra light on the data comes from the scattered Cherenkov light. As for the shape, the data seems to be thinner than the simulation, this means that probably the simulation emits less Cherenkov light than the one present on the data since on the previous section the scattered light didn't change considerably the shape of the light sum.

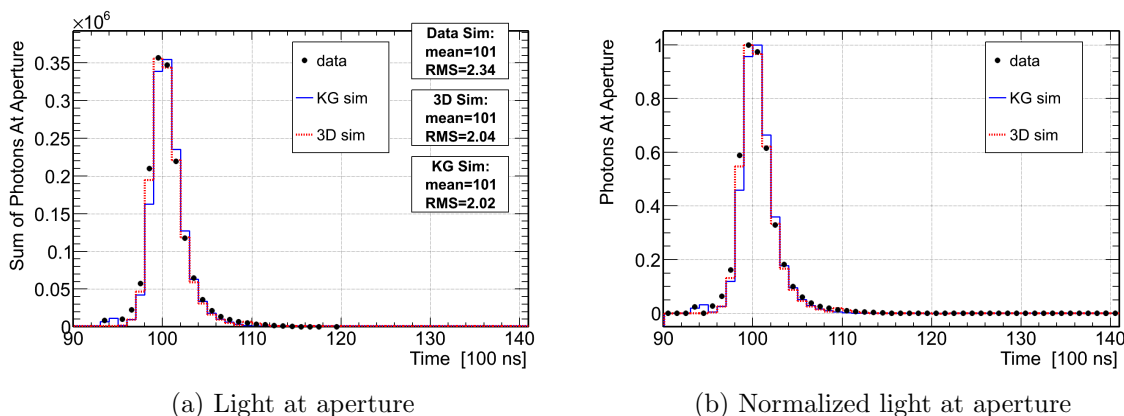


Figure 4.23: Sum of the photons at the diaphragm for all events as function of ADC time bins (left). The same normalized profiles on the right. In black dots, blue and red lines are the data, KG and 3D simulations respectively. Only fluorescence and direct Cherenkov light were produced on the simulations.

The next step is to analyse the energy and X_{max} of the events. To this aim, the events need to be reconstructed, which means, the light needs to be converted into dE/dX and the time into $X[\text{g}/\text{cm}^2]$. Both simulations were reconstructed with the standard reconstruction and the dE/dX were fitted to the Gaisser-Hillas function, where the X_{max} is obtained and the integral is proportional to the energy.

The reconstruction depends on the estimation of the light components matrix that relates the all the light with the deposited energy profile, on eq. 3.24, for a particular geometry. The Cherenkov light is very dependent on the shower geometry, as well as the matrix Cherenkov parameters. A small difference on the shower could lead to different estimation of deposited energy.

The Cherenkov is dependent on the angular distance to the shower axis, denoted here as α_{sh} . In the figure 4.24a the light at aperture is plotted as function of the α_{sh} , according with the

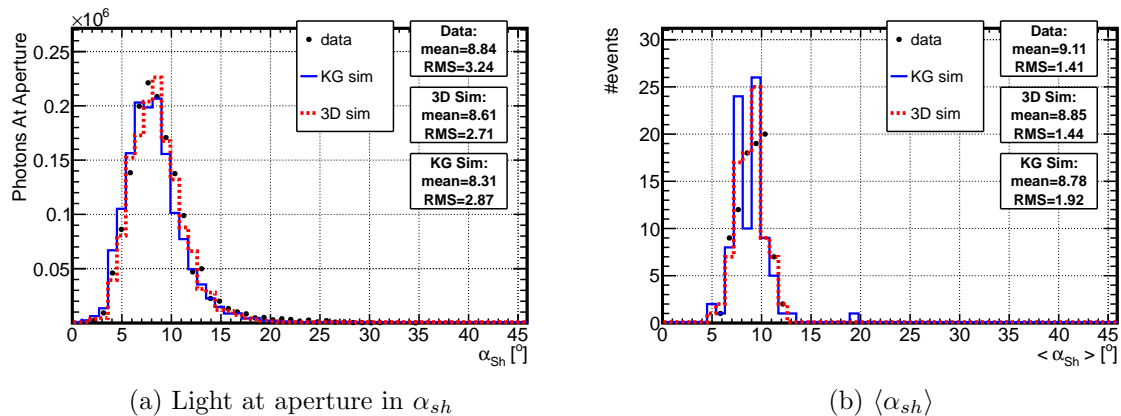


Figure 4.24: Sum of the photons at the diaphragm for all events as function of α_{sh} (a). The mean α_{sh} , $\langle \alpha_{sh} \rangle$, weighted by the light on the events. In black dots, blue and read lines are the data, KG and 3D simulations respectively. Only fluorescence and direct Cherenkov light were produced on the simulations.

geometry. The KG and 3D simulations are slightly shifted with respect to the data, meaning that the energy matrix could be a little changed. In the figure 4.24b, the mean α_{sh} , weighted by the light is plotted. They are similar, but the data is slightly higher than the simulations.

In figure 4.25, the reconstructed shower energy is presented with the $\log_{10}(E/\text{eV})$ distribution, where it is compared to the reconstructed energy of the events in the real data. On the right, the distributions of the relative difference between the reconstructed energy in both simulations and that of the data sample is displayed.

The light profiles being relatively similar, the reconstructed energy for the 3D simulation is about -1% lower than the generated (data) energy. The KG energy is also quite similar to the generated with a average difference of -4% . In respect to the standard simulation, it should be noted that the reconstructions and simulations are based on the same principles and parametrizations, which means, it should be in agreement. The 3D simulation on another side, uses the intrinsic time of the SkyBins, and distributions contained in it. With this information, the standard simulation could have difficulty to recover the energy.

Just to remember again, this sample has events with about $\sim 85\%$ Cherenkov light and the reconstruction must correctly estimate the matrix with the different light components of equations 3.24 and 3.25 (on section 3.2.4). A slightly difference on the geometric reconstruction would change the values of α_{sh} , changing the parameters in the matrix, with subsequent wrong recovered energy deposited, dE/dX . Also, since the Cherenkov events are much shorter in time (compare figure 4.23 with 4.8), this means the shower geometry is less constrain and less reliable. In the data, these steps are not completely reliable, so they are not used in most of the analyses. Also, if the reconstruction has problems on those events, then the generated energy coming from the data could not correspond to the real energy of that event.

Instead of looking for the shower energy (proportional to the integral of the dE/dX profile) it may be worthwhile to look at the dE/dX_{max} of the profile. In the figure 4.26, the distribution of dE/dX_{max} (left) and the distribution of $(dE/dX_{max,k} - dE/dX_{max,data}) / dE/dX_{max,data}$ is plotted for the 3D and KG simulation, data and generated values. As can be expected, the KG value is very close to the one on the data, since it was approximately the value that was simulated by it. Nevertheless, the generated values are around 20% higher and the 3D around $\sim 13\%$. A shift on the α_{sh} values could explain the difference, but also, the data might have a difference, for the same reason, with respect to the real energy deposited profile. This means that probably the simulated sample doesn't correspond exactly to the data, but has a bias on the reconstruction, seen in the 3D simulation and generated. Despite the dE/dX_{max} being higher in the 3D simulation than in the KG, the integral (for the energy) obtained is similar and the energy reconstruction compatible.

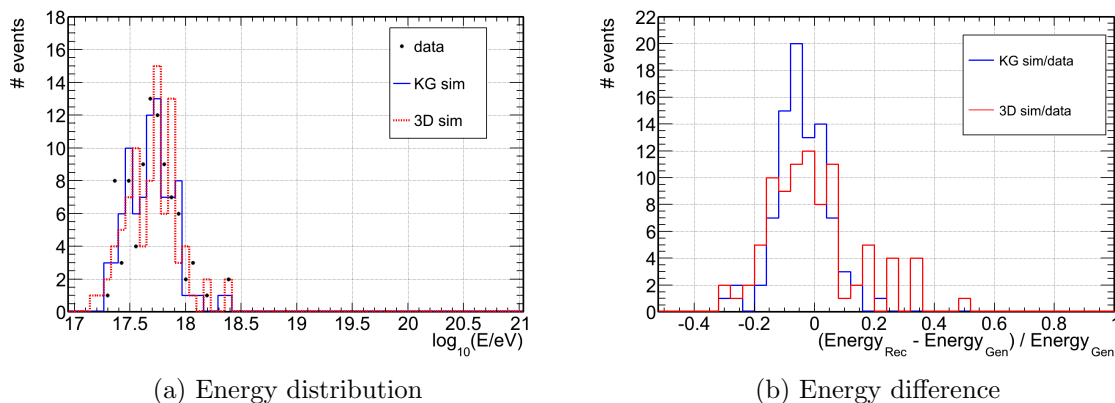


Figure 4.25: The reconstructed energy, $\log_{10}(E/eV)$, distribution for the data sample (black dots), KG (blue) and 3D (red) simulations (left); on the right the $(E_k - E_{gen}) / E_{gen}$ distribution. The generated energy matches the reconstructed energy in Data.

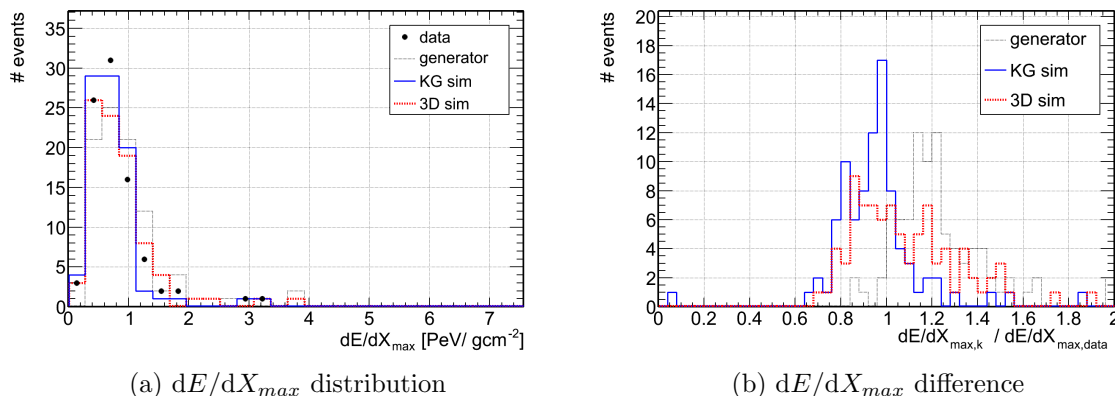


Figure 4.26: The reconstructed longitudinal maximum profile, dE/dX_{max} , the data sample (black dots), KG (blue) and 3D (red) simulations (left); and the $(dE/dX_{max,k} - dE/dX_{max,data}) / dE/dX_{max,data}$ distribution (right).

In order to compare the X_{max} , the generated one will be considered again. The X_{max} distribution and the differences between the value of X_{max} at generation and in simulation are displayed in figure 4.27, whereas, on the right, the relative difference (in g/cm^2) between the reconstructed values of X_{max} for both simulations and the corresponding X_{max} values at generator level. In average, both simulation methods yield reconstructed X_{max} values slightly bias to the generated value. In average, the simulations gives around $+7.3 \pm 38$ and $-14 \pm 45 \text{ g/cm}^2$ (for 3D and KG respectively) with respect to the generated values. For both simulations, the difference between generated and reconstructed X_{max} values is below 2%. The X_{max} is worst reconstructed here than in the fluorescence sample, but it is comparably good taking into account the previous problems. All previous results are written on the table 4.3.

In the figure 4.28, the dE/dX is summed for all events as function of $X' = X - X_{max}$, for the two simulated samples and for data. All events with the translation in X , should became similar and the fluctuations decreases, so it's easy to see if there are some regions with more or less production of light. However, it is very dependent on the X_{max} reconstruction and in the

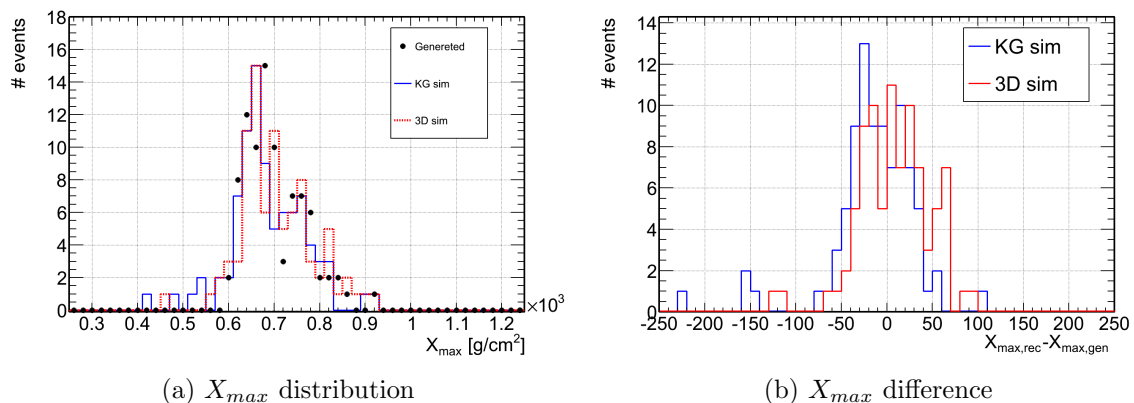


Figure 4.27: X_{max} (left) and $(X_{max} - X_{max})/X_{max}$ (right) distributions are displayed for the generated events (black dots) and for the simulated sets, 3D (red) and KG (blue).

x	$\langle x_{gen} \rangle$	$\langle x_{KG} \rangle$	$\langle x_{3D} \rangle$	$\langle \frac{x_{KG} - x_{gen}}{x_{gen}} \rangle$	$\langle x_{KG} - x_{gen} \rangle$	$\langle \frac{x_{3D} - x_{gen}}{x_{gen}} \rangle$	$\langle x_{3D} - x_{gen} \rangle$
$\phi(^{\circ})$	-	-	-	0.006 ± 0.023	0.17 ± 0.46	-0.002 ± 0.016	-0.11 ± 0.55
$\theta(^{\circ})$	-	-	-	0.004 ± 0.006	0.16 ± 0.54	0.003 ± 0.009	0.23 ± 0.39
$\log_{10}(E/eV)$	17.71 ± 0.22	17.77 ± 0.26	17.70 ± 0.23	-0.052 ± 0.126	-0.032 ± 0.119	-0.004 ± 0.154	-0.006 ± 0.065
$X_{max,gen} [\text{g/cm}^2]$	700.7 ± 64.4	685.3 ± 80.1	704.9 ± 79.9	-0.021 ± 0.068	-14.4 ± 45.5	0.006 ± 0.068	7.3 ± 38.7
$dE/dX_{max,gen} [\text{PeV}/\text{g/cm}^2]$	0.940 ± 0.596	0.727 ± 0.457	0.846 ± 0.559	-0.218 ± 0.135	-0.213 ± 0.190	-0.103 ± 0.193	-0.094 ± 0.189
$dE/dX_{max,data} [\text{PeV}/\text{g/cm}^2]$	0.776 ± 0.469	0.727 ± 0.457	0.846 ± 0.559	-0.047 ± 0.200	-0.049 ± 0.123	0.086 ± 0.232	0.070 ± 0.167
$L_{data} [\text{g/cm}^2]$	250.8 ± 23.5	257.1 ± 20.2	241.0 ± 23.9	0.033 ± 0.128	8.8 ± 29.2	-0.049 ± 0.129	-11.4 ± 30.3

Table 4.3: Average values of the reconstructed geometry, energy, dE/dX_{max} , X_{max} and L for the simulated samples with KG and 3D methods. The difference and relative difference between the reconstructed parameters of the simulations and the generated ones, along with the rms of the distributions. The value dE/dX_{max} of the data and generated is considered separately in the lines 5 and 6. The results are presented as *mean* \pm *RMS*.

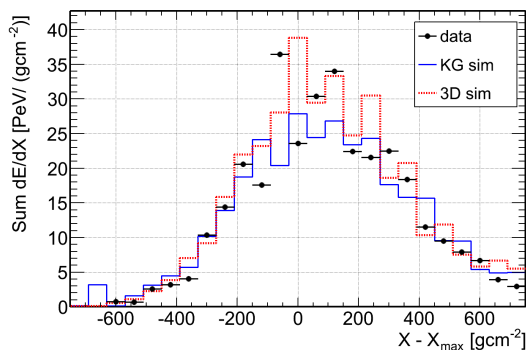
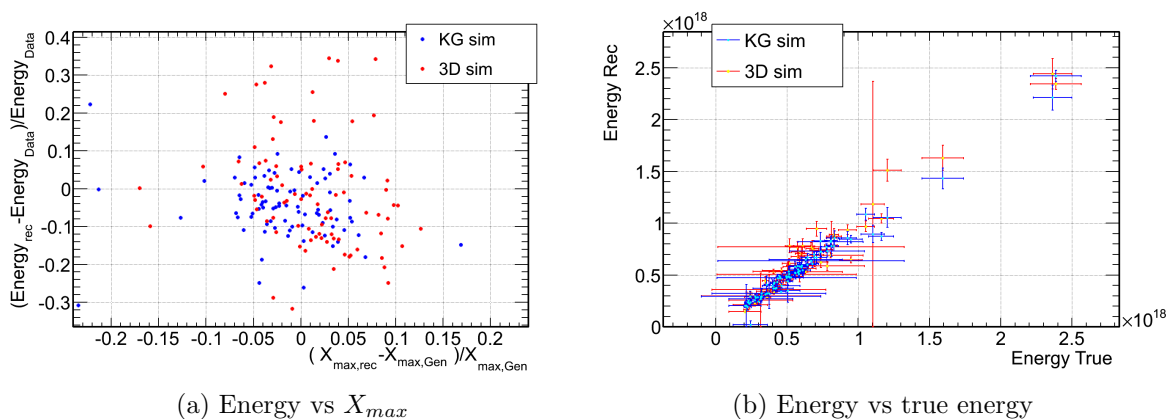


Figure 4.28: dE/dX sum of all events, as a function of $X' = X - X_{max}$ of each event, for the two simulated sets, 3D simulation (red) and KG Simulation (blue) and compared to the corresponding distribution on data (dots).



(a) Energy vs X_{max}

(b) Energy vs true energy

Figure 4.29: Relative difference between the reconstructed shower energy in the simulations and the reconstructed shower energy for data versus the relative difference between the reconstructed X_{max} value obtained for the simulations and at generation level. The KG simulation is represented by the blue dots and the 3D simulation by the red dots.

case of the Cherenkov sample, where the X_{max} is worst reconstructed may not be so conclusive. The KG distribution is similar to the data since the reconstruction, while around $X' = 0$, the 3D simulation is similar to the data since the dE/dX is higher.

In figure 4.29a, the $(E - E_{data})/E_{data}$ is plotted as function of $(X_{max} - X_{max,data})/X_{max,data}$, for both simulated sets. The 3D distribution has a higher spread than the KG due to the worst reconstruction. On the right it is also the reconstructed energy as function of the generated one (from data). Despite the difference in the USP and in the dE/dX_{max} , the reconstructed energy from both simulation is compatible along the considered energies. In the fig. 4.30, the L parameter of equation 2.48, $L = \sqrt{|X'_0|\lambda}$, which is basically the longitudinal width of the shower, is plotted. The KG have a longitudinal width higher than the 3D simulation and higher than the data, this is why the KG energy is similar to the other one even with lower dE/dX_{max} . The same feature applies to the 3D simulation with a thinner L and higher maximum given

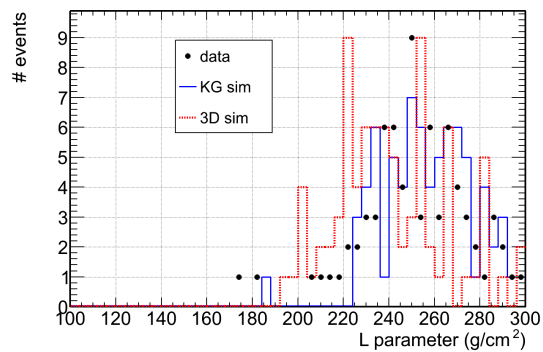


Figure 4.30: a) width L distribution (3D and KG simulation in red and blue, and data in black points).

similar energies in the end.

4.3.2.3 Lateral parameters

After validating the longitudinal light profiles, now it is possible to analyse the lateral distributions.

In the figure 4.31 the light at the diaphragm is plotted as function of ζ from equation 4.8. The 3D simulation have slightly more photons than the KG, but the general shape is very similar as can be seen in the log scale. Both simulations have less photons than the detected in data. At higher ζ angles there are much more light in data, this happens due to the multiple scattering that is not taking into account on the simulations. The multiple scattering is more important here than on the fluorescence sample, because the fluorescence events are close-by, but going from the telescope into the Auger array, while the Cherenkov events go from the array into the telescopes, accumulating more scattered light.

With respect to the distributions in the ξ angular distance, eq. 4.9 (figure 4.32) both simulation

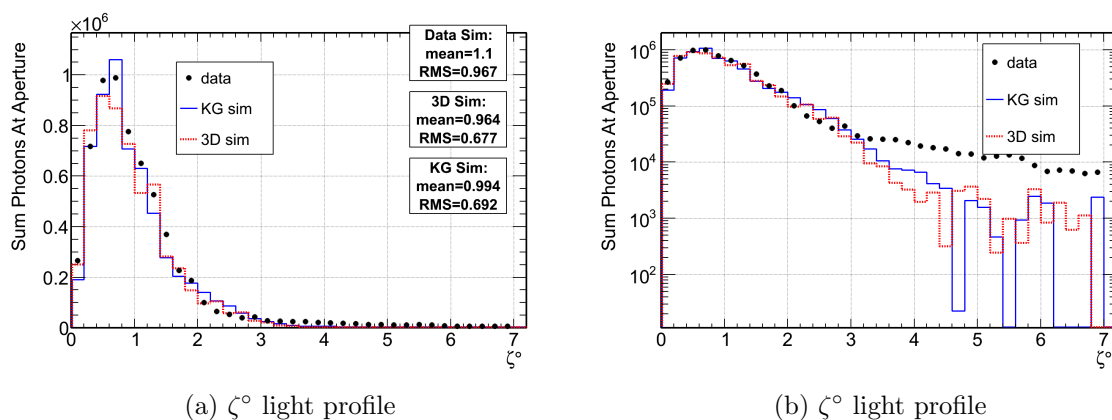


Figure 4.31: Light profile as function of ζ , in normal (left) and \log_{10} scale (right), for the 3D (red), KG (blue) simulations and data (black).

are narrower than the data. At lower angles, the 3D simulation have more light than the one presented in the data. The extra light photons presented on the data for bigger angles than $\sim 3^\circ$ are due to the multiple scattering, which is not implemented on the 3D or KG simulations. Here the contribution is more important than in the previous sample, since the shower points into the telescope direction.

The event reconstruction doesn't consider all ζ light but only the fraction within the ζ_{optimum} . In figure 4.33, it is plotted for the simulations and data. For the Cherenkov sample the ζ_{optimum} is basically the same for the simulations and data, as opposite to the fluorescence sample in figure 4.18. The Cherenkov events have a smaller lateral width and are dominated by the Cherenkov light, showing that the difference in the ζ_{optimum} comes from the fluorescence distribution.

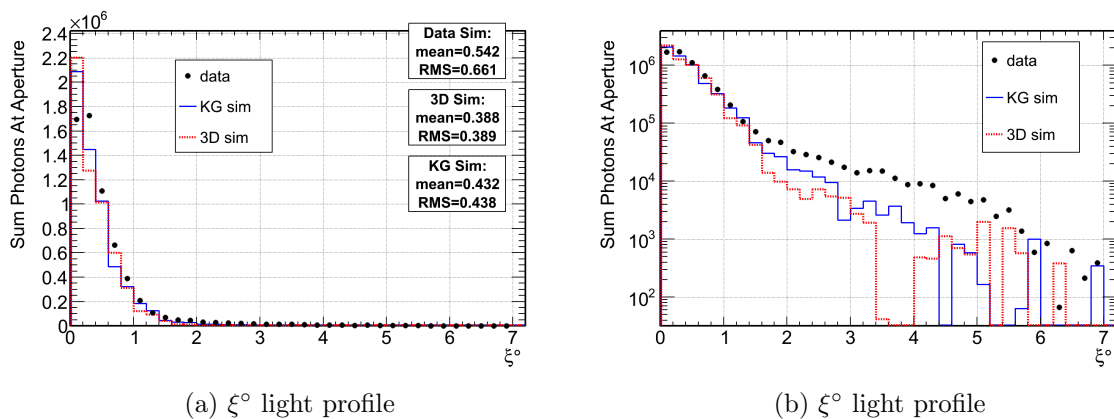


Figure 4.32: Light profile as function of ξ , in normal (left) and \log_{10} scale (right), for the 3D (red), KG (blue) simulations and data (black).

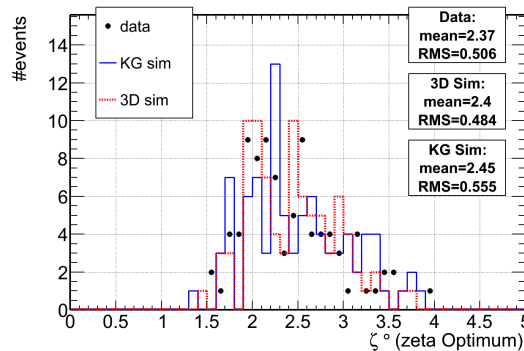


Figure 4.33: Zeta optimum, ζ_{optimum} considered in the reconstruction, for the 3D (red), KG (blue) simulations and data (black), in the Cherenkov sample.

4.3.2.4 Review

With the BinTheSky framework, it was possible to simulate the Cherenkov without any given lateral parametrizations. With the previous distributions the Cherenkov light is consistent with

the data and similar to the parametrizations in the KG simulation. However, a 3D reconstruction should be applied, since the standard reconstruction is tuned to the standard simulation and some bias appeared in the longitudinal reconstructions. The KG simulation used the same parametrizations as the reconstruction and they are based on the same approach, moreover, they are tuned with each other, which mean they should be very similar.

4.3.3 Cherenkov Pool

The Cherenkov emissions were treated only within the Auger telescopes field of view. Nevertheless, with this framework, it is possible to simulate all Cherenkov light arriving on the ground and discriminate it with different vertical field of views.

Using all SkyBins information, in all α and ϕ' directions (figure 4.20), it is possible to see the Cherenkov patterns on the ground. All Cherenkov light emitted by the charged particles in a specific (α, ϕ') directions is propagated and attenuated until they reach a surface.

In the figure 4.34 the Cherenkov density arriving on a surface at Auger height, are shown for all possible field of views or photon directions. The core position is located at the center of the coordinate system. The black line represent the projection on the ground of the shower axis. Each point on the graphic gives the density of photons, that a detector with 180° FOV would detect. In the figure 4.34a is the ground pattern for a vertical event, with 10^{18} eV, completely symmetrical around the core. While on the 4.34b the pattern appears distorted due to the shower inclination of 60° (for an energy $7 \cdot 10^{17}$ eV).

The photons arriving on the ground can be discriminated for their FOV. As follows, the light arriving to HEAT telescope and a normal telescope (like Coihuenco) can be analysed. On the figures 4.35a and 4.35b, the photons on the ground, with the the HEAT FOV detected direction

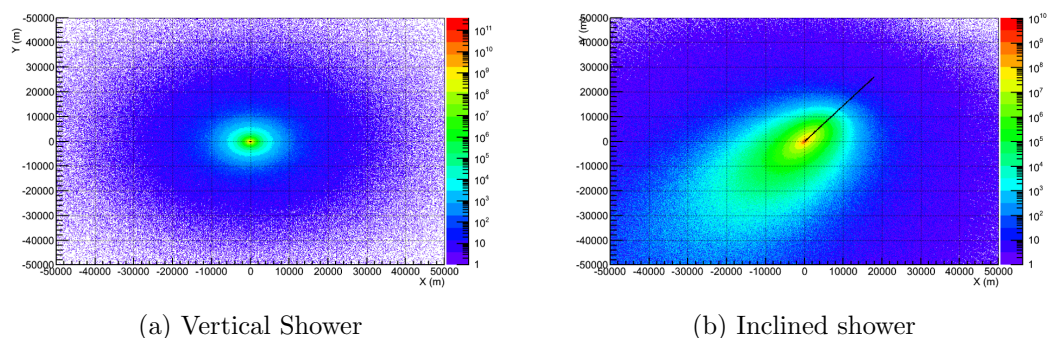


Figure 4.34: Cherenkov photon density arriving on the ground at Auger height, for all possible photon directions with respect to the vertical direction. (a) obtained from a vertical event with 10^{18} eV, (b) obtained from a shower with 60° and $7 \cdot 10^{17}$ eV. The black line represents the shower propagation direction.

(which is approximately between $\sim 30^\circ - 60^\circ$) are plotted, for the vertical and inclined event respectively. HEAT already detects a considerable amount of light between $10^3 - 10^4$ photons per meter square compared to the maximum light at the core with around $\sim 10^{10}$ photons per meter square, on a vertical event. In the inclined event, close to the core, HEAT would detect around $\sim 10^7$ photons per meter square. In the HEAT field of view, since the inclined shower has 60° , the light is only detected if the detector is below the shower axis. If the telescope were in the front of the shower its field of view would be above the shower.

On the figures 4.35c 4.35d are the plots for the same events, but for a field of view corresponding to the normal telescopes (around $\sim 0^\circ - 30^\circ$). In a vertical event, the amount of direct Cherenkov light, detected in the normal telescopes field of view, is negligible. However, if the event is inclined, the normal telescopes could detect a big quantity of light close to the core, and more distant if the telescope is in the front of the shower.

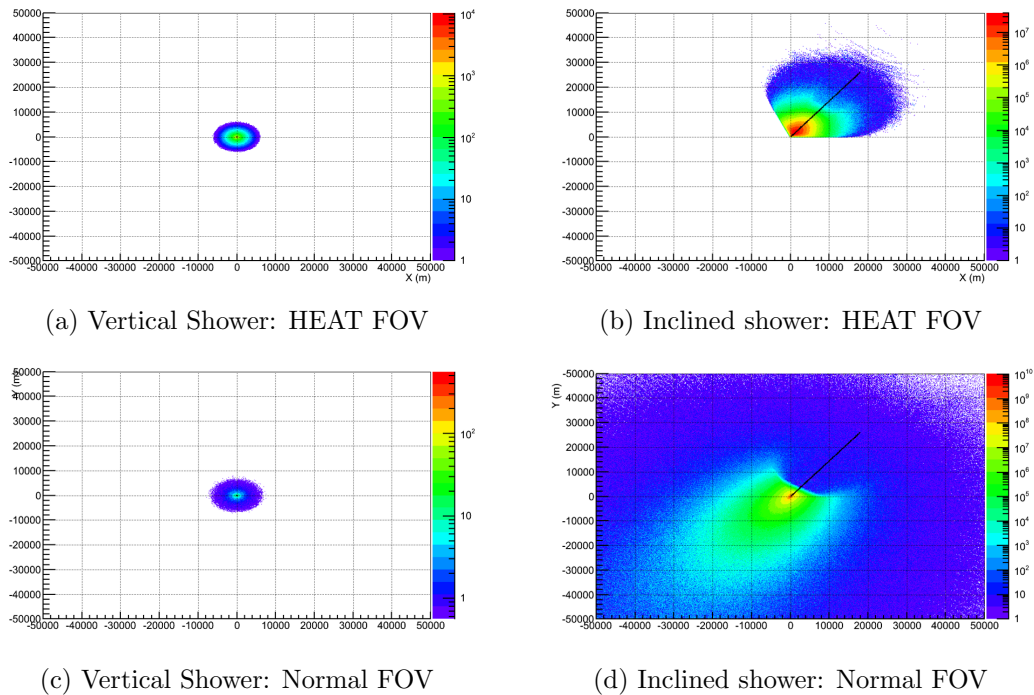


Figure 4.35: Cherenkov photon density arriving on the ground at Auger height, for the HEAT FOV (a) and (b) and normal telescopes FOV (c) and (d). Profiles (a) and (c) obtained from a vertical event with 10^{18} eV, profiles (b) and (d) obtained from a shower with 60° and $7 \cdot 10^{17}$ eV. The black line represents the shower propagation direction.

4.3.3.1 Lateral Cherenkov profile on the ground

The lateral Cherenkov density profile on the ground can also be studied. For this purpose, to simplify, only vertical showers will be considered. In the figure 4.36, an example of a lateral profile density of Cherenkov photons per m^2 , obtained with the 3D simulation is shown for an event with energy 10^{18} eV.

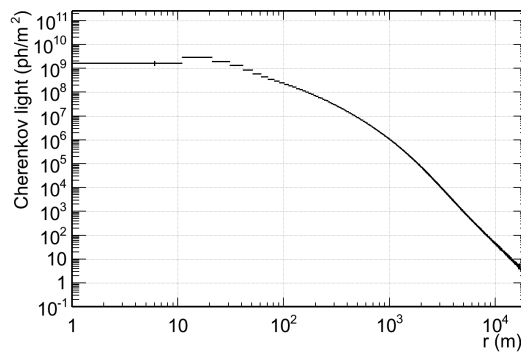


Figure 4.36: Cherenkov photons density (per m^2) as function of the radius $r(m)$ for an event with energy 10^{18} eV, considering all possible photon directions (all field of view).

In order to observe the lateral shape for several energies and to be less dependent on the X_{max} fluctuations, ten events per energy bin were simulated on CORSIKA. It was considered four samples with energies : 10^{16} , 10^{17} , 10^{18} and 10^{19} eV.

On the figure 4.37, the lateral profiles are shown for the four simulated energies. Each profile is an average of the ten simulated events. Since normally the experiments don't reach all possible field of view, the Cherenkov photons were divided accordingly with their angular direction θ with respect to the vertical direction. They are divided in 3 θ intervals for each energy and plotted on the corresponding profile.

The most vertical photons, with $0^\circ < \theta < 30^\circ$, in relation to the shower axis, are represented in red. The blue profiles corresponds to the photon with $30^\circ < \theta < 60^\circ$, which is approximately the FOV of the Auger HEAT telescopes. In green is the density of photons with $60^\circ < \theta < 90^\circ$, corresponding approximately to the FOV of the normal telescopes. The total number of photon arriving on the ground, for all photon inclinations, is in black, which is equal to the sum of the three profiles.

The profiles are similar depending mostly on the normalization and on the considered angular direction. If the detectors are not pointing upwards (align vertically), most of the Cherenkov light will not be detected, however, it can be higher compared with the fluorescence light.

The standard simulation (KG) can be changed in order to obtain the KG lateral Cherenkov light. It is possible to use the number of charged particles of the events (from the CORSIKA longitudinal profiles), with the Offline parametrizations to convert it into photons, and use the probability of Cherenkov photon emission accordingly with their angular direction to obtain the KG lateral Cherenkov profile for the ten events.

On the figure 4.38, the KG and 3D lateral profiles are shown together for all photon directions. The overall shape is similar, but the KG profiles seems to have at least one discontinuity on the second derivative, while the 3D profiles is more similar along the r axis, which mean the KG behaves like the sum of two components. In mid radius they look consistent with each other. At

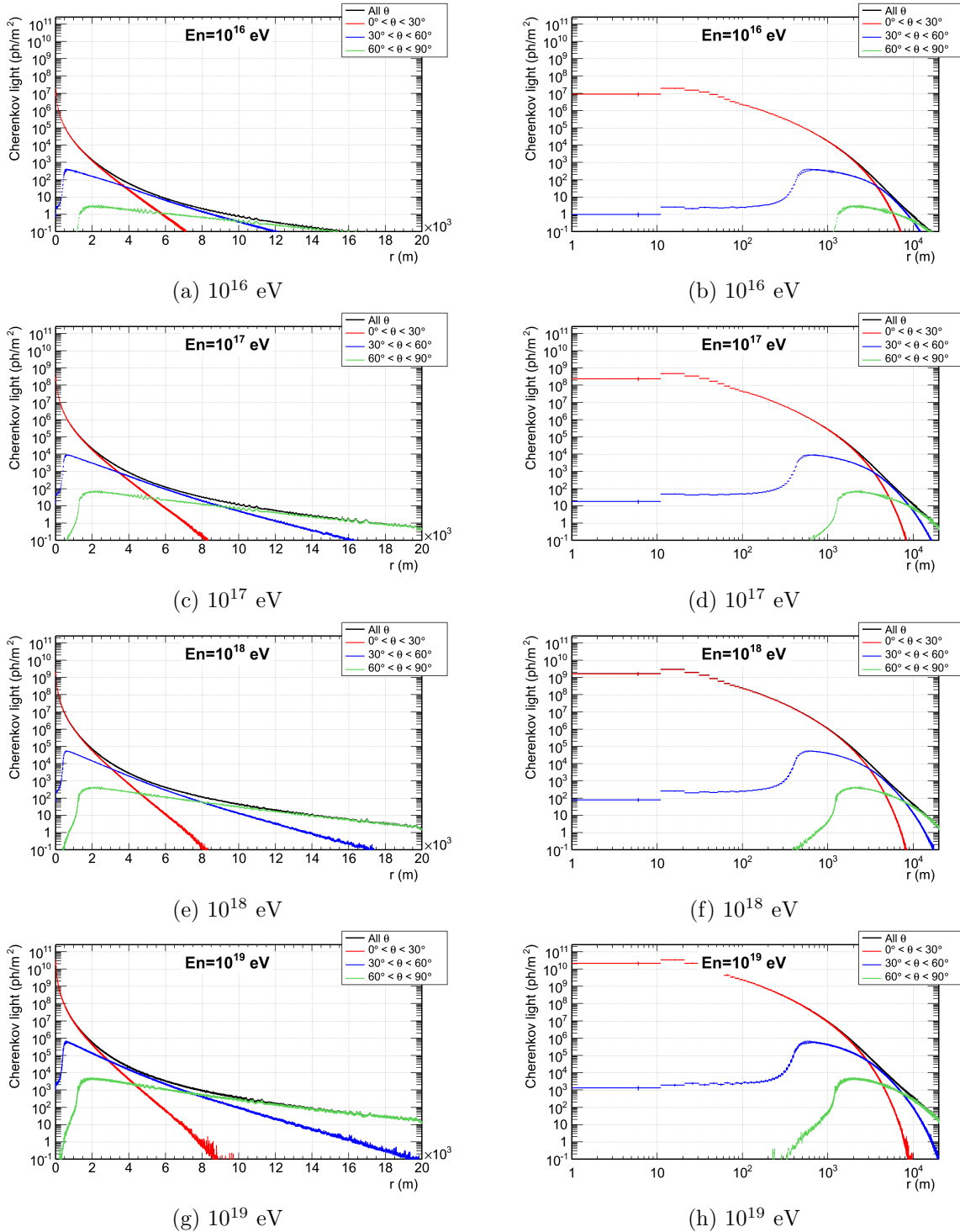


Figure 4.37: Cherenkov photons densities (per m^2) as function of the radius $r(m)$, for several energies. All photons in black, photons with directions $0^\circ < \theta < 30^\circ$, $30^\circ < \theta < 60^\circ$ and $60^\circ < \theta < 90^\circ$ are in red, blue and green respectively.

small radius (corresponding to vertical directions) the KG predicts more Cherenkov photons as well as at higher radius were the KG simulations fall far from the 3D simulation. Nonetheless, at large radius the number of Cherenkov photons is reduced and at lower angles (small radius)

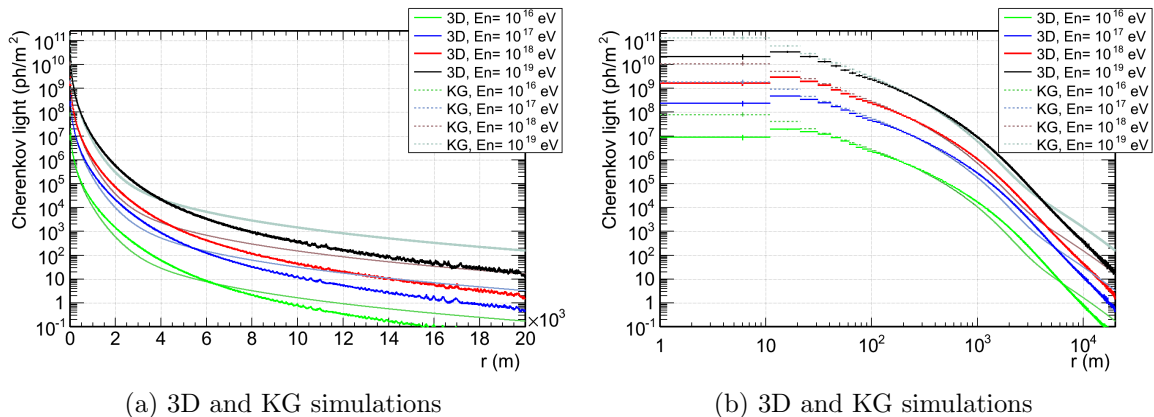


Figure 4.38: Cherenkov photons densities (per m^2) as function of the radius $r(m)$, for several energies, including all directions (FOV). The darker colors corresponds to the 3D simulation results and the lighter color to the KG simulations.

the Auger telescopes don't have angular range to detect them. This means that the overall light produced on the Offline by both simulations is similar, not deteriorating the simulation.

The 3D results for the Cherenkov light can be compared with others results in the literature. For example, the Tunka experiment, referred on the previous chapter, detects the Cherenkov light of the EAS. Tunka-25[210] consists of 25 detectors arranged on the square of $340 \times 340 m^2$ at 675 m ($\sim 950 g/cm^2$) above sea level with the distance between detectors of 85 m. Each detector has a field of view around 45° with respect to the vertical direction.

The Tunka parametrization was performed for showers within 10^{12} eV and 10^{16} eV, in a squared detection area with 45° FOV. Tunka's extrapolations are shown on the figure 4.39 in dashed lines together with the 3D results at same height with similar FOV. The Tunka extrapolation is completely different from the 3D and KG simulations, as can be seen, showing that this function cannot be considered at UHE cosmic rays. Nevertheless, in the end of the Tunka energy range, 10^{16} eV its results are compatible with the simulations.

The Tunka results don't use data of pure vertical shower, but rather vertical showers with some resolution, flattening the results close to the core. At 10^{16} eV, where the results should be similar, the big difference is at larger radius. For $r > 1000$ m, the parametrization is lower than the 3D simulation density. This happens, due to the Tunka small size, being less sensible at those radius. Also, Tunka detectors have squared FOV and in the simulations the cut were photons with less than 45° (which means, circular aperture), changing the photon suppression at large radius. Tunka gives a parametrization which works well in their energy range and limited distance to the core.

There were been also proposals to measure the Cherenkov light at Chacaltaya mountain, Bolivia, with similar squared detectors. This mountain is at $536 g/cm^2$, ~ 5200 m. On the figure 4.40, the points at Chacaltaya, from [211, 212] are drawn and compared with the 3D simulation at similar configuration. The normalization and shape are similar, becoming slightly

different when the radius increases, due to the squared shape in [211] and array size.

The 3D simulation is in a good agreement to the Chacaltaya and Tunka lateral Cherenkov densities, validating the simulation at this level. Further away, using the BinTheSky framework is possible to implement several types of arrays and simulated them. Inclusive the Tunka array allowing better comparisons with results and parametrizations.

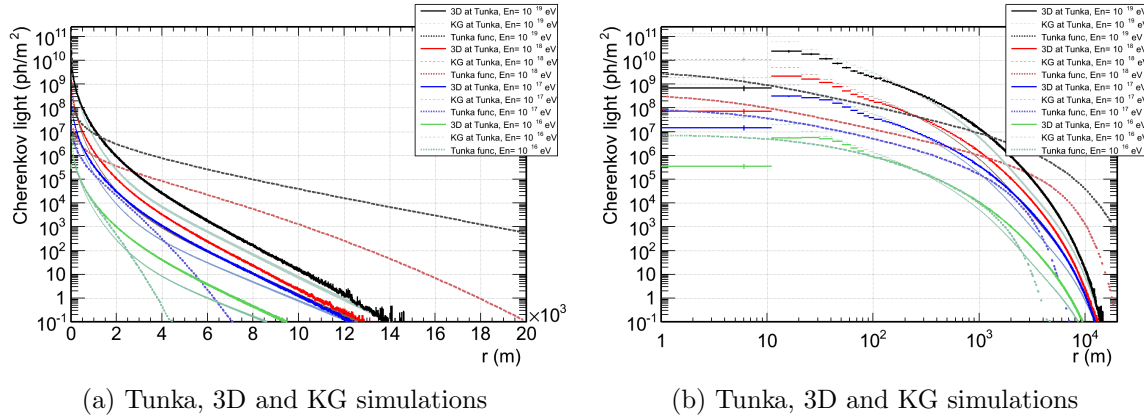


Figure 4.39: Cherenkov photons densities (per m^2) as function of the radius $r(m)$, for several energies, at Tunka height ($\sim 950g/cm^2$) for photons with $\theta < 45^\circ$ with respect to the vertical direction. The darker colors corresponds to the 3D simulation results and the lighter color to the KG simulations. In dashed line are the extrapolations from the Tunka lateral parametrization, from [210].

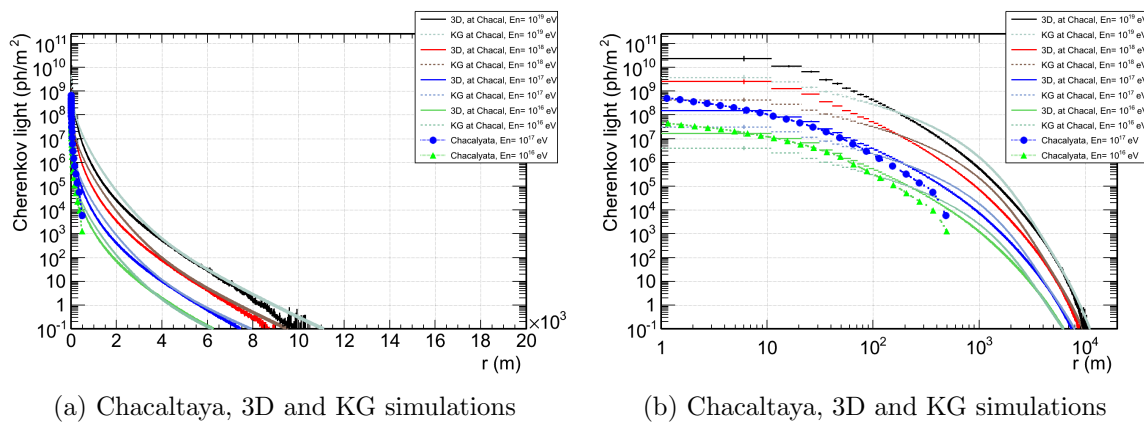


Figure 4.40: Cherenkov photons densities (per m^2) as function of the radius $r(m)$, for several energies, at Chacaltaya mountain with ~ 5200 m height, ($\sim 950g/cm^2$), for photons with $\theta < 45^\circ$ with respect to the vertical direction. The darker colors corresponds to the 3D simulation results and the lighter color to the KG simulations. In open circles are the results at Chacaltaya from [211, 212].

4.4 Summary and prospects

The BinTheSky framework described in this chapter, enables to perform a 3D simulation for Extensive Air Showers detected by the Fluorescence Detector of the Pierre Auger Observatory.

Summary

The 3D information of the shower, needed for the 3D simulation, were retrieved from the CORSIKA generator in a new framework called BinTheSky. Then, the information in the BinTheSky was inserted into Offline, to simulate and reconstruct the shower events, in a dedicated module, the ShowerSimulatorLX. This module replace the modules used for light simulation and propagation to the detector, in the shower simulations based on the longitudinal profile. In the new module, without lateral parametrizations, the light is produced, propagated and attenuated to the telescope diaphragms and the Auger detectors were afterwards simulated in the standard configurations.

In this chapter, in order to validate the developed framework, data events close to the telescopes with very small fraction of Cherenkov (fluorescence samples) and dominated by Cherenkov light (Cherenkov sample) were selected. Its characteristics were simulated with the standard and 3D simulations and after that, both simulations were reconstructed with the standard reconstructions. Finally, the fluorescence and direct Cherenkov emission simulations were compared with the data they represent with compatible results.

It was verified that the 3D BinTheSky simulation for fluorescence results on a geometric reconstruction of the shower axis with an accuracy comparable to that obtained with the standard longitudinal profile based simulation, after applying similar reconstruction procedures. Moreover, the two main variables extracted from the reconstruction of the longitudinal profiles, the energy of the shower and the depth of shower maximum (X_{max}), are reconstructed with similar accuracy by both the 3D and the KG simulation methods.

The selected data events used in the validation of the BinTheSky method are very close to the telescopes, and only a part of the shower is therefore visible. Furthermore, the depth of shower maximum in many events, lies inside, but close to the edge of the detector's field of view. This results in a less accurate X_{max} reconstruction both for the present data sample and for the corresponding simulated samples, when compared to the average standard performance of the reconstruction algorithms in Auger Data. Additionally, there were missing photons on the longitudinal profiles, since Cherenkov light production and reconstruction, were turned off in the simulated sets. Also, on the lateral profile, as function of ζ , above 3° the simulation had less photons, since the multiple scattering were not implemented.

With respect to the direct Cherenkov, in the Cherenkov sample, the energy and X_{max} recovered in the 3D simulation is worse (but within the statistical error), than the KG simulation,

since the reconstruction is tuned and uses the same parametrizations as in the KG simulation, as can be seen on the table 4.3. It should be noted that, usually, these events are not considered in the analysis, since the fluorescence light is around 10 – 15% of the total light and undistinguishable from the remaining 85 – 90%. The reconstruction must correctly estimate the matrix with the different light components; a slight difference in the geometric reconstruction would change the values of α_{sh} (figure 4.24), changing the parameters in the energy matrix, with subsequent wrong recovered energy deposited, dE/dX and also energy and X_{max} . Furthermore, the light profiles at the diaphragm, before the energy reconstruction converting fluorescence into dE/dX , are considerable more similar between the 3D and the data.

After the validation, it would be important to simulate a bigger sample and reconstruct it with the 3D reconstruction in order to see the fluctuation around the average lateral and longitudinal parametrizations.

Prospects

The BinTheSky framework was developed with the purpose of keeping the spatial information related to the development of EAS inside the shower particle generator and using this information directly in the production of fluorescence and Cherenkov light, without having to use a parametrization for the transverse distribution of the shower particles. This 3D simulation will be very important to implement together with a 3D reconstruction method. In the standard simulation, in each time slot, the signals are summed in nearby pixels for the profile reconstruction, despite the fact that the same time on different pixels corresponds to different emission times. The 3D reconstruction can use the relevant time bins in the pixels and consider a disk shower propagation. In this way, the fluctuations on the shower spacial structure could be analysed, lateral profile could be studied and compared with the lateral signals on the ground.

This framework was validated throughout this chapter, showing that it is possible to use on several applications. An important application of the BinTheSky framework in Auger would be to simulate the laser in the calibration tasks. A laser with the corresponding scattered light could be simulated outside the Offline with GEANT4, using different atmospheric properties and the corresponding information saved in the BinTheSky framework. This information can be used to calculate the first light scattering and propagate the photons into the telescopes inside the Auger Offline framework, in the ShowerSimulatorLX. Or, while the multiple scattering is not implemented, the laser could be simulated on the atmosphere including all scatterings and use the framework as connection with the Offline.

The BinTheSky framework can also be used to simulate the Cherenkov light in other detectors configurations, such Tunka and others, as was seen. It is a quick framework to introduce multiple detectors arrays.

Prospects for the Cherenkov scattering

To produce the scattered Cherenkov light is much more difficult without using parametrizations. It happens because the scattered light that goes into one pixels depends on the direct Cherekov light crossing the pixels FOV from everywhere in the shower.

The simple way to do it without parametrizations, is to begin by calculating the amount of Cherenkov on a particular position p , on the i th pixel field of view, at a specific time t_p . The total light at the position p and time t_p is the sum of the Cherenkov produced in the SkyBin j that obey the relation $(t_{emission\ j} + d_{j,p}/c) = t_p$, where $t_{emission\ j}$ is the emission time in the SkyBin j and $d_{j,p}$ is the distance between the position p and the SkyBin. The total Cherenkov light, after the given attenuations between the position and the SkyBin, will be given by:

$$n_{ph,Ckov}^{pixel\ i}(d_{eye,p}, t_p) = \sum_{SkyBin\ j} T_{j,p} \cdot n_{ph,Ckov}^{SkyBin\ j,\alpha,\phi'} \quad , (t_{emission\ j} + d_{j,p}/c) = t_p . \quad (4.14)$$

Using the total Cherenkov light in the point p it is possible to calculate the scattered light $f_s(\beta_i) \cdot n_{ph,Ckov}^{pixel\ i}(d_{eye,p}, t_p)$ with the scatter probability f_s , which depends on the photons directions, β_i , between the shower axis and the eye. At this stage the scattered light at a pixel i , in a given time t_i is just the sum of the scattered light in all possible positions inside the pixel FOV obeying $d_{eye,p} = (t_i - t_p)/c$. The total scattered light at the pixel i is given by:

$$\begin{aligned} n_{ph,Cs}^{dia\ i}(t_i) &= \sum_p \frac{A_{dia}}{4\pi d_{eye,p}^2} \cdot T_{i,p} \cdot f_s(\beta_i) \cdot n_{ph,Ckov}^{pixel\ i}(d_{eye,p}, t_i - d_{eye,p}/c) \quad , d_{eye,p} = (t_i - t_p)/c \\ &= \sum_p \frac{A_{dia}}{4\pi [(t_i - t_p)/c]^2} \cdot T_{i,p} \cdot f_s(\beta_i) \cdot n_{ph,Ckov}^{pixel\ i}[(t_i - t_p)/c, t_p] \quad , t_p = t_i - d_{eye,p}/c . \end{aligned} \quad (4.15)$$

These sums are possible to perform, however they would be unnecessarily, extremely time consuming. A better option should be reassessed in order to use only the 3D information.

Energy Calibration using WCT signals

The Auger surface detectors measure the electromagnetic particles (e^\pm/γ) and the muons (μ), on the Earth surface. In the present SD configuration, the Electromagnetic signal component (EM) and Muonic signal component (MU) are measured at the same time. The ground signals at a reference core distance are then used as an energy estimator, which is calibrated against the FD calorimetric measurement. However, the FD measures the electromagnetic component, so the energy calibration, currently performed using the Total signal component (TOT) of the tank, should be done with the electromagnetic component. The energy obtained, with the total signal, can thus be highly correlated with the number of muons.

The muonic component is not directly achievable, it is only possible to recover it indirectly, using algorithms to distinguish between the electromagnetic and muonic signals or in very inclined events. It is known that the muonic signal does not agree with the models predictions, for example, there is a deficit of the muons predicted by the models [197, 199] (see section 3.7). Nonetheless, the electromagnetic component is more compatible with the models assuming some specific composition. In this way, a new detector with the purpose to measure the muons directly is important to overcome the inconsistencies and measure the muon content evolution with energy, in a way uncorrelated with the energy calibration procedure.

A new muon detector, which allow to disentangle between both electromagnetic and muonic component is very important. Such a detector could be the MARTA project[213, 214]. It would provide an accurate measurements of the muonic shower component, independently from the signals in the tanks. Combining the information from MARTA with the WCT data, would enable to disentangle the electromagnetic and muonic content of the showers, providing an almost independent measurement of both shower components. So, the energy resolution of the SD is expected to improve and the evolution of the muon content with energy obtained with smaller systematic errors.

In this chapter, the energy calibration is accomplished using the electromagnetic component, following the usual calibration procedure, replacing the SD signal by the EM signal and the FD

energy by the simulated one. The energy calibration is done using the Constant Intensity Cut (CIC) method [153, 215]. The likelihood used to fit the Lateral Distribution Function (LDF) will be described. From the fit, the β parameter will be parametrized to minimize the S_{1000} fluctuations. Then, the S_{1000} attenuation curves are obtained using the CIC method and the S_{38} calculated. Finally, this electromagnetic S_{38} will be used as the energy estimator and calibrated with the MC energy. The same procedure was repeated for the total signal (usual calibration) and for the muonic signal, and compared.

A sample of proton and iron simulated events[216] was used in this analysis, with QGSJET-II model, with energy ranging from $10^{16.5}$ eV to $10^{19.5}$ eV , with a uniform distribution in $\cos^2\theta$ (zenith angle), ranging from 0° to 60° . We used 191954 proton simulations and 142773 iron simulations.

5.1 Shower Size Determination

In this section, the shower size (S_{1000}) will be estimated, to be used later in the energy calibration. To summarize the approach I will take, the first step is to fit event by event, all events, and get an estimation for the shower size S_{1000} and the parameter β (accordingly with the description given in section 5.1.1). We should then parametrize the β parameter as function of S_{1000} and zenith angle (section 5.1.2). At last, perform the fits event by event again, using the β parametrizations, and get the new S_{1000} to be used in the CIC method (section 5.2).

5.1.1 Fitting approach

To estimate the shower size, as we saw in section 3.1.3.1, we need to estimate the ground signal at 1000 m (S_{1000}), which is close to the zone more stable for the fitting procedures with current PAO geometry.

The ground signal are mostly azimuthally symmetric, only changing in moderately inclined events, due to different atmospheric depth between close and far tanks to the core, so we model the profile with a radial dependence.

The lateral shape also depends on the energy and on the angle, in this way, we describe the ground signal with a function depending on the radius r , energy E and zenith angle θ ,

$$S = S_{1000} \cdot f_{LDF}(r, E, \theta), \quad (5.1)$$

where S_{1000} is the signal at $r = 1000$ m from the shower core with the requirement that $f_{LDF}(1000, E, \theta) = 1$.

Our current f_{LDF} parametrization is a modified NKG equation (see equation 2.50) given by:

$$f_{LDF}(r, E, \theta) = \left(\frac{r}{r_{opt}} \right)^\beta \cdot \left(\frac{r + r_{scale}}{r_{opt} + r_{scale}} \right)^{(\beta+\gamma)}, \quad (5.2)$$

where $r_{opt} = 1000$ m is the optimum distance for $S(r_{opt}) = S_{1000}$, the best energy estimator, $r_{scale} = 700$ m is the modification of the Moliere radius (see section 3.1.3 and [71]). The slope parameters are $\beta = \beta(E, \theta)$ and $\gamma = \gamma(E, \theta)$ are functions of the shower age.

In figure 5.1, we can see two MC events for 10 deg and for 40 deg with the EM and MU components discriminated. These lateral profiles are relatively steep and the different slopes are caused by attenuation during propagation through the atmosphere and other effects. Accordingly, β and γ change with energy and shower zenith angle, for both EM and MU components. The lateral profiles of the shower get flatter while propagating through the atmosphere (or with shower age).

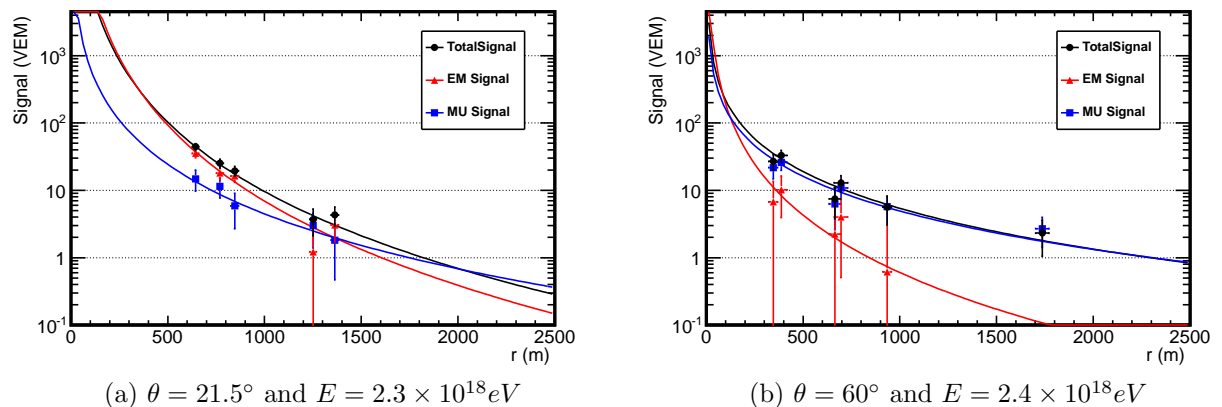


Figure 5.1: Total, EM and MU signals for two SD events from the simulated sample [216]. The total, EM and MU signals are shown in black, blue and red, respectively. The event on the left has $\theta = 21.5^\circ$ and $E = 2.3 \times 10^{18}$ eV, while the event on the right has $\theta = 60^\circ$, $E = 2.4 \times 10^{18}$ eV. The curves correspond to the fits of eq. 5.21 to the signal. The obtained fit parameters for each event are displayed in table 5.1. Error from equation 5.3

Table 5.1: Results to the fit of eq. 5.21 for two events in the simulated set displayed in figure 5.1.

Event	$\theta=21.5^\circ$ $E=2.3 \times 10^{18} eV$			$\theta=60^\circ$ $E=2.34 \times 10^{18} eV$		
	Total	EM	MU	Total	EM	MU
S_{1000}	9.6	6.9	4.4	5.4	0.6	4.9
β	-2.2	-2.5	-1.6	-1.2	-1.9	-1.1

The signal in the tanks is measured in units of VEM (see section 3.1.1), which means Vertical Equivalent Muons. Since we use this unit, and the WCT measure the electromagnetic and muonic particles at different angles, we will obtain different Poissonian accuracies. The uncertainty on the signal is taken as (see [140] and [217]):

$$\sigma_S(\theta) = f_S(\theta)\sqrt{S} \quad (5.3)$$

$$f_S(\theta) = (0.32 + 0.42/\cos\theta) \quad (5.4)$$

$f_S(\theta)$ is plotted in the figure 5.2. This equation was obtained analysing the signals in two twin stations, each pair placed together at two consecutive position (1500 m apart). Each pair should measure approximately the same lateral position of a shower (they are a few meter apart, compared with the normal width of a shower). Then the fluctuations between each other should corresponds to the Poissonian fluctuations on the tanks, due to different probabilities of being hit by a particle.

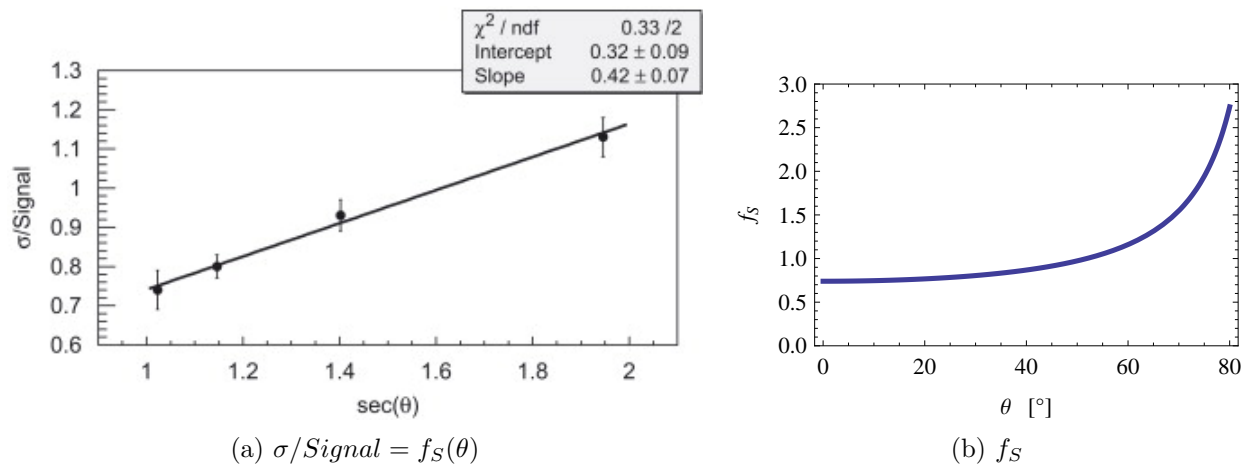


Figure 5.2: On the left, fit to the $\sigma/\text{Signal} = f_S(\theta)$ from [217], giving the result $f_S(\theta) = [(0.32 \pm 0.09) + (0.42 \pm 0.07) \times \sec \theta] \sqrt{S}$; on the right, f_S as function of θ .

The WCT detects both electromagnetic and muonic particles. Particles with a vertical incidence in the tanks cross approximately 120 cm water thick, which corresponds to approximately 3 radiation length for electrons and gammas. So, the electromagnetic particles and the respective cascades will be highly absorbed in the water for all incident directions and the Poissonian accuracy should be mainly independent on the angle.

For the muons, the signal detected in the tank is proportional to the track length. The same signal at high incident angles corresponds to less equivalent particles than at low angles (since we measure in units of VEM). Or in the other way around, the same number of particles would produce a higher signal at higher angles. So for large angles the fluctuations should be higher than \sqrt{S} , as we can see in figure 5.2. For vertical showers we obtain an accuracy better than \sqrt{S} . This happens because we use units of VEM. At lower zenith angles, we have a strong electromagnetic component, since they are less energetic, many particles are needed to deposit 1 VEM and the fluctuations are lower. For higher zenith angles, the EM component is attenuated and we are dominated by the muonic behaviour.

To reconstruct the data we implement a maximum likelihood method as fitting procedure. We also need to point out, that in Offline standard reconstruction, this fit is coupled with the geometric fit, since the distance r depends on the determination of the shower core. Nonetheless, we will consider the geometry determined in the Offline and only fit the LDF (which means,

using the Offline reconstructed shower core). These option simplifies very much the fitting procedure and the geometry error is normally very small. Note that the geometry parameters come from the same kind of fits to the total component on Offline.

In order to use the silent stations, or active stations with 0 signal, we need to use a maximum Likelihood method; the χ^2 method would not be appropriate, giving biased results, also simply because in mathematical sense it would be wrong (It would not be possible to use the zero stations with zero error). However, to use a *ML* method, it's necessary to have a conversion factor from the signals (that should reflect the electron-gamma to muon ratio), which will be described in the following.

In order to perform the Maximum Likelihood method, we need to know the statistics corresponding to the signal of the WCT. Which means, we need to know the number of particles in the detector. The WCT detects the Cherenkov photons of the particles passing the tanks, and the number of these photons depends strongly on the particle type, injection point and incident angle. There is no simple conversion between the registered photons and the real number of passing particles.

The ground signal of the shower comes from muons, electrons and photons which give different responses in the WCT. We begin by considering the total number of particles crossing a tank

$$\begin{aligned} n &= n_\mu + n_e + n_\gamma \\ &= n_\mu + n_{e,\gamma} , \end{aligned} \tag{5.5}$$

each value depends on the energy, cosmic ray composition and zenith angle. We can also write the particle numbers according to the muon fraction k_μ as

$$\begin{aligned} n_\mu &= k_\mu n \\ n_{e,\gamma} &= (1 - k_\mu)n . \end{aligned} \tag{5.6}$$

Each signal component in the WCT should be given by the number of particles of one kind (n_j) times the response signal on the detector (a_j) for that kind of particle:

$$S_\alpha = a_\alpha n_\alpha, \quad \alpha = \mu, e, \gamma , \tag{5.7}$$

for this purpose we can consider $S_{e,\gamma} = S_e + S_\gamma = a_{e,\gamma} n_{e,\gamma}$. The muon converting factor a_μ is approximately 1, assuming a mean signal of 1 VEM per muon. But the electromagnetic factor is much smaller than a_μ and the average factor for Auger tanks holds $0 < a < 1$. The total signal is:

$$\begin{aligned} S &= \sum_j a_j . n_j = n_\mu + a_{e,\gamma} n_{e,\gamma} \\ &= [k_\mu + a_{e,\gamma}(1 - k_\mu)]n , \end{aligned} \tag{5.8}$$

with the equation 5.8, we can relate the total signal with the total number of particles. Therefore we introduce the Poisson factor p :

$$n = p . S \tag{5.9}$$

n is the effective number of particles. The factor p was parametrized in [140] and is given by (see also fig. 5.3):

$$p = p(\theta) = \begin{cases} f_S(\theta)^{-2} & ; \text{if } f_S(\theta) \geq 1 \\ 1 & ; \text{if } f_S(\theta) < 1 \end{cases} \quad (5.10)$$

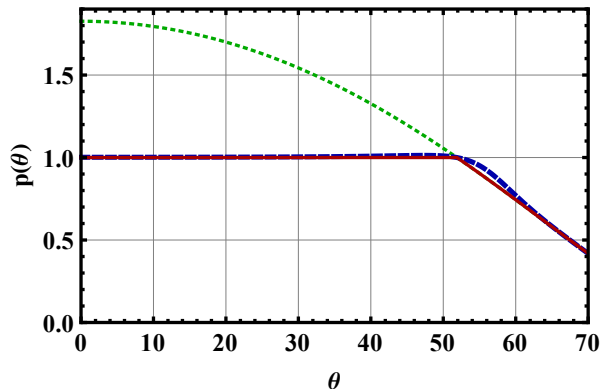


Figure 5.3: In dotted green line the function $f_S(\theta)^{-2}$ is plotted. The $p_S(\theta)$ as function of θ are drawn in dashed blue and full red for the old parametrization (eq. 5.10) and the new one (eq. 5.11) respectively. $p_S(\theta)$ comes from [140]. We can see that both p_S function have the same behaviour and there is no problem to use the new one.

The $p(\theta)$ is obtained from the f_S in eq. 5.4. So we should have $p(\theta) = f_S(\theta)^{-2}$. However, this f_S is an effective factor for EM and MU components at the same time. For higher angles, we should use $f_S(\theta)^{-2}$, since f_S is higher than 1, that means we are dominated by muons and we should use this factor to have a good estimation on the effective number of particles. Nevertheless, for lower angles, we have a lot of EM particles close to the core, where the value $f_S < 1$ holds, but for bigger radius, we begin to be dominated by muons where $f_S < 1$ doesn't hold. But if we look at the next subsection, to the definition of the Maximum Likelihood, we can see that close to the core, where we have a huge number of particles, the $\sigma_S(\theta)$ is more important. While far from the core, we have Poissonian statistics, with small number of particles (dominated by muons), where the $\sigma_S(\theta)$ doesn't matter and the p_S is very important. In this way, if $f_S(\theta)$ is lower than 1, we should use $p_S(\theta) = 1$, to not give a wrong weight to muons far from the core. The equation 5.10 was substituted by eq. 5.11, by technical purposes, because the original function has a kink, which was leading to an undefined first derivative of the likelihood function. Since we don't distinguish directly each kind of particles, we should use an effective number of particles for the statistics. But it needs to be noted that those particles are not to be considered a realistic number of particle in a particular station, due to very different signals from each kind, and because the fractions of each component changes with cosmic rays zenith angles and the radius of the station to the core.

$$p = p(\theta) = \frac{1}{1 + e^z} + \frac{1 - \frac{1}{1 + e^z}}{f_S^2(\theta)}, \quad z = 20(f_S(\theta) - 1.05), \quad (5.11)$$

$p(\theta)$ is plotted in figure 5.3. We can see that the new eq. 5.11 describe the same behaviour of the old equation.

5.1.1.1 Maximum likelihood

The Likelihood function chosen is divided in four terms, for low signals stations, high signal stations, saturated stations and zero signal stations respectively

$$L = \prod_i f_P(n_i, \mu_i) \prod_i f_G(n_i, \mu_i) \prod_i F_{sat}(n_i, \mu_i) \prod_i F_{zero}(n_i, \mu_i). \quad (5.12)$$

And the log likelihood function gives

$$\ell = \sum_i \ln f_P(n_i, \mu_i) + \sum_i \ln f_G(n_i, \mu_i) + \sum_i \ln F_{sat}(n_i, \mu_i) + \sum_i \ln F_{zero}(n_i, \mu_i), \quad (5.13)$$

n_i is the effective number of particles and μ_i is the expected particle number at station i . According to the equation 5.9, they are given by:

$$\begin{aligned} n_i &= p(\theta) S_i \\ \mu_i &= p(\theta) S_{exp,i} = p(\theta) \cdot S_{1000} \cdot f_{LDF}(r_i) \\ \sigma_i &= f_S(\theta) \sqrt{S_{exp,i}}. \end{aligned} \quad (5.14)$$

The construction of each term will be discussed in the following.

In our surface detector, we have a trigger that rejects low signals events (silent stations, see chapter 3.1.2) and we have a region where the linearity of the photomultiplier behaviour is lost (saturated stations). Nevertheless, we can still use them, the first as a probability of having a lower signal than a $S_{upperlimit}$, and the second as probability of having a signal higher than $S_{lowerlimit}$ [217] [218] [140] (an updated version with the Offline software distribution).

5.1.1.2 Low Signal stations

The stations with an effective particle numbers $n < 30$ are considered with low signal and modelled with a Poissonian p.d.f.:

$$\begin{aligned} f_P(n_i, \mu_i) &= \frac{\mu_i^{n_i} e^{-\mu_i}}{n_i!}, \\ \ln f_P(n_i, \mu_i) &= n_i \ln \mu_i - \mu_i - \sum_{j=1}^{n_i} \ln j. \end{aligned} \quad (5.15)$$

5.1.1.3 High Signal Stations

For large signals we consider a Gaussian distribution, so for $n > 30$ we have:

$$\begin{aligned} f_G(n_i, \mu_i) &= \frac{1}{\sqrt{2\pi}\sigma_i} \exp\left(-\frac{(n_i - \mu_i)^2}{2\sigma_i^2}\right), \\ \ln f_G(n_i, \mu_i) &= -\frac{(n_i - \mu_i)^2}{2\sigma_i^2} - \ln \sigma_i - \frac{1}{2} \ln 2\pi. \end{aligned} \quad (5.16)$$

5.1.1.4 Saturated Signal Stations

If the tank is saturated, the value n_i is used as a lower limit of the actual signal. Hence, the probability of detecting a WCT above the limit will be the integration of f_G for all values larger than n_i ,

$$F_{Sat}(n_i, \mu_i) = \int_{n_i}^{\infty} f_G(n_i, \mu_i) dn = \frac{1}{2} \operatorname{erfc} \left(\frac{n_i - \mu_i}{\sqrt{2}\sigma_i} \right), \quad (5.17)$$

where $\operatorname{erfc}(x) = 1 - \operatorname{erf}(x)$ ¹ is the complementary error function.

5.1.1.5 Zero Signal Stations

The WCT will not trigger with signal below some threshold. In this way, if the signal $n_i < n_{th}$, then the tank will be silent with no data recorded. The probability of this happening is the sum over all the Poissonian probabilities with expected values of μ_i and actual particles $n_i < n_{th}$,

$$F_{zero}(n_{th}, \mu_i) = \sum_{n=0}^{n_{th}} f_P(n, \mu_i), \quad (5.18)$$

$$\ln F_{zero}(n_{th}, \mu_i) = -\mu_i + \ln \left(\sum_{n=0}^{n_{th}} \frac{\mu_i^n}{n!} \right).$$

There could be complications due to different local trigger algorithms. We can approximate the threshold trigger to be $S_{th} \approx 3VEM$ or $n_{th} = 3$. The probability can now be approximated by:

$$\ln F_{zero}(3, \mu_i) = -\mu_i + \ln \left(1 + \mu_i \left(1 + \frac{\mu_i}{2} \left(1 + \frac{\mu_i}{3} \right) \right) \right), \quad (5.19)$$

if $\mu_i < 0.03$ we can further approximate by

$$\ln F_{zero}(3, \mu_i) = -\frac{\mu_i^4}{24}. \quad (5.20)$$

We should note that compared with normal stations, these zero signal stations will have a very small contribution for the overall likelihood (if the fit behaves well enough, these zero stations really corresponds to low values in the LDF below some threshold). The threshold was chosen to be $n_{th} = 3$ which corresponds approximately to $S_i \approx 3$ VEM, however the TOT (time over threshold) normally has a threshold $S_i \approx 1.7$ VEM. We chose the values 3 to be in agreement with the Offline and because the 1.7 VEM is unlikely to trigger at larger radii [140].

After the construction of the likelihood for the tanks we are in a position to perform the fits of the Lateral Profile distribution.

5.1.2 LDF Parameterization

Before performing the fits, if we look at equations 5.2 and 5.1, our fits will depend on S_{1000} , β and γ . To simplify, we consider $\gamma = 0$ and we get only 2 degrees of freedom. γ doesn't change

¹ $\operatorname{erf}(x)$ is called the Gauss error function and $\operatorname{erf}(x) = \frac{2}{\sqrt{\pi}} \int_0^x e^{-t^2} dt$

too much the LDF shape, however in the future, we could also fit this parameter. We can now rewrite our fitting function as

$$S_{LDF}(r, \beta, S_{1000}) = S_{1000} \left(\frac{r}{1000} \right)^\beta \left(\frac{700 + r}{1000 + 700} \right)^\beta. \quad (5.21)$$

For a better LDF stability, afterwards, we will parametrize the beta parameter, as it was done in the standard SD event reconstruction described in [219], since at that step, the important value to obtain is the S_{1000} , which in the following will be used to get the energy estimator. Different values for β were found to describe the total signal, the muonic and electromagnetic LDFs.

To this analysis we used the two samples (proton and iron) of simulated events, described in the beginning of this chapter and [216]. The events used to parametrize the slope β should fulfil some requirements. The events should have a level trigger of T5. To have a good estimation of the slope we need to require that we have enough stations around S_{1000} ($r = 1000$), to ensure a station distribution giving enough lever arm for the fit and, a minimum of 5 stations. This criterion was formulated in [220] and corresponds to:

- at least two stations with $500 \text{ m} < r_n < 1500 \text{ m}$ and $|r_i - r_j| > 500 \text{ m}$, or;
 - at least three stations with $500 \text{ m} < r_n < 1500 \text{ m}$ and at least one pair of those with $|r_i - r_j| > 400 \text{ m}$, or;
 - at least four stations with $500 \text{ m} < r_n < 1500 \text{ m}$ and at least one pair of those with $|r_i - r_j| > 300 \text{ m}$.
- (5.22)

We also require a minimum energy threshold, since cutting in number of stations would give rise to different energies for different zenith angles. Other cuts are $\chi^2/ndf < 2.5$, $0.5 < \beta < 9$ and $Error_{\beta,i} < 4$, to avoid some outliers due to fit problems. And if the closest station to the core is saturated and unrecoverable, we would only get a lower limit on the station signal and therefore it could bias the fitting of the slope. So we also cut SD with unrecovered saturated signals. In table 5.2, the cuts are displayed for both proton and iron sample.

Table 5.2: Event cut efficiencies to fit the slope β . Each cut is explained on the text. The number of events passing each cut is displayed and also the efficiency of that cut.

Cut	Value	Proton sample		Iron sample	
All events		191954	100%	142773	100%
Quality Trigger	T5	94584	49.3%	74489	52.2%
$N_{stations} \leq 5$	eq. 5.22	46394	49.1%	42367	56.9%
Lever arm cut					
Threshold	$lgE > 18.3$	17622	38.0%	12918	30.5%
Other cuts		11371	64.5%	8617	66.7%

5.1.2.1 Beta Parametrization

In figures 5.4 and 5.5, we can see the average β for the remaining events after the cuts. Each point is an average in bins of $\log_{10}(S_{1000})$ and $\sec \theta$.

The slope parameter is then parametrized with the remaining events. The β is simply described by a linear dependency on $\log_{10}(S_{1000})$ and a polynomial of second order in $\sec \theta$, given by eq. (5.23), where a_0, a_1, b_0, b_1, c_0 and c_1 are the fit parameters.

$$\beta = [a_0 + a_1 \log_{10}(S_{1000})] + [b_0 + b_1 \log_{10}(S_{1000})] \sec \theta + [c_0 + c_1 \log_{10}(S_{1000})] \sec^2 \theta . \quad (5.23)$$

The fits, however, are performed without binning, event-by-event, minimising the χ^2 defined by the next equation (there isn't any necessity for binning the β values).

$$\chi^2 = \sum_i^N \frac{\beta_i - \beta(\theta_i, S_{1000,i})}{\sigma_i^2} \quad (5.24)$$

$$\sigma_i^2 = \sigma_\beta^2 + \left(\frac{d\beta(\theta_i, S_{1000,i})}{d\theta_i} \cdot \sigma_{\theta_i} \right)^2 + \left(\frac{d\beta(\theta_i, S_{1000,i})}{dS_{1000,i}} \cdot \sigma_{S_{1000,i}} \right)^2 \quad (5.25)$$

Figure 5.4 and 5.5 shows the fits to β for the three component, note that the 10 $\sec \theta$ intervals as a function of $\log_{10}(S_{1000})$ are only for demonstration purpose. The fits were performed using all events separately.

Separate fits were performed with eq. 5.23 for each signals component in the simulated samples to obtain β_{TOT} , β_{EM} and β_{MU} , whose dependences on $\log_{10}(S_{1000})$ and $\sec \theta$ are expected to differ. The β event-by-event were fitted to the equation 5.23 with χ^2 from eq. 5.25 and the results are written on table 5.3 (printed as well on figures 5.4 and 5.5).

We get a χ^2/ndf between 0.67 and 0.97 for the 6 fits (3 for each primary). We can see the evolution of β_{TOT} , β_{EM} and β_{MU} with S_{1000} , where each graphic is a bin in $\sec \theta$. We can see that the electromagnetic part has an higher beta than the muonic one, due to higher attenuation of EM particles on the atmosphere. The TOT part is in middle of both.

On the figure 5.6, the values $(\beta_i - \beta_{Model})/\beta_i$ distribution is plotted. According with the distribution, from the previous parametrization, we can obtain β values with a mean deviation of 0.012 and a *RMS* of 0.11 for the total component in proton sample, as for iron sample is a mean deviations 0.014 and *RMS* 0.10. In the EM component we get a mean deviation 0.00095 and *RMS* of 0.10, and 0.0030 with *RMS* of 0.11 for proton and iron sample respectively. The MU component we get a mean deviation 0.012 with *RMS* of 0.16 and 0.017 with *RMS* about 0.15 for proton and iron respectively. We got deviations less than 1.7% and *RMS* of the order of 11% (16% for muons). This shows that we can recover the β with a good resolution for both samples.

On the figure 5.7, it is displayed the β_{TOT} for the first and last bin of $\sec \theta$ for the proton and iron simulations. The total signal is the sum of the electromagnetic and muonic signals, so the β_{TOT} should lie between β_{EM} and β_{MU} . Since the iron showers have more muons than the proton showers, this means that β_{TOT} for iron should be closer to the value of the muons β . In

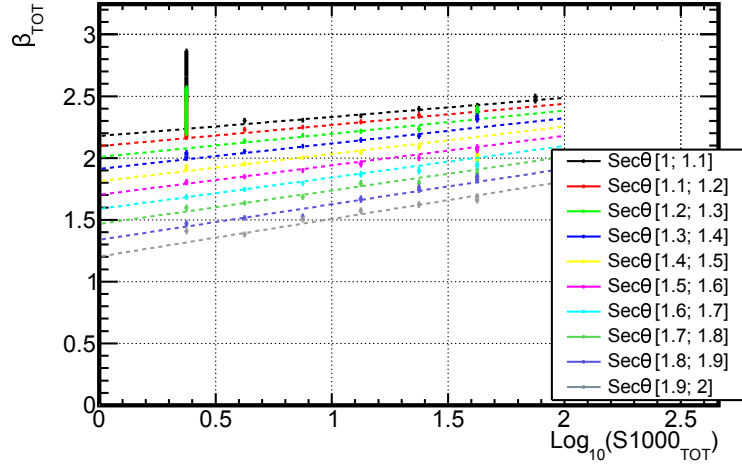
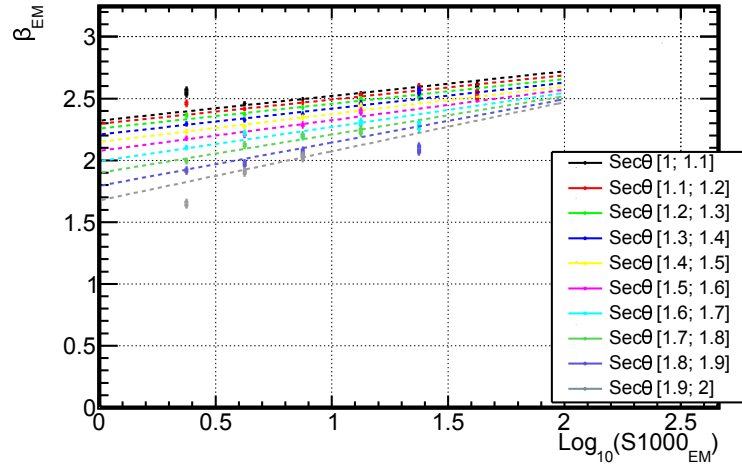
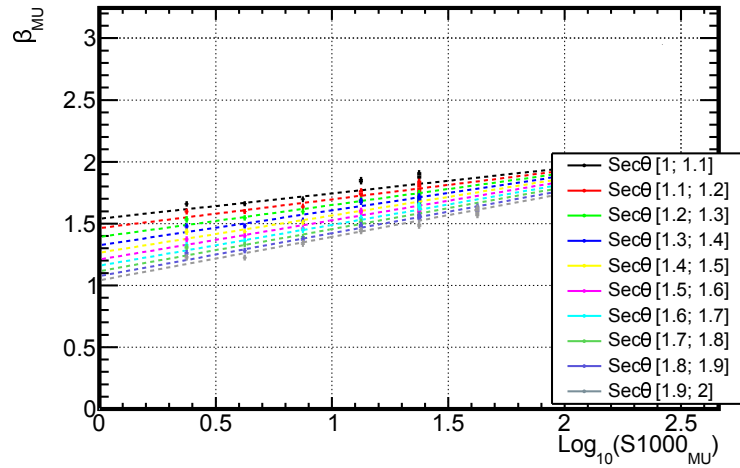
(a) β_{TOT} (b) β_{EM} (c) β_{MU}

Figure 5.4: The 3 plots are the Total signal β_{TOT} , EM signal β_{EM} and MU signal β_{MU} respectively. The events remaining after cuts from table 5.2 are binned in $\text{log}_{10}(S_{1000})$ intervals for several $\text{sec}\theta$ ranges, for demonstrations purposes. The lines are the fit to equation 5.23, with all events (not binned) and the fit results are written in the table 5.3. These results corresponds to the proton Sample.

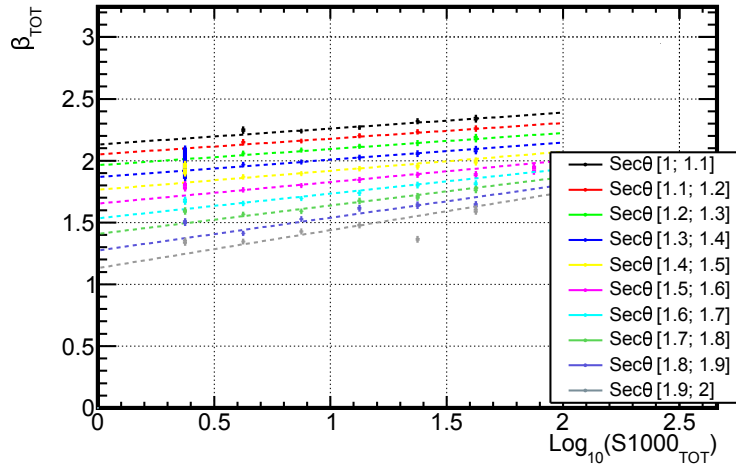
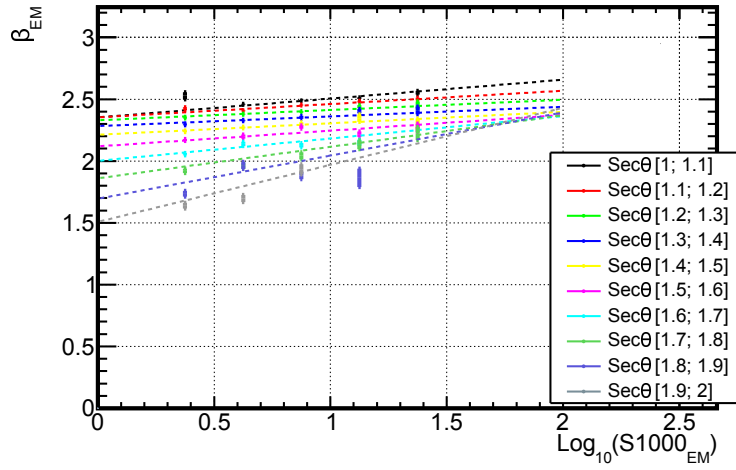
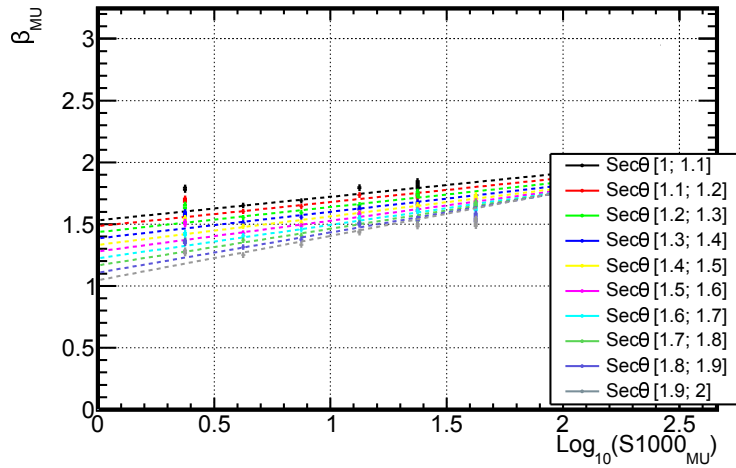
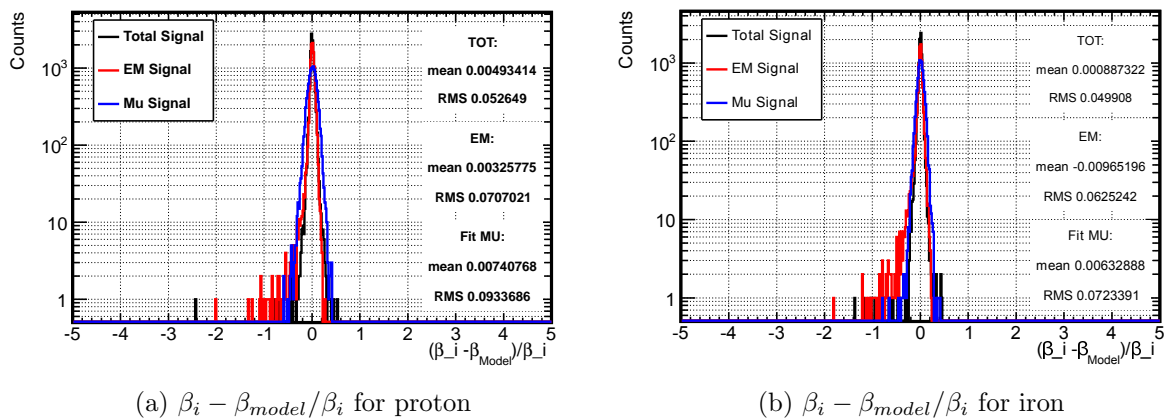

 (a) β_{TOT}

 (b) β_{EM}

 (c) β_{MU}

Figure 5.5: LDF β for the total signal, EM signal and MU signal, after cuts from table 5.2, displayed in $\log_{10}(S_{1000})$ bins and for several $\sec\theta$ ranges, for demonstration purposes. The lines are the fit to equation 5.23, with all events (not binned) and the fit results are written in the table 5.3. These results corresponds to the iron Sample.

Table 5.3: Parameters describing the dependence of β on $\log_{10}(S_{1000})$ and $\sec\theta$, resulting from the fit of eq. 5.23 to the selected sample of simulated events (proton and iron) from table 5.2. .

Proton Sample						
Parameter	TOT signal		EM signal		MU signal	
	value	uncertainty	value	uncertainty	value	uncertainty
a_0	-2.637	0.085	-1.905	0.008	-2.666	0.109
a_1	+0.027	0.092	-0.602	0.011	+0.282	0.154
b_0	+0.089	0.118	-0.995	0.009	+1.352	0.149
b_1	-0.176	0.130	+0.708	0.012	-0.625	0.209
c_0	+0.331	0.039	+0.570	0.004	-0.266	0.050
c_1	+0.003	0.044	-0.309	0.007	+0.154	0.069
χ^2/ndf	0.921		0.679		0.947	

Iron Sample						
Parameter	TOT signal		EM signal		MU signal	
	value	uncertainty	value	uncertainty	value	uncertainty
a_0	-2.507	0.007	-0.928	0.010	-1.919	0.009
a_1	-0.467	0.007	-1.812	0.013	-0.358	0.011
b_0	-0.048	0.006	-2.593	0.010	+0.279	0.008
b_1	+0.602	0.006	+2.617	0.015	+0.346	0.009
c_0	+0.386	0.003	+1.177	0.005	+0.087	0.004
c_1	-0.266	0.003	-0.987	0.008	-0.178	0.004
χ^2/ndf	0.973		0.671		0.918	

Figure 5.6: $\beta_i - \beta_{model}/\beta_i$ distribution for proton (left) and iron (right). Black line for total component, red for EM and blue for MU components.

the figure, on both $\sec\theta$ bins, the β_{TOT} for protons are shifted with relation to the irons, being the proton β_{TOT} higher (closer to β_{EM}) as explained before. The same behaviour is observed on the other bins as can be seen in the figure 5.10.

The muonic β_{MU} for proton and iron showers are practically equal as can be seen in the figure 5.12 at the end of the section. Nevertheless, the parameter for the parametrization of the

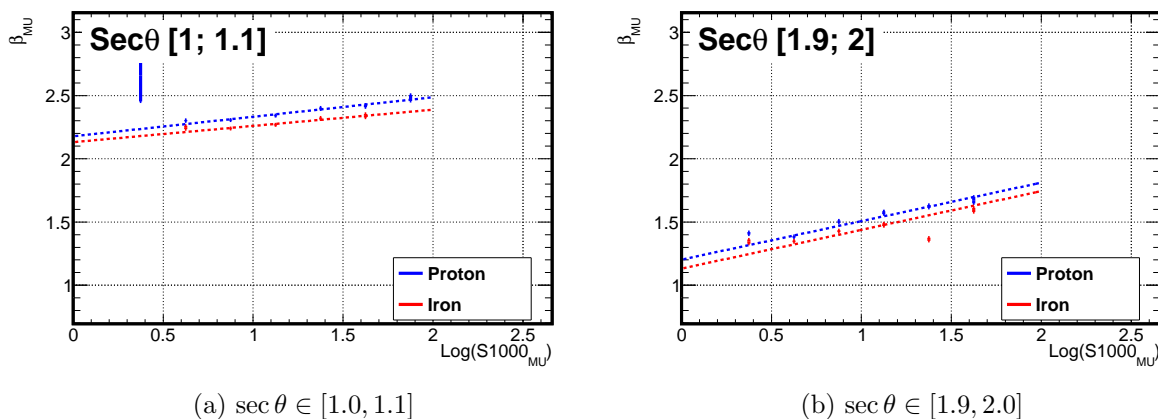


Figure 5.7: The β dependence as function of $\log_{10}(S_{1000})$ for the intervals $\sec \theta \in [1, 1.1]$ (left) and $\sec \theta \in [1.9, 2.0]$ (right), for proton (blue lines) and iron (red lines). The lines are the fit to equation 5.23. The others $\sec \theta$ bins are plotted on figure 5.10.

β_{MU} are different (see table 5.3). This means we have an higher degree of freedoms in the β parametrization (eq. 5.23) than what would be necessary, or equivalently, some parameters are correlated.

In the electromagnetic part, the β_{EM} for the first signal is also practically equal for both proton and iron shower as can be seen in figure 5.11 in the end of the section. For the last bins in $\sec \theta$ (corresponding to more inclined events), the β_{EM} are slightly different for the primaries but within the error bars. We should note that at those angles the EM signal is much lower, giving more fluctuations and that's the reason for the difference in the calibration.

The figures 5.13 and 5.14 are also added for a better comparison of each component within the same primary. The first figure is for the proton sample where β_{TOT} , β_{EM} and β_{MU} (the three components) are displayed for the 10 bins in $\sec \theta$. The second figure is the same for the iron sample. The behaviour on both samples is quite similar. At vertical events (low $\sec \theta$) the β_{TOT} is close to the one found for β_{EM} while for the most inclined events of the sample (high $\sec \theta$), β_{TOT} decreased until values very close to the values for β_{MU} . This reflects the increasing importance of the muonic component with zenith angle. Like was said before, the EM component is very attenuated in atmosphere, so for higher zenith angles it will be much smaller (while muons are almost constant).

The interest of parametrizing beta is to afterwards obtain a better S_{1000} estimation. So, after obtaining the parametrization for β for the 3 components, we perform the fits again, event by event, but fixing β with these values, in order to observe the behaviour of the S_{1000} for β free and β fixed.

On the figures 5.9, we can see the values of $RMS(S_{1000}/Energy)/\langle S_{1000}/Energy \rangle$ plotted as a function of $\cos^2(\theta)$ for the three component separately (and both primaries). Since S_{1000} changes with energy and with $\cos^2(\theta)$ (according to CIC attenuation) this is the best plot to observe the fluctuations on the shower size (S_{1000}) before and after fixing the parameter β on

the LDF. We can see that when we fix the β on the fits we have a consistently lower RMS. This will mean that our energy estimator will have a lower RMS and the final energy reconstruction will have a better resolution.

We can also see that the error on S_{1000} obtain when fixing the values of β is lower as expected. In the figure 5.8, we have plotted $\sigma_{S_{1000}}/S_{1000}$ as function of $\log_{10}(S_{1000})$ and we can see a consistently lower $\sigma_{S_{1000}}$ when fixing β compared with free β .

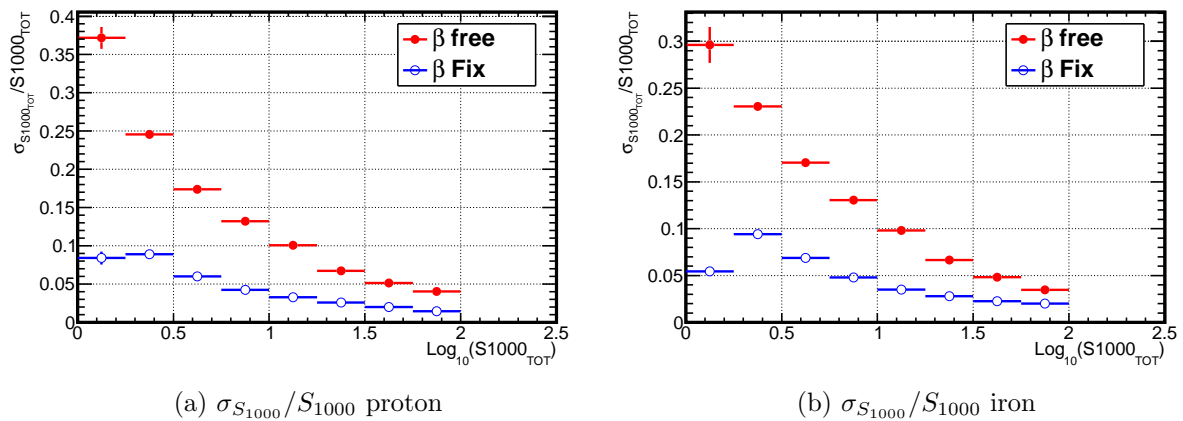


Figure 5.8: $\sigma_{S_{1000}}/S_{1000}$ as function of $\log_{10}(S_{1000})$ for the total component. The values for β free and β fixed are plotted on red and blue respectively. We have the proton and iron samples on the left and right respectively.

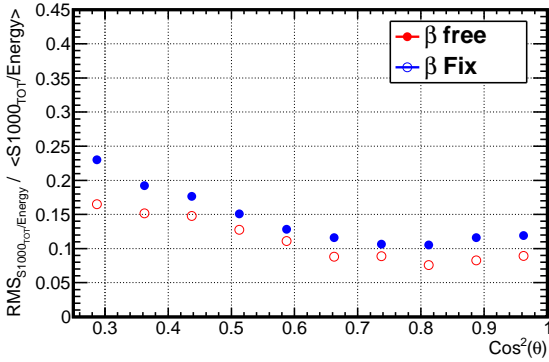
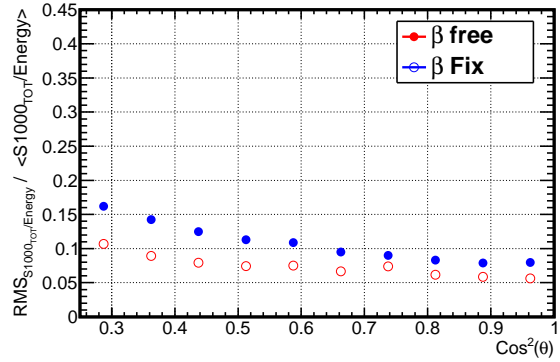
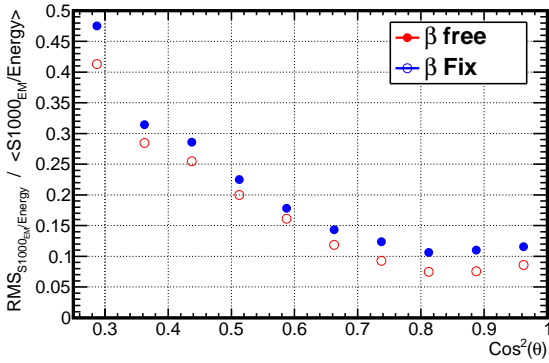
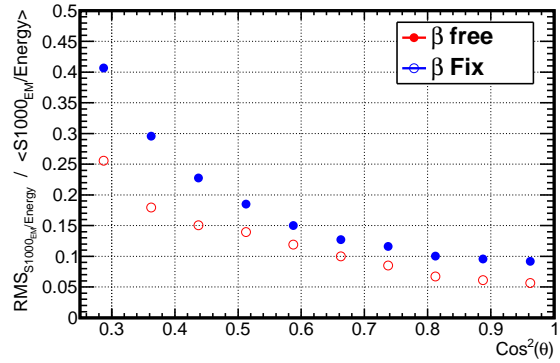
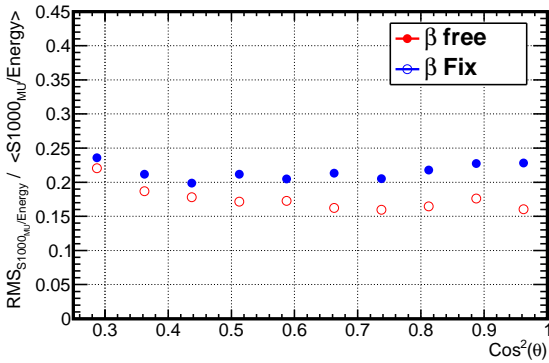
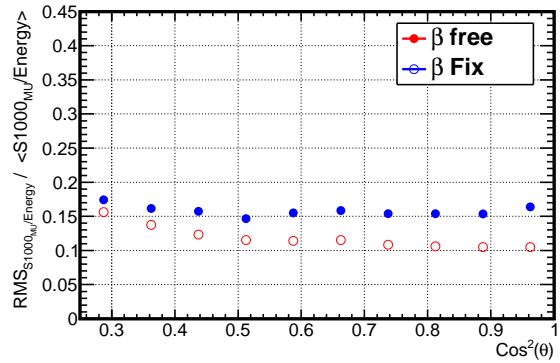

 (a) $RMS(S_{1000,TOT}/Energy) / \langle S_{1000,TOT}/Energy \rangle$, for proton

 (b) $RMS(S_{1000,TOT}/Energy) / \langle S_{1000,TOT}/Energy \rangle$, for Iron

 (c) $RMS(S_{1000,EM}/Energy) / \langle S_{1000,EM}/Energy \rangle$, for proton

 (d) $RMS(S_{1000,EM}/Energy) / \langle S_{1000,EM}/Energy \rangle$, for Iron

 (e) $RMS(S_{1000,MU}/Energy) / \langle S_{1000,MU}/Energy \rangle$, for proton

 (f) $RMS(S_{1000,MU}/Energy) / \langle S_{1000,MU}/Energy \rangle$, for Iron

Figure 5.9: $RMS(S_{1000}/Energy) / \langle S_{1000}/Energy \rangle$ plotted as a function of $\cos^2(\theta)$ for the three component separately (and both primaries). On the left the values for the proton primary sample, while on the right for the iron sample. In the top, center and bottom we have the TOT, EM and MU components respectively. In blue we have the values when fixing β and in red the values for free β .

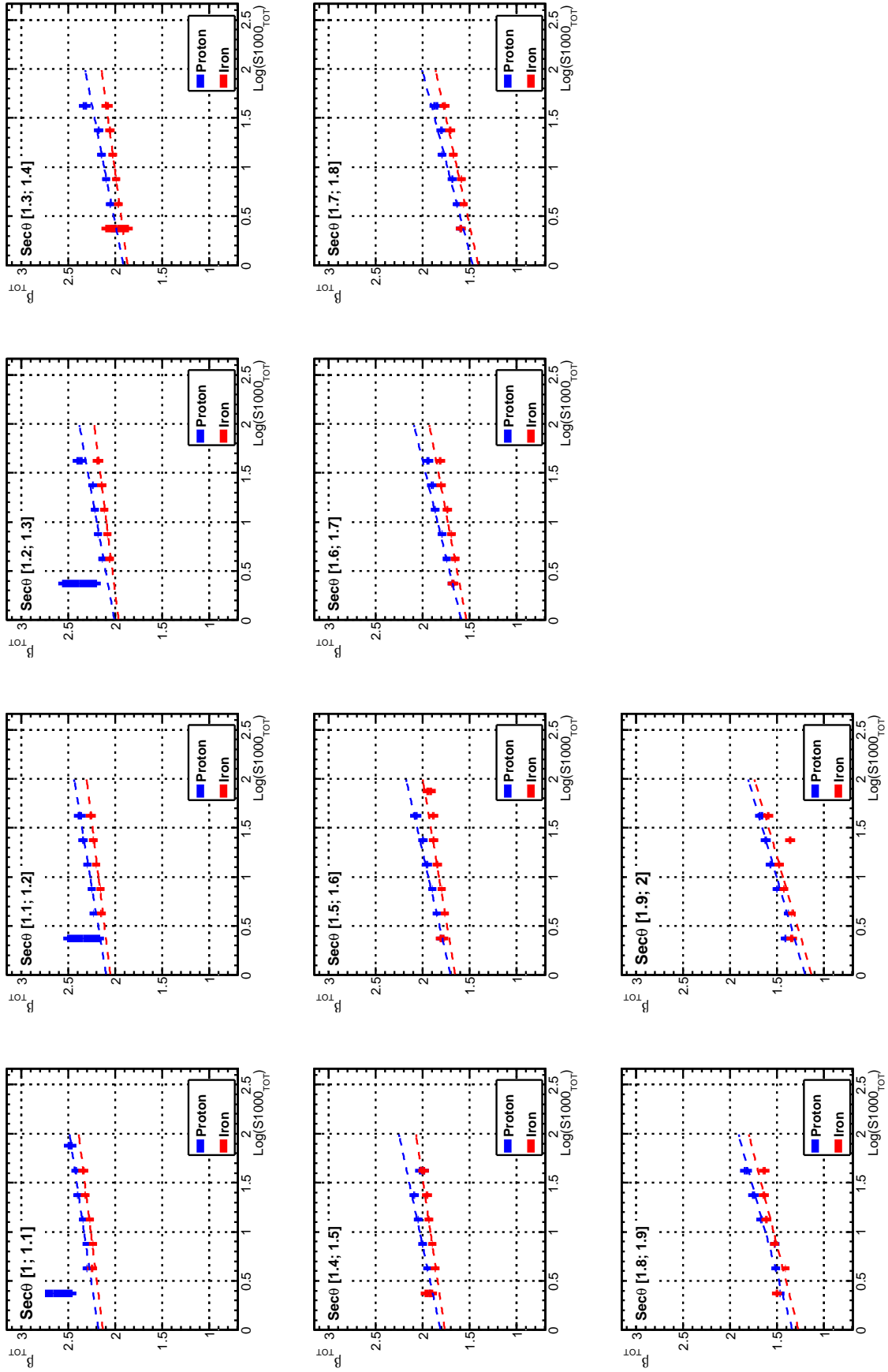


Figure 5.10: LDF β for the total signal as function of $\log_{10}(S_{1000})$ intervals for different $\sec\theta$ ranges. Blue is for proton sample and red is for iron sample. On dashed lines are the fits to the equation 5.23, with parameters in table 5.23, for the components.

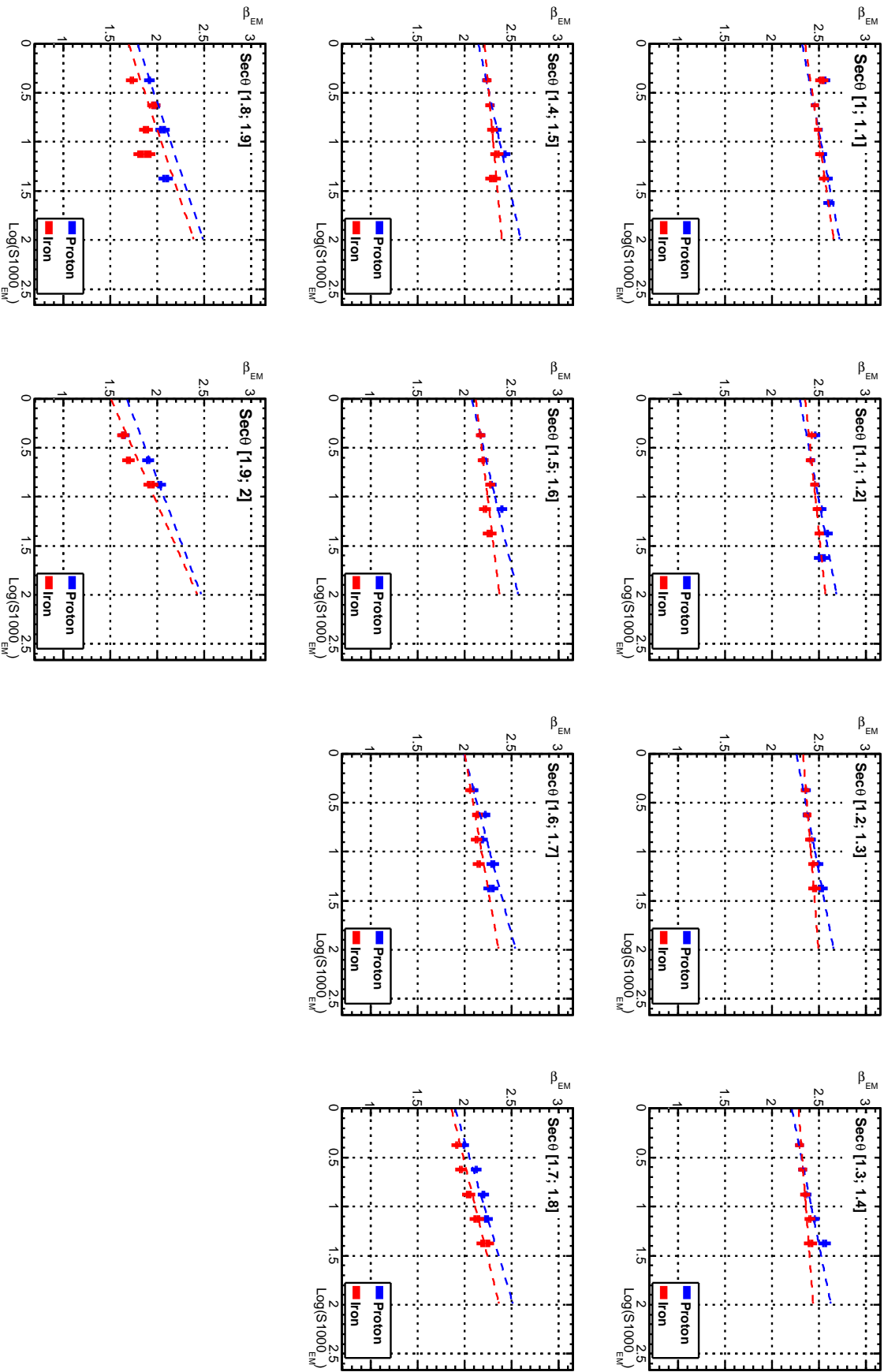


Figure 5.11: LDF β for the EM signal as function of $\log_{10}(S_{1000})$ intervals for different $\text{sec } \theta$ ranges. Blue is for proton sample and red is for iron sample. On dashed lines are the fits to the equation 5.23, with parameters in table 5.3, for the components.

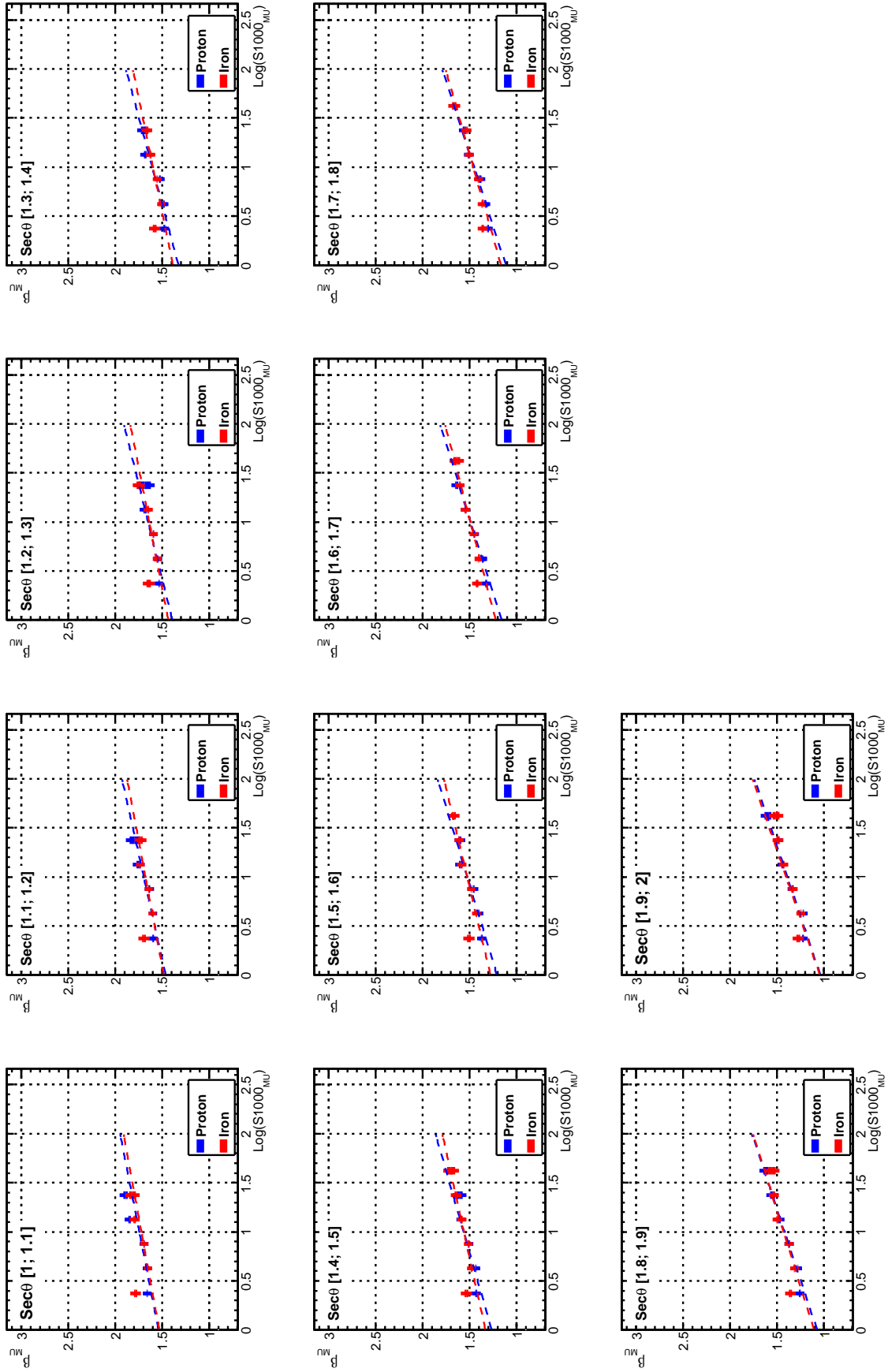


Figure 5.12: LDF β for the MU signal as function of $\log_{10}(S_{1000})$ intervals for different $\text{sec}\theta$ ranges. Blue is for proton sample and red is for iron sample. On dashed lines are the fits to the equation 5.23, with parameters in table 5.3, for the components.

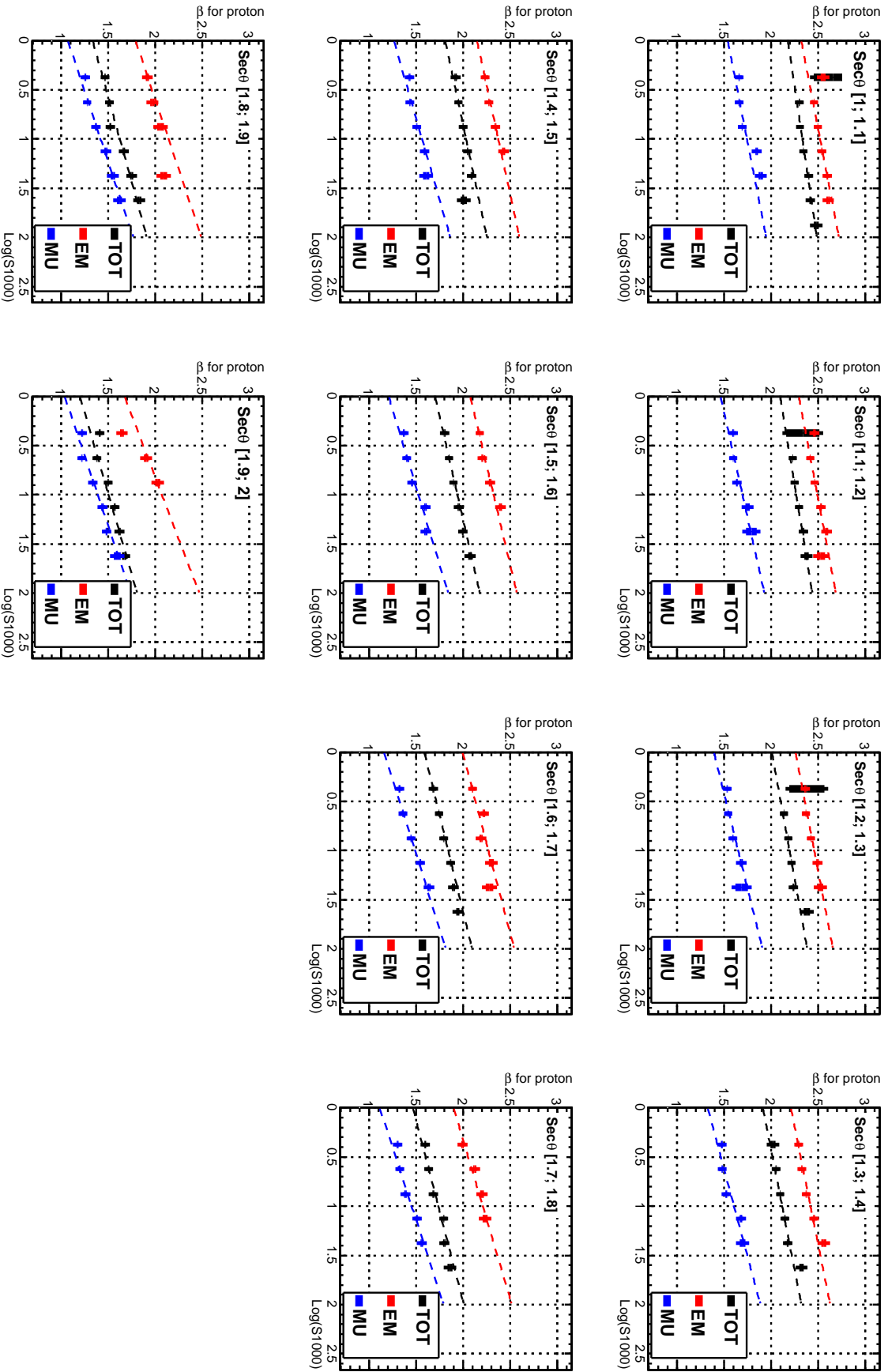


Figure 5.13: β for the three components for proton sample (balck for TOT, red for EM and blue for MU) and data (in green) coming from [221]. Each plot corresponds to a differente $\text{sec}\theta$ bin. On dashed lines are the fits to the equation 5.23, with parameters in table 5.3, for the components.

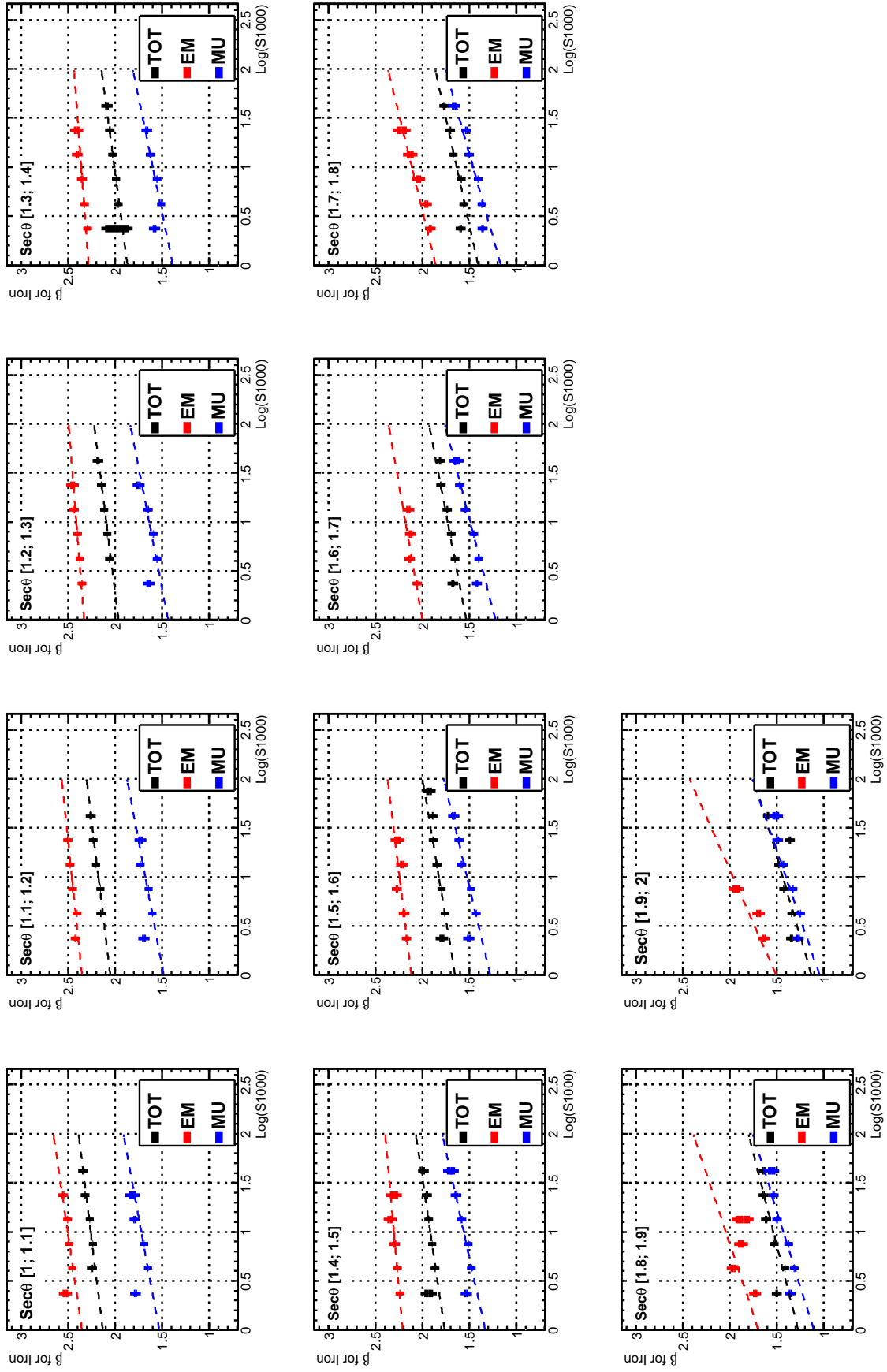


Figure 5.14: β for the three components for iron sample (black for TOT, red for EM and blue for MU) and data (in green) coming from [221]. Each plot corresponds to a different $\sec\theta$ bin. On dashed lines are the fits to the equation 5.23, with parameters in table 5.3, for the components.

5.2 Energy Calibration

On the previous section, the LDF parametrization was discussed and the likelihood method for fitting the signals on the ground was explained. It was also verified that fixing the parameter β reduces the fluctuations on the S_{1000} . In this section we want to obtain an energy estimator for the SD. The better way is to consider the S_{1000} as a value proportional to the shower size or energy, but it can not be used directly as explained in the following.

At this step, we perform the fit to equation 5.23 again, but this time fixing the β to the values found in table 5.3, because in this way, we reduce the fluctuations on the parameter S_{1000} , that interests us to perform the energy calibration. With the new fits, we can obtain the S_{1000} parameter which should be almost proportional to the energy of the primary cosmic ray. Nevertheless, we cannot use the S_{1000} directly as a energy estimator. If we look at figure 5.1, we can see that the two events have approximately the same energy, however the $S_{1000,TOT}$ is different, being 9.6 VEM and 5.4 VEM for the showers with 24.5° and 60° respectively. This happens, because at different zenith angles, the ground corresponds to different atmospheric depth crossed by the shower. So in more inclined events, the shower would cross an higher atmospheric depth, and the particles would be more attenuated. This means that even for the same primary energy, the S_{1000} will be higher in vertical events (with less attenuation).

To obtain an energy estimator, we should correct the S_{1000} for the attenuation, reducing it to the equivalent S_{1000} at a reference zenith angle of 38° . This value has been chosen because is the median of zenith angle distribution of SD events. It is also assumed that the attenuation functional is the same at different energies. This procedure would be simpler if we could choose an energy bin to obtain the angular attenuation and then correct the ground signal. However to choose the energy bin, we would need to have the energy estimator already. The way to solve this problem is to use the Constant Intensity Cut (CIC) described in the next section. To use this method we need a constant frequency of events in $\cos^2\theta$, and we have it as we can see in figures 5.15 and 5.16.

In the CIC analysis, only events with energy greater than $3 \cdot 10^{18} eV$ fulfilling standard SD cuts were used.

5.2.1 Intensities

The constant intensity cut method (see [153]) is widely used in the cosmic rays field for many years (see [223, 224, 225]). This approach implies two conditions, that the cosmic rays are isotropic and the second, that the detector acceptance as function of zenith angle is known. In the range of energies of these studies, the cosmic rays are basically isotropic. At $E > 3$ EeV the SD is full efficient and up to 60° it's acceptance is purely geometric. The assumption of equal cosmic ray flux per solid angle at a given energy holds for energies lower than $E < 20$ EeV (as seen in [226] and lower energies than $E < 10^{17}$ eV are not in the scope of Auger). So the flux

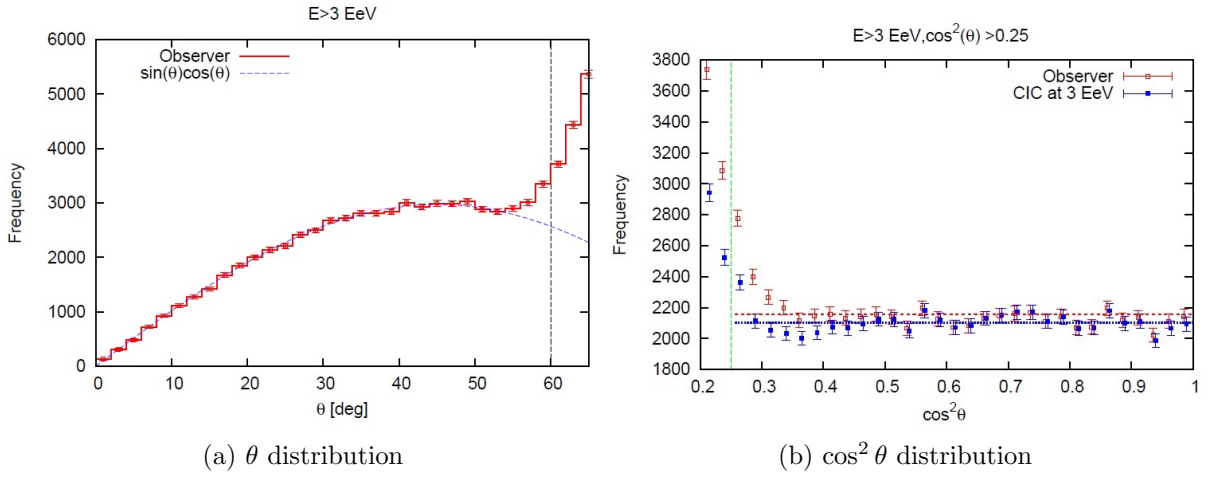


Figure 5.15: Frequency of cosmic rays as function of zenith angle(left) and $\cos^2 \theta$ (right). Since the cosmic rays are mainly isotropic, according with our geometry, we will have approximately the same number of event in equal $\cos^2 \theta$ bins. Plots from [222]

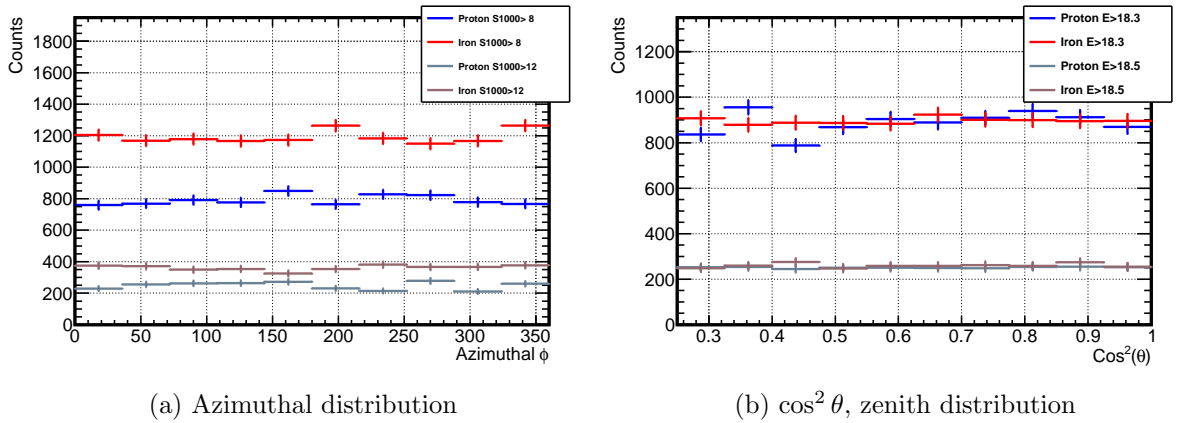


Figure 5.16: Event frequency from the proton and iron sample as function of azimuthal angle ϕ (left) and zenith angle $\cos^2(\theta)$ (right). In red and blue we have the iron and proton samples respectively. The azimuthal distributions were made using events with $S_{1000} > 8$ VEM and > 12 VEM (normal and darker color). As for $\cos^2(\theta)$ distributions we cut at $\log_{10}(En) > 18.3$ and > 18.5 (for normal and darker color). We can see that we have approximately the same events per bin allowing us to perform the CIC method.

per solid angles $dJ/d\Omega$ is equal for all directions for a energy above some threshold with full efficiency. With $\Omega = \sin \theta d\theta d\phi$, we have a flat distribution in the azimuthal directions (ϕ) of CR. In the figure 5.16 left, we have the azimuthal distribution plotted for $S_{1000} > 10$ and $S_{1000} > 5$ for proton and iron samples. The distributions in our simulation have a constant distribution in ϕ allowing us to use this method.

We need to find the zenith angle distribution for CR. So, with the assumption that the CR

flux is equal in bins of solid angle, then the flux should be given by:

$$\frac{dJ}{d\Omega} = \frac{d}{d\theta} \left(\frac{1}{A \cdot \cos \theta} \frac{dN^3}{dt dE \sin \theta d\theta d\phi} \right) = 0, \quad (5.26)$$

where θ is the zenith angle, with the effective area $A \cdot \cos \theta$, E and t gives the energy and time dependence and ϕ is the azimuthal dependence. The time t and area A don't depend neither on zenith or azimuthal angles, so we can integrate over t and ϕ and get:

$$\frac{dN^3}{dE \cos \theta \sin \theta d\theta} = \text{constant}. \quad (5.27)$$

Since CR are isotropic and the energy dependence is a steeply falling spectrum, we can say that the integration above a threshold is given by:

$$\frac{dN^3}{\cos \theta \sin \theta d\theta} \Big|_{E > E_0} = \text{constant}. \quad (5.28)$$

The frequency of CRs as function of zenith is then proportional to $\cos \theta \sin \theta$ (fig 5.15 left). This means that above some threshold with full efficient trigger, the CR have the same statistics in equal bins of $\cos^2 \theta$ or $\sin^2 \theta$ (fig 5.15 right).

In the figure 5.16 right, we can see that our samples have a constant distribution on $\cos^2 \theta$. This is the feature that allows us to calibrate S_{1000} independent of an energy scale.

At this point, we introduce the Intensity distributions, which are the cumulative number of events with signals above S_{1000} , for each $\cos^2 \theta$ bin. The intensity I is defined as:

$$I(S_{1000}, \theta) = N_{event\theta}(S_{1000}^* > S_{1000}) = \int_{S_{1000}}^{\infty} \frac{dN(S_{1000}^*)}{d \cos^2 \theta} dS_{1000}^*. \quad (5.29)$$

So, I is the number of events above a given signal S_{1000} per $\cos^2 \theta$ bin.

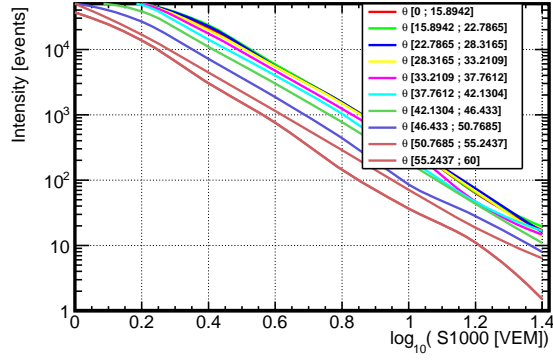
If we chose some intensity like $I(S_{1000}, \theta) = 85$, we are choosing the 85 most energetic events within the θ interval. Each $\cos^2 \theta$ bin has the same statistics and it also has the same energy spectrum, therefore, a given intensity (selecting the most energetic events) corresponds to the same lower energy cut, given different S_{1000} values per each $\cos^2 \theta$ bin.

An horizontal line in the figures 5.17, with equal intensity, corresponds to a line with constant energy. So we can easily obtained the attenuation curve or the CIC curves, ie the S_{1000} at constant intensity as a function of $\cos^2 \theta$.

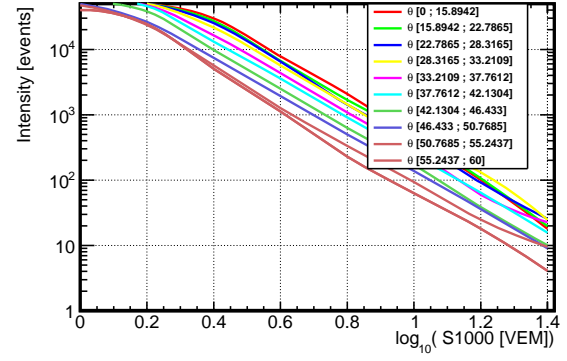
5.2.2 Constant Intensity Cut (CIC)

In this analysis, 10 $\cos^2 \theta$ intervals were used (for the intensity distributions and consequently 10 points to CIC curves). With the Intensities plots, we can choose several intensity cuts (horizontal lines) that corresponds to different energy cuts and obtains the attenuation curves.

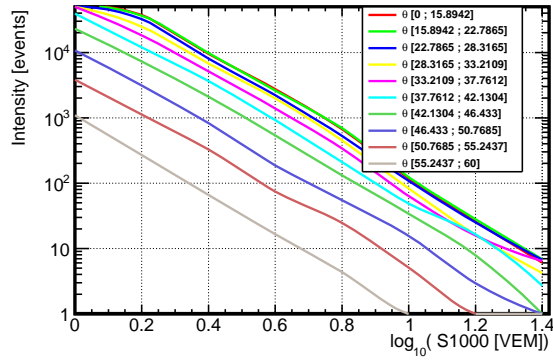
For each 10 $\cos^2 \theta$ intensity distributions, we have the S_{1000} axis binned. So, at a fix $\cos^2 \theta$,



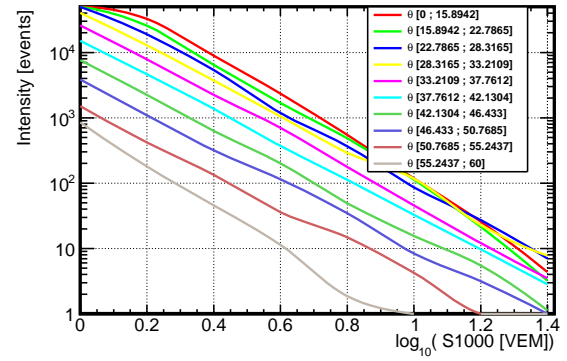
(a) Total component, proton



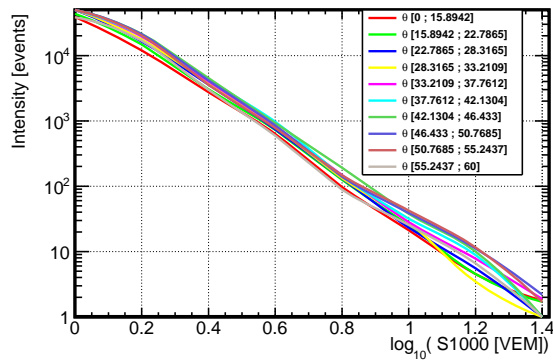
(b) Total component, iron



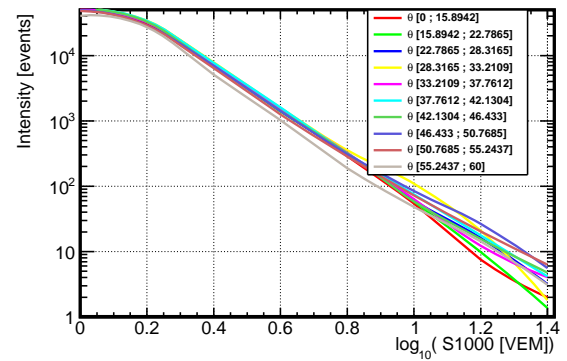
(c) EM component, proton



(d) EM component, iron



(e) MU component, proton



(f) MU component, iron

Figure 5.17: The intensity I plots given by equation 5.29, in 10 bins of $\cos^2 \theta$, for the total signal (top), EM signal (Center) and MU signal (bottom). On left is the proton sample, on right for iron sample.

to obtain the signal between two adjacent points (I', S') and (I'', S'') , we can do an linear interpolation corresponding to a power law:

$$\begin{aligned}\log I' &= n + m \cdot \log S' , \\ \log I'' &= n + m \cdot \log S'' .\end{aligned}\tag{5.30}$$

The value S_{1000} , S , at a given intensity I , between the two closest available points I' and I'' , is calculated by:

$$S(I) = S'' \left(\frac{I}{I''} \right)^{\frac{\log_{10}(S'/S'')}{\log_{10}(I'/I'')}} = S'' \left(\frac{I}{I''} \right)^{\frac{\log_{10}(S'/S'')}{\log_{10}(1+\Delta I/I'')}} ,\tag{5.31}$$

where $\Delta I = I'' - I'$. The points I' and I'' are correlated, but to estimate the error in S , we use the fact that ΔI and I'' for example are uncorrelated, so the statistical uncertainty in S is given by:

$$\sigma_S^2 = (S(I'', \Delta I) - S(I'' + \sigma_{I''}, \Delta I))^2 + (S(I'', \Delta I) - S(I'', \Delta I + \sigma_{\Delta I}))^2 .\tag{5.32}$$

As I is an event counting value, we assume Poisson distribution and we have $\sigma_{I''} = \sqrt{I''}$ and $\sigma_{\Delta I} = \sqrt{\Delta I}$.

In figure 5.18, these curves are shown for four different intensity cuts for each signal (5 for the total). The three from the left corresponds to the proton sample, while at the right we have the iron sample.

The S_{1000} behaviour with $\cos^2\theta$ should be the same for all energies, only changing the absolute value. With this evolution we can transform the S_{1000} value, of a given angle, into the value it should have at zenith 38° , where we have more statistics. As follows, we have an energy estimator independent of the angle.

Each attenuation curve can be parametrized with equation 5.33, yielding the S_{38} energy estimator.

$$\begin{aligned}S_{1000} &= S_{38} \times CIC(\theta) \\ &= S_{38}(1 + a[\cos^2\theta - \cos^2(38^\circ)] + b[\cos^2\theta - \cos^2(38^\circ)]^2) ,\end{aligned}\tag{5.33}$$

S_{38} , a , and b are the parameters, the CIC fit parameters obtained for *Intensity* = 170 are presented in table 5.4. The parameter S_{38} here is only a normalization factor that don't interest for our analyses, only the functional part ($CIC(\theta)$) is important.

In fact, the normalization factors should differ for proton and iron, due to two reasons. On one side, we don't have the same number of events on both simulations. So an equal cut in intensity would not correspond to the same cut in energy. On other side, if the signal on the ground for proton and iron is not the same, then the normalization is not the same.

The TOT signal CIC for proton and iron seems very similar. The proton one, looks more curved than for iron, as we can see in the parameter b (higher for proton).

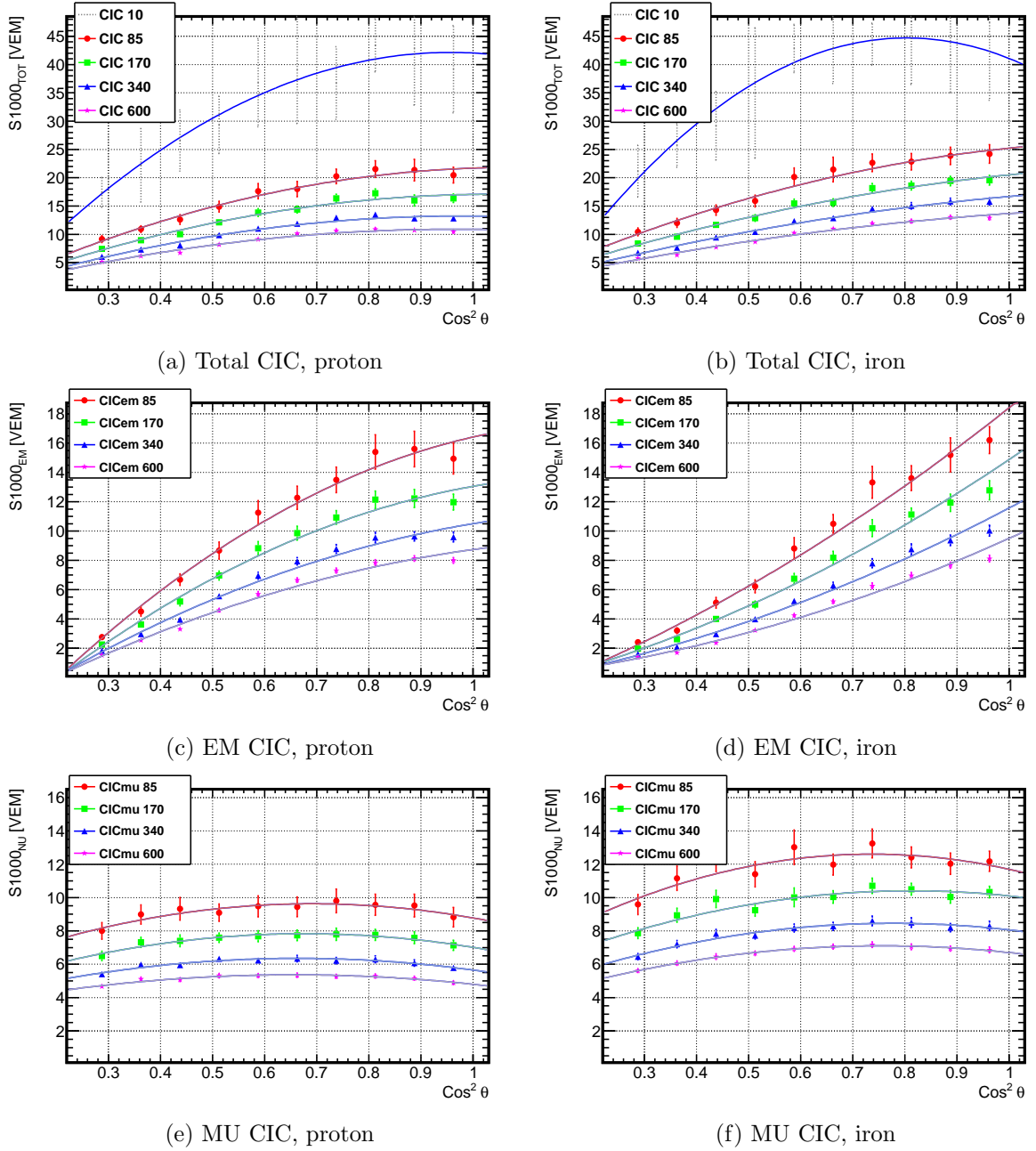


Figure 5.18: Attenuation curves, for several signal intensities. In the top, mid and bottom we have the CIC curves for Total, EM and MU signal respectively. These curves were made for intensity cuts with 85, 170, 340 and 600 events (in red, green, blue and pink respectively). The fit results for the parameters for $Intensity = 170$ (green color) are presented in table 5.4.

The EM CIC for iron has a steepest slope than the proton CIC, probably due to the higher multiplicity in iron, that produces less energetic electromagnetic particles, which will decay more quickly.

The Muonic CIC is almost uniform, since the muons are much less attenuated. The small shape in the CIC comes from the geometry of the tanks with the direction of the particle injection. The Muonic CIC for the proton sample is very similar to the iron sample, as should be expected.

Table 5.4: Fit parameters obtained from the fit of eq. 5.33 for a $CIC = 170$, to the total, EM and MU signals (for proton and iron sample).

Signal	S_{38}	a	b	χ^2/ndf
Proton primary				
Total	14.00 ± 0.28	1.04 ± 0.07	-1.24 ± 0.29	7.6/7
EM	8.85 ± 0.17	1.79 ± 0.07	-1.43 ± 0.26	11.1/7
MU	7.80 ± 0.16	0.11 ± 0.06	-1.01 ± 0.29	1.3/7
Iron primary				
Total	15.33 ± 0.32	1.16 ± 0.07	-0.73 ± 0.31	4.5/7
EM	6.95 ± 0.14	2.57 ± 0.09	1.14 ± 0.33	12.7/7
MU	10.09 ± 0.20	0.33 ± 0.05	-0.85 ± 0.27	5.2/7

If the analysis is consistent, the CICs curves for several intensities should differ only in the normalization. So the normalized attenuation curves for different intensity cuts, enable us to test the universality of the method. They are displayed, normalized to the S_{38} , in the figure 5.19 for the total signal LDF, and for its EM and MU components. In the figures 5.19, we have all normalized $CIC(\theta)$ plotted and the shadow band corresponds to the error of the average of the various intensities cuts per signal type and primary. We can see that, for each type, all intensity curves overlap. This is a key consideration for the consistency of the method.

The CIC for muons are approximately constant and extremely different from the other two. The electromagnetic CIC is steeper than the total CIC, and it is clear that the total CIC should be dominated by muons at low $\cos^2(\theta)$ (high zenith θ).

Again, we can better see that the muonic CIC is extremely similar between proton and iron. The EM CIC is steeper for iron as said before. And the TOT CIC is slightly different for high $\cos^2(\theta)$ (low θ) due to the difference in the EM fraction. The averages CIC curves were fitted to eq.5.33 and the results are written on table 5.5. In the next section, to get the S_{38} , we use the parametrizations of the average intensities curves from that table.

The results of the fits have χ^2/ndf between 0.22 and 1.1 which is very good. The χ^2 for EM CIC is worst than for the other two, because the behaviour is much steeper than for the others and it is more difficult to accommodate the points.

Since the muonic CIC is mainly constant, that means that the parameter a and b will have low values with a big error compared to the parameter value itself.

The uncertainty coming from the CIC parametrizations are dependent on the zenith angles, in the fig. 5.20, we can see the $\sigma_{S_{38}}/S_{38}$ for the total component, on proton (blue shadow) and iron showers (red shadow). The uncertainty varies from less than 0.5% around 38° , since CIC is a polynomial around $\theta = 38^\circ$, to $\approx 6\%$ at 0° and 60° . The iron error band is slightly bigger

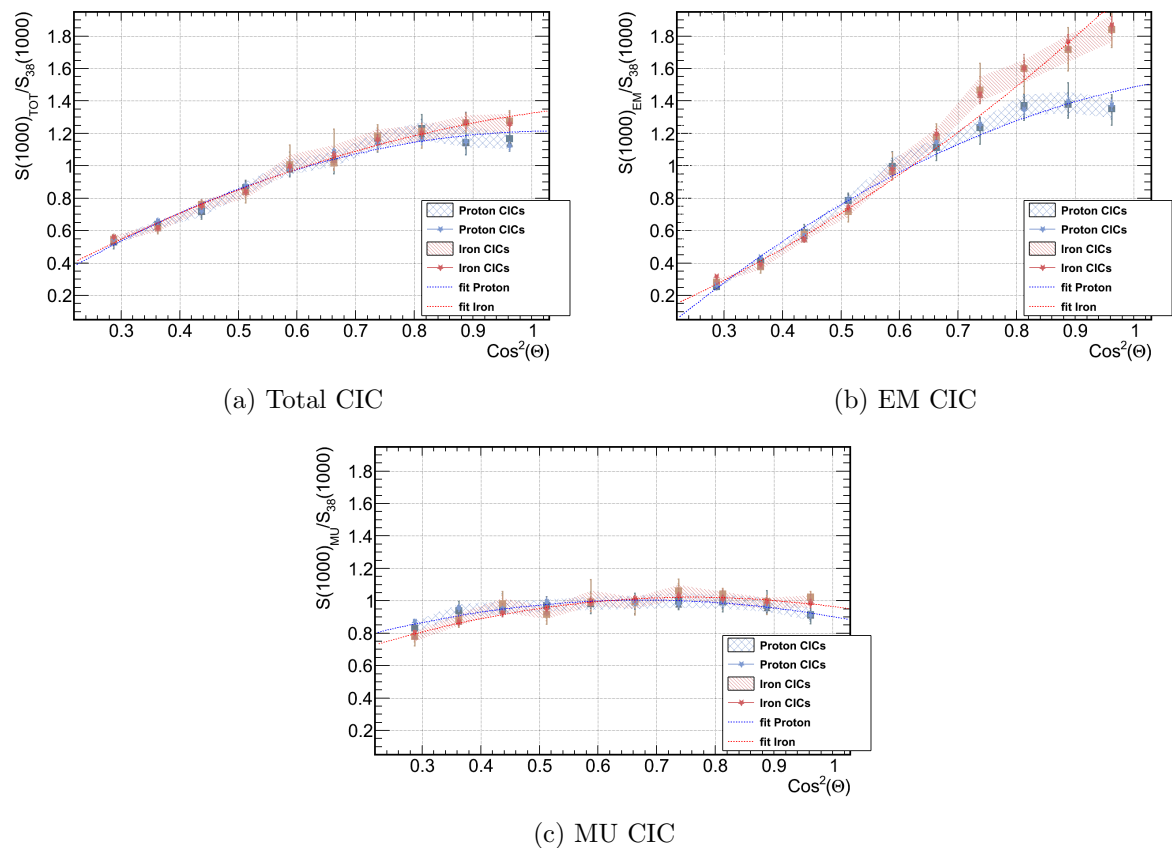


Figure 5.19: The four intensity CIC curves are shown (normalized to the S_{38}). In red the results for iron sample and blue for proton sample. In the top left is the total signal CIC, in right the EM signal CIC and at the bottom we have the muonic signal CIC. The fit of eq. 5.33 to the average are plotted for all components and primaries and whose parameter are on table 5.5.

due to a bigger error in CIC parametrization, but of the same order.

In the figure 5.21, we plotted the ratios CIC_{EM}/CIC_{TOT} and CIC_{EM}/CIC_{MU} to understand the relative importance of each component.

First, we can also see that, the fractions for each 4 intensities are overlapped, within the error bars. The same was found in the figure 5.19. This means that they are similar, differing only in the normalization, as it should be if the analysis is consistent.

According with the plots, for low $\cos^2(\theta)$ (or more inclined showers), the total signal is dominated by the muon component. The electromagnetic particle are absorbed in the atmosphere while the muons are much less attenuated, and since for higher angles we cross more depth in atmosphere, that means, the EM component will be more attenuated than the muonic part. So we will have a lower EM signal. On vertical shower (higher $\cos^2(\theta)$), we are closer to the X_{max} , so the EM particles dominates against muons.

The same behaviour is obviously observed on both iron and proton primaries. Nevertheless, the muons begins to dominate for lower zenith angles. We can even see that even in vertical

Table 5.5: Fit parameters obtained from the fit of eq. 5.33 for the CIC average of the CIC curves with intensities 85, 170, 340 and 600 (present in the figure 5.18, whose average is in fig 5.19). The total, EM and MU signals results are present (for proton and iron sample).

Signal	S_{38}	a	b	χ^2/ndf
Proton primary				
Total	1.00 ± 0.02	1.04 ± 0.06	-1.26 ± 0.28	7.0/7
EM	1.00 ± 0.02	1.80 ± 0.07	-1.37 ± 0.24	11.2/7
MU	1.00 ± 0.02	0.107 ± 0.055	-0.970 ± 0.272	1.4/7
Iron primary				
Total	1.00 ± 0.02	1.15 ± 0.07	-0.83 ± 0.29	5.6/7
EM	1.00 ± 0.02	2.55 ± 0.09	$+1.08 \pm 0.30$	12.6/7
MU	1.00 ± 0.02	0.281 ± 0.051	-0.999 ± 0.260	5.2/7

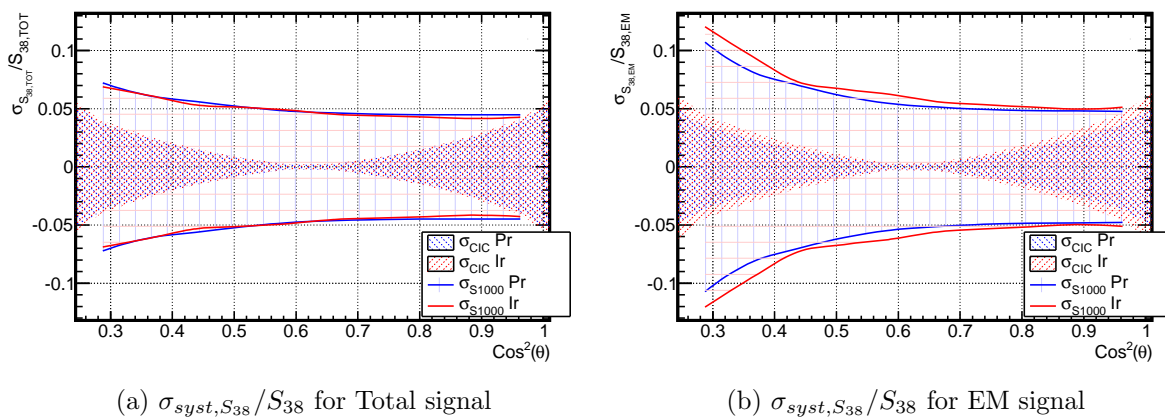


Figure 5.20: The Bands represents the $\sigma_{syst,S_{38}}/S_{38}$ as function of $\cos^2(\theta)$ for the Total signal component. The blue and red fill color corresponds to proton and iron.

showers, the muons are very important in iron primaries. This happens because X_{max} for iron is smaller (higher in atmospheric height), so the shower develops early and the ground is at a later stage of development than for proton primary. The EM particles in iron shower would be already more attenuated on the ground than the ones coming from a proton.

Also, the iron shower produces more muons than protons. And, as we saw before, the EM component is steeper for iron than for proton. All this together, explain the features in the fig 5.21.

For the proton primary, the muonic component dominates the CIC for zenith angles with $\cos^2 \theta < 0.5$ while for iron it dominates basically until $\cos^2 \theta < 0.85$.

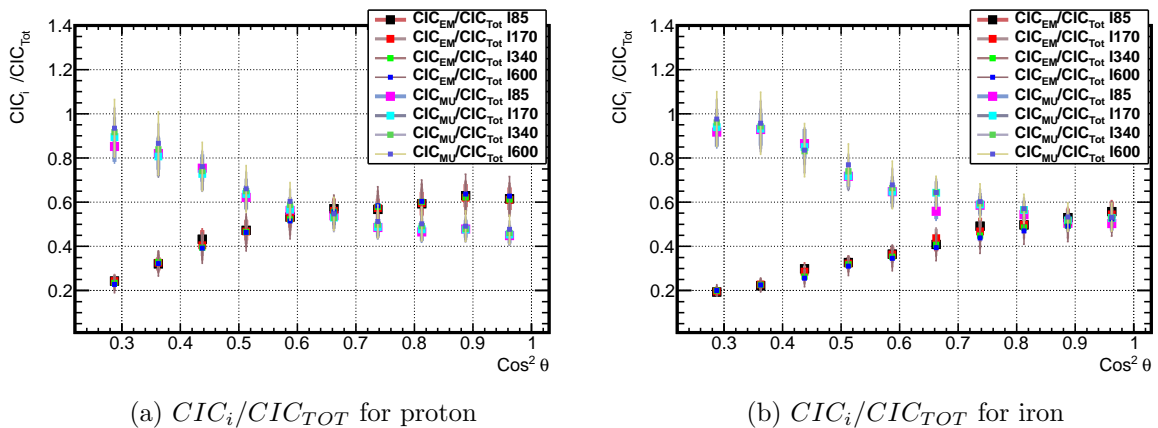


Figure 5.21: Ratios between the EM and MU signal and the corresponding total signal for different values of $\cos^2 \theta$. The points are for intensities of 85, 170, 340 and 600. In left the proton sample and in right the iron sample.

5.2.3 Energy Estimator

The S_{38} estimator of the shower energy is calibrated with the FD energy, in the case of the data. For the present analysis the MC energy was used instead of FD energy. The performance of the S_{38} estimators for the total, EM and MU signals were evaluated in the calibration of the SD assuming a linear $\log(S_{38})$ - $\log(\text{Energy})$ dependence. We use all events with energy above $10^{18.3}$ eV.

We estimate the S_{38} uncertainty to be given by:

$$\sigma_{S_{38}} = \sigma_{CIC(\theta)}^2 + \sigma_{\cos \theta}^2 + \sigma_{S_{1000}}^2, \quad (5.34)$$

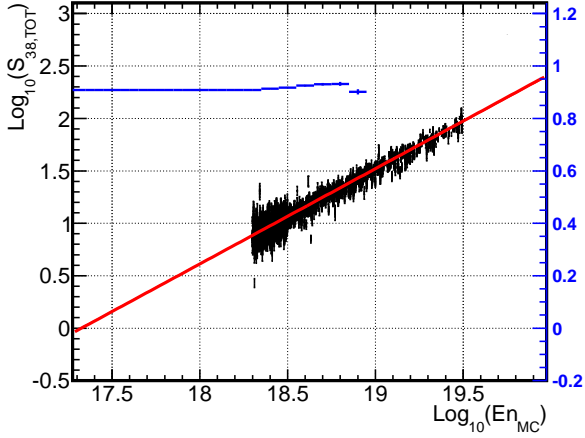
where $\sigma_{CIC(\theta)}^2$ comes from the propagation of the errors of the parameters a and b from $CIC(\theta)$ fit in equation 5.33. $\sigma_{\cos \theta}^2$ comes from the error in the angular accuracy of the event. And $\sigma_{S_{1000}}^2$ is the uncertainty from the S_{1000} parameter. This error comes from the fit to the LDF eq. 5.2. The $\log(S_{38})$ - $\log(\text{Energy})$ dependence are fitted with equation 5.35 for the three components. In figures 5.22, the $\log_{10}(S_{38})$ is plotted as function of $\log_{10}(E)$ with the respective linear fit of the calibration. The calibration parameters obtained from the fit for the S_{38} estimator for the total, EM and MU signals are presented in table 5.6.

$$\log_{10}(S_{38}^{tot,EM,MU}) = A + B \times \log_{10}(E^{tot,EM,MU}). \quad (5.35)$$

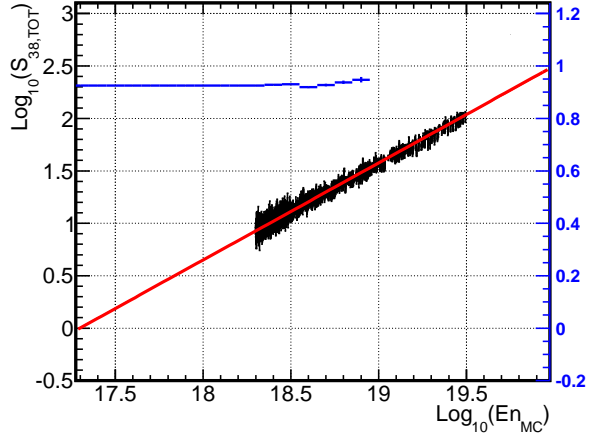
Inverting the equation 5.35 in order to the energy, the SD energy estimator is :

$$\begin{aligned} \log_{10}(E^{tot,EM,MU}) &= a + b \times \log_{10}(S_{38}^{tot,EM,MU}) \\ E_{S_{38}} &= 10^a \cdot S_{38}^b, \end{aligned} \quad (5.36)$$

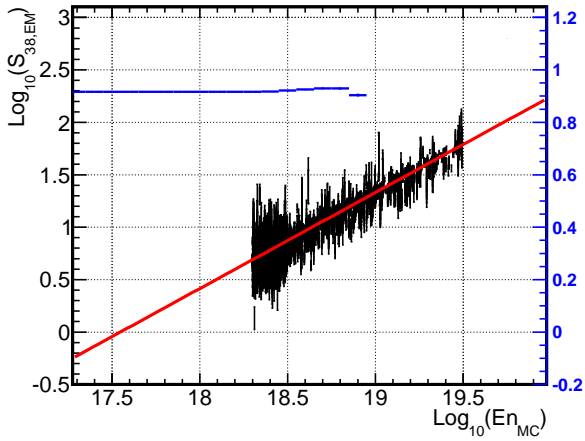
where $a = -A/B$ and $b = 1/B$ (from equation 5.35). The parameters a and b are also written on the same table.



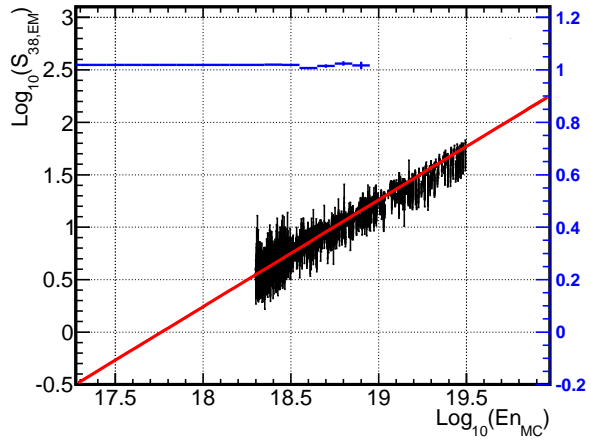
(a) Total signal, for proton



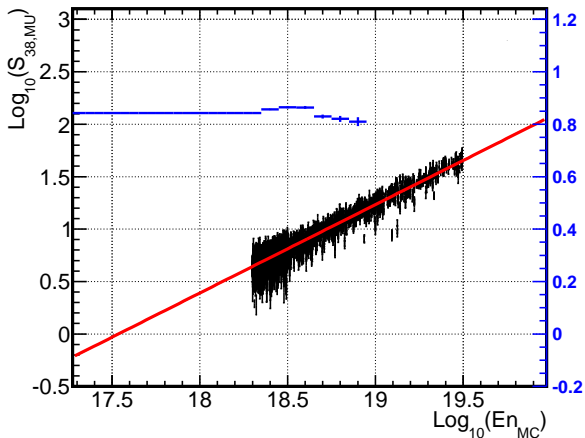
(b) Total signal, for iron



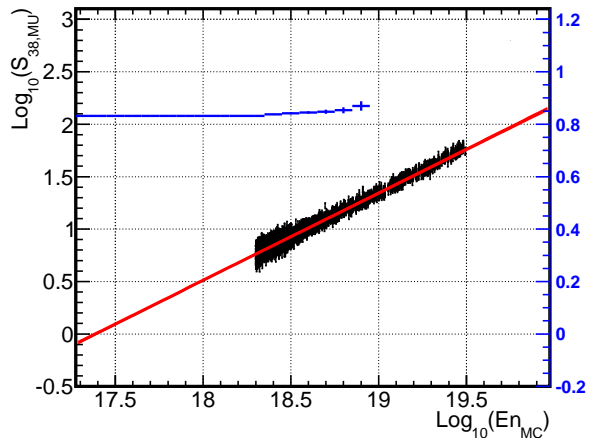
(c) EM signal, for proton



(d) EM signal, for iron



(e) MU signal, for proton



(f) MU signal, for iron

Figure 5.22: S_{38} energy estimator for the total signal (top) and the EM signal (center) and muonic signal component (bottom) in the SD as function of MC Energy. The red lines correspond to the linear calibration with equation 5.35 and the blue lines are the calibration slopes B (whose magnitude can be read in the blue axis on the right), taking into account all the points with Energy equal or above the MC energy in each bin.

Table 5.6: Energy Calibration of the S_{38} estimator parameters of equation 5.35 for the total, EM and MU signals in the SD. Results for the proton and iron sample separately.

Signal	A	B	χ^2/ndf	a	b
Proton primary					
Total	-15.74 ± 0.03	0.908 ± 0.001	4.81	17.33 ± 0.03	1.100 ± 0.002
EM	-16.20 ± 0.03	0.943 ± 0.002	5.63	17.56 ± 0.03	1.060 ± 0.002
MU	-14.78 ± 0.04	0.843 ± 0.002	3.40	17.54 ± 0.05	1.187 ± 0.003
Iron primary					
Total	-16.00 ± 0.03	0.925 ± 0.001	2.06	17.30 ± 0.03	1.080 ± 0.002
EM	-18.10 ± 0.03	1.019 ± 0.002	2.44	17.76 ± 0.03	0.981 ± 0.002
MU	-14.45 ± 0.04	0.831 ± 0.002	1.55	17.38 ± 0.04	1.202 ± 0.003

The uncertainty on this measurement is then given by,

$$\sigma_{E_{SD}}^2 = \sigma_{E_{SD}(Calib)}^2 + \sigma_{E_{SD}(S_{38})}^2 \quad (5.37)$$

$$\begin{aligned} \sigma_{E_{SD}(Calib)} &= \sqrt{[\ln(10)10^a S_{38}^b]^2 \sigma_a^2 + [\log_{10}(S_{38})10^a S_{38}^b]^2 \sigma_b^2} \\ \sigma_{E_{SD}(S_{38})} &= 10^a S_{38}^{b-1} b \cdot \sigma_{S_{38}} \end{aligned} \quad (5.38)$$

In our fit we got χ^2/ndf ranging from 1.6 to 5.6. The fact that the calibration with the muon have a lower χ^2 , comes from the CIC fit. The muonic CIC is mainly constant, however we fit the same functional used in the other components, which means that the parameter are less constrained that in the EM and TOT case. A simpler *CIC*, with less parameters can be considered in the future to the muonic component.

To understand the performance of the energy calibration we plot the distribution of $(E_{MC} - E_{SD})/E_{MC}$ on the figure 5.23. We got mean deviations of similar magnitude for iron and proton sample, with values between 0.2% and 1.7%, but all bellow 5%. The mean deviations are very small in the iron sample and around $\approx 1\%$ in the proton sample.

The RMS of the distributions, that give us the fluctuations of the energy estimation are on the order of 10% to 18%. The RMS for the iron sample are much smaller in all components, since iron has an higher multiplicity in the development of the air shower cascade, which means much less fluctuations.

The muonic RMS is higher due to the intrinsic fluctuations coming from the determination of the muonic S_{1000} that fluctuates more than the other ones (with RMS 18% and 11% for proton and iron respectively). The total component has RMS of 14.8% and 9.0% for proton and iron, while the EM has RMS of 17.2% and 11.6% respectively. The EM signal calibration seems to have more fluctuation than using the TOT signal, which should go against the idea to use EM as an energy estimator instead of the TOT. The problem is that the electromagnetic CIC, is much more steeper than for the other two. This mean, on one side, that for example, the EM signal for inclined events is $\approx 14\%$ of the value for vertical events at the same energy. In this

way, we can have a lot of fluctuation in some event and much less fluctuation in others at the same energy. On other side, if the CIC function is somewhat different with respect to what it should be, because the distribution in $\cos^2(\theta)$ is not constant, then we will have bias on some zenith angles. While for muons some difference in the $\cos^2(\theta)$ distribution would give smaller bias.

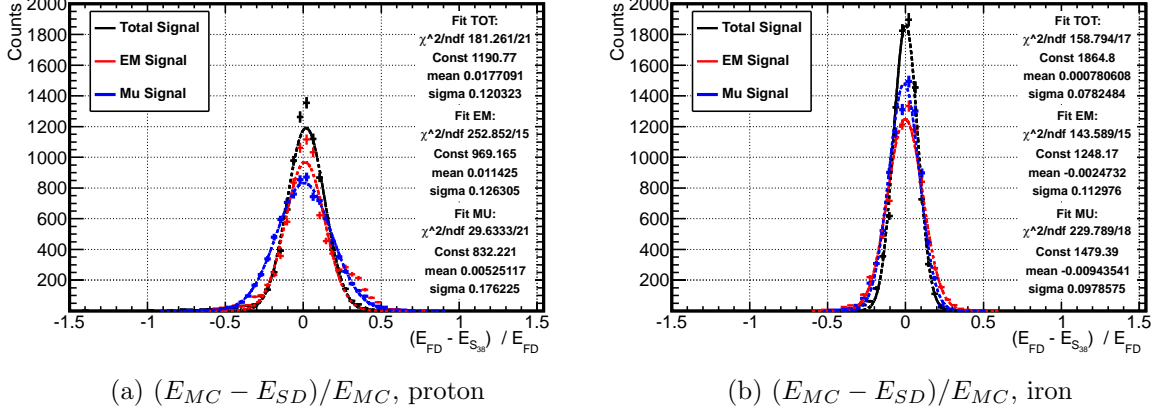


Figure 5.23: Distribution of $(E_{MC} - E_{SD})/E_{MC}$ for the proton (left) and iron (right) samples. On black, red and blue we have the distributions for the total signal, EM signal and Muonic signal component. In a dashed line we have gaussian fits to each distributions with the respective parameters written on the plots. The distributions have for proton $mean_{TOT} = 0.010$, $RMS_{TOT} = 0.148$, $mean_{EM} = 0.040$, $RMS_{EM} = 0.172$ and $mean_{MU} = 0.006$, $RMS_{MU} = 0.180$. For iron we got $mean_{TOT} = 0.003$, $RMS_{TOT} = 0.084$, $mean_{EM} = 0.004$, $RMS_{EM} = 0.116$ and $mean_{MU} = -0.010$, $RMS_{MU} = 0.107$.

Before continuing to confirm the uncertainties associated with the parameters and consecutive errors propagations, for each event, the P factor was calculated with the equation 5.39.

$$P = \frac{E_{MC} - E_{SD}}{\sqrt{\sigma_{E_{SD}}^2 + \sigma_{E_{FD}}^2}}, \quad (5.39)$$

in this case $\sigma_{E_{FD}}^2 = 0$, because we use MC events. The distribution of the P factor are plotted on the figure 5.24. For the iron sample, the P value is approximately 1 for the three component. For the proton sample, we got P from 0.7 to 1.55. This means, that for the proton sample, the error that we obtain in the final calibration are comparable with the fluctuation of the estimator. While for the iron, the errors are smaller than the fluctuations of the energy estimator. The values are considerably close to one, which mean that at the level of the error magnitude the analysis is consistent. It can be noticed that the P value for the electromagnetic component, considering all zenith angle range is not better than the one from the total signal. This was explained before, so it is worth to go back and look at the $(E_{MC} - E_{SD})/E_{MC}$ distribution for some zenith intervals afterwards.

To understand the errors intervening in the systematic uncertainty of the energy estimator, in the figure 5.25 the final error and it's components are plotted as function of the energy. The

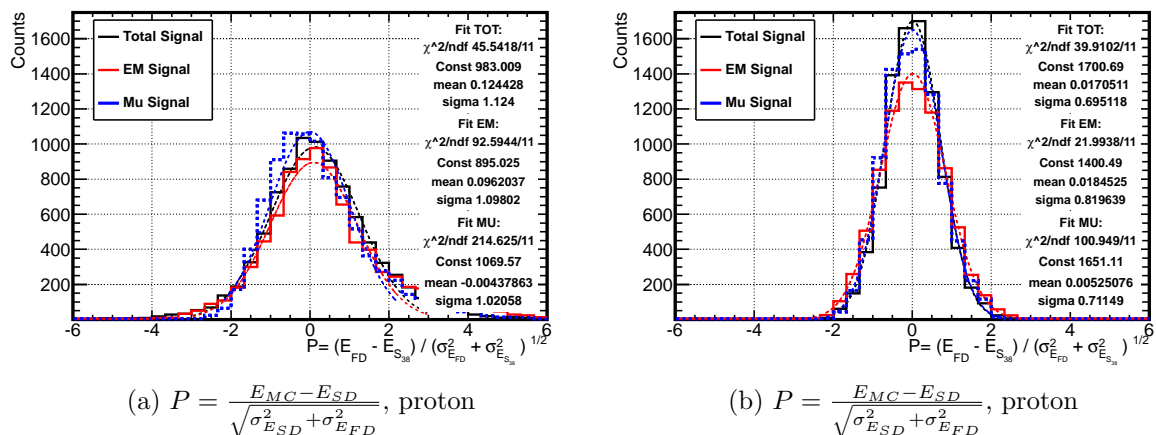


Figure 5.24: Distribution of $P = \frac{E_{MC} - E_{SD}}{\sqrt{\sigma_{E_{SD}}^2 + \sigma_{E_{FD}}^2}}$ for the proton (left) and iron (right) samples.

On black, red and blue we have the distributions for the total signal, EM signal and Muonic signal component. In a dashed line we have gaussian fits to each distributions with the respective parameters written on the plots. The distributions have for proton $mean_{TOT} = 0.22$, $RMS_{TOT} = 1.37$, $mean_{EM} = 0.430$, $RMS_{EM} = 1.55$ and $mean_{MU} = 0.21$, $RMS_{MU} = 1.27$. For iron we got $mean_{TOT} = 0.02$, $RMS_{TOT} = 0.70$, $mean_{EM} = 0.02$, $RMS_{EM} = 0.82$ and $mean_{MU} = 0.01$, $RMS_{MU} = 0.72$.

plot has the fraction of the error over the energy. The total error is given by equation 5.37. The error components are $\sigma_{E_{SD}(calib)}$, $\sigma_{E_{SD}(CIC)}$ and $\sigma_{E_{SD}(S_{1000})}$, which are the errors in the final energy estimator that comes from the energy calibration parameters, CIC parameters and from the S_{1000} error (and they are written in equation 5.38).

As should be expected the final error decreases with energy, since the error that comes from the $\sigma_{S_{1000}}$ decreases with energy. At low energies $\sigma_{E_{SD}(S_{1000})}$ is much higher because we will have very few muons. That way, at lower energies the error coming from $\sigma_{S_{1000}}$ dominates, while for higher energies the error coming from the energy calibration parameters and CIC dominates. The systematic errors for the EM and TOT components are very similar, but the errors in the MU part are higher. In all range, the $\sigma_{E_{SD}(calib)}$ is much higher for the muon component due to the intrinsic muonic fluctuations.

The errors as a function of $\cos^2(\theta)$ are also displayed in the figures 5.26. The fraction of error that comes from the energy calibration are approximately constant with $\cos^2(\theta)$ for the three component.

The error that comes from the S_{1000} are approximately constant for the muon signals, because the muons are approximately constant with zenith angle, so the muon fluctuations should not change with zenith angle. Nevertheless, the TOT and the EM signal have attenuations curves (CIC), which means the signal for inclined event would be smaller and then, have more fluctuations. Since the EM CIC is steeper than the TOT, consequently the fluctuations in the EM signal changes more with zenith angle. The iron fluctuations changes more with zenith since his CICs are steeper than for proton.

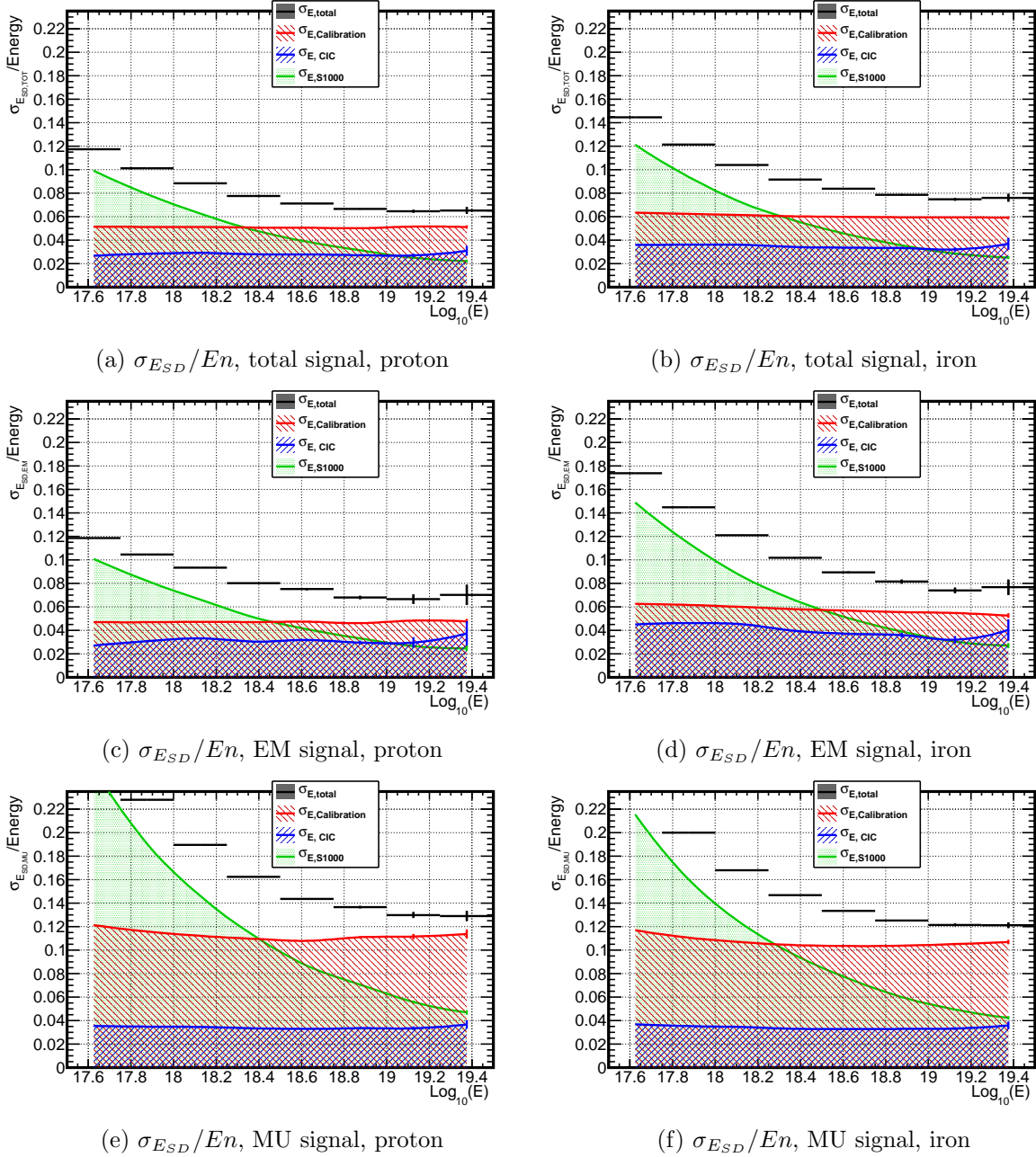


Figure 5.25: Evolution of the Energy estimator error E_{SD} as function of the energy given by equation 5.37. And the error components that come from the energy calibration parameters ($\sigma_{E_{SD}(calib)}$), from the CIC parameters ($\sigma_{E_{SD}(CIC)}$) and from the S_{1000} ($\sigma_{E_{SD}(S_{1000})}$) given on eq. 5.38.

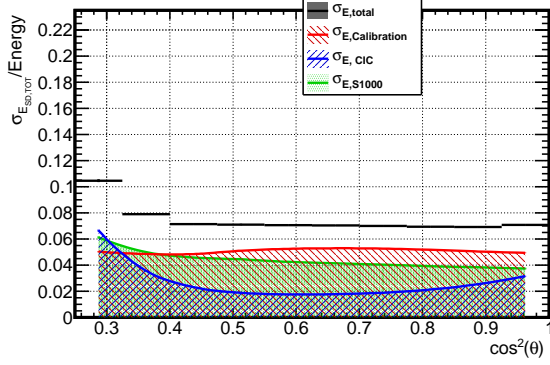
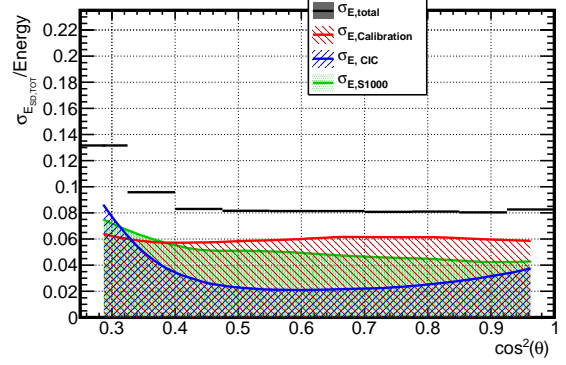
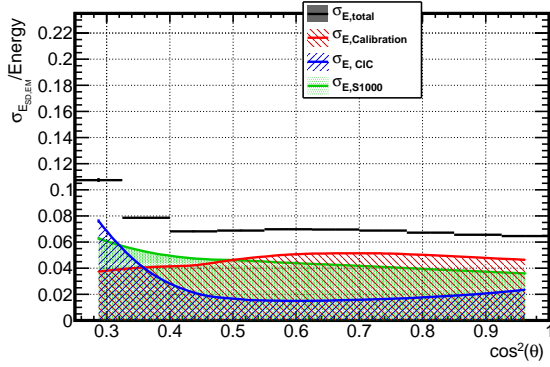
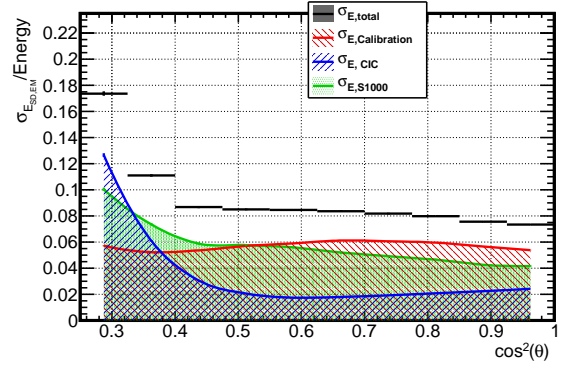
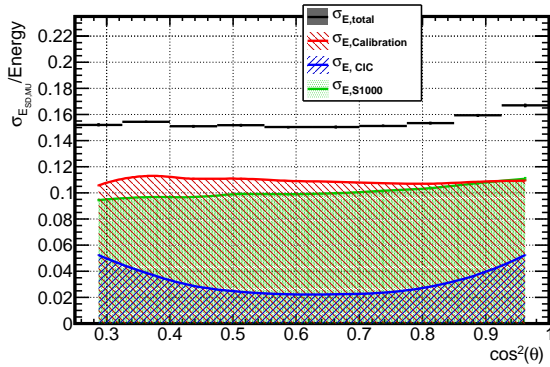
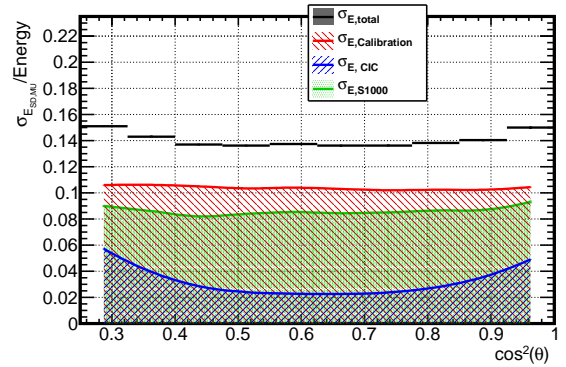
(a) $\sigma_{E_{SD}}/En$, total signal, proton(b) $\sigma_{E_{SD}}/En$, total signal, iron(c) $\sigma_{E_{SD}}/En$, EM signal, proton(d) $\sigma_{E_{SD}}/En$, EM signal, iron(e) $\sigma_{E_{SD}}/En$, MU signal, proton(f) $\sigma_{E_{SD}}/En$, MU signal, iron

Figure 5.26: Evolution of the Energy estimator error E_{SD} as function of the $\cos^2(\theta)$ given by equation 5.37. And the error components that come from the energy calibration parameters ($\sigma_{E_{SD}(calib)}$), from the CIC parameters ($\sigma_{E_{SD}(CIC)}$) and from the S_{1000} ($\sigma_{E_{SD}(S_{1000})}$) given on eq. 5.38.

The error that comes from the CIC parameter has a lower value at $\theta = 38^\circ$, once the CIC is a polynomial around $\cos^2(38^\circ)$. The electromagnetic signal error is almost dominated by the CIC error at low $\cos^2(\theta)$ (inclined events), being much smaller for the other zenith angles.

To see if there is any dependence of the fluctuation on energy in the previous energy calibration fit, in the figures 5.27, the evolution of $(E_{MC} - E_{SD})/E_{MC}$ is plotted with logarithm of the energy. We can see that both on proton (5.27a) and on iron (5.27b) samples, the mean deviations are approximately constant in energy. So the parameter B in eq. 5.35 is adequate to the calibration.

The RMS is also approximately constant on energy, meaning also that the *CIC* function remains similar at different energies (using this calibration). There is also a bias on the energy reconstructed for energies below $\approx 10^{18}$ eV in the iron sample, which is not that relevant because it is an extrapolation of the energy range used in the fit. The same appears for the muon part on the proton sample where we are overestimating the energy at those energies.

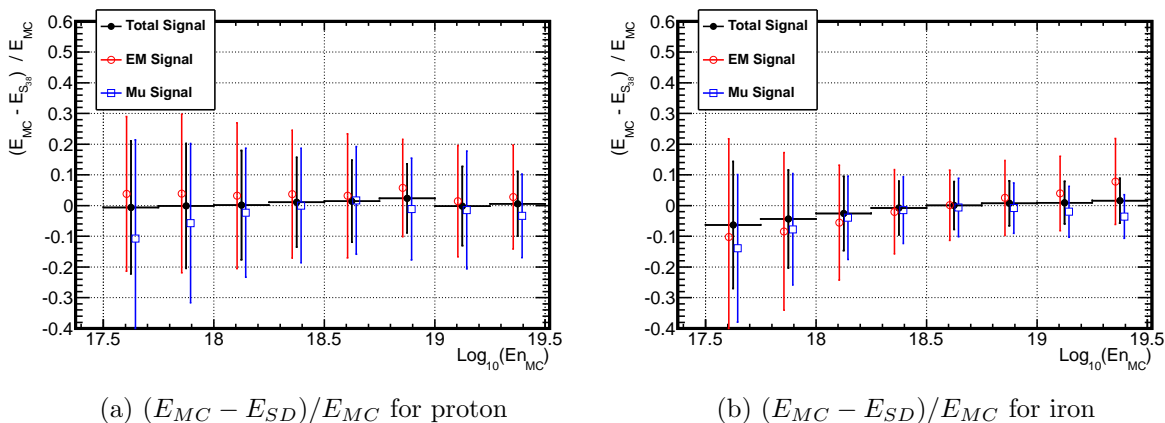


Figure 5.27: Evolution of $(E_{MC} - E_{SD})/E_{MC}$ with logarithm of the energy for the proton (a) and iron (b) samples, for the fit to equation 5.35 with the results on table 5.6. The fits were performed for $\log_{10}(E) > 18.3$, but here, the resolution was extended to $\log_{10}(E) > 17.5$. In black circles, red open circles and blue squares, the Total, EM and MU signals are plotted, respectively. Each samples were divided in equal energy bins for the three signals. The bin center coincide with the Total signal bins centers. The points for EM and MU signals were slightly displaced on x axis for better view.

The resolution of the energy calibration for the three signals is different for several zenith angles. In the figures 5.28, we have the evolution of $(E_{MC} - E_{SD})/E_{MC}$ with zenith angle θ , for the fit to equation 5.35 with the results on table 5.6, for proton (left) and iron (right). The mean deviations and RMS for muons are approximately constant, which mean it is almost independent of θ . This happens, since the *CIC* function is mostly constant. Basically, since the muons interacts much less in atmosphere, the number of muons that arrive on the ground should be approximately the same. So the ground signal depends mainly on the geometry of the detector in relation to the incident muons. In this way, the *CIC* is almost constant between 0° and 60° , and the resolution independent of θ .

The EM and TOT signal, however, have a bias in the mean deviation of $(E_{MC} - E_{SD})/E_{MC}$ for low $\cos^2(\theta)$ (higher angles), and the RMS also increases with zenith angle. This feature also happens due to the *CIC* behaviour. The EM particles are very attenuated across the atmosphere and the shower will cross an higher atmospheric depth for higher θ . This means that for higher angles we should have less EM component and the electromagnetic *CIC* has a big slope. The relative EM signal changes from around 0.2 at $\sim 60^\circ$ to 1.5 at $\sim 0^\circ$ (see figure 5.19). If we have much less signal for higher angles, we will also have a worst resolution (with much more fluctuations). These fluctuations will increase in amplitude when we convert it to S_{38} , since for example, at $\sim 55^\circ$ we have $\approx 20\%$ of the signal at 38° . The EM signal RMS is very small for low angles (even a little smaller than for the TOT signal). However, the calibration deteriorate for higher angles and we have a big deviation and RMS at 60° . For the TOT signal we have an intermediate situation between the MU and EM signal. It is good at low angle but not as bad as EM at high angles.

In relation to the $(E_{MC} - E_{SD})/E_{MC}$ bias with $\cos^2(\theta)$ we see a structure which is related with two factors. On one hand, the distribution of number of events in $\cos^2(\theta)$ is not completely constant, which means that we are overestimating or underestimating the value S_{1000} used in the *CIC* at some $\cos^2(\theta)$ bin. This difference should be accounted in the error (given by \sqrt{N}). On other side, we can see that the structure is oscillating, which means that the differences come also from the residuals between the actual place where the point in the *CIC* curves are and the place where the *CIC* fit is. This difference should be accommodated within the error coming from the *CIC* parameters, except for the first points of the electromagnetic signal.

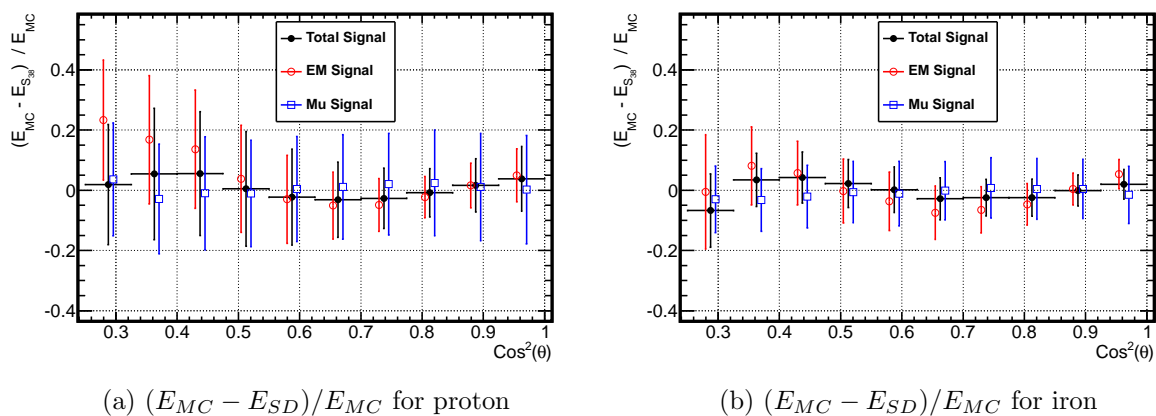


Figure 5.28: Evolution of $(E_{MC} - E_{SD})/E_{MC}$ with $\cos^2(\theta)$ (Zenith angle), for the fit to equation 5.35 with the results on table 5.6. The TOT, EM and MU signal are plotted with black circles, red open circles and blue squares respectively. The samples were divided in 10 bins of $\cos^2(\theta)$ like in the *CIC* procedure, but the points for EM and MU signals were slightly displaced for better view. It was only used events with $\log_{10}(E) > 18.3$.

The fluctuations in the EM component for high angles are very high, so to understand the resolution we could get, we should not look at an energy calibration with all zenith angle range,

but perform the energy calibration (eq. 5.35) for different interval of zenith angle. The linear $\log_{10}(S_{38}) - \log_{10}(Energy)$ dependence was fitted again for 4 different θ intervals separately. After performing the energy calibration again for the events with zenith angle within $\theta \in [0^\circ, 29.9^\circ]$, the $(E_{MC} - (E_{SD})/E_{MC}$ distribution is plotted on the figure 5.29 for the three components and for proton (left) and iron (right) samples similar to the plots in fig. 5.23. The same distribution is also displayed on the figure 5.30 for the zenith angle interval $\theta \in [48^\circ, 60^\circ]$.

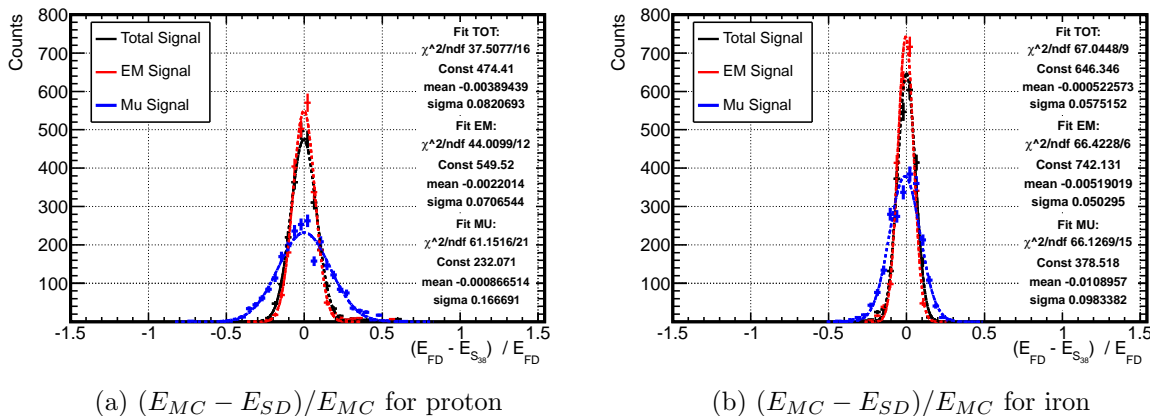


Figure 5.29: Distribution of $(E_{MC} - (E_{SD})/E_{MC}$ for the proton (left) and iron (right) samples for the zenith interval $\theta \in [0^\circ, 29.9^\circ]$. On black, red and blue we have the distributions for the total signal, EM signal and Muonic signal component. In a dashed line we have gaussian fits to each distributions with the respective parameters written on the plots. The distributions have for proton $mean_{TOT} = 0.002$, $RMS_{TOT} = 0.096$, $mean_{EM} = 0.004$, $RMS_{EM} = 0.085$ and $mean_{MU} = 0.002$, $RMS_{MU} = 0.171$. For iron we got $mean_{TOT} = 0.001$, $RMS_{TOT} = 0.0616$, $mean_{EM} = 0.001$, $RMS_{EM} = 0.0534$ and $mean_{MU} = -0.006$, $RMS_{MU} = 0.102$.

In the first figure we can see that the calibration with the EM signal for vertical events is as good as the one for the total signal. The RMS for the EM component is 8.5% and 5.3% (for proton and iron) while the total RMS is 9.6% and 6.2% (for proton and iron). This means that the EM component can be used for the energy calibration at low zenith angles. In relation to the last zenith bin, the EM calibration is much worst for both proton and iron, since as said before it has much more fluctuations.

In figure 5.31, the RMS of $(E_{SD} - E_{MC})/E_{MC}$ is plotted for four bins of zenith angle. For $\theta < 29.9^\circ$ the RMS of the EM component is significantly lower than the RMS of the total signal. While for the higher zenith angle bins, for $\theta > 38^\circ$, it rises quickly due to the EM attenuation, yielding larger statistical fluctuations. At this region, the signals starts to be dominated by muons. If there is variation in the muon number (and they are different from the hadronic models), it will be reflected in the SD energy. We need to be careful when using the total signal to calibrate the energy and to estimate the number of muons, because they will be highly correlated (we used the same signal for both variables).

Nonetheless, a better accuracy in the shower energy will be attained at least for $\theta < 38^\circ$, if the EM signal component is used in the energy calibration instead of the total signal in the SD.

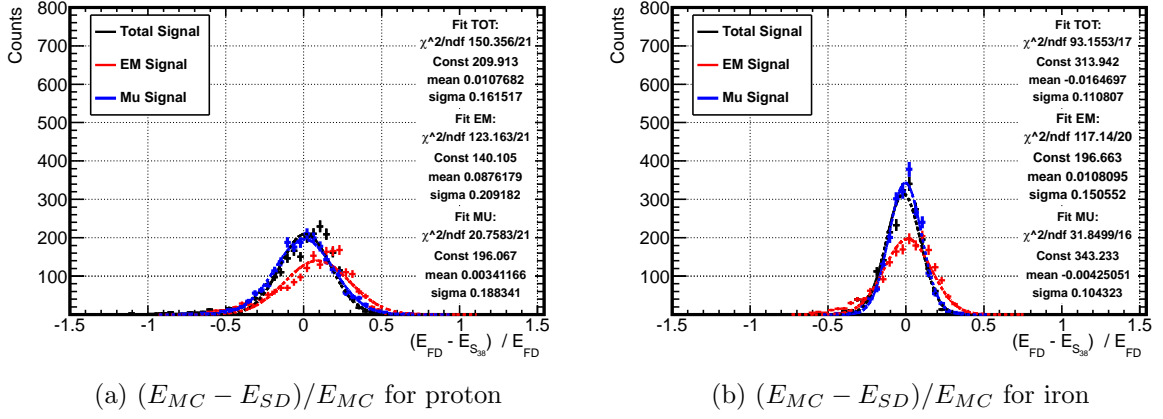


Figure 5.30: Distribution of $(E_{MC} - (E_{SD})/E_{MC}$ for the proton (left) and iron (right) samples for the zenith interval $\theta \in [48^\circ, 60^\circ]$. On black, red and blue we have the distributions for the total signal, EM signal and Muonic signal component. In a dashed line we have gaussian fits to each distributions with the respective parameters written on the plots. The distributions have for proton $mean_{TOT} = -0.007$, $RMS_{TOT} = 0.209$, $mean_{EM} = 0.066$, $RMS_{EM} = 0.229$ and $mean_{MU} = 0.002$, $RMS_{MU} = 0.198$. For iron we got $mean_{TOT} = -0.021$, $RMS_{TOT} = 0.122$, $mean_{EM} = 0.008$, $RMS_{EM} = 0.172$ and $mean_{MU} = -0.002$, $RMS_{MU} = 0.108$.

This way, combining a detector that allow us to separate Total signal from muonic signal (like MARTA), we could have a region where the energy calibration on SD would be considerable independent on the muon number. And the other detector would give the value for the muon number.

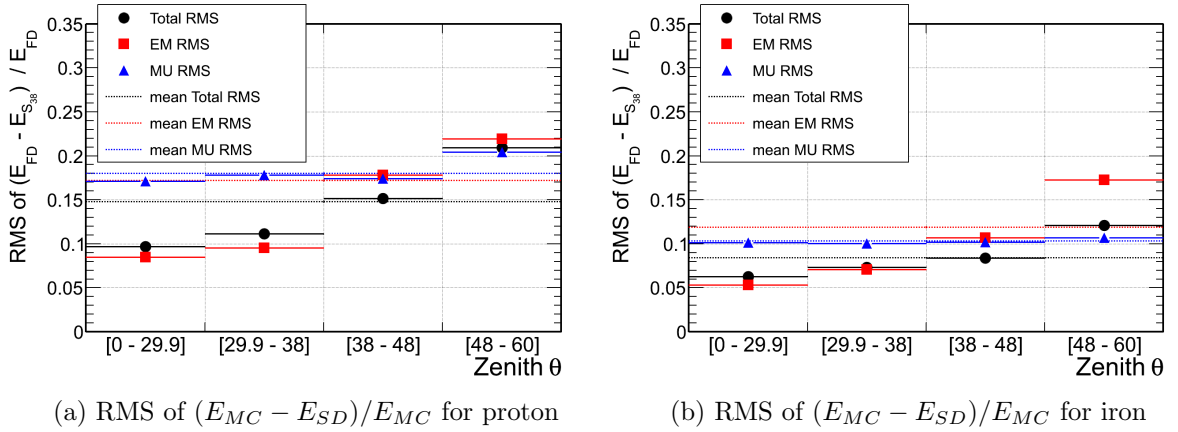


Figure 5.31: RMS of $(E_{SD} - E_{MC})/E_{MC}$ in four bins of zenith angle with approximately the same statistics. The black circles, red square and the blue triangles corresponds to the total, EM and MU component respectively. The dashed lines correspond to the RMS of all angles, with the same colors rule. The fits to the linear $\log_{10}(S_{38}) - \log_{10}(Energy)$ dependence of eq. 5.35 were perform for each bin separately.

Table 5.7: RMS of $(E_{SD} - E_{MC})/E_{MC}$ in four bins of zenith angle with approximately the same statistics and in all angle range. E_{SD} is the energy estimated using the S_{38} estimator. The results for proton and iron samples. The fits to the linear $\log_{10}(S_{38}) - \log_{10}(Energy)$ dependence of eq. 5.35 were performed for each bin separately.

Signal	$RMS_{[0-60]}$	$RMS_{[0-29.9]}$	$RMS_{[29.9-38]}$	$RMS_{[38-48]}$	$RMS_{[48-60]}$
Proton primary					
Total	0.148	0.096	0.11	0.15	0.21
EM	0.172	0.085	0.95	0.18	0.22
Mu	0.180	0.17	0.18	0.17	0.20
Iron primary					
Total	0.084	0.062	0.073	0.084	0.12
EM	0.116	0.053	0.071	0.11	0.17
Mu	0.107	0.10	0.10	0.10	0.11

5.3 Mixture Composition

The real cosmic ray results, suggest a mixture of several compositions. On this section, the previous analysis was applied considering a sample with half proton events and half iron events (basically adding the proton and iron sample with the same statistics).

Constant Intensity Cut

After the intensity plots were obtained, the CIC method was performed and the CIC curve, for each signal component, is displayed in the figure 5.32. The plots are normalized to $S_{38} = 1$ and the point with intensities $I = 85, 170, 340$ and 600 events are shown. The gray region corresponds to the four intensities average, the average fit to equation 5.33 is shown in red and parameters written on the table 5.8. The separate fits to each sample are also superimposed on dashed lines.

The three CIC curves were very similar, so the 50%/50% sample is also similar with each component individually. This means that a mixture of composition don't change this picture and the energy calibration can be analysed on the following.

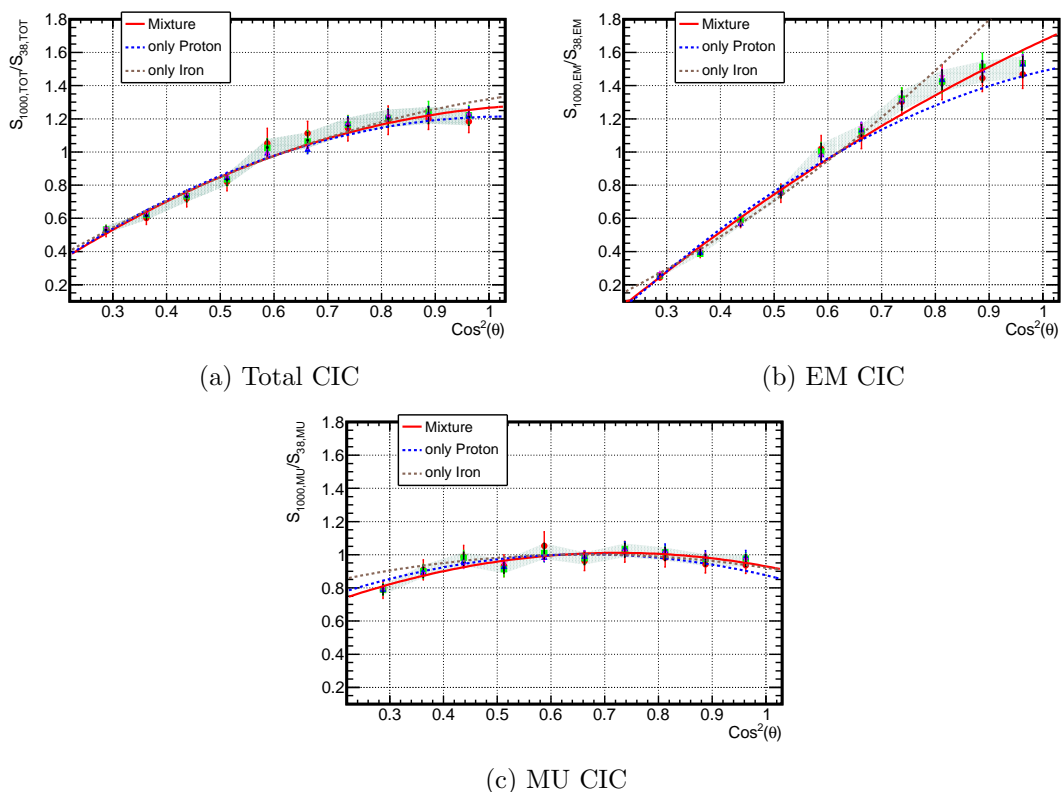


Figure 5.32: Attenuation curves, for several signal intensities: Total (a), EM (b) and MU (c) signals. These curves were made for intensity cuts with 85, 170, 340 and 600 events (in red, green, blue and pink respectively) and are normalized to the S_{38} . The average curve is shown in the gray fill with the respective fit to equation 5.33 (and parameters written on table 5.8). There are also the CICs obtained for the proton and iron sample individually and written on table 5.5.

Table 5.8: Fit parameters obtained from the fit of eq. 5.33 for the CIC average of the CIC curves with intensities 85, 170, 340 and 600 (similar to figure 5.18). The total, EM and MU signals results are present (for the 50% proton 50% iron sample).

Signal	S_{38}	a	b	χ^2/ndf
Mixture of 50% proton 50% iron primary				
Total	1.00 ± 0.02	1.11 ± 0.06	-1.09 ± 0.28	7.2/7
EM	1.00 ± 0.02	2.03 ± 0.07	-0.69 ± 0.26	13.4/7
MU	1.00 ± 0.02	0.22 ± 0.05	-1.06 ± 0.27	4.6/7

Energy Calibration

The attenuation curve with equation 5.33, allows to obtain the energy estimator S_{38} . At this step the estimator can be calibrated with the events energy. In the figures 5.33, the estimator S_{38} is plotted as function of energy with the respective fit to eq. 5.35 (on red line), for each kind of signals. The dashed lines corresponds to each proton and iron sample fits, performed separately. The calibration parameters of the mixture are written on table 5.9.

The energy calibration of the mixture is between the proton and iron curve for the muon and

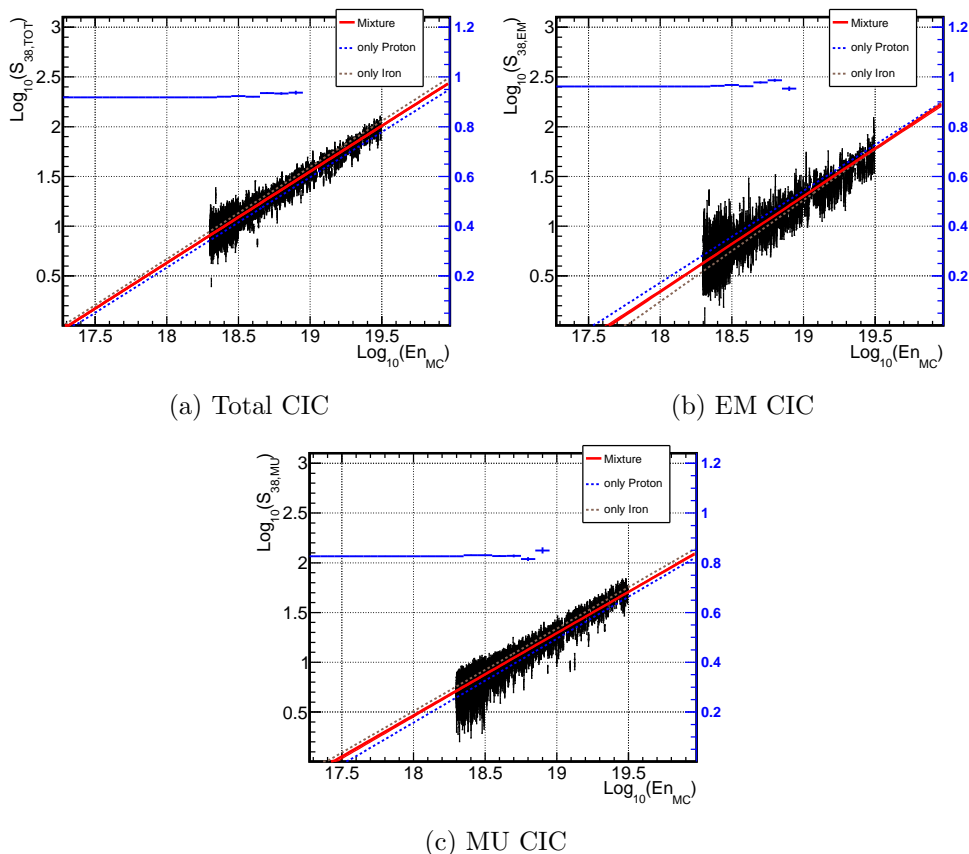


Figure 5.33: S_{38} energy estimator for the total (a), EM (b) and muonic (c) signal components in the SD as function of MC Energy. The red lines correspond to the linear calibration with equation 5.35 (parameter written on table 5.9. The dashed lines corresponds to the proton and iron samples separately, with parameter from table 5.7. The blue lines are the calibration slopes B (whose magnitude can be read in the blue axis on the right), taking into account all the points with energy equal or above the MC energy in each bin. .

Table 5.9: Energy Calibration of the S_{38} estimator parameters of equation 5.35 for the total, EM and MU signals in the SD. Results for the 50% proton 50% iron sample.

Signal	A	B	χ^2/ndf	a	b
	Mixture of 50% proton 50% iron primary				
Total	-15.89 ± 0.02	0.918 ± 0.001	5.0	17.31 ± 0.02	1.089 ± 0.001
EM	-16.97 ± 0.02	0.961 ± 0.001	7.3	17.65 ± 0.02	1.040 ± 0.001
MU	-14.41 ± 0.03	0.826 ± 0.001	5.8	17.43 ± 0.06	1.210 ± 0.002

total signal. There, the iron events have an higher signal than the proton events. In the case of the electromagnetic signal, at high energies, the proton and iron events seems to have similar signal, and at lower energies the proton is slightly higher, probably due to the difference on the X_{max} and consequent attenuations between the X_{max} and the ground.

To understand the performance of the energy calibration, the distribution of $(E_{MC} - E_{SD})/E_{MC}$

is plotted in the figure 5.34. The bias are less than 2.5% and the RMS are around 0.12 – 0.22, similar to the one obtained for proton (figure 5.23). With respect to the P value of eq. 5.39, the picture is worst since the RMS is slightly higher than one, around 1.40 – 1.63. It should be noticed that, these distributions for the muonic components are no longer Gaussians, since the iron signals are higher than the signals on proton events (as seen in the figure 5.33).

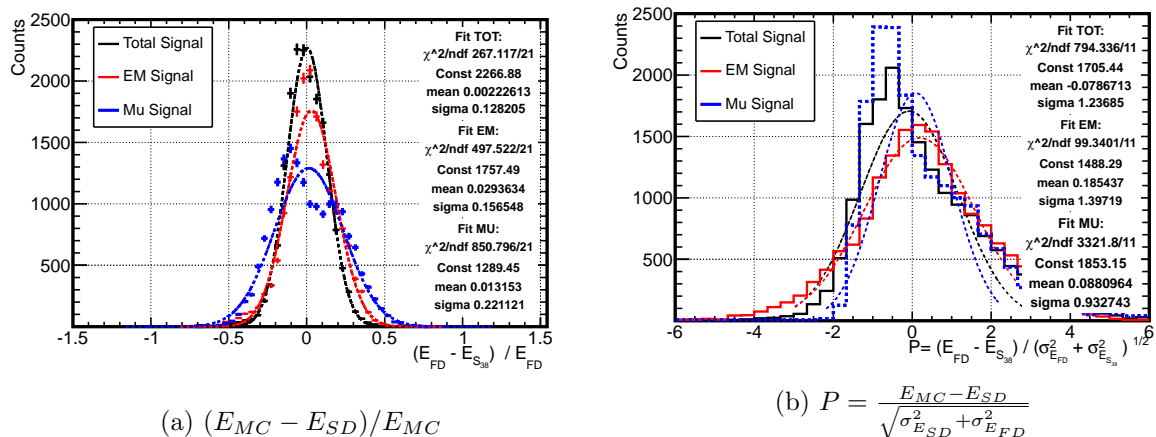


Figure 5.34: Distribution of $(E_{MC} - E_{SD})/E_{MC}$ (a) and $P = \frac{E_{MC} - E_{SD}}{\sqrt{\sigma_{E_{SD}}^2 + \sigma_{E_{FD}}^2}}$ (b) for the mixture composition sample. On black, red and blue we have the distributions for the total signal, EM signal and Muonic signal component. In a dashed line we have gaussian fits to each distributions with the respective parameters written on the plots. The distributions have in a) $mean_{TOT} = -0.002$, $RMS_{TOT} = 0.14$, $mean_{EM} = 0.025$, $RMS_{EM} = 0.163$ and $mean_{MU} = 0.009$, $RMS_{MU} = 0.215$. In b) it gives, $mean_{TOT} = 0.21$, $RMS_{TOT} = 1.51$, $mean_{EM} = 0.27$, $RMS_{EM} = 1.63$ and $mean_{MU} = 0.294$, $RMS_{MU} = 1.40$.

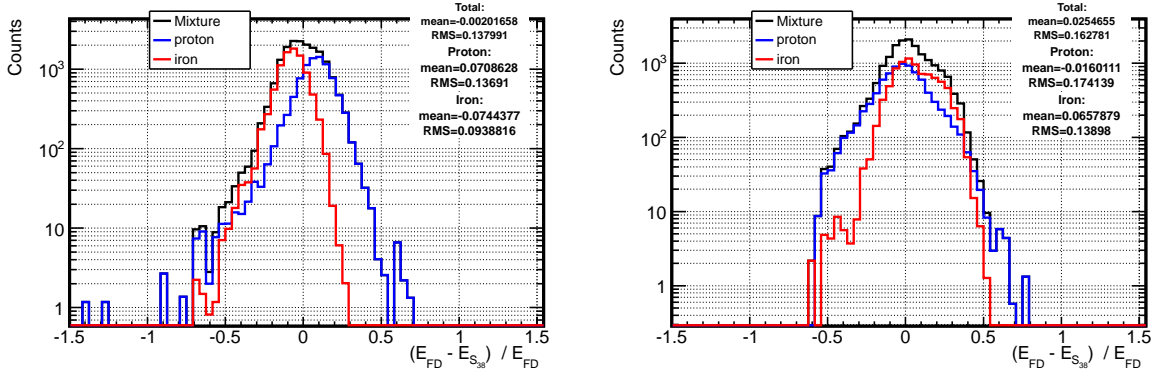
In the figure 5.35, the $(E_{MC} - E_{SD})/E_{MC}$ distribution are displayed for the three components again, but showing the contributions of the proton and iron events. In the case of the energy calibration using the muonic signals, the proton events obtain an energy underestimated by around 17.4% and the iron events are overestimated around 15.5%, despite almost no bias including all events. This means that in a scenario with different cosmic ray compositions, the muonic signal lead to some bias. This signal is used in the very inclined events, so if there were 50% protons and 50% irons, then the final number of muon in the iron events would be underestimated and overestimated on the protons.

For example, if the X_{max} is recovered from the ground signal, like in section 7.3.1 or from the rising time, using the muonic signal to estimate the energy, it would bias the final results. Considering a 50% proton/iron composition, the proton events X_{max} would be bias to higher values, while the iron would be bias into smaller values. Since the proton X_{max} is higher than the iron one, this would means that the final X_{max} RMS would be higher than what was expected. The RMS would be bias by an order of magnitude around 9 g/cm^2 .

The $(E_{MC} - E_{SD})/E_{MC}$ electromagnetic signal, fitted with the mixture, presents lower bias for each component. The proton events energy are overestimated around 1.6% and the iron

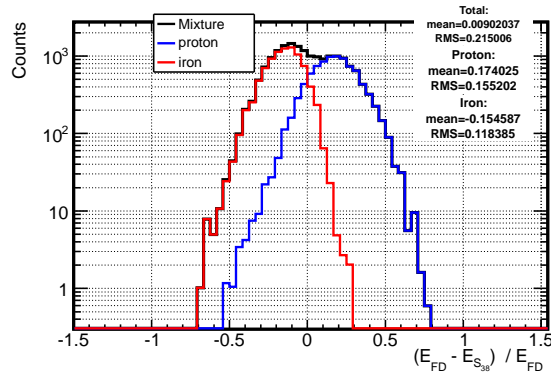
underestimated by 6.5%. This means that is much safer to consider an energy calibration on the ground signal using the electromagnetic signal. Nonetheless, at higher zenith angles it can not be used, since the electromagnetic signal is too low and the fluctuations increases.

The total signal calibration behaviour is between the others signals. In that calibration, the protons events have an energy underestimated by 7% and irons energy overestimated by 7.4%.



(a) $(E_{MC} - E_{SD})/E_{MC}$ for Total signal

(b) $(E_{MC} - E_{SD})/E_{MC}$ for EM signal



(c) $(E_{MC} - E_{SD})/E_{MC}$ for MU signal

Figure 5.35: Distribution of $(E_{MC} - E_{SD})/E_{MC}$ for the total (a), electromagnetic (b) and muonic (c) signals, in the 50% proton/iron sample. The contributions from the proton and iron events are discriminated as well.

5.4 Summary and prospects

Throughout this chapter, the energy calibration of the SD tank were performed, using the total, electromagnetic and muonic signals separately.

The LDF were fitted event-by-event with a likelihood and the β parameter were parametrized as function of zenith angle and size parameter S_{1000} . The β were afterwards fixed on the fitting procedure to reduce the S_{1000} fluctuations.

The cosmic ray flux is constant on $\cos^2(\theta)$, above the energy of the SD full efficiency. In this way, the Constant Intensity Cut method can be applied to correct the shower size parameter S_{1000} into S_{38} , since the statistics is higher at 38° . The signal must be corrected using the CIC, because for different zenith angles, the atmospheric depth crossed by the shower is different and the signal on the ground is different, being more or less attenuated. The muon CIC were mainly constant, as a result of the low attenuation of muons on air.

The electromagnetic signal was highly attenuated with the atmospheric depth, the EM signal for inclined events is $\sim 14\%$ of the value for vertical events at the same energy (as seen on the CIC). In this way we have a lot of fluctuation in some events and much less fluctuation in others at the same energy.

The size shower parameter S_{38} were used as an energy estimator for each component separately. After calibrating the energy with the S_{38} , considering all zenith angle range ($[0^\circ, 60^\circ]$), the reconstructed energy had biases less than 2% for proton and iron for the three components. The fluctuations are around 15% and 9% for proton and iron, considering the total signal, while they are around 17% and 12% for proton and iron considering the electromagnetic signal. These result could disregard the premise of using the electromagnetic signal as an energy estimator. Nonetheless, it was seen that the electromagnetic is very attenuated on the atmosphere, so the electromagnetic signal changes considerably with zenith angle, being less reliable at higher zenith angles.

At lower zenith angles, it was seen that the electromagnetic energy resolution is comparable or slightly better than the one obtained from the total signal (table 5.7). Under the circumstances, the electromagnetic signal could be used to estimate the SD energy at zenith angle below around 40° . The energy estimation would be in this way less correlated with other analysis on the muon content, allowing a better understand of the data.

Moreover, considering a mixture of 50% protons and 50% iron events, it was seen that the average calibration would bias the energy of each one in about 7% on the total signal due to the different muonic content, while the electromagnetic would give a smaller bias (+1% to -6% for proton and iron), being mostly related to the different X_{max} positions. Other studies could also be carried out as described on section 7.3.1.

Comparison between data and QGSJETII-04

The LDF β parameter, attenuation CIC curve and energy calibration curves have been determined on the data for the total component, so it is possible to compare them with the proton and iron simulation predictions of the QGSJET-II model used on the previous chapter 5.

On the first section of that chapter 5 the β parameter of the LDF (in eq. 5.2) was parametrized as function of $\sec\theta$ and $\log_{10}(S_{1000})$ for the total signal in the tanks. The parametrization was obtained from the hadronic interaction model QGSJET-II for proton and iron primaries. These values are compared to the actual value obtained for the β on the data in the section 6.1.

The CIC function and the calibration function were also determined for the model QGSJET-II and will be compared to the data in sections 6.2 and 6.3 respectively.

The size parameter N_{19} and R_{μ} on the inclined events can also be compared to the muonic S_{38} , since the signals on the very inclined events are essentially muons (section 6.3).

6.1 Beta Parameter

It was seen in the previous chapter, that the ground signal can be described by the LDF written in the equation 5.21. The β can be described by a linear dependency on $\log_{10}(S_{1000})$ and a polynomial of second order in $\sec\theta$, given by:

$$\beta = [a_0 + a_1 \log_{10}(S_{1000})] + [b_0 + b_1 \log_{10}(S_{1000})] \sec\theta + [c_0 + c_1 \log_{10}(S_{1000})] \sec^2\theta \quad (6.1)$$

where a_0, a_1, b_0, b_1, c_0 and c_1 are the fit parameters.

After performing the fits with the β and S_{1000} free and applying the cuts present on the table 5.2 the behaviour of the β parameter is obtained. The figures 6.1 are plotted here again for clear description. There, the average β for the remaining events after the cuts, can be seen for the model QGSJET-II for proton and Iron primaries. Each point is an average on bins of $\log_{10}(S_{1000})$ and $\sec\theta$.

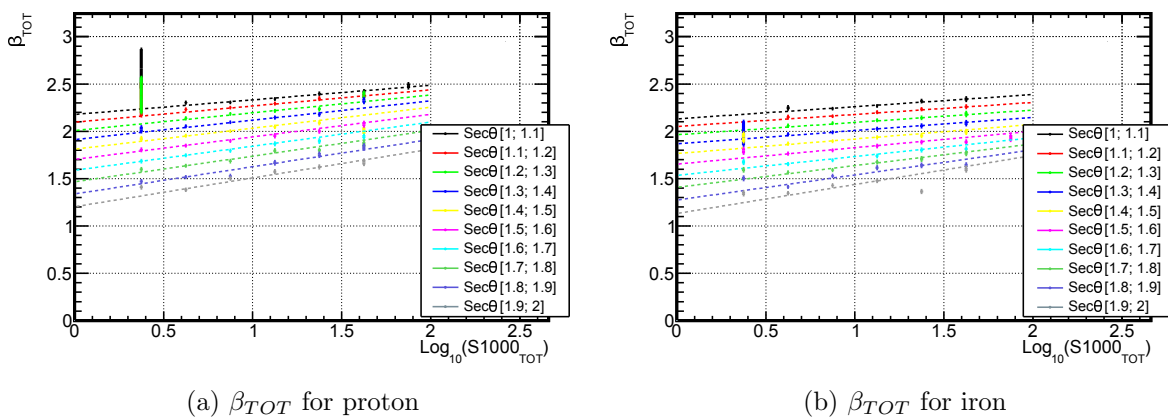
(a) β_{TOT} for proton(b) β_{TOT} for iron

Figure 6.1: The β dependence as function of $\log_{10}(S_{1000})$, for 10 bins in $\sec\theta$. The events remaining after cuts from table 5.2, are binned in $\log_{10}(S_{1000})$ intervals for several $\sec\theta$ ranges, for demonstrations purposes. The lines are the fit to equation 6.1, with all events (not binned) and the fit results are written in the table 6.1. On the left and right are the results for proton and iron primaries respectively, with QGSJET-II model.

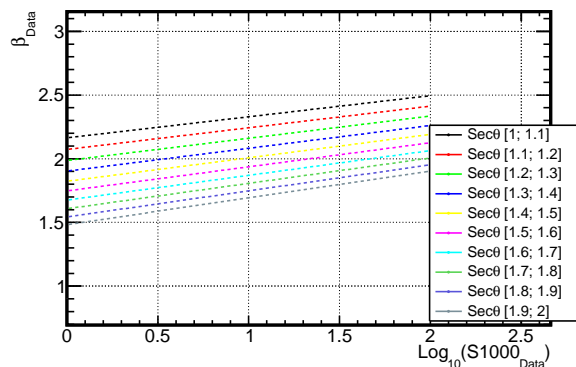


Figure 6.2: The β dependence obtained for data in [221] is plotted as function of $\log_{10}(S_{1000})$, for 10 bins in $\sec\theta$. The values from data corresponds to the total signal.

The fit to equation 6.1, to fix β , however, is performed without binning, event by event, minimising the χ^2 (there isn't any necessity for binning the β values). The β evolution is drawn in the figure 6.1 with dashed lines for both primaries and the same hadronic interaction model and the parameters results are written on the table 6.1.

The same analysis was performed to the data events and can be found in [221]. On the figure 6.2, the β parametrization found in data is plotted as function of $\log_{10}(S_{1000})$, for 10 bins in $\sec\theta$ as before. The parameters of equation 6.1 are written on the table 6.1.

To compare both samples with Data, in the following, the β for the proton and iron primaries are plotted together with the Data for different $\sec\theta$ bins.

On the figure 6.3, the β for the total signal, for the proton and iron samples and data are

Table 6.1: Parameters describing the dependence of β on $\log_{10}(S_{1000})$ and $\sec\theta$, resulting from the fit of eq. 6.1 to the selected sample of simulated events (proton and iron) and to data from [221].

Parameter	Data fit from [221]		Proton simulation		Iron simulation	
	value	uncertainty	value	uncertainty	value	uncertainty
a_0	-3.35	0.23	-2.637	0.085	-2.507	0.007
a_1	-0.125	0.151	0.0272	0.0924	-0.467	0.007
b_0	1.33	0.31	0.0889	0.1182	-0.0483	0.0063
b_1	-0.0324	0.2114	-0.176	0.130	0.602	0.006
c_0	-0.191	0.105	0.331	0.039	0.386	0.003
c_1	-0.00573	0.07210	0.00317	0.04442	-0.266	0.003
χ^2/ndf	1.443		0.921		0.973	

drawn on the same plots, for the first and last $\sec\theta$ bin. On the left is for $\sec\theta \in [1, 1.1]$ and on the right for $\sec\theta \in [1.9, 2.0]$. On the figure 6.7 the same plots are displayed for all $\sec\theta$ bins. For low zenith angles the Data and the TOT parametrization for proton samples are in a very good agreement. Nevertheless, we should say that the values obtained for proton and iron, despite being different, they are both compatible within the uncertainty, and also compatible with the Data.

For the last 3 $\sec\theta$ bins they begin to differ, being the β_{TOT} of the simulation, lower than for the Data one. This can be observed on the figure 6.3 right (for the last $\sec\theta$ bin). This feature is in contradiction to what would be expected. First we should note that the β values for proton and iron in the simulations are always a little shifted. This happens because β_{TOT} for total signal should lie between the β_{EM} and β_{MU} , the TOT LDF is a sum of EM and MU signals. If the number of muons is high, then the β_{TOT} should be closer to β_{MU} . Since the total signal in iron showers have more muons, then the β_{TOT} should be closer to the β_{MU} than the proton showers (both β_{EM} and β_{MU} can be seen in figures 5.11 and 5.12).

Considering the deficit in muons in our models, the β_{TOT} on the data should be closer to the muons β_{MU} , and the β_{TOT} from simulation should be higher than the Data. However, for higher zenith angles, where the muonic component dominates, we can see that the β for the data is higher than in simulation being in contradiction with a deficit in muon on the hadronic models (seen in the section 3.7.3.2), unless the muons lateral distributions are not correctly described. These would mean that the Lateral distribution for muons is not well described in the model QGSJET-II .

In the figures 6.8 and 6.9, we can see the evolution of β_{TOT} , β_{EM} and β_{MU} with S_{1000} , where each graphic is a bin in $\sec\theta$. On the same plots, the line from Data fit are also superimposed. We can see that the electromagnetic part as an higher beta than the muonic one, due to higher attenuation of EM particles on the atmosphere, as said before. The TOT part is in middle of both. For low zenith angles the Data and the TOT parametrization are a very good agreement, but they are different at higher zenith angles.

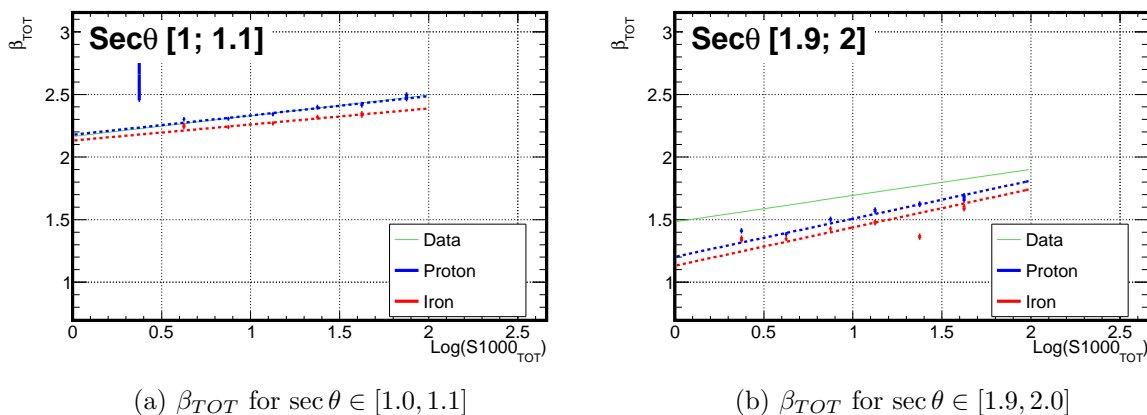


Figure 6.3: The β dependence as function of $\log_{10}(S_{1000})$ for the intervals $\sec \theta \in [1, 1.1]$ (left) and $\sec \theta \in [1.9, 2.0]$ (right), for proton (blue lines) and iron (red lines). The Data are superimposed in green. The lines are the fit to equation 6.1.

6.2 CIC Function

In the section 5.2.2, we perform the Constant Intensity Cut (CIC) for the proton and iron showers simulations with QGSJET-II. The cuts were performed for intensities $I = 85, 170, 340$ and 600 events (drawn on figure 5.18). The CIC behaviour can be parametrized with a polynomial around $\cos^2(38^\circ)$ in equation 6.2 (repeated here):

$$S_{1000} = S_{38} \times CIC(\theta) \quad (6.2)$$

$$CIC(\theta) = (1 + a[\cos^2 \theta - \cos^2(38^\circ)] + b[\cos^2 \theta - \cos^2(38^\circ)]^2).$$

The difference in each cut is the normalization factor, so the CIC curves are all plotted with $S_{38} = 1$ on the figure 5.19. The normalized CIC curves are displayed again in the figure 6.4, where the shadow bands correspond to the average CIC. In red and blue are the CICs for iron and proton showers. The equation 6.2 is then fitted to the average profile and the results are written on the table 6.2. Both proton and iron CIC are very similar changing for low zenith angles ($\cos^2(\theta) \approx 1$).

On the table 6.2, the CIC parameters obtained for the total signal on Data coming from [227] are also written, and it is drawn in a green line, in figure 6.4, together with the simulations. In this analysis, we get a total signal proton CIC similar to the Data. The total iron CIC is a little different due to the difference in the EM CIC, but within the error bars. The relative shower size at high zenith angle (low $\cos^2(\theta)$) for data and simulations are in agreement, which is not in contradiction with the differences on β . The β parameter is the shape of the LDF, while the S_{1000} is the size (normalization) of the LDF.

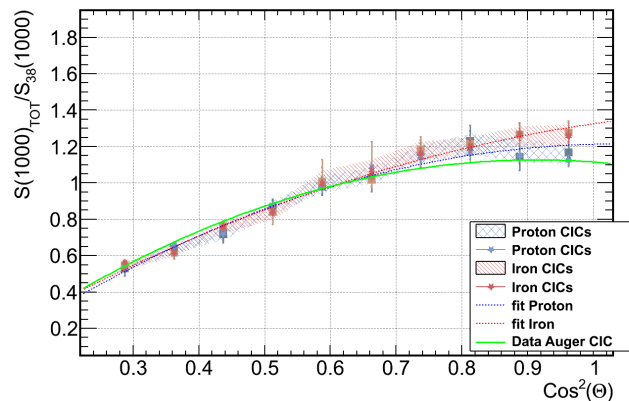


Figure 6.4: The four intensity CIC curves are shown (normalized to the S_{38}) for the total signal. In red the results for iron sample and blue for proton sample. In green we have the Auger Data CIC [227] for the total signal (which is very similar to the total signal proton CIC).

Table 6.2: *CIC* parameters of eq. 6.2 for the total signal of the Data from [227] and proton and iron showers simulated with the hadronic interaction model QGSJET-II .

	a	b	χ^2/ndf
Data from [227]	0.87 ± 0.04	-1.49 ± 0.20	-
Proton primary	1.04 ± 0.06	-1.26 ± 0.28	7/7
Iron primary	1.15 ± 0.07	-0.83 ± 0.30	5.2/7

6.3 Calibration Function

After applying the CIC method, the energy estimator S_{38} can be calibrated with the equation:

$$\begin{aligned} \log_{10}(S_{38}^{tot,EM,MU}) &= A + B \times \log_{10}(E^{tot,EM,MU}) \\ \log_{10}(E^{tot,EM,MU}) &= a + b \times \log_{10}(S_{38}^{tot,EM,MU}) \end{aligned} \quad (6.3)$$

In the figure 6.5, the S_{38} for the total signal is plotted as function of the energy for the proton and iron showers (on the left and right respectively) for the hadronic interaction model QGSJET-II .

The values can be compared to the calibration of the data performed in [155]. The curve corresponding to the data is the green dashed line plotted in the previous figure. The parameters obtain for the data and simulations are written on the table 6.3.

The simulation parameters for iron and proton are similar, but they are not compatible with the Data values within the error bars. Once the EM and MU signal don't have the same slope, then the slope of the S_{38} Calibration should lie between both EM em MU values. According to

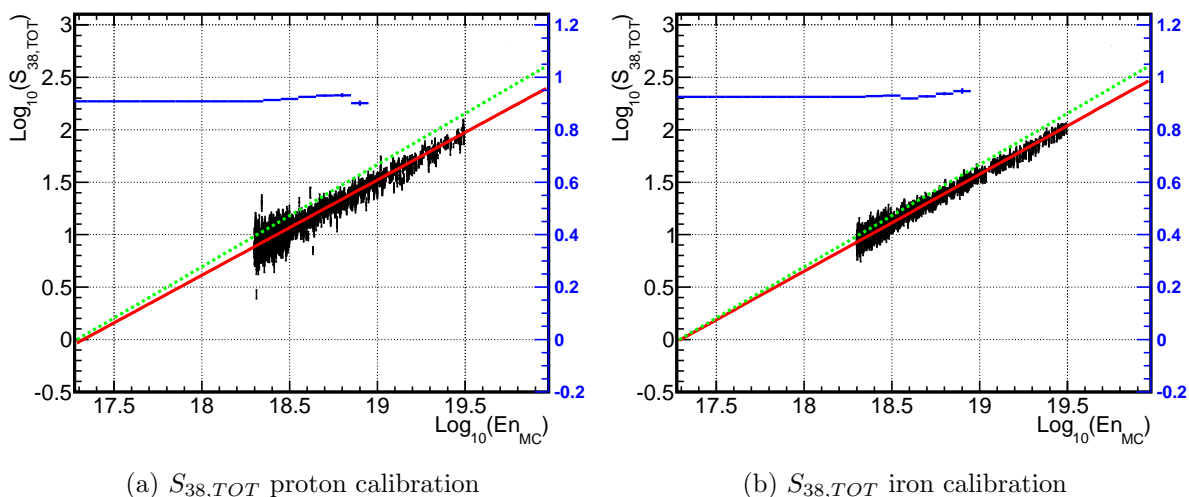


Figure 6.5: S_{38} energy estimator for the total signal in the SD as function of MC Energy. The red lines correspond to the linear calibration with equation 6.3 and the blue lines are the calibration slopes B (whose magnitude can be read in the blue axis on the right), taking into account all the points with Energy equal or above the MC energy in each bin. Data from [155] are displayed in a green line.

Table 6.3: Energy Calibration of the S_{38} estimator parameters of equation 6.3 for the total signals in the SD. Results for the proton and iron sample separately and Data results from [155].

Sinal	A	B	χ^2/ndf	a	b
Data results from [155]					
Total	-16.86 ± 0.12	0.975 ± 0.007	–	17.28 ± 0.011	1.025 ± 0.007
Proton primary					
Total	-15.74 ± 0.03	0.908 ± 0.002	4.80	17.33 ± 0.03	1.100 ± 0.002
Iron primary					
Total	-16.00 ± 0.03	0.925 ± 0.002	2.06	17.30 ± 0.03	1.080 ± 0.002

the previous chapter, in section 5.2.3, the MU slope B is ≈ 0.84 while the EM is about ≈ 0.94 , so the TOT slope B should be in the middle.

In the Data, $A = 0.975$ while for the simulations the values are $A = 0.908$ (proton) and $A = 0.925$ (iron). This means that probably for both A_{EM} and A_{MU} the value on the data is higher than on the simulations.

The Pierre Auger Observatory, currently doesn't have a dedicated muon detector in the full array, however the muon content can be inferred on the normal signals (see section 3.7.3.2). For very inclined events, the electromagnetic component is very attenuated in the atmosphere, so the total signal is dominated by the muons. Subsequently, considering that the signals for events with $\theta > 62^\circ$ are mainly muons, the muonic content can be measured. We can determine the signal at 1000 m, S_{1000} , for these events with high zenith angles, and normalized it to the value

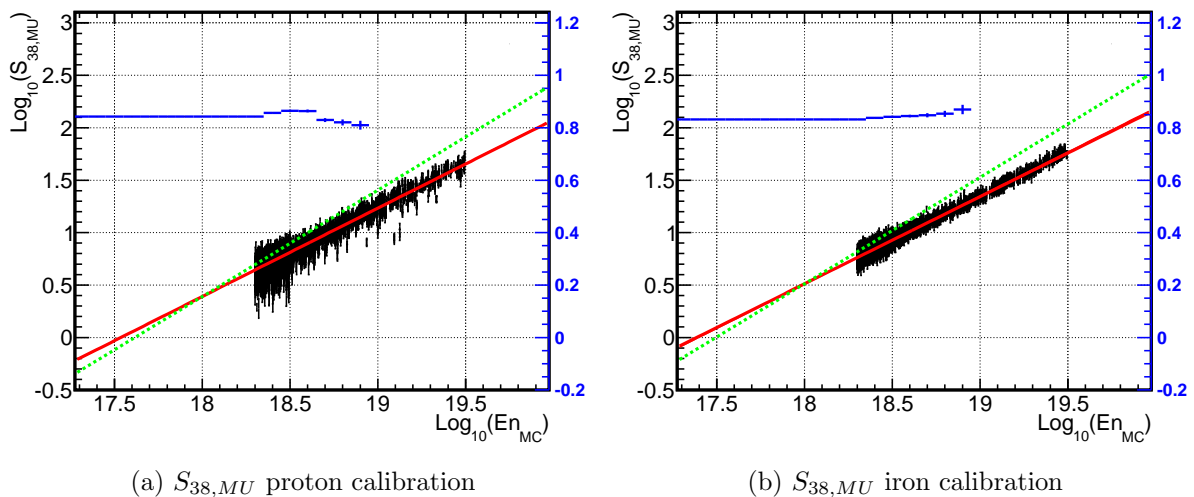


Figure 6.6: S_{38} energy estimator for the muonic signal in the SD as function of MC Energy. The red lines correspond to the linear calibration with equation 6.3 and the blue lines are the calibration slopes B (whose magnitude can be read in the blue axis on the right), taking into account all the points with Energy equal or above the MC energy in each bin. Data result of the N_{19} from ICRC 2013 [155] are displayed in a green line. The Data curve is normalized to the value of the S_{38} calibration at 10^{18} eV.

at 10^{19} eV of QGSJET-II protons, which is known as N_{19} estimator (instead of S_{38}).

In the figures 6.6, the S_{38} for muon signal is plotted as function of the energy with the respective calibration for the proton (left) and iron (right) simulations. The parameters obtained for the calibration are written on the table 6.4.

In [155] and [228], the N_{19} is calibrated and the parameters are also written on table 6.4. We should note that the constant a and A are not suppose to be the same as in N_{19} and $S_{38,MU}$, since we are not measuring exactly the same units, the N_{19} is related to the model QGSJET-II. However, the slope should be similar. On the figure 6.6, the N_{19} calibration curve from ICRC 2013 is displayed in a green line, but normalized to the S_{38} calibration at 10^{18} eV.

The recent calibration parameter of the R_{μ} are also written on table 6.4. The R_{μ} , described on section 3.7.3.2, is the N_{19} corrected to the true muon number on the generator, so the constants a and A are not comparable, but the slope should be.

The result obtained in the previous chapter are completely different from the ones obtained on the Data for the N_{19} analysis. From this analysis the slope is approximately 1, while in the simulation is around 0.84. Accordingly to the modified Heitler model (section 2.3.2.1), the b parameter would range between $b \simeq 0.84$ and $\simeq 0.92$, depending on the multiplicities. The muon results on the simulation seems compatible with the predictions from the Heitler model, for the QGSJET-II model. The N_{19} parameter takes correction for electromagnetic contaminations and muonic halo, resulting in a bias, which is not important for the energy calibration, since it is absorbed.

Similar to the results in the β parameter at high zenith angles, these differences pointing

Table 6.4: Energy Calibration of the S_{38} estimator parameters of equation 6.3 for the muonic signals in the SD. Results for the proton and iron sample separately and Data results from [196, 155, 228] for the N_{19} .

Sinal	A	B	χ^2/ndf	a	b
Data results from R_μ paper [196]					
MU	-19.29 ± 1.043	1.029 ± 0.054	–	18.74 ± 1.41	0.972 ± 0.051
Data results from N_{19} ICRC2013 [155]					
MU	-17.30 ± 0.38	0.985 ± 0.02	–	17.56 ± 0.53	1.015 ± 0.021
Data results from N_{19} ICRC2011 [228]					
MU	-17.72 ± 0.95	0.95 ± 0.05	–	18.65 ± 1.40	1.053 ± 0.055
Proton primary					
MU	-14.78 ± 0.04	0.843 ± 0.002	3.40	17.53 ± 0.05	1.187 ± 0.003
Iron primary					
MU	-14.45 ± 0.04	0.831 ± 0.002	1.55	17.38 ± 0.04	1.203 ± 0.003

out to a difference on the detected muons signal, evolution with energy, relatively to the model predictions. This effect could appear from a change in the composition. Nevertheless, even a composition transition from proton to iron, would not be sufficient to describe the evolution with energy in the R_μ parameter (see reference [196]). We should remember also, that such composition is not favoured by the FD measurements.

6.4 Summary and prospects

On this chapter the results of the chapter 5 were compared to the data. Only the values for the total signal can be compared to the current data, despite it would be interesting to analyse the electromagnetic and muonic component separately.

The β parameter of the total signal on data, at lower zenith angles, are in agreement with the proton simulated sample, but the iron sample is also compatible within the error band. At high zenith angles the β parameter seems to be much higher than expected from both simulations (of proton and iron). The muon β is lower than the electromagnetic one. In this context, since the models have a deficit on muons, as referred on section 3.7.3.2, the total β on data should be closer to the muonic β , which means that the parameter should be smaller than the one seen on the simulations. Nonetheless, the β parameter is higher than the simulations. The only possible explanation for this to happens is that the lateral distribution for muons in the model QGSJET-II is not in agreement with the data. Probably, that can point to an harder muon spectrum in the data than predicted.

The data CIC function is compatible with both proton and iron simulations within the error bars (figure 6.4). At high zenith angles they are very similar despite the β differences on this range.

The calibration curves found on the simulation are different from the one on the data. The one found on the data is around 0.97, while the simulations it is around 0.91 – 0.93 for proton and iron.

With respect to the muon signals calibration, it can be compared to the N_{19} . Nevertheless, the data slope is close to 1, with around 0.98, while from the simulations the slope is around 0.84, consistent with the modified Heitler model predictions. Similar to the results in the β parameter at high zenith angles, these differences pointing out to a difference on the detected muons signal, evolution with energy, relatively to the model predictions.

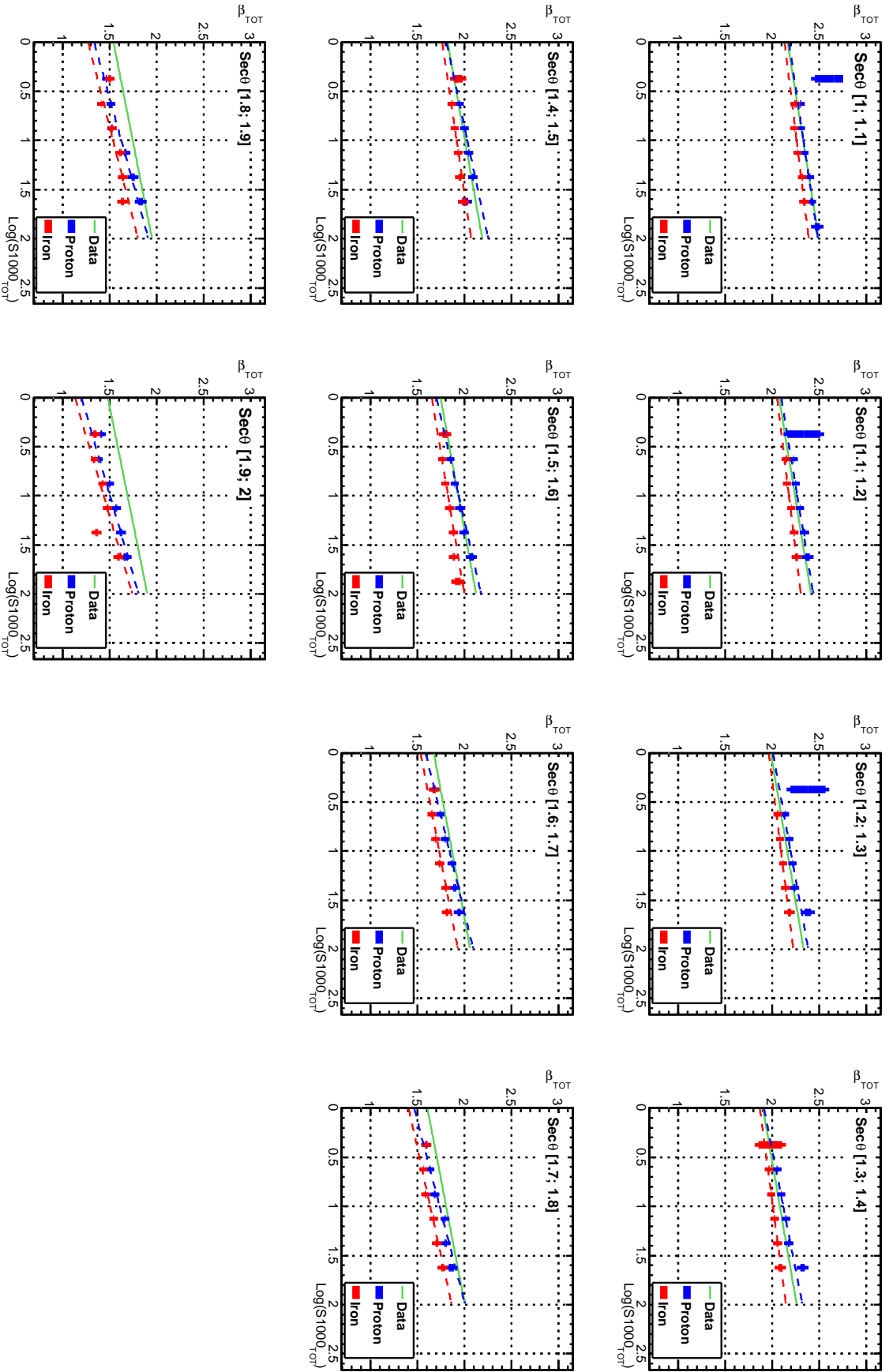


Figure 6.7: LDF β for the total signal as function of $\log_{10}(S_{1000})$ intervals for different $\sec\theta$ ranges. Blue is for proton sample and red is for iron sample. On dashed lines are the fits to the equation 5.23, with parameters in table 5.3, for the components. In green is the Data fit from [221] (see table 6.1).

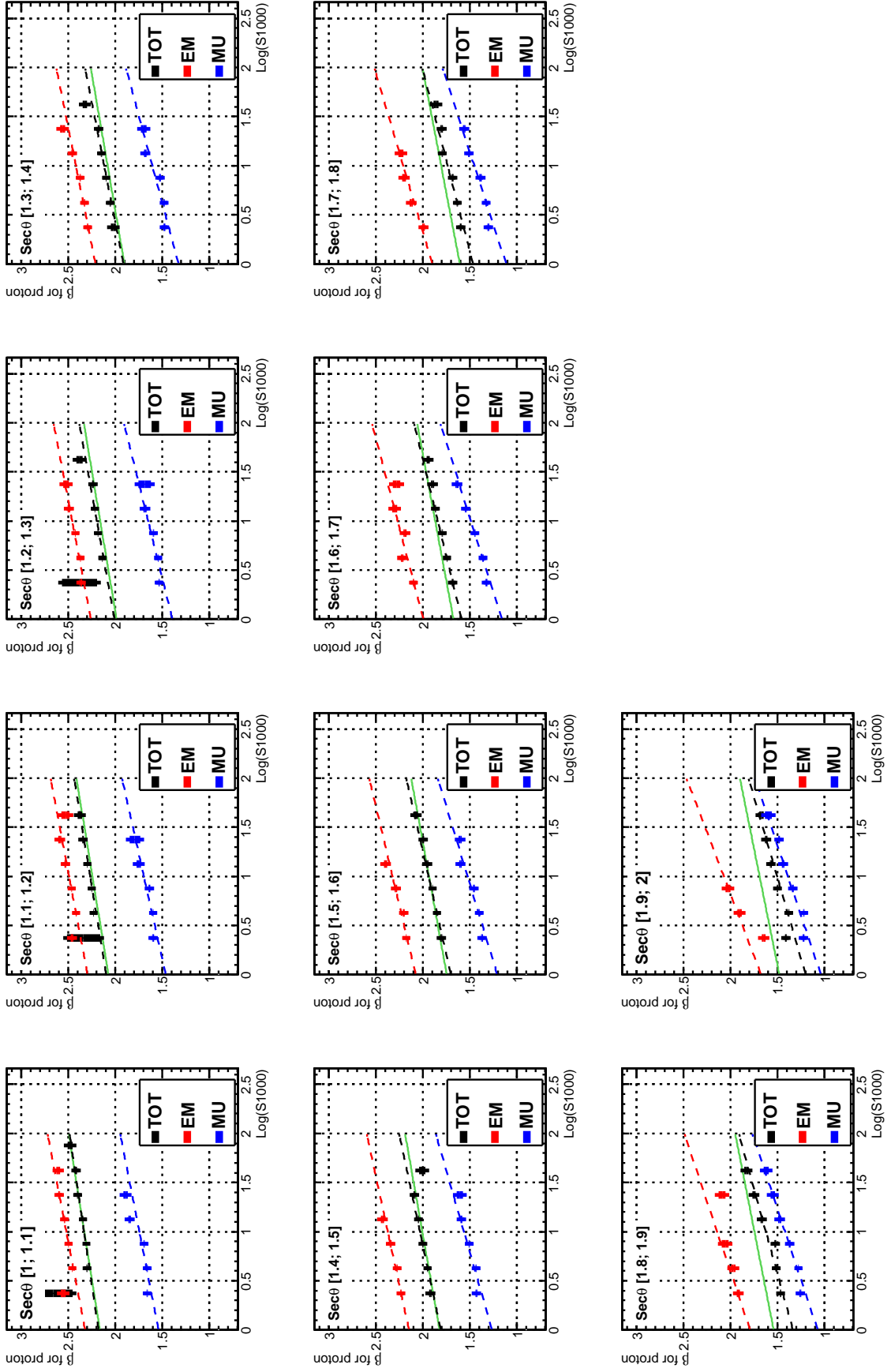


Figure 6.8: β for the three components for proton sample (black for TOT, red for EM and blue for MU) and data (in green) coming from [221]. Each plot corresponds to a different $\text{sec}\theta$ bin. On dashed lines are the fits to the equation 5.23, with parameters in table 5.3, for the components. In green is the Data fit from [221] (see table 6.1).

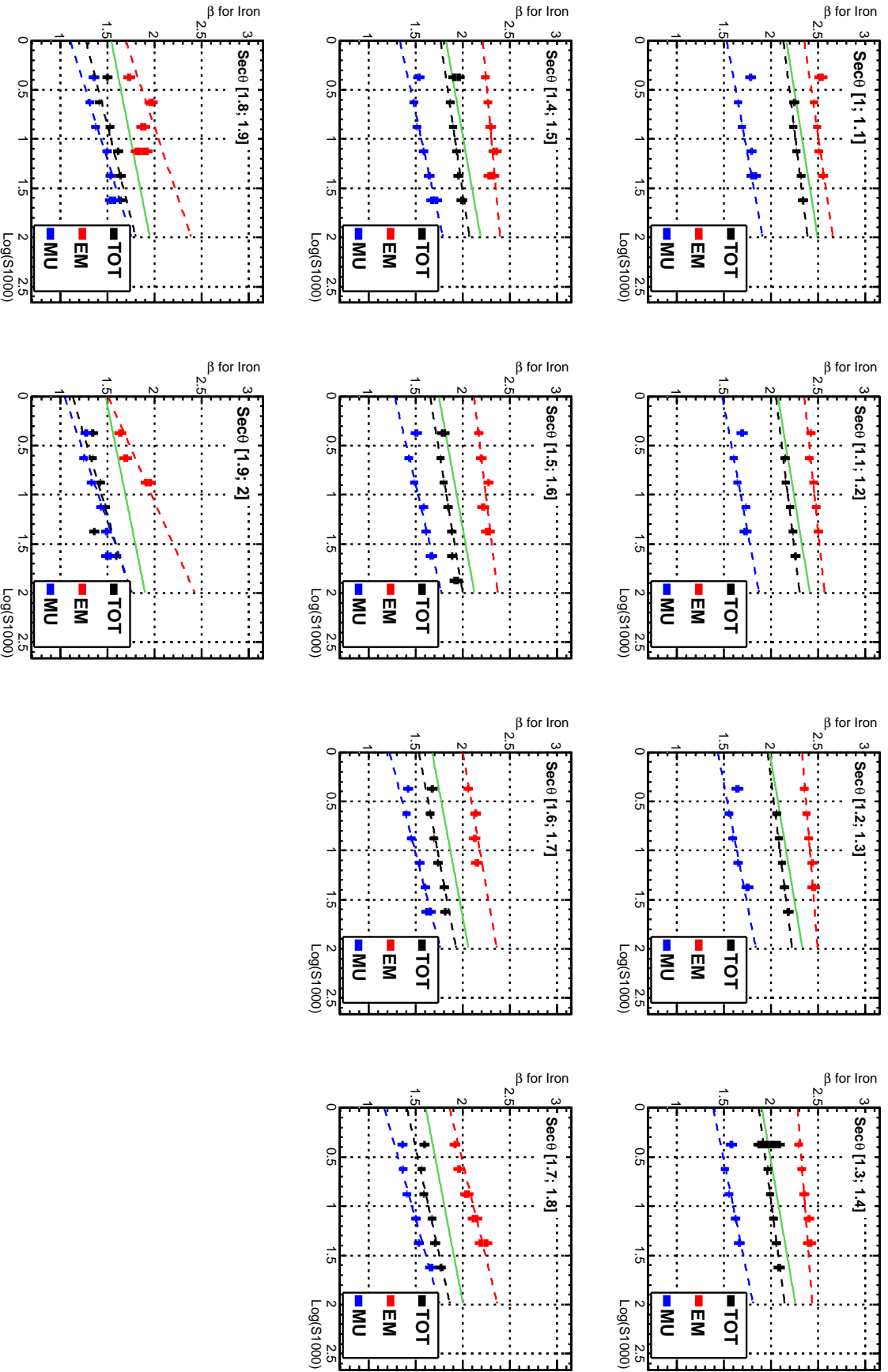


Figure 6.9: β for the three components for Iron sample (black for TOT, red for EM and blue for MU) and data (in green) coming from [221]. Each plot corresponds to a different $\text{sec}\theta$ bin. On dashed lines are the fits to the equation 5.23, with parameters in table 5.3, for the components. In green is the Data fit from [221] (see table 6.1).

Studies with MARTA (Muon Auger RPC for the Tank Array)

The Pierre Auger results are very puzzling with respect to the cosmic ray composition at ultra high energies (UHE). The observatory measurements (on section 3.7), after accumulating statistics, suggest a composition change scenario towards heavier composition[188]. Regardless, the composition scenario can not be disentangled from a change in the hadronic interactions above a certain energy or probably both can occur together. The confirmation of the composition or hadronic change would give an important understanding on the cosmic rays and particle interactions.

The main data inconsistencies come from the comparison between the electromagnetic sector (X_{max}) and the muonic sector (N_μ). In order to address these problems, a future Auger upgrade would be important to measure each component separately. On one hand, it would be important to measure the average (and RMS) of the muon number, as well as the longitudinal Muon Production Depth (MPD). The muon component derives from the charged pion decays, being more closely related to the hadronic shower than the electromagnetic component. Currently, the muons are not directly detected, but they have the most discrepant results, showing the importance of a dedicated muon detector. On other hand, the energy estimator from the SD signals is strongly correlated with the muon number. So, it would be important to perform a more accurate energy measurement based on the SD electromagnetic signal (independent of the muon content), as seen on chapter 5.

A Muon measurement would be also relevant to identify photon initiated showers (enhancing hadronic background rejections) and to reduce the systematics on the shower missing energy.

An R&D project capable of separating the muon and electromagnetic component is the Muon Auger RPC for the Tank Array (MARTA)[213, 214]. This detector array would allow to : measure the energy evolution of the distribution of the muons number in the showers; disentangle mass composition changes from a change in hadronic interactions at high energies; improve the energy measurement by subtracting the muon component from the tank signal; increase the primary photon discrimination power; and improve the estimation of the missing energy in air

showers.

The used of RPCs on cosmic ray is not new, it is a well established technique in accelerator and had been used at Haverah Park in the 90's [229].

In this chapter, the MARTA array will be briefly described (section 7.1) and some future analyses to be carried on with it. On the section 7.2, the average muonic LDFs will be built from the MARTA signals, in an attempt to assess the composition of cosmic rays (using the LDF β parameter). On the section 7.3.1, the electromagnetic X_{max} is obtained from the signals $S_{1000,em}/S_{1000,\mu}$. Finally, the MPD analysis could be extended in the future, and the difference $\Delta X = X_{max} - X_{max}^{\mu}$ compared with the electromagnetic longitudinal length L , on section 7.3.2.

7.1 MARTA project

The idea of the project is to measure the muon content independently from the SD, while maintaining the Observatory present capabilities. In this way, it is possible to measure the electromagnetic profiles with an accurate determination of the energy, while the uncertainties on the muon measurements and energy are not strongly correlated. See the energy calibration using the electromagnetic component on the chapter 5.

The strategy is to place a new detector under the standard Auger Cherenkov tanks. The SD units are sensitive to all charged particles and absorb a big fraction of the electromagnetic component, allowing the underneath detector to measure the muons. The new detector must be able to reach an energy of at least 10^{19} eV, measure the muons down to at least 500 m from the core, even for heavy primaries such as iron (one of the initial requirements). So, they need to be sensitive to measure from a single muon (far from the core) to hundreds of muons. The standard Auger array is not modified, so this new array is backward compatible.

7.1.1 MARTA design

The Muon Auger RPC for the Tank Array proposed here [213], consist of placing a muon detector underneath each tank. The chosen muon detectors are RPC[230]. The RPC were chosen due to their capability of covering very large areas at low cost, excellent performance in many aspects, being used in nuclear and high energy physics and cosmic ray physics research in experiments such as COVER-PLASTEX at Haverah Park[229], ATLAS at LHC and ARGO/YBJ[231].

A scheme of one MARTA unit is represented in the figure 7.1. The baseline configuration is a concrete precast below the SD tank, where four RPC chambers are placed, with a total area about 7 m². The tank and precast act as an absorber, reducing the electromagnet component of the shower in the MARTA measurements. In a first design, the precast above the RPCs has around 20 g of concrete (~ 50 g/cm²). The trigger, timing, communication and power of the RPCs are provided by the SD tank. The RPC module is constrained by the tank area, readout

pad structure (number of channels) and must be able to work with low maintenance, which mean low gas flux operation and low power consumption.

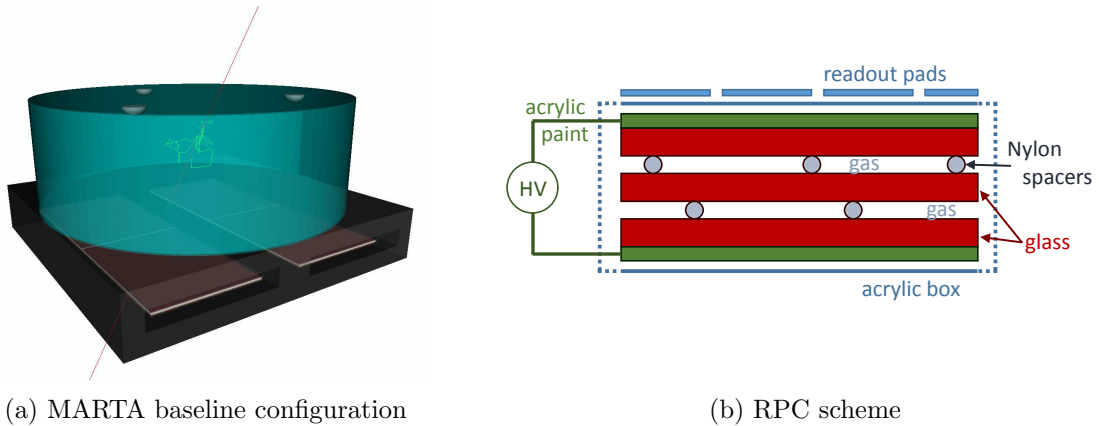


Figure 7.1: (a) Water tank (in green), concrete precast (in black) and RPC chambers (in brown) in the MARTA baseline configuration [213]. (b) RPC scheme with two gaseous gaps, high voltage plates and readout.

7.1.1.1 RPC (Resistive Plate Chambers)

The Resistive Plate Chambers (RPC)[230] are fast gaseous detectors widely used as muon detectors (for example at LHC). It consist in two plates of highly resistive material separated by a gap of gas of the order of the millimetre. The outer surfaces of these plates are coated with a conductor and a high voltage is applied (few kV) (see figure 7.1b). The idea is that when a particle passes through the gas gap, it ionises the gas and the high electric field amplifies this ionization by an electron avalanche. The resistive plates stop the avalanche development in each gap, but a fast signal can be induced by the movement of the electrons and pickup at electrodes. Narrow gap width allows to achieve good time resolution while several gaps can be used to achieve high efficiency.

The use of RPCs at Auger requires several specific points to be fulfilled, such as: very reduced gas flow for reduced maintenance (aiming at 1 kg/year); impervious to humidity, mostly because of its effect on high-voltage (HV) insulation, internal and external; stable efficiency within large temperature excursions; reasonably dark counting rate; low construction, installation and operation costs.

In the baseline design, each RPC module[232] has $1.5 \times 1.2 \text{ m}^2$. After several tests [233], it was chosen a structure of two gaseous gaps of 1 mm, with the glass separated by Nylon monofilaments (fishing line). The high voltage is applied in a layer of resistive acrylic paint, on the outer glass surfaces. The set is closed inside a permanently glued acrylic box, with only two output for the high voltage and two for gas input and output. The Tetrafluorethane (R-134a), a common refrigeration gas, is used for the gaseous gap. It is the main component of the gas mixture used in most modern RPC installations. The RPC gas box is then covered with the readout plane

with several pads, the cables are attached to each pad and the ground cables are soldered into an aluminium plate bolted into the cover plates. Then, everything is enclosed in a 3 mm thick aluminium shielding box.

Each RPC chamber will consist in a grid of 64 pads with dimensions $15 \times 20 \text{ cm}^2$ arranged in a 8×8 matrix and the electronics has 256 acquisition channels.

7.1.2 MARTA studies

The water on the SD tank acts as an absorber of the electromagnetic component with around $\sim 120 \text{ g/cm}^2$ of material. The precast concrete, also provide further additional shielding of 50 g/cm^2 . Nevertheless, there are particles entering by the sides of the tank crossing a smaller depth of absorber and the electromagnetic contamination will be higher. The slant mass crossed by the particles in the station before reaching each of the RPC pads is displayed in the figure 7.2a, for a 40° zenith angle shower. On the red region, the slant mass crossed is higher and the electromagnetic contamination lower, so a fiducial area can be defined in the analysis, on an event by event basis, by selecting only the pads with low electromagnetic contamination. An electromagnetic contamination threshold of 0.5 of the total signal was set in defining the fiducial area.

After selecting a fiducial area, is important to see the ratio of the signal from the shower electromagnetic component to the signal from muons (including muon decays, and hadrons) as a function of the distance to the shower axis (in the figure 7.2b). The ratio is below or of the order of 30% for 40° showers and 50% for vertical showers, at distances of 500 m to the core. Moreover, for 60° showers the electromagnetic contamination is negligible at all distances and the fiducial area can be considered as essentially the total RPC area.

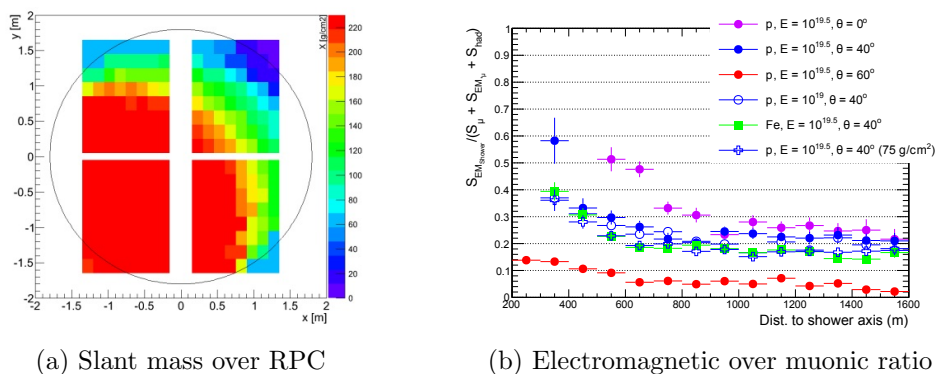


Figure 7.2: (a) Slant mass crossed by the particles in the station before reaching each of the RPC pads, for an incidence shower with 40° . (b) Electromagnetic over muonic (including muon decays, and hadrons) ratio, selecting a fiducial area with electromagnetic contamination below 0.5. From [213] by B. Tomé.

Tank calibration

The number of atmospheric particles in each pad per minute is higher than 300, so they can be

used to calibrate each RPC pad. More important, the usual tank calibration uses atmospheric muons as referred on chapter 3, so on the figure 7.3a, the SD signal from atmospheric particles is plotted in black. The muon peak can be seen at around 1.2 VEM with the low signal peak, mainly due to e.m. particles. Requiring a coincidence with MARTA RPCs, the usual tank calibration can be improved. The low energy peak is suppressed requiring a single hit in one RPC pad, red line. Increasing the requirement to one hit only in a central region ($r < 0.5$ m), the electromagnetic component and clipping muons signal are essentially eliminated.

Furthermore, the muon peak shape, requiring one RPC hit, change with the tank Tyvek reflectivity, being a good observable for the tank operation (figure 7.3b). The sensitivity to this effect can be further improved by selecting trajectories.

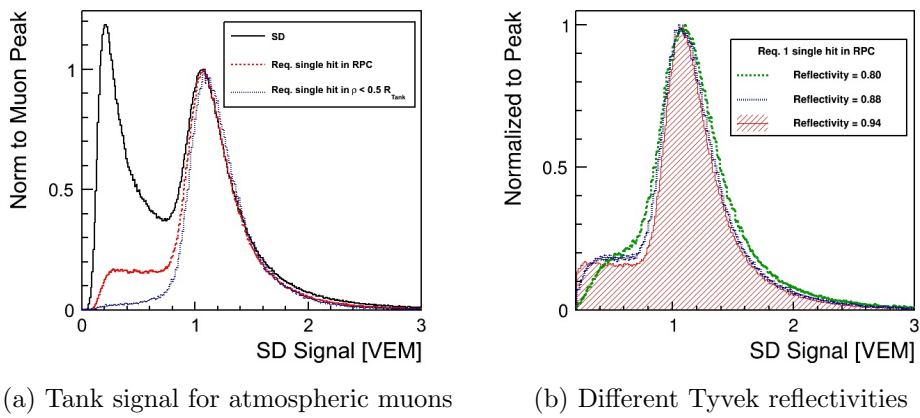


Figure 7.3: (a) The total tank response in black, events with single hit (in one RPC pad) in red and one single hit in a pad in a central region of the RPCs (radius $r < 0.5$ m) in blue. (b) Tank signal for atmospheric muons requiring one single hit in the RPC for different Tyvek reflectivities. From [214] by R. Conceição.

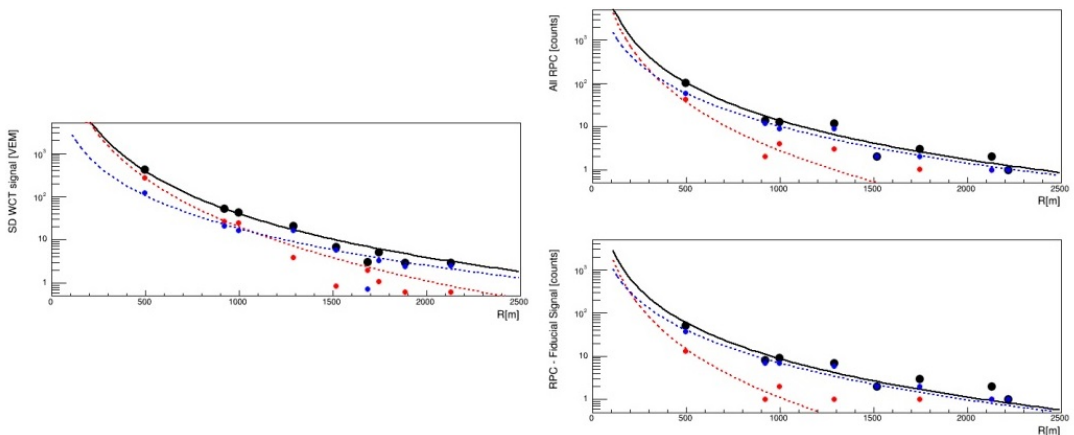


Figure 7.4: Combined fit for one event (proton, QGSJET-II.04 , $E=10$ EeV, at 38°) in the tank and RPC's total and fiducial area. The electromagnetic (red) muonic (blue) and total (black) components displayed. From [214] by S. Andringa.

Segmentation EM and MU

The SD tanks are sensitive to both electromagnetic and muonic component, while MARTA is more sensible to muon (especially the fiducial area). In this way, doing combined fits to the LDFs measured both in the MARTA fiducial and non-fiducial areas as well as in the tank, allows to estimate the electromagnetic and muonic contents of the shower. These fits must take into account the effective areas, the absorption, the conversion VEM / particles and EM/MU halo (considered as $\sim 10\%$, but changes with particle spectrum as a function of r). The shape of the fits change accordingly to the zenith angle and energy as seen in section 5.1.2.1. In the figure 7.4, it is shown for one event with the respective fits.

MARTA array can also improve the MPD reconstruction and other variables could be used to analyse the shower as will be seen on the following.

7.2 LDF's on MARTA

The MARTA array would allow to study the lateral distribution of muons on the ground. For instance, it is possible to build an average LDF of the muon content. In the figure 7.5, the average lateral profile, obtained by averaging 300 events with 10^{19} eV and 38° zenith, are plotted for several primaries. The normalization is different (the size ρ_{1000}) and the shape parameter, such as the slope β of the LDF, could be used to distinguish composition.

As seen on the section 3.1.3.1, the LDF can be described as a NKG function (eq. 3.10). For the case of the muons, the Auger $f_{LDF}(r, \theta, E)$ will be considered:

$$\rho(r) = \rho_{1000} \left(\frac{r}{1000} \right)^\beta \left(\frac{r_s + r}{r_s + 1000} \right)^\beta, \quad (7.1)$$

where $\rho(r)$ is the muon density as function of the distance r to the core, $r_s = 700$ m, ρ_{1000} and β are the parameter to fit. In the figures 7.6a and 7.5 the density of muons in the fiducial area is represented, note that the fiducial area can vary from about ~ 5 m² to ~ 7 m², which means that a density $\rho = 1$ could correspond to about seven muons.

There are several ways to recover every β and ρ parameters, we can choose two way with mathematical sense. One is fitting each event with a likelihood similar to the one defined on section 5.1.1 and obtain an average value of the parameters for the events (they will be denoted as $\beta_{LH} < \beta >$ and $\rho_{1000,LH} < \rho_{1000} >$). To apply the likelihood of eq. 5.12, it is not necessary to convert the MARTA signals into number of particles, since it counts particles.

The other way is to add all events in an average profile and fit the function minimizing a χ^2 , since after adding several events, the errors can be considered as Gaussian (they will be denoted as $\beta_{\chi^2} < LDF >$ and $\rho_{1000,\chi^2} < LDF >$). To fit the average profile, the fitting range is very important, because if the fit begins too early, it would get saturated stations and the average signal would have a flat baseline at small radius. If the radius is high, problems from the silent

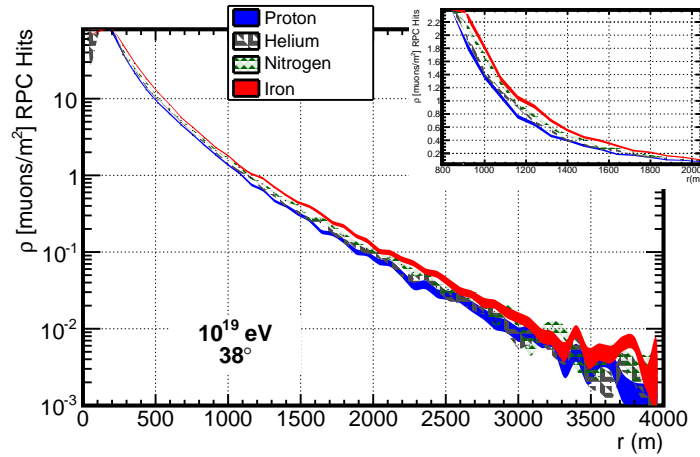


Figure 7.5: Average lateral profile on MARTA for proton, helium, nitrogen and iron for 38° and 10^{19} eV.

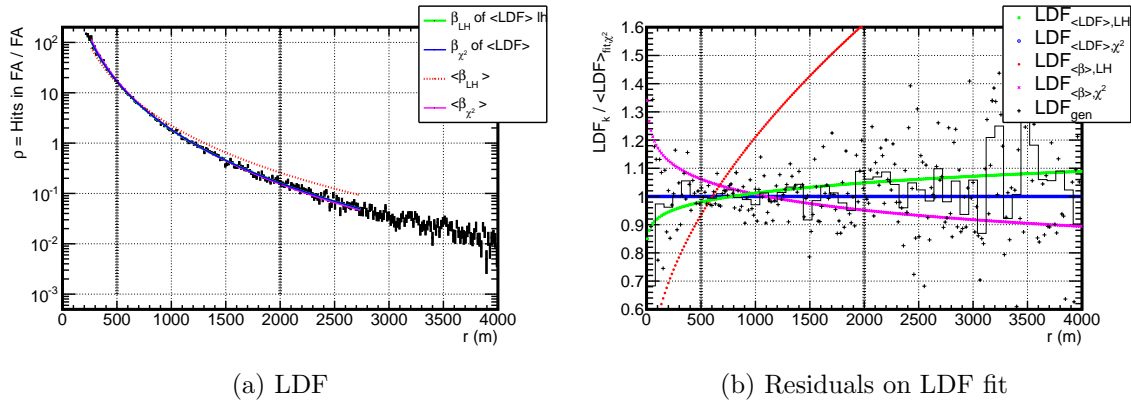


Figure 7.6: Average lateral profile with the several fits (a) and the residuals (b) with respect to the fit results of the average LDF with χ^2 (considering 300 events). In blue and green are the fit to the average LDF using a χ^2 minimization, or the likelihood (eq. 5.1.1) respectively. The average $\langle \beta \rangle$ and $\langle \rho_{1000} \rangle$ event-by-event fitted with the likelihood or the χ^2 are in red and pink respectively. The lateral profile in the toy is plotted with the stars and re-binned in the black lines.

stations would arrive. The fitting range considered on this chapter will be $r \in [500, 2000]$ m. In this way the saturation station will not be considered and at this step the silent station don't present a problem, since they are not present (see section 7.2.3 for further details).

It is also possible to fit the defined likelihood to the average and minimizing the χ^2 event-by-event, to observe the result, but they don't have mathematical sense. The best way to fit the lateral distributions is to use a χ^2 minimization instead of the likelihood used on the section 5.1.1. To see the stability of the fit a toy model was done considering the 1500 m array, with signal on the stations obtained from a known LDF. In each station fluctuations with the Poisson distribution were added to the LDF value of that station. The signals on the station were

determined several times, where each LDF has a random core and the parameters $\rho_{1000} = 1.85$ and $\beta = 2.1$ (similar values to proton shower with 10^{19} eV and 38°). To each parameter, β and ρ_{1000} , were added a Gaussian fluctuation with $\sigma = 0.15$, which is on the same order of the β and ρ_{1000} RMS, event-by-event.

The result of each parameter are plotted in the figure 7.7, as function of the number of events added to the mean LDF, or to the average parameter event-by-event. As can be seen, the best estimators would be the ones obtained from the χ^2 minimization. The values obtained using the likelihood defined previously have a bias both on the β and ρ_{1000} .

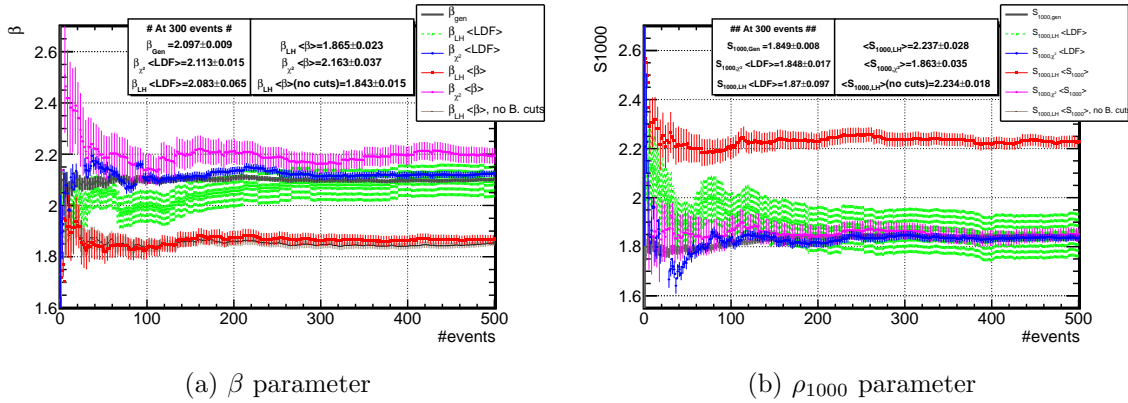


Figure 7.7: Fitting result of the parameters β and ρ_{1000} as function of the number of events considered for it. In dark grey is the generated values, in blue and green are the fit to the average LDF using a χ^2 minimization, or the likelihood (eq. 5.1.1) respectively. The average $\langle \beta \rangle$ and $\langle \rho_{1000} \rangle$ event-by-event fitted with the likelihood or the χ^2 are in red and pink respectively. On brown is the average event-by-event with likelihood applying the Billoir cuts, of eq. 5.22.

In the figure 7.6a, the average lateral profile is plotted with corresponding fits. Again, the χ^2 fit seems the best one. On right, figure 7.6b, the residual are plotted with respect to the χ^2 fit. The average shape is on average similar to the χ^2 fit, but as expected the likelihood fit event-by-event over-estimate the signals for large radius. Since at large radius the statistics is Poissonian, while at lower radius the statistics is Gaussian, with much less fluctuations, that means the likelihood behaviour would be dominated by the high statistics stations. The χ^2 minimization, by its turn, has similar weights along the radius and gives better β and ρ_{1000} estimators.

These results seem to contradict the method used in chapter 5, nevertheless, the SD energy calibration must be performed on an event-by-event basis and there are no problem in having a bias since it would be corrected in the CIC and calibration curve. The important on the calibration method is to reduce the fluctuations on the S_{1000} and correct it on the energy calibration curve.

Since the statistics at Auger is not infinite, it would be wise to analyse the parameter considering a realistic number of events. On the figure 7.7, it can be seen that at 300 events the parameter have a value close to the one with higher statistics and the parameter don't change too much

by adding more events. In this way, on the further fits, only 300 events will be considered.

7.2.1 Fixed energy bin

Several sample of events were simulated using MARTA configuration in `Offline`, with the fixed energies of $10^{18.5}$, 10^{19} and $10^{19.8}$ eV, for the fixed zenith angles 21° , 38° and 52° . The QGSJET-II.04 model were used on these samples and 300 events will be considered on this section. On data there are no fixed energy bins, so it is not possible to connect the event numbers with a time interval of data acquisition. Nevertheless, considering a data binning with $\Delta \log_{10} E \sim 0.1$ and three bins on angle (between $0^\circ - 60^\circ$), at 10^{19} eV, 300 events are roughly one year of data, while at $10^{19.8}$ eV it corresponds to about ~ 22 years of data.

The average lateral profile (LDF) of muon density in MARTA for proton, helium, nitrogen and iron can be seen on the figure 7.5 for 38° with 10^{19} eV. The profile for the different compositions looks different, so in this section, the parameter β and ρ_{1000} will be analysed as possible composition estimators.

The fits to the average profiles were performed on the range $r \in [500, 2000]$ m, for all energies, angles and composition including 300 events. On the figure 7.8 is an example of one event with respective parameters fitted with the χ^2 minimization.

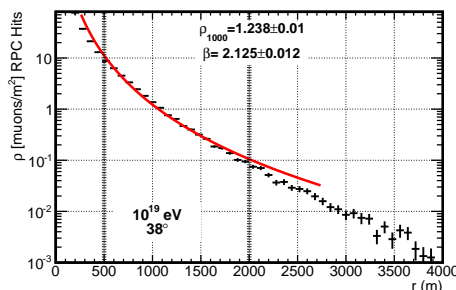


Figure 7.8: Fit from a χ^2 minimization to the average of 300 event, of proton with 38° , 10^{19} eV and in the range $r \in [500, 2000]$.

The evolution with angle and energy of the slope β_{χ^2} (fitting the average $\langle LDF \rangle$) is plotted in the figure 7.9a, while the β_{LH} (fitted event-by-event with the likelihood) is the figure 7.9b. The $\langle \beta_{LH} \rangle$ is relatively different between different energy samples, however between compositions it is very similar. That was also seen for proton and iron in the muonic tank signal on section 5.1.2.1. The $\langle \beta_{LH} \rangle$ is not a good composition estimator. The β_{χ^2} on other side, shows smaller differences between the energy bins, but larger differences for the different compositions. The main reason for this to happen, is that by construction, the likelihood gives an high weight to the high signal stations, biasing the result (figure 7.7), while the χ^2 minimization of the average profile gives similar weight in all radius range, with closer result to the actual slope value. As follows, the slope β_{χ^2} should be considered as a discriminator variable between the compositions. Together with other parameters, it could be an important estimator as will

be analysed on the subsequent text.

The slope β evolves with zenith angle. In the figures can be seen that the slope decreases with zenith, since the ground at higher zenith correspond to a later stage on the shower development, the muons are less energetic, have been produced with more p_t and have more scattering.

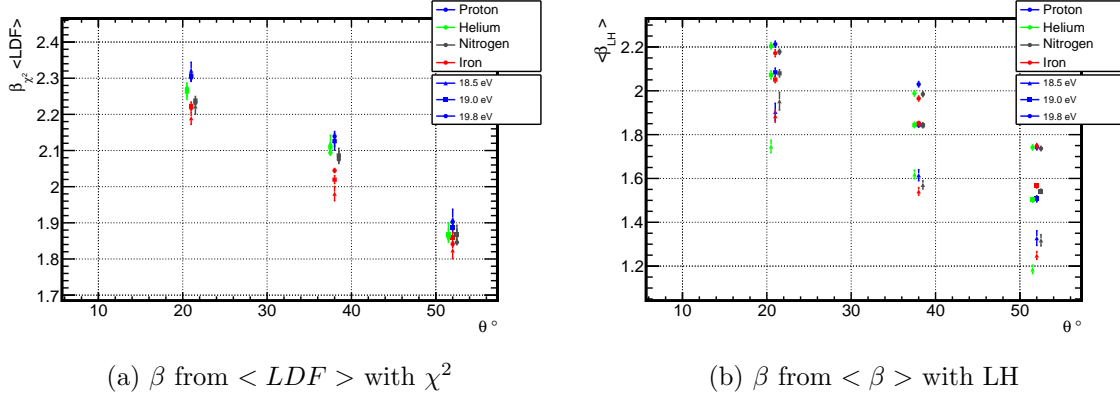


Figure 7.9: The slope β evolution with zenith angle, for fixed angle and energy, for the χ^2 minimization to the average $\langle LDF \rangle$ (a) and the average $\langle \beta \rangle$ to the likelihood event-by-event (b).

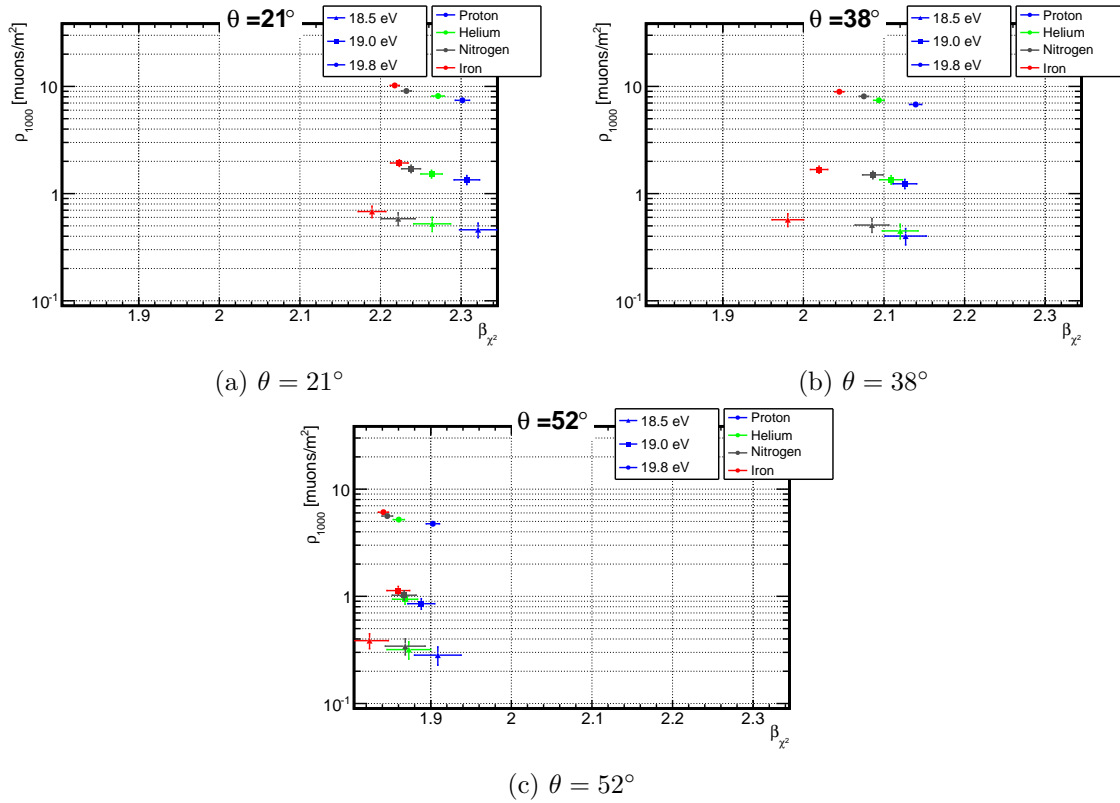


Figure 7.10: ρ_{1000} and β parameter from the χ^2 minimization for several primaries, for the samples with energy and zenith (θ) fixed.

Table 7.1: Parameter separation (according to eq. 7.2) from proton and iron, for the samples with energy and zenith (θ) fixed.

	$E = 10^{18.5}$ eV			$E = 10^{19}$ eV			$E = 10^{19.8}$ eV		
	21°	38°	52°	21°	38°	52°	21°	38°	52°
β	4.6	4.5	2.3	4.4	5.8	1.3	8.0	10.0	5.9
$\beta + \rho$	5.0	4.8	2.6	5.3	6.3	2.3	9.5	11.0	7.0
$\beta + X_{max}$	4.8	4.8	2.6	4.6	6.0	2.0	8.1	10.1	6.1
$\beta + N_\mu$	4.8	4.7	2.4	4.5	5.9	1.5	8.2	10.1	6.1

Considering only the β_{χ^2} from the average LDF, the minimization gives the parameter β and ρ_{1000} . On the figure 7.10, the parameter ρ_{1000} is discriminated against the β_{χ^2} . There are a considerably distance between the proton points (blue) and iron points (red). The combination of both variables could be used as composition discriminator. Since the statistics is reduced, it could be noted that within the error bars, the points are not at the same distance between each others. The β for 38° at 10¹⁹ eV for proton and helium is very similar, but that is expected at low statistics and such similar nuclei.

In order to better understand the separation between the proton and iron, it is possible to define the relative distance between the proton and iron with respect to the systematic errors. Considering the errors uncorrelated, a separation could be defined as:

$$\Delta = \sqrt{\Delta_x^2 + \Delta_y^2}, \quad (7.2)$$

where in this case, $\Delta_x = |\beta_p - \beta_i| / \sqrt{\sigma_{\beta,p}^2 + \sigma_{\beta,i}^2}$ and $\Delta_y = |\rho_{1000,p} - \rho_{1000,i}| / \sqrt{\sigma_{\rho_{1000,p}}^2 + \sigma_{\rho_{1000,i}}^2}$. On the table 7.1, Δ is written for ρ_{1000} and Δ_x alone for β . Those values show that the parameter β is a good estimator for composition and eventually comparison with hadronic models.

It is also possible to look for other parameter, like the $\langle X_{max} \rangle$ and $\langle N_\mu \rangle$, together with β to distinguish primaries. On the figures 7.11a, 7.11c and 7.11e the $\langle X_{max} \rangle$ are plotted together with β and $\langle N_\mu \rangle$ with β on figures 7.11b, 7.11d and 7.11f. Using both variables, the separation is similar and Δ is also written on table 7.1. The parameter that most separate the composition is the β , which shows that the slope of muonic lateral profile is related to the primary type. The number of muons N_μ is obtained by integrating the fitted NKG to the LDF, in the range [500, 2000] m, obtaining a muon number with respect to the generated CORSIKA, with negligible bias and RMS around 10%[234].

The difference between the N_μ and ρ_{1000} is that the second one is the LDF normalization at $r = 1000$ m, being more independent on the β parameter, while the N_μ is basically the ρ_{1000} times the LDF integral, which depends on the β parameter.

It is also significant to note that the parameter β is dependent on the X_{max} position (see figures 7.11a, 7.11c and 7.11e). The slope β is also related with the stage of the shower development on the ground. A lower β is obtained if the X_{max} is far away from the ground, since the particles

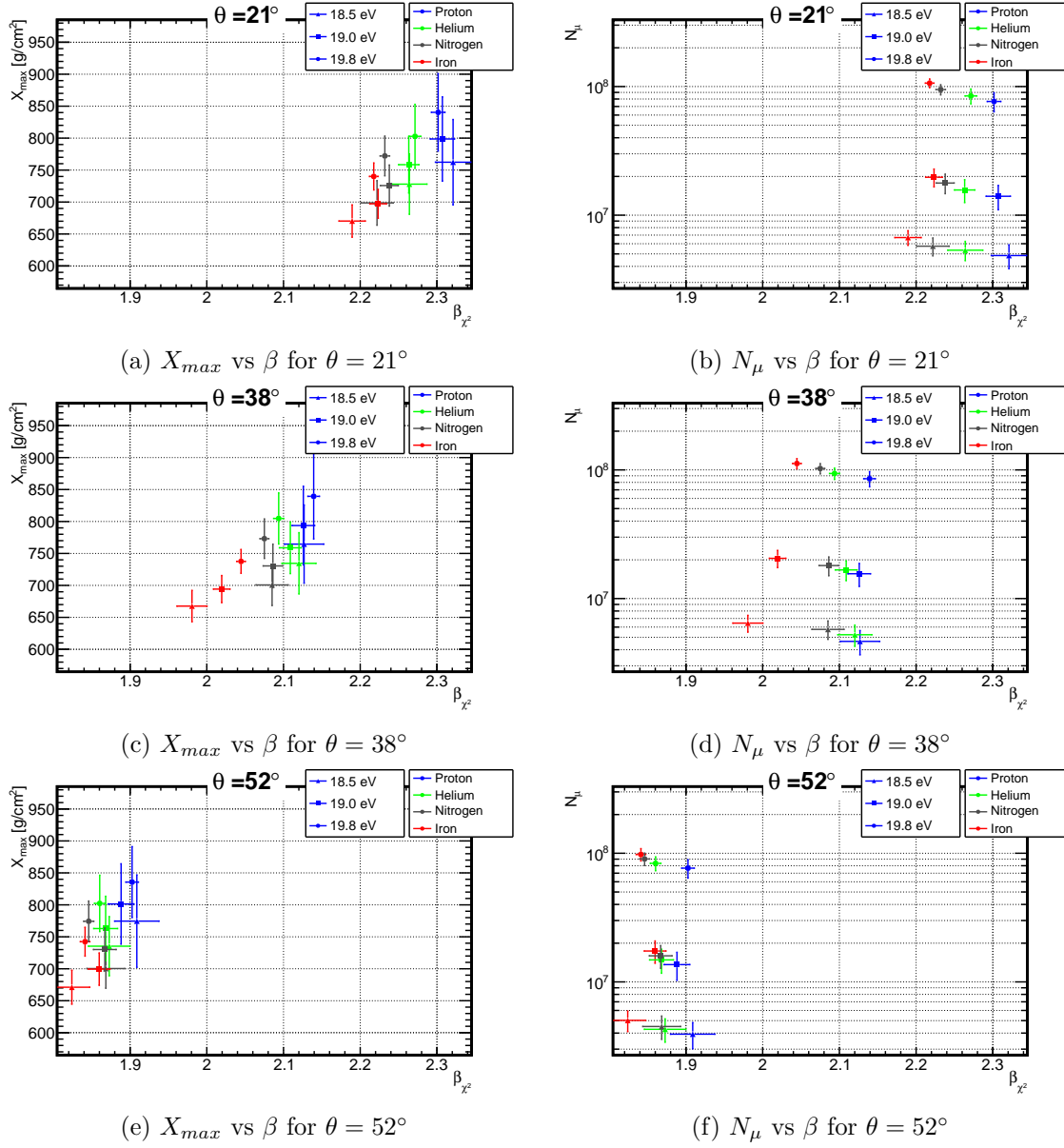


Figure 7.11: Pairs $\langle X_{max} \rangle, \beta$ and $\langle N_\mu \rangle, \beta$ (β from the χ^2 minimization) for several primaries, for the samples with energy and zenith (θ) fixed.

are more scattered, so it is dependent on the distance from X_{max} to the ground.

Difference between QGSJet-II.04 and Epos-LHC

These fixed energy and angle samples were also simulated with the model EPOS-LHC and similar behaviour was found. In the table 7.2, the parameter $\Delta = \sqrt{\Delta_x^2 + \Delta_y^2}$ is written, comparing the proton sample with QGSJET-II.04 and EPOS-LHC . All values are small and in the worst cases $\Delta \sim 2$, which mean that combining β with others parameters is difficult to distinguish between the two models. Nevertheless, it could be important to estimate different compositions.

In the figure 7.12 bands representing the QGSJET-II.04 and EPOS-LHC models are drawn. Both models are consistent, but the average LDF applied to data could constrain the composition and test the consistency of the hadronic models since the slope parameter β is the particle dispersion from the primary direction, related with the p_t , multiplicities and elasticities of the interactions.

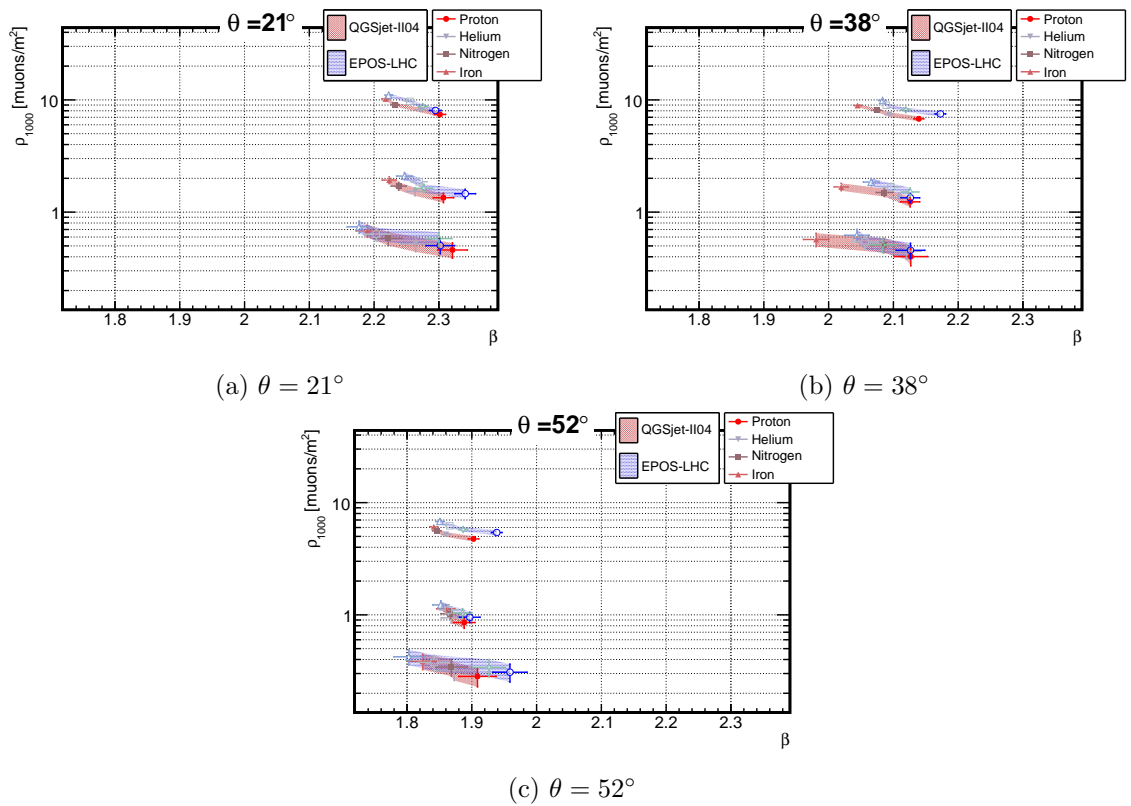


Figure 7.12: ρ_{1000} and β parameter from the χ^2 minimization for several primaries, for the samples with energy and zenith (θ) fixed. The red and blue band corresponds to the QGSJET-II.04 and EPOS-LHC models respectively. In the ascending order of ρ_{1000} the bands corresponds to the energies $10^{18.5}$, 10^{19} and $10^{19.8}$ eV.

Table 7.2: Parameter separation (according to eq. 7.2 using $\Delta_x = |\beta_{p,QGSjet} - \beta_{p,EPOS}|/(\sigma_{\beta,p,QGSjet} + \sigma_{\beta,p,EPOS})$ and $\Delta_y = |\rho_{1000,p,QGSjet} - \rho_{1000,p,EPOS}|/(\sigma_{\rho_{1000,p,QGSjet}} + \sigma_{\rho_{1000,p,EPOS}})$) between EPOS-LHC and QGSJET-II.04, for the proton samples with energy and zenith (θ) fixed.

	$E = 10^{18.5}$ eV			$E = 10^{19}$ eV			$E = 10^{19.8}$ eV		
	21°	38°	52°	21°	38°	52°	21°	38°	52°
β	0.6	0	1.3	1.5	0	0.4	0.6	3	3.1
$\beta + \rho$	0.7	0.5	1.3	1.6	0.6	0.8	1.2	3.3	3.5
$\beta + X_{max}$	0.6	0.1	1.3	1.5	0.2	0.4	0.6	3	3.1
$\beta + N_\mu$	0.7	0.4	1.3	1.5	0.3	0.5	0.7	3	3.1

7.2.2 Continuous energy bin

Studying samples with zenith angle and energy fixed is not sufficient because it is not possible to have such pure samples on the data. On this section, two samples were simulated with energies [18.85, 19.15] and [19.6, 19.8] eV, with a continuous distribution on zenith angle in the range $\theta \in [0^\circ, 60^\circ]$, for each primary (proton, helium, nitrogen and iron).

To account for the energy resolution and bin crosstalk due to the energy and zenithal reconstruction, the samples were divided into a central smaller bin on the reconstructed energy and in six bins in the reconstructed cosine of zenith angle ($\cos \theta$). The considered energy bins were [18.85, 19.05] and [19.65, 19.75]. It was used 300 events at 10^{19} eV, per zenith bin, which corresponds roughly to one and half years of data. At the $10^{19.7}$ eV were used 100 events per zenith bin, however that is unrealistically high, since it would correspond to about 15 years of data.

On the figure 7.13 is the evolution of the β as function of zenith angle, in the case of the fit to the average LDF (figure 7.13a) and event-by-event (figure 7.13b). Even considering a continuous energy bin, the previous picture of figure 7.9 doesn't change and the composition is not separated on a event-by-event basis with the likelihood, while using the χ^2 minimization to the average LDF the composition seems to be separated.

Combining the parameter β from the χ^2 with the respective ρ_{1000} (figure 7.14), $\langle X_{max} \rangle$ (figure 7.15) and with $\langle N_\mu \rangle$ (figure 7.16), some separation can be achieved, as can be seen. The values from eq. 7.2, comparing proton and iron are written on table 7.3.

The separation proton-iron is on the same order as the one found in the fixed energy bins. In this way, the parameter β can be used as a composition estimator on data using the MARTA array. It can be seen, again, that the parameter β is related with the X_{max} , on a similar way for each zenith angles.

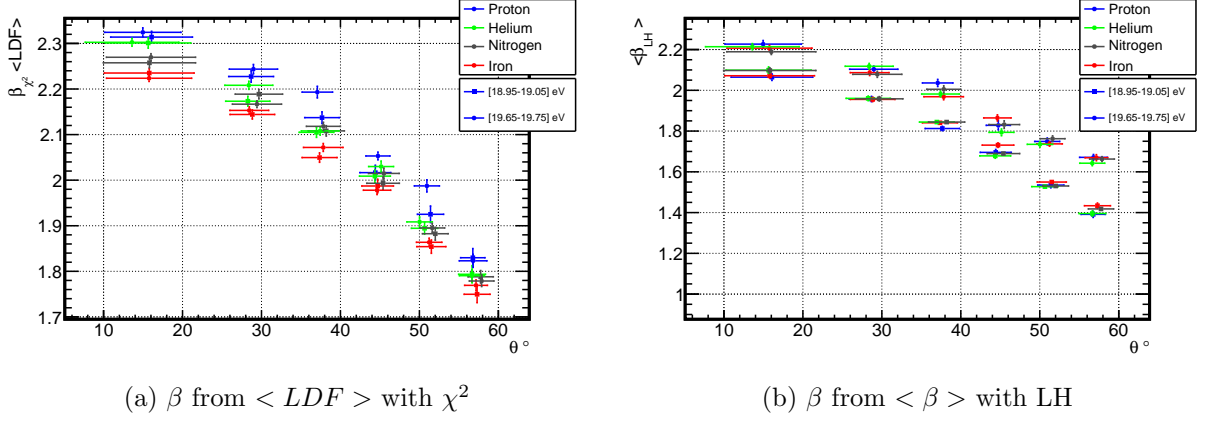


Figure 7.13: The slope β evolution with angle and energy for the χ^2 minimization to the average $\langle LDF \rangle$ (a) and the average $\langle \beta \rangle$ to the likelihood event-by-event (b), for the continue energy and zenith angle intervals.

Table 7.3: Parameter separation (according to eq. 7.2) from proton and iron, for the samples with the continue energy and zenith (θ) angle intervals.

	\log_{10} Energy	Zenith $\cos^2(\theta) \in$					
		[1, 0.875]	[0.875, 0.750]	[0.750, 0.625]	[0.625, 0.500]	[0.500, 0.375]	[0.375, 0.250]
β	[18.95 – 19.05]	4.9	5.2	5.3	1.3	3.0	2.9
	[19.65 – 19.75]	8.3	6.9	7.8	5.8	7.6	2.9
$\beta + \rho$	[18.85 – 19.05]	6.0	6.1	6.2	2.4	3.6	3.3
	[19.65 – 19.75]	9.5	7.6	8.3	6.8	7.9	3.1
$\beta + X_{max}$	[18.95 – 19.05]	5.0	5.3	5.5	1.9	3.3	3.3
	[19.65 – 19.75]	8.4	7.0	7.9	6.0	7.7	3.2
$\beta + N_\mu$	[18.95 – 19.05]	5.0	5.3	5.4	1.6	3.1	3.0
	[19.65 – 19.75]	8.5	7.0	7.9	6.0	7.7	3.0

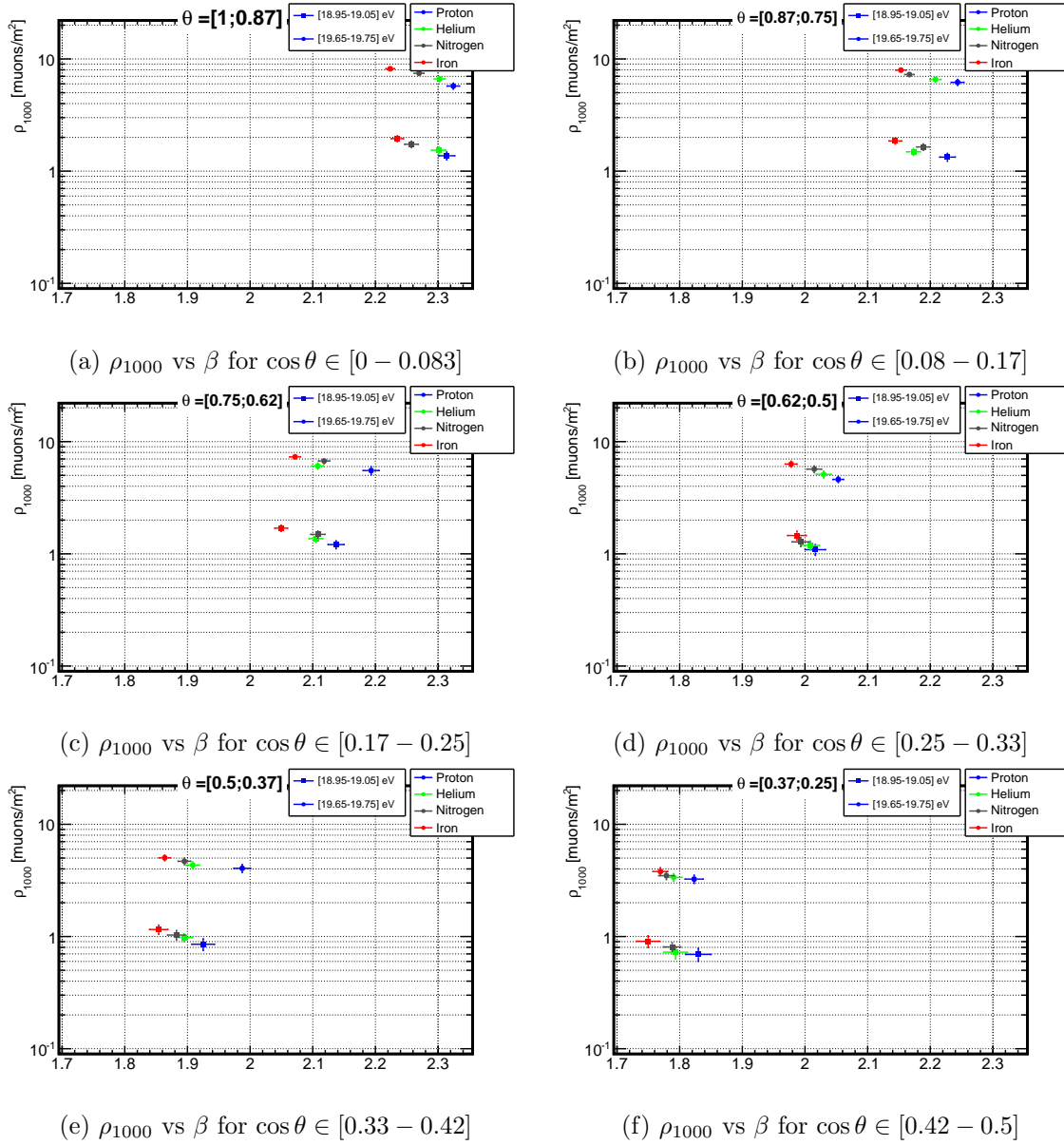


Figure 7.14: ρ_{1000} and β parameter from the χ^2 minimization for several primaries, for the samples with the continue energy and zenith (θ) angle intervals.

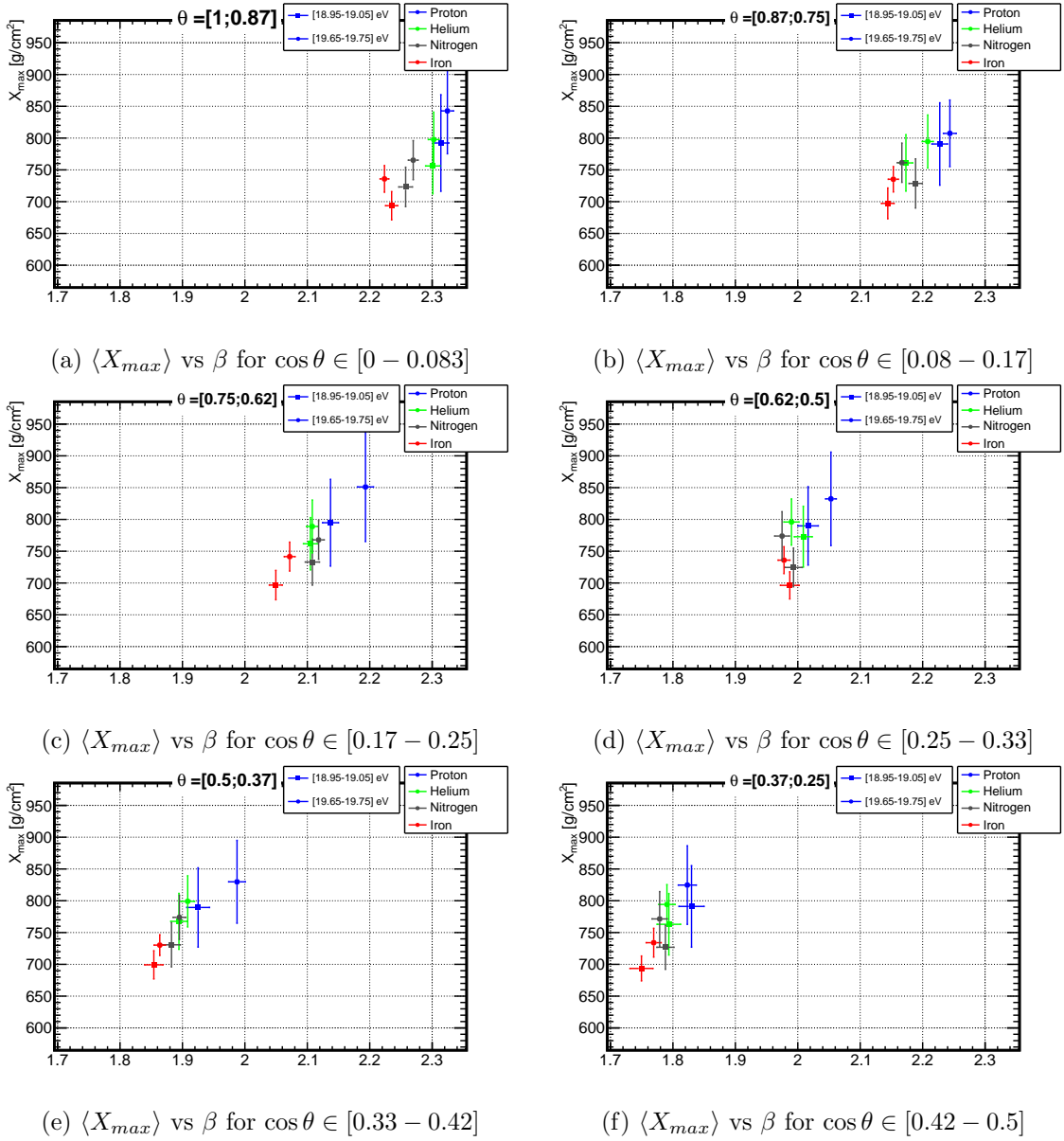


Figure 7.15: $\langle X_{max} \rangle$ and β parameter from the χ^2 minimization for several primaries, for the samples with the continue energy and zenith (θ) angle intervals.

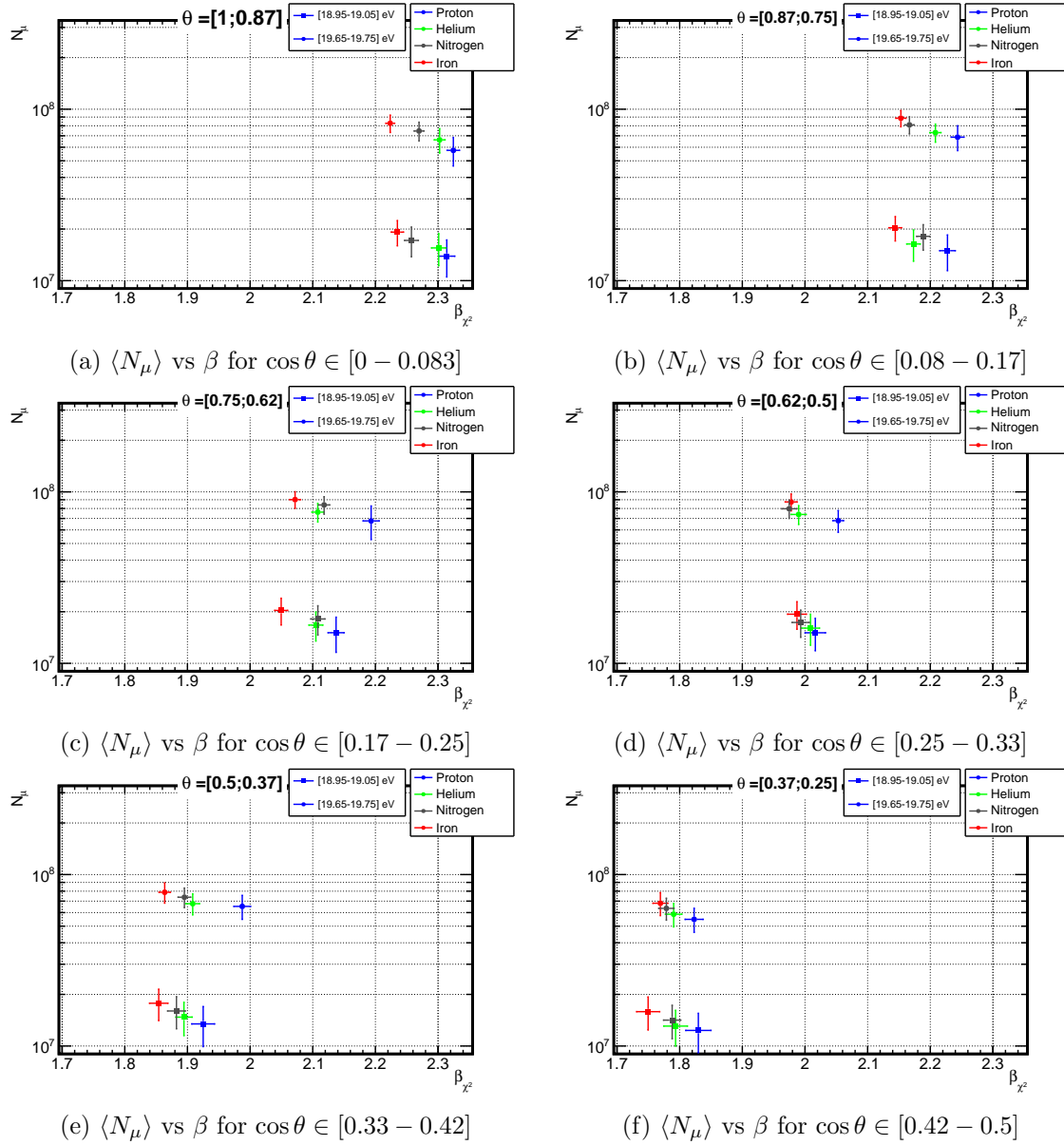


Figure 7.16: $\langle N_\mu \rangle$ and β parameter from the χ^2 minimization for several primaries, for the samples with the continue energy and zenith (θ) angle intervals.

7.2.3 Applying the tank trigger

On the previous section 7.2.2, it was seen that the parameter β can be used as composition estimator. Nevertheless, this variable comes from the χ^2 minimization to the average lateral density measured with all MARTA array stations. The purposed design MARTA array uses the tank trigger, this means that there are some MARTA station without trigger that otherwise would have signal. The tank only trigger above a chosen signal (usually 1.7 VEM).

The absence of those stations changes the LDF shape, with different behaviour accordingly to the way those silent stations are used. If the silent stations are not used, then at larger radius the signal is overestimated (only stations that fluctuates above the trigger cut appears) and a flat baseline emerge. On other side, if a zero signal is associated with the silent stations, then stations that would have a signal above zero and bellow the cut will be considered as zero and the shape falls rapidly. These two features can be seen on the figures 7.17.

On the MARTA array, even if the SD is used as a trigger, the CDAS could ask for the RPC's signal in a radius around the triggered event, which would solve that question. However, the RPC's electronic should continually save the data, during some time, in order to send it to the CDAS, if necessary.

Without solving the silent stations, there are two problems on the average LDF.

On one side, the fitting range on the LDF should be fixed. It was chosen to consider distance above 500 m to avoid the saturation stations (that gives similar problem as the silent stations). The maximum limit of 2000 m were chosen to minimize the silent station effect at energies above 10^{19} eV. The radius, at which the silent station effect is considerable, change with zenith angles, energy and primary composition, so the max limit of the fit could vary. Nevertheless, by changing the maximum limit, it would be extremely difficult to compare the results between the zenith/energy bin, but more important, also between the primaries.

The other problem is that the tank trigger of 1.7 VEM don't correspond to about 1.7 muons in the RPCs. The tank also measure electromagnetic particles and some muons that don't arrive to the RPC. In this way, the signal cut in the each tank don't correspond to the same signal on the corresponding MARTA signal. This mean that to use a convolution of Poisson (with some lower cut) with the LDF would need a conversion factor from the signal to the particles number. This conversion change with angle and energy, since the signal of one muon change with its track length and the electromagnetic particles don't give the same signal.

The silent stations are important at lower radius in lower energy events and inclined events, since the signals are lower (figure 7.17). It also change with composition, since the number of muons changes. Thus, this fit will only be reliable at high energies, otherwise it also measure the radius at which the silent stations appears. and the fit is not measuring the same thing in different compositions.

On the figure 7.18, the β is drawn as a function of the zenith angle, including silent stations as zero signal and without silent stations. The picture now is different from the figure 7.9 and the compositions are not consistently separated. The new parameters β are drawn against the

normal β in the figure 7.19. At energies around 10^{19} eV, the slope on the studied range doesn't change, since there were few silent stations, nonetheless, at lower energies the slopes changes, enabling to use it as composition estimator.

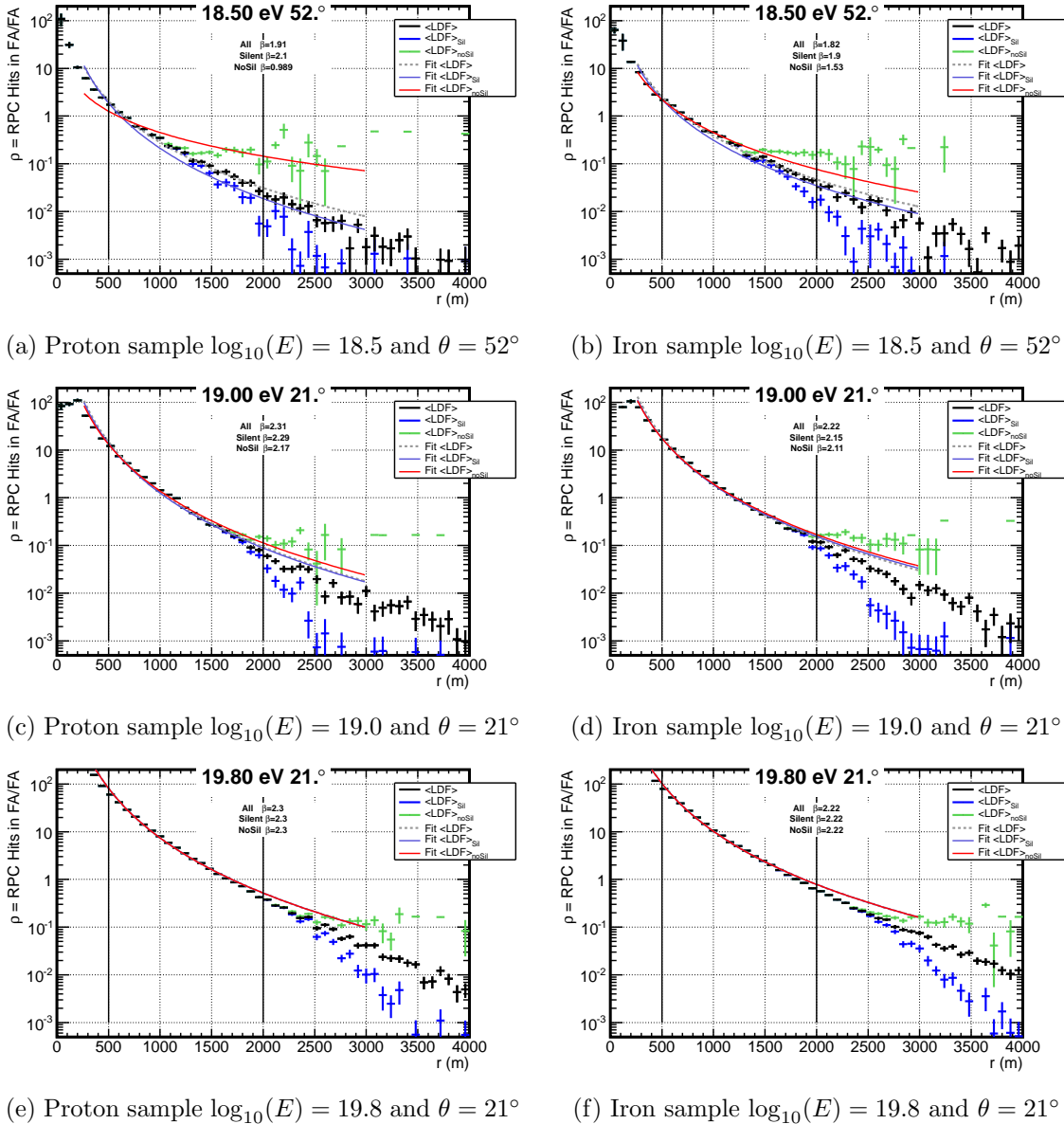


Figure 7.17: Average $\langle LDF \rangle$ of the RPC densities hits on the MARTA stations. On black all stations are considered, in green and blue are the profile without the silent stations and include them as zero signal, respectively. The fits are also included (grey, red and blue for all, without silent and zero signal on silent stations, respectively).

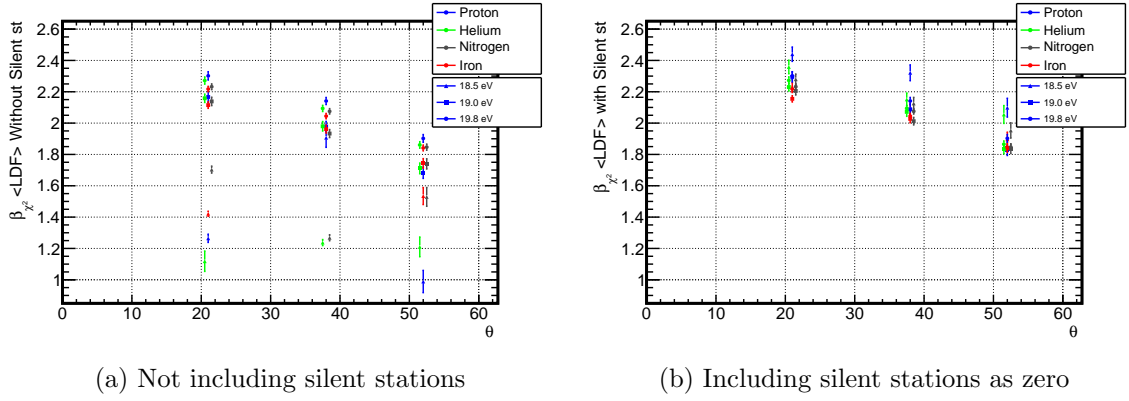


Figure 7.18: The evolution of the slope β , with energy and zenith angle, for the fixed energy bins from the average LDF, including zero signal silent stations (b) and without silent stations (a).

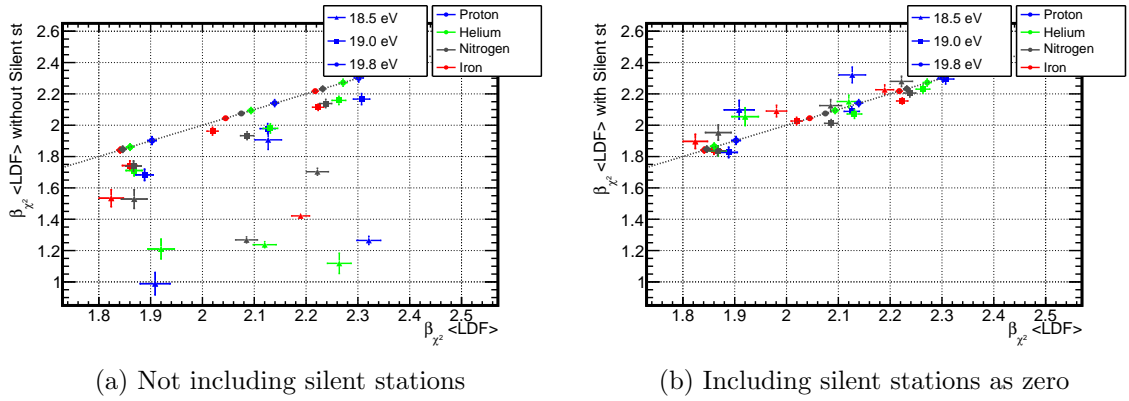


Figure 7.19: The slope β from the LDF including silent stations as zero signal (b) and without silent stations (a) as function of the β including all stations.

Signals on the SD tank

The slope β of the total signal LDF in the SD tank has the problem of the silent stations as well (figure 7.20). Moreover, the tank measures both muonic and electromagnetic component, which means that the *LDF* contains different fraction of muons as function of zenith angle, but more important also as a function of the composition. In this way, the parameter β is not measuring the same physics in the same fitting range on different compositions and angles. At lower zenith angle the electromagnetic part will be important, while at higher angles the muon dominates. Also, at heavier compositions, the muonic component is more important even at lower angles. A final comparison between the LDF is in this way difficult as can be seen on the figure 7.21. Both figures 7.21 and 7.22 show that the new β parameter on the tank signals are not exactly suitable to use as composition estimator. The compositions are not well separated. The interpretation would change with zenith angle and energy. And moreover, the data has different muonic/electromagnetic components, being difficult to compared it with simulations.

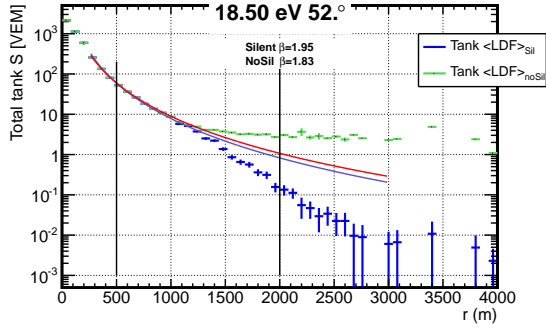
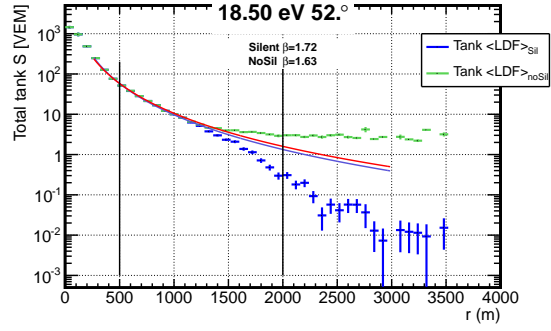
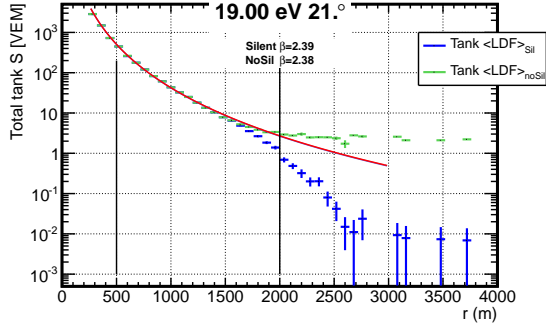
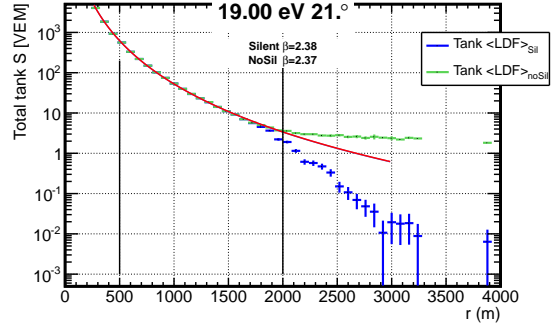
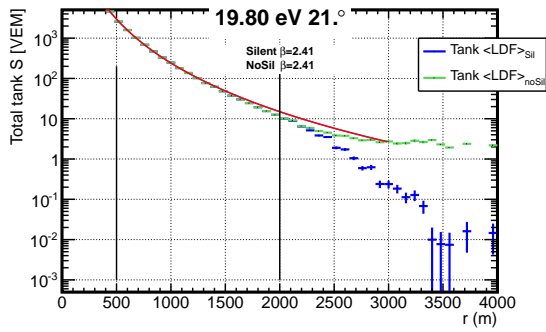
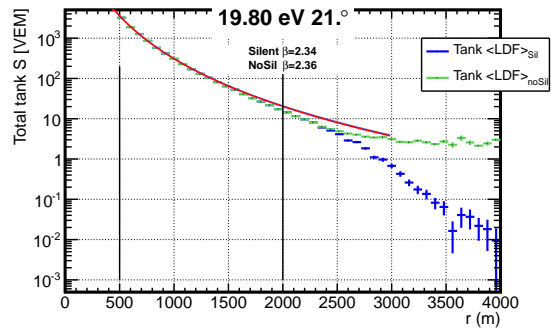

 (a) Proton sample $\log_{10}(E) = 18.5$ and $\theta = 52^\circ$

 (b) Iron sample $\log_{10}(E) = 18.5$ and $\theta = 52^\circ$

 (c) Proton sample $\log_{10}(E) = 19.0$ and $\theta = 21^\circ$

 (d) Iron sample $\log_{10}(E) = 19.0$ and $\theta = 21^\circ$

 (e) Proton sample $\log_{10}(E) = 19.8$ and $\theta = 21^\circ$

 (f) Iron sample $\log_{10}(E) = 19.8$ and $\theta = 21^\circ$

Figure 7.20: Average $\langle LDF \rangle$ of the SD tank signals. In green and blue are the profile without the silent stations and include them as zero signal, respectively. The fits are also included (red and blue for profiles with zero signal on silent stations and without silent stations, respectively).

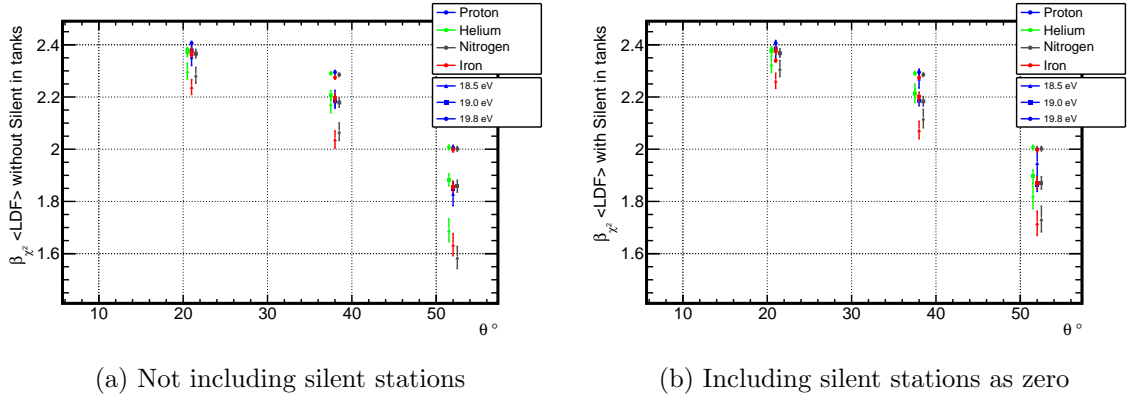


Figure 7.21: The slope β evolution with energy and zenith angle for the fixed energy bins. Results from the average LDF, without silent stations (a) and including zero signal silent stations (b).

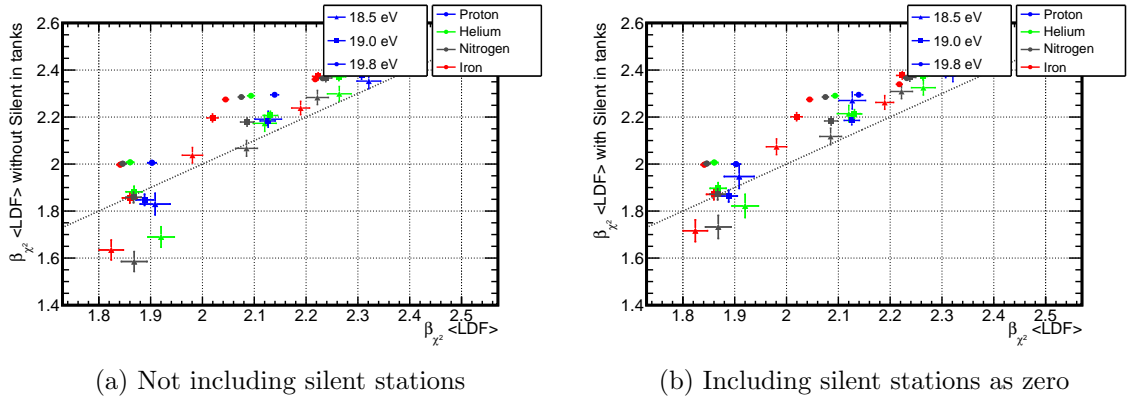


Figure 7.22: The slope β from LDF on the tanks, including silent stations as zero signal (b) and without silent stations (a) as function of the β including all stations on MARTA.

7.3 Perspective studies

The use of an array with the MARTA array capabilities allows to perform several studies as seen before. The direct measurement of muon is very important to obtain an average N_μ and its RMS at the same time that the electromagnetic part is measured. Moreover, the X_{max}^μ could be further improved due to the RPC time resolution and the possibility to measure the muon closer to the core.

7.3.1 Xmax reconstruction from signal fractions

Other kinds of analysis can also be performed. For example, the difference in depth between the electromagnetic X_{max} and the ground is related to the fraction of the $S_{1000,em}/S_{1000,\mu}$. This fraction could be easily obtained in the combined fit between the SD tank and MARTA (figure 7.4). In a first approximation the X_{max} can be parametrized as a polynomial of the first

order of the fraction $S_{1000,em}/S_{1000,\mu}$ (see figure 7.23). A exponential function would be more correct, since the $S_{1000,em}$ would depend on the distance between the X_{max} and the ground, in a proportion given by the longitudinal Gaisser-Hillas. The S_{μ} is less depend on the X_{max} position, and in the fraction, it gives the energy dependence.

The X_{max} can be given by:

$$X_{max} = b(\theta) + m(\theta) (S_{1000,em}/S_{1000,\mu}) . \quad (7.3)$$

Since for a given X_{max} , its difference to the ground changes with the zenith angle, then the parameters $b(\theta)$ and $m(\theta)$ are parametrized as function of $\sec\theta$, similar to the section 5.1.2.1, for the β parameter.

$$\begin{aligned} b(\theta) &= b_0 \\ m(\theta) &= m_0 + m_1 \sec(\theta) + m_2 \sec^2(\theta) . \end{aligned} \quad (7.4)$$

The precision that could be obtained using this calibration, is analysed with the iron and proton samples used on the chapter 5. The parameters $S_{1000,em}$ and $S_{1000,\mu}$ come from the fits to the tanks signals, from section 5.2. The fits were performed to all events. On the figure 7.23, the $S_{1000,em}/S_{1000,\mu}$ is plotted, for proton and iron, with the respective fits. The results are written on table 7.4. The evolution of each parameter with the zenith angle is drawn in the figure 7.24. Above $S_{1000,em}/S_{1000,\mu} = 2$, in the proton sample, the more vertical $\sec\theta$ bins appears to be constant due to the ground effect, since the X_{max} would be close to the surface.

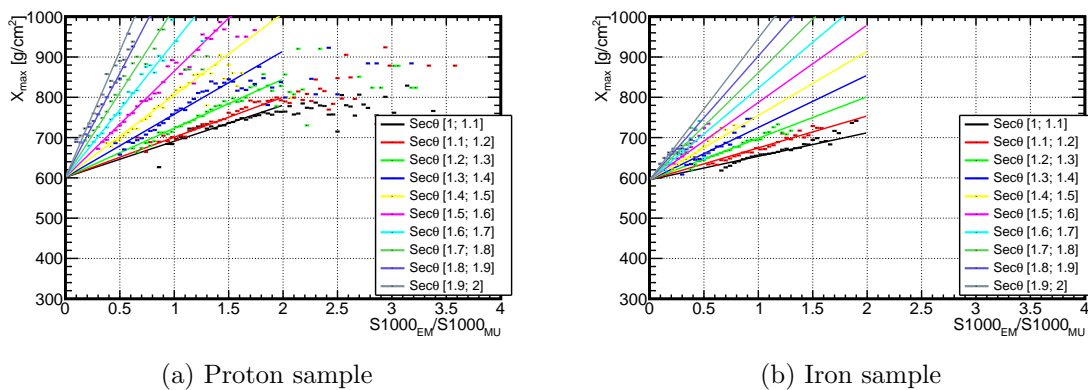
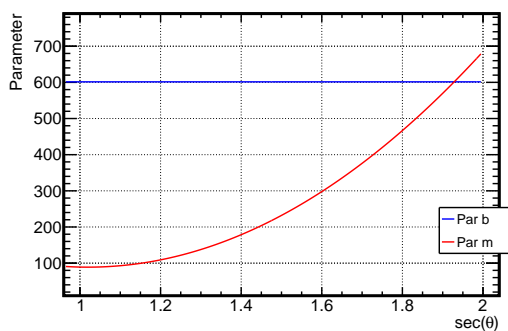


Figure 7.23: X_{max} as function of $S_{1000,em}/S_{1000,\mu}$ for the proton (a) and iron (b) samples from section 5.2 and fit to eq. 7.3.

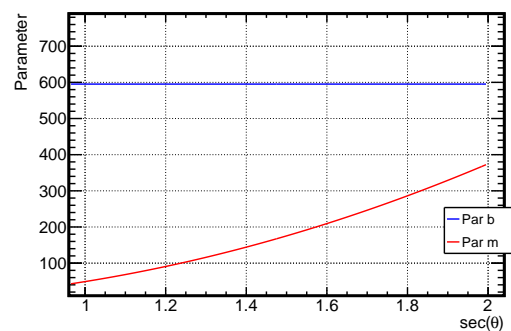
On the figure 7.25, the electromagnetic X_{max} reconstructed is compared with the generated X_{max} . The RMS of $X_{max}^{MC} - X_{max}^{rec}$ is about 45 g/cm^2 and 23 g/cm^2 for the proton and iron sample, with a negligible bias. These resolutions are comparable with the one obtained with MDP method for the X_{max}^{μ} . Using this approach or similar one, would be possible to recover the elongation rate for the electromagnetic component, with the SD events, increasing its statistics and enabling to reach higher energies. It can also be noticed that, the resolution and bias in the

Table 7.4: Parameter from the fit to equation 7.3, for the proton, iron and mix primary samples from section 5.2.

sample	b_0	m_0	m_1	m_2	χ^2/ndf
proton	601 ± 1.71	734 ± 17	$-1.26e + 03 \pm 26.8$	620 ± 10.9	519/251
Iron	595 ± 2.39	14.7 ± 25.4	-112 ± 39.4	146 ± 15.7	240/147
50% proton 50% iron	557 ± 0.438	371 ± 8.05	-707 ± 12.6	430 ± 4.9	3230/332



(a) Proton sample



(b) Iron sample

Figure 7.24: Parameters b and m from the fit to equation 7.3 (values on table 7.4).

recovered X_{max} , is similar for the lower and higher zenith angles, showing a reduced dependency on the angle.

The UHE cosmic rays seems to have a mixture composition. So, the same method was applied to the extreme case (currently disfavoured) of a composition with half protons and half irons. In the figure 7.26 is the X_{max} calibration with the fraction $S_{1000,em}/S_{1000,\mu}$ and the corresponding $X_{max}^{MC} - X_{max}^{rec}$. The χ^2/ndf of the fit to the joint samples is worst but the $X_{max}^{MC} - X_{max}^{rec}$ RMS is about 43 g/cm^2 , similar to the RMS of pure proton and a bias around -9 g/cm^2 . These extreme cases, show that this could be applied even with mixtures of composition. Nevertheless, with this joint sample, the protons and irons suffers some bias, around $+13 \text{ g/cm}^2$ and -32 g/cm^2 respectively.

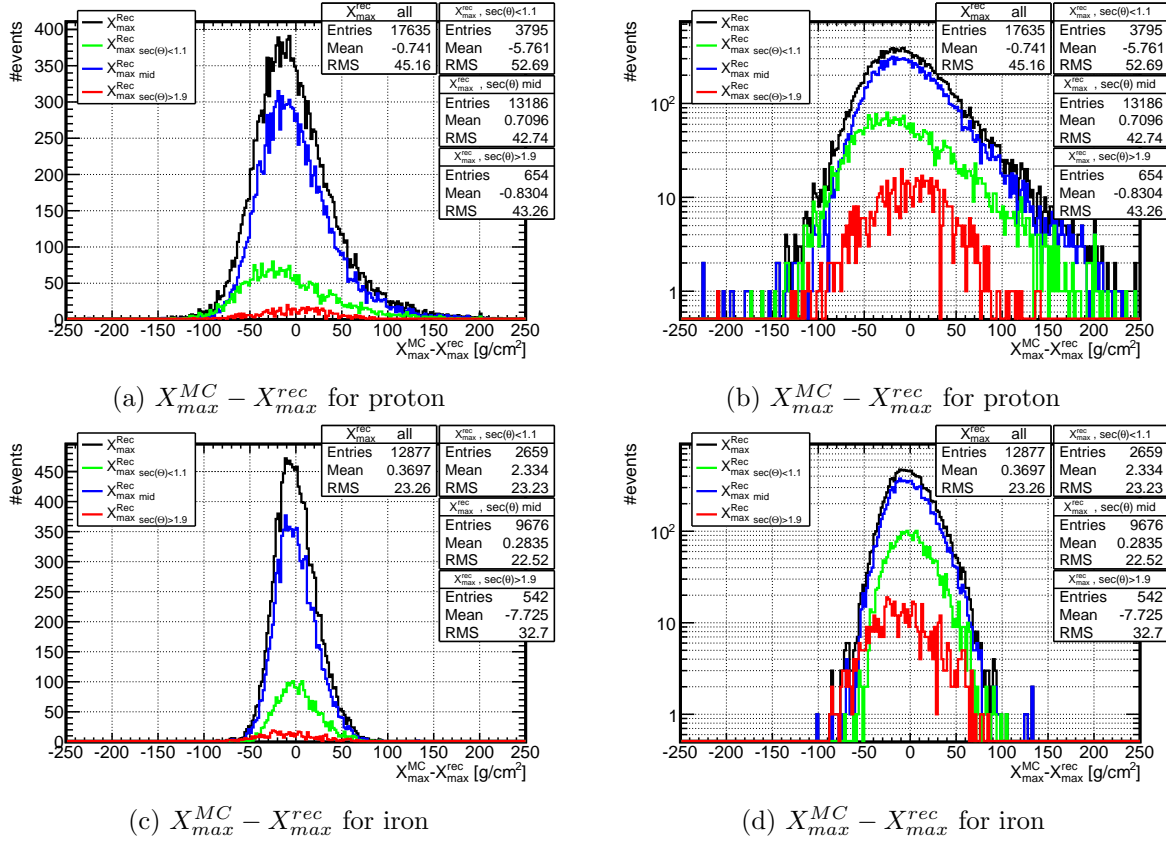


Figure 7.25: Resolution to the $X_{max}^{MC} - X_{max}^{rec}$ for the iron and proton sample. In black all events are plotted, in blue, red and green are the events with $\sec(\theta) < 1.1$, $\sec(\theta) > 1.9$ and the others, respectively.

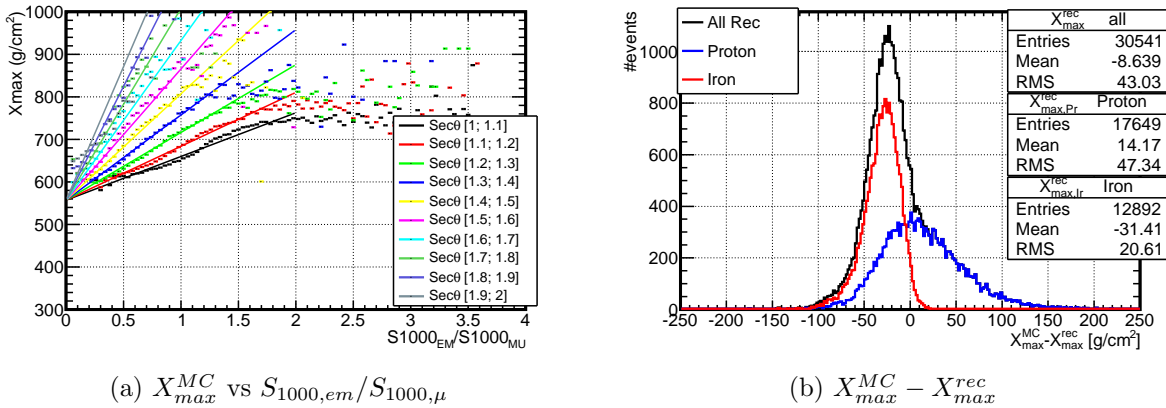


Figure 7.26: a) X_{max}^{MC} as function of $S_{1000,em}/S_{1000,\mu}$ for the mix sample with 50% proton, 50% iron and fit to eq 7.3. b) $X_{max}^{MC} - X_{max}^{rec}$ of the same sample. In black all events are plotted, in blue and red are the proton and iron events, respectively, considered the joint reconstruction.

7.3.2 MPD and L width

A new array similar to MARTA allows to detect the muon directly and understand the problems on the muon content. In this context, the MPD can be obtained in much more events, not only on the inclined ones, and also, it can use the tanks close to the core in the MPD reconstruction increasing the statistics of the measured X_{max}^μ .

The muon longitudinal profile is closely related to the hadronic cascade, since the muons come directly from the charged pion decays. In contrast, the electromagnetic longitudinal development, descent mainly from the neutral pion decay. This means that the inflection point on the Gaisser-Hillas (of the electromagnetic cascade) should be related to the maximum production of neutral pions. Above the inflection point the electromagnetic cascade is less feed, since the maximum π^0 production had already happened. Since the π^0 decay almost instantly, their maximum production point must be the charge pion maximum, above the energy threshold for the π^\pm to interact with air (and not decay). Pions below that energy threshold would mainly decay and contribute less to the electromagnetic shower. The maximum number of muons above a specific threshold would be close to the pion maximum and the electromagnetic inflection point. Looking at the equations 2.46 and 2.48, the electromagnetic inflection point of the Gaisser-Hillas is at the position $X_{max} - L$, where L is the profile width. In these way, the width of the shower can be related to the difference between the X_{max} and X_{max}^μ .

In the figure 7.27a, the electromagnetic $\langle X_{max} \rangle$ is shown again (from [182]), together with the muonic $\langle X_{max}^\mu \rangle$ on the figure 7.27b (from [195]). Both maximums, show a composition getting heavier with energy, being heavier on the X_{max}^μ . The difference between both maximums are plotted on the figure 7.28a. It is around $\sim 160 - 180 \text{ g/cm}^2$, the data shows a behaviour above the difference for proton, but within the systematics.

Currently, this plot is not possible to be obtained event-by-event, since the muonic maximum is obtained only at very inclined events (the largest event selection from [195]). From these

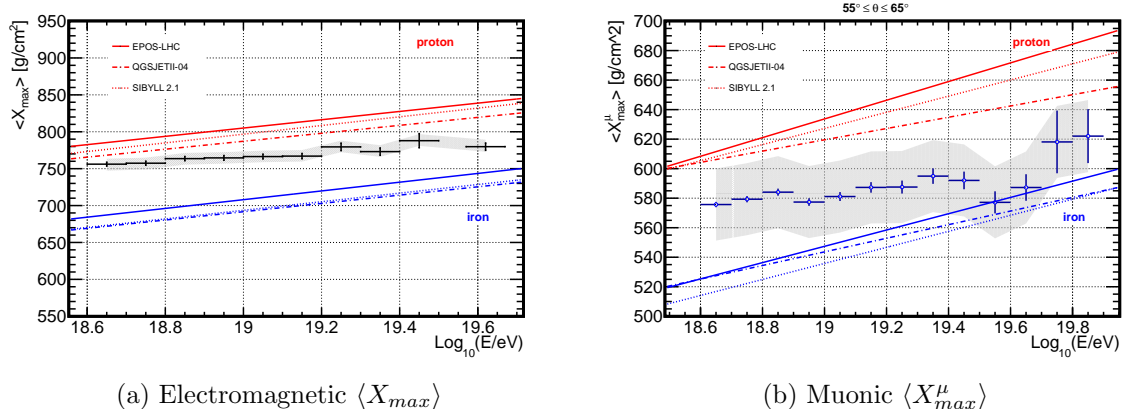


Figure 7.27: Electromagnetic X_{max} (a) and muonic X_{max}^μ (b) results, from [182] and [195] respectively.

~ 10000 inclined events, only 10% are hybrid and these, around less than 30% pass the fiducial cuts and quality cut on the FD. Moreover, to compare it with the L width even less events are accessible.

The shower width L is displayed in the figure 7.28b with values around $\sim 225 - 235 \text{ g/cm}^2$. Similar to the maximum differences, the L data also shows values above the models proton predictions. The maximum differences however, doesn't correspond exactly to the width L , but are smaller with differences around $\sim 60 - 80 \text{ g/cm}^2$. This is expected since the muonic maximum was the true muon maximum, including all muons with energies below the critical energy threshold for pions interactions.

The previous muonic maximum is corrected accordingly to the simulations, but it can be obtained directly from the tanks (usually referred as the apparent MPD), which corresponds to the maximum with the natural energy cut in the muons, from the atmosphere and detector. The apparent MPD maximum is displayed in the figure 7.29a and the difference between the electromagnetic and muonic part is plotted in the figure 7.29b.

The models are less consist on the apparent MPD due to the internal differences on the muon production energies, considering all muons the models seem similar. Now the difference between the electromagnetic and muonic part is around $\sim 240 - 270 \text{ g/cm}^2$, being now higher than the L width. The EPOS-LHC model for proton and iron falls outside the data systematic band. In the future, the difference between the X_{max} and X_{max}^μ compared with the L width can bring new insights on the consistency in the electromagnetic/muonic sector and pions production.

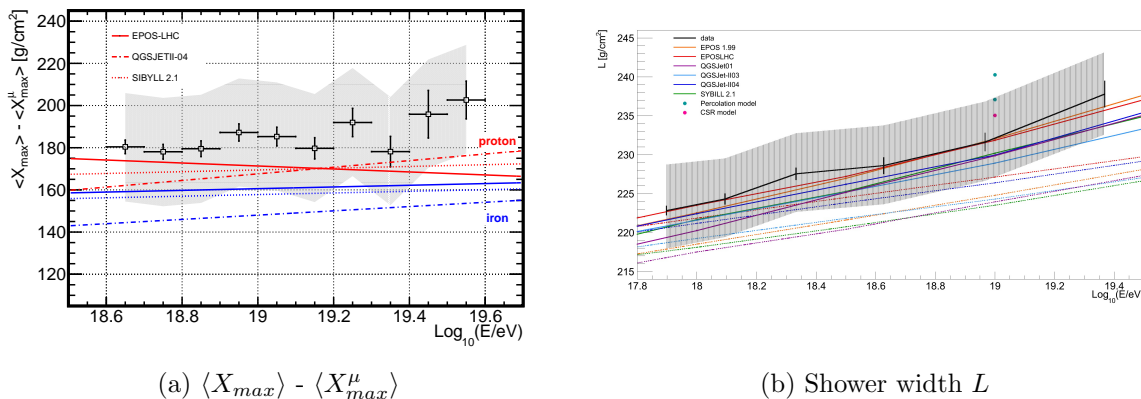


Figure 7.28: The shower maximums difference $\langle X_{max} \rangle - \langle X_{max}^\mu \rangle$ (a) and the shower width L (b) (from [76]).

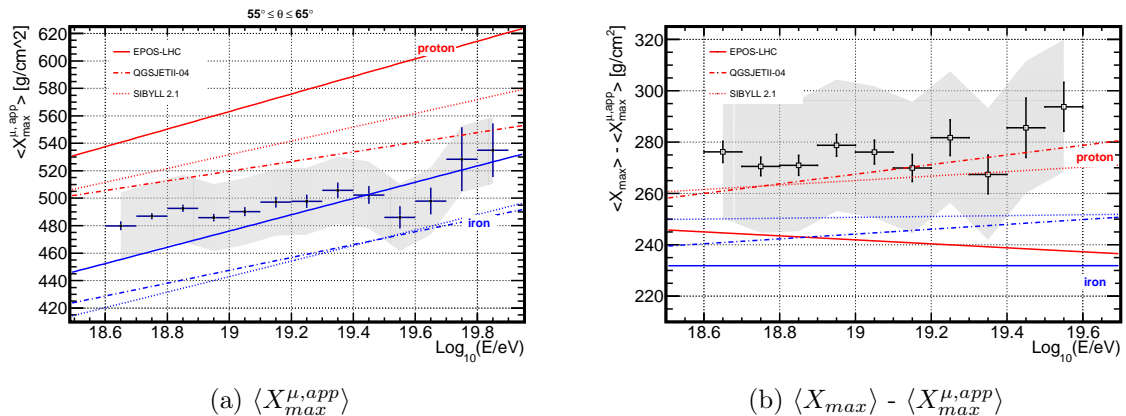


Figure 7.29: Apparent muonic maximum $X_{max}^{\mu,app}$ (a)[195] and $\langle X_{max} \rangle - \langle X_{max}^{\mu,app} \rangle$ (b).

7.4 Summary and prospects

The MARTA array, or some similar muon purpose detector array, can allow new studies and possibilities in an observatory like Auger.

The MARTA array at Auger would allow to enhance the SD tank calibrations. It is possible to monitor the tank ageing, with the deterioration of the Tyvek and lower reflectivity, which is very important for the data stability along the operation time.

Since this array is a muon detector purpose, it allow to disentangle the muonic and electromagnetic components. In this way, the muon content problem could be directly addressed and the SD energy calibrated in a relatively independent way of the muon signals.

With the MARTA project new analyses are possible, for instance, the muon number, its RMS and the X_{max}^{μ} can be accessed directly and with much more statistics than today.

A first analysis was developed and tested using simulations to build muonic LDFs in an attempt to assess the composition of cosmic rays. Two approaches can be used: The first one, an LDF was fit on an event-by-event basis and the slope of the LDFs (β) was averaged. The event by event approach to fit the β was used in chapter 5, minimizing the fluctuations in the energy calibration, but is not the best for a composition estimator.

On the second approach, a mean LDF was built from several events and then fitted to extract the β parameter. On this chapter, it was seen that the average LDF β in the muonic signal (between 500 m and 2000 m) can be used to disentangle composition and eventually constrain the hadronic models, on a similar way to the L and R studies on reference [76]. The β and ρ_{1000} obtained from the fit to the average LDF, were used as composition estimators, giving a separation around 3σ between proton and iron. The tests were performed using QGSJET-II.04 and EPOS-LHC with compatible results. Moreover, they are MARTA only variables and can be associated with the other variables in the electromagnetic sector to constrain the consistency of the hadronic models.

In the future, if MARTA array uses the SD tank trigger, then the MARTA signals on silent stations can not be achieved, so the average LDF could be difficult to analysed. Without the silent station, considering only stations with tank signal above the threshold, a flat baseline appears above some radius. This position change with energy, position and composition. If the silent stations are considered as zero, then the profile would decrease too quickly in an artificial way. In this case, the analyses of the β parameter is related also with the radius of the silent stations, so it not measures the same thing at different compositions and energies. Looking at the SD tank β is worst, since the β will measure the slope of the electromagnetic and muonic together. Since their fraction change with zenith angle and composition, the parameter measures different physics on the same radius fitting range. It should be carefully considered as a new parameter.

Combining the tank and MARTA signals, in addition to being able to calibrate the energy with the electromagnetic component only (chapter 5), they would permit to determine the ratio $S_{1000,EM}/S_{1000,\mu}$. It was seen that this ratio is related with the electromagnetic X_{max} position. Basically, the $S_{1000,EM}$ gives the difference between the ground and the X_{max} (at the same energy). Since both total, electromagnetic and muonic signals are proportional to the energy (chapter 5) and the $S_{1000,\mu}$ is relatively constant with crossed slant depth, then it can give the energy evolution. The X_{max} is possible to obtain as function of the ratio $S_{1000,EM}/S_{1000,\mu}$ and zenith angle, with a resolution ($X_{max}^{MC} - X_{max}^{rec}$) obtained around 45 g/cm^2 and 23 g/cm^2 , for proton and iron respectively, with negligible bias.

In the future, with this method the X_{max} can be determined with more statistics than today (due to the small FD duty cycle) and in this way, reach higher energies on the elongation rate. Moreover, the X_{max}^{μ} could also be obtained with more statistics applying the MPD on the MARTA Array. Considering both variables, the difference $\Delta X = X_{max} - X_{max}^{\mu}$ could be studied. Currently, despite the trend to heavier compositions found on both X_{max} , the difference of the average of those X_{max} , points to lighter composition. With a muon detector, this could be seen event-by-event. And, the consistency, between the electromagnetic and muonic development of each model could be compared with the expected electromagnetic development length L .

Summary and Conclusions

The ultra high energy cosmic rays grant access to an energy range well above that achieved with man-made accelerators, providing an unique window to study particle physics and astrophysics. The access of new information is not straightforward, as said in the thesis beginning, since the particle composition is not known. The primary particles are inferred indirectly from the atmospheric shower development leading to many inconsistencies and unsolved problems.

The objective of this thesis was to build tools that would allow to better understand the data and to increase the sensitivity both to the primary mass composition and to the high energy hadronic models using the Fluorescence Detector and Surface Detectors, and the new MARTA project in the Pierre Auger Observatory.

Currently, the Auger Offline framework simulate the atmospheric cascades in a one dimensional, longitudinal analyses, losing the 3D shower information. And, afterwards it recovers the 3D structure using average lateral profiles. In this context, the BinTheSky framework was developed as a tool to save the generators spacial information and use it inside Offline. The fluorescence and direct Cherenkov emission were implemented, validated and compared with data in chapter 4.

The fluorescence emission was validated in comparison with the standard Offline. The standard longitudinal reconstructions, such as the geometric reconstruction, energy, X_{max} were on average very similar, with identical bias and resolutions. The Cherenkov emission was also compatible with the longitudinal parameters, but shows that the simulation and reconstruction are not describing the shower shape as well as the fluorescence emission (namely the dE/dX_{max} , USP and L). The events with high Cherenkov light component are not considered in most standard analysis, due to the high uncertainty recovering the light components matrix. Nevertheless, a 3D simulation together with a 3D reconstruction would allow to improve the reconstruction using the spacial information of these events, especially with the new HEAT data. These tools would also allow to study fluctuations on the spacial shape of the shower, resulting from a double bang event, for example.

The first and multiple scattering are not yet implemented and further algorithm improvement is

needed in order to do not use average parametrizations. The framework can, anyhow be applied to the laser simulations using both Offline and external GEANT4simulation of the light with the first scattering easily implemented. Moreover, the Cherenkov light profiles on the ground were determined and compared to available references, such as Tunka results. The direct Cherenkov emission was consistent with those parametrizations.

The electromagnetic lateral profile, detected by the FD, can arrive on the ground, and through the Auger surface detectors be detected simultaneously with muons. Both Electromagnetic signal component and Muonic signal component are not directly distinguishable, in the current Auger status. The ground signals at a reference core distance are used as an energy estimator, which is calibrated against the FD energy measurement. So, the SD energy obtained can be highly correlated with the number of muons.

The FD measures the electromagnetic component, similar to a calorimetric measurement. So the energy calibration on the SD, currently performed using the total tank signal, should be done with the SD electromagnetic component.

Moreover, the muonic measurements in Auger show a disagreement with the models, such as the deficit on the predicted muons [197, 199] (see section 3.7). Nonetheless, the electromagnetic component is more compatible with the models assuming some specific composition. Also, it should be remembered that the muonic component is not directly achievable, it is only possible to recover the muon content indirectly, using algorithms to distinguish between the electromagnetic and muonic signals or in very inclined events. In this way, a new detector with the purpose to measure the muons directly is important to overcome the inconsistencies and measure the muon content evolution with energy, in a way uncorrelated with the energy calibration procedure.

In chapter 5, the size shower parameter S_{38} were used as an energy estimator for each component separately. The calibration was done using the Constant Intensity Cut (CIC) method. The LDF was fitted with a likelihood in which β can be parametrized to minimize the S_{1000} fluctuations. The $S_{1000}(\theta)$ attenuation curves were obtained using the CIC method and the S_{38} calculated. Then, this electromagnetic S_{38} was used as the energy estimator and calibrated with the MC energy. It was shown that the SD energy can be calibrated using the electromagnetic component with better performance as the one currently obtained (for the total signal), below zenith angles $\sim 40^\circ$. In that region, the energy can be calibrated using the electromagnetic signal recovered from the tank, and the muons can be measured with MARTA, in a mostly independent way and with much more statistics. The overall calibration performance, from 0° to 60° in zenith angle, gave negligible bias. The statistical error of the reconstructed energy is higher when the EM component is used than when the total signal is used, on inclined events. This happens, since in inclined events the electromagnetic signal is small and the fluctuations are high. On vertical events, with lower zenith angles, the precision obtained from the EM signal is better than that obtained with the total SD signal. For instance, between 0° and 29° , the RMS is about 9.6% and 6.2%, in the total component, for the proton and iron simula-

tions respectively, while for the electromagnetic signal, it gives about 8.5% and 5.3% respectively.

The LDF β parameter, attenuation CIC curve and energy calibration curves have been determined on the data for the total component, so it is possible to compare them with the proton and iron simulation predictions of the QGSJET-II.04 model used on the chapter 5. In chapter 6, it was seen that the slope β was similar between the proton and iron simulations, when separately considering the electromagnetic or the muonic LDF. The total slope β on the simulations was less similar between the primaries, but the iron sample had a flatter total LDF (smaller β), reflecting the higher muon content. In the vertical events, the data is compatible with the proton predictions, however in more horizontal events, the slope is much higher in the data than in the simulations. This is in apparent contradiction with the deficit of muons indicated by other analyses, which should lower the total β closer to the muonic β . It seems to indicate that the muonic LDF, for now not measured in data, is different from the one predicted in the models. That can point to an harder muon spectrum in the data than predicted.

Another difference is found on the calibration of S_{38} to the FD energy. The linear slope (on the $\log_{10}(S_{38}) - \log_{10}(Energy)$ in data is 0.975, much higher than that from simulations, which was around 0.908 and 0.925 for proton and iron respectively. That does not seem to come from the CIC attenuation curves, which are fully compatible with proton and within 3σ with iron.

From simulations, we know that the calibration with the muonic S_{38} gives a lower slope, around 0.84 (see chapter 5), in agreement with the modified Heitler model predictions. The Heitler model predicts values between $\sim 0.84 - 0.92$ (depending on the model multiplicities). In data, S_{38} is not measured for muons only, but the muonic signals can be measured in inclined events by the parameter N_{19} and R_{μ} and compared with the simulated S_{38} . They give much higher slopes in the calibration, about 0.985 and 1.03, again pointing out to a difference on the detected muons signal, evolution with energy, relatively to the model predictions (similar to the total β). This effect could appear from a change in the composition disfavoured by the electromagnetic results.

The MARTA project allows the possibility for, for instance, the muon number, its RMS and the X_{max}^{μ} to be accessed directly and with much more statistics than today (seen on the chapter 7). And the electromagnetic and muonic sector could be compared.

A first analysis was developed and tested using simulations to build muonic LDFs in an attempt to assess the composition of cosmic rays. Two approaches can be used:

The first one, an LDF was fit on an event-by-event basis and the slope of the LDFs (β) was averaged. The event by event approach to fit the β was used in chapter 5, minimizing the fluctuations in the energy calibration, but is not the best for a composition estimator. On the second approach, a mean LDF was built from several events and then fitted to extract the β parameter. The β and the ρ_{1000} obtained from the fit to the average LDF, were used as composition estimators, giving a separation around 3σ between proton and iron. The tests were performed using QGSJET-II.04 and EPOS-LHC with compatible results.

Furthermore, employing the MARTA capabilities to separate electromagnetic and muonic components, it is possible to reconstruct the electromagnetic X_{max} using the fraction $S_{1000,em}/S_{1000,\mu}$, event-by-event. As shown in chapter 5, both $S_{1000,em}$ and $S_{1000,\mu}$ depend linearly on energy, for a given zenith angle θ . The $S_{1000,\mu}$ is almost independent of the X_{max} and can fix the event energy, while the $S_{1000,em}$ has also the information of the attenuation due to the distance between the ground and the X_{max} . Then, the X_{max} could be obtained as function of the $S_{1000,em}/S_{1000,\mu}$ ratio and zenith angle. This method would allow to dramatically increase the statistics and reach higher energies. It would give a resolution ($X_{max}^{MC} - X_{max}^{rec}$) of at least $\sim 45 \text{ g/cm}^2$ and 23 g/cm^2 , for proton and iron respectively, with negligible bias.

With such a detector, in the future, the X_{max} can be determined with more statistics than today. Moreover, the X_{max}^{μ} could also be obtained with more statistics applying the MPD on the MARTA Array. With both variables, the difference $\Delta X = X_{max} - X_{max}^{\mu}$ could be studied. Currently, despite the trend to heavier compositions found on both X_{max} , the different of the average of those X_{max} , points to lighter composition (like the L parameter). With a muon detector, these could be seen event-by-event. The consistency, between the electromagnetic and muonic development of each model could be compared with the expected electromagnetic development length L .

All these effort took us closer to to the UHECRs composition and to the knowledge of the hadronic interactions at extremely high energies.

Bibliography

- [1] J. Abraham et al. “Properties and performance of the prototype instrument for the Pierre Auger Observatory”. In: *Nuclear Instruments and Methods in Physics Research Section A: Accelerators, Spectrometers, Detectors and Associated Equipment* 523.1-2 (2004), pp. 50–95. ISSN: 0168-9002. DOI: 10.1016/j.nima.2003.12.012. URL: <http://www.sciencedirect.com/science/article/pii/S0168900203033497>.
- [2] J. Unger. “Higgs Boson Production in the Atmosphere of the Earth”. CERN-THESIS-2014-313. MA thesis. Dresden University of Technology, 2014.
- [3] T. Wulf. “Über den Einfluss des Druckes auf die elektromotorische Kraft der Gaselektroden/On the influence of the pressure on the electromotive force of the gas electrode”. In: *Physikalische Zeitschrift* 10 (1909).
- [4] T. Wulf. “Beobachtungen über die Strahlung hoher Durchdringungsfähigkeit auf dem Eiffelturm/Observations on the radiation of high penetration power on the Eiffel Tower”. In: *Physikalische Zeitschrift* 11 (1910).
- [5] D. Pacini. “La radiazione penetrante alla superficie ed in seno alle acque”. In: *Nuovo Cimento* VI/3 (1912). arXiv: 1002.1810.
- [6] D. Pacini. “La radiation pénétrante sur la mer”. In: *Le Radium* VIII (1911). arXiv: 1101.3015.
- [7] A. Angelis. “Domenico Pacini, uncredited pioneer of the discovery of cosmic rays”. In: *Rivista del Nuovo Cimento* 33 (2010). arXiv: 1103.4392.
- [8] V. F. Hess. “Über Beobachtungen der durchdringenden Strahlung bei sieben Freiballonfahrten/On the observation of the penetrating radiation in seven free balloon campaigns”. In: *Physikalische Zeitschrift* 13 (1912).
- [9] W. Kolhörster. “Messungen der durchdringenden Strahlung im Freiballon in größeren Höhen./Measurements of the penetrating radiation in free balloon at higher altitudes.” In: *Physikalische Zeitschrift* 14 (1913).
- [10] W. Kolhörster. “Gekoppelte Höhenstrahlen/Coupled high-altitude rays”. In: *Naturwissenschaften* 26.35 (1938).
- [11] P. Auger et al. “Grandes gerbes cosmiques atmosphériques contenant des corpuscules ultra-pénétrante”. In: *Comptes rendus Acad. Sci.* 206 (1938).
- [12] Pierre Auger et al. “Extensive Cosmic-Ray Showers”. In: *Review Modern Physics* 11 (3-4 1939), pp. 288–291. DOI: 10.1103/RevModPhys.11.288. URL: <http://link.aps.org/doi/10.1103/RevModPhys.11.288>.
- [13] W. Bothe and W. Kolhörster. “Das Wesen der Höhenstrahlung/The essence of cosmic radiation”. In: *Zeitschrift für Physik* 56.11-12 (1929), pp. 751–777. ISSN: 0044-3328. DOI: 10.1007/BF01340137.
- [14] H.J. Bhabha and W. Heitler. “The Passage of Fast Electrons and the Theory of Cosmic Showers”. In: *Royal Society of London Proceedings Series A* A.159 (Apr. 1937). DOI: 10.1098/rspa.1937.0082.

- [15] J. F. Carlson and J. R. Oppenheimer. “On Multiplicative Showers”. In: *Physics Review* 51 (4 1937), pp. 220–231. DOI: 10.1103/PhysRev.51.220. URL: <http://link.aps.org/doi/10.1103/PhysRev.51.220>.
- [16] Carl D. Anderson. “The Apparent Existence of Easily Deflectable Positives”. In: *Science* 76.1967 (1932). DOI: 10.1126/science.76.1967.238.
- [17] J. Linsley. “Evidence for a Primary Cosmic-Ray Particle with Energy 10^{20} eV”. In: *Physics Review Letter* 10 (1963). DOI: <http://dx.doi.org/10.1103/PhysRevLett.10.146>.
- [18] M. M. Winn et al. “The cosmic-ray energy spectrum above 10^{17} eV”. In: *Journal of Physics G: Nuclear Physics* 12.7 (1986), pp. 653–660. DOI: 10.1088/0305-4616/12/7/015. URL: <http://stacks.iop.org/0305-4616/12/i=7/a=015>.
- [19] M. A. Lawrence, R. J. O. Reid, and A. A. Watson. “The cosmic ray energy spectrum above 4.10^{17} eV as measured by the Haverah Park array”. In: *Journal of Physics G: Nuclear and Particle Physics* 17.5 (1991), pp. 733–757. DOI: 10.1088/0954-3899/17/5/019. URL: <http://stacks.iop.org/0954-3899/17/i=5/a=019>.
- [20] M. N. Dyakonov, N. N. Efimov, and T. A. Egorov. “Cosmic rays of extremely high energy”. In: *Nauka, Novosibirsk, USSR* (1991).
- [21] M. Nagano and M. Teshima. “Present status of Akeno 100 km² air shower array (AGASA)”. In: *Nuclear Physics B - Proceedings Supplements* 28.2 (Nov. 1992), pp. 28–35. ISSN: 0920-5632. DOI: 10.1016/0920-5632(92)90105-2. URL: <http://www.sciencedirect.com/science/article/pii/0920563292901052>.
- [22] R.M. Baltrusaitis et al. “The Utah Fly’s Eye detector”. In: *Nuclear Instruments and Methods in Physics Research Section A: Accelerators, Spectrometers, Detectors and Associated Equipment* 240.2 (1985), pp. 410–428. ISSN: 0168-9002. DOI: 10.1016/0168-9002(85)90658-8. URL: <http://www.sciencedirect.com/science/article/pii/0168900285906588>.
- [23] H. Kawai et al. “Telescope Array Experiment”. In: *Nuclear Physics B - Proceedings Supplements* 175-176.0 (2008). Proceedings of the XIV International Symposium on Very High Energy Cosmic Ray Interactions, pp. 221–226. ISSN: 0920-5632. DOI: 10.1016/j.nuclphysbps.2007.11.002. URL: <http://www.sciencedirect.com/science/article/pii/S0920563207007992>.
- [24] R. Battiston et al. “Cosmic ray physics from low to extreme energies: Status and perspectives”. In: *Advances in Space Research* 37.10 (2006). Astrophysics, pp. 1834–1840. ISSN: 0273-1177. DOI: <http://dx.doi.org/10.1016/j.asr.2006.03.015>. URL: <http://www.sciencedirect.com/science/article/pii/S0273117706001438>.
- [25] B. Klecker. “Anomalous Cosmic Rays: Our present understanding and open questions”. In: *Advances in Space Research* 23.3 (1999). The Transport of Galactic and Anomalous Cosmic Rays in the Heliosphere: Observations, Simulations and Theory, pp. 521–530. ISSN: 0273-1177. DOI: 10.1016/S0273-1177(99)80006-4. URL: <http://www.sciencedirect.com/science/article/pii/S0273117799800064>.
- [26] K.A. Olive et al. (Particle Data Group). “Review of Particle Physics”. In: *Chinese Physics C* 38.9 (2014). DOI: 090001.
- [27] T. Antoni et al. In: *Astroparticle Physics* 24.1-2 (2005), pp. 1–25. ISSN: 0927-6505. DOI: 10.1016/j.astropartphys.2005.04.001. URL: <http://www.sciencedirect.com/science/article/pii/S0927650505000691>.
- [28] J. Hörandel. “Models of the knee in the energy spectrum of cosmic rays”. In: *Astroparticle Physics* 21.3 (2004), pp. 241–265. ISSN: 0927-6505. DOI: 10.1016/j.astropartphys.2004.01.004. URL: <http://www.sciencedirect.com/science/article/pii/S0927650504000209>.
- [29] W. D. Apel et al. “Kneelike Structure in the Spectrum of the Heavy Component of Cosmic Rays Observed with KASCADE-Grande”. In: *Physical Review Letters* 107 (17 2011), p. 171104. DOI: 10.1103/PhysRevLett.107.171104. URL: <http://link.aps.org/doi/10.1103/PhysRevLett.107.171104>.

- [30] R. Abbasi et al. “Cosmic ray composition and energy spectrum from 1-30 PeV using the 40-string configuration of IceTop and IceCube”. In: *Astroparticle Physics* 42.0 (2013), pp. 15–32. ISSN: 0927-6505. DOI: <http://dx.doi.org/10.1016/j.astropartphys.2012.11.003>. URL: <http://www.sciencedirect.com/science/article/pii/S0927650512002009>.
- [31] D. R. Bergman and J. W. Belz. “Cosmic rays: the Second Knee and beyond”. In: *Journal of Physics G: Nuclear and Particle Physics* 34.10 (2007), R359. DOI: 10.1088/0954-3899/34/10/R01. URL: <http://stacks.iop.org/0954-3899/34/i=10/a=R01>.
- [32] J. Hörandel. “The composition of cosmic rays at the knee”. In: *AIP Conference Proceedings, in Centenary Symposium 2012: Discovery of Cosmic Rays*. Vol. 1516. 1. AIP Scitation, 2013, pp. 185–194. DOI: <http://dx.doi.org/10.1063/1.4792566>. URL: <http://scitation.aip.org/content/aip/proceeding/aipcp/10.1063/1.4792566>.
- [33] W. F. G. Swann. “A Mechanism of Acquirement of Cosmic-Ray Energies by Electrons”. In: *Physics Review* 43 (4 1933), pp. 217–220. DOI: 10.1103/PhysRev.43.217. URL: <http://link.aps.org/doi/10.1103/PhysRev.43.217>.
- [34] A. M. Hillas. “The Origin of Ultra-High-Energy Cosmic Rays”. In: *Annual Review of Astronomy and Astrophysics* 22 (4 1984), pp. 425–444. DOI: 10.1146/annurev.aa.22.090184.002233. URL: <http://www.annualreviews.org/doi/pdf/10.1146/annurev.aa.22.090184.002233>.
- [35] E. Fermi. “The Origin of Ultra-High-Energy Cosmic Rays”. In: *Annual Review of Astronomy and Astrophysics* 22 (4 1984), pp. 425–444. DOI: 10.1146/annurev.aa.22.090184.002233. URL: <http://www.annualreviews.org/doi/pdf/10.1146/annurev.aa.22.090184.002233>.
- [36] J.R. Protheroe. “Acceleration and Interaction of Ultra High Energy Cosmic Rays”. In: *”Topics in cosmic-ray astrophysics” ed. M. A. DuVernois*. Ed. by M. A. Duvernois. Vol. ADP-AT-98-9. 1999, p. 247. DOI: [arXiv:astro-ph/9812055](https://arxiv.org/abs/astro-ph/9812055). arXiv: [astro-ph/9812055](https://arxiv.org/abs/astro-ph/9812055).
- [37] L. Anchordoqui et al. “Ultrahigh Energy Cosmic Rays: The state of the art before the Auger Observatory”. In: *International Journal of Modern Physics A* 18.13 (2003), pp. 2229–2366. DOI: 10.1142/S0217751X03013879. arXiv: [hep-ph/0206072](https://arxiv.org/abs/hep-ph/0206072). URL: <http://www.worldscientific.com/doi/abs/10.1142/S0217751X03013879>.
- [38] P. Bhattacharjee and G. Sigl. “Origin and propagation of extremely high-energy cosmic rays”. In: *Physics Reports* 327.3-4 (2000), pp. 109–247. ISSN: 0370-1573. DOI: [http://dx.doi.org/10.1016/S0370-1573\(99\)00101-5](http://dx.doi.org/10.1016/S0370-1573(99)00101-5). URL: <http://www.sciencedirect.com/science/article/pii/S0370157399001015>.
- [39] M. Settimo and for The Pierre Auger Collaboration. “An update on a search for ultra-high energy photons using the Pierre Auger Observatory”. In: *32nd International Cosmic Ray Conference (ICRC 2011)*. Vol. 2. The Pierre Auger Observatory III: Other Astrophysical Observations. Beijing, China, July 2011, pp. 55–58. DOI: 10.7529/ICRC2011/V02/0393. arXiv: [1107.4805](https://arxiv.org/abs/1107.4805).
- [40] P. Pieroni and for the Pierre Auger Collaboration. “Ultra-high energy neutrinos at the Pierre Auger Observatory”. In: *33rd International Cosmic Ray Conference (ICRC 2013)*. Rio de Janeiro, 2013, pp. 76–79. arXiv: [1307.5059](https://arxiv.org/abs/1307.5059).
- [41] D. Harari, S. Mollerach, and E. Roulet. “The toes of the ultra high energy cosmic ray spectrum”. In: *Journal of High Energy Physics* 1999.08 (1999), p. 022. DOI: 10.1088/1126-6708/1999/08/022. arXiv: [astro-ph/9906309](https://arxiv.org/abs/astro-ph/9906309). URL: <http://stacks.iop.org/1126-6708/1999/i=08/a=022>.
- [42] J. W. Cronin. “The highest-energy cosmic rays”. In: *Nuclear Physics B - Proceedings Supplements* 138.0 (2005). Proceedings of the Eighth International Workshop on Topics in Astroparticle and Underground Physics, pp. 465–491. ISSN: 0920-5632. DOI: 10.1016/j.nuclphysbps.2004.11.107. URL: <http://www.sciencedirect.com/science/article/pii/S0920563204006723>.

- [43] T.E. Clarke, P.P. Kronberg, and H. Böehringer. “A New radio-X-ray probe of galaxy cluster magnetic fields”. In: *The Astrophysical Journal Letters* 547.2 (2001), pp. L111–L114. DOI: 10.1086/318896. arXiv: astro-ph/0011281 [astro-ph]. URL: <http://stacks.iop.org/1538-4357/547/i=2/a=L111>.
- [44] A. A. Penzias and R. W. Wilson. “A Measurement of Excess Antenna Temperature at 4080 Mc/s.” In: *Astrophysical Journal* 142 (July 1965), pp. 419–421. DOI: 10.1086/148307.
- [45] K. Greisen. “End to the Cosmic-Ray Spectrum?” In: *Physical Review Letters* 16 (17 1966), pp. 748–750. DOI: 10.1103/PhysRevLett.16.748. URL: <http://link.aps.org/doi/10.1103/PhysRevLett.16.748>.
- [46] G. T. Zatsepin and V. A. Kuz'min. “Upper Limit of the Spectrum of Cosmic Rays”. In: *Soviet Journal of Experimental and Theoretical Physics Letters* 4 (Aug. 1966), p. 78.
- [47] A.M. Hillas. “The energy spectrum of cosmic rays in an evolving universe”. In: *Physics Letters A* 24.12 (1967), pp. 677–678. ISSN: 0375-9601. DOI: 10.1016/0375-9601(67)91023-7. URL: <http://www.sciencedirect.com/science/article/pii/0375960167910237>.
- [48] A.P. Szabo and R.J. Protheroe. “Implications of particle acceleration in active galactic nuclei for cosmic rays and high energy neutrino astronomy”. In: *Astroparticle Physics* 2.4 (1994), pp. 375–392. ISSN: 0927-6505. DOI: 10.1016/0927-6505(94)90027-2. arXiv: astro-ph/9405020. URL: <http://www.sciencedirect.com/science/article/pii/0927650594900272>.
- [49] A. Mücke et al. “Monte Carlo simulations of photohadronic processes in astrophysics”. In: *Computer Physics Communications* 124.2-3 (Feb. 2000), pp. 290–314. ISSN: 0010-4655. DOI: 10.1016/S0010-4655(99)00446-4. arXiv: astro-ph/9903478.
- [50] T. Stanev et al. “Propagation of ultrahigh energy protons in the nearby universe”. In: *Physical Review D* 62 (9 2000), p. 093005. DOI: 10.1103/PhysRevD.62.093005. URL: <http://link.aps.org/doi/10.1103/PhysRevD.62.093005>.
- [51] T. Stanev. *High Energy Cosmic Rays*. Springer Praxis Books / Astronomy and Planetary Sciences Series. Springer London, Limited, 2011. ISBN: 9783642073731. URL: <http://books.google.ca/books?id=nmEEkgAACAAJ>.
- [52] D. Allard. “Extragalactic propagation of ultrahigh energy cosmic-rays”. In: *Astroparticle Physics* 39-40.0 (2012). Cosmic Rays Topical Issue, pp. 33–43. ISSN: 0927-6505. DOI: 10.1016/j.astropartphys.2011.10.011. URL: <http://www.sciencedirect.com/science/article/pii/S092765051100199X>.
- [53] V. Berezhinsky, A. Gazizov, and S. Grigorieva. “On astrophysical solution to ultrahigh energy cosmic rays”. In: *Physical Review D* 74 (4 2006), p. 043005. DOI: 10.1103/PhysRevD.74.043005. URL: <http://link.aps.org/doi/10.1103/PhysRevD.74.043005>.
- [54] F. Aharonian and J. Cronin. “Influence of the universal microwave background radiation on the extragalactic cosmic-ray spectrum”. In: *Physical Review D* 50 (3 1994), pp. 1892–1900. DOI: 10.1103/PhysRevD.50.1892. URL: <http://link.aps.org/doi/10.1103/PhysRevD.50.1892>.
- [55] M Risse and P. Homola. “Search for ultra-high energy photons using air showers”. In: *Modern Physics Letters A* 22.11 (2007), pp. 749–766. DOI: 10.1142/S0217732307022864. URL: <http://www.worldscientific.com/doi/abs/10.1142/S0217732307022864>.
- [56] K. Karl-Heinz et al. “CRPropa 2.0 - A public framework for propagating high energy nuclei, secondary gamma rays and neutrinos”. In: *Astroparticle Physics* 42.0 (2013), pp. 41–51. ISSN: 0927-6505. DOI: 10.1016/j.astropartphys.2012.12.001. URL: <http://www.sciencedirect.com/science/article/pii/S0927650512002186>.
- [57] R. Aloisio et al. “SimProp: a simulation code for ultra high energy cosmic ray propagation”. In: *Journal of Cosmology and Astroparticle Physics* 10 (2012), p. 7. arXiv: 1204.2970 [astro-ph.HE].

- [58] L. Anchordoqui et al. “High energy physics in the atmosphere: phenomenology of cosmic ray air showers”. In: *Annals of Physics* 314.1 (2004), pp. 145–207. ISSN: 0003-4916. DOI: 10.1016/j.aop.2004.07.003. URL: <http://www.sciencedirect.com/science/article/pii/S0003491604001381>.
- [59] M. Risse. “Properties of Extensive Air Showers”. In: *Acta Physica Polonica B* 35 (June 2004), p. 1787. arXiv: [astro-ph/0402300](https://arxiv.org/abs/astro-ph/0402300).
- [60] B. Rossi. *High Energy Particles*. Prentice-Hall, Inc., EnglewoodCliffs, 1952.
- [61] CRC Press Group. *CRC Handbook of Chemistry and Physics*. 91th. CRC Press, Taylor & Francis Group, 2009.
- [62] M.J. Berger and S.M. Seltzer. *Tables of Energy Losses and Ranges of Electrons and Positrons*. National Aeronautics and Space Administration Report NASA-SP-3012, 1964.
- [63] W. Heitler. *The Quantum Theory of Radiation*. Oxford University Press, 1944.
- [64] M. Risse et al. “Photon air showers at ultra-high energy and the photonuclear cross-section”. In: *Czechoslovak Journal of Physics* 56.1 (2006), A327–A336. ISSN: 0011-4626. DOI: 10.1007/s10582-006-0166-7.
- [65] A. Donnachie and P.V. Landshoff. “New data and the hard pomeron”. In: *Physics Letters B* 518.1-2 (2001), pp. 63–71. ISSN: 0370-2693. DOI: [http://dx.doi.org/10.1016/S0370-2693\(01\)01048-6](http://dx.doi.org/10.1016/S0370-2693(01)01048-6). arXiv: [hep-ph/0105088](https://arxiv.org/abs/hep-ph/0105088). URL: <http://www.sciencedirect.com/science/article/pii/S0370269301010486>.
- [66] J. Matthews. “A Heitler model of extensive air showers”. In: *Astroparticle Physics* 22.5-6 (2005), pp. 387–397. ISSN: 0927-6505. DOI: 10.1016/j.astropartphys.2004.09.003. URL: <http://www.sciencedirect.com/science/article/pii/S0927650504001598>.
- [67] L.D. Landau and I.Ya. Pomeranchuk. “Electron-cascade processes at very high energies”. In: *Doklady Akademii Nauk SSSR* 92 (1953), pp. 735–738.
- [68] A. B. Migdal. “Bremsstrahlung and Pair Production in Condensed Media at High Energies”. In: *Physical Review* 103 (6 1956), pp. 1811–1820. DOI: 10.1103/PhysRev.103.1811. URL: <http://link.aps.org/doi/10.1103/PhysRev.103.1811>.
- [69] K. Greisen. “Cosmic Ray Showers”. In: *Annual Review of Nuclear Science* 10.1 (1960), pp. 63–108. DOI: 10.1146/annurev.ns.10.120160.000431.
- [70] Koichi Kamata and Jun Nishimura. “The Lateral and the Angular Structure Functions of Electron Showers”. In: *Progress of Theoretical Physics Supplement* 6 (1958), pp. 93–155. DOI: 10.1143/PTPS.6.93. eprint: <http://ptps.oxfordjournals.org/content/6/93.full.pdf+html>.
- [71] H. A. Bethe. “Molière’s Theory of Multiple Scattering”. In: *Physical Review* 89 (6 1953), pp. 1256–1266. DOI: 10.1103/PhysRev.89.1256. URL: <http://link.aps.org/doi/10.1103/PhysRev.89.1256>.
- [72] J. Alvarez-Muñiz et al. “Hybrid simulations of extensive air showers”. In: *Physical Review D* 66 (3 2002), p. 033011. DOI: 10.1103/PhysRevD.66.033011. URL: <http://link.aps.org/doi/10.1103/PhysRevD.66.033011>.
- [73] T. K. Gaisser and A. M. Hillas. “Reliability of the method of constant intensity cuts for reconstructing the average development of vertical showers”. In: *15th International Cosmic Ray Conference (ICRC 1977)*. Vol. 8. Plovdiv, Bulgaria, 1977, pp. 353–357.
- [74] S. Andringa, R. Conceição, and M. Pimenta. “Increased sensitivity to electromagnetic and hadronic features of air showers from a new parameterization of the longitudinal profiles”. In: *31st International Cosmic Ray Conference (ICRC 2009)*. Lodz, Poland, 2009, pp. 7–15.
- [75] S. Andringa, R. Conceição, and M. Pimenta. “Mass composition and cross-section from the shape of cosmic ray shower longitudinal profiles”. In: *Astroparticle Physics* 34.6 (2011), pp. 360–367. ISSN: 0927-6505. DOI: 10.1016/j.astropartphys.2010.10.002. URL: <http://www.sciencedirect.com/science/article/pii/S0927650510001830>.

- [76] S. Andringa et al. *Measurement of the shape parameters of FD average profiles*. Tech. rep. 2014-004. Pierre Auger GAP-Notes, 2014.
- [77] D. Góra et al. “Universal lateral distribution of energy deposit in air showers and its application to shower reconstruction”. In: *Astroparticle Physics* 24.6 (2006), pp. 484–494. ISSN: 0927-6505. DOI: 10.1016/j.astropartphys.2005.09.007. URL: <http://www.sciencedirect.com/science/article/pii/S0927650505001453>.
- [78] G. Battistoni et al. “The FLUKA code: description and benchmarking”. In: *AIP Conference Proceedings: Hadronic Shower Simulation Workshop*. Ed. by M. Albrow and R. Raja. Vol. 896. American Institute of Physics Conference Series. Mar. 2007, pp. 31–49. DOI: 10.1063/1.2720455. URL: <http://scitation.aip.org/content/aip/proceeding/aipcp/10.1063/1.2720455>.
- [79] H. Fesefeldt. *Simulations of Hadronic Showers, Physics and Applications*. Tech. rep. 1985.
- [80] S.A. Bass et al. “Microscopic models for ultrarelativistic heavy ion collisions”. In: *Progress in Particle and Nuclear Physics* 41 (1998), pp. 255–369. ISSN: 0146-6410. DOI: 10.1016/S0146-6410(98)00058-1. arXiv: nucl-th/9803035 [nucl-th]. URL: <http://www.sciencedirect.com/science/article/pii/S0146641098000581>.
- [81] I. C. Mariş et al. “Influence of low energy hadronic interactions on air-shower simulations”. In: *Nuclear Physics B Proceedings Supplements* 196 (Dec. 2009), pp. 86–89. ISSN: 0920-5632. DOI: 10.1016/j.nuclphysbps.2009.09.013. arXiv: 0907.0409 [astro-ph.CO]. URL: <http://www.sciencedirect.com/science/article/pii/S0920563209006495>.
- [82] V.N. Gribov. “A Reggeon Diagram Technique”. In: *Soviet Physics: Journal of Experimental and Theoretical Physics* 26 (1968), pp. 414–422.
- [83] S. Ostapchenko. “Non-Linear Effects in High Energy Hadronic Interactions”. In: Jan. 2005. arXiv: hep-ph/0501093.
- [84] T. Pierog and K. Werner. “EPOS Model and Ultra High Energy Cosmic Rays”. In: *Nuclear Physics B Proceedings Supplements* 196 (Dec. 2009), pp. 102–105. ISSN: 0920-5632. DOI: 10.1016/j.nuclphysbps.2009.09.017. arXiv: 0905.1198 [hep-ph]. URL: <http://www.sciencedirect.com/science/article/pii/S0920563209006537>.
- [85] E.J. Ahn et al. “Cosmic ray interaction event generator SIBYLL 2.1”. In: *Physical Review D* 80.9, 094003 (Nov. 2009), p. 094003. DOI: 10.1103/PhysRevD.80.094003. arXiv: 0906.4113 [hep-ph]. URL: <http://link.aps.org/doi/10.1103/PhysRevD.80.094003>.
- [86] Pierog, T. et al. “Future of Monte Carlo simulations of atmospheric showers”. In: *AtmoHEAD 2014: Atmospheric Monitoring for High Energy AstroParticle Detectors*. Ed. by EPJ Web of Conferences. Vol. 89. 2015, p. 01003. DOI: 10.1051/epjconf/20158901003. URL: <http://dx.doi.org/10.1051/epjconf/20158901003>.
- [87] R. Ulrich, R. Engel, and M. Unger. “Hadronic multiparticle production at ultrahigh energies and extensive air showers”. In: *Physical Review D* 83.5, 054026 (Mar. 2011), p. 054026. DOI: 10.1103/PhysRevD.83.054026. arXiv: 1010.4310 [hep-ph]. URL: <http://link.aps.org/doi/10.1103/PhysRevD.83.054026>.
- [88] G. R. Farrar and J. D. Allen. “A new physical phenomenon in ultra-high energy collisions”. In: *UHECR 2012 - International Symposium on Future Directions in UHECR Physics*. Ed. by EPJ Web of Conferences. Vol. 53. European Physical Journal Web of Conferences. June 2013, p. 7007. DOI: 10.1051/epjconf/20135307007. arXiv: 1307.2322 [hep-ph].
- [89] J. Alvarez-Muñiz et al. “Percolation and high energy cosmic rays above 10^{17} eV”. In: *Astroparticle Physics* 27 (Apr. 2007), pp. 271–277. ISSN: 0927-6505. DOI: 10.1016/j.astropartphys.2006.11.006. arXiv: hep-ph/0608050. URL: <http://www.sciencedirect.com/science/article/pii/S0927650506001836>.

- [90] S. J. Sciutto. “AIRES: A system for air shower simulations (Version 2.2.0)”. In: *ArXiv Astrophysics e-prints* (Nov. 1999). arXiv: astro-ph/9911331 [astro-ph].
- [91] D. Heck et al. *CORSIKA: A Monte Carlo Code to Simulate Extensive Air Showers*. 1998.
- [92] T. Pierog et al. “First results of fast one-dimensional hybrid simulation of EAS using CONEX”. In: *Nuclear Physics B Proceedings Supplements* 151 (Jan. 2006), pp. 159–162. ISSN: 0920-5632. DOI: 10.1016/j.nuclphysbps.2005.07.029. arXiv: astro-ph/0411260. URL: <http://www.sciencedirect.com/science/article/pii/S0920563205009205>.
- [93] H.J. Drescher and G. R. Farrar. “Air shower simulations in a hybrid approach using cascade equations”. In: *Physical Review D* 67.11, 116001 (June 2003), p. 116001. DOI: 10.1103/PhysRevD.67.116001. arXiv: astro-ph/0212018. URL: <http://link.aps.org/doi/10.1103/PhysRevD.67.116001>.
- [94] K. de Souza et al. “Design studies for a very large detector array to study cosmic rays at the highest energies”. In: *Nuclear Physics B - Proceedings Supplements* 28.2 (1992), pp. 135–142. ISSN: 0920-5632. DOI: 10.1016/0920-5632(92)90119-D. URL: <http://www.sciencedirect.com/science/article/pii/092056329290119D>.
- [95] A.U. Abeysekara et al. “On the sensitivity of the HAWC observatory to gamma-ray bursts”. In: *Astroparticle Physics* 35.10 (2012), pp. 641–650. ISSN: 0927-6505. DOI: <http://dx.doi.org/10.1016/j.astropartphys.2012.02.001>. URL: <http://www.sciencedirect.com/science/article/pii/S0927650512000291>.
- [96] K. Kamata et al. “Akeno air shower project”. In: *AIP Conference Proceedings*. Vol. 49. 1. 1979, pp. 443–450. DOI: <http://dx.doi.org/10.1063/1.31637>. URL: <http://scitation.aip.org/content/aip/proceeding/aipcp/10.1063/1.31637>.
- [97] N. Chiba et al. “Akeno Giant Air Shower Array (AGASA) covering 100 km² area”. In: *Nuclear Instruments and Methods in Physics Research Section A: Accelerators, Spectrometers, Detectors and Associated Equipment* 311.1-2 (1992), pp. 338–349. ISSN: 0168-9002. DOI: 10.1016/0168-9002(92)90882-5. URL: <http://www.sciencedirect.com/science/article/pii/0168900292908825>.
- [98] T. Antoni et al. “The cosmic-ray experiment KASCADE”. In: *Nuclear Instruments and Methods in Physics Research Section A: Accelerators, Spectrometers, Detectors and Associated Equipment* 513.3 (2003), pp. 490–510. ISSN: 0168-9002. DOI: 10.1016/S0168-9002(03)02076-X. URL: <http://www.sciencedirect.com/science/article/pii/S016890020302076X>.
- [99] W.D. Apel et al. “The KASCADE-Grande experiment”. In: *Nuclear Instruments and Methods in Physics Research Section A: Accelerators, Spectrometers, Detectors and Associated Equipment* 620.2-3 (2010), pp. 202–216. ISSN: 0168-9002. DOI: 10.1016/j.nima.2010.03.147. URL: <http://www.sciencedirect.com/science/article/pii/S0168900210007734>.
- [100] A. Etchegoyen. “AMIGA, Auger Muons and Infill for the Ground Array”. In: (Oct. 2007). arXiv: 0710.1646 [astro-ph].
- [101] M. Aglietta et al. “The EAS-TOP array at $E_0 = 10^{14} - 10^{16}$ eV: Stability and resolutions”. In: *Nuclear Instruments and Methods in Physics Research Section A: Accelerators, Spectrometers, Detectors and Associated Equipment* 277.1 (1989), pp. 23–28. ISSN: 0168-9002. DOI: 10.1016/0168-9002(89)90531-7. URL: <http://www.sciencedirect.com/science/article/pii/0168900289905317>.
- [102] Denis A. Suprun, Peter W. Gorham, and Jonathan L. Rosner. “Synchrotron radiation at radio frequencies from cosmic ray air showers”. In: *Astroparticle Physics* 20.2 (2003), pp. 157–168. ISSN: 0927-6505. DOI: 10.1016/S0927-6505(03)00177-4. URL: <http://www.sciencedirect.com/science/article/pii/S0927650503001774>.
- [103] Markus Risse and Dieter Heck. “Energy release in air showers”. In: *Astroparticle Physics* 20.6 (2004), pp. 661–667. ISSN: 0927-6505. DOI: 10.1016/j.astropartphys.2003.10.006. URL: <http://www.sciencedirect.com/science/article/pii/S0927650503002664>.

- [104] M. Boháčová. “Study of the Air Fluorescence by AIRFLY”. In: *Nuclear Physics B - Proceedings Supplements* 190.0 (2009). Proceedings of the Cosmic Ray International Seminars, pp. 266–271. ISSN: 0920-5632. DOI: 10.1016/j.nuclphysbps.2009.03.098. URL: <http://www.sciencedirect.com/science/article/pii/S0920563209003375>.
- [105] T. Waldenmaier et al. “Measurement of the air fluorescence yield with the airlight experiment”. In: *Nuclear Instruments and Methods in Physics Research Section A: Accelerators, Spectrometers, Detectors and Associated Equipment* 597.1 (2008). Proceedings of the 5th Fluorescence Workshop, pp. 67–74. ISSN: 0168-9002. DOI: 10.1016/j.nima.2008.08.047. URL: <http://www.sciencedirect.com/science/article/pii/S0168900208012813>.
- [106] M. Nagano et al. “New measurement on photon yields from air and the application to the energy estimation of primary cosmic rays”. In: *Astroparticle Physics* 22.3-4 (2004), pp. 235–248. ISSN: 0927-6505. DOI: 10.1016/j.astropartphys.2004.08.002. URL: <http://www.sciencedirect.com/science/article/pii/S0927650504001434>.
- [107] P. Colin et al. “Measurement of air and nitrogen fluorescence light yields induced by electron beam for UHECR experiments”. In: *Astroparticle Physics* 27.5 (2007), pp. 317–325. ISSN: 0927-6505. DOI: 10.1016/j.astropartphys.2006.11.008. URL: <http://www.sciencedirect.com/science/article/pii/S092765050600185X>.
- [108] S. Agostinelli et al. “Geant4—a simulation toolkit”. In: *Nuclear Instruments and Methods in Physics Research Section A: Accelerators, Spectrometers, Detectors and Associated Equipment* 506.3 (2003), pp. 250–303. ISSN: 0168-9002. DOI: [http://dx.doi.org/10.1016/S0168-9002\(03\)01368-8](http://dx.doi.org/10.1016/S0168-9002(03)01368-8). URL: <http://www.sciencedirect.com/science/article/pii/S0168900203013688>.
- [109] F. Kakimoto et al. “A measurement of the air fluorescence yield”. In: *Nuclear Instruments and Methods in Physics Research Section A: Accelerators, Spectrometers, Detectors and Associated Equipment* 372.3 (1996), pp. 527–533. ISSN: 0168-9002. DOI: 10.1016/0168-9002(95)01423-3. URL: <http://www.sciencedirect.com/science/article/pii/0168900295014233>.
- [110] J.W. Belz et al. “Measurement of pressure dependent fluorescence yield of air: Calibration factor for UHECR detectors”. In: *Astroparticle Physics* 25.2 (2006), pp. 129–139. ISSN: 0927-6505. DOI: <http://dx.doi.org/10.1016/j.astropartphys.2005.12.008>. URL: <http://www.sciencedirect.com/science/article/pii/S092765050500188X>.
- [111] M. Ave et al. “Precise measurement of the absolute fluorescence yield of the 337 nm band in atmospheric gases”. In: *Astroparticle Physics* 42 (Feb. 2013), pp. 90–102. ISSN: 0927-6505. DOI: 10.1016/j.astropartphys.2012.12.006. arXiv: 1210.6734 [astro-ph.IM]. URL: <http://www.sciencedirect.com/science/article/pii/S092765051200223X>.
- [112] F. I. Boley. “Atmospheric Čerenkov Radiation from Cosmic-Ray Air Showers”. In: *Review Modern Physics* 36 (3 1964), pp. 792–808. DOI: 10.1103/RevModPhys.36.792. URL: <http://link.aps.org/doi/10.1103/RevModPhys.36.792>.
- [113] F. Nerling. *Thesis: Description of Cherenkov Light Production in Extensive Air Showers*. Tech. rep. 2005-063. Pierre Auger GAP-Notes, 2005.
- [114] F. Nerling et al. “Universality of electron distributions in high-energy air showers-Description of Cherenkov light production”. In: *Astroparticle Physics* 24.6 (2006), pp. 421–437. ISSN: 0927-6505. DOI: 10.1016/j.astropartphys.2005.09.002. URL: <http://www.sciencedirect.com/science/article/pii/S0927650505001325>.
- [115] A. Bucholtz. “Rayleigh-scattering calculations for the terrestrial atmosphere”. In: *Applied Optics* 34.15 (1995), pp. 2765–2773. DOI: 10.1364/AO.34.002765. URL: <http://ao.osa.org/abstract.cfm?URI=ao-34-15-2765>.

- [116] J. Diaz, M. Amaral, and R. Shellard. *Weakly Interacting Particles Viewed by Fluorescence Detectors*. Tech. rep. Pierre Auger GAP-Notes, 2000.
- [117] T Abu-Zayyad et al. “The prototype high-resolution Fly’s Eye cosmic ray detector”. In: *Nuclear Instruments and Methods in Physics Research Section A: Accelerators, Spectrometers, Detectors and Associated Equipment* 450.2-3 (2000), pp. 253–269. ISSN: 0168-9002. DOI: 10.1016/S0168-9002(00)00307-7. URL: <http://www.sciencedirect.com/science/article/pii/S0168900200003077>.
- [118] The MAGIC Collaboration et al. “Unprecedented study of the broadband emission of Mrk 421 during flaring activity in March 2010”. In: *ArXiv e-prints* (Dec. 2014). arXiv: 1412.3576.
- [119] F. Aharonian et al. “Observations of the Crab nebula with HESS”. In: *Astronomy and Astrophysics* 457 (Oct. 2006), pp. 899–915. DOI: 10.1051/0004-6361:20065351. arXiv: astro-ph/0607333.
- [120] M. Persic. “CTA: the future of ground-based γ -ray astrophysics”. In: *Nuclear Physics B - Proceedings Supplements* 239-240.0 (2013). Proceedings of the 9th workshop on Science with the New Generation of High Energy Gamma-ray Experiments: From high energy gamma sources to cosmic rays, one century after their discovery, pp. 210–215. ISSN: 0920-5632. DOI: 10.1016/j.nuclphysbps.2013.05.048. URL: <http://www.sciencedirect.com/science/article/pii/S0920563213004271>.
- [121] S. F. Berezhnev et al. “The Tunka-133 EAS Cherenkov light array: Status of 2011”. In: *Nuclear Instruments and Methods in Physics Research A* 692 (Nov. 2012), pp. 98–105. DOI: 10.1016/j.nima.2011.12.091. arXiv: 1201.2122.
- [122] J. V. Jelley et al. “Radio Pulses from Extensive Cosmic-Ray Air Showers”. In: *Nature* 205 (Jan. 1965), pp. 327–328. DOI: 10.1038/205327a0.
- [123] J. Nichimura. “Radio wave emitted by an extensive air showers in 10 KHz to 1 MHz region”. In: *19th International Cosmic Ray Conference (ICRC 1985)*. Vol. 7. La Jolla, USA, Aug. 1985, pp. 308–311.
- [124] K. Boruah et al. “Low frequency radio-emission associated with UHE cosmic rays”. In: *Nuclear Physics B - Proceedings Supplements* 212-213.0 (2011). Proceedings of the Cosmic Ray International Seminars (CRIS 2010) 100 years of Cosmic Ray Physics: from pioneering experiments to physics in space, pp. 317–322. ISSN: 0920-5632. DOI: 10.1016/j.nuclphysbps.2011.03.042. URL: <http://www.sciencedirect.com/science/article/pii/S0920563211000752>.
- [125] H. Falcke et al. “Detection and imaging of atmospheric radio flashes from cosmic ray air showers”. In: *Nature* 435 (May 2005), pp. 313–316. DOI: 10.1038/nature03614. arXiv: astro-ph/0505383.
- [126] D. Ardouin et al. “Radio-detection signature of high-energy cosmic rays by the CODALEMA experiment”. In: *Nuclear Instruments and Methods in Physics Research Section A: Accelerators, Spectrometers, Detectors and Associated Equipment* 555.1-2 (2005), pp. 148–163. ISSN: 0168-9002. DOI: 10.1016/j.nima.2005.08.096. URL: <http://www.sciencedirect.com/science/article/pii/S0168900205017468>.
- [127] F. Schröder for the Pierre Auger Collaboration. “Radio detection of air showers with the Auger Engineering Radio Array”. In: *33rd International Cosmic Ray Conference (ICRC 2013)*. Rio de Janeiro, 2013, pp. 88–91. arXiv: 1307.5059.
- [128] R. Gaio for the Pierre Auger Collaboration. “Detection of cosmic rays using microwave radiation at the Pierre Auger Observatory”. In: *33rd International Cosmic Ray Conference (ICRC 2013)*. Rio de Janeiro, 2013, pp. 96–99. arXiv: 1307.5059.
- [129] P. W. Gorham et al. “Observations of microwave continuum emission from air shower plasmas”. In: *Physical Review D* 78 (3 2008), p. 032007. DOI: 10.1103/PhysRevD.78.032007. URL: <http://link.aps.org/doi/10.1103/PhysRevD.78.032007>.
- [130] S. Baur et al. *On the Microwave Signal of Air Showers Observed with CROME*. Tech. rep. 2012-061. Pierre Auger GAP-Notes, 2012.

- [131] P. Allison for the Pierre Auger Collaboration. “Microwave detection of cosmic ray showers at the Pierre Auger Observatory”. In: *32nd International Cosmic Ray Conference (ICRC 2011)*. Vol. 3. The Pierre Auger Observatory V: Enhancements. Beijing, China, 2011, pp. 141–144. DOI: 10.7529/ICRC2011/V03/0733. arXiv: 1107.4807.
- [132] P. Facal San Luis et al. “Microwave detection of air showers with MIDAS”. In: *Nuclear Instruments and Methods in Physics Research Section A: Accelerators, Spectrometers, Detectors and Associated Equipment* 662, Supplement 1.0 (2012). 4th International workshop on Acoustic and Radio EeV Neutrino detection Activities, S118–S123. ISSN: 0168-9002. DOI: 10.1016/j.nima.2010.11.020. URL: <http://www.sciencedirect.com/science/article/pii/S0168900210024629>.
- [133] R. Salamida et al. “First Experimental Characterization of Microwave Emission from Cosmic Ray Air Showers”. In: *Physical Review Letters* 113 (22 2014), p. 221101. DOI: 10.1103/PhysRevLett.113.221101. URL: <http://link.aps.org/doi/10.1103/PhysRevLett.113.221101>.
- [134] I. Allekotte et al. “The surface detector system of the Pierre Auger Observatory”. In: *Nuclear Instruments and Methods in Physics Research Section A: Accelerators, Spectrometers, Detectors and Associated Equipment* 586.3 (2008), pp. 409–420. ISSN: 0168-9002. DOI: 10.1016/j.nima.2007.12.016. URL: <http://www.sciencedirect.com/science/article/pii/S0168900207024680>.
- [135] The Pierre Auger Collaboration. “The Pierre Auger Cosmic Ray Observatory”. In: *submitted to Nuclear Instruments and Methods in Physics Research Section A: Accelerators, Spectrometers, Detectors and Associated Equipment* (Feb. 2015). arXiv: 1502.01323 [astro-ph.IM].
- [136] M. Aglietta for the Pierre Auger Collaboration. “Calibration of the surface array of the Pierre Auger Observatory”. In: *29th International Cosmic Ray Conference (ICRC 2005)*. Vol. 7. Pune, 2005, pp. 279–282.
- [137] M. Aglietta for the Pierre Auger Collaboration. “Response of the Pierre Auger Observatory Water Cherenkov Detectors to Muons”. In: *29th International Cosmic Ray Conference (ICRC 2005)*. Vol. 7. Pune, 2005, pp. 83–86.
- [138] A. Etchegoyen et al. “Muon-track studies in a water Cherenkov detector”. In: *Nuclear Instruments and Methods in Physics Research Section A: Accelerators, Spectrometers, Detectors and Associated Equipment* 545.3 (2005), pp. 602–612. ISSN: 0168-9002. DOI: 10.1016/j.nima.2005.02.016. URL: <http://www.sciencedirect.com/science/article/pii/S016890020500759X>.
- [139] J. Abraham et al. “Trigger and aperture of the surface detector array of the Pierre Auger Observatory”. In: *Nuclear Instruments and Methods in Physics Research Section A: Accelerators, Spectrometers, Detectors and Associated Equipment* 613.1 (2010), pp. 29–39. ISSN: 0168-9002. DOI: 10.1016/j.nima.2009.11.018. URL: <http://www.sciencedirect.com/science/article/pii/S0168900209021688>.
- [140] Markus Roth Darko Veberic. *SD Reconstruction; Offline Reference Manual*. Tech. rep. 2005-035. Pierre Auger GAP-Notes, 2005.
- [141] D. Newton, J. Knapp, and A.A. Watson. “The optimum distance at which to determine the size of a giant air shower”. In: *Astroparticle Physics* 26.6 (2007), pp. 414–419. ISSN: 0927-6505. DOI: 10.1016/j.astropartphys.2006.08.003. URL: <http://www.sciencedirect.com/science/article/pii/S0927650506001216>.
- [142] J. Abraham et al. “The fluorescence detector of the Pierre Auger Observatory”. In: *Nuclear Instruments and Methods in Physics Research Section A: Accelerators, Spectrometers, Detectors and Associated Equipment* 620.2-3 (2010), pp. 227–251. ISSN: 0168-9002. DOI: 10.1016/j.nima.2010.04.023. URL: <http://www.sciencedirect.com/science/article/pii/S0168900210008727>.
- [143] R. Sato and C. O. Escobar. “The Performance of the Corrector Lenses for the Auger Fluorescence Detector”. In: *29th International Cosmic Ray Conference (ICRC 2005)*. Vol. 8. 2005, p. 13.

- [144] D.Allard et al. *A New Method for the Longitudinal Profile Reconstruction of the AUGER Fluorescence Detector Events*. Tech. rep. 2006-026. Pierre Auger GAP-Notes, 2006.
- [145] J.T. Brack et al. “Absolute photometric calibration of large aperture optical systems”. In: *Astroparticle Physics* 20.6 (2004), pp. 653–659. ISSN: 0927-6505. DOI: 10.1016/j.astropartphys.2003.09.004. URL: <http://www.sciencedirect.com/science/article/pii/S0927650503002469>.
- [146] M. Unger et al. “Reconstruction of longitudinal profiles of ultra-high energy cosmic ray showers from fluorescence and Cherenkov light measurements”. In: *Nuclear Instruments and Methods in Physics Research Section A: Accelerators, Spectrometers, Detectors and Associated Equipment* 588.3 (2008), pp. 433–441. ISSN: 0168-9002. DOI: 10.1016/j.nima.2008.01.100. arXiv: 0801.4309 [astro-ph]. URL: <http://www.sciencedirect.com/science/article/pii/S0168900208001587>.
- [147] M Giller et al. “Energy spectra of electrons in the extensive air showers of ultra-high energy”. In: *Journal of Physics G: Nuclear and Particle Physics* 30.2 (2004), p. 97. URL: <http://stacks.iop.org/0954-3899/30/i=2/a=009>.
- [148] M. D. Roberts. “The role of atmospheric multiple scattering in the transmission of fluorescence light from extensive air showers”. In: *Journal of Physics G: Nuclear and Particle Physics* 31.11 (2005), p. 1291. URL: <http://stacks.iop.org/0954-3899/31/i=11/a=012>.
- [149] J. Pekala et al. “Atmospheric multiple scattering of fluorescence and Cherenkov light emitted by extensive air showers”. In: *Nuclear Instruments and Methods in Physics Research Section A: Accelerators, Spectrometers, Detectors and Associated Equipment* 605.3 (2009), pp. 388–398. ISSN: 0168-9002. DOI: 10.1016/j.nima.2009.03.244. arXiv: 0904.3230. URL: <http://www.sciencedirect.com/science/article/pii/S0168900209007347>.
- [150] M. Unger. *Shower Profile Reconstruction from Fluorescence and Cherenkov light*. Tech. rep. 2006-010. Pierre Auger GAP-Notes, 2006.
- [151] M. Unger et al. “Reconstruction of longitudinal profiles of ultra-high energy cosmic ray showers from fluorescence and Cherenkov light measurements”. In: *Nuclear Instruments and Methods in Physics Research Section A: Accelerators, Spectrometers, Detectors and Associated Equipment* 588.3 (2008), pp. 433–441. ISSN: 0168-9002. DOI: 10.1016/j.nima.2008.01.100. arXiv: 0801.4309. URL: <http://www.sciencedirect.com/science/article/pii/S0168900208001587>.
- [152] M. Mostafa. “The hybrid performance of the Pierre Auger Observatory”. In: *29th International Cosmic Ray Conference Pune (ICRC 2005)*. Pune, India, 2005.
- [153] J. Hersil et al. “Observations of Extensive Air Showers near the Maximum of Their Longitudinal Development”. In: *Physical Review Letters* 6 (1 1961), pp. 22–23. DOI: 10.1103/PhysRevLett.6.22. URL: <http://link.aps.org/doi/10.1103/PhysRevLett.6.22>.
- [154] The Pierre Auger Collaboration. “Reconstruction of inclined air showers detected with the Pierre Auger Observatory”. In: *Journal of Cosmology and Astroparticle Physics* 8, 019 (Aug. 2014), p. 19. DOI: 10.1088/1475-7516/2014/08/019. arXiv: 1407.3214 [astro-ph.HE]. URL: <http://stacks.iop.org/1475-7516/2014/i=08/a=019>.
- [155] A. Schulz and for the Pierre Auger Collaboration. “The measurement of the energy spectrum of cosmic rays above 3×10^{17} eV with the Pierre Auger Observatory”. In: *33rd International Cosmic Ray Conference (ICRC 2013)*. Rio de Janeiro, Brasil, 2013, pp. 27–30. arXiv: 1307.5059.
- [156] L. Valore for the Pierre Auger Collaboration. “Measuring Atmospheric Aerosol Attenuation at the Pierre Auger Observatory”. In: *33rd International Cosmic Ray Conference (ICRC 2013)*. Rio de Janeiro, 2013, pp. 100–103. arXiv: 1307.5059.
- [157] B. Fick et al. “The Central Laser Facility at the Pierre Auger Observatory”. In: *Journal of Instrumentation* 1.11 (2006), P11003. URL: <http://stacks.iop.org/1748-0221/1/i=11/a=P11003>.

- [158] The Pierre Auger Collaboration. “Techniques for measuring aerosol attenuation using the Central Laser Facility at the Pierre Auger Observatory”. In: *Journal of Instrumentation* 8.04 (2013), P04009. DOI: 10.1088/1748-0221/8/04/P04009. arXiv: 1303.5576. URL: <http://stacks.iop.org/1748-0221/8/i=04/a=P04009>.
- [159] A. Aab et al. “Origin of atmospheric aerosols at the Pierre Auger Observatory using studies of air mass trajectories in South America”. In: *Atmospheric Research* 149.0 (2014), pp. 120–135. ISSN: 0169-8095. DOI: 10.1016/j.atmosres.2014.05.021. arXiv: 1405.7551. URL: <http://www.sciencedirect.com/science/article/pii/S0169809514002300>.
- [160] A. Filipčić et al. “Scanning lidar based atmospheric monitoring for fluorescence detectors of cosmic showers”. In: *Astroparticle Physics* 18 (Feb. 2003), pp. 501–512. DOI: 10.1016/S0927-6505(02)00162-7. arXiv: hep-ex/0202015. URL: <http://www.sciencedirect.com/science/article/pii/S0927650502001627>.
- [161] S. Y. BenZvi et al. “Measurement of the aerosol phase function at the Pierre Auger Observatory”. In: *Astroparticle Physics* 28 (Nov. 2007), pp. 312–320. DOI: 10.1016/j.astropartphys.2007.06.005. arXiv: 0704.0303. URL: <http://www.sciencedirect.com/science/article/pii/S0927650507000953>.
- [162] J. Chirinos for the Pierre Auger Collaboration. “Cloud Monitoring at the Pierre Auger Observatory”. In: *33rd International Cosmic Ray Conference (ICRC 2013)*. Rio de Janeiro, 2013, pp. 108–109. arXiv: 1307.5059.
- [163] K. Louedec for the Pierre Auger Collaboration. “Atmospheric Monitoring at the Pierre Auger Observatory - Status and Update”. In: *32nd International Cosmic Ray Conference (ICRC 2011)*. Vol. 2. The Pierre Auger Observatory IV: Operation and Monitoring. Beijing, China, 2011, pp. 63–66. DOI: 10.7529/ICRC2011/V02/0568. arXiv: arXiv:1107.4806.
- [164] P. Abreu et al. “Identifying clouds over the Pierre Auger Observatory using infrared satellite data”. In: *Astroparticle Physics* 50-52.0 (2013), pp. 92–101. ISSN: 0927-6505. DOI: 10.1016/j.astropartphys.2013.09.004. arXiv: 1310.1641. URL: <http://www.sciencedirect.com/science/article/pii/S0927650513001461>.
- [165] S. BenZvi et al. “New method for atmospheric calibration at the Pierre Auger Observatory using FRAM, a robotic astronomical telescope”. In: *30th International Cosmic Ray Conference (ICRC 2007)*. Merida, Mexico, June 2007. arXiv: 0706.1710.
- [166] B. Keilhauer et al. “Atmospheric Profiles at the Southern Pierre Auger Observatory and their Relevance to Air Shower Measurement”. In: *29th International Cosmic Ray Conference (ICRC 2005)*. Pune, India, July 2005. eprint: astro-ph/0507275.
- [167] T. Mathes for the Pierre Auger Collaboration. “The HEAT Telescopes of the Pierre Auger Observatory Status and First Data”. In: *32nd International Cosmic Ray Conference (ICRC 2011)*. Vol. 3. The Pierre Auger Observatory V: Enhancements. Beijing, China, 2011, pp. 153–156. DOI: 10.7529/ICRC2011/V03/0761. arXiv: arXiv:1107.4807.
- [168] F. Suarez for the Pierre Auger Collaboration. “The AMIGA muon detectors of the Pierre Auger Observatory: overview and status”. In: *33rd International Cosmic Ray Conference (ICRC 2013)*. Rio de Janeiro, 2013, pp. 80–83. arXiv: 1307.5059.
- [169] T. Huege for the Pierre Auger Collaboration. “Probing the radio emission from cosmic-ray-induced air showers by polarization measurements”. In: *33rd International Cosmic Ray Conference (ICRC 2013)*. Rio de Janeiro, 2013, pp. 92–95. arXiv: 1307.5059.
- [170] A. Aab et al. “Probing the radio emission from air showers with polarization measurements”. In: *Physical Review D* 89 (5 2014), p. 052002. DOI: 10.1103/PhysRevD.89.052002. arXiv: 1402.3677. URL: <http://link.aps.org/doi/10.1103/PhysRevD.89.052002>.

- [171] S. Argirò et al. “The Offline Software Framework of the Pierre Auger Observatory”. In: *Nuclear Instrument Methods A580* (2007), pp. 1485–1496. DOI: 10.1016/j.nima.2007.07.010. arXiv: 0707.1652 [astro-ph]. URL: <http://www.sciencedirect.com/science/article/pii/S0168900207014106>.
- [172] J. Allen et al. “The Pierre Auger Observatory offline software”. In: *Journal of Physics: Conference Series* 119.3 (2008). 16th International Conference on Computing in High Energy and Nuclear Physics (CHEP 2007), p. 032002. DOI: 10.1088/1742-6596/119/3/032002. URL: <http://stacks.iop.org/1742-6596/119/i=3/a=032002>.
- [173] T. Abu-Zayyad et al. “Energy spectrum of ultra-high energy cosmic rays observed with the Telescope Array using a hybrid technique”. In: *Astroparticle Physics* 61.0 (2015), pp. 93–101. ISSN: 0927-6505. DOI: <http://dx.doi.org/10.1016/j.astropartphys.2014.05.002>. arXiv: 1305.7273. URL: <http://www.sciencedirect.com/science/article/pii/S0927650514000668>.
- [174] R. U. Abbasi et al. “First Observation of the Greisen-Zatsepin-Kuzmin Suppression”. In: *Physical Review Letters* 100 (10 2008), p. 101101. DOI: 10.1103/PhysRevLett.100.101101. arXiv: astro-ph/0703099. URL: <http://link.aps.org/doi/10.1103/PhysRevLett.100.101101>.
- [175] M. Takeda et al. “Energy determination in the Akeno Giant Air Shower Array experiment”. In: *Astroparticle Physics* 19.4 (2003), pp. 447–462. ISSN: 0927-6505. DOI: 10.1016/S0927-6505(02)00243-8. arXiv: astro-ph/0209422. URL: <http://www.sciencedirect.com/science/article/pii/S0927650502002438>.
- [176] Véron-Cetty, M.P. and Véron, P. “A catalogue of quasars and active nuclei: 13th edition*”. In: *Astronomy and Astrophysics* 518 (2010), A10. DOI: 10.1051/0004-6361/201014188. URL: <http://dx.doi.org/10.1051/0004-6361/201014188>.
- [177] A. Aab et al. “Searches for Anisotropies in the Arrival Directions of the Highest Energy Cosmic Rays Detected by the Pierre Auger Observatory”. In: *The Astrophysical Journal* 804.1 (2015), p. 15. DOI: 10.1088/0004-637X/804/1/15. arXiv: 1411.6111.
- [178] W. H. Baumgartner et al. “The 70 Month Swift-BAT All-sky Hard X-Ray Survey”. In: *The Astrophysical Journal Supplement Series* 207.2 (2013), p. 19. URL: <http://stacks.iop.org/0067-0049/207/i=2/a=19>.
- [179] I. Sidelnik and for the Pierre Auger Collaboration. “Measurement of the first harmonic modulation in the right ascension distribution of cosmic rays detected at the Pierre Auger Observatory: towards the detection of dipolar anisotropies over a wide energy range”. In: *33rd International Cosmic Ray Conference (ICRC 2013)*. Rio de Janeiro, 2013, pp. 56–59. arXiv: 1307.5059.
- [180] A. Aab et al. “Large Scale Distribution of Ultra High Energy Cosmic Rays Detected at the Pierre Auger Observatory With Zenith Angles up to 80° ”. In: *Astrophysical Journal* 802.2 (2015), p. 111. DOI: 10.1088/0004-637X/802/2/111. arXiv: 1411.6953 [astro-ph.HE].
- [181] The Pierre Auger Collaboration and The Telescope Array Collaboration. “Searches for Large-scale Anisotropy in the Arrival Directions of Cosmic Rays Detected above Energy of 10^{19} eV at the Pierre Auger Observatory and the Telescope Array”. In: *The Astrophysical Journal* 794.2 (2014), p. 172. DOI: 10.1088/0004-637X/794/2/172. arXiv: 1409.3128. URL: <http://stacks.iop.org/0004-637X/794/i=2/a=172>.
- [182] A. Aab et al. “Depth of maximum of air-shower profiles at the Pierre Auger Observatory. I. Measurements at energies above $10^{17.8}$ eV”. In: *Physical Review D* 90 (12 2014), p. 122005. DOI: 10.1103/PhysRevD.90.122005. arXiv: 1409.4809. URL: <http://link.aps.org/doi/10.1103/PhysRevD.90.122005>.
- [183] Y. Tsunesada and for the Telescope Array Collaboration. “Highlights from Telescope Array”. In: *32nd International Cosmic Ray Conference (ICRC 2011)*. Vol. 12. Beijing, China, 2011, p. 67. DOI: 10.7529/ICRC2011/V12/H05. arXiv: 1111.2507 [astro-ph.HE].
- [184] R. U. Abbasi et al. “Indications of Proton-Dominated Cosmic-Ray Composition above 1.6 EeV”. In: *Physical Review Letters* 104 (16 2010), p. 161101. DOI: 10.1103/PhysRevLett.104.161101. URL: <http://link.aps.org/doi/10.1103/PhysRevLett.104.161101>.

- [185] R. Abbasi et al. “Report of the Working Group on the Composition of Ultra High Energy Cosmic Rays”. In: *2014 Conference on Ultrahigh Energy Cosmic Rays (UHECR2014)*. 2015. arXiv: 1503.07540 [astro-ph.HE].
- [186] The Pierre Auger Collaboration. “Interpretation of the depths of maximum of extensive air showers measured by the Pierre Auger Observatory”. In: *Journal of Cosmology and Astroparticle Physics* 2, 026 (Feb. 2013), p. 26. DOI: 10.1088/1475-7516/2013/02/026. arXiv: 1301.6637 [astro-ph.HE]. URL: <http://stacks.iop.org/1475-7516/2013/i=02/a=026>.
- [187] Eun-Joo Ahn and for the Pierre Auger Collaboration. “Inferences about the mass composition of cosmic rays from data on the depth of maximum at the Auger Observatory”. In: *33rd International Cosmic Ray Conference (ICRC 2013)*. Rio de Janeiro, Brasil, 2013, pp. 38–39. arXiv: 1307.5059 [astro-ph.HE].
- [188] A. Aab et al. “Depth of maximum of air-shower profiles at the Pierre Auger Observatory. II. Composition implications”. In: *Physical Review D* 90 (12 2014), p. 122006. DOI: 10.1103/PhysRevD.90.122006. arXiv: 1409.5083. URL: <http://link.aps.org/doi/10.1103/PhysRevD.90.122006>.
- [189] D. Garcia-Pinto and for The Pierre Auger Collaboration. “Measurements of the Longitudinal Development of Air Showers with the Pierre Auger Observatory”. In: *32nd International Cosmic Ray Conference (ICRC 2011)*. Vol. 2. The Pierre Auger Observatory II: Studies of Cosmic Ray Composition and Hadronic Interaction models. Beijing, China, July 2011, pp. 87–90. DOI: 10.7529/ICRC2011/V02/0709. arXiv: 1107.4804 [astro-ph.HE].
- [190] P. Abreu et al. “Measurement of the proton-air cross-section at $\sqrt{s} = 57$ TeV with the Pierre Auger Observatory”. In: *Physical Review Letters* 109 (6 2012), p. 062002. DOI: 10.1103/PhysRevLett.109.062002. arXiv: 1208.1520 [hep-ex]. URL: <http://link.aps.org/doi/10.1103/PhysRevLett.109.062002>.
- [191] R. U. Abbasi et al. “Measurement of the Proton-Air Cross Section with Telescope Array’s Middle Drum Detector and Surface Array in Hybrid Mode”. In: *ArXiv e-prints* (May 2015). arXiv: 1505.01860 [astro-ph.HE].
- [192] L. Cazon. “Modelling the muon time distribution in extensive air showers.” ISBN 84-9750-467-4. Universidade de Santiago de Compostela, 2005.
- [193] L. Cazon et al. “A model for the transport of muons in extensive air showers”. In: *Astroparticle Physics* 36.1 (2012), pp. 211–223. ISSN: 0927-6505. DOI: 10.1016/j.astropartphys.2012.05.017. arXiv: 1201.5294. URL: <http://www.sciencedirect.com/science/article/pii/S0927650512001223>.
- [194] A. Aab et al. “Muons in air showers at the Pierre Auger Observatory: Measurement of atmospheric production depth”. In: *Physical Review D* 90 (1 2014), p. 012012. DOI: 10.1103/PhysRevD.90.012012. arXiv: 1407.5919. URL: <http://link.aps.org/doi/10.1103/PhysRevD.90.012012>.
- [195] E. Santos. “Measurement of the muon production depth with a time-domain fit at the Pierre Auger Observatory”. GAP note 2014-014. PhD thesis. Instituto Superior Tecnico, 2014.
- [196] The Pierre Auger Collaboration. “Muons in air showers at the Pierre Auger Observatory: Mean number in highly inclined events”. In: *ArXiv e-prints* 91 (3 2015), p. 032003. DOI: 10.1103/PhysRevD.91.032003, 10.1103/PhysRevD.91.059901. arXiv: 1408.1421 [astro-ph.HE]. URL: <http://link.aps.org/doi/10.1103/PhysRevD.91.032003>.
- [197] B. Kégl and for the Pierre Auger Collaboration. “Measurement of the muon signal using the temporal and spectral structure of the signals in surface detectors of the Pierre Auger Observatory”. In: *33rd International Cosmic Ray Conference (ICRC 2013)*. Rio de Janeiro, 2013, pp. 48–51. arXiv: 1307.5059.
- [198] J. Espadanal for The Pierre Auger Collaboration. “Measurement of the Muon content of Extensive Air Showers with the Pierre Auger Observatory”. In: *XXX-th HEPFT 2014*. Protvino, Russia, 2014. arXiv: 1505.05527 [astro-ph.HE].

- [199] Glennys R. Farrar and the Pierre Auger Collaboration. “The muon content of hybrid events recorded at the Pierre Auger Observatory”. In: *33rd International Cosmic Ray Conference (ICRC 2013)*. Rio de Janeiro, 2013, pp. 52–55. arXiv: 1307.5059.
- [200] A. Aab et al. “A Search for Point Sources of EeV Photons”. In: *The Astrophysical Journal* 789.2 (2014), p. 160. DOI: 10.1088/0004-637X/789/2/160. arXiv: 1406.2912.
- [201] The Pierre Auger Collaboration1 et al. “A Search for Point Sources of EeV Neutrons”. In: *The Astrophysical Journal* 760.2 (2012), p. 148. DOI: 10.1088/0004-637X/760/2/148. arXiv: 1211.4901.
- [202] A. Aab et al. “A Targeted Search for Point Sources of EeV Neutrons”. In: *The Astrophysical Journal Letters* 789.2 (2014), p. L34. DOI: 10.1088/2041-8205/789/2/L34. arXiv: 1406.4038.
- [203] A. Aab et al. “Improved limit to the diffuse flux of ultrahigh energy neutrinos from the Pierre Auger Observatory”. In: *Physical Review D* 91 (9 2015), p. 092008. DOI: 10.1103/PhysRevD.91.092008. arXiv: 1504.05397. URL: <http://link.aps.org/doi/10.1103/PhysRevD.91.092008>.
- [204] M. Pato, S. Andringa, and M. Pimenta. “Poster: 3D Reconstruction of Extensive Air Showers from Fluorescence Data”. In: *30th International Cosmic Ray Conference (ICRC 2007)*. Mérida, Mexico, 2007.
- [205] R. Brun and F. Rademakers. “ROOT - An object oriented data analysis framework”. In: *Nuclear Instruments and Methods in Physics Research Section A: Accelerators, Spectrometers, Detectors and Associated Equipment* 389.1-2 (1997). New Computing Techniques in Physics Research V, pp. 81–86. ISSN: 0168-9002. DOI: [http://dx.doi.org/10.1016/S0168-9002\(97\)00048-X](http://dx.doi.org/10.1016/S0168-9002(97)00048-X). URL: <http://www.sciencedirect.com/science/article/pii/S016890029700048X>.
- [206] P. Assis et al. *Reference manual of fluorescence detector simulation in Offline*. Tech. rep. 2008-014. Pierre Auger GAP-Notes, 2008.
- [207] J. Espadanal et al. *3D simulation of EAS for the FD: validation with a fluorescence rich data sample*. Tech. rep. 2012-039. Pierre Auger GAP-Notes, 2012.
- [208] J. Vélez. “Analysis of the air fluorescence induced by electrons for application to cosmic-ray detection”. PhD thesis. Universidad Complutense de Madrid, 2011.
- [209] M. Espirito Santo. *The CUSCALX framework*. Tech. rep. Presented in Auger Collaboration Meeting. LIP, 2010.
- [210] A. A. Al-Rubaiee et al. “Parametrization for Cherenkov light lateral distribution function in Extensive Air Showers”. In: *ArXiv e-prints* (Mar. 2011). arXiv: 1104.2510 [physics.gen-ph].
- [211] A. Mishev and J. Stamenov. “Lateral distribution of Cerenkov light in extensive air showers at high mountain altitude produced by different primary particles in wide energy range”. In: (2005). arXiv: astro-ph/0512432 [astro-ph].
- [212] A. L. Mishev and J. N. Stamenov. “Some Characteristics of Extensive Air Showers at Chacaltaya Observation Level”. In: *28th International Cosmic Ray Conference (ICRC 2008)*. Vol. 1. Tsukuba, Japan, July 2003, p. 247.
- [213] The MARTA teams. *MARTA (Muon Auger RPC for the Tank Array) Design Report*. Tech. rep. 2013-020. Pierre Auger GAP-Notes, 2013.
- [214] The MARTA teams. *MARTA (Muon Auger RPC for the Tank Array) 1st Progress Report*. Tech. rep. 2013-052. Pierre Auger GAP-Notes, 2013.
- [215] J. Espadanal et al. *SD Energy Calibration based on the Electromagnetic Signal*. Tech. rep. 2013-054. Pierre Auger GAP-Notes, 2013.
- [216] Auger DataBase. <http://augerdb.lal.in2p3.fr>. URL: <http://augerdb.lal.in2p3.fr:8080/augerdb/simdb/Library-en.do?libraryId=57617361andhttp://augerdb.lal.in2p3.fr:8080/augerdb/simdb/Library-en.do?libraryId=57617351>.

- [217] M. Ave et al. “The accuracy of signal measurement with the water Cherenkov detectors of the Pierre Auger Observatory”. In: *Nuclear Instruments and Methods in Physics Research Section A: Accelerators, Spectrometers, Detectors and Associated Equipment* 578.1 (2007), pp. 180–184. ISSN: 0168-9002. DOI: 10.1016/j.nima.2007.05.150. URL: <http://www.sciencedirect.com/science/article/pii/S0168900207010248>.
- [218] M. Ave and T. Yamamoto. *Signal Fluctuation of the Auger Surface Array Detector*. Tech. rep. 2003-030. Pierre Auger GAP-Notes, 2003.
- [219] T. Schmidt. *Measurement of the Flux of Ultra High Energy Cosmic Rays using very inclined Extensive Air Showers measured at the Pierre Auger Observatory*. Tech. rep. 2010-046. Pierre Auger GAP-Notes, 2010.
- [220] Pierre Billoir. *Email to the auger collaboration mailing list. Auger Collaboration Mailing List*.
- [221] T. Schmidt, I. Maris, and M. Roth. *Fine Tuning of the LDF parameterisation and the Influence on S1000*. Tech. rep. 2007-106. Pierre Auger GAP-Notes, 2007.
- [222] D. Harari et al. *The CIC: beyond the quadratic fit and its energy dependence*. Tech. rep. 2012-122. Pierre Auger GAP-Notes, 2012.
- [223] D.M. Edge et al. “The cosmic ray spectrum at energies above 10^{17} eV”. In: *Journal of Physics A: Mathematical, Nuclear and General* 6.10 (1973), pp. 1612–1634. DOI: 10.1088/0305-4470/6/10/019. URL: <http://stacks.iop.org/0301-0015/6/i=10/a=019>.
- [224] M. Chikawa et al. “Energy estimation of AGASA events”. In: *27th International Cosmic Ray Conference (ICRC 2001)*. Vol. 1. Hamburg, Germany, 2001, p. 329.
- [225] J.C. Arteaga-Velázquez et al. *The Constant Intensity Cut Method applied to the KASCADE-Grande muon data*. Proceedings of the XV International Symposium on Very High Energy Cosmic Ray Interactions (ISVHECRI 2008). 2009. DOI: 10.1016/j.nuclphysbps.2009.09.033. URL: <http://www.sciencedirect.com/science/article/pii/S0920563209006690>.
- [226] X. Bertou et al. “Calibration of the surface array of the Pierre Auger Observatory”. In: vol. 568. 2. 29th International Cosmic Ray Conference, Pune, India. 2006, pp. 839–846. DOI: 10.1016/j.nima.2006.07.066. URL: <http://www.sciencedirect.com/science/article/pii/S0168900206013593>.
- [227] R. Pesce and for the Pierre Auger Collaboration. “Energy calibration of data recorded with the surface detectors of the Pierre Auger Observatory: an update”. In: *32nd International Cosmic Ray Conference (ICRC 2011)*. Vol. 2. The Pierre Auger Observatory I: The Cosmic Ray Energy Spectrum and Related Measurements, pp. 214–217. DOI: 10.7529/ICRC2011/V02/1160. arXiv: 1107.4809 [astro-ph.HE].
- [228] H. Dembinski and for The Pierre Auger Collaboration. “The Cosmic Ray Spectrum above 4×10^{18} eV as measured with inclined showers recorded at the Pierre Auger Observatory”. In: *32nd International Cosmic Ray Conference (ICRC 2011)*. Vol. 2. The Pierre Auger Observatory I: The Cosmic Ray Energy Spectrum and Related Measurements. Beijing, China, July 2011, pp. 101–104. DOI: 10.7529/ICRC2011/V02/0724. arXiv: 1107.4809 [astro-ph.HE].
- [229] G.A. Agnetta et al. “Use of RPC in EAS physics with the COVER-PLASTEX experiment”. In: *Nuclear Instruments and Methods in Physics Research Section A: Accelerators, Spectrometers, Detectors and Associated Equipment* 381.1 (1996), pp. 64–72. ISSN: 0168-9002. DOI: [http://dx.doi.org/10.1016/0168-9002\(96\)00677-8](http://dx.doi.org/10.1016/0168-9002(96)00677-8). URL: <http://www.sciencedirect.com/science/article/pii/0168900296006778>.
- [230] R. Santonico and R. Cardarelli. “Development of resistive plate counters”. In: *Nuclear Instruments and Methods in Physics Research* 187.2-3 (1981), pp. 377–380. ISSN: 0167-5087. DOI: [http://dx.doi.org/10.1016/0029-554X\(81\)90363-3](http://dx.doi.org/10.1016/0029-554X(81)90363-3). URL: <http://www.sciencedirect.com/science/article/pii/0029554X81903633>.

- [231] B. Bartoli et al. “The analog Resistive Plate Chamber detector of the ARGO-YBJ experiment”. In: *Astroparticle Physics* 67 (July 2015), pp. 47–61. DOI: 10.1016/j.astropartphys.2015.01.007. arXiv: 1504.01510 [astro-ph.IM].
- [232] L. Lopes et al. “Resistive Plate Chambers for the Pierre Auger array upgrade”. In: *Journal of Instrumentation* 9.10 (2014), p. C10023. URL: <http://stacks.iop.org/1748-0221/9/i=10/a=C10023>.
- [233] The MARTA teams. *MARTA (Muon Auger RPC for the Tank Array) Design Report*. Tech. rep. 2013-016. Pierre Auger GAP-Notes, 2013.
- [234] The MARTA teams. *MARTA (Muon Auger RPC for the Tank Array) Design Report*. Tech. rep. 2013-018. Pierre Auger GAP-Notes, 2013.

